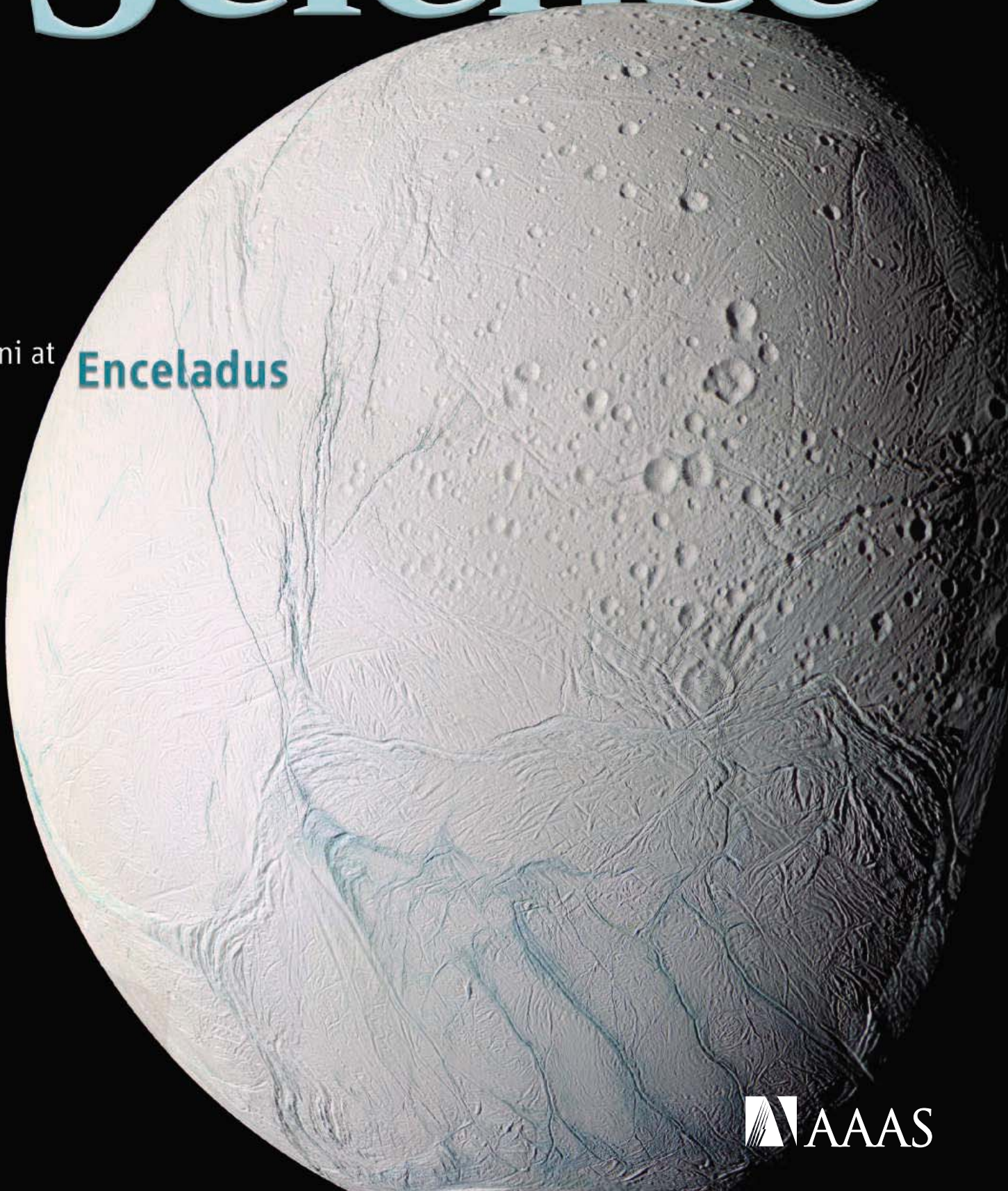


10 March 2006 | \$10

Science

Cassini at **Enceladus**



 AAAS

Mx3005P™ System
Most Flexible

Mx3000P® System
Most Affordable



Performance runs in the family.

Choose the personal QPCR system that's right for you.

Stratagene now offers two affordable, fully-featured quantitative PCR (QPCR) systems. The new five-color Mx3005P™ QPCR System includes expanded features to support a wider range of real-time QPCR applications, such as simultaneous five-target detection and alternative QPCR probe chemistries. The Mx3000P® QPCR System is still the most affordably priced four-color 96-well system available.

- A four- or five-color instrument, with user-selected filters
- Advanced optical system design for true multiplexing capability, and wider application support
- QPCR Software with enhanced data analysis and export functionality

Need More Information? Give Us A Call:

Stratagene USA and Canada

Order: (800) 424-5444 x3

Technical Services: (800) 894-1304 x2

Stratagene Japan K.K.

Order: 03-5159-2060

Technical Services: 03-5159-2070

Stratagene Europe

Order: 00800-7000-7000

Technical Services: 00800-7400-7400

www.stratagene.com

Mx3000P® is a registered trademark of Stratagene in the United States.
Mx3005P™ is a trademark of Stratagene in the United States.

Purchase of this product is accompanied by a license under the foreign counterparts of U.S. Patent Nos. 4,683,195, 4,683,202 and 4,965,188 covering the Polymerase Chain Reaction ("PCR") process, where such process is covered by patents. This instrument is an Authorized ThermalCycler for use with applications licenses available from Applied Biosystems. Its use with Authorized Reagents also provides a limited PCR license in accordance with the label rights accompanying such reagents.



introducing the

Time MACHINE



the MINI PREP 96

Fully Automatic plasmid and
genomic DNA purification at
the push of a button.



Your time is valuable.

MacCONNELL
RESEARCH

800.466.7949 www.macconnell.com



Greater flexibility in histidine-tagged protein purification

Ni Sepharose™ products from GE Healthcare give you greater flexibility and the highest binding capacity available for histidine-tagged protein purification. They also assure maximum target protein activity, thanks to their tolerance of a wide range of additives and negligible nickel ion leakage.

His MultiTrap™ prepacked multiwell plates let you directly apply unclarified lysate for greater convenience and minimized degradation of sensitive target proteins. Ni Sepharose is also available prepacked in His SpinTrap™, His GraviTrap™, HisTrap™ and bulk packs to ensure maximum flexibility in histidine-tagged protein purification.

www.gehealthcare.com/his



imagination at work



COVER

Saturn's enigmatic moon Enceladus is a jumbled world of fresh snow plains, old cratered terrains, and long cracks dusted in green organic material. A special section in this issue presents multiple views of Enceladus taken from the Cassini spacecraft during three close flybys. See page 1388.

Image: NASA/Jet Propulsion Laboratory/
C. C. Porco

SPECIAL SECTION

Cassini at Enceladus

INTRODUCTION

Tiger, Tiger, Burning Bright 1388

PERSPECTIVES

Enceladus: Cosmic Gymnast, Volatile Miniworld 1389
J. S. Kargel

Does Enceladus Govern Magnetospheric Dynamics at Saturn? 1391
M. G. Kivelson

RESEARCH ARTICLES

Cassini Observes the Active South Pole of Enceladus 1393
C. C. Porco et al.

Cassini Encounters Enceladus: Background and the Discovery of a South Polar Hot Spot 1401
J. R. Spencer et al.

REPORTS

Identification of a Dynamic Atmosphere at Enceladus with the Cassini Magnetometer 1406
M. K. Dougherty et al.

The Interaction of the Atmosphere of Enceladus with Saturn's Plasma 1409
R. L. Tokar et al.

Enceladus' Varying Imprint on the Magnetosphere of Saturn 1412
G. H. Jones et al.

Cassini Dust Measurements at Enceladus and Implications for the Origin of the E Ring 1416
F. Spahn et al.

Cassini Ion and Neutral Mass Spectrometer: Enceladus Plume Composition and Structure 1419
J. H. Waite Jr. et al.

Enceladus' Water Vapor Plume 1422
C. J. Hansen et al.

Composition and Physical Properties of Enceladus' Surface 1425
R. H. Brown et al.

DEPARTMENTS

1339 Science Online
1341 This Week in Science
1347 Editors' Choice
1350 Contact Science
1353 NetWatch
1355 Random Samples
1375 Newsmakers
1485 New Products
1486 Science Careers

EDITORIAL

1345 Summers and Harvard
by Donald Kennedy



NEWS OF THE WEEK

Last-Minute Nuclear Deal Has Long-Term Repercussions 1356

The Sun's Churning Innards Foretell More Solar Storms 1357

NASA Agrees to Review What's on the Chopping Block 1359

SCIENCESCOPE 1359

Dates Revise Easter Island History 1360

>>Science Express Report by T. L. Hunt and C. P. Lipo

Theory of Shock Waves Clears Up the Puzzling Graininess of Crystals 1361

Austria's Bid for an Instant MIT Meets Opposition From Researchers 1363

Legislator Wants NSF to Offer \$1 Billion Energy Prize 1363

NEWS FOCUS

The End of Angkor Local Elites Cast New Light on Angkor's Rise 1364

Samuel Bodman: With Energy to Spare, an Engineer Makes the Case for Basic Research 1369

A Dose of Reform to Treat the Malaise Gripping French Science 1371

Speciation Standing in Place 1372

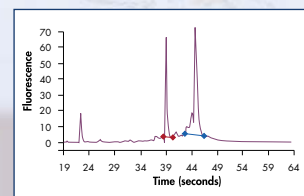
CONTENTS continued >>

Systems Biology — RNA Purification

Standardized RNA solutions guarantee comparable results



Convenient RNA purification



Purification of high-quality RNA

Advance your gene expression research with standardized solutions for RNA purification!

QIAGEN RNA solutions standardize the purification of RNA from biological samples.

Benefits include:

- **Reliability** — highly pure, intact RNA for standardized results in all downstream applications
- **Convenience** — easy-to-use kits with minimal protocol steps
- **Speed** — ready-to-use RNA purified in as little as 25 minutes
- **Versatility** — manual and automated kits for a wide range of sample types, sizes, and throughputs

Visit www.qiagen.com/goto/RNAsolutions to find out more!

For up-to-date trademarks and disclaimers, see www.qiagen.com. GEXRNA0106S1WW © 2006 QIAGEN, all rights reserved.



WWW.QIAGEN.COM

Qs & AAAS



www.sciencedigital.org/subscribe

For just US\$99, you can join AAAS TODAY and start receiving *Science* Digital Edition immediately!

Qs & AAAS



www.sciencedigital.org/subscribe

For just US\$99, you can join AAAS TODAY and start receiving *Science* Digital Edition immediately!



SCIENCE EXPRESS

www.sciencexpress.org

PHYSICS

Generating Optical Schrödinger Kittens for Quantum Information Processing

A. Ourjoumsev, R. Tualle-Brouri, J. Laurat, P. Grangier

Subtraction of a photon from a squeezed coherent light pulse produces a small flying Schrödinger cat state (with an unbound photon), an essential element for quantum communication.

10.1126/science.1122858

GENETICS

Genome-Wide Detection of Polymorphisms at Nucleotide Resolution with a Single DNA Microarray

D. Gresham et al.

Hybridization of yeast DNA from a test strain to a microarray with redundant reference DNA simply and rapidly identifies most of the polymorphisms between two strains.

10.1126/science.1123726

ARCHAEOLOGY

Late Colonization of Easter Island

T. L. Hunt and C. P. Lipo

Radiocarbon dates imply that voyaging Polynesians arrived on Easter Island around 1200 A.D., later than previously thought, and soon began depleting timber and other natural resources and erecting statues.

>> *News story p. 1360*

10.1126/science.1121879

PLANT BIOLOGY

Rice Domestication by Reducing Shattering

C. Li, A. Zhou, T. Sang

The retention of rice grains on the plant after ripening—a trait important for domestication—is the result of a single nucleotide change in a transcription factor gene.

10.1126/science.1123604

LETTERS

Finding Good in the Bad and Vice Versa *D. Johns* 1376

Diversity in Tropical Forests *W. F. Laurance*

Genetic Polymorphism of Fc *J. P. Pandey*

Response *J. M. Woof*

Hyposmocoma molluscivora Description *D. Rubinoff and W. P. Haines*

GPS: A Military/Civilian Collaboration *J. F. Zumberge*

Decline of Vultures in Asia *R. E. Green*

BOOKS ET AL.

The Weather Makers How Man Is Changing the Climate and What It Means for Life on Earth *T. Flannery*; **The Weather Makers** The History and Future Impact of Climate Change *A. Lane* 1379

reviewed by B. Chameides

POLICY FORUM

Fusion Power: Will It Ever Come? 1380

W. E. Parkins

PERSPECTIVES

Total Information Awareness for Worm Genetics 1381

S. R. Eddy

>> *Report p. 1481*

Five Golden Rings 1382

D. W. Christianson

>> *Report p. 1464*

Resonances in Reaction Dynamics 1383

R. N. Zare

>> *Reports pp. 1440 and 1443*

One Misfolded Protein Allows Others to Sneak By 1385

G. P. Bates

>> *Report p. 1471*

Fungi, Weathering, and the Emergence of Animals 1386

L. A. Derry

>> *Report p. 1446*

BREVIA

ATMOSPHERIC SCIENCE

Diffusive Separation of the Lower Atmosphere 1429

Y. Adachi, K. Kawamura, L. Armi, R. F. Keeling

As long predicted, diffusion can overcome turbulence in the troposphere under specific conditions to separate heavy and light atoms and molecules.

RESEARCH ARTICLE

STRUCTURAL BIOLOGY

Structure of the Hydrophilic Domain of 1430

Respiratory Complex I from *Thermus thermophilus*

L. A. Sazanov and P. Hinchliffe

The x-ray crystal structure of the peripheral part of the largest bacterial respiratory electron-transport complex shows the folds, contacts, and positions of the redox cofactors.

REPORTS

CHEMISTRY

Ultrafast Interfacial Proton-Coupled Electron Transfer 1436

B. Li, J. Zhao, K. Onda, K. D. Jordan, J. Yang, H. Petek

Return of an electron from a methanol film to a semiconductor induces rapid (30 femtoseconds) stabilizing motion in the substrate and coupled transfer of a proton.

CHEMISTRY

Observation of Feshbach Resonances in the 1440

$F + H_2 \rightarrow HF + H$ Reaction

M. Qiu et al.

Signatures of H_2CO Photodissociation from 1443

Two Electronic States

H. M. Yin, S. H. Kable, X. Zhang, J. M. Bowman

Spectroscopy and computations reveal the nuclear vibrations and other motions involved in the dissociations of excited, transient molecules and in collision reactions.

>> *Perspective p. 1383*

CONTENTS continued >>

Molecular Biology Summer Workshops



We are pleased to announce the twenty-first annual Molecular Biology Summer Workshops, sponsored by New England Biolabs in conjunction with Smith College. Workshops are held at the Clark Science Center, Smith College, Northampton, MA, USA. Over 3,000 people have graduated from this intensive training program in the past twenty years.

Learn Molecular Biology in 2 Weeks!

This intensive, two-week course emphasizes hands-on molecular biology laboratory work and covers a wide variety of topics and techniques.

when:

Session 1: June 4 – June 17, 2006

Session 2: June 18 – July 1, 2006

Session 3: July 9 – July 22, 2006

where:

Clark Science Center
Smith College
Northampton, MA USA

to apply:

apply online at
<http://www.science.smith.edu/neb>
or

Mail a recent resume and one paragraph explaining your interest to:

Molecular Biology Summer Workshops
Dr. Steven A. Williams
Clark Science Center
Smith College
Northampton, MA 01063

Topics/Techniques:

- :: **gene cloning (cDNA and genomic)**
- :: **gene expression analysis**
- :: **PCR and quantitative RT-PCR**
- :: **genomics and bioinformatics**
- :: **DNA sequencing and DNA fingerprinting**
- :: **RNAi, siRNA and microarrays**
- :: **and much more – visit our website for a complete list**

Application Information:

No previous experience in molecular biology is required or expected. Fifty participants per session will be selected from a variety of disciplines and academic backgrounds.

FEE: \$4000 per participant includes lab manual, use of all equipment and supplies, and room and board (all rooms are singles).

APPLICATION DEADLINE: First come, first served (apply now!).

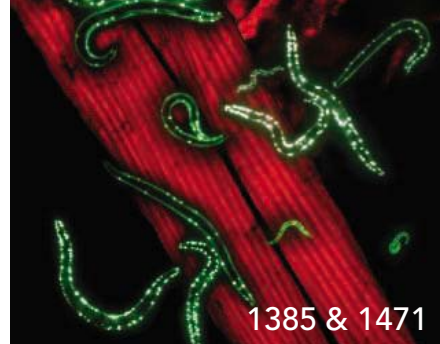
PAYMENT DEADLINE: Three weeks following receipt of your application.

Late applications will be accepted! Your application should include a recent resume and one paragraph explaining your reasons for taking the course.

Please specify the session to which you are applying (1, 2, or 3) and indicate a second choice from one of the other sessions.

For additional information,
please call (413) 247-3004
or visit the Summer Workshop web site:
<http://www.science.smith.edu/neb>





REPORTS CONTINUED...

ATMOSPHERIC SCIENCE

Late Precambrian Oxygenation; Inception of the Clay Mineral Factory 1446

M. Kennedy, M. Droser, L. M. Mayer, D. Pevear, D. Mrofka

The development of an oxygen-rich atmosphere during the Neoproterozoic was the result of an increase in the rate of clay deposition caused by the spread of terrestrial vegetation.

>> *Perspective p. 1386*

CLIMATE CHANGE

The Last Deglaciation of the Southeastern Sector of the Scandinavian Ice Sheet 1449

V. R. Rinterknecht et al.

Dating of glacial deposits near the margins of the Scandinavian Ice Sheet reveals that it began to retreat about 19,000 years ago, contributing to an abrupt rise in sea level.

PLANETARY SCIENCE

Exposed Water Ice Deposits on the Surface of Comet 9P/Tempel 1 1453

J. M. Sunshine et al.

Deep Impact has found three patches of water ice on comet Tempel 1, but these cannot account for the water output of outgassing, implying a subsurface source.

EVOLUTION

***Laonastes* and the "Lazarus Effect" in Recent Mammals** 1456

M. R. Dawson, L. Marivaux, C. Li, K. C. Beard, G. Métais

A recently discovered living rodent is a survivor of a family thought to have been extinct for 11 million years.

ECOLOGY

Opposing Effects of Native and Exotic Herbivores on Plant Invasions 1459

J. D. Parker, D. E. Burkepile, M. E. Hay

A meta-analysis of 71 experimental studies shows that invasions by exotic plants tend to be suppressed by native herbivores but enhanced by exotic herbivores.

ECOLOGY

A Major Ecosystem Shift in the Northern Bering Sea 1461

J. M. Grebmeier et al.

Warming has caused the highly productive northern part of the Bering Sea to change from an arctic to a subarctic marine ecosystem.



ADVANCING SCIENCE. SERVING SOCIETY

SCIENCE (ISSN 0036-8075) is published weekly on Friday, except the last week in December, by the American Association for the Advancement of Science, 1200 New York Avenue, NW, Washington, DC 20005. Periodicals Mail postage (publication No. 484460) paid at Washington, DC, and additional mailing offices. Copyright © 2006 by the American Association for the Advancement of Science. The title SCIENCE is a registered trademark of the AAAS. Domestic individual membership and subscription (51 issues): \$139 (\$74 allocated to subscription). Domestic institutional subscription (51 issues): \$650; Foreign postage extra: Mexico, Caribbean (surface mail) \$55; other countries (air assist delivery) \$85. First class, airmail, student, and emeritus rates on request. Canadian rates with GST available upon request, GST #1254 88122. Publications Mail Agreement Number 1069624. Printed in the U.S.A.

Change of address: Allow 4 weeks, giving old and new addresses and 8-digit account number. Postmaster: Send change of address to Science, P.O. Box 1811, Danbury, CT 06813-1811. Single-copy sales: \$10.00 per issue prepaid includes surface postage; bulk rates on request. Authorization to photocopy material for internal or personal use under circumstances not falling within the fair use provisions of the Copyright Act is granted by AAAS to libraries and other users registered with the Copyright Clearance Center (CCC) Transactional Reporting Service, provided that \$18.00 per article is paid directly to CCC, 222 Rosewood Drive, Danvers, MA 01923. The identification code for Science is 0036-8075/03 \$18.00. Science is indexed in the Reader's Guide to Periodical Literature and in several specialized indexes.

BIOCHEMISTRY

Structure and Mechanism of the Lantibiotic Cyclase Involved in Nisin Biosynthesis 1464

B. Li et al.

The enzyme that performs the final step in the biosynthesis of the antimicrobial food preservative nisin constructs five thioether rings of different sizes in this peptide.

>> *Perspective p. 1382*

BIOPHYSICS

Engineering Cooperativity in Biomotor-Protein Assemblies 1468

M. R. Diehl, K. Zhang, H. J. Lee, D. A. Tirrell

Artificial assembly of kinesin proteins on scaffold molecules shows that their transport activity is enhanced by their proximity.

CELL BIOLOGY

Progressive Disruption of Cellular Protein Folding in Models of Polyglutamine Diseases 1471

T. Gidalevitz et al.

In experiments in nematodes that may simulate some neurodegenerative diseases, abnormal, glutamine-rich proteins disrupt the cell's normal disposal of misfolded proteins.

>> *Perspective p. 1385*

EPIDEMIOLOGY

The Global Impact of Scaling Up HIV/AIDS Prevention Programs in Low- and Middle-Income Countries 1474

J. Stover et al.

Implementation of AIDS prevention measures targeting sexual transmission and drug users could prevent 30 million new infections in the next 10 years.

NEUROSCIENCE

Combinatorial Effects of Odorant Mixes in Olfactory Cortex 1477

Z. Zou and L. B. Buck

Specific neurons in the olfactory cortex act as coincidence detectors, responding to a mixture of two odors but not to the individual components of the mixture.

GENETICS

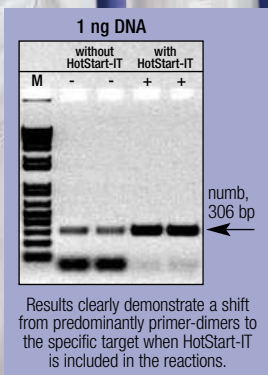
Genome-Wide Prediction of *C. elegans* Genetic Interactions 1481

W. Zhong and P. W. Sternberg

Construction of a comprehensive gene interaction network for *C. elegans*, guided by data from yeast and fruit flies, identifies previously undescribed interacting protein pairs.

>> *Perspective p. 1381*

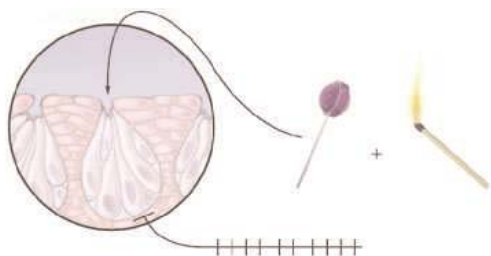
IS YOUR
hot-start method
giving you more questions
THAN ANSWERS?



“Are my PCR reactions specific enough? Will my experiment be contaminated from animal-sourced antibodies? Will the DNA be damaged from extensive heat denaturation? Will my results be compromised?” If these are some of the questions you’re asking yourself, try HotStart-IT.™ Developed by USB scientists, HotStart-IT is an elegant new method that doesn’t use antibodies or chemically modified enzymes. Instead, HotStart-IT relies on a unique protein that binds and sequesters primers at lower temperatures which prevents mispriming and the formation of primer-dimers. When PCR is initiated, the protein is inactivated during the heat denaturation step and the primers are free to participate in the subsequent amplification cycles. The result? Higher specificity. Higher yield. And, most importantly, a higher level of confidence for you.



For a **FREE** sample of new HotStart-IT,
call 800.321.9322 or visit www.usbweb.com/hotstart



Tasting sweet.

SCIENCE'S STKE

www.stke.org SIGNAL TRANSDUCTION KNOWLEDGE ENVIRONMENT

PERSPECTIVE: Thermal Gating of TRP Ion Channels— Food for Thought?

E. R. Liman

Heat may enhance the perception of taste by modulating the putative taste transduction channel.

FORUM: Open Forum on Methodology

Post a question or tip about cell signaling research.



Weighing in on calorie restriction.

SCIENCE'S SAGE KE

www.sageke.org SCIENCE OF AGING KNOWLEDGE ENVIRONMENT

NEWS FOCUS: Craving an Answer

M. Leslie

After 70 years, researchers might be closing in on how calorie restriction extends life.

CLASSIC PAPER: Action of Food Restriction in Delaying the Aging Process

E. J. Masoro, B. P. Yu, H. A. Bertrand

Decreased metabolic rate might not explain why food restriction slows aging; *Proc. Natl. Acad. Sci. U.S.A.* **79**, 4239 (1982).

SCIENCE NOW

www.sciencenow.org DAILY NEWS COVERAGE

A Hummingbird Never Forgets

Stellar recall skills prevent birds from wasting time with the wrong flower.

Getting the Most Out of Your Shrink

"Learning drug" enhances benefits of social anxiety therapy.

Pesticides Common in U.S. Streams

Danger to humans is unlikely, but aquatic and fish-eating wildlife face health threats.



On-target cover letters.

SCIENCE CAREERS

www.sciencecareers.org CAREER RESOURCES FOR SCIENTISTS

US: Writing a Winning Cover Letter

J. Borchardt

A good cover letter says you're a good fit for the department and the position you're seeking.

EUROPE: New Research Centers in Southern Europe

E. Pain

Next Wave looks into the research and job opportunities at new science centers in southern Europe.

MISCINET: Minority Admissions—Countering Cultural Blocks

A. Sasso

The college application process may be responsible for low numbers of minority students.

US: NIH Electronic Submission

Grant Doctor

What does the future of biomedical grant submissions look like?

Separate individual or institutional subscriptions to these products may be required for full-text access.

SPECIAL INTRODUCTORY OFFER

See our website for details.



NEW ENGLAND BIOLABS



music to your ears.

Competent Cells from New England Biolabs

SUPERIOR COMPETENT *E. COLI* STRAINS FOR CLONING AND PROTEIN EXPRESSION

For many years staff scientists at New England Biolabs have been using their own line of optimized chemically competent *E. coli* cells for cloning and protein expression. These strains have made all the difference to a highly demanding research and production program. Now when you are looking for a versatile cloning strain, rapid colony growth, or tight control of protein expression, you can benefit from the superior performance and high quality of these strains.

- **NEB Turbo Competent *E. coli*** **C2984H**
Ligate, transform, plate and pick colonies in one day
- **NEB 5-alpha Competent *E. coli*** **C2991H**
Versatile cloning strain
- **T7 Express Competent *E. coli*** **C2566H**
High efficiency transformation and protein expression
- **T7 Express I^q Competent *E. coli*** **C2833H**
Tight control of protein expression
- **dam⁻/dcm⁻ Competent *E. coli*** **C2925H**
Grow plasmids free of dam and dcm methylation

Advantages:

- Ready to transform – packaged in single-use transformation tubes (20 x 0.05 ml)
- Free of animal products
- 5 minute transformation protocols
- Supplied with outgrowth media and control DNA

	NEB Turbo	NEB 5-alpha	T7 Express	T7 Express I ^q	dam ⁻ /dcm ⁻
Transformation Efficiency (cfu/μg)	>10 ⁹	1-3 x 10 ⁹	2-6 x 10 ⁸	2-6 x 10 ⁸	>2 x 10 ⁸
Strain	K12	K12	B	B	K12
T1 Phage Resistant	✓	✓	✓	✓	✓
Blue/White Screening	✓	✓	-	-	-
lac I ^q	✓	✓	-	✓	-
Colonies Visible after 8 hours	✓	-	-	-	-
Endonuclease I Deficient	✓	✓	✓	✓	✓
Protease Deficient	-	-	✓	✓	-
Restriction Deficient	✓	✓	✓	✓	✓
M13 Phage Capable (F ⁺)	✓	✓	-	✓	-
RecA Deficient	-	✓	-	-	-

Chemically Competent *E. coli* Strain Characteristics

For more information and international distribution network, please visit www.neb.com

- **New England Biolabs Inc.** 240 County Road, Ipswich, MA 01938 USA 1-800-NEB-LABS Tel. (978) 927-5054 Fax (978) 921-1350 info@neb.com
- **Canada** Tel. (800) 387-1095 info@ca.neb.com
- **Germany** Tel. 0800/246 5227 info@de.neb.com
- **UK** Tel. (0800) 318486 info@uk.neb.com
- **China** Tel. 010-82378266 beijing@neb-china.com





Ecosystem Effects of Climate Change

Contemporary climate changes affect the geographical distribution of a number of species of terrestrial and marine organisms. **Grebmeier *et al.*** (p. 1461) observed responses to climate change in an entire ecosystem, the northern Bering Sea. This ecosystem is relatively shallow, with a rich benthic prey source that supports bottom-feeding marine mammals and seabirds that are hunted by local human populations. During the past decade, there has been a geographic displacement of marine mammal population distributions northward, a reduction of benthic prey populations, an increase in pelagic fish, a reduction in sea ice, and an increase in air and ocean temperatures.

Unraveling Chemical Collisions

Gas-phase spectroscopy and accompanying theoretical computations have been used to resolve two long-standing puzzles in the interplay of electronic and nuclear molecular motion in chemical reactions (see the Perspective by **Zare**). **Yin *et al.*** (p. 1443) probed the impact of electronic state on the unimolecular dissociation of formaldehyde (H_2CO) into H and HCO products. Their results suggest that bond scission in the ground state produces rapidly rotating HCO, whereas dissociation in the excited triplet state yields vibrationally excited HCO. **Qiu *et al.*** (p. 1440) studied a bimolecular reaction: collision of an F atom with H_2 to yield HF and H. At a specific collision energy, the experiments and theory point to a transient complex, termed a Feshbach resonance, in which the colliding partners vibrate several times before rearranging to products.

Clay and Atmospheric Oxygen

The oxygen content of Earth's atmosphere increased dramatically and permanently during the Neoproterozoic and has remained high since then, which suggests that the mechanisms underlying this increase must have included some irreversible change in the global biogeochemical cycle. **Kennedy *et al.*** (p. 1446, published online 2 February; see the Perspective by **Derry**) hypothesize that oxygenation of the atmosphere resulted from an increase in the rate of burial of organic carbon caused by the accelerated production of clays. In shallow marine environments, clays

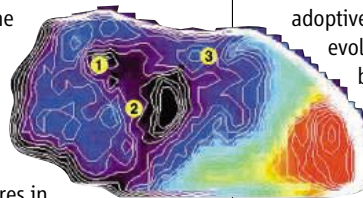
retard the oxidation of organic matter and facilitate their burial. The authors use this insight, along with mineralogical and geochemical evidence of an increase in clay deposition in the Neoproterozoic, to show how the stepwise transition from a low- O_2 atmosphere to one with abundant O_2 could have occurred.

Scandinavian Deglaciation

The Scandinavian Ice Sheet, the second largest Northern Hemisphere ice sheet at the end of the last glacial period, must have contributed significantly to glacial-interglacial sea level and regional climate changes. However, the timing of the decay of the Scandinavian Ice Sheet remains poorly constrained. **Rinterknecht *et al.*** (p. 1449) present a suite of cosmogenic ^{10}Be ages and radiocarbon dates of glacial deposits that define more precisely the timing of major fluctuations of the southern margin of the Scandinavian Ice Sheet in central and eastern Europe.

Exposed Cometary Ice

Exposed deposits containing water ice have been found on the surface of the comet 9P/Tempel 1. Images obtained by **Sunshine *et al.*** (p. 1443, published online 2 February) with cameras on board the Deep Impact spacecraft reveal several patches that are bluer than the rest of the surface. Absorption features in infrared spectra confirm the presence of water ice in these spots and suggest it is present in aggregates of grains that are tens of micrometers in size. The deposits are relatively impure



and contain only a few percent water ice and are too small in area to be the main source of water vapor that outgases from the nucleus.

Rodent Resurrection

When the new species of rodent *Laonastes* was described last year, it attracted broad attention because it was claimed as a representative of an entirely new family of living mammals. **Dawson *et al.*** (p. 1456) compared *Laonastes* with the Diatomyidae, a poorly known group of rodents from the Oligocene and Miocene of Asia. Anatomical comparisons of a new fossil Miocene diatomyid with *Laonastes* confirmed that *Laonastes* is actually a living member of this "extinct" clade. Hence, *Laonastes* "resurrects" a clade of mammals that was formerly thought to have been extinct for more than 10 million years.

Invasive Chain Reaction

Biological invasions by exotic species are a leading threat to native biodiversity and entail enormous monetary costs. In a meta-analysis of field studies from a wide range of ecosystems, **Parker *et al.*** (p. 1459) challenge the hypothesis that invasive exotic plants become a problem in their adoptive lands because they left their co-evolved herbivores behind. Instead, herbivores in the invaded communities are better able to resist invaders than do the enemies of those plants in their original home. By the same token, introduced herbivores are harder on native plants in lands they invade than on introduced plants, including those with which they coevolved. Thus, the

Continued on page 1343



www.roche-applied-science.com



Genome Sequencer 20 System

First to the Finish

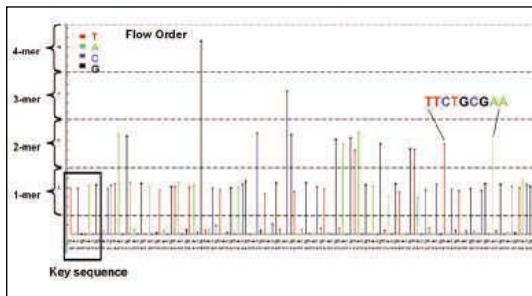
Sequence genomes like never before

- Compare microbial genomes in weeks, not years
- *De novo* sequence a bacterial genome in fewer than 5 days
- Sequence more than 100 BACs per month
- Sequence >200,000 miRNAs, SAGE tags, or ditags (e.g., CAGE) in 5.5 hours

Coming soon:

Ultra-deep sequencing of amplicons – identify rare SNP patterns or cancer-associated mutations from complex samples

Harness the horsepower of the newest revolution in sequencing today — visit www.roche-applied-science.com/sis/sequencing/genome or contact your local sales representative.



Flowgram of a GS 20 read

454 LIFE
SCIENCES



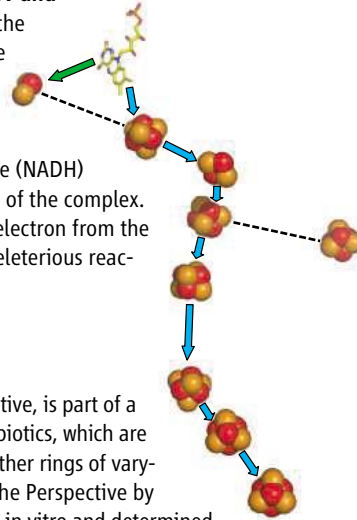
Diagnostics

Continued from page 1341

replacement of native with exotic herbivores triggers an invasional “meltdown” whereby one exotic species facilitates invasions by others.

Redox Stages in Respiration

In bacteria and mitochondria, a flavin cofactor within complex I of the membrane accepts reducing equivalents, converts some of the energy into a proton gradient, and passes electrons onward via a quinone carrier to other membrane-bound enzymes. **Sazanov and Hincliffe** (p. 1430, published online 9 February) describe the crystal structure of the eight-subunit hydrophilic portion (the part outside the membrane) of respiratory complex I from *Thermus thermophilus* and describe the environments of the flavin and the nine iron-sulfur clusters that transport the electrons from the dihydronicotinamide adenine dinucleotide (NADH) binding site into the hydrophobic (proton-pumping) domain of the complex. They propose that the outermost cluster accepts the second electron from the flavin, which helps to reduce the generation of potentially deleterious reactive oxygen species.



Closing Nisin's Rings

Nisin, an antimicrobial peptide widely used as a food preservative, is part of a group of posttranslationally modified peptides known as lantibiotics, which are characterized by thioether structures. Nisin contains five thioether rings of varying size formed by the enzyme NisC. **Li et al.** (p. 1464; see the Perspective by **Christianson**) have reconstituted the nisin cyclization process in vitro and determined the x-ray crystal structure of the NisC enzyme. NisC is structurally similar to mammalian farnesyl transferases with an active-site zinc ion that activates nucleophilic cysteine residues during cyclization.

Global Problems in Protein Folding in Polyglutamine Diseases?

A number of distinct, seemingly unrelated mechanisms have been proposed for polyglutamine, or trinucleotide repeat diseases, which include spinocerebellar ataxia type 3. These mechanisms include dysregulation of transcription, protein degradation, and mitochondrial function, as well as activation of apoptosis. **Gidalevitz et al.** (p. 1471, published online 9 February; see the Perspective by **Bates**) have taken a genetic approach and find that polyglutamine expansions in *Caenorhabditis elegans* cause global perturbation in protein folding. This progressive disturbance of protein folding may provide an explanation for the multitude of cellular pathways affected in conformational diseases.

Prevention Is Cheaper Than Treatment

In strategies to fight the AIDS epidemic, considerable emphasis has been placed on treatment options and costs. **Stover et al.** (p. 1474, published online 2 February) have evaluated the cost-effectiveness of prevention approaches on the basis of UNAIDS/WHO predictions of prevalence. By their calculations, roughly 30 million new infections could be prevented between 2005 and 2015 if a package of 15 prevention approaches targeting sexual transmission and transmission among injecting drug users were used in 125 low- and middle-income countries. These averted infections translated into dramatic savings because of the diminished needs for treatment and care.

Mixing Scents

How are odors represented in the higher processing areas of the brain? **Zou and Buck** (p. 1477) compared the responses of mouse olfactory cortical neurons to binary mixtures of odorants versus their individual components. They monitored neuronal activity in the anterior piriform cortex of the same animals in response to individual odors and mixtures. The technique used enabled the authors to monitor neuronal activity in response to two temporally segregated experiences. The results suggest that olfactory cortical neurons receive convergent input from multiple odorant receptors and that a subpopulation may require such convergent input for activation.

Browse our new web site with over 1500 recombinant cytokines, growth factors, chemokines and neurotrophins. Competitive pricing and daily shipping to most locations.

www.CytokineCenter.com



www.cellsciences.com

- **BMPs**
- **Cytokines**
Wide range of proteins of many species, including human, mouse, rat & porcine
- **Chemokines**
Recombinant and chemically synthesized
- **Defensins**
BD-1, -2, -3, NP-1
- **Endotoxins**
CD14, LALF, LBP, LL37, PMB
- **FGFs**
- **GM-CSFs**
- **Growth Factors**
IGF-I, IGF-II, BPs 1-7
- **Growth Hormones**
HGH, & other species
- **Interferons**
IFN- α , - β , - γ & more
- **Interleukins**
IL-1 α , thru IL-31
- **Neurotrophins**
- **Signal Transduction Proteins & Kinases**
- **TNFs**
- **VEGFs**

Secure ordering on our web site. € payments, VISA and MasterCard are accepted. Daily shipping worldwide.

Call toll free in USA & Canada:

888 769-1246

Cell Sciences
480 Neponset Street, Bldg. 12A
Canton, MA 02021 USA
Tel: 781 828-0610 Fax: 781 828-0542
email: info@cellsciences.com

new!

The power of small²

NanoDrop introduces a Fluorospectrometer



1 μ l samples • No cuvettes • 10-second measurements • Broad spectral output

Small footprint. Revolutionary technology. The NanoDrop[®] ND-3300 Fluorospectrometer is a powerful new tool for fluorescence spectrometry. Choose from many pre-defined methods or configure your own.

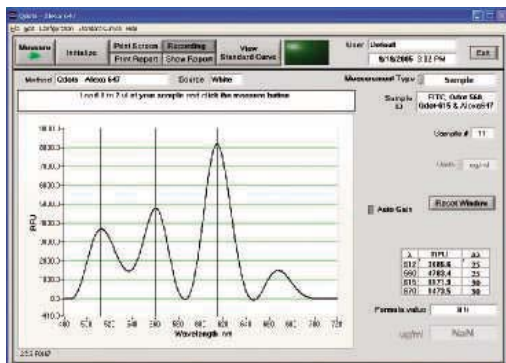
- **Nucleic acids:** Determine concentration of dsDNA using PicoGreen[®] assay (2 pg), Quant-iT[™] DNA assay or Hoechst 33258 dye; RNA using RiboGreen[®] dye.
- **Proteins:** Determine concentration using Quant-iT[™] protein assay.
- **More:** FITC (fluorescein), Cy-Alexa Fluor dyes, B-Phycoerythrin, Quinine Sulfate, Sulforhodamine and 4-MU.

Measurement is as easy as pipette and read, requiring only 1-2 μ l of sample. No cuvettes are necessary — simply wipe the optical surfaces and you're ready for your next sample. A broad excitation range is achieved using UV, blue and white LED sources. The uniquely clean optics of the patented retention system, combined with proprietary white LED signal processing, enables measurements across a wide range of wavelengths without the need for filter changes. The ND-3300 is small, simple and powerful enough for your most challenging and precious samples.

And for the power of small in absorbance measurement, the NanoDrop[®] ND-1000 UV/Vis Spectrophotometer can detect down to 2ng/ μ l and up to 3700 ng/ μ l of dsDNA without dilutions.

Ready to experience the power of small? Contact us today and try the ND-3300 or ND-1000 in your own lab.

FREE one week evaluation
Call for details (302)479-7707 www.nanodrop.com



 **NanoDrop**



Donald Kennedy is
Editor-in-Chief of *Science*.

Summers and Harvard

What has happened at Harvard University over the past year is important to *Science* readers for all sorts of reasons. Harvard was the first university established in the United States, and its excellence as well as its tradition have made it the symbol of higher education for the U.S. public and for many aspiring students in other parts of the world. Why else would last month's departure of President Lawrence Summers, after a turbulent 5-year tour of duty, as well as some of the earlier incidents that led to this denouement, have been covered above the fold on the front page of the *New York Times*?

What fascinates me, as a Harvard alumnus and the former president of a university that does many of the same things as Harvard, is the extraordinary array of explanations given for these events. Summers' resignation preceded a meeting of the Faculty of Arts and Sciences, which had previously passed a no-confidence vote and looked ready to do it again. But many have asked why a university, proud of doing the academic decathlon, left the faculties of Law, Medicine, Business, and Education out of such an important referendum? The faculty-versus-Summers theme has been a Rorschach test for outside observers interested in academic governance, management styles, constituency relationships, and obligations to undergraduate education. The *Economist* called Summers the wrong messenger with the right message, after a lead describing Harvard as "a world-beater in academic back-stabbing." Observers who watched Summers in the U.S. Treasury Department, first as undersecretary and then as secretary, saw him as brilliant and accomplished, including his boss and predecessor Robert Rubin, who was influential in his appointment. On the other hand, many of his academic critics have found Summers arbitrary, blunt, and even arrogant. The *Washington Post* bought little of that, implying in an editorial that the future of academic leadership is in peril when the inmates are running the asylum.



So it goes. Every crisis has multiple interpretations, with the differences often resting on the interests of the interpreters. For some at Harvard and elsewhere, the problem was that in a list of possible explanations for the relative scarcity of women in the sciences, Summers had included genetic gender differences. Had that possibility been introduced with tact and some reservations, it is doubtful that it would have produced the same furor. Summers' notion that Harvard should change—not a bad idea—was introduced through a series of conversations in which his listeners were made to feel part of the problem, not of the solution. Managerial style, in short, was plainly part of Summers' difficulties. But some critics saw the faculty reaction in more harshly political terms: The ubiquitous Harvard Law professor Alan Dershowitz even persuaded the *Economist* to publish his improbable thesis that the "hard left" of the faculty had accomplished a coup d'état.

This multiplicity of perspectives makes it difficult to draw out useful lessons, but it does reveal some realities about presidential power in the university. Professor James March, a valued colleague of mine at Stanford, often pointedly reminded me that power in academia is primarily horizontal. There is little hierarchy in the organization, and the professoriate consists of smart, independent-minded people who don't always do what they're told. Governments are different, and Summers may have been unprepared for a venue in which failure to consult is costly the first time and unforgivable when repeated.

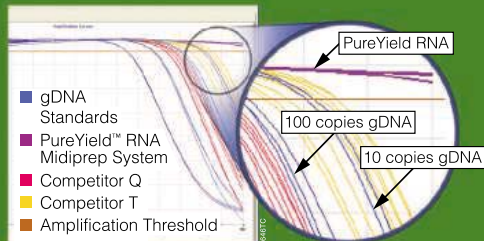
I was happy with his appointment and thought his challenge to Harvard was timely. It failed not because of political differences or constituency mischief, though his image and its contrast with Harvard's has tempted many observers to misallocate blame. The real story here is a classic tragedy: a brilliant thinker and scholar, capable of great leadership, brought low by flaws of personal style. Well, the finger-pointing will finally stop and give us time to notice that, having experienced a very bad bump in the road, Harvard then brought off the perfect rescue. Derek Bok had served a successful 20-year term at Harvard: quite possibly the most successful U.S. university presidency since World War II. Harvard has talked him out of his productive study and into interim leadership, and they're fortunate that he answered the call. That's the good news for higher education, at least for now.

—Donald Kennedy

10.1126/science.1126858



Is unexpected DNA worming its way into your RNA?



qPCR analysis shows no detectable genomic DNA contamination in PureYield™ RNA samples.

The PureYield™ RNA Midiprep System uses a novel, non-DNase method to remove genomic DNA prior to RNA isolation. PureYield reduces your chances of inaccurate results by eliminating DNA from your RNA preps. You get pure, total RNA with no detectable genomic DNA contamination. No surprises. No starting over.

Request a FREE sample* at: www.promega.com/rna

* Samples to qualified customers where available, while supplies last.
©2006 Promega Corporation. 13386-AD-MD

PROMEGA CORPORATION • www.promega.com



Promega

HIGHLIGHTS OF THE RECENT LITERATURE

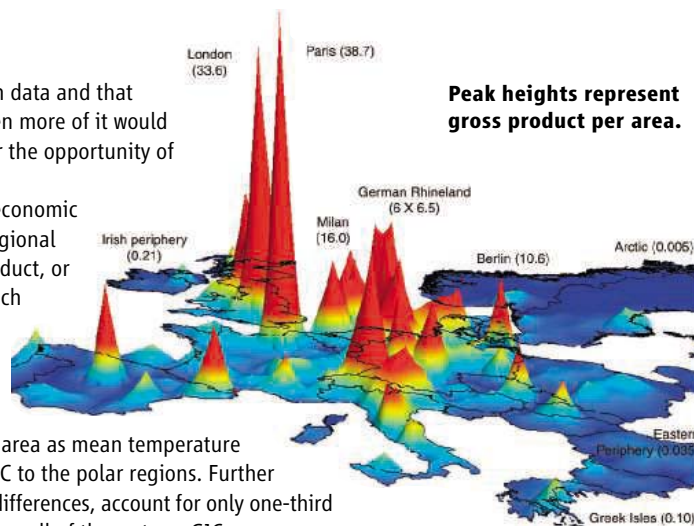
ECONOMICS

Highlands and Lowlands

It might seem that nowadays we're already drowning in too much data and that devoting more energy to interpreting it and less to collecting even more of it would be advisable. On the other hand, large amounts of data can offer the opportunity of looking at old questions in new ways.

Nordhaus describes the construction of a geographically scaled economic data set (G-Econ) that transforms the economic quantity gross regional product (where a region can be a nation, as in gross national product, or a smaller political subdivision) along geophysical dimensions, such as temperature or coastal proximity. Aggregating economic data across multiple sources and scaling output to a cell size of 1° longitude by 1° latitude yields the gross cell product or GCP. The established finding that output per person increases with distance from the equator converts into a decrease in output per area as mean temperature decreases, with a decline of 10^5 from the maximum at about 10°C to the polar regions. Further analysis reveals that country-specific effects, such as institutional differences, account for only one-third of this variation, with geography contributing to but not explaining all of the rest. — GJC

Proc. Natl. Acad. Sci. U.S.A. **103**, 10.1073/pnas.0509842103 (2006).



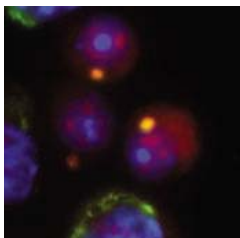
Peak heights represent gross product per area.

MOLECULAR BIOLOGY

Gathering in the Clouds

The chromatoid body, an electron-dense structure in the cytoplasm of mammalian male germ cells, was first described more than a century ago (see review by Parvinen); it may correspond to *Drosophila nuage*, which is a cloud-like fibrous material seen in germ cells. During spermatogenesis, the chromatoid body moves around, associating with the Golgi complex, mitochondria, and nuclear pores. The absence of DNA and the presence of RNA and the RNA helicase MVH (the mouse VASA homolog) have contributed to the belief that this structure is involved in the handling and storage of messenger RNAs (mRNAs).

Kotaja *et al.* demonstrate that the chromatoid body contains the same kinds of molecules that are found in the processing



MVH (green) and mRNA (red) in chromatoid bodies.

bodies of mammalian somatic cells and yeast. The endonuclease Dicer generates small RNAs that are then assembled with Argonaute into an RNA-induced silencing complex (RISC), which mediates the degradation and translational arrest of mRNAs. The authors show that Dicer interacts with MVH and that Dicer, Argonaute, and mRNA all

localize to the chromatoid body. They suggest that, as an early step in posttranscriptional regulation of gene expression, both mRNAs and small RNAs may be captured by the chromatoid body as they transit the nuclear pores. — GJC

Int. J. Androl. **28**, 189 (2005); *Proc. Natl. Acad. Sci. U.S.A.* **103**, 2647 (2006).

CHEMISTRY

Enantioselective Emulsions

Although enzymes achieve extraordinary selectivity in catalyzing biochemical reactions, they operate in relatively dilute environments. To adapt enzymatic catalysis for cost-effective industrial-scale synthesis, it would be desirable to increase the reagent concentrations substantially. One approach has been to solubilize reagents by adding an organic co-solvent to aqueous solutions of the enzyme; however, the reaction rates in such biphasic systems are hindered by slow mixing kinetics.

Gröger *et al.* have used mini-emulsions to improve mixing efficiency by increasing the interface area between dissolved enzymes and substrates. They focused specifically on lipase-catalyzed kinetic resolutions of racemic α - and β -amino acid esters to the respective homochiral free acids. Through ultrasound sonication of aqueous solutions containing 1% surfactant and 1% hydrophobic hexadecane, the authors generated stable emulsions of 100-nm-diameter droplets containing the ester. The exceptionally

high ester concentration under these conditions cut the reaction time to less than half that for a traditional biphasic system, while maintaining >99% enantioselectivity. — MSL

Angew. Chem. Int. Ed. **45**, 1645 (2006).

CELL BIOLOGY

Reinforcing the Scaffold

During cell division, chromosomes condense into their stereotypical compact rod-like shapes, and this allows them to be manipulated efficiently by the mitotic spindle for partitioning into the daughter cells. Using fluorescence microscopy on live cells, Gerlich *et al.* examined the roles of the condensin proteins I and II in chromosome restructuring during mitosis. Condensin II remained associated with chromosomes throughout mitosis, whereas condensin I began to associate with chromosomes in prometaphase, after compaction had been completed in prophase. As mitosis progressed, the levels of chromosome-associated condensin I increased, until chromosomes had lined up on the mitotic spindle, for partitioning during anaphase. When levels of condensin I were reduced experimentally, chromosomes condensed normally, but during alignment and separation, the compacted chromosomes were mechanically unstable and more readily disrupted. In contrast, when levels of condensin II were reduced, condensed chromosomes remained robust enough to withstand partitioning. Thus, it

Continued on page 1349

Create!



INNOVATION @ WORK

with Sigma, the new leader in RNAi create your advantage

Faster siRNA manufacturing? 100% transduction efficiency of shRNA constructs? Long and short term silencing? Sigma has developed the most comprehensive array of cutting edge products for every step of your RNAi experimental design – creating for you a real advantage.

- Taking siRNA manufacturing to a new level by providing a rapid turnaround, high throughput and cost effective service that caters to your siRNA needs
- MISSION™ TRC shRNA libraries, comprising 150,000 pre-cloned shRNA constructs targeting 15,000 human genes and 15,000 mouse genes
- Lentiviral shRNA delivery that boasts flexibility of long and short term silencing, 100% transduction efficiency and enables experimentation with difficult to study cell types such as non-dividing or primary cells

So whether you are determining gene function, analyzing signal transduction or screening for potential drug targets, why not discover how you can create your RNAi advantage.

sigma.com/rnai

Accelerating Customers' Success through **Leadership** in **Life Science**, **High Technology** and **Service**
SIGMA-ALDRICH CORPORATION • BOX 14508 • ST. LOUIS • MISSOURI 63178 • USA



Member of the RNAi Consortium

MISSION is a trademark belonging to Sigma-Aldrich Co. and its affiliate Sigma-Aldrich Biotechnology LP. The RNAi Consortium shRNA library is produced and distributed under license from the Massachusetts Institute of Technology.

SIGMA®

Continued from page 1347

seems that condensin I reinforces the scaffold of condensed chromosomes and helps them to withstand the forces applied as they interact with the mitotic spindle. — SMH

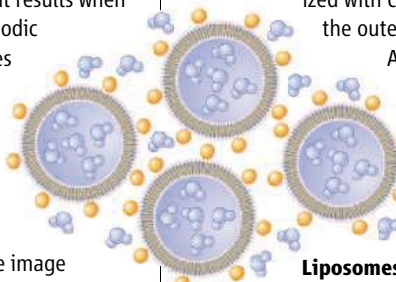
Curr. Biol. **16**, 333 (2006).

APPLIED PHYSICS

Scanning Nanobarcodes

Screening technologies for biological and chemical monitoring often depend on the ability to identify and track labeled substrates. Although carrier beads can be encoded optically with fluorescence, infrared, or Raman spectroscopic signatures, the number of discriminable markers or tags available via these techniques is limited.

To expand the pool of markers, Galitonov *et al.* introduce an alternative method, based on the characteristic diffraction patterns produced by nanostructured barcodes. The operating principle relies on the distinctive image that results when laser light is scattered from a periodic grating, with the diffraction angles of the first and higher-order lines determined by the grating's periodicity. Each grating thus encodes a unique signature; moreover, superposition of two or more gratings creates a complex pattern, distinct from the image produced by either grating alone. By fabricating 100- μm -long barcodes from just three superposed gratings, the authors demonstrate the capacity to create a library of 68,000 distinctive tags, each readily readable by a helium-neon laser. With library sizes expected to increase as more gratings are superposed and fabrication resolution is improved, the method should find



use in a variety of high-throughput screening applications. — ISO

Opt. Express **14**, 1382 (2006).

MATERIALS SCIENCE

Like Repels Like

Liposomes—microscopic compartments surrounded by a phospholipid bilayer shell—are of interest for targeted drug delivery. However, their high surface curvature renders them vulnerable to fusing when they collide, which can result in the premature release of their contents; many efforts to address this deficiency have relied on significant modifications of the liposome surface structure.

Zhang and Granick have stabilized 200-nm-diameter liposomes against fusion through a minor modification: the adhesion of negatively charged nanoparticles (polystyrene functionalized with carboxylate groups) to the outer membrane surface.

Although only one-quarter of the surface was occluded by the nanoparticles, charge repulsion was sufficient to pre-

Liposomes held apart by adsorbed nanoparticles (orange).

vent fusion, stabilizing a 16% by volume liposome suspension for 50 days. The authors further demonstrated the robustness of the structures by filling them with a fluorescent dye and observing no leakage over 4 days. — PDS

Nano Lett. **6**, 10.1021/nl052455y (2006).



www.stke.org

<< The Ups and Downs of Kinases

Jeffrey *et al.* explored the role of the nuclear-localized dual specificity phosphatase (DUSP) isoform known as phosphatase of activated cells 1 (PAC-1, which is encoded by the DUSP2 gene) in the regulation of leukocyte activity and in a mouse model of autoimmune arthritis. Surprisingly, cells from *Dusp2^{-/-}* mice showed decreased induction of inflammatory arthritis (delayed onset of symptoms and diminished histological and clinical features). Stimulated macrophages and bone marrow-derived mast cells from these mice exhibited reduced gene expression and secretion of inflammatory mediators; in addition, cultured mast cells exhibited greater apoptosis and decreased cell survival. Despite *in vitro* evidence that the mitogen-activated protein kinases (MAPKs) p38 and ERK are substrates of PAC-1, their activities decreased in the *Dusp2^{-/-}* mast cells and macrophages. In contrast, phosphorylation of the MAPK c-Jun N-terminal kinase (JNK) increased. PAC-1 deficiency reduced gene expression by the transcriptional regulator Elk1, and inhibition of JNK in PAC-1 deficient cells rescued ERK phosphorylation and Elk1-mediated transcription, suggesting that the JNK pathway regulates the ERK pathway so that when JNK activity goes up, ERK activity goes down. These results point to therapeutic targeting of PAC-1 as a modulator of MAPK signaling in immune cells, especially for treatment of autoimmune disease. — NRG

Nat. Immunol. **7**, 274 (2006).

AAAS Travels

We invite you to travel with AAAS in the coming year. You will discover excellent itineraries and leaders, and congenial groups of like-minded travelers who share a love of learning and discovery.

Africa Safari

June 23–July 6, 2006

Join lion expert **Dr. David Bygott** on safari! Visit Samburu, Lake Nakuru, Ngorogoro Crater & the Serengeti!

Tibetan Plateau

July 7–25, 2006

Discover Tibet, a place of fascination for naturalists & explorers for centuries. \$3,295 + air.



A Walk in the Swiss Alps

July 21–August 2, 2006

Discover some of the finest areas in Switzerland for walking: Appenzell and Engelberg, plus Lucerne & St Gallen. \$2,995 + air.



Peru & The Incas

August 3–15, 2006

Discover the Inca civilization and Peru's cultural heritage with expert **Dr. Douglas Sharon**. Explore Lima, Cuzco, Machu Picchu, the Nazca Lines & more! \$3,695 + air.

Xinjiang & Hunza

August 3–22, 2006

Discover the Silk Road in far western China with **Dr. Chris Carpenter**. Visit Turpan, Kanas Lake National Park, Urumqi, Kashgar, Tashkurgan, Altai, and see the Karakoram and Hunza.



Madagascar

August 15–31, 2006

Discover the lemurs and unique natural heritage at Perinet, Nosy Be, Asole, and Berenty. \$3,695 + air.

Andalucia

October 13–25, 2006

A marvelous adventure in Southern Spain, from Granada to Seville, El Rocio, Grazalema, and Coto Donada.

Backroads China

October 20–November 5, 2006

Join our guide **David Huang** and discover the delights of Southwestern China, edging 18,000-foot Himalayan peaks, the most scenic & culturally rich area in China. \$3,295 + air.



Call for trip brochures & the Expedition Calendar

(800) 252-4910

AAAS Travels

17050 Montebello Road
Cupertino, California 95014

Email: AAASinfo@betchartexpeditions.com
On the Web: www.betchartexpeditions.com

1200 New York Avenue, NW
Washington, DC 20005

Editorial: 202-326-6550, FAX 202-289-7562
News: 202-326-6500, FAX 202-371-9227

Bateman House, 82-88 Hills Road
Cambridge, UK CB2 1LQ

+44 (0) 1223 326500, FAX +44 (0) 1223 326501

SUBSCRIPTION SERVICES For change of address, missing issues, new orders and renewals, and payment questions: 800-731-4939 or 202-326-6417, FAX 202-842-1065. Mailing addresses: AAAS, P.O. Box 1811, Danbury, CT 06813 or AAAS Member Services, 1200 New York Avenue, NW, Washington, DC 20005

INSTITUTIONAL SITE LICENCES please call 202-326-6755 for any questions or information

REPRINTS: Author Inquiries 800-635-7181

Commercial Inquiries 803-359-4578

Corrections 202-326-6501

PERMISSIONS 202-326-7074, FAX 202-682-0816

MEMBER BENEFITS Bookstore: AAAS/BarnesandNoble.com bookstore www.aaas.org/bn; Car purchase discount: Subaru VIP Program 202-326-6417; Credit Card: MBNA 800-847-7378; Car Rentals: Hertz 800-654-2200 CDP#343457, Dollar 800-800-4000 #AA1115; AAAS Travels: Betchart Expeditions 800-252-4910; Life Insurance: Seabury & Smith 800-424-9883; Other Benefits: AAAS Member Services 202-326-6417 or www.aaasmember.org.

science_editors@aaas.org (for general editorial queries)

science_letters@aaas.org (for queries about letters)

science_reviews@aaas.org (for returning manuscript reviews)

science_bookrevs@aaas.org (for book review queries)

Published by the American Association for the Advancement of Science (AAAS), *Science* serves its readers as a forum for the presentation and discussion of important issues related to the advancement of science, including the presentation of minority or conflicting points of view, rather than by publishing only material on which a consensus has been reached. Accordingly, all articles published in *Science*—including editorials, news and comment, and book reviews—are signed and reflect the individual views of the authors and not official points of view adopted by the AAAS or the institutions with which the authors are affiliated.

AAAS was founded in 1848 and incorporated in 1874. Its mission is to advance science and innovation throughout the world for the benefit of all people. The goals of the association are to: foster communication among scientists, engineers and the public; enhance international cooperation in science and its applications; promote the responsible conduct and use of science and technology; foster education in science and technology for everyone; enhance the science and technology workforce and infrastructure; increase public understanding and appreciation of science and technology; and strengthen support for the science and technology enterprise.

INFORMATION FOR CONTRIBUTORS

See pages 102 and 103 of the 6 January 2006 issue or access www.sciencemag.org/feature/contribinfo/home.shtml

EDITOR-IN-CHIEF **Donald Kennedy**

EXECUTIVE EDITOR **Monica M. Bradford**

DEPUTY EDITORS NEWS EDITOR

R. Brooks Hanson, Katrina L. Kelner Colin Norman

EDITORIAL SUPERVISORY SENIOR EDITORS Barbara Jasny, Phillip D. Szurromi; **SENIOR EDITOR/PERSPECTIVES** Lisa D. Chong; **SENIOR EDITORS** Gilbert J. Chin, Pamela J. Hines, Paula A. Kiberstis (Boston), Beverly A. Purnell, L. Bryan Ray, Guy Riddihough (Manila), H. Jesse Smith, Valda Vinson, David Voss; **ASSOCIATE EDITORS** Marc S. Lavine (Toronto), Jake S. Yeston; **ONLINE EDITOR** Stewart Wallis; **ASSOCIATE ONLINE EDITOR** Tara S. Marathe; **BOOK REVIEW EDITOR** Sherman J. Suter; **ASSOCIATE LETTERS EDITOR** Etta Kavanagh; **INFORMATION SPECIALIST** Janet Kegg; **EDITORIAL MANAGER** Cara Tate; **SENIOR COPY EDITORS** Jeffrey E. Cook, Harry Jach, Barbara P. Ordway; **COPY EDITORS** Cynthia Howe, Alexis Wynne Mogul, Jennifer Sills, Trista Wagoner; **EDITORIAL COORDINATORS** Carolyn Kyle, Beverly Shields; **PUBLICATION ASSISTANTS** Ramatoulaye Diop, Chris Filiatreau, Joi S. Granger, Jeffrey Hearn, Lisa Johnson, Scott Miller, Jerry Richardson, Brian White, Anita Wynn; **EDITORIAL ASSISTANTS** Lauren Kmec, Patricia M. Moore, Brendan Nardozi, Michael Rodewald; **EXECUTIVE ASSISTANT** Sylvia S. Kihara

NEWS SENIOR CORRESPONDENT Jean Marx; **DEPUTY NEWS EDITORS** Robert Coontz, Jeffrey Mervis, Leslie Roberts, John Travis; **CONTRIBUTING EDITORS** Elizabeth Culotta, Polly Shulman; **NEWS WRITERS** Yudhijit Bhattacharjee, Adrian Cho, Jennifer Couzin, David Grimm, Constance Holden, Jocelyn Kaiser, Richard A. Kerr, Eli Kintisch, Andrew Lawler (New England), Greg Miller, Elizabeth Pennisi, Robert F. Service (Pacific NW), Erik Stokstad, Katherine Unger (intern); **CONTRIBUTING CORRESPONDENTS** Barry A. Cipra, Jon Cohen (San Diego, CA), Daniel Ferber, Ann Gibbons, Robert Iron, Mitch Leslie (NetWatch), Charles C. Mann, Evelyn Strauss, Gary Taubes, Ingrid Wickelgren; **COPY EDITORS** Linda B. Felaco, Rachel Curran, Sean Richardson; **ADMINISTRATIVE SUPPORT** Scherraine Mack, Fannie Groom BUREAUS: Berkeley, CA: 510-652-0302, FAX 510-652-1867, New England: 207-549-7755, San Diego, CA: 760-942-3252, FAX 760-942-4979, Pacific Northwest: 503-963-1940

PRODUCTION DIRECTOR James Landry; **SENIOR MANAGER** Wendy K. Shank; **ASSISTANT MANAGER** Rebecca Doshi; **SENIOR SPECIALISTS** Jay Covert, Chris Redwood; **SPECIALIST** Steve Forrester **PREFLIGHT DIRECTOR** David M. Tompkins; **MANAGER** Marcus Spiegler; **SPECIALIST** Jessie Mudjitaba

ART DIRECTOR Joshua Moglia; **ASSOCIATE ART DIRECTOR** Kelly Buckheit; **ILLUSTRATORS** Chris Bickel, Katharine Suttifit; **SENIOR ART ASSOCIATES** Holly Bishop, Laura Creveling, Preston Huey; **ASSOCIATE** Nayomi Kevitiyagala; **PHOTO EDITOR** Leslie Blizard

SCIENCE INTERNATIONAL

EUROPE (science@science-int.co.uk) **EDITORIAL:** INTERNATIONAL MANAGING EDITOR Andrew M. Sugden; **SENIOR EDITOR/PERSPECTIVES** Julia Fahrenkamp-Uppenbrink; **SENIOR EDITORS** Caroline Ash (Geneva: +41 (0) 222 346 3106), Stella M. Hurlley, Ian S. Osborne, Stephen J. Simpson, Peter Stern; **ASSOCIATE EDITOR** Joanne Baker **EDITORIAL SUPPORT** Alice Whaley; Deborah Dennison **ADMINISTRATIVE SUPPORT** Janet Clements, Phil Marlow, Jill White; **NEWS:** INTERNATIONAL NEWS EDITOR Eliot Marshall **DEPUTY NEWS EDITOR** Daniel Cley; **CORRESPONDENT** Gretchen Vogel (Berlin: +49 (0) 30 2809 3902, FAX +49 (0) 30 2809 8365); **CONTRIBUTING CORRESPONDENTS** Michael Balter (Paris), Martin Enserink (Amsterdam and Paris), John Bohannon (Berlin); **INTERN** Michael Schirber

ASIA Japan Office: Asca Corporation, Eiko Ishioka, Fusako Tamura, 1-8-13, Hirano-cho, Chuo-ku, Osaka-shi, Osaka, 541-0046 Japan; +81 (0) 6 6202 6272, FAX +81 (0) 6 6202 6271; asca@os.gulf.or.jp; **ASIA NEWS EDITOR** Richard Stone +66 2 662 5818 (rstone@aaas.org) **JAPAN NEWS BUREAU** Dennis Normile (contributing correspondent, +81 (0) 3 3391 0630, FAX 81 (0) 3 5936 3531; dnormile@gol.com); **CHINA REPRESENTATIVE** Hao Xin, +86 (0) 10 6307 4439 or 6307 3676, FAX +86 (0) 10 6307 4358; haoxin@earthlink.net; **SOUTH ASIA** Pallava Bagla (contributing correspondent +91 (0) 11 2271 2896; pbagla@vsnl.com)

EXECUTIVE PUBLISHER **Alan I. Leshner**

PUBLISHER **Beth Rosner**

FULFILLMENT & MEMBERSHIP SERVICES (membership@aaas.org) **DIRECTOR** Marlene Zenzel; **MANAGER** Waylon Butler; **SYSTEMS SPECIALIST** Andrew Vargo; **SPECIALISTS** Pat Butler, Laurie Baker, Tamara Alfson, Karen Smith, Vicki Linton; **CIRCULATION ASSOCIATE** Christopher Refice

BUSINESS OPERATIONS AND ADMINISTRATION DIRECTOR Deborah Rivera-Wienhold; **BUSINESS MANAGER** Randy Yi; **SENIOR BUSINESS ANALYST** Lisa Donovan; **BUSINESS ANALYST** Jessica Tierney; **FINANCIAL ANALYST** Michael LoBue, Farida Yeasmin; **RIGHTS AND PERMISSIONS:** ADMINISTRATOR Emilie David; **ASSOCIATE** Elizabeth Sandler; **MARKETING:** DIRECTOR John Meyers; **MARKETING MANAGERS** Darryl Walter, Allison Pritchard; **MARKETING ASSOCIATES** Julianne Wielga, Mary Ellen Crowley, Catherine Featherston, Alison Chandler; **DIRECTOR OF INTERNATIONAL MARKETING AND RECRUITMENT ADVERTISING** Deborah Harris; **INTERNATIONAL MARKETING MANAGER** Wendy Sturley; **MARKETING/MEMBER SERVICES EXECUTIVE:** Linda Rusk; **JAPAN SALES** Jason Hannaford; **SITE LICENSE SALES:** DIRECTOR Tom Ryan; **SALES AND CUSTOMER SERVICE** Mehan Dossani, Kiki Forsythe, Catherine Holland, Wendy Wise; **ELECTRONIC MEDIA:** Amanda K. Kelzabeth Harman; **PRODUCTION ASSOCIATES** Sheila Mackall, Manda K. Skelton, Lisa Stanford, Nichelle Johnston; **APPLICATIONS DEVELOPER** Carl Saffell

ADVERTISING DIRECTOR WORLDWIDE AD SALES Bill Moran

PRODUCT (science_advertising@aaas.org); **MIDWESTWEST COAST/W. CANADA** Rick Bongiovanni: 330-405-7080, FAX 330-405-7081 • **EAST COAST/E. CANADA** Christopher Breslin: 443-512-0330, FAX 443-512-0331 • **UK/EUROPE/ASIA** Tracey Peers (Associate Director): +44 (0) 182 752530, FAX +44 (0) 1782 752531 **JAPAN** Mashyo Yoshikawa: +1 (81) 33235 5961, FAX +81 (0) 33235 5852 **TRAFFIC MANAGER** Carol Maddox; **SALES COORDINATOR** Deiana Simms

CLASSIFIED (advertise@sciencecareers.org); **U.S. SALES DIRECTOR** Gabrielle Boguslawski: 718-491-1607, FAX 202-289-6742; **INSIDE SALES MANAGER** Daryl Anderson: 202-326-6543; **WEST COAST/MIDWEST** Kristine von Zedlitz: 415-956-2531; **EAST COAST** Jill Downing: 631-580-2445; **CANADA, MEETINGS AND ANNOUNCEMENTS** Kathleen Clark: 510-271-8349; **LINE AD SALES** Emmet Teslaye: 202-326-6740; **SALES COORDINATORS** Erika Bryant; Rohan Edmonson Christopher Normile, Joyce Scott, Shirley Young; **INTERNATIONAL SALES MANAGER** Tracy Holmes: +44 (0) 1223 326525, FAX +44 (0) 1223 326532; **SALES** Christina Harrison, Svetlana Barnes; **SALES ASSISTANT** Helen Moroney; **JAPAN:** Jason Hannaford: +81 (0) 52 789 1860, FAX +81 (0) 52 789 1861; **PRODUCTION MANAGER** Jennifer Rankin; **ASSISTANT MANAGER** Deborah Tompkins; **ASSOCIATES** Christine Hall; Amy Hardcastle; **PUBLICATIONS ASSISTANTS** Robert Buck; Natasha Pinol

AAAS BOARD OF DIRECTORS **RETIRING PRESIDENT**, Chair Gilbert S. Omenn; **PRESIDENT** John P. Holdren; **PRESIDENT-ELECT** David Baltimore; **TREASURER** David E. Shaw; **CHIEF EXECUTIVE OFFICER** Alan I. Leshner; **BOARD ROSINA M. Bierbaum**; John E. Dowling; Lynn W. Enquist; Susan M. Fitzpatrick; Alice Gast; Thomas Pollard; Peter J. Stang; Kathryn D. Sullivan



ADVANCING SCIENCE. SERVING SOCIETY

SENIOR EDITORIAL BOARD

John I. Brauman, *Chair, Stanford Univ.*
Richard Losick, *Harvard Univ.*
Robert May, *Univ. of Oxford*
Marcia McNutt, *Monterey Bay Aquarium Research Inst.*
Linda Partridge, *Univ. College London*
Vera C. Rubin, *Carnegie Institution of Washington*
Christopher R. Somerville, *Carnegie Institution*
George M. Whitesides, *Harvard University*

BOARD OF REVIEWING EDITORS

R. McNeill Alexander, *Leeds Univ.*
David Altshuler, *Broad Institute*
Arturo Alvarez-Buylla, *Univ. of California, San Francisco*
Richard Amasino, *Univ. of Wisconsin, Madison*
Meinrat O. Andreae, *Max Planck Inst., Mainz*
Kristi S. Anseth, *Univ. of Colorado*
Cornelia I. Bargmann, *Rockefeller Univ.*
Brenda Bass, *Univ. of Utah*
Ray H. Baughman, *Univ. of Texas, Dallas*
Stephen J. Benkovic, *Pennsylvania St. Univ.*
Michael J. Bevan, *Univ. of Washington*
Tom Bisseling, *Wageningen Univ.*
Mina Bissell, *Lawrence Berkeley National Lab*
Peer Bork, *EMBL*
Dennis Bray, *Univ. of Cambridge*
Stephen Buratowski, *Harvard Medical School*
Jilliam M. Burriak, *Univ. of Alberta*
Joseph A. Burns, *Cornell Univ.*
William P. Butz, *Population Reference Bureau*
Doreen Cantrell, *Univ. of Dundee*
Peter Carmeliet, *Univ. of Leuven, VIB*
Gerbrand Ceder, *MIT*
Mildred Cho, *Stanford Univ.*
David Clapham, *Children's Hospital, Boston*
David Clary, *Oxford University*
J. M. Claverie, *CNRS, Marseille*

Jonathan D. Cohen, *Princeton Univ.*
F. Fleming Crim, *Univ. of Wisconsin*
William Cumberland, *UC/CA*
George O. Daley, *Children's Hospital, Boston*
Caroline Dean, *John Innes Centre*
Judy DeLoache, *Univ. of Virginia*
Edward DeLong, *MIT*
Robert Desimone, *MIT*
Dennis Discher, *Univ. of Pennsylvania*
Julian Downward, *Cancer Research UK*
Denis Duboule, *Univ. of Geneva*
Christopher Dye, *WHO*
Richard Ellis, *Cal Tech*
Gerhard Ertl, *Fritz-Haber-Institut, Berlin*
Douglas H. Erwin, *Smithsonian Institution*
Barry Everitt, *Univ. of Cambridge*
Paul G. Falkowski, *Rutgers Univ.*
Ernst Fehr, *Univ. of Zurich*
Tom Fenchel, *Univ. of Copenhagen*
Alain Fischer, *INSERM*
Jeffrey S. Flier, *Harvard Medical School*
Chris D. Frith, *Univ. College London*
R. Gadagkar, *Indian Inst. of Science*
John Gearhart, *Johns Hopkins Univ.*
Jennifer M. Graves, *Australian National Univ.*
Christian Haass, *Ludwig Maximilians Univ.*
Dennis L. Hartmann, *Univ. of Washington*
Chris Hawkesworth, *Univ. of Bristol*
Martin Heimann, *Max Planck Inst., Jena*
James A. Hendler, *Univ. of Maryland*
Ary A. Hoffmann, *La Trobe Univ.*
Evelyn L. Hu, *Univ. of California, SB*
Meyer B. Jackson, *Univ. of Wisconsin Med. School*
Stephen Jackson, *Univ. of Cambridge*
Daniel Kahne, *Harvard Univ.*
Bernhard Keimer, *Max Planck Inst., Stuttgart*
Alan B. Krueger, *Princeton Univ.*
Lee Kump, *Penn State*
Virginia Lee, *Univ. of Pennsylvania*

Anthony J. Leggett, *Univ. of Illinois, Urbana-Champaign*
Michael J. Lenardo, *NIH, MD, MD*
Norman L. Levin, *Beth Israel Deaconess Medical Center*
Olle Lindvall, *Univ. Hospital, Lund*
Richard Losick, *Harvard Univ.*
Andrew P. MacKenzie, *Univ. of St. Andrews*
Raul Madariaga, *Ecole Normale Supérieure, Paris*
Rick Maizels, *Univ. of Edinburgh*
Michael Malim, *King's College, London*
Eve Marder, *Brandeis Univ.*
George M. Martin, *Univ. of Washington*
William McGinnis, *Univ. of California, San Diego*
Virginia Miller, *Washington Univ.*
H. Yasushi Miyashita, *Univ. of Tokyo*
Edward Moser, *Norwegian Univ. of Science and Technology*
Andrew Murray, *Harvard Univ.*
Naoto Nagawa, *Univ. of Tokyo*
James Nelson, *Stanford Univ. School of Med.*
Roeland Nolte, *Univ. of Nijmegen*
Helga Nowotny, *European Research Advisory Board*
Elinor N. Olson, *Univ. of Texas, SW*
Erin O'Shea, *Univ. of California, SF*
Rinor Ostrom, *Indiana Univ.*
John Pendry, *Imperial College*
Philippe Poulin, *CNRS*
Mary Power, *Univ. of California, Berkeley*
David J. Read, *Univ. of Sheffield*
Les Real, *Emory Univ.*
Clint Renfrew, *Univ. of Cambridge*
 Trevor Robbins, *Univ. of Cambridge*
 Nancy Ross, *Virginia Tech*
 Edward M. Rubin, *Lawrence Berkeley National Labs*
 Gary Ruvkun, *Mass. General Hospital*
 J. Roy Sambles, *Univ. of Exeter*
 David S. Schime, *National Center for Atmospheric Research*
 Georg Schulz, *Albert-Ludwigs-Universität*
 Paul Schulze-Lefert, *Max Planck Inst., Cologne*
 Terrence J. Sejnowski, *The Salk Institute*
 David Sibley, *Washington Univ.*
 George Somero, *Stanford Univ.*

Christopher R. Somerville, *Carnegie Institution*
Joan Steitz, *Yale Univ.*
Edward I. Stiefel, *Princeton Univ.*
Thomas Stocker, *Univ. of Bern*
Jerome Strauss, *Univ. of Pennsylvania Med. Center*
Tomoyuki Takahashi, *Univ. of Tokyo*
Marc Tatar, *Brown Univ.*
Glenn Telling, *Univ. of Kentucky*
Marc Tessier-Lavigne, *Genentech*
Craig B. Thompson, *Univ. of Pennsylvania*
Michiel van der Kifts, *Astronomical Inst. of Amsterdam*
Derek van der Kooy, *Univ. of Toronto*
Bert Vogelstein, *Johns Hopkins*
Christopher A. Walsh, *Harvard Medical School*
Christopher T. Walsh, *Harvard Medical School*
Graham Warren, *Yale Univ. School of Med.*
Colin Watts, *Univ. of Dundee*
Julia R. Weertman, *Northwestern Univ.*
Daniel M. Wegner, *Harvard University*
Ellen D. Williams, *Univ. of Maryland*
R. Sanders Williams, *Duke University*
Ian A. Wilson, *The Scripps Res. Inst.*
Jerry Workman, *Stowers Inst. for Medical Research*
John R. Yates III, *The Scripps Res. Inst.*
Martin Zatz, *NIMH, NIH*
Walter Zieglgansberger, *Max Planck Inst., Munich*
Huda Zoghbi, *Baylor College of Medicine*
Mina Zuber, *MIT*

BOOK REVIEW BOARD

John Aldrich, *Duke Univ.*
David Bloom, *Harvard Univ.*
Londa Schiebinger, *Stanford Univ.*
Richard Swedner, *Univ. of Chicago*
Ed Wasserman, *DuPont*
Lewis Wolpert, *Univ. College, London*

Explore the Store... and More!
Visit appliedbiosystems.com for
web specials.

Now! Real-Time PCR results in under 40 minutes!



Real Affordable
Applied Biosystems
7300 Real-Time PCR System



Real Versatile
Applied Biosystems
7500 Real-Time PCR System



Real Fast
Applied Biosystems
7500 Fast Real-Time PCR System

Looking for faster real-time PCR results?

Our new Applied Biosystems 7500 Fast Real-Time PCR

System, the choice for labs in a hurry, is the latest addition to the innovative family of real-time PCR systems from Applied Biosystems. It enables 96-well format high-speed thermal cycling, easily integrating into your lab's workflow. Whichever system you choose, you'll get the gold standard combination of TaqMan[®] assays and the proven performance of the industry leader—plus unbeatable real-time chemistry choices, powerful software, and a comprehensive selection of reagents and consumables. For the real deal in real-time PCR, visit <http://info.appliedbiosystems.com/realtimepcr>

AB Applied Biosystems



For Research Use Only. Not for use in diagnostic procedures. Practice of the patented polymerase chain reaction (PCR) process requires a license. The Applied Biosystems 7300/7500 Real-Time PCR Systems are Authorized Thermal Cyclers for PCR and may be used with PCR licenses available from Applied Biosystems. Their use with Authorized Reagents also provides a limited PCR license in accordance with the label rights accompanying such reagents. Purchase of this instrument does not convey any right to practice the 5' nuclease assay or any of the other real-time methods covered by patents owned by Roche or Applied Biosystems.

Applied Biosystems is a registered trademark and AB (Design) and Applera are trademarks of Applera Corporation or its subsidiaries in the US and/or certain other countries. TaqMan is a registered trademark of Roche Molecular Systems, Inc. Information is subject to change without notice. © 2006 Applied Biosystems. All rights reserved.

ADVANCED TRAINING COURSE IN BIOMEDICAL RESEARCH

Modern Technologies in Gene Expression Detection and Data Integration

July 18–26, 2006, Debrecen, Hungary

Debrecen Clinical Genome Center, University of Debrecen

Applications are invited for this HHMI-sponsored international course for graduate students, postdoctoral fellows, and junior faculty.

This hands-on course explores technologies for detecting and quantifying gene expression in mammalian cells and tissues, such as DNA microarrays, real-time PCR, chromatin immunoprecipitation (ChIP)-on-chip technologies, and bioinformatics of integrated datasets. Topics include transcription factor-regulated gene networks, epigenetic modifications, the role of siRNA and microRNAs, and novel methods for visualizing gene expression.

Application deadline: April 30, 2006

Information: www.hhmi.org/grants/courses

HHMI
HOWARD HUGHES MEDICAL INSTITUTE
International Program

Moving? Change of Address? New E-mail Address?

Continue your AAAS membership and get *Science* after you move!

Contact our membership department and be sure to include your membership number. You may:

- Update online at AAASmember.org
- E-mail your address change to membership4@aaas.org
- Call us:
Within the U.S.: 202-326-6417
Outside the U.S.: +44 (0) 1223 326 515



LET US
KNOW!



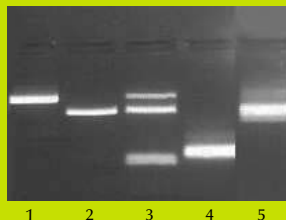
Breakthrough in PCR analysis

NO DNA ISOLATION !

Go from Biological Sample Directly to PCR with

DNAzol[®] DIRECT Reagent^{*}

- Lyse sample in DNAzol[®] Direct
- Add lysate into PCR
- PCR



Amplified DNA fragments

1. Human saliva - LCT
2. Human blood - cfos
3. Human blood/Multiplex
- LCT - cfos - cox 2
4. Rat liver- GAPDH
5. Wheat - 5S rRNA

Works for animal, plant, yeast, bacterial and viral samples; whole blood, plasma, serum, saliva, buccal swabs, blood cards and formalin-fixed tissue.

Standard, multiplex and real-time PCR.

Sample ready for PCR in 15 minutes, no column, no DNA precipitation.

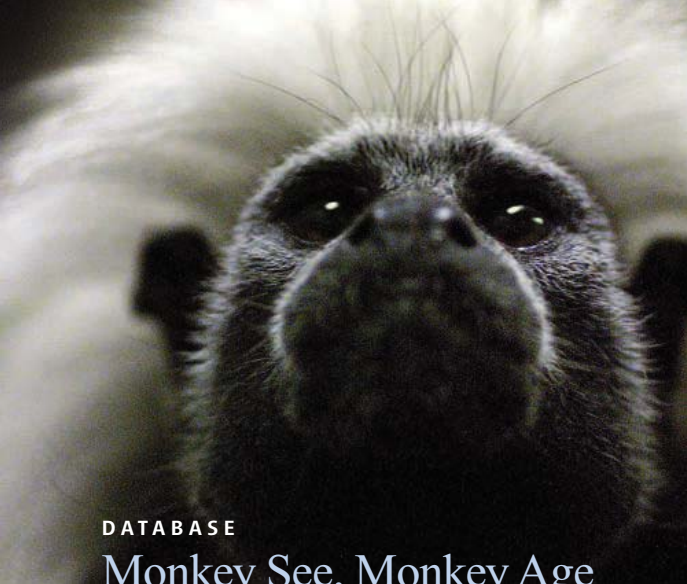
Minimal amount of sample required, down to few picograms of DNA.

Sensitive PCR detection of bacterial and viral DNA.

* Patent pending

Contact Molecular Research Center, Inc.,

www.mrcgene.com or call toll-free 888-841 0900



DATABASE

Monkey See, Monkey Age

Researchers studying aging, primate physiology, and related topics will find a trove of baseline data at this site from the Wisconsin National Primate Research Center in Madison. The internet Primate Aging Database (iPAD) stockpiles measurements of putative aging biomarkers—variables such as blood glucose level, bone thickness, and white blood cell count that might clock the ravages of time. Eleven U.S. labs have contributed information on 16 types of primates, from the Western lowland gorilla to the cotton-top tamarin (*Saguinus oedipus*; above). Searches serve up some of the 400,000 data points or provide statistical summaries. You can sift the results by the animals' age, diet, sex, or housing conditions. The free database is open to academics and commercial researchers, but potential users must apply for access. >>

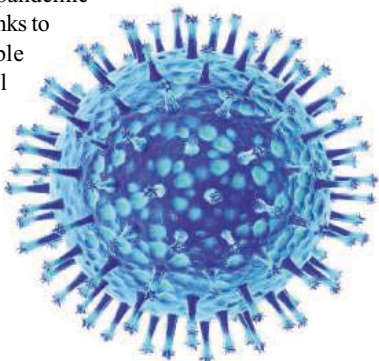
ipad.primat.wisc.edu

RESOURCES

The Encyclopedia Influenzae

A solid source of information about the deadly H5N1 avian influenza virus and its potential to trigger a human pandemic is the Flu Wiki, a user-written collaboration in the spirit of Wikipedia. A primer dissects the influenza virus and follows it into the body to see how it damages the respiratory system. Other pages discuss the limitations of anti-flu drugs such as Tamiflu and theorize about what deadly traits the 1918 flu strain and H5N1 share. These viruses might unleash a flood of immune system messengers termed a cytokine storm. Visitors can scan different countries' pandemic influenza plans. The site also links to resources on the flu's possible economic, legal, and ethical implications. For example, a recent white paper estimates that even a mild pandemic would cut the world's economic output by \$330 billion and kill 1.4 million people. >>

www.fluwiki.com



TOOLS

Meta Analysis

Metazome from the U.S. Department of Energy and the University of California, Berkeley, lets researchers compare animal genomes to tease out gene lineages. The site currently holds complete genome sequences for 11 species—including *Homo sapiens*, the zebrafish, and the malaria-spreading *Anopheles gambiae* mosquito—that represent branch points in animal, or metazoan, evolution. Searching “jawed vertebrates” for a particular gene, for instance, returns all the genes in that group descended from an ancestral gene. Links provide more information about the genes and their proteins. >> www.metazome.net

IMAGES

Fossils on Parade >>

The bones and shells on display at the new 3D Museum are about as close to hands-on as the Internet gets.

Hosted by the Vertebrate Paleobiology Lab at the University of California, Davis, the growing exhibit houses remains of more than 20 extinct and living animals, from branching coral to a woolly mammoth tooth. Java windows let you rotate and zoom in on three-dimensional scans of objects such as the shell of the ammonite *Toxoceratoides taylari* (above), a squid relative from the Cretaceous period. >> 3dmuseum.org



FUN

Still Life, With Test Tube

The dearth of well-rounded scientific characters in the arts and popular culture provided one inspiration for LabLit. Jennifer Rohn, a London-based microbiology Ph.D., edits the Web magazine and writes some of the content. The title refers to realistic fiction about scientists at work and to Rohn's hope to shed light on “a largely unknown or obscure world ... the culture of science.”

To illuminate that world, Rohn posts everything from reviews of science-themed plays and novels to a profile of an ex-Massachusetts Institute of Technology mathematician whose company offers advice to screenwriters. In one “Lab Rats” feature, a postdoc writes up his anecdotal evidence that “My specialty is neuroscience” isn't such a bad a pickup line. The LabLit List tallies movies, books, plays, and TV shows that pass the reality test. It's longer than you might expect and includes works by writers such as Tom Stoppard and Barbara Kingsolver. >> www.lablit.com

Send site suggestions to >> netwatch@aaas.org

Archive: www.sciencemag.org/netwatch

Get the experts behind you.



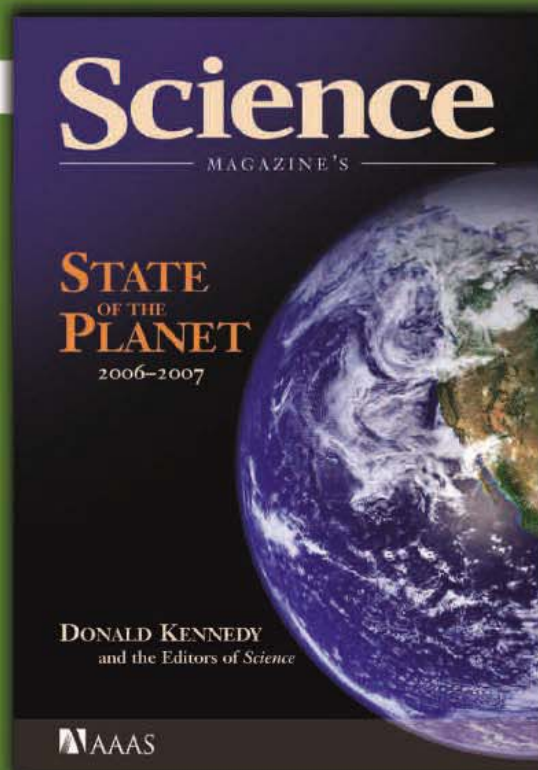
www.ScienceCareers.org

- Search Jobs
- Next Wave — now part of
ScienceCareers.org
- Job Alerts
- Resume/CV Database
- Career Forum
- Career Advice
- Meetings and Announcements
- Graduate Programs

*All of the features on
ScienceCareers.org are
FREE to job seekers.*

ScienceCareers.org

We know science



Science Magazine's
State of the Planet
2006-2007

Donald Kennedy, Editor-in-Chief,
and the Editors of *Science*
The American Association for
the Advancement of Science

**The most authoritative voice
in American science, *Science* magazine,
brings you current knowledge on
the most pressing environmental
challenges, from population growth to
climate change to biodiversity loss.**

COMPREHENSIVE • CLEAR • ACCESSIBLE

 **ISLANDPRESS**

Science
AAAS

islandpress.org

Tambora caldera.

LOST KINGDOM FOUND?

A team of volcanologists claims to have rediscovered the lost kingdom of Tambora. In April 1815, a volcanic eruption on the Indonesian island of Sumbawa buried the kingdom and resulted in the deaths of some 90,000 people. The event, which generated an extended episode of global cooling, still ranks as the largest and deadliest eruption in recorded history.

In 2004, a team led by Haraldur Sigurdsson of the University of Rhode Island (URI), Narragansett, excavated a wooden house buried below a 3-meter-deep gully in the volcanic deposits. There they found the bones of two adults as well as artifacts including bronze bowls and ceramic pots. Team member Lewis Abrams, a geophysicist at the University of North Carolina, Wilmington, says the house was clearly destroyed by the eruption, as evidenced by the finding of melted glass and carbonized wood beams. Sigurdsson says this site must be Tambora, which was known throughout the East Indies for its honey and wood products, because no other sites in the vicinity have yielded significant artifacts.

The team plans to return next year, and Sigurdsson hopes to unearth a palace he believes is buried there. But some researchers question the magnitude of the find. Roland Fletcher, an archaeologist at the University of Sydney in Australia, says he doubts that the community was powerful enough to boast a palace. URI announced the discovery last week; a spokesperson says the team had delayed going public due to an agreement with *National Geographic*.

Stars in the Head

A Japanese astronomer wants you to ponder the heavens even as you engage in earthier activities. His idea: astronomical toilet paper. Every 70 centimeters, the paper tells, with pictures and text, of the formation, evolution, and death of a star. "By reading this toilet paper, I'm hoping people will realize they are part of the universe and possibly develop an interest in astronomy," says its inventor, University of Tokyo Ph.D. candidate Masaaki Hiramatsu. Over the past year, observatories and science museums have sold 13,000 rolls at \$2.25 apiece (see www.tenpla.net/atp).

Hiramatsu hopes to extend his market by playing to the intense Japanese interest in astrology: His next roll will feature "interesting heavenly objects in the vicinity of the zodiac constellations."



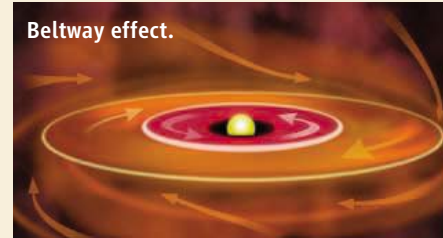
CREDITS (TOP TO BOTTOM): HARALDUR SIGURDSSON; BILL SAXTON/NRAO/AUI/NSEF; ATP

Dueling Space Disks

Like leaves in a whirlpool, planets around a star always orbit in the same direction. Or so astronomers thought. Now they've discovered two distinct disks of gas rotating in opposite directions around a gestating star 500 light-years away.

Because planets might arise from each gas disk, the unique system could theoretically spawn two sets of planets orbiting in opposite directions, says Anthony Remijan of the National Radio Astronomy Observatory in Charlottesville, Virginia, who with Jan Hollis of NASA's Goddard Space Flight Center in Greenbelt, Maryland, reports the finding in a study to appear in the 1 April *Astrophysical Journal*. But theorist Richard Lovelace of Cornell University says that's unlikely because strong shearing motions between the disks may cancel out the spins and force the gas to fall onto the star in less than a million years—probably not enough time for big planets to assemble.

Beltway effect.



THE "MYTH" OF THE BIASED DOC

"Physician [racial] bias" is often blamed for disparities between the health care of blacks and whites in the United States. But far more important is the fact that blacks and whites live in different areas and so are treated by different hospitals and doctors, according to health researchers speaking last month at the American Enterprise Institute in Washington, D.C.

For example, a 1996 Duke University study showing that whites were more likely than blacks to be treated aggressively for heart disease is often cited as evidence of physician bias. But Peter Bach, a pulmonologist at the Center for Medicare and Medicaid Services in Baltimore, Maryland, said most of the whites in the study had private practice physicians whereas the blacks were in community health plans—so the discrepancy had more to do with the type of providers than with racial bias. Bach also said a survey of 84,000 U.S. primary care physicians showed that only 20% of doctors handle 80% of black patients. Doctors in that 20%, he said, are less likely to be board certified, and they are more likely to practice in low-income areas and to be black themselves.

Brian Smedley, director of a 2002 Institute of Medicine report on health disparities, said physician bias cannot be discounted and cited studies showing that doctors presented with hypothetical cases may make different diagnoses depending on a patient's race. But lawyer Jonathan Klick of Florida State University in Tallahassee, author, with psychiatrist Sally Satel, of a new book, *The Health Disparities Myth*, said such studies don't reflect real life: "When whites and blacks see the same doctors in the same hospitals in the same areas, they get the same care."

Rapid decline on
Easter Island

1360

Prize fever to
hit NSF?

1363

PROLIFERATION

Last-Minute Nuclear Deal Has Long-Term Repercussions

NEW DELHI—The watershed agreement announced here last week by U.S. President George W. Bush and Indian Prime Minister Manmohan Singh rewrites the rules of the nuclear game. It would allow India to import nuclear technology and fuel to meet rising energy needs; in exchange, India—a nuclear weapons state that has long refused to sign the Nuclear Nonproliferation Treaty (NPT)—

Science and Technology Commission with a \$60 million war chest will fund projects in biotechnology and other areas. India has committed to taking two U.S. payloads, including a mineral mapper, on its first moon mission, scheduled for 2008. And a new \$100 million, 3-year initiative will support agricultural research exchanges to nurture what Bush hopes will be a “second green revolution.”



Atomic bonding. Bush and Singh have anchored their new “strategic partnership” on the nuclear pact.

would open a majority of its nuclear power plants to international inspections. Although India has earned respect for keeping a lid on its nuclear secrets, the U.S. invitation to trade with the nuclear club is something new—and it will likely spur other nations to seek concessions.

But the agreement is far from complete. In the coming weeks, Congress will scrutinize the fine print before deciding whether to make the changes in U.S. law needed to bring about a sea change in nonproliferation policy. The outlook is uncertain. Legislators praise the White House for strengthening ties with India, an emerging power and rival to China. But one big hurdle remains: The Bush Administration must convince Congress that the momentous agreement would make the world safer.

Lost in the hullabaloo over nuclear power is another set of agreements signed last week that will result in a significant expansion of bilateral research cooperation. The new

All the drama, however, centered on the nuclear accord, which Bush and Singh had agreed to in principle last July. Filling in the details proved difficult, especially on a provision that India segregate its nuclear program into two categories: civilian facilities open to international inspection and nuclear trade, and military installations off limits to both. Negotiations over the separation plan grew tense last December, when India put all R&D facilities, including its prototype fast breeder reactors, which run on plutonium, and CIRUS, a reactor in Mumbai presumed to have produced plutonium for weapons, on the military list (*Science*, 20 January, p. 318). In an interview with *Science* last month, Indian atomic chief Anil Kakodkar said that the U.S. desire to see the breeders brought under safeguards amounted to “changing the goalposts” and vowed that India would not open up more facilities to inspections (*Science*, 10 February, p. 765).

Negotiations went down to the wire, with the sides talking through the night of Bush’s arrival in New Delhi on 1 March. Morning light saw a deal in which India would put 14 of 22 planned or existing nuclear power reactors on the civilian list—leaving eight to use for military plutonium and tritium production, if it so desired. India has tagged all other facilities as military and retains the right to decide which future indigenous reactors to place under safeguards, although all reactors imported from now on would be subject to inspections. In the end, India made two key concessions: The “India-specific” safeguards, yet to be negotiated, would last in perpetuity—as long as countries do not withhold nuclear fuel. Singh told Parliament on 7 March that India would shut down CIRUS in 2010 and relocate Apsara, a light-water reactor, for safeguarding.

Indian scientists praise the deal and their resolute negotiators. “It’s a fantastic achievement,” says nuclear scientist V. S. Ramamurthy, secretary of the Department of Science and Technology. He adds that Kakodkar prevailed “against incredible odds.” Kakodkar too is pleased: “I am convinced this [agreement] is the practical way to move forward.”

U.S. nonproliferation analysts, meanwhile, have their knives out. “The Bush Administration is sacrificing or selling out on what until this day have been some core U.S. nonproliferation values,” argues Daryl Kimball, executive director of the Arms Control Association, based in Washington, D.C. He and others say U.S. officials caved in. “We probably could have put more restraints on the fast breeder reactor program, but Bush stopped the negotiations,” says Stephen Cohen, a senior fellow of the Brookings Institution and member of the U.S. National Academies’ Committee on International Security and Arms Control.

Both sides agree that the deal places no constraints on India’s nuclear weapons program. Even though India would sacrifice about a third of its warhead plutonium production if it closes CIRUS, it could erase that deficit by reprocessing plutonium in spent fuel from nonsafeguarded power reactors. This fuel currently contains about 9 metric tons of plutonium, says Kimball, enough for hundreds of bombs. But India could not convert it to weapons use easily: “They haven’t got the capability to reprocess that much plutonium unless they build major new plants,” notes Matthew Bunn, a nonproliferation expert at Harvard University.

There’s another concern: India has scant domestic uranium resources, and lifting the ▶

CREDIT: P. BAGLA/SCIENCE



What happened at Angkor Wat?

1364



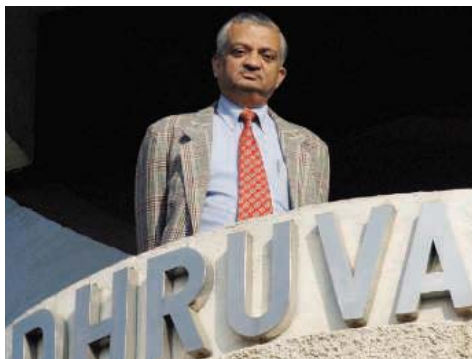
Samuel Bodman's big challenge

1369



Speciation without separation

1372



ban on uranium sales “could indirectly assist India’s military program” by freeing up more uranium, argues Kimball. Others doubt that India will seek to greatly expand its arsenal. The pact “should not be seen as a ploy to pro-

Drove a hard bargain. Indian scientists credit Anil Kakodkar with keeping breeder reactors off the table.

duce more and more fissile material for weapons. Getting access to cheaper uranium for energy production is the main driver,” says T. S. Gopi Rethinaraj, an arms-control expert at the National University of Singapore. Cohen worries that the deal could further devalue the NPT, which is already “severely damaged” by the defiant actions of Iran and North Korea.

U.S. legislators are waiting to see the details of the pact in a bill being drafted by the Administration. Before U.S. companies can dive into the Indian nuclear energy market, Congress must approve that bill and amend a 1978 nonproliferation law. Senator Joseph Biden of Delaware, a key Democrat on the panel that will vet the

agreement, wants the Administration to show that the deal will not help India evade NPT restrictions or create a “double standard” that will encourage other countries to do so. Despite such misgivings, many analysts anticipate that Congress will give the pact a thumbs-up. “Shutting down CIRUS will help,” Rethinaraj says.

Congressional approval would likely tumble a row of nuclear dominoes. For one, it would prompt the 45-nation Nuclear Suppliers Group to alter its rules, which for 30 years have prevented members from selling nuclear technology to India. It would also give a green light to India and France to implement a bilateral nuclear deal inked last month. Other nuclear suitors for Indian contracts would soon follow.

—RICHARD STONE AND PALLAVA BAGLA

With reporting by Katherine Unger in Washington, D.C.

SOLAR PHYSICS

The Sun's Churning Innards Foretell More Solar Storms

Astronauts, power grid operators, and satellite managers had better watch out in 2012, a group of solar physicists warns. Drawing on their computer simulation of the circulation in the sun's interior, researchers at the National Center for Atmospheric Research (NCAR) predict that the next peak in sunspots will come a little late but will be far bigger than the last peak—bigger, in fact, than all but one of the 12 solar maxima since 1880. The accompanying solar storms could play havoc with satellite communications and threaten space station astronauts.

The key to predicting solar activity years ahead, according to solar physicists Mausumi Dikpati, Peter Gilman, and Giuliana de Toma, is including data from enough past sunspot cycles. Every 11 years, the sun's dark spots and accompanying flares wax and wane. Predictions based on just the present strength of the magnetic field near the sun's poles—that is, the lingering remnants of the previous cycle's sunspots—call for an especially weak sunspot cycle coming up.

But the NCAR group, located in Boulder, Colorado, thought that several past cycles might influence the coming one. When they ran their new model of the solar interior, they fed it with

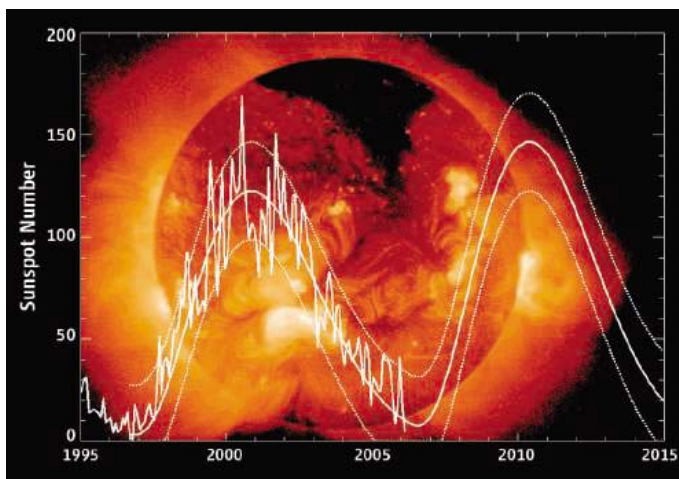
observations since 1880 to see how past cycles might assert their influence. They found that it takes a good 20 years for the magnetic remnants of past sunspots to recirculate deep into the interior, where the twisting action of the sun's rota-

50% stronger than the last solar cycle,” she told a media teleconference this week. The next cycle will begin 6 to 12 months later than average, in late 2007 or early 2008, according to the model, and will peak in 2012.

The model-based prediction “is exciting stuff, the first new thing to come along” in decades, says Ernest Hildner, the recently retired director of the Space Environment Center in Boulder, the federal group charged with forecasting solar activity. It's especially exhilarating because “it finally answers the 150-year-old question: What causes the sunspot cycle?” solar astronomer David Hathaway of NASA's Marshall Space Flight Center in Huntsville, Alabama, told the teleconference. New work by Hathaway and colleagues supports the NCAR group's findings.

If the sun is indeed gearing up for an especially active maximum, managers of everything from the Global Positioning System (which solar storms can disrupt) to low-orbiting satellites (which storms can drag down) could begin taking the threat into account. But as exciting as the forecast is, promising techniques for predicting the future have failed before, Hildner points out: “You still have to wait and see.”

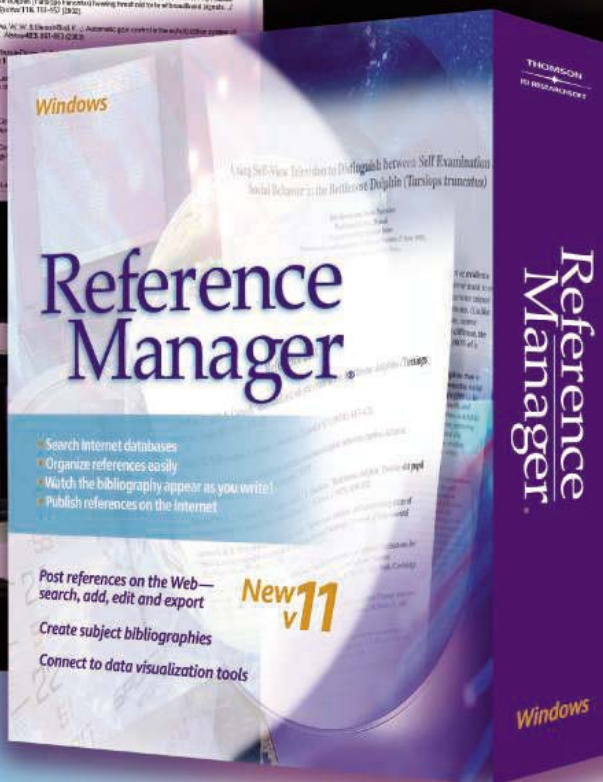
—RICHARD A. KERR



Onward and upward. Solar physicists are predicting that the next peak in sunspots and other disruptive solar activity will exceed the previous solar max (squiggly line) because the previous three peaks contribute.

tion amplifies them, and to rise back to the surface near the equator as the next cycle's sunspots. The model did an impressively accurate job “hindcasting” the size and timing of past cycles. That track record made Dikpati confident that “the next solar cycle will be 30% to

BIBLIOGRAPHY CENTRAL



Your High-Tech Command and Control Center for References.

Introducing Reference Manager 11—a powerful upgrade to the bibliographic software that streamlines research, writing and publishing.

Reference Manager has served corporate, government and academic researchers worldwide for over 20 years. And now version 11 delivers new ways to share and view your reference collections: Post your databases to the Web. Collaborate with colleagues over a network. Link to full text pdf files.

These are just some of the powerful features that await you. Reference Manager is your command and control center for all things reference related.

What's new in v11:

- Publish Reference Manager databases to the Web or intranet
- Create subject bibliographies instantly
- Access new and updated content files at www.refman.com
- Share traveling libraries with colleagues
- Connect to data visualization tools

Put innovation into action. Order or upgrade today. Available for Windows in a single-user and network edition. Phone: 800-722-1227 • 760-438-5526 • info@isiresearchsoft.com

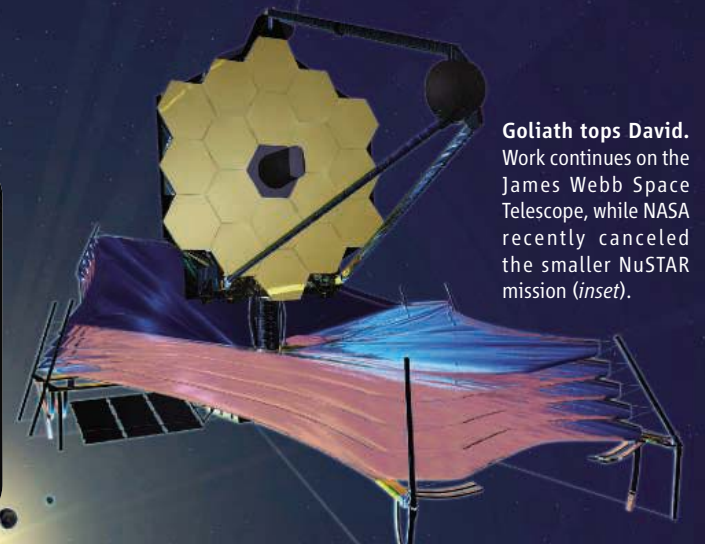
Download a Free Demo Today
www.refman.com

THOMSON
ISI RESEARCHSOFT

© Copyright 2004 Thomson. Reference Manager is a registered trademark of Thomson. All other trademarks are the property of their respective companies.



Goliath tops David. Work continues on the James Webb Space Telescope, while NASA recently canceled the smaller NuSTAR mission (inset).



SPACE SCIENCE

NASA Agrees to Review What's On the Chopping Block

NASA's science chief has offered space and earth scientists half a loaf in response to withering complaints about cuts in the agency's proposed 2007 budget. Even so, it's a better offer than the one NASA Administrator Michael Griffin made last week to life and microgravity scientists: He announced a new timetable for finishing the international space station that will leave almost no room in the next 4 years for U.S. research projects.

Testifying before the House Science Committee, NASA's Mary Cleave pledged to rethink the space agency's proposed cuts after legislators and researchers complained about their impact on young researchers and smaller missions. (One of those missions, to two asteroids, was canceled the same day.) Cleave said there was a catch, however: Shifting money back into those areas could spell doom for flagship spacecraft now under development for astronomers, earth scientists, and solar physicists. But senior researchers at the hearing said they would be willing to consider such a tradeoff.

That same afternoon, Griffin announced that NASA will not pursue most of the planned research activity on the space station before the orbiting base is complete in 2010. The change results from a cost- and timesaving reduction in the number of space shuttle flights needed to boost the hardware into space—missions that would have allowed astronauts to carry out a host of experiments. Speaking at a press conference at Kennedy Space Center in Florida with the leaders of other space agencies, Griffin declined to discuss the U.S. research agenda after 2010, but it appears bleak. Russian Federal Space Agency chief Anatoly Perminov says NASA will provide the Russian section of the station with additional electrical power.

NASA's cancellation of the Dawn mission,

awaiting a June launch to the Vesta and Ceres asteroids, drew a swift response from scientists. "I was shocked that after testifying before your committee yesterday, the first thing Dr. Mary Cleave did upon returning to her office was to cancel the Dawn Discovery mission," wrote Mark Sykes, director of the Planetary Science Institute in Tucson, Arizona, to committee chair Representative Sherwood Boehlert (R-NY). Although Sykes maintains that critical technical issues have been resolved, Cleave told *Science* that a recent review found expected cost overruns exceeding 20% and the project facing more than a 1-year delay. Her office was in the process of notifying scientists before the hearing, she noted, but legislators did not ask her about the mission.

At the hearing, both Republican and Democratic legislators expressed outrage at cuts, proposed last month in NASA's 2007 budget, to a host of robotic science missions as well as to biology on the space station. A panel of scientists also lambasted NASA for proposing to reduce research grants, typically 3-year awards of less than \$100,000, and small missions. The cuts "would be disproportionately felt by the younger members of the community," warned Joseph Taylor, a physicist at Princeton University. "Without research support to pay for their time, this group will be forced to turn to other fields—or leave the sciences altogether."

Pressed by Boehlert to offer an alternative, Taylor pointed to the servicing mission for the Hubble Space Telescope and to the James Webb Space Telescope. The Webb telescope remains \$1 billion over budget, despite recent attempts to cut back its costs, and the Hubble mission is the second largest effort within NASA's astronomy plan. Taylor said he would consider sacrificing one of those to rescue grants and small missions. Astrophysicist ▶

Knock Hockey

The heat was on a 12-person National Research Council committee last week as it tackled the politically charged debate over how scientists have gauged temperatures from the past millennium or two. Chair Gerald North of Texas A&M University in College Station kept the audience on a tight leash, including principal protagonists Michael Mann of Pennsylvania State University in State College and his critics, Stephen McIntyre of the University of Toronto, Canada, and Ross McKittrick of the University of Guelph, Canada. House Science Committee Chair Representative Sherwood Boehlert (R-NY) had requested the study in the wake of attacks on Mann's "hockey stick" temperature curve showing an abrupt, presumably human-induced warming over the last century (*Science*, 1 July 2005, p. 31).

Mann made himself scarce throughout the proceedings, even abruptly departing as McIntyre stood to make a final comment. Others, however, had already provided independent support for temperature trends resembling Mann's, and Mann himself pointed out that he had sworn off the criticized analytical method years ago. The committee has promised a report on the science of millennial temperatures in June.

—RICHARD A. KERR

Species Law Backed

Thousands of biologists and the Union of Concerned Scientists are asking the U.S. Senate to heed "sound scientific principles" and preserve the Endangered Species Act (ESA). Last September, the House narrowly passed a bill that would overhaul the ESA, taking private economic interests into account when deciding which species to protect and how (*Science*, 30 September 2005, p. 2150). Now it's the Senate's turn to weigh the proposed changes.

"There is a great deal right with the Endangered Species Act," says conservation biologist Stuart Pimm of Duke University in Durham, North Carolina. Pimm is a leader of the effort, which has garnered 5738 biologists supporting a letter calling for a "strengthened" ESA that is fully funded and implemented. They say the ESA is "the ultimate safety net in our life-support system." Opponents say the ESA hinders development and is ineffective at species recovery. But supporters say that less than 1% of listed species have gone extinct, as opposed to 10% of species waiting to be listed. Senate legislation is expected to be introduced in the next few weeks.

—KATHERINE UNGER

Fran Bagenal of the University of Colorado, Boulder, added that restoring money to those two areas would “justify a delay in flagships” such as the Solar Dynamics Observatory, to be launched in 2008 to examine solar variability.

Some flagship missions already have been delayed or canceled. A 2010 launch for NASA’s \$850 million Global Precipitation Measurement mission has been stretched to 2013, and NASA has twice canceled plans for a major spacecraft to study Jupiter’s moon Europa. “This marks the first time in 4 decades

when we have no solar system flagship at all,” noted Wes Huntress, a geophysicist at the Carnegie Institution of Washington and a former NASA space science chief.

That somber situation might look good to life and microgravity scientists, who would be largely shut out over the next 4 years of space station construction and perhaps longer. Before the Columbia disaster, NASA planned 28 shuttle flights, many carrying scientific equipment to and from the facility. Now the number stands at 16. “It is the same

space station,” Griffin said. “But we are largely deferring utilization.”

In good news for the station’s partners, NASA agreed to launch the European and Japanese scientific modules earlier than planned so that non-U.S.-based research could begin in 2008. In exchange for not launching a Russian power module, NASA also will funnel power to the Russian portion of the station. A portion of that power was once designated for experiments aboard the U.S. lab module.

—ANDREW LAWLER



Monumental price. The building of immense statues helped deforest Easter Island.

ARCHAEOLOGY

Dates Revise Easter Island History

When Dutch explorers landed on a remote Pacific island a few days after Easter Day 1722, they found eerie carvings of huge stone statues, a barren landscape, and natives with dwindling supplies of food and wood. Ever since, Easter Island, now known as Rapa Nui, has been considered a textbook example of a once-thriving culture that doomed itself by destroying its own fragile habitat.

Now a paper appearing online in *Science* this week (www.sciencemag.org/cgi/content/abstract/1121879) revises that story, implying that construction of the statues and degradation of the environment both began almost immediately after humans set foot on the island. New radiocarbon dates and a reanalysis of old ones put humans first on Rapa Nui at about 1200 C.E., 400 to 800 years later than previously estimated and just 100 years before the palm trees begin to vanish. “You don’t have this Garden of Eden period for 400 to 800 years,” says lead author Terry Hunt of the University of Hawaii, Manoa. “Instead, they have an immediate impact. The destruction-of-the-environment story is on steroids.”

Other researchers, such as archaeologist Patrick Kirch of the University of California, Berkeley, agree that the new dates raise serious questions about whether the Easter Island residents ever lived sustainably on the island. But some question the team’s dismissal of some older radiocarbon dates. “I’m not convinced they made the case for a later occupation,” says Kirch.

By the time the Dutch landed, the Easter Islanders—and the Polynesian rats that had stowed away in their canoes—had destroyed most of the subtropical trees and giant palms that provided wood for canoes and for transporting statues, as well as fuel for fire. The settlers also had wiped out many species of birds. But most researchers thought that there was a period during which the islanders had lived in harmony with the environment, before they taxed their resources with a complex culture and statue building. Earlier radiocarbon dates seemed to support that idea, suggesting colonization between 800 C.E. and 1200 C.E. and ecological collapse, as indicated by the disappearance of

palm trees, starting at least 400 years later.

Hunt and co-author Carl Lipo of California State University, Long Beach, took eight samples of wood charcoal from the bottom of the oldest known archaeological site on the island, called Anakena. When they got radiocarbon dates that clustered at about 1200 C.E., Hunt at first assumed the dates were wrong and put them aside. But later he and Lipo decided to scrutinize all earlier dates from Anakena, to make sure they did not contain carbon from marine organisms or old wood, which can skew dates too old. After discarding what they considered unreliable dates, the pair found a high probability (50%) for the first human settlement starting just after 1200 C.E. The evidence does not rule out an occupation at 1000 C.E., but the probability is very low, says Hunt. The new dates are a “significant improvement” over the old ones, says radiocarbon-dating expert Tim Higham of Oxford University, U.K.

Although several researchers welcome the rigorous analysis of dates, not everyone agrees with the criteria the team used. “Some of his criteria are fair; others are not,” says zoologist David Steadman of the Florida Museum of Natural History in Gainesville, whose 1000 C.E. dates for Anakena were left in the pair’s analysis.

The new results are in keeping with a trend in the past decade toward later dates for colonization of some of the outermost Pacific islands. “This is an important paper, because it is part of a revision on the chronology of the Pacific that shows there is a big gap between settling west Polynesia [e.g., Samoa] and the marginal areas of south and east Polynesia,” such as New Zealand, says archaeologist Atholl Anderson of the Australian National University in Canberra.

The new dates won’t be the final word on the first colonization of Easter Island, researchers say. “The chances you’re going to find the first campfire are pretty slim,” says Steadman. “It will enliven the debate and force everybody to take a critical look at their dates.”

—ANN GIBBONS

CREDIT: TERRY HUNT

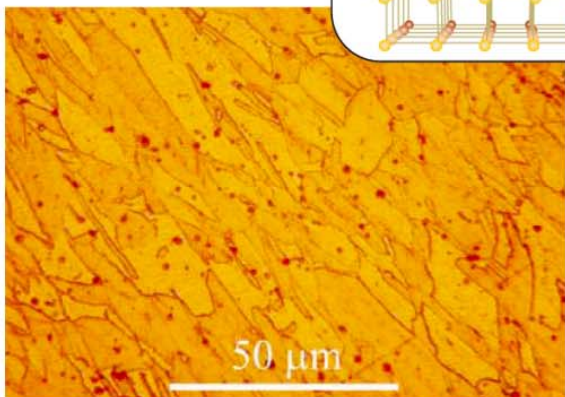
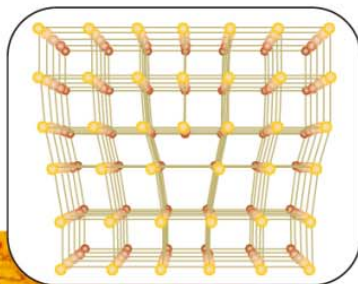
SOLID STATE PHYSICS

Theory of Shock Waves Clears Up the Puzzling Graininess of Crystals

Ideally, a crystalline material ought to be a realm of perfect atomic order. Real-world crystals, however, consist of small grains and cells that lock together higgledy-piggledy, like so many stones in a wall. For decades, physicists have struggled to explain where the boundaries delineating grains and cells come from. Now theorists have shown how these walls form out of stringy imperfections in the crystal called dislocations.

The advance could lead to a deeper understanding of the grainy character of crystals—which determines their hardness and other mechanical properties—and give engineers a new tool for analyzing the wear of metal parts. “If the theory is correct, it’s very important,” says Michael Zaiser, a theorist at the University of Edinburgh, U.K.

Within a crystal, atoms snuggle into orderly planes like checkers filling a checkerboard, and the planes stack to form a regular three-dimensional (3D) structure. A real crystal also contains many threadlike dislocations, which arise when, for



Mosaic. Within the orderly arrangement of atoms in a crystal, 1-dimensional dislocations (*inset*) coalesce to form the 2-dimensional boundaries of grains, like these in copper.

example, one plane of atoms wedges partway between two others. The edge of the extra plane then creates a 1D irregularity running through the crystal. These 1D dislocations coalesce to form 2D walls that separate the grains and cells.

Physicists have tried to simulate that process in computer models that track the motion of each atom. But those simulations work only for idealized 2D crystals one plane of atoms thick, Zaiser says. Simulating a 3D crystal is “one of the most computationally intense simulations known to man,” he says.

So Surachate Limkumnerd and James Sethna of Cornell University took a different tack. They described the atoms with a continuous “tensor field” that quantified how far and in which direction each one had been displaced from its position in the ideal crystal. A tensor field roughly resembles the arrow-filled weather maps on which forecasters plot wind directions and speeds. Each dislocation corresponds to a tornadolike eddy within the field.

Using a computer, the researchers then calculated how, starting from random variations, the tensor field interacts with itself and evolves. Wherever dislocations accumulate, stress within the crystal can jump significantly from one side of the accumulation to the other. The “stress jump” attracts more dislocations in a runaway process that mathematically resembles the

formation of a shock wave. Ultimately, the dislocations squeeze into sharply defined walls, the researchers report in a paper to be published in *Physical Review Letters*.

Other physicists had attempted continuum models as much as 50 years ago, but all failed to produce walls. Their mathematical approaches led to vexing infinities that the tensor field avoids, Sethna says. Even so, Sethna and Limkumnerd had to employ special computational tools to deal with the slightly less troublesome jumps.

The model is an important first step, says Stefano Zapperi, a theorist at the National Institute for the Physics of Matter in Rome, Italy, but it doesn’t yet account for some key ingredients. For example, physicists know that grains, which form when a crystal solidifies, generally subdivide into cells only when a crystal is stressed. In the model, the dividing happens spontaneously. “The key would be to put something more realistic into it and see if you can make predictions that you can test experimentally,” Zapperi says.

Sethna agrees and says that, for example, including the tendency of dislocations to tangle might impede the spontaneous division of grains. Still, at this stage Sethna is encouraged that he and Limkumnerd have managed just to hit a wall.

—ADRIAN CHO

White House Sticks to The Basics

High-energy physics is certainly basic science. But it’s not what the Bush Administration is promoting when it talks about doubling basic research in the physical sciences over 10 years at three federal agencies. “There are exciting opportunities in high-energy physics, ... but these are not emphasized in the ACI [American Competitiveness Initiative],” presidential science adviser John Marburger told the High Energy Physics Advisory Panel for the Department of Energy’s Office of Science, which is included in the ACI (*Science*, 17 February, p. 929). ACI focuses on nanotechnology, high-end computing, and basic energy sciences that promise a direct technological payoff, Marburger explained. University of Chicago physicist Melvyn Shochet, the panel’s chair, called Marburger’s words “sobering ... and honest.”

—ADRIAN CHO

Slammer Awaits Science Terrorists

Six members of an animal-rights group will be sentenced in June after a federal jury in Trenton, New Jersey, last week found them guilty of stalking and harassment. Their target was Huntingdon Life Sciences (HLS), a British animal testing company that moved most of its operations to the United States several years ago to escape the group’s activities. Called Stop Huntingdon Animal Cruelty, the group’s now-defunct U.S. Web site had listed “terror tactics” and personal information about HLS employees.

The case is the first to be brought under a 2002 federal law that covers “animal enterprise terrorism.” Individual charges carry maximum sentences ranging from 3 to 5 years and \$250,000 fines.

—CONSTANCE HOLDEN

Glug, Glug, Go U.S. Subs

The National Oceanic and Atmospheric Administration (NOAA) is trying to keep open five undersea research facilities caught in a budget squeeze this year. The facilities are run by several East Coast universities and offer diving and robotic equipment needed for studies including deep-sea fisheries research and coral science. Last fall, Congress cut \$8 million from NOAA’s \$12 million National Undersea Research Program, which also supports two West Coast centers. NOAA’s Barbara Moore says internal money could keep at least one center open. And the White House has asked Congress to restore the funds for 2007.

—ELI KINTISCH

You could be next

Yes, it *can* happen to you:

If you're making inroads in neurobiology research and you've received your M.D. or Ph.D. within the last 10 years, the Eppendorf & *Science* Prize for Neurobiology has been created for YOU!

**\$25,000
Prize**

This annual research prize recognizes accomplishments in neurobiology research based on methods of molecular and cell biology. The winner and finalists are selected by a committee of independent scientists, chaired by the Editor-in-Chief of *Science*. Past winners include post-doctoral scholars and assistant professors.

If you're selected as next year's winner, you will receive \$25,000, have your work published in the prestigious journal *Science* and be invited to visit Eppendorf in Hamburg, Germany.

What are you waiting for? Enter your research for consideration!

Deadline for entries:

June 15, 2006

For more information:

www.eppendorf.com/prize

www.eppendorfsceinceprize.org

"This is a unique award because it recognizes young neuroscientists for their work and their ability to communicate with a broad audience. I was surprised and honored to be a winner."

Miriam B. Goodman, Ph.D.
Assistant Professor
Stanford University
School of Medicine
2004 Winner



**eppendorf
& Science**
**PRIZE FOR
NEUROBIOLOGY**

UNIVERSITIES

Austria's Bid for an Instant MIT Meets Opposition From Researchers

A plan to create a new elite university in Austria that once had the backing of politicians and top scientists has lost the support of many prominent researchers. On 2 March, the Austrian cabinet approved a law that will establish the Austrian Institute of Science and Technology, with \$545 million in funding over 10 years. But early backers of a plan to draw world-class researchers to a technology-focused graduate school have withdrawn their support over what they say are overly political decisions on the new institute's location and direction.

The bandwagon to create an institution may be "unstoppable," says molecular geneticist Barry Dickson of the Research Institute of Molecular Pathology in Vienna. But without more input from scientists, he says, the school has no chance of reaching the world's top ranks. "It's a completely missed opportunity," he says.

Austria is the latest country to attempt to boost its research profile by creating a new institution on the model of the Massachusetts Institute of Technology in Cambridge.



Under pressure. Scientists say Austrian education minister Elisabeth Gehring's plans for an elite university are driven by politics.

Germany and France have also launched elite funding schemes, and politicians in the European Union are keen to create a European Institute of Technology (*Science*, 3 March, p. 1227).

Many European universities have a sprinkling of world-class research groups, says physicist Anton Zeilinger of the University of Vienna, but none has the critical mass of

America's top institutions. Two years ago, Zeilinger proposed starting a new graduate-level institution, which he hoped would provide healthy competition for Austria's existing universities, he says.

But scientists and politicians often have different goals. Those differences came to a head in mid-February when the government announced that the proposed school would be located in a small village 45 minutes outside Vienna on the campus of a psychiatric hospital. Critics say this ignored two other locations that scientists preferred and that were within the city, closer to existing research institutes. Dickson and others say political considerations weighed in favor of Gugging, where the local governor is a political ally of the national government.

The problems go beyond the location, Zeilinger says. It is crucial, he says, to bring in independent international experts to guide the university's first steps. But the steering committee members announced last week are almost exclusively Austrian, and most have reason to protect their current universities and institutes, Zeilinger says: "It's like asking the heads of Skoda and Mitsubishi to create a new Mercedes."

International experts will guide the new school's scientific direction, says Jürgen Mittelstrass, head of Austria's Science Council and a professor of philosophy at the University of Konstanz in Germany, who will head the national steering committee. He agrees that the Gugging site "is not optimal." But after national elections this fall, he says, it may be possible to develop a second campus nearer the city.

—GRETCHEN VOGEL

U.S. SCIENCE POLICY

Legislator Wants NSF to Offer \$1 Billion Energy Prize

Could a \$1 billion prize help end the U.S. addiction to foreign oil? Representative Frank Wolf (R-VA) thinks it might. Last week, he urged the National Science Foundation (NSF) to raise such a prodigious amount from private sources and then give it to scientists offering ideas on how to make the United States energy independent.

"Why not challenge industry and private foundations to come up with \$1 billion?" Wolf asked NSF Director Arden Bement at a 2 March hearing on the agency's 2007 budget request. Singling out the billions for public health research from the Bill and Melinda Gates Foundation as an example of how philanthropists are eager to support technological solutions to societal needs, he speculated that many organizations would be willing to donate to a program run by NSF's world-class system of merit review. "I think you should try to raise the money by the end of year. ... And I'll put some language into your bill"

that would allow NSF to move forward, he said.

The audacious proposal may force modifications in a plan NSF has been developing in conjunction with the National Academies on earlier orders from Wolf's spending panel, which has jurisdiction over NSF and several other science agencies (*Science*, 2 December 2005, p. 1417). NSF has already criticized one draft of a proposal to stimulate innovative research, Bement told Wolf, and expects a second version in a few weeks. "Our plan was to inaugurate the program in 2007 and award the first prizes in 2008," Bement explained.

Without presuming any dollar amount, the academies' Stephen Merrill says that body's report examines "how to make a splash in terms



Jackpot. Representative Frank Wolf wants NSF to think big.

of selecting the topics, advertising it, and the ground rules for the competition. The idea is to induce a solution to a major problem by getting the community involved." Merrill says the academies' team was thinking "along the lines of an [Ansari] X Prize," the \$10 million for privately funded space travel won in 2004 by SpaceShipOne.

Admitting after the 3-hour hearing that he hadn't worked out the details, Wolf acknowledged that such a privately funded, government-run program would be unprecedented.

But he said that shouldn't deter NSF. When NSF Assistant Director Kathie Olsen suggested that "we need to talk to our lawyers to see what we are allowed to do," Wolf shot back, "I think you can [do it]." —JEFFREY MERVIS



The collapse of a great medieval city suggests that environmental miscalculations can spell doom for even the most highly engineered urban landscapes

The End of Angkor

SIEM REAP, CAMBODIA—Crouching in the bottom of a gully, Roland Fletcher traces with his finger the beveled edge of a pitted, grayish-red rock. The carved laterite block with a sloping face fits snugly in a groove in the block below. “It’s a fancy piece of work,” says Fletcher, an archaeologist at the University of Sydney, Australia. Centuries ago, the people of Angkor built immense sandstone palaces and temples on foundations of laterite, a spongy, iron-laden soil that hardens when exposed to air. In excavations begun last year, Fletcher’s team discovered that the half-meter-long block is just one piece of a dilapidated platform extending 20 meters underground in either direction. The platform appears to be the remnants of a massive spillway, possibly used to disperse floodwaters unleashed by monsoon rains. “Nobody had ever seen a structure of this kind here before,” Fletcher says.

The spillway helps resolve one debate, showing that the majestic waterworks of Angkor—a Khmer kingdom from the 9th to 15th centuries C.E. that at its height encompassed much of

modern-day Cambodia, central Thailand, and southern Vietnam—were designed for practical purposes as well as religious rituals. But this singular piece of medieval engineering may also offer clues to a more profound riddle—not because the spillway exists, but because it was destroyed.



Ever since Portuguese traders in the late 16th century described the lotus-shaped towers of Angkor Wat rising from the forest canopy, people have wondered why the once-gilded temple devoted to Vishnu—humanity’s largest religious monument—and the city connected with it were abandoned about 500 years ago. The list of suspects proposed so far includes marauding invaders, a religious

Beguiling. A once-gilded Angkor Wat tower.

change of heart, and geological uplift.

Now Fletcher and his colleagues have new evidence that the very grandeur of Angkor’s

complex plumbing, the lifeblood of the city, left it vulnerable to collapse. In a provocative new interpretation of Angkor’s demise, Fletcher, co-director of the Greater Angkor Project (GAP), a 5-year survey and excavation sponsored by the Australian Research Council, proposes that the trigger may have been a combination of rigid infrastructure, environmental degradation, and abrupt changes in monsoons. He and other scholars caution that the case is not closed. “It’s hard to put a finger on any one reason for the collapse,” says Charles Higham, an anthropologist at the University of Otago in Dunedin, New Zealand, whose startling finds at earlier Thai sites are illuminating the origins of Angkor (see p. 1366).

If the GAP team is right, Angkor—the most extensive city of its kind in the preindustrial world, with a population numbering in the hundreds of thousands in its heyday—would not be the first civilization unraveled by environmental change. For example, many archaeologists now hold that a series of devastating droughts doomed the Maya and their sprawling city-states on the Yucatán Peninsula between 800 and 900 C.E. Angkor’s downfall may be a cautionary tale for modern societies on the knife-edge of sustainability, such as Bangladesh. “The lesson to learn from all of this,” says Higham, “is don’t abuse the environment.”



Waterworld. (Left) Angkor's ponds, canals, and reservoirs sustained a vast city and its grand temples. (Above, left to right) The monuments still impress, including heavenly apsaras at Angkor Wat; a statue of a god outside Angkor Thom; and giant faces smiling placidly from the towers of the Bayon temple.

Seeing the big picture

On a hazy January morning about 30 kilometers north of Siem Reap, the modern town near Angkor, Donald Cooney banks his ultralight plane hard right and heads toward a stand of trees a half-kilometer away. Soaring over forested lowland crisscrossed with waterways, rice paddies, and traditional wooden houses on stilts, some of the more stupendous Angkorian features are impossible to miss, including a gigantic 1000-year-old earthen reservoir called the West Baray, 2.2 kilometers wide and 8 kilometers long. Dozens of immense stone temples reflect Hindu cosmogony; the temples represent Mount Meru, the mythical home of Hindu gods, and the moats represent encircling oceans. Bas reliefs on sandstone facades depict everyday scenes—two men bent over a chessboard, for instance—as well as sublime visions such as the apsaras, alluring female dancers in elaborate headdresses who served as messengers between humans and the gods. Yet much of the kingdom remains inscrutable, like the giant faces that stare serenely from the towers of the Bayon in Angkor Thom, the walled heart of the kingdom.

Cooney, a pilot based in Knoxville, Tennessee, takes a hand off the control bar and gestures toward a thicket of banyan trees. “Do you see the temple?” he asks, his voice crackling over the headset. Even from 300 meters up, the umber towers of a walled temple complex built by Yashovarman I in the late 800s emerge from the canopy only when the aircraft is nearly on top of it. “It’s easy to see how so much of Angkor was hidden from view for so long,” he says.

Cooney’s flights have helped the 30-person GAP team chart new Angkorian features, such as canal earthworks that are easy to overlook on foot. “It’s ground-truthing from the air,” says Fletcher, who co-directs the \$700,000 project with Sydney colleagues Michael Barbetti and Daniel Penny, as well as Ros Borath—a deputy director general of the APSARA Authority, the Cambodian agency that manages

Angkor—and Christophe Pottier of the French Research School of the Far East (EFEO).

Although archaeologists have long marveled over Angkor’s sculptures and temples, the aerial views have been particularly revealing of the extensive waterworks that sustained them. In 1994, a radar snapshot from the Space Shuttle Endeavor espied eroded segments of the Great North Canal, which shunted water from the Puok River to two reservoirs. Then a few years later, archaeologist Elizabeth Moore of the University of London used radar to spot undiscovered Bronze Age and Iron Age settlement mounds at Angkor.

Some epic legwork has also revealed the transformation the medieval Khmers wrought on the landscape. In remote sensing and ground surveys conducted on foot in the 1990s, Pottier, an architect and archaeologist, mapped hundreds of hitherto unknown house mounds and shrines clustered around artificial ponds, called water tanks.

For Pottier, the surveys were an epiphany. “The people of Angkor changed everything

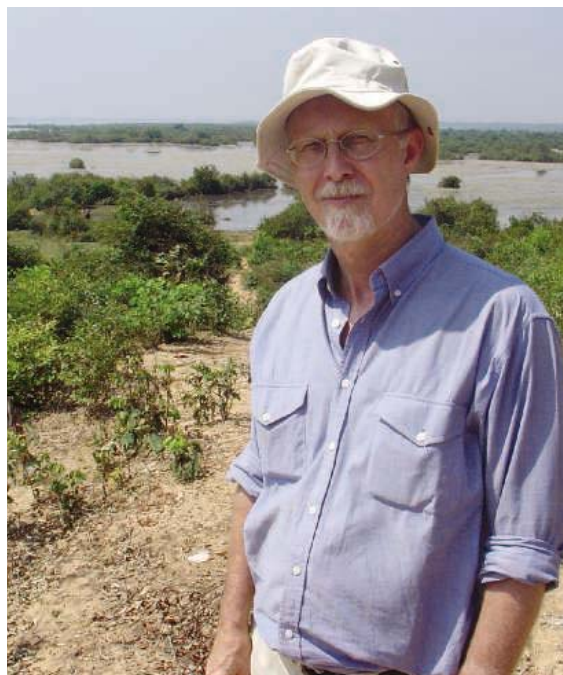
about the landscape,” he says. “It’s very difficult to distinguish what is natural and what is not.”

That transformation was extensive, as Fletcher, a specialist on the growth and decline of settlements, and University of Sydney graduate student Damian Evans learned by scrutinizing NASA radar images commissioned by GAP. They found Angkorian dwellings and water tanks scattered across roughly 1000 square kilometers and connected by a skein of roads and canals, many now barely discernible.

The surveys also revealed the outlines of the ingenious water-management system, centered on three great reservoirs, or barays. A labyrinth of channels north of the barays and of the complexes of Angkor Thom and Angkor Wat diverted water from the Puok, Roluos, and Siem Reap rivers to the reservoirs (see map on p. 1367). The system “brought large amounts of water to a halt and then bled the water off into other channels as required,” explains Fletcher. Canals leading south and eastward from the barays dispersed the water across the landscape, for irrigation and to blunt seasonal flooding. This allowed the growth of a vast urban complex: a low-density patchwork of homes, temples, and rice paddies.

Angkor’s growth, and the king’s power, depended on sustained rice yields. “If the king runs short of rice, he’d have to go cap in hand to other Khmer lords in the kingdom,” says Fletcher. Reliable yields required ample water at the right times of year. Angkor’s water system, therefore, was the wellspring of power for its rulers.

Surprisingly—and frustratingly—the roughly 1200 inscriptions in Sanskrit and Khmer chiseled on Angkorian walls are mum on the water system. “They’re full of references to boundary stones and land ownership, but virtually silent on water issues and water rights,” says Higham. Apart from the inscriptions, not a single written Angkorian word has been recovered. The oldest inscribed palm leaves, a likely medium for records, date from the early 18th century.



Practical minded. Roland Fletcher, on the bank of the West Baray, argues that Angkor’s reservoirs were for irrigation and flood control, not just rituals.

Angkor's inscriptions also betray nothing of the kingdom's decline. By the 14th century, "we really don't know what's going on in Angkor," says Fletcher. Siamese annals recount how an army from a nearby kingdom seized Angkor in 1431. Why the city was ultimately abandoned is an enigma—although the consequences must have been devastating. "When a low-density city collapses," Fletcher says, "it takes out the entire region."

Angkor's past has remained mysterious in part because Cambodia's grim recent history deterred research here. Civil war, the brutal reign of the Khmer Rouge, and finally the invasion of Vietnamese forces turned Angkor into a no-go zone for nearly 20 years. Although the heritage park with the major monuments is safe for tourists, some terrain north of the barays still has landmines and unexploded ordnance. "You can't go bushwalking here," Fletcher says. Fortunately, the warring sides left Angkor largely untouched.

Then when Pottier reopened EFEO in 1992, the emphasis was on restoring the temples. Centuries of neglect had turned some complexes into tumbled ruins, whereas others required urgent measures to stabilize them or restore sandstone facades. More than 20 teams

from around the world are working here, says APSARA archaeologist So Peang. He points to masons repairing a 12th century causeway that bisects one of Angkor Wat's moats. "Many blocks have decayed. Rains wash away the sands," he says.

The vital repairs, not to mention efforts to interpret the structures and inscriptions, have conspired to keep attention riveted on the monuments. "Archaeologists here have tended to focus on what they can see," Fletcher says. "Imagine trying to learn about life in New York City by only examining its churches." As a result, says Pottier, "Huge parts of the site remain complete blanks."

For that reason, one can stumble upon hidden treasures. Walking on the bank of the East Baray, Fletcher spots a triangular, dark-gray object in the sandy grass. He picks up the palm-sized stone fragment and points to some squiggly lines. "It looks like old writing," he says. An EFEO expert later confirms that the inscription is from the reign of Yashovarman I. "So much here is just waiting to be discovered," Fletcher says.

Going with the flow

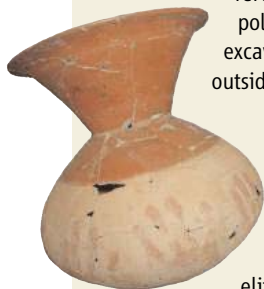
On the western edge of the Mebon, an artificial island in the middle of the West Baray, a tangle of grass and vines hides some laterite foundations. Seventy years ago, during the dry season, a villager looting the Mebon stumbled upon part of a gigantic bronze torso jutting from the muck near the foundations. He alerted an EFEO curator, explaining that the Buddha told him in a dream that he was buried in the Mebon and couldn't breathe. French excavations later unearthed the 2-meter-tall head and shoulders of a statue of Vishnu.

Beyond the baray, a swelling red sun is just meeting the horizon. "Imagine the rays of the setting sun glinting off Vishnu," says Fletcher, standing beside the remnants of the temple wall. Pressure from the reservoir's water column would have forced water through the base of the statue and out of Vishnu's navel. Pollen grains preserved in mud inside the temple show that lotus plants flourished in the pond gracing either side of a causeway leading from the temple to the statue.

A controversy has simmered over whether the magnificent Mebon and West Baray were brought into being solely to inspire awe. Some advocates of the purely ritual argument

Local Elites Cast New Light On Angkor's Rise

PHIMAI, THAILAND—In a square pit that could swallow a two-story house, a dozen skeletons are seeing the light of day for the first time in 20 centuries. Two adults have more than a dozen seashell bangles on each arm, and a third has a pair of marble bangles. In one corner, small painted clay pots contain infant bones. Above each skull, of adults and children alike, lies a single bivalve shell, probably representing fertility or rebirth, says anthropologist Charles Higham, who is excavating the Ban Non Wat site outside the city of Phimai.



At the edge of the pit, Higham points to a string of pots jutting from the soil below the layer of the skeletons. "These are

almost certainly from a 'superbial,' " he says: an elite grave brimming with shell and marble jewelry and bronze tools and ornaments. After a few more days of digging earlier this month, his 60-strong team of academics, Thai laborers, and volunteers from the conservation nonprofit Earthwatch International capped their field season by unearthing a clutch of ritualistic, princely burials. These wealthy graves date from the Early Bronze Age, more than 18 centuries before the civilization of Angkor rose to greatness.

Such early riches are helping to rework views of Angkor's origins. Archaeologists long thought that the import of Indian culture between 200 and



Rewriting history. Charles Higham's team has uncovered rich early graves, as shown by a pot from a Bronze Age superbial next to his left knee.

400 C.E., during the Iron Age, transformed scattered communities of benighted farmers into civilized societies. A smattering of Bronze Age digs in Southeast Asia had yielded remarkably few grave goods, creating a picture of farmers and fishers eking out hardscrabble lives. Elsewhere in Asia and in Europe, meanwhile, the advent of metalworking in the early Bronze Age had clearly widened the gap between elites, merchants, and commoners. But Higham has uncovered a very different story.

From a patch of land half the size of an Olympic swimming pool, his team over five field seasons has unearthed 470 graves spanning the Neolithic to the Iron Age, from 2200 B.C.E. to 500 C.E. Most spectacular are the 3000-year-old superbials. The team's largely unpublished findings reveal that Southeast Asian societies were stratified into elite classes more than 1000 years before Indianization began. "By the Bronze Age, people here were sophisticated," says Higham, of the University of Otago in Dunedin, New Zealand,

whose team includes Otago research fellow Rachanie Thosarat and Nigel Chang of James Cook University in Townsville, Australia.

Moreover, Higham says, the excavations show that the people of Phimai "were able to control water flow long before the development of Angkor's reservoirs." Those reservoirs and associated canals were vital to Angkor's power (see main text).

Higham's work is "pathbreaking," says archaeologist Miriam Stark of the University of Hawaii, Manoa, who co-directs another dig in the region. Ban Non Wat shows that Southeast Asia's Bronze Age societies were not out of step with the rest of the world.

—R.S.

long claimed that no canals exited the massive reservoir—so how could it have been used for irrigation?

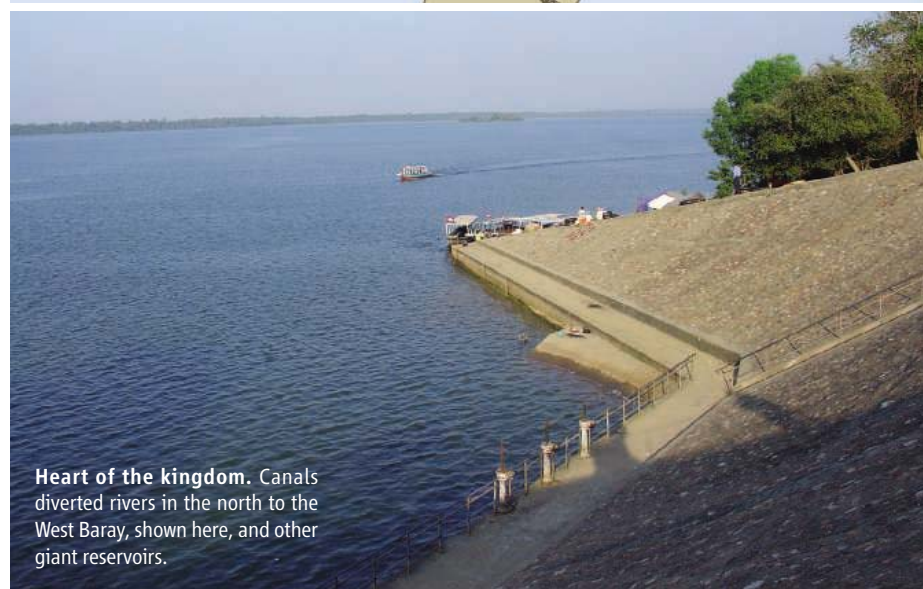
In the last few years, the GAP team has amassed new details on the vestiges of outlets, some lined with laterite blocks, from both the West and East Barays. To many experts, it's now beyond dispute that the reservoirs were used to store water for irrigation during the dry season and possibly to prevent flooding of houses and fields. "I'm really impressed with what the GAP team is doing," says Yale University anthropologist Michael Coe, an expert on the Maya and Angkor civilizations. They "have pretty much laid this debate to rest."

But the question remains as to how Angkor's endgame played out, as scholars over the years have engaged in a lively Angkorian version of whodunit. Some experts hold that shifting economic, political, or religious winds trimmed Angkor's sails. A "building orgy" of Jayavarman VII, who in the late 12th century ordered the construction of numerous temples and Angkor Thom with its then-gilded Bayon, might have emptied the kingdom's coffers and thus reduced its influence. Another possibility is the growth of maritime trade, with centers of wealth shifting south, closer to the sea. Or perhaps Angkor's star dimmed when Theravada Buddhism and its tenet of social equality began to eclipse Hinduism in the kingdom in the 13th and 14th centuries.

A prevailing view is that crop yields declined precipitously. Nearly 30 years ago, EFEO researchers Bernard-Philippe Groslier and Jacques Dumarçay speculated that the waterways and barays filled with silt, choking off irrigation during the dry winter months. The mechanism might have been deforestation, as fields were cleared for planting to feed a booming population—making Angkor a victim of its own success.

To test these ideas, Fletcher and others set out to unravel the details of Angkor's canals and barays. They found a number of clues hinting at problems with the grand waterworks. Engineering flaws may have doomed the East Baray, at least. "By modern engineering standards, it was a total failure," says Heng Thung of the Regional Centre for Archaeology and Fine Arts in Bangkok, a specialist in satellite data. To construct the baray, workers simply piled up earthen dikes on the sides. A canal diverted water from the Siem Reap River to the baray, but because the reservoir's bed was no deeper than that canal, the baray was perpetually shallow during the dry season. Water would have evaporated rapidly when the land is thirstiest.

The engineers got smarter when they built the West Baray a century later. This reservoir was excavated in places by as much as 1 meter, presumably deep enough to retain water throughout the dry season. What doomed the West Baray, Thung asserts, is something that Khmer engineers or astrologers could never have foreseen:



Heart of the kingdom. Canals diverted rivers in the north to the West Baray, shown here, and other giant reservoirs.

geological uplift. He says the beds of the Siem Reap and other rivers unmistakably deepened during the Angkor era. This must have occurred as the upward movement of the crust gradually raised the flow gradient, making the meandering rivers run faster and cut deeper. River levels would have decreased relative to the surrounding land, until eventually the rivers were too low during the dry season to feed into the West Baray. "When the water was needed, the canals couldn't supply the reservoir," Thung says.

Whatever the problems with the barays, some researchers contend that their importance for irrigation has been vastly overstated. The engineered system would have provided water to grow enough rice to support between 100,000 and 200,000 people, less than half of the presumed population. The land between the barays and the Tonle Sap, a lake south of Angkor, is so flat that it's hard to imagine large amounts of water supplying a broad expanse of

irrigated rice land, says archaeologist John Miksic of the National University of Singapore and an expert on early Indonesian cultures. Most of the populace tended banded rice paddies that captured water during the monsoons or grew rice in saturated soil left after monsoon floodwaters receded.

Thung, Fletcher, and others do not dispute that baray-fed irrigation alone would not have sustained the populace. Rather, they suggest, the barays provided extra capacity that could have ensured survival rations during a poor harvest. The irrigation system "may have been a risk-management strategy for a bad monsoon year," Fletcher says—a strategy that would have failed if the barays didn't fill. Another practical purpose of the barays might have been flood control by diverting waters from swollen rivers: "Insurance policies maybe, in case the monsoons were heavy," Fletcher says. He proposes that the great embankments and canals are central features of

an artificial wetland aimed at reducing the risk of flood damage.

Remarkably, the GAP team is the first to attempt a comprehensive assessment of Angkor's climate and waterworks. Penny, an expert on past climates, is analyzing pollen grains to uncover shifts in vegetation cover. From this he hopes to reconstruct changes in land use during Angkor's waning centuries. So far, he says, results indicate that Angkor's demise was "patchy, both over time and space," undercutting traditional explanations for the city's last days. Other scientists are focused on the canals and barays—and tackling the perplexing riddle of the spillway.

Dowsing for the truth

The spillway might never have come to light if Khmer Rouge laborers hadn't dug an irrigation trench through it. Around the end of the 9th century C.E., with Angkor blossoming, engineers excavated a long canal that altered the course of the Siem Reap River, diverting it southward to the East Baray. The spillway extends westward from the northern end of the canal and would have functioned, Fletcher infers, to protect that canal from excess flooding, comparable to a bathtub's overflow slot.

The conundrum is that the spillway's meticulous construction is badly damaged. The Khmer Rouge trench has largely eroded away; the Angkorian workmanship was far superior. Nevertheless, most of the spillway's laterite blocks lie in a jumble under sandy soil. "It was torn apart," says Fletcher. It's possible, he says, that an engineering flaw caused the spillway to give way. But Angkorian structures were built to last, which propels Fletcher toward a different conclusion. "It seems they ripped the spillway out themselves," he says. "Perhaps something had gone wrong."

Fletcher tends to see the hand of necessity, not neglect. He hypothesizes that the structure was damaged by flooding, then dismantled for its materials, after which Angkor workers buried the ruins to prevent the diversion canal from breaking out of its channel and flowing west.

The story of the spillway and other clues from the GAP team's work indicate that over the centuries, Angkor's vaunted water system grew ever more complex to support the sprawling city. "We know that something was going wrong, mechanically, with their water system," Fletcher says. For instance, one of the great southern



Mapping in style. Donald Cooney's bird's-eye views of Angkor and its temples (*top*) have helped researchers detect subtle features, such as eroded canal earthworks.

canals was filled with cross-bedded sand, indicating considerable and rapid water flow as well as sedimentation. "The sand buried the canals," he says. The water infrastructure "became so inflexible, convoluted, and huge that it could neither be replaced nor avoided, and had become both too elaborate and too piecemeal."

The more complicated and delicately balanced the system grew, the harder it would have been to compensate for unusual events, such as extreme flooding or drought. "They engineered a completely artificial environment, and it was a fragile environment," Pottier says.

Add climate change to this volatile mix, and you have a recipe for disaster. The GAP team is probing whether monsoons became "really erratic" during the Little Ice Age, between 1300 and 1600 C.E. There's good evidence that cooling in the Northern Hemisphere not only weakened monsoons in mainland Southeast

Asia during this period but also triggered sharp declines in crop yields in Europe. William Boyd, a geologist at Southern Cross University in Lismore, Australia, who's collaborating with Higham, finds GAP's scenario reasonable; he suspects that the Angkor region would have become drier.

The idea is "really intriguing," says archaeologist Miriam Stark of the University of Hawaii, Manoa, who has studied the pre-Angkor Funan kingdom of Cambodia's Mekong delta. But archaeologists say more climate data are needed. "A definitive answer," says Miksic, "would require a study of the ecology of the Tonle Sap Basin over the past 2000 years."

Fletcher concurs, and he and Penny hope to receive permission from Cambodian authorities to go caving in search of evidence. Stalagmites add new layers every year; the isotopic chemistry of the layers captures a record of climatic conditions during accrual. (Stark and Paul Bishop of the University of Glasgow hope to gather similar data from caves in the Mekong delta region in the coming year.) Deciphering the isotope record in suitably old stalagmites should yield insights into past climate. Other evidence could be gleaned from changes in vegetation or lake water levels, and Chinese trade records, says Boyd.

As Angkor was rising, halfway around the world a similar loss of equilibrium brought the Maya to their knees. Overpopulation and environmental degradation had weakened their Mesoamerican

cities. Beset by droughts and a "paroxysm of warfare," the civilization crumbled, Coe says. "The demise of Angkor is directly comparable to the great Maya collapse," he says. And it could happen again. "When populations in tropical countries exceed the carrying capacity of the land, real trouble begins," Coe says.

Fletcher says there are lessons for developed nations as well. He compares Angkor's plumbing woes to modern cities having to cope at great cost with extensive, decaying sewers or cumbersome road systems.

On their quest to understand the end of Angkor, the GAP team will continue to excavate and analyze deposits from its water features and reconstruct its environmental history. Angkor, says Thung, "is a never-ending story." Or, rather, it's an ending often rewritten, and with a lesson for society that gets gloomier each time.

—RICHARD STONE

PROFILE: SAMUEL BODMAN

With Energy to Spare, an Engineer Makes the Case for Basic Research

As secretary of energy, Samuel Bodman leads a campaign for research that will result in new energy technologies. Even critics find reason to applaud

Samuel Bodman relishes a challenge. Even before President George W. Bush nominated him in late 2004 to be secretary of energy, the chemical engineer and former CEO of the Cabot chemical giant in Boston, Massachusetts, had decided that the government was underfunding “math, chemistry, physics, and engineering.” But the Administration’s 2006 budget request that he inherited called for a 3% cut in the Department of Energy’s (DOE’s) \$3.6 billion Office of Science, the primary federal backer of fundamental physics. Bodman gamely defended that request as in line with “the president’s deficit-reduction goals.” But back at the department’s fortresslike headquarters in downtown Washington, D.C., he set out not only to reverse the cuts in DOE’s basic science but also to lobby the White House for new applied energy efforts.

Last month, Bodman enjoyed the fruits of his efforts: Within a span of a week, Bush devoted an unprecedented nine paragraphs of his State of the Union Address to research and science education and proposed a 14% increase in the 2007 budget for DOE’s

Office of Science. A nuclear energy initiative drew mixed reviews, and environmentalists applauded the Administration’s belated endorsement of solar power and biomass programs (see table, p. 1370).

Overnight, Bodman had changed from faceless bureaucrat to a hero of science. “He has his values at the right location,” says nuclear physicist Konrad Gelbke, director of DOE’s National Superconducting Cyclotron Laboratory at Michigan State University in East Lansing. “Our last secretary was also an advocate for science, but this is in a different way: hands on,” said Office of Science Director Raymond Orbach last year about a grueling 2-hour budget briefing session with Bodman.

The self-effacing 67-year-old says he doesn’t relish the spotlight: “I don’t view myself as a role model.” He credits his success partly to hard work: Even before he was confirmed as DOE’s 11th secretary, he devoured several fat three-ring briefing binders describing the \$24 billion behemoth he was about to manage, which has responsi-

bility for everything from the nation’s nuclear weapons arsenal to appliance standards. And he’s quick to spread the credit around. “I’m a good judge of horseflesh,” he says, noting that Orbach has been nominated for the additional title of undersecretary of science, a position Bodman successfully lobbied Congress to create last year. But he is as results-oriented as any CEO, targeting “areas that are best positioned to yield results in our lifetime, more specifically, in my lifetime.”

Although energy scientists aren’t willing to bet that Bodman will be able to transform an energy industry whose fundamental technologies have changed little in 30 years, they think his academic and energy qualifications give him a better shot at succeeding than his predecessors. That roster includes a dentist, a lawyer, and two former senators with no technical background. Former CIA director and DOE official John Deutch says Bodman may be “the most qualified secretary we’ve ever had.” Bodman, they argue, represents the best shot in decades at changing how America uses energy.

Follow the money

Trained as a chemical engineer at Cornell University and the Massachusetts Institute of Technology (MIT), Bodman was quickly attracted to the fledgling world of venture capitalism. An associate professor at MIT in the 1960s, he simultaneously worked at the Boston-based American Research and Development Corp., among the first venture capital companies to benefit from the emerging U.S. academic research juggernaut. Bodman then took a job assessing energy and chemical technology for Fidelity Investments’ nascent venture unit, spending more than a decade at the mutual fund giant and rising to chief operating officer. As Cabot CEO, he won plaudits as the \$2 billion company expanded into natural gas and electronics. With Fidelity, he met Don Evans, a Bush family friend who became commerce secretary and recruited Bodman as his deputy. Bodman oversaw the department’s research portfolio, which includes the National Institute of Standards and Technology (NIST) and the National Oceanic and Atmospheric Administration.

Yet despite a career focused on technology—“I’m an engineer, not a scientist,” he’s quick to remind reporters—Bodman often talks about the need to beef up U.S. fundamental research. And he’s extremely grateful for the \$2200-a-year National Science Foundation (NSF) fellowship that put him through graduate school in the early 1960s. “What I’m concerned about is that America retain leadership, that America continue to be the place that offers the maximum opportunity for a young scientist or a young engineer ... to participate in the great



Bowling partners. Speaking at DOE’s National Science Bowl, Samuel Bodman has given Office of Science Director Raymond Orbach (left) an enhanced role in decision-making during his first year as energy secretary.

CREDIT: DOE

discovery process that is science,” he told *Science* in an interview last week in his well-appointed seventh-floor office.

Bodman is pushing the president’s new American Competitiveness Initiative, which promises a 10-year doubling of basic science funding in DOE’s Office of Science, NSF, and NIST’s core lab programs. On his office coffee table sits a well-worn copy of an October report from the National Academies on bolstering U.S. leadership in science (*Science*, 21 October 2005, p. 423).

His corporate and technical experience helps him understand how basic science can feed into new energy technologies, Bodman says, and he’s quick to challenge proposed solutions. Joe Jones of Skyonic, a carbon-chemistry start-up in Austin, Texas, says during a recent meeting Bodman “snapped back between chemical engineering professor and board of director; ... [it was] the equivalent of my [graduate school] orals.”

Befitting a former corporate manager, Bodman likes to set specific market goals. For biofuels, he wants to improve the conversion of cellulose—think corn waste or wood chips—into ethanol for cars, making it competitive with gasoline in 6 years. Starch in corn kernels is currently converted into the fuel and used as an additive in millions of U.S. autos, but DOE’s Doug Kaempf says a 30-fold drop in the cost of enzymes that convert cellulose to sugar helped persuade Bodman to boost biofuels research dollars by 65%—focusing on fermentation. Similarly, progress in photovoltaics persuaded Bodman to boost applied solar work such as silicon manufacturing and crystal growth techniques, aiming to make solar energy as cheap as retail electricity by 2015.

Previous DOE attempts to promote similar programs have been rebuffed by a White House with close ties to the energy industry. High gasoline prices helped Bodman this time around, but so did his inside-the-Beltway mettle, lobbyists attest. Former Commerce official Phillip Bond, now with Monster.com, says Bodman repeatedly secured healthy funding requests for NIST labs by describing what its science “meant for the business sector.” From his office window, Bodman can gaze upon the Capitol dome. “That’s where the money is,” he says.

Flying under the banner “work together,” Bodman has declared war on DOE’s infamous bureaucratic stovepiping. Scientists involved with DOE’s supercomputing efforts, for example, say that separate programs con-

nected to weapons and basic science are talking more to one another, with good results. Bodman has also elevated Orbach’s role as science adviser to the secretary, consulting with him before deciding to support the National Ignition Facility, a superlaser at Lawrence Livermore National Laboratory in California that faced the budget ax last year. The materials scientist also helped decide the fate of several troubled cleanup sites, giving guidance “as to what kind of glass they were using,” Bodman says. “I think [Bodman] brought back the notion that the head of the Office of Science is going to provide him

and weatherization programs undermine the president’s stated goal of curing “America’s oil addiction.” Green groups, in turn, cheer the ethanol studies but say the government could reduce carbon emissions faster by mandating more efficient cars. Citing high fuel prices, Bodman says “there is plenty of sacrifice to go around.”






The \$250 million nuclear initiative, in particular, is a lightning rod for critics. Bodman says results from DOE labs “seem to indicate” potential for advanced recycling of waste, reducing the need for a geologic repository. Critics say that billions could be wasted in a

futile attempt to convince the nuclear industry. Others, such as Princeton University physicist Frank von Hippel, question whether the system could work without producing fissile material that terrorists could use to build bombs. Bodman says that effort—and a similar demonstration project on an advanced coal plant called FutureGen—is focused on convincing the industry to eventually buy in. But MIT’s Deutch warned in a paper last year that congressional mood swings and a lack of “necessary skills” at DOE have doomed a number of previous demonstration projects, including the Clinch River Breeder Reactor and several synthetic fuel plants.

Others question the scope of Bodman’s vision. Although chemist Nate Lewis of the California Institute of Technology in Pasadena welcomes new solar funding, he notes that poor storage technology means homes with solar panels must draw from the grid at night, suggesting that only transformational advances in photovoltaics and batteries would create true independence. Hoffert says Bodman’s new efforts “are a good idea but [are] pitifully small compared to the magnitude of the problem.” National Venture Capital Association President Mark Heesen fears Bodman’s employees won’t conquer “the mindset that big companies are the only ones who solve big issues,” missing potential breakthroughs.

Bodman is careful not to oversell the department’s various taxpayer-funded gambles, including the nuclear reprocessing initiative, using lingo taken in equal parts from his business and academic backgrounds. “If we do the work and the industry expresses zero interest, either we will try to convince them otherwise, or we won’t proceed,” Bodman told *Science*. After all, he says, “this is research.”

—ELI KINTISCH

DOE Research Priorities		2006 Budget (\$ millions)	President’s 2007 Request (\$ millions)	Percentage Change
	Office of Science	3596	4102	+14%
	Advanced Nuclear Fuel Cycle	79	243	+207%
	Biomass/Biofuels	91	150	+65%
	Solar Energy	83	148	+78%
	Efficiency and Weatherization	644	531	-18%

Growth industry. President George W. Bush has requested healthy increases next year for DOE’s basic research efforts and several applied programs.

basic scientific input on general science issues,” says MIT theoretical physicist Arthur Kerman, a longtime DOE consultant.

That faith in his deputies has ruffled some feathers. In January, Bodman dismissed the top science advisory board at DOE—6 months after it released a report critical of DOE’s management of its weapons complex. Senator Carl Levin (D-MI) called the move “troubling,” and longtime DOE adviser and physicist Richard Garwin sees it as “a very bad idea.” Peter McPherson, chair of the now-shuttered group and president of the National Association of State Universities and Land-Grant Colleges, is less concerned. Bodman, he says, “can get input from other sources.” And Bodman says he prefers to receive advice from those “on the payroll.”

A treacherous path

Many energy watchers are skeptical of DOE’s new priorities. Some experts complain that Bodman, whose entourage uses a limousine and big black SUVs, plays down saving energy. The American Council for an Energy-Efficient Economy says that Bodman’s proposed cuts for energy-efficiency research



RESEARCH POLICY

A Dose of Reform to Treat the Malaise Gripping French Science

Two years after protesters launched a massive revolt against government science policy, France has adopted a law that promises to reform the establishment

PARIS—Just 700 protesters showed up for a final march against the French government's research policy last week, according to the police. Like so much in this uprising, the number of marchers is disputed: The organizers claim there were at least 2000. It was by any estimate a far cry from the tens of thousands of angry researchers and supporters who took to the streets 2 years ago to air grievances about the system. And last week, the protest ended in anticlimax: After walking the short distance from the Musée d'Orsay to the National Assembly, the crowd dissipated quickly into the evening rush hour; it didn't even make the TV news.

The object of the protesters' ire—a plan drawn up by civil servants to infuse new life into French research—is also coming to a quiet conclusion. A bill authorizing reforms was expected to pass the full National Assembly easily on 7 March and was slated to be approved by both legislative houses on 16 March after differences are ironed out. The package includes a raft of measures aimed at luring young people into labs and making innovation the engine of a flagging economy. But few except education and science minister Gilles de Robien and minister delegate François Goulard, who shepherded the bill to a vote, seem excited about it.

The powerful trade unions and the protest movement *Sauvons la Recherche* (Let's Save Research, or SLR), which organized last week's protest, criticize the plan for falling short of their goals. Others cite its positive elements: The research budget will grow from €19.9 billion in

2005 to €24 billion in 2010. Along with providing more money, the new law attempts to simplify research management and empowers a new National Research Agency (ANR) to dole out funds for projects based on merit reviews, a novelty in France. But the scientific community had hoped for a bigger financial boost. "I have very mixed feelings," says physicist Edouard Brézin, president of the Academy of Sciences, who says the bill bespeaks a "lack of ambition."

Few dispute that French science is, as an academy panel chaired by the academy's permanent secretary Jean-François Bach put it last year, "in a serious crisis." Studies have concluded that it is lagging behind the rest of Europe and the United States, based upon the declining quantity and quality of research output as well as the small number of new patents and biotech start-ups that stem from French research. Low wages and scarce lab resources have made the profession unattractive for young people. And the prime advantage of joining the vast scientific civil service—security for life—hardly stimulates creativity.

Government labs such as the mammoth CNRS and INSERM, where most research takes place, are at arm's length from higher education, and university scientists are overburdened with teaching tasks, the academy report concluded.

End of the road. Researchers formed a nationwide movement to protest inadequate pay and a stagnant work environment. The government response, due to be voted on this week, wins few plaudits.

Bureaucratic rules waste precious time and money, too, says Bernard Meunier, who quit as CNRS president in January to protest "excessive" bureaucracy and now leads Palumed, a biotech firm developing antimalarials and antibiotics.

Many successful scientists opted out of the French system. Molecular biologist Catherine Dulac, who runs a lab at Harvard studying olfactory signaling, says she was determined to return to France after a postdoc job in the United States—until she realized how limited her resources would be. "It would have been scientific suicide," she says. Attracting fresh foreign blood to France is even more difficult than retaining French talent, says Brézin.

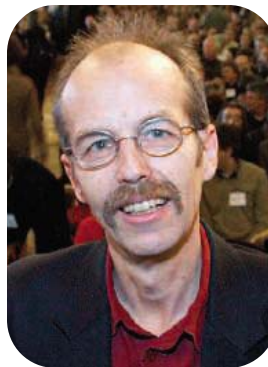
Some labs have tried to bring about change on a small scale. The Curie Institute in Paris, for instance, lures top researchers by offering them better paid, 5-year contracts, and more money to spend on equipment and support staff. It can do so because, as a foundation, it is blessed with both public and private money, says Curie Director Daniel Louvard. However, strict labor laws put limits on its flexibility.

Discontent reached a boiling point in early 2004, after the government made cuts in the science budget and proposed to replace 550 permanent jobs with temporary contracts. More than 3500 lab leaders threatened to stop performing their administrative duties, and streets around the country filled with protesters in lab coats (*Science*, 13 February 2004, p. 948).

Surprised by the scale of the backlash, the government backed down, and President Jacques Chirac promised a "Pact for Research." The scientific community organized a nationwide debate, culminating in a 2-day meeting in Grenoble and a consensus wish list (*Science*, 5 November 2004, p. 956).

Geochemist Claude Allègre, who served as science minister in a Socialist cabinet from 1997 until 2000, says the scientists' movement accomplished less than it might have because it engaged in a "naïve" debate about structural changes it

wanted in the science system. "They lost 2 years," Allègre says. "Money, money, money—that's the only thing that's important at the moment." But Brézin notes that scientists had their recommendations ready in November 2004; it's the government that kept postponing the bill, in part because of a complete cabinet reshuffle after a public vote rejected the European constitution in May 2005.



Voice of protest. *Sauvons la Recherche* spokesperson Alain Trautmann.

Still, money remains a key issue. The budget increase to €24 billion—which would be even higher if Goulard can deliver on a commitment, made during the debate, to correct for inflation—will help pay for 3000 new jobs. “The hemorrhage has stopped; that’s positive,” says SLR co-founder and spokesperson Alain Trautmann. But Trautmann and other critics say the bill falls far short of what’s needed to revamp anemic government labs. Roughly one-third of the new money comes in the form of tax deductions for industry, which, Brézin notes, does little for basic research. To his critics’ surprise, Goulard also made a turnaround and promised to try to raise Ph.D. students’ salaries to 1.5 times the minimum wage. But it’s a commitment that could easily be forgotten if there’s no money or if Goulard is replaced, Trautmann says.

The law authorizes new “Regional Centers for Science and Education” to bring scientists from government institutes and universities together, but the plan doesn’t go far enough to provide the

needed relief for university research, says Bach. Researchers are also “nervous” about the bill’s vagueness, he says; for example, it’s not clear whether a new High Council for Science and Technology—which researchers had lobbied hard for—will be truly independent or merely decorative. Goulard sees a major advance: “Never, and I mean never, has so much been done for French science,” he said last week.

Opinions are divided, meanwhile, about the new grants agency ANR, which started operating last year with temporary authority. Bach believes it will create a new way to support talented young people, provided it stays free of political interference. But SLR and the trade unions oppose the new agency, which they worry will not improve flexibility as much as it will reduce certainty for the average researcher. Indeed, one reason SLR lost steam, Meunier says, is that it had become increasingly aligned with the trade unions, which argue for more money but have opposed substantive change. Despite the banners, the balloons,

and the whistles, the research unions tend to be conservative, protecting the interests of those inside the system with good jobs at the expense of younger people, he says.

Trautmann acknowledges that there has been a “convergence” between SLR and the unions and that it has caused some early members to turn their backs on the movement. He says he isn’t happy with this himself, as SLR was started primarily to address the plight of young scientists. “We don’t want to be a new union,” he says. Now that the landmark reform bill has passed, SLR will decide on own its fate at a general meeting on 11 March. Although Trautmann says he wants to continue “analyzing and communicating” about science policy in some way, he says the group could decide to dissolve.

For now, most scientists are hoping for better times. If the left comes to power in the 2007 elections, the research budget will get a 10% annual increase, Socialist Party leader François Hollande promised last week. —MARTIN ENSERINK

EVOLUTIONARY BIOLOGY

Speciation Standing In Place

Surprising some evolutionary biologists, studies of birds, fish, trees, and insects show that it doesn’t take a mountain chain, island, or other geographic quirks to create a species



It’s not often that one witnesses speciation in action, but some birdwatchers in Africa may be having that privilege. Michael Sorenson, an evolutionary ecologist at Boston University, and Robert Payne of the University of Michigan, Ann Arbor, have monitored African indigobirds at a field site in Cameroon for the past decade. The opportunistic birds lay their eggs in the nests of different species of finches. The newborn indigobirds then look and act as if they belong there, and as adults, incorporate the twills and whistles of their foster parents into their own mating calls.

Recently, the researchers observed one species, called the blue indigobird, lay eggs in the nests of both the African firefinch and the

Black-bellied firefinch. The resulting indigobirds learned the songs of their respective finches and now seem to have developed into two “races.” Although all the blue indigobirds can still mate with one another—which means the races are not yet distinct species—females prefer suitors who know the same finch song they do. And they pass their preferences on: Female indigobirds that grow up in an African firefinch nest, for example, tend to lay eggs in the same kind of nest rather than in one belonging to a Black-bellied firefinch. “We have a nice example of early stages of speciation in this group,” concludes Sorenson.

This bird tale, described in an upcoming *Behavioral Ecology* paper, is one of several recent

Nesting behavior. By sneaking into nests of two kinds of finches, the blue indigobird is on its way to splitting into two species.

volleys in the continuing debate over how speciation occurs. For the past 50 years or so, many influential evolutionary biologists, notably the late Ernst Mayr, have held that physical separation among members of a species, such as that caused by the emergence of a mountain chain, typically drives the splitting of one species into two. Populations separated by geographic barriers can’t interbreed and eventually evolve into distinct species. Examples of this speciation process, called allopatry, abound.

Charles Darwin recognized allopatry as a driving force of speciation. But he also thought populations could diverge into separate species in the absence of physical barriers, an idea now called sympatric speciation, or simply sympatry. However, his successors were at a loss to explain how this could happen, and they could find few examples. By 1907, textbooks dismissed sympatric speciation, and 35 years later, Mayr virtually tossed the idea out of modern evolutionary thinking with his strong antisympatry rhetoric. Since then, few researchers have taken sympatry seriously.

Now the situation is changing fast. The indigobird study, combined with recently published reports of sympatric speciation among cichlid fish and palm trees, have offered compelling new support for the concept. Although some researchers are not yet convinced, sympatric events can now be detected with unprecedented certainty, says evolutionary biologist Axel Meyer of the University of Konstanz, Germany, who led the new cichlid fish study. Even supposedly airtight examples of allopatry

have sprouted leaks; a new study questions whether certain mammalian groups arose through allopatry, as researchers have long thought.

Instead of asking if sympatry occurs at all, “the question has now become ‘How frequently does sympatry underlie the genesis of new taxa?’” says Jeffrey Feder, an evolutionary biologist at the University of Notre Dame, Indiana.

The case for sympatry

Sympatry has been slow to catch on in part because it is hard to envision why members of one group in a population would predominantly mate only with each other. “There has to be some sort of assortative mating, or you don’t get [species-defining] genetic differences creeping in,” says Kenneth Petren, an evolutionary ecologist at the University of Cincinnati, Ohio. With allopatry, it’s simple: Geographic barriers leave individuals little to no opportunity to breed with their peers. But with sympatry, “ecological” barriers—genetic, morphological, or behavioral quirks that lead to changes in food preferences, courtship colors, breeding season, and so forth—cause group members to prefer or have contact with a specific type of mate.

Sympatry is hard to spot. To find it in a world seemingly dominated by allopatry, evolutionary biologists must identify a place where it is highly unlikely that physical barriers have separated members of a species. They must identify closely related, but nonetheless different, species and measure the amount of “gene flow” between the two species. In sympatry, where some interbreeding occurs throughout the speciation processes, gene flow is rampant, especially at first. As a result, the two species look similar—genetically speaking—except for the particular genes underlying the changes in behavior, morphology, etc., that make the two species different. In contrast, in allopatry, physical barriers essentially cut off gene flow, freeing entire genomes to evolve in different directions. Thus, the pattern of genetic differences provides a key clue about the method of speciation.

One of the oft cited cases of sympatry is a 1994 report by Ulrich Schliewen, an ichthyologist at the Zoological State Collection

New territory. Fruit flies that originally lived off hawthorne trees have now colonized apple trees and evolved a dislike for hawthorne fruit, which may ultimately create a new fly species.



in Munich, Germany, and his colleagues. They concluded, based on mitochondrial DNA studies, that 11 cichlid species living in a small lake in Cameroon arose sympatrically from a common ancestor trapped in the



Backdoor speciation. In a Cameroonian lake, the slender Konia cichlid (*top*) hybridized with another species and gave rise to the fatter, sponge-eating Pungu cichlid (*bottom*).

2.5-kilometer-wide space. Schliewen attributed this burst of sympatry to the original species evolving in ways that, for example, helped the fish thrive at different depths. Schliewen’s work has been widely heralded as one of the best examples of sympatric speciation, in part because it’s unlikely that this isolated lake would have been colonized enough times by outside species to create the current diversity, says Feder.

In 2004, Schliewen described a new twist on the evolution of this tightly knit group of fish. With more extensive genetic testing, he found that at least one of the 11 species arose as a hybrid of two other species, suggesting yet another avenue of speciation among sympatric species.

Schliewen had few molecular techniques at his disposal when he did his initial work in the early 1990s, which left some people skeptical of the sympatry claim at the time. But in the 8 February issue of *Nature*, a team led by Meyer and one led by Vincent Savolainen and William Baker of the Royal Botanic Gardens, Kew, in Richmond, U.K., apply new genetic analyses to come up with two additional compelling examples of sympatry.

Meyer and his colleagues examined two fish species, the arrow and Midas cichlids, that live in an isolated 5-kilometer-wide volcanic lake in Nicaragua. By comparing the species’ mitochondrial genes, variable DNA sequences called microsatellites, and other genetic landmarks, the researchers demonstrated that the arrow cichlid evolved from the Midas cichlid fewer than 10,000 years ago. They argue that the lake is too small for this to have resulted from physical separation. Instead, they believe that competition for food may have pushed members of the ancestral species to go in different ways. The Midas cichlid is an algae-eating bottom feeder with a deep body, whereas the arrow cichlid, whose slender shape is built for swimming, often dines on winged insects. Other researchers have shown that the two prefer to mate with their own kind and that when forced to interbreed, they fail to produce young.

Savolainen and Baker also picked a remote spot to search for sympatry: Lord Howe Island, a 12-square-kilometer speck of volcanic rock 580 kilometers east of Australia. There they studied two indigenous palm tree species, the kentia palm, which is used throughout the world as a houseplant, and the much shorter curly palm. A DNA-based family tree of all the island’s palm species indicated that the curly palm descended from the kentia palm about 1 million to 2 million years ago. Although the two species coexist in 20% of the island sites surveyed, the timing of their flowering now keeps them separate, say Savolainen and Baker.

The pair suggests that soil differences on Howe Island created the ecological barrier that drove this sympatric speciation. Today, kentia palms thrive on the island's basic soil, whereas curly palms stick to acidic soils. Savolainen and Baker suggest that as the kentia palm spread onto different soils, its flowering time was delayed, possibly because the genes needed to adapt to the

slow egg development, such that their eggs hatch at peak apple season. Feder and his colleagues' recent work also shows that the two kinds of maggots remain separate in part because they are attracted to the odor of their particular fruit and are repulsed by other fruits.

Other insects seem to be following a similar path to a sympatric split. Last year, Thibaut

tough call since we were not there at the time of speciation," says Feder.

Coyne also worries that the genetic evidence of close kinships may be misleading. In the case of the Lord Howe Island palms, for example, the second palm species may have arisen elsewhere. If wind blew some of that palm's pollen to Lord Howe and hybrids resulted, then the intermingling of the genomes of the two species would make them seem more closely related than they really are. "It's a judgment call," Coyne says. "There are other alternatives that have to be taken seriously."

Richard Glor, an evolutionary biologist at the University of California (UC), Davis, has found such an alternative explanation for the diversity of anole lizards on Cuba. Cuba is a relatively small island with 60 species of Anole lizards, and some researchers have proposed that sympatric speciation underlies much of the lizards' diversity. In 2004, Glor and his colleagues analyzed genetic differences among three green canopy-dwelling lizards to determine when the species separated. They concluded that the speciations occurred more than 5 million years ago, at a point when a rise in sea level had broken Cuba into multiple islands. Thus, physical separation, not sympatry, gave rise to the three species, which are reunited on a single island today, says Glor.

Still, that ambiguity cuts both ways. Some cases of mammalian speciation attributed to allopatry have recently been called into question. UC Davis evolutionary biologist Michael Turelli admits that he had hoped to quiet sympatry sympathizers with a new study, appearing in the March issue of *Evolution*. He and his former student Benjamin Fitzpatrick gathered data on the ranges of 14 groups of mammals—"where no one thinks that sympatric speciation is going on," says Turelli.

The study's rationale was simple: If two closely related mammals arose through geographic isolation as allopatry demands, then they should have ranges that were disconnected, at least early in their evolutionary history. (Over time, these species might expand their ranges such that the two would intersect somewhat.) With sympatric speciation, the opposite should be true, Turelli explains. By definition, sympatric species start off in the same place and only over time do their ranges diverge.

The analysis firmly established allopatry for gophers but not for two-thirds of the other mammals. "We saw clade after clade where there was no clear signal," says Turelli. "The punch line is it's less obvious that it's all allopatry all the time."

Indeed, even the most fervent fans of allopatric speciation are becoming more open-minded. Just as Mayr did later in his career, Coyne is softening his stance, for example. At least, says Giacomo Bernardi, an evolutionary biologist at UC Santa Cruz, "evolutionary biologists are at last essentially agreeing that sympatric speciation is possible."

—ELIZABETH PENNISI

Castaway. Cuban lizards became diverse after the island was partially submerged and divided into isolated islets.



altered pH affected the transmission of those involved in flowering. The new flowering schedule jump-started the speciation process.

The studies are "a good beginning" to demonstrating sympatry, says Jerry Coyne, an evolutionary biologist at the University of Chicago, Illinois, who has in the past been skeptical of proposed cases of sympatric speciation.

Sympatry on the fly

Some apparent cases of speciation in action, such as that of the indigobirds, are also bolstering the case for sympatry. Back in the 1860s, local farmers noticed that some fruit maggots had switched their mating and breeding grounds from hawthorns, which are native to America, to apples, a domesticated fruit species. A century later, Guy Bush of Michigan State University in East Lansing proposed that this type of ecological separation might be a common mechanism by which fructivore insects diverge into new species. Although not yet genetically distinct enough to be separate species, the apple and hawthorn maggots are proving a strong example of incipient sympatry, says Feder. The two types of maggots have begun to develop some subtle genetic differences. For example, apple maggots are much more likely to have genetic variants that

Malausa, at the Université Paul-Sabatier in Toulouse, France, and his colleagues found very little intermating in the wild between European corn-borers that prefer corn and ones that prefer hop or mugwort, even though all belong to the same species. Further enforcing this reproductive isolation, says Malausa, is that corn-feeding caterpillars of the species emerge as moths later than caterpillars with a hop-mugwort diet do (*Science*, 8 April 2005, p. 258).

Judgment calls

Fans of sympatric speciation are still working to win over many evolutionary biologists. For every researcher who sees a solid example of sympatry, there's a skeptic ready to poke holes in the case. "It's hard to rule out some sort of geographic separation, even if it's micro-separation," notes Petren. Hop versus corn, or apples versus hawthorn, could easily be interpreted as geographic isolation on a small scale, for example. And seemingly sympatric species isolated on islands or in lakes may have divided their territories enough to enforce reproductive isolation, Petren points out. The arrow and Midas cichlids divided their lake by depth; the kentia and curly palms stick to particular soil types. "It's always a



Awards **WOMEN IN SCIENCE.**

Colleagues call Jennifer Graves the “weird animal lady” for her work with kangaroos, wallabies, and platypuses. Now, the comparative genomicist from Australia National University has earned another title: laureate.

Graves, 64, is one of five women to receive the L’Oréal-UNESCO For Women in Science Award, a \$100,000 prize that recognizes women leaders in

life sciences or materials sciences. Born in Adelaide, South Australia, Graves earned her Ph.D. in molecular biology at the University of California, Berkeley, but later returned to Australia to study the country’s indigenous mammals. Graves’s research on the evolution of the Y chromosome suggests that the male chromosome is quickly losing genes and may disappear in several million years.

Graves hopes the awards will encourage young women to pursue careers in science. “We can’t afford to wait for recognition by others,” she notes. “We need to start by each recognizing the value of our own unique insights.” Other Women in Science honorees are Pamela Bjorkman of the California Institute of Technology in Pasadena, Christine Van Broeckhoven of Universiteit Antwerpen in Belgium, Habiba Bouhamed Chaabouni of the University of Tunis El Manar in Tunisia, and Esther Orozco of the Instituto de las Mujeres del Distrito Federal in Mexico. The awards were presented 2 March in Paris.



MOVERS HONORED CRITIC.

One of Australia’s most vocal proponents of genetically modified (GM) food crops has been named the government’s chief scientist. Plant molecular biologist Jim Peacock,

68, is widely recognized for leading the plant industry division of the Commonwealth Scientific and Industrial Research Organisation to international respect during his 25-year stint as head.

The current president of the Australian Academy of Science, Peacock is no stranger to controversy. Four years after receiving a share of the first Prime Minister’s Science Prize in 2000, Miller publicly challenged the administration’s overemphasis on “the delivery end of science,” warning that “we should never neglect investment in fundamental science.” Peacock has publicly supported GM food crops, even though all Australian state governments have imposed moratoria on planting them. And despite widespread public opposition to nuclear power, he recently suggested that nuclear plants may be a way to fight global warming.

“We applaud the appointment,” says Gerard Sutton, vice-chancellor of the University of Wollongong and president of

the Australian Vice-Chancellors’ Committee, “and we expect to be able to work with him very effectively.”

SMITHSONIAN SHUFFLE. Entomologist Scott Miller, 46, is trading his post as associate director for science at the National Zoo for a more central role in advising the leaders of the Smithsonian Institution in Washington, D.C. He succeeds Steven Monfort, who will step into Miller’s zoo job.

As the new senior program officer for science, Miller (below) will develop institute-wide initiatives in systematics, conservation, and other areas. “Scott brings a wealth of understanding of biology programs throughout the Smithsonian,” says Paula DePriest, director of the Smithsonian Center for Materials Research and Education. Miller will engender partnerships both within the Smithsonian and with outside organizations, DePriest says.

Miller plans to keep his lab at the National Museum of Natural History and continue field research on moths in Papua New Guinea. Miller also runs the Consortium of the Barcode of Life, a program to characterize all organisms by their DNA.



Dennis Bartels, the new director of the famed Exploratorium science museum in San Francisco, California, sees no reason why the city can’t fuse its youth culture and its high-tech industries to become “the science education capital of the world.” But innovating at a 37-year-old museum known for innovation won’t be easy, admits the 43-year-old science educator, currently president of TERC, an education R&D center in Boston.

Q: What’s new in informal science education?

A: A decade ago, everybody was talking about edutainment as a way to attract young people. But that didn’t work out. The real challenge for museums today is to deliver a bona fide educational experience: adult education, teacher training, or whatever else people want.

Q: How can the Exploratorium do that?

A: Since 1998, it’s been offering a 2-year science program for new teachers in the area that’s turned out to be a lifesaver for those with emergency credentials or teaching out of field. And 95% of those teachers are still in the classroom, which is an incredible retention rate.

Q: Can it be a national force for teacher training?

A: Yes, we have an Institute for Inquiry that has trained more than 1000 curriculum coordinators, and now it’s moved online. And the Center for Informal Learning in Schools has worked with more than 400 teacher educators from museums around the country to share best practices.

Got a tip for this page? E-mail people@aaas.org

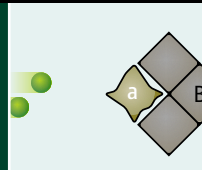
Costs of climate change

1379



Genetic interaction maps

1381



LETTERS | BOOKS | POLICY FORUM | EDUCATION FORUM | PERSPECTIVES

LETTERS

edited by Etta Kavanagh

Finding Good in the Bad and Vice Versa

DONALD KENNEDY'S EDITORIAL "GOOD NEWS—AND BAD" (13 JAN., P. 145) on the intelligent design Dover, Pennsylvania, court decision and the South Korean stem cell scandal overlooks some of the bad news in the good and the good news in the bad. The fraud perpetrated by at least some members of Hwang's research group is indeed bad news. But the good news is that the fraud was caught very soon after publication, and it is being dealt with. This is an example of science working, largely by reason of its openness and institutionalized commitment to testing and debate. Compare this scandal to deception in the business and political realms. Enron's fraud was hidden for years. Abramoff and DeLay similarly operated for years before indictment. Indeed, even supposedly democratic governments classify their fraudulent or other illegal actions, using the cloak of national security, and crimes can remain buried for decades. There is good reason to resist efforts to increase secrecy in any realm of human endeavor. With secrecy, the tail ends up wagging the dog and corruption becomes a way of life.

There is no question that the court decision in the Dover case was a good one. The opinion written by Judge Jones is rigorous and thorough—

and yes, quite elegant. There is a substantial dark side to this decision, however, that reflects poorly on the scientific community. How did it come to this court fight? How, in a country as "developed" as the United States, have the school system, the media, and the scientific community failed so miserably to educate the majority of Americans about the nature of science in general and evolution in particular?

—Johns

DAVID JOHNS
School of Government, Portland State University, Post Office Box 751, Portland, OR 97207, USA. E-mail: johnsd@pdx.edu

Diversity in Tropical Forests

IN HER ARTICLE "RARE TREE SPECIES THRIVE IN local neighborhoods" (News of the Week, 27 Jan., p. 452) discussing a study by C. Wills *et al.* ("Nonrandom processes maintain diversity in tropical forests," Reports, 27 Jan., p. 527), E. Pennisi states that "Biodiversity may be threatened worldwide, but small pockets of tropical-forest trees are surprisingly becoming more diverse over time." However, the key implication of Wills *et al.*'s study is that, in several tropical forests on two different continents, strong density- and frequency-dependent mortality tends to favor rare over common tree species locally (at a scale of tens to hundreds of square meters), and that this is a key process that helps to maintain (but not increase) tree diversity at a forest-wide scale.

Hence, Wills *et al.* have helped to reveal the mechanisms by which tropical forests maintain

their extraordinary biological diversity, but there is nothing in their study to suggest that the number of species in these forests is somehow increasing.

WILLIAM F. LAURANCE

Smithsonian Tropical Research Institute, Apartado 2072, Balboa, Republic of Panama. E-mail: laurancew@si.edu

Genetic Polymorphism of Fc

J. M. WOOF'S PERSPECTIVE "TIPPING THE SCALES toward more effective antibodies" (2 Dec. 2005, p. 1442) presents a good commentary on how Fc γ receptors (Fc γ R) could contribute to the observed variation in immunoglobulin G (IgG) subclass responses to pathogens and tumor antigens. The author briefly points out the importance of Fc γ R gene polymorphism in differential binding to human IgG subclasses. I would like to add that the genetic variation in the Fc domain might also contribute to the effector functions of the IgG molecules. Surprisingly, virtually all studies—whether

involving interaction of Fc and Fc γ R or engineering mouse-human chimeric antibodies for immunotherapy—have treated the Fc region as if it were monomorphic. The Fc region of IgG (both human and mice) is not monomorphic. For instance, Fc regions of γ 1, γ 2, and γ 3 chains possess polymorphic determinants (called GM allotypes) coded by genes on chromosome 14 in humans (1). It is possible that particular Fc γ R and Fc (GM) alleles epistatically interact and contribute to specific effector responses mediated by IgG molecules, providing a mechanistic explanation for numerous associations observed between various Fc γ R and GM alleles and immunity to infectious, autoimmune, and malignant diseases. This would be analogous to the reported interaction between HLA and NK cell inhibitory receptor genes in the resolution of hepatitis C virus infection (2).

JANARDAN P. PANDEY

Department of Microbiology and Immunology, Medical University of South Carolina, 171 Ashley Avenue, Charleston, SC 29425, USA.

Qs & AAAS



www.sciencedigital.org/subscribe

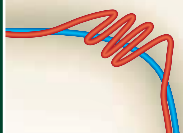
For just US\$99, you can join AAAS TODAY and start receiving *Science* Digital Edition immediately!

Qs & AAAS



www.sciencedigital.org/subscribe

For just US\$99, you can join AAAS TODAY and start receiving *Science* Digital Edition immediately!



Resonances in
chemical reactions

1383



Aggravating
aggregates

1385

References

1. R. Grubb, *Exp. Clin. Immunogenet.* **12**, 191 (1995).
2. S. I. Khakoo *et al.*, *Science* **305**, 872 (2004).

Response

PANDEY'S LETTER RAISES THE ISSUE OF IGG allotypes, allelic variants of IgG that vary at one or more amino acids at defined positions in their heavy chain constant regions. Although his arguments perhaps have most bearing on the outcome of an individual's IgG immune response to infectious agents, there are good reasons for considering the IgG allotype of monoclonal antibodies that are administered therapeutically. First, if the allotype of an administered antibody does not match that of the recipient, an immune response to an allotype-specific epitope on the administered IgG could necessitate termination of multiple-dose treatment. To avoid such a possibility, one option would be to generate a panel of IgGs representing all the different allotypes and match the allotype to each patient. However, this strategy is not considered commercially feasible, and usually, the most common allotype would be selected for general use. A practicable improvement, now being considered for some applications, is to create an artificial "null" allele and so reduce the likelihood of immune response in most recipients (1).

Second, as Pandey suggests, particular IgG polymorphisms might influence the ability of the antibody to interact with and trigger Fcγ receptors (FcγR). However, as yet, the evidence for this possibility is limited. The few studies addressing this point that have used "matched" Ig allotypes (i.e., with identical variable domains) have tended not to find significant differences in the ability of particular FcγR to interact with different human IgG allotypes (2–4). Before a definitive picture can emerge on whether IgG polymorphisms affect FcγR binding, further experiments to ascertain the interaction characteristics of matched IgG allotypes with every human FcγR variant will be necessary.

JENNY M. WOOF

Division of Pathology and Neuroscience, University of Dundee Medical School, Ninewells Hospital, Dundee, DD1 9SY, UK. E-mail: j.m.woof@dundee.ac.uk

References

1. K. L. Armour *et al.*, *Blood*, in press; published online 1 Dec. 2005 (10.1182/blood-2005-03-0989).
2. M. Brüggemann *et al.*, *J. Exp. Med.* **166**, 1351 (1987).
3. T. Paterson, J. Innes, L. McMillan, I. Downing, M. C. M. Carter, *Immunotechnology* **4**, 37 (1998).
4. K. L. Armour, A. Atherton, L. M. Williamson, M. R. Clark, *Biochem. Soc. Trans.* **30**, 495 (2002).

Hypsmocoma molluscivora Description

IN OUR BREVIA "WEB-SPINNING CATERPILLAR stalks snails" (22 July 2005, p. 575), we reported a new species of cosmopterigid moth, *Hypsmocoma molluscivora*. The species description was given in the Supporting Online Material; however, according to the International Code of Zoological Nomenclature, the formal description must appear in print to make the name officially available. The description follows.



Hypsmocoma molluscivora. Type Male genitalia ventral aspect specimen.



Hypsmocoma molluscivora Rubinoff & Haines, new species

Adult

Male.

Length of forewing: 6 mm, ($n = 1$). Head. Creamy dull white with scattered fuscous scales. Labial palpi prominent, recurved, mostly black. Antenna uniformly black, unscaled except for small white mark on dorsal side of elongated first basal segment; vertex same color as rest of head. Thorax. Dorsal scaling similar to that of head centrally but with more fuscous scales, abruptly becoming black at periphery where joining at base of costal margin of wing. Underside black toward head, abruptly becoming white with few fuscous scales toward abdomen. Legs. Prothoracic legs mostly black. Mesothoracic legs basally white abruptly becoming black, metathoracic legs same pattern. Tibial spurs prominent, off-white. Forewing: (see left panel of figure) very elongate, narrow, 6 times longer than broad. Ground color a lustrous white overlaid extensively with indistinct pattern of fuscous scales over upper (costal) 2/3 of wing, sometimes dense enough to appear as black spots, posterior 1/3 mostly white, fuscous scales becoming very sparse with distinct, undulating margin, except apical lower 1/3 remaining mostly fuscous like rest of forewing. Hindwing. More lanceolate than forewing, 7 times longer than broad. Subcostal brush (fig. S1) (1) prominent, dark brown, extending 2/3 the length of hindwing. Lustrous light gray with long colorous fringe maximum length nearly half as long as hindwing. Abdomen uniformly dark

gray. Genitalia as in the right panel of the figure and fig. S2 (1). Pseuduncus elongate, curved, attenuated distally into sharp point; aedeagus stout, prominent, blunt tipped; anellus lobes 1/2 length of uncus, broadened and setose distally, left lobe with distinctly broader tip; valva broadened distally, with four prominent, broad, uniformly spaced spurs, sequentially longer distally.

Male. HOLOTYPE. HAWAII: Maui, Makawao Forest Reserve. Elevation 920 m. GPS coordinates (UTM, NAD83): 04Q 783924, 2305563. Adult emerged III-23-05. (W. Haines, C. King collectors). Deposited in the University of Hawaii Insect Museum, on indefinite loan to the Bishop Museum, Honolulu, Hawaii.

Diagnosis

Hypsmocoma molluscivora is most similar and may be sympatric with *Hypsmocoma lebetella* Walsingham in montane wet forest areas of East Maui. The taxa can be easily distinguished by differences in forewing pattern, and the presence of the subcostal brush in *H. molluscivora*, but absent in male *H. lebetella*.

Larval Habits

Hypsmocoma molluscivora larvae form elongate, almost cylindrical cases of silk, algae, and small snail shells. The larvae use silk to attach resting snails to leaves and then force their way out into the snail's shell to feed (fig. S3) (1).

DANIEL RUBINOFF AND WILLIAM P. HAINES

Department of Plant and Environmental Protection Sciences, University of Hawaii, Honolulu, HI 96822, USA.

References and Notes

1. Supporting Online Material is available at www.sciencemag.org/cgi/content/full/311/5766/1377a/DC1.
2. We thank M. Bryce, F. Starr, and K. Starr for bringing specimens to our attention; B. Holland and R. Cowie of the University of Hawaii for identifying snail specimens; and F. Duvall for access to the Makawao Forest Reserve. J. Powell of UC Berkeley provided very helpful comments. W. Haines was supported by a National Science Foundation GK-12 grant (#DGE-0232016) awarded to the University of Hawaii's Center for Conservation Research and Training, K. Y. Kaneshiro, principal investigator.

GPS: A Military/Civilian Collaboration

DANIEL CLERY'S ARTICLE "EUROPE'S ANSWER TO GPS could be a boon for research" (News of the Week, 23 Dec. 2005, p. 1893) did a fine job of describing how Galileo (the European equivalent of the U.S.'s GPS) will extend the research value of global satellite navigation systems and help further develop new applications pioneered by GPS, including weather forecasting, ocean altimetry, surface roughness, and wave height.

Science readers should be aware that, although GPS is operated and maintained by the U.S. military, it is designed as a dual-use system and is managed by a joint military-civil committee. The official U.S. Government policy (www.navcen.uscg.gov/gps/default.htm) states that "The United States Government recognizes that GPS plays a key role around the world as part of the global information infrastructure and takes seriously the responsibility to provide the best possible service to civil and commercial users worldwide. This is as true in times of conflict as it is in times of peace." One other point of clarification is that a single GPS receiver in low Earth orbit can detect hundreds of atmospheric occultation signals every day, not just "a few."

JAMES F. ZUMBERG

Jet Propulsion Laboratory, Pasadena, CA 91109, USA.

Decline of Vultures in Asia

THE RANDOM SAMPLES ITEM "VULTURE CULTURE" (3 Feb., p. 587) presents the appearance of large numbers of Eurasian griffon vultures in Rajasthan, India, as good news, but this is far from the case. In India, populations of three species of vultures endemic to South Asia (oriental white-backed, long-billed, and slender-billed) have declined to less than 3% of what they were about

a decade ago and the decline continues (1). The Eurasian griffons are mostly immature birds from Central Asia, Tibet, and Mongolia that return there to breed, probably attracted in larger numbers by plentiful supplies of livestock carcasses left uneaten now that the resident species have almost disappeared. There is now substantial published evidence that the cause of the Asian vulture decline is veterinary use of the drug diclofenac, which vultures take in when they feed on the carcass of a cow or water buffalo treated with the drug (1–3). Eurasian griffons are as susceptible to kidney failure caused by diclofenac as their Asian relatives (4), so it is likely that the source populations of this species that winter in India will also be affected. Such an effect will not be detected soon, however, because there is virtually no systematic monitoring of numbers of vultures breeding in these inaccessible areas. Numbers of immature Eurasian griffons wintering in India may continue to grow, but this will probably just indicate a growing drain on their source populations. A ban on the veterinary use of diclofenac, announced by the Indian prime minister in March 2005 (5), will therefore probably benefit Eurasian griffons as well as the resident species, but only if it can be implemented successfully.

The Random Samples item also contained inaccuracies about recently published findings on the safety to vultures of meloxicam, an alter-

native to diclofenac that could help to save the vultures by speeding the removal of diclofenac from their food supply (6). The vultures used in the experiments were captive, but not captive-bred, and 72 birds (not 35) were treated, of which 66 were given meloxicam itself, rather than meat from treated cattle.

RHYS E. GREEN

Department of Zoology, University of Cambridge, Downing Street, Cambridge CB2 3EJ, UK.

References

1. R. E. Green *et al.*, *J. Appl. Ecol.* **41**, 793 (2004).
2. J. L. Oaks *et al.*, *Nature* **427**, 630 (2004).
3. S. Shultz *et al.*, *Proc. R. Soc. London Ser. B (Suppl.)* **271**, S458. DOI 10.1098/rsbl.2004.0223 (2004).
4. G. E. Swan *et al.*, *Biol. Lett.* doi:10.1098/rsbl.2005.0425 (2006).
5. P. Bagla, *Science* **307**, 1851 (2005).
6. G. E. Swan *et al.*, *PLoS Biol.* **4** (no. 3), e66 (2006).

Letters to the Editor

Letters (~300 words) discuss material published in *Science* in the previous 6 months or issues of general interest. They can be submitted through the Web (www.submit2science.org) or by regular mail (1200 New York Ave., NW, Washington, DC 20005, USA). Letters are not acknowledged upon receipt, nor are authors generally consulted before publication. Whether published in full or in part, letters are subject to editing for clarity and space.



MEETING CHAIRS

J. Charles Barbour
Sandia National Laboratories
jcbarbo@sandia.gov

Paul S. Drzaic
Alien Technology Corporation
pdrzaic@alien-technology.com

Gregg S. Higashi
Applied Materials
gregg_s_higashi@amat.com

Viola Vogel
Swiss Federal Institute of
Technology, ETH
viola.vogel@mat.ethz.ch

For additional meeting information,
visit the MRS Web site at

www.mrs.org/meetings/

or contact:



Member Services
Materials Research Society

506 Keystone Drive
Warrendale, PA 15086-7573
Tel 724-779-3003
Fax 724-779-8313
E-mail: info@mrs.org
www.mrs.org

2006 MRS SPRING MEETING

www.mrs.org/meetings/spring2006/

SYMPOSIA

MICROELECTRONIC DEVICE PROCESSING AND FABRICATION

- A: Amorphous and Polycrystalline Thin-Film Silicon Science and Technology
B: Silicon Carbide—Materials, Processing, and Devices
C: Sub-Second Rapid Thermal Processing for Device Fabrication
D: Transistor Scaling—Methods, Materials, and Modeling
E: Gate Stack Scaling—Materials Selection, Role of Interfaces, and Reliability Implications
F: Materials, Technology, and Reliability of Low-k Dielectrics and Copper Interconnects
G: Science and Technology of Nonvolatile Memories
H: Chalco-genide-Based Phase-Change Materials for Reconfigurable Electronics

PHOTONICS, ELECTRONICS, MAGNETICS, AND SENSORS

- I: Silicon-Based Microphotonics
J: Negative Index Materials—From Microwave to Optical
K: Materials Research for THz Applications
L: Materials for Next-Generation Display Systems
M: Conjugated Organic Materials—Synthesis, Structure, Device, and Applications
N: Molecular-Scale Electronics
O: Hybrid Organic/Inorganic/Metallic Electronic and Optical Devices
P: Semiconductor Nanowires—Fabrication, Physical Properties, and Applications
Q: Magnetic Thin Films, Heterostructures, and Device Materials
R: Nanostructured Materials and Hybrid Composites for Gas Sensors and Biomedical Applications
S: Smart Nanotextiles

COMPLEX AND BIOLOGICAL NANOSCALE MATERIALS AND SYSTEMS

- T: Nanomanufacturing
U: Organic and Inorganic Nanotubes—From Molecular to Submicron Structures
V: Structure and Dynamics of Charged Macromolecules at Solid-Liquid Interfaces
W: Colloidal Materials—Synthesis, Structure, and Applications
Y: Nanostructured Probes for Molecular Bio-Imaging
Z: Mechanics of Nanoscale Materials and Devices
AA: Molecular Motors, Nanomachines, and Engineered Bio-Hybrid Systems
BB: Mechanotransduction and Engineered Cell-Surface Interactions
CC: Electrobiological Interfaces on Soft Substrates

ENERGY AND ENVIRONMENT

- DD: Solid-State Lighting Materials and Devices
EE: Hydrogen Storage Materials
FF: Materials and Basic Research Needs for Solar Energy Conversion
GG: Current and Future Trends of Functional Oxide Films
HH: Recent Advances in Superconductivity
II: Materials in Extreme Environments
JJ: Materials Science of Water Purification

FORUM

- KK: Education in Nanoscience and Engineering

GENERAL

- X: Frontiers of Materials Research

MEETING HIGHLIGHTS

SYMPOSIUM TUTORIAL PROGRAM

Available only to meeting registrants, the symposium tutorials will concentrate on new, rapidly breaking areas of research and are designed to encourage the exchange of information by meeting attendees during the symposium.

EXHIBIT

A major exhibit encompassing the full spectrum of equipment, instrumentation, products, software, publications, and services is scheduled for April 18-20 in Moscone West, convenient to the technical session rooms.

SYMPOSIUM ASSISTANT OPPORTUNITIES

Graduate students who are interested in assisting in the symposium rooms during the 2006 MRS Spring Meeting are encouraged to apply for a Symposium Assistant position. By assisting in a minimum of four half-day sessions, students will receive a complimentary student registration, a one-year MRS student membership commencing July 1, 2006, and a stipend to help defray expenses. Applications will be available on our Web site by November 1.

CAREER CENTER

A Career Center for MRS members and meeting attendees will be offered in Moscone West during the 2006 MRS Spring Meeting.

PUBLICATIONS DESK

A full display of over 885 books will be available at the MRS Publications Desk. Symposium Proceedings from both the 2005 MRS Spring and Fall Meetings will be featured.

GRADUATE STUDENT AWARDS

The Materials Research Society announces the availability of Gold and Silver Awards for graduate students conducting research on a topic to be addressed in the 2006 MRS Spring Meeting symposia. Applications will be available on our Web site by October 1 and must be received at MRS headquarters by January 6, 2006.

CLIMATE CHANGE

Humanity Usurps Nature

Bill Chameides

Scientists overwhelmingly agree that we must act now to avert dangerous climate change. Despite that consensus, debate rages on in the public arena. Opposing viewpoints grace the pages of weekly newspapers, magazines, Web sites, and blogs. *The Weather Makers* is Tim Flannery's contribution to the fray. Already a hit in Australia, the book is now being released in the United States and Britain. Do we really need another lay book on global warming? Is there anything new to add? In this case, the answer is yes.

Flannery, the director of the South Australian Museum, is without question an extraordinary scientist. He may well hold the world's record for the discovery and description of mammal species, and his *Mammals of New Guinea (1)* is considered the authoritative reference on the subject. He entered the arena of science popularization about a decade ago, with the publication of his bestseller *The Future Eaters (2)*. His fame (perhaps in some minds notoriety) in Australia is akin to the reputation in America of the now-passed icon Carl Sagan.

Flannery's popular works are epic in scope, entertaining, poetic, and iconoclastic. In the *Future Eaters*, he argues that mass extinction of Australia's large terrestrial vertebrates some 50,000 years ago was caused by the arrival of humans—the "blitzkrieg" theory of mass extinction. A similar theme appears in his more recent *The Eternal Frontier (3)*, an ecological tribute to North America.

Given the author's views on the role of humanity in mass extinctions, it is no surprise that *The Weather Makers* is both a passionate explication of human influence on climate change and a call to action. Flannery offers an engaging—at times, spellbinding—read, which he develops along three major narrative lines.

The first follows Flannery's "slow awakening" to the dangers of global warming. It begins in 1981, when he discovered that forests are invading the alpine grasslands on Mt. Albert Edward in New Guinea. He suspected that this is symptomatic of rising temperatures, but did not pursue the question as he turned to

other, more immediate problems. Like many of us, Flannery greeted the warnings of global warming in the late 1980s with skepticism. (He notes that his initial reaction is not unusual as scientists are "trained skeptics," a relevant point given that the so-called "climate skeptics" seem to have appropriated the word for themselves.) Only later, in 2001, as the scientific claims of global warming grew more insistent, did he recall his 1981 observation and realize that he had "to learn more." Thus began his climate journey, which is both metaphorical (a discussion of the mysteries of Earth's climate) and a literal journey around the world to visit climate experts.

The second story is that of Earth or, for Flannery, Gaia—the term coined by James Lovelock to describe the interconnectedness of Earth's biological, atmospheric, oceanic, and geological systems. Readers are treated to an exposition of Earth's great climatic shifts over the past 65 million years. By detailing our growing understanding of the causes of these shifts, the author explodes the skeptics' arguments that past climate change has yet to be explicated and that we are therefore helpless to make sense of the human role in cur-

rent changes. We also travel with Flannery to critically important and unique ecosystems where global warming has already begun to wreak havoc. This is perhaps the most evocative part of the book, with Flannery describing "the delicate web of life [that] is being torn apart" by human interference in the climate.

The third story line presents the reader with two contrasting futures. In one, we fail to act and Earth's climate passes a tipping point that leads to disastrous consequences. Humanity is thrown either into a dark age or a dictatorial world regime ruled by the "Earth Commission

for Thermostatic Control." Bleak? Yes. Possible? Yes, but not likely.

The alternate future is one where disastrous climate change is averted by concerted international action that includes those countries Flannery deems the bad actors—the United

States and Australia. His discussion here is a little muddled. Flannery conflates the market-based, cap-and-trade approach adopted in Kyoto with carbon taxes. He also presents the technologies used to bring about a low-carbon economy as policy choices for governments rather than pathways determined by the marketplace in a cap-and-trade system. He claims we are at a crossroads: we can opt for either (i) a centralized system based on hydrogen and nuclear power and dominated by big corporations or

(ii) a distributed system based on wind and solar energy that places the power of production in the hands of individuals. Flannery, of course, favors the second path. I suspect, however, that the notion of such a clear crossroads is a bit oversimplified.

The book has some scientific missteps, for example: Nitrogen oxides (NO_x) are emitted from the burning of fossil fuels and lead to the production of ozone, not nitrous oxide. We would not "soon run out of oxygen and suffocate" without plants and algae—the depletion of atmospheric oxygen would require a couple of million years. And the connection between El Niño and global warming is not nearly as well established as Flannery would have readers believe. But these are minor flaws in a tour de force.

The book's title refers to the controllers or "makers" of the weather. It reflects a parable that weaves in and out of Flannery's three story lines. In this parable, Gaia was formerly the weather maker, but her rightful place has been usurped by humanity and our profligate use of fossil fuels. In the optimistic conclusion of Flannery's parable, humanity frees itself of fossil fuels and Gaia once again assumes control of Earth's climate. Hopeful? Yes. Possible? I think so.

References

1. T. F. Flannery, *Mammals of New Guinea* (Robert Brown, Carina, Queensland, Australia, 1990).
2. T. F. Flannery, *The Future Eaters: An Ecological History of the Australasian Lands and People* (Reed, Chatswood, New South Wales, Australia, 1994).
3. T. F. Flannery, *The Eternal Frontier: An Ecological History of North America and Its Peoples* (Atlantic Monthly Press, New York, 2001).

The Weather Makers

How Man Is Changing the Climate and What It Means for Life on Earth

by Tim Flannery

Atlantic Monthly Press, New York, 2006. 381 pp. \$24. ISBN 0-87113-935-9.

The Weather Makers

The History and Future Impact of Climate Change

Allen Lane, London, 2006. £20. ISBN 0-713-99921-7.



Lost treasure. Was Costa Rica's golden toad (*Bufo perigrines*) the first species to have become extinct as a result of climate change?

The reviewer is in the MIT Anthropology Program, 77 Massachusetts Avenue, Room 16-267, Cambridge, MA 02139-4307, USA. E-mail: guster@mit.edu

Fusion Power: Will It Ever Come?

William E. Parkins[†]

In the early 1950s, the hydrogen bomb awakened public awareness to the explosive power of nuclear fusion and launched hope in the physics community to use fusion as a power source. Fission made the trip to utility reasonably quickly, and now, 14% of the world's electricity is produced in that way. But although practical, controlled energy release from fission followed the discovery of that process by only 3 years, fusion power is still a dream-in-waiting. The explanation has more to do with engineering than with physics.

Two achievements are essential to produce electricity from a primary fuel: attaining the temperature needed to convert the source into heat and extracting the heat from the reacting region. In a nuclear fission reactor, uranium-235 can undergo the chain reaction with neutrons of ordinary temperature, and heat can be extracted directly by coolant circulated through the reactor. The scheme is compact, and it is cheap enough to compete with combustion plants.

There is no shortage of pairs of isotopes of light elements that can be made to fuse, but a potential energy barrier must be exceeded by the energy of collision. The combination requiring the least energy is D-T (deuterium-tritium). It requires a stable, long-lived plasma of reasonably high density with a temperature of about 100,000,000 K, but many efforts have failed to reach these conditions for a net power-producing plasma. The other plausible candidate (D-D) requires a temperature five times as high with no feasible means of heat removal.

Heat removal is troublesome even with the D-T reaction. A large amount of energy (17.4 MeV) is released from each fusion. Although 14 MeV is carried away by a neutron—to be slowed and absorbed in a blanket containing lithium and thus “breed” more tritium—the energy released will make everything radioactive out to the radiation shield beyond the blanket. Worse, the material of the reactor vessel will undergo radiation damage, which alters its physical properties. Any material used for the reactor vacuum vessel will become increasingly brittle. Back in the 1970s, design studies indicated that the vessel would need periodic replacement (1–3).

Another operational problem entails maintenance of vacuum integrity. The reactor vessel will have to approach much as 20 m in its major

dimension and would need many connections to heat transfer and auxiliary systems. It must operate at very high temperatures and undergo stresses from thermal cycling. Vacuum leaks would be inevitable and problem-solving would require remotely controlled equipment (4).

During the 1970s, projects in the United States, the United Kingdom, and Japan worked on conceptual full-scale fusion plant designs. Cost for the UWMAK-III design from the University of Wisconsin was estimated by the Bechtel Corporation to be between four and six times those of coal-fueled and nuclear plants of the period (5, 6).

Although the importance of reducing reactor dimensions was well recognized, recent work has focused on trying to achieve the necessary conditions in the plasma. In 1991, a team in California designed a plant with an output of 1000 megawatt-electric (MWe), comparable to modern nuclear power stations. The result, ARIES-I, was based partly on technologies yet to be developed (7). The reactor vessel was 17 m in its major dimension, fabricated from a silicon carbide composite. It operated at 650°C and benefited from an imagined average heat transfer rate of 1.2 MW/m²—six times the design rate for reactors that use helium coolants and twice that of pressurized water reactors.

Finally, the construction cost for any future fusion plant can be estimated by examining the blanket-shield component. Its area equals that of the vessel, so that its thickness is determined simply by choosing an average heat transfer rate. A 1000 MWe plant requires a thermal power of about 3000 MW, 20% of which must be absorbed by the vessel wall. If we assume an average heat transfer rate of 0.3 MW/m², the vessel wall and blanket-shield each must have an area of 2000 m². To absorb the 14 MeV neutrons and to shield against the radiation produced requires a blanket-shield thickness of ~1.7 m of expensive materials. This is a volume of 3400 m³, which, at an average density of about 3 g/cm³, would weigh 10,000 metric tons. A conservative cost would be ~\$180/kg, for a total blanket-shield cost of \$1.8 billion. This amounts to \$1800/kWe of rated capacity—more than nuclear fission reactor plants cost today (8). This does not include the vacuum vessel, magnetic field windings with their associated cryogenic system, and other systems for vacuum pumping, plasma heating, fueling, “ash” removal, and hydrogen isotope separation. Helium compressors, primary heat exchangers, and power conversion components would have to be housed outside of the steel containment building—

Prospects for practical applications of fusion power to solve our energy problems appear dubious on engineering grounds.

required to prevent escape of radioactive tritium in the event of an accident. It will be at least twice the diameter of those common in nuclear plants because of the size of the fusion reactor.

Scaling of the construction costs from the Bechtel estimates suggests a total plant cost on the order of \$15 billion, or \$15,000/kWe of plant rating. At a plant factor of 0.8 and total annual charges of 17% against the capital investment, these capital charges alone would contribute 36 cents to the cost of generating each kilowatt hour. This is far outside the competitive price range.

The history of this dream is as expensive as it is discouraging. Over the past half-century, fusion appropriations in the U.S. federal budget alone have run at about a quarter-billion dollars a year. Lobbying by some members of the physics community has resulted in a concentration of work at a few major projects—the Tokamak Fusion Test Reactor at Princeton, the National Ignition Facility (NIF) at Lawrence Livermore National Laboratory, and the International Thermonuclear Experimental Reactor (ITER), the multinational facility now scheduled to be constructed in France after prolonged negotiation. NIF is years behind schedule and greatly over budget; it has poor political prospects, and the requirement for waiting between laser shots makes it a doubtful source for reliable power. ITER was born in 1987, but no dirt has been dug, and U.S. membership is temporarily in moratorium.

New physics knowledge will emerge from this work. But its appeal to the U.S. Congress and the public has been based largely on its potential as a carbon-sparing technology. Even if a practical means of generating a sustained, net power-producing fusion reaction were found, prospects of excessive plant cost per unit of electric output, requirement for reactor vessel replacement, and need for remote maintenance for ensuring vessel vacuum integrity lie ahead. What executive would invest in a fusion power plant if faced with any one of these obstacles? It's time to sell fusion for physics, not power.

References and Notes

1. W. D. Metz, *Science* **192**, 1320 (1976).
2. W. D. Metz, *Science* **193**, 38 (1976).
3. W. D. Metz, *Science* **193**, 307 (1976).
4. W. E. Parkins *et al.*, *Phys. Today* **1997**, 15 (March 1997).
5. B. Badger *et al.*, Report UWFD-150 (Fusion Technology Institute, University of Wisconsin, Madison, 1975).
6. W. E. Parkins, *Science* **199**, 1403 (1978).
7. F. Najmabadi *et al.*, Report UCLA-PPG-1323 (University of California at Los Angeles, 1991).
8. J. A. Lake *et al.*, *Sci. Am.* **2002**, 73 (January 2002).

[†] William E. Parkins worked on uranium separation at the University of California during World War II and later was chief scientist at Rockwell International. This Policy Forum was edited to shorter length by the Editor-in-Chief from a manuscript received just before Parkins's death last October.

GENETICS

Total Information Awareness for Worm Genetics

Sean R. Eddy

Genetic analysis is an art. Just by studying the effect of mutations in genes, geneticists try to deduce how organisms work. This has been compared to trying to figure out how cars work by waiting outside the factory, tying the hands of individual workers as they go in, and studying the defects of cars that come out (*1*). Nowadays, as a result of high-throughput genomics, those metaphorical factory workers—the genes—live in a veritable police state, and geneticists have friends in high places. We can tap into vast databases of gene sequences, gene expression patterns, biochemical interactions, the published literature, and more—so we know the identities of genes, where they go and when, whom they talk to, and what’s being said about them. But we face the same problem as less benevolent police states: How can we (and should we?) use unreliable, disparate intelligence databases to learn what genes are actually doing? On page 1481 of this issue, Zhong and Sternberg (*2*) report the development of an integrated database system that predicts genetic interactions in the model worm *Caenorhabditis elegans*, marking a step toward total information awareness in genetic analysis.

A genetic interaction is one of the more subtle clues that geneticists use to tease apart the mechanistic details of a biological system. Two genes *A* and *B* “genetically interact” when the phenotype generated as the result of mutations in both genes (double mutant *ab*) is unexpectedly not just a combination of the phenotypes of the two single mutants *a* and *b*. A genetic interaction is called “suppression” when the phenotype of double mutant *ab* is more normal than expected and “enhancement” when the mutant *ab* phenotype is more defective than expected. An “interaction” is thus a logical one between genes, not necessarily a physical one between gene products, and there are many possible mechanistic explanations for it (see the figure). By themselves, genetic interactions are usually not enough to infer how a biological process works. Rather, genetic interactions are used to identify additional genes that might play a role in a process of interest.

One classic example is from studies of the development of the fruit fly eye (*3*). The phenotypes of flies with single-gene mutations had

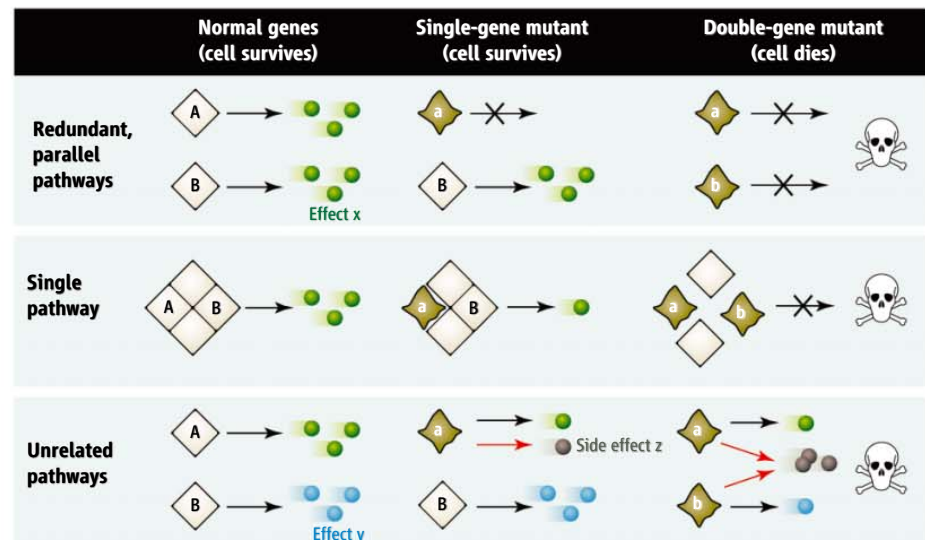
revealed two important genes, *sevenless* and *boss* (encoding a receptor and its cognate ligand, respectively), that function at an early stage of a signaling pathway, directing one cell type (R7) to become a photoreceptor. The genes encoding the rest of the signaling pathway remained unknown. One possibility was that the pathway was an essential shared subsystem—so important elsewhere in the fly that any mutations in genes of the pathway would be lethal. An elegant screen was crafted, using a weak mutation of the *sevenless* gene, to make R7 cells uniquely sensitive to small perturbations in the signaling pathway; weak mutants in other essential genes of the pathway might then produce defective R7 cells but not kill the flies. This approach worked, and seven essential genes involved in the signaling pathway were identified. The genes turned out to be components of one of the fundamental signaling pathways in biology, the Ras/mitogen-activated protein kinase (MAP kinase) cascade.

Many genetic interaction screens involve hypothesis-driven detective work. Only the simplest screens lend themselves to the assembly lines of modern high-throughput biology. Zhong

A comprehensive genetic interaction map of *C. elegans* can be derived from a database of information about *C. elegans* genes, proteins and their interactions, augmented with similar data from *Drosophila* and yeast.

and Sternberg aim to augment the geneticist, not replace him, by focusing attention on specific suspects predicted by integration of other types of high-throughput data. Recent technologies for targeted disruption of gene function (such as RNA interference) allow a geneticist to test specific pairs of genes quickly, instead of having to mutagenize and screen the entire genome.

Informative genetic interactions are expected to involve genes that are expressed at the same time and place (or coexpressed), that might physically interact, and that might show a similar phenotype when mutated individually. Zhong and Sternberg therefore integrated systematic data sets of *C. elegans* for gene expression, physical interaction of gene products, and functional annotation curated from the literature. However, these worm data sets are far from complete. A crucial part of the authors’ strategy is that not only do they use *C. elegans* data sets, they also integrate comparable data sets from two other major genetic model systems, the fruit fly *Drosophila melanogaster* and the yeast *Saccharomyces cerevisiae*. Many homologous genes function similarly in worms, flies, and yeast, so data sets from one



A genetic interaction, but what kind? Suppose that two genes encode products *A* and *B* (diamond shapes) that are involved in certain cellular functions (colored circles). What if mutations in both genes (double mutant, resulting in altered products *a* and *b*) show an unexpectedly strong visible phenotype relative to either single-gene mutation by itself? This would be considered genetic enhancement, but we don’t know immediately what the relationship is between the products of normal genes *A* and *B*. **(Top)** The two genes could act in redundant, parallel pathways. **(Middle)** They could encode subunits of a physical complex that tolerates loss of one subunit, but fails to produce an effect upon losing both. **(Bottom)** The gene products might have nothing special to do with each other, but both defects produce a synergistic side effect, such as a cellular stress response, that is overwhelmed by the loss of both genes. Thus, there are many possible mechanistic explanations for the genetic enhancement that is observed.

The author is with the Howard Hughes Medical Institute and the Department of Genetics, Washington University School of Medicine, St. Louis, MO 63108, USA. E-mail: eddy@genetics.wustl.edu

species should be partially informative for other species. All this information is weighted and integrated by a standard statistical classifier (linear regression), trained on examples of known pairs of interacting *C. elegans* genes.

Does it work? Zhong and Sternberg test predicted interactions generated by this approach for two genes known to function in two different signaling pathways: the *let-60/ras* gene in the MAP kinase signaling cascade, and the *itr-1* gene that encodes an inositol 1,4,5-trisphosphate receptor. Using RNA interference to create worms with simultaneous defects in both genes, they looked for either enhancement or suppression relative to single-gene defect phenotypes. They confirmed 12 of 49 novel predicted interactions for *let-60/ras*, and 2 of 6 for *itr-1*. The phenotypes they score are quantitative and far from obvious, such as the worm's pharynx pumping rate of 200 times a minute instead of

180 times a minute. This points to an advantage of focusing on a short list of suspects—it would be heroic to detect such small phenotypic effects in a genomewide mutagenesis screen.

Mind you, Zhong and Sternberg would likely be the first to tell you that it's not rocket science to guess that two *C. elegans* genes might show a genetic interaction if they are coexpressed, have similar mutant phenotypes, and have homologs that are already known to genetically interact in another organism. The difficulty is not making predictions from the available data—the difficulty is knowing the data are available. Humans lack the time and patience to manually cross-correlate huge genomic databases across several model organisms. Integrative database analysis augments our strong deductive ability by making up for our limited informational bandwidth.

Zhong and Sternberg have made lists of predicted genetic interactions for every gene in *C.*

elegans available at their Web site (4). Worm geneticists will soon be perusing the lists for their favorite genes. We can expect the same computational technology to be applied to the other model genetic systems, now that Zhong and Sternberg have provided such a clear demonstration of its potential. Someday soon, a *Drosophila* geneticist will download a list of genes that might interact with a favorite wing-development gene—a new and happier kind of “no-fly list” produced by database integration technology.

References

1. W. T. Sullivan, <http://bio.research.ucsc.edu/people/sullivan/savedoug.html>.
2. W. Zhong, P. W. Sternberg, *Science* **311**, 1481 (2006).
3. M. A. Simon, *Dev. Biol.* **166**, 431 (1994).
4. <http://tenaya.caltech.edu:8000/predict>

10.1126/science.1125655

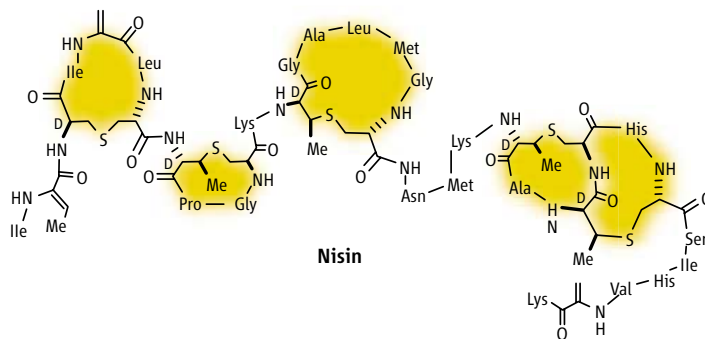
BIOCHEMISTRY

Five Golden Rings

David W. Christianson

The growing problem of antibiotic resistance has inspired myriad studies of antibacterial agents and their biosynthesis in recent years. Surprisingly, despite its worldwide use as a food preservative for more than four decades, the antibiotic nisin has not induced widespread biological resistance (1–4), making its biosynthesis particularly intriguing.

Nisin (see the figure) belongs to the family of lantibiotics, ribosomally synthesized antimicrobial peptides that are unusual in the extent and novelty of their posttranslational modifications. Their common structural feature is lanthionine—two alanine amino acids that are covalently cross-linked by a thioether linkage. Lanthionine is required for the function and stability of a cyclic peptide architecture (1). The prototypical lantibiotic is nisin, a 3.4-kD peptide secreted by the Gram-positive bacterium *Lactococcus lactis* (1, 2). Nisin binds to lipid II, a bacterial cell wall precursor, and consequently forms pores in the plasma membranes of Gram-positive bacteria. Membrane permeabilization accordingly results in cell death. Nisin exhibits nanomolar potency against a wide range of Gram-positive bacteria,



Five golden rings. The peptide antibiotic nisin contains extensive and unusual post-translational modifications, the most notable of which are five thioether rings of varying sizes and conformations. A single enzyme, nisin cyclase, utilizes a zinc ion to activate five cysteine thiol groups in the dehydrated prenisin substrate for sequential nucleophilic addition reactions that generate the five thioether rings of nisin.

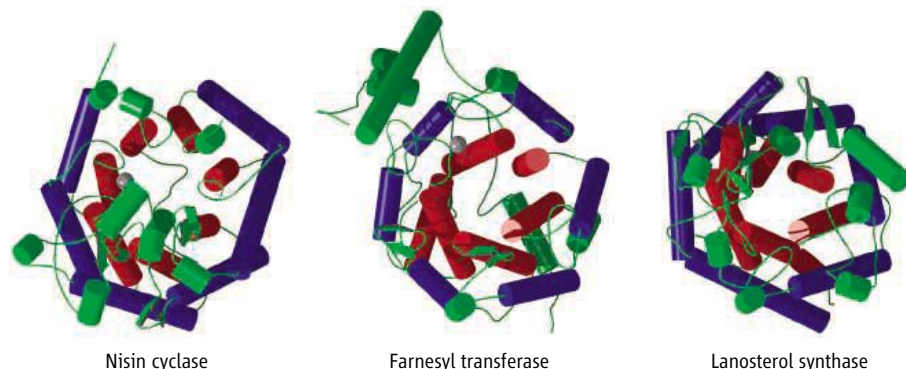
including those that cause botulism and listeriosis (3, 4). *L. lactis* itself escapes the toxic effect of nisin by the action of specific immunity proteins. The study by Li *et al.* (5) on page 1436 of this issue marks an important advance in our understanding of nisin biosynthesis. The authors report the crystal structure of nisin cyclase and provide compelling evidence that this zinc enzyme catalyzes five distinct cyclization reactions to generate the five thioether rings of nisin. Even though these thioether rings vary dramatically in size and shape, a hallmark of nisin cyclase catalysis is the exquisite regiochemical and stereochemical control over each thioether ring-forming reaction. As a versatile template for catalysis, nisin cyclase is sufficiently promiscuous to chaperone each of

The antibiotic nisin bears five rings of different sizes in its structure. The enzyme that catalyzes the five distinct cyclization reactions is flexible, yet stringent, enough to form each ring in the correct order and conformation.

five distinct cyclization reactions, but it is also sufficiently stringent to disallow nonproductive cyclization reactions.

The structure of nisin cyclase illuminates fascinating aspects of the cyclization mechanism, which requires the intramolecular addition of a cysteine thiolate to the α,β -unsaturated bond of either 2,3-didehydroalanine or (Z)-2,3-didehydrobutyrine in a Michael-type reaction to generate each of the five rings of nisin. Thiol coordination to the active-site zinc ion activates each cysteine for nucleophilic attack, a catalytic strategy shared with other zinc enzymes such as farnesyl transferase (which catalyzes the addition of a farnesyl moiety onto cysteine residues of certain proteins) (6, 7). The authors propose that conserved residues His²¹² and Arg²⁸⁰ in nisin cyclase function in the deprotonation of the cysteine nucleophile and the protonation of the enolate intermediate in the ring-forming reaction. Given its relatively weak acidity (pK_a of ~12.5), it is unusual for the guanidinium group of arginine to be considered in acid-base catalysis at physiological pH. Unless its pK_a were perturbed, the energetic cost of arginine deprotonation could compromise its potential catalytic utility. However, compelling results with certain enzymes implicate arginine residues in acid-base catalysis (8), so further stud-

The author is at the Roy and Diana Vagelos Laboratories, Department of Chemistry, University of Pennsylvania, Philadelphia, PA 19104–6323, USA. E-mail: chris@sas.upenn.edu



Nisin cyclase

Farnesyl transferase

Lanosterol synthase

Unexpected company. Nisin cyclase, farnesyl transferase, and the C-terminal domain of lanosterol synthase (a terpenoid cyclase), share similar double α -barrel folds (Protein Data Bank accession codes 2G02, 1KZO, and 1W6), respectively) despite their lack of amino acid sequence similarity.

ies of nisin cyclase are clearly warranted to pinpoint the catalytic importance of Arg²⁸⁰.

An equally surprising result emanating from the nisin cyclase structure (5) is the unexpected resemblance of its double α -barrel topology to that of farnesyl transferase (7) and of terpenoid cyclases such as squalene-hopene cyclase (9) and lanosterol synthase (10), despite low amino acid sequence identity (see the figure). The enzymes of terpene metabolism catalyze strikingly different chemical reactions using hydrocarbon isoprenoid substrates, yet they bear noteworthy structural and functional similarities with nisin cyclase. Farnesyl transferase uses a zinc-activated substrate thiolate for nucleophilic attack at farnesyl diphosphate (6, 7). The terpenoid cyclases serve as stringent templates that enforce the folding of a long, flexible polyisoprenoid substrate in the conformation required for the proper sequence, regiochemistry, and stereochemistry of multiple carbon-carbon bond-forming reactions—just as nisin cyclase serves as a stringent template that enforces the folding of a long, flexible peptide substrate in the conformation required for the proper sequence, regiochemistry, and stereochemistry of multiple carbon-sulfur bond-forming reactions. However, the ring-forming reactions catalyzed by a terpene cyclase occur in a multistep carbocation-mediated cascade initiated by a single enzyme-substrate complex, whereas the ring-forming reactions catalyzed by nisin cyclase occur sequentially. That is, the substrate must shift in the enzyme active site to activate each cysteine residue, one at a time, for thioether ring formation. Thus, biosynthetic fidelity and promiscuity must be balanced in the nisin cyclase active site to accommodate the regiochemical and stereochemical requirements of multiple substrate-binding modes, much as fidelity and promiscuity appear to be balanced in the terpene cyclase active site to accommodate multiple carbocation intermediates in catalysis (11).

The occurrence of double α -barrel protein folds among disparate cyclases suggests that this particular fold lends itself to facile evolution and

optimization as a template for complex cyclization reactions in biology. Another variation of the α -helical fold is found in terpenoid cyclases that generate smaller hydrocarbon products in the biosynthesis of menthol and the anticancer drug paclitaxel (taxol) (11). Future studies of these systems promise to exploit biosynthetic promiscuity and fidelity in cyclization reactions using

natural and unnatural (12) substrates in the never-ending search for blockbuster antibiotics. Such studies may well prove the five thioether rings of nisin to be golden indeed.

References and Notes

1. C. Chatterjee, M. Paul, L. Xie, W. A. van der Donk, *Chem. Rev.* **105**, 633 (2005).
2. J. Delves-Broughton, P. Blackburn, R. J. Evans, J. Hugenoltz, *Antonie van Leeuwenhoek* **69**, 193 (1996).
3. E. Breukink *et al.*, *Science* **286**, 2361 (1999).
4. S.-T. D. Hsu *et al.*, *Nat. Struct. Mol. Biol.* **11**, 963 (2004).
5. B. Li *et al.*, *Science* **311**, 1436 (2006).
6. C.-C. Huang, P. J. Casey, C. A. Fierke, *J. Biol. Chem.* **272**, 20 (1997).
7. H. W. Park, S. R. Boduluri, J. F. Moomaw, P. J. Casey, L. S. Beese, *Science* **275**, 1800 (1997).
8. Y. V. Guillén Schlippe, L. Hedstrom, *Arch. Biochem. Biophys.* **433**, 266 (2005).
9. K. U. Wendt, K. Poralla, G. E. Schulz, *Science* **277**, 1811 (1997).
10. R. Thoma *et al.*, *Nature* **432**, 118 (2004).
11. D. W. Christianson, *Chem. Rev.*, in press.
12. X. Zhang, W. Ni, W. A. van der Donk, *J. Org. Chem.* **70**, 6685 (2005).
13. D.W.C. thanks the NIH for support (grant GM56838) and L. Di Costanzo, D. Dowling, H. Gennadios, and G. Gomez for helpful discussions.

10.1126/science.1125298

CHEMISTRY

Resonances in Reaction Dynamics

Richard N. Zare

Resonances—sharp changes in behavior when particles interact—in chemical reactions can reveal the vibration and rotation of reactants and products. This approach has been applied to the dissociation of formaldehyde and the reaction of fluorine with hydrogen.

Whenever one object collides with another, the objects can merely bounce off each other like billiard balls, or they can undergo some process of change and interaction (for example, a chemical reaction). The probability for such an interactive or reactive process to occur sometimes varies rapidly as a function of collision energy. Observing

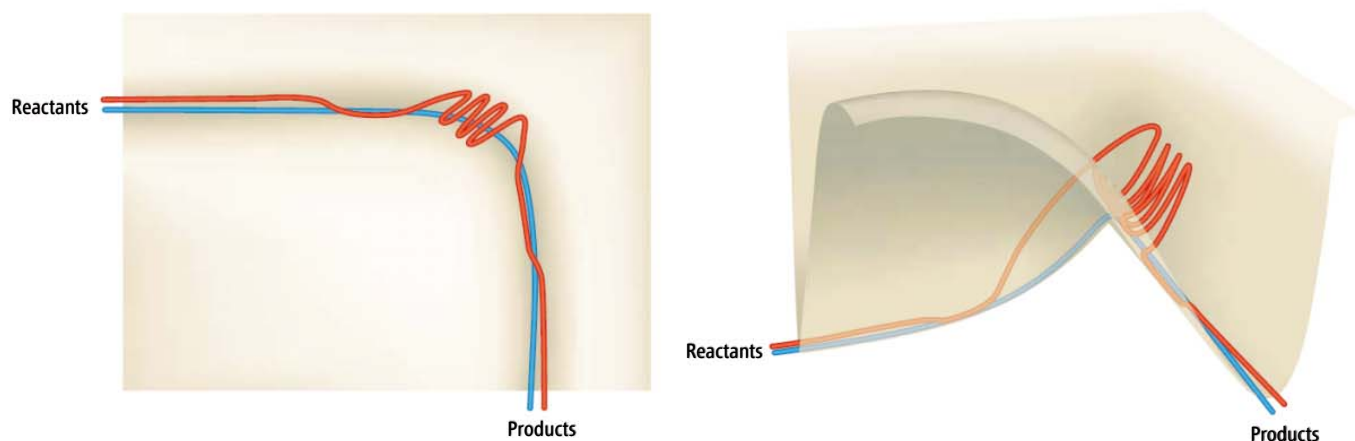
these sharp variations, known as resonances, is the most common way to detect short-lived intermediates in nuclear and particle physics. In the world of atomic and molecular physics, however, resonances are rarely observed, probably owing to the higher density of energy levels of the target system (which would smear out any resonance) and the experimental difficulty of obtaining sufficient velocity and angle resolution of the reactants and scattered prod-

ucts. It is very exciting, therefore, to see the observation of resonances in the reaction $F + H_2 \rightarrow HF + H$, reported by Qiu *et al.* (1) on page 1440, and the photodissociation of formaldehyde, reported by Yin *et al.* (2) on page 1443 of this issue. Such resonances may give us deep insight into how various elementary chemical steps actually occur. In each study, the intimate interplay between theory and experiment is needed to clarify what is actually happening.

The first report of a scattering resonance in atoms was the observation by Schulz of a sharp change in the intensity of electrons transmitted through helium atoms (3, 4). The incoming electron excites one of the two electrons of helium from its 1s orbital to a 2s orbital and then remains bound to the excited helium atom, forming a temporary helium negative ion. Below the energy threshold for promoting the helium 1s-to-2s transition, the temporary bound state can only decay by having the helium atom return to its (1s)² ground state, allowing the other electron to escape. Above this threshold, the temporary bound state of the helium nega-

Enhanced online at
www.sciencemag.org/cgi/
content/full/311/5766/1383

The author is in the Department of Chemistry, Stanford University, Stanford, CA 94305, USA. E-mail: zare@stanford.edu



Over the top. In a bimolecular reaction, the transformation of reactants to products resembles a hike over a mountain pass (top-down view at left, three-dimensional view at right). The minimum-energy path (blue curve) is referred to as the reaction coordinate. In a resonance (red curve), relative motion of the colliding reactants becomes temporarily converted into internal motion of

the collision complex not directed along the reaction path. This quasi-bound state persists until energy reflows into relative motion along the reaction coordinate. The drawings are very simplified—four dimensions are needed to portray accurately the motion, three for the internal degrees of freedom and one for the energy.

tive ion can also decay by having the electron escape while leaving the helium atom in its excited $1s2s$ electron configuration. The first decay mode is into a channel that hardly overlaps with the decaying state, whereas the second decay mode is into a channel with a much larger overlap. Consequently, the decay probability increases dramatically as the collision energy of the electron passes through threshold, an effect that is indicated by the width of the resonance as a function of the electron collision energy. Soon after Schulz's work with helium, the same type of phenomenon was observed in the scattering of electrons from molecules.

Scattering resonances might be regarded as rather esoteric, of intense interest to those who study simple atoms and molecules in isolation but of little relevance to living processes. This perception would be quite false. For example, most of the energy deposited in living cells by ionizing radiation causes the production of secondary electrons. These electrons, even at energies insufficient to trigger ionization, induce breaks in single- and double-stranded DNA, which are caused by rapid decays of transient molecular resonances localized on the nitrogen-containing bases of DNA (5).

A molecule is a collection of nuclei held together by electrostatic attraction. A bound system of N nuclei can vibrate in $3N - 6$ different ways (normal modes) in which the system's center of mass remains fixed while all nuclei move with the same frequency but in general with different amplitudes. Some of these motions are along the reaction coordinate—that is, they are directed from reactants to products—whereas many other motions do not couple to the reaction coordinate (see the figure). Energy in these noncoupled modes cannot be used to surmount the barrier that commonly separates reactants from products, and the system must wait some time (the decay time of the resonance) for its

energy to redistribute itself and find its way to modes along the reaction coordinate for the collision partners to separate.

In the photodissociation of formaldehyde, CH_2O , the reaction products are HCO and H as well as CO and H_2 . For the $\text{H}_2 + \text{CO}$ channel, the H_2 molecule can be formed directly or it can result from the frustrated escape of the H and HCO fragments (6). In the latter case, the H and HCO partners fail to separate because part of the energy is tied up in vibrational motion of the HCO fragment, which does not couple to the H-HCO coordinate. The loosely bound H atom then bounces around in the attractive potential of the complex until it comes close enough to the H -end of HCO to pull off this H atom, yielding hot (vibrationally excited) H_2 and cold CO . This wandering behavior of the light H atom followed by the production of internally excited H_2 closely resembles what has been observed in the reaction of $\text{H} + \text{HBr} \rightarrow \text{H}_2 + \text{Br}$ (7). Two different pathways can yield the $\text{H} + \text{HCO}$ fragments. One of them is on the barrierless ground-state singlet potential energy surface (S_0) for which the two electron spins on H and HCO are paired, and the energy is distributed statistically among the different vibrational and rotational motions of the products. The other is on the low-barrier triplet-state potential energy surface (T_1) for which the electron spins are unpaired, resulting in more impulsive dynamics that directs the energy into the separating photofragments in a distinctly nonstatistical manner. The combined experimental and theoretical studies by Yin *et al.* represent a major step forward in our understanding of how this simple molecule is decomposed by radiation to yield photofragments having so many disparate attributes. The coupling of electronic and nuclear motions in which more than one potential energy surface is accessed is particu-

larly striking. Even for this relatively small molecule, breaking up is never easy.

The $\text{F} + \text{H}_2$ reaction, made famous by the pioneering crossed molecular beam experiments of Lee and co-workers (8), is of practical importance as the driver for the powerful infrared HF chemical laser. Qiu *et al.* fire a pulsed beam of F atoms at a pulsed beam of molecular hydrogen that is prepared almost exclusively in its vibrationless, rotationless ground state $\text{H}_2(v = 0, J = 0)$ (where v is the vibrational quantum number and J is the rotational quantum number). The resulting H -atom products are detected by converting them to high-lying atomic Rydberg states. By measuring the velocity distribution of the H atoms, it is possible to extract the corresponding vibrational-rotational internal state distribution of the HF products from conservation of energy. Moreover, the H atoms can be detected at different laboratory scattering angles, allowing the center-of-mass angular distribution of the HF products to be obtained. Qiu *et al.* find a pronounced forward-scattering peak for the $\text{HF}(v = 2)$ product, where forward means in the same direction as the incoming F atom—a result never observed before for this benchmark reaction system. This feature shows a rather abrupt change with collision energy, which is attributed to the trapped motion in the $\text{H-HF}(v = 3)$ vibrationally adiabatic potential energy surface before the opening of this channel. The authors suggest that both a ground-state and a first-excited-state van der Waals resonance in the exit channel constructively interfere to account for the observed behavior. This work is one of the most striking examples of the existence of resonances in a heavy-particle collision system.

Why study more resonances in reaction dynamics? They surely exist, as shown quite convincingly for the $\text{F} + \text{HD} \rightarrow \text{HF} + \text{D}$ reaction

system (9). The answer is that resonances reveal the quasi-bound levels of the reaction complex with unique clarity. Until we are able to determine more confidently what theoretical approximations can be trusted, we need the close interplay between theory and experiment to help us understand how elementary chemical processes take place.

References

1. M. Qiu *et al.*, *Science* **311**, 1440 (2006).
2. H. M. Yin *et al.*, *Science* **311**, 1443 (2006).
3. G. J. Schulz, *Phys. Rev. Lett.* **10**, 104 (1963).
4. M. A. Biondi, A. Herzenberg, C. E. Kuyatt, *Phys. Today* **32** (10), 44 (1979).
5. B. Boudaïffa, P. Cloutier, D. Hunting, M. A. Huels, L. Sanche, *Science* **287**, 1658 (2000).
6. D. Townsend *et al.*, *Science* **306**, 1158 (2004); published

online 21 October 2004 (10.1126/science.1104386).

7. A. E. Pomerantz *et al.*, *J. Am. Chem. Soc.* **127**, 16368 (2005).
8. D. M. Neumark, A. M. Wodtke, G. N. Robinson, C. C. Hayden, Y. T. Lee, *J. Chem. Phys.* **82**, 3045 (1985).
9. K. Liu, R. T. Skodje, D. E. Manolopoulos, *PhysChemComm* **5**, 27 (2002).

10.1126/science.1124421

BIOMEDICINE

One Misfolded Protein Allows Others to Sneak By

Gillian P. Bates

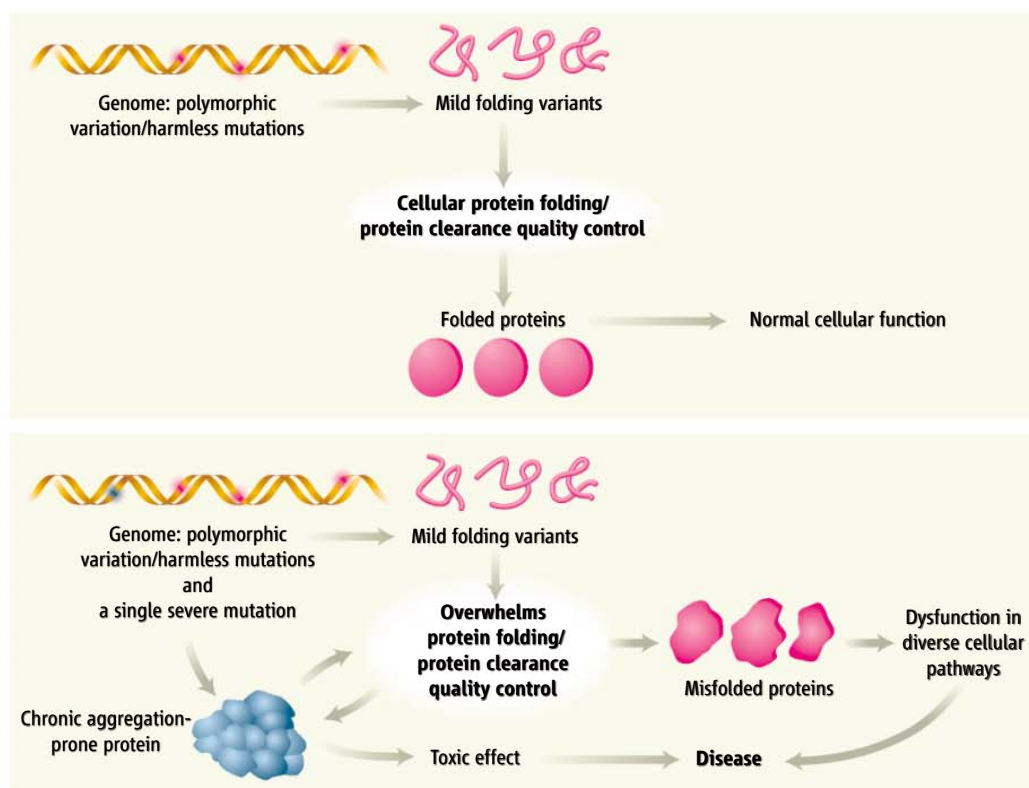
Huntington's disease, Parkinson's disease, Alzheimer's disease, and amyotrophic lateral sclerosis—these neurodegenerative disorders are among many inherited diseases that have been linked to genetic mutations that result in the chronic aggregation of a single specific protein. Cellular and animal models of these disorders are consistent with misfolded conformers, oligomers, and/or aggregates of the proteins huntingtin, α -synuclein, amyloid- β peptide, and superoxide dismutase-1 as the respective toxic culprits of these late-onset degenerations. What has been puzzling about the progression of each of these diseases is the perturbation of a wide range of cellular pathways (transcription, energy metabolism, microtubule transport, synaptic function, and apoptosis, among others), and this collective dysfunction of processes has also been proposed to underlie the pathogenesis of these diseases. Could a single "aggregation-prone" protein wreak so much havoc? A report by Gidalevitz *et al.* on page 1471 of this issue (1) has questioned whether there might be a general mechanism by which an aggregation-prone protein can have so many cellular effects.

The mutations that cause polyglutamine (polyQ) diseases, including Huntington's disease and a number of spinocerebellar ataxias, result in the expansion of a tract of glutamine residues to a length beyond a threshold of generally 35 to 40 glutamines, render-

ing the protein in which the tract is harbored as pathogenic. This correlates with a dramatic increase in the rate at which the polyQ tract can self-assemble into fibrillar aggregates (2). Morimoto and colleagues have previously used the nematode *Caenorhabditis elegans* to model polyQ disease by expressing

Proteins prone to aggregate in cells have been linked to neurodegenerative diseases. As cells try to eliminate such aggregates, other misfolded proteins may go undetected, making the cell susceptible to their toxic effects.

pathogenic and nonpathogenic polyQ peptides that are fused to yellow or green fluorescent proteins in muscle (3) and neuronal (4) cells. Fluorescent polyQ aggregates and a corresponding phenotype were observed in worms expressing pathogenic polyQ, whereas nonpathogenic peptides had no effect.



The global consequences of an aggregation-prone protein on cellular protein folding homeostasis. (Top) Under normal physiological conditions, polymorphisms in genes can result in the expression of proteins that are mild folding variants that are correctly folded or cleared out of the cell by protein quality control mechanisms. (Bottom) In the presence of a chronic aggregation-prone protein such as those associated with neurodegenerative diseases, the protein folding and clearance process becomes overwhelmed. Proteins that are normally innocuous are no longer correctly folded, leading to dysfunction in a diverse set of cellular pathways. In turn, these structurally and functionally unrelated proteins generate a positive feedback loop and exacerbate the misfolding of the aggregation-prone protein, thereby acting as modifiers of this process.

The author is at King's College London School of Medicine, London SE1 9RT, UK. E-mail: gillian.bates@genetics.kcl.ac.uk

To uncover the cellular consequences of the chronic expression of an aggregation-prone protein, Gidalevitz *et al.* used functionally unrelated temperature-sensitive mutations and selected the polyQ worm as a model of a protein conformation disease. Such mutations are highly dependent on their cellular environment and do not display a phenotype at a “permissive” temperature. However, when the temperature is raised to become “restrictive,” they cause disturbances in the folding of their host protein, with deleterious consequences. The phenotypes of the temperature-sensitive mutants chosen for this study are rarely observed at 15°C but are present in more than 95% of the worms at 25°C, and they include early embryonic and larval lethality, slow movement in adults, abnormal body shape, and an egg-laying defect. These temperature-sensitive strains were crossed to worms that express either polyQ40 (pathogenic) or polyQ24 (nonpathogenic) in muscle cells. The specific temperature-sensitive phenotype was exposed in worms expressing pathogenic polyQ40, but not polyQ24, at 15°C. One of these temperature-sensitive strains (UNC-15) has a mutation in the homolog of paramyosin, a muscle structural protein, which at 25°C forms paracrystalline structures that are quite distinct from aggregates of proteins with a polyQ tract. In the presence of pathogenic polyQ40, UNC-15 animals formed these paracrystalline structures at the permissive temperature. The expression of pathogenic polyQ40 thus disturbed the global balance of protein folding quality control in the muscle of these animals and exposed the phenotypes of distinct temperature-sensitive mutations at the permissive temperature. Gidalevitz *et al.* showed that

this phenomenon extends to the expression of pathogenic polyQ in neuronal cells and that its effect on the mutant phenotype reflects specific molecular interactions within a cell type rather than an overall decrease in the fitness of the organism. Therefore, the chronic expression of polyQ40, an aggregation-prone protein, can compromise the function of many structurally and functionally unrelated proteins.

The authors further questioned whether the misfolding of a temperature-sensitive protein could in turn enhance the misfolding of the polyQ-containing protein. They found that aggregation of pathogenic polyQ40 at the permissive temperature dramatically increased when worms also harbored a temperature-sensitive mutation in genes encoding either paramyosin or the small GTP-binding protein ras. The mutations in these genes have no adverse effects under normal physiological conditions, yet they substantially enhanced the aggregation of the polyQ-containing proteins. This demonstrates that mild folding variants in proteins that are not involved in protein folding or clearance pathways can behave as modifiers of pathogenic polyQ phenotypes and toxicity.

This work indicates that the chronic expression of a misfolded protein can upset the cellular protein folding homeostasis under physiological conditions. These results have implications for pathogenic mechanisms in protein conformational diseases. The human genome harbors a load of polymorphic variants and mutations that might be prevented from exerting deleterious effects by protein folding and clearance quality control mechanisms in the cell. However, should these mechanisms become overwhelmed, as in a

protein conformation disease, mild folding variants might contribute to disease pathogenesis by perturbing an increasing number of cellular pathways (see the figure). Therefore, the complexity of pathogenic mechanisms identified for protein conformation diseases could in part result from the imbalance in protein folding homeostasis. These folding-defective proteins may in turn compromise the overall folding capacity of the cell and act as genetic modifiers of disease. In the case of Huntington’s disease, this may contribute to the 40% of the variance in age of onset that is not attributed to polyQ repeat length but to genes other than the HD gene (5) and to the wide variation in disease presentation between individuals with the same polyQ mutation. In a genetic screen of the worm, Nollen *et al.* identified close to 200 genes with diverse functions that could modify polyQ protein aggregation (6). As genetic modifiers of Huntington’s disease and other protein conformation diseases are identified, it will be intriguing to test whether they too can have an impact on protein homeostasis.

References

1. T. Gidalevitz, A. Ben-Zvi, K. H. Ho, H. R. Brignull, R. I. Morimoto, *Science* **311**, 1471 (2006); published online 9 February 2006 (10.1126/science.1124514).
2. E. Scherzinger *et al.*, *Proc. Natl. Acad. Sci. U.S.A.* **96**, 4604 (1999).
3. J. F. Morley, H. R. Brignull, J. J. Weyers, R. I. Morimoto, *Proc. Natl. Acad. Sci. U.S.A.* **99**, 10417 (2002).
4. H. R. Brignull, S. Tang, R. I. Morimoto, personal communication.
5. N. S. Wexler *et al.*, *Proc. Natl. Acad. Sci. U.S.A.* **101**, 3498 (2004).
6. E. A. Nollen *et al.*, *Proc. Natl. Acad. Sci. U.S.A.* **101**, 6403 (2004).

10.1126/science.1125246

ATMOSPHERIC SCIENCE

Fungi, Weathering, and the Emergence of Animals

Louis A. Derry

As any high-school biology text will explain, eukaryotes have separate nuclei and other organelles and thus possess a more complex level of cellular organization than the simpler prokaryotic archaea and bacteria. Eukaryotes form a large group that include some algae, protists, fungi, plants, and animals. We also know that the origin of animals followed the appearance of their eukaryotic ancestors by more than a billion years. The existence of such a long interval between the advent of complex cells and the advent of com-

plex organisms remains a fascinating and fundamental puzzle in the history of Earth and life. The first fossil evidence for ancestral animals is found in strata from about 575 million years ago (1, 2), and recent analyses of molecular clocks suggest that the genetic divergence of animals occurred only 50 million years or so earlier (3). Animals emerged in a period of Earth history characterized by extreme climatic shifts and profound developments in biogeochemical cycles. During the Neoproterozoic (850 to 544 million years ago) there were three global glaciations, and toward the end of that interval geochemical evidence suggests increased oxygenation of Earth’s atmosphere. On page 1446 of this issue, Kennedy *et al.*

A billion years separated the advent of one-celled eukaryotes from that of multicellular animals. This rise of the animals may have been triggered by increases in atmospheric oxygen resulting from mineral weathering accelerated by ancient soil biota.

(4) propose that weathering processes on land, perhaps accelerated by the expansion of an early terrestrial biosphere, helped create conditions suitable for the emergence of animals.

The temporal correspondence between dramatic environmental change and the appearance of early multicellular animals (metazoans) has led many scientists to propose that the evolutionary changes were a consequence of either new environmental pressures, or the relaxation of a previous environmental constraint. Increased atmospheric oxygen in the late Proterozoic is one such candidate. The appearance of large animals more than half a meter in diameter by about 560 million years ago itself suggests a strong

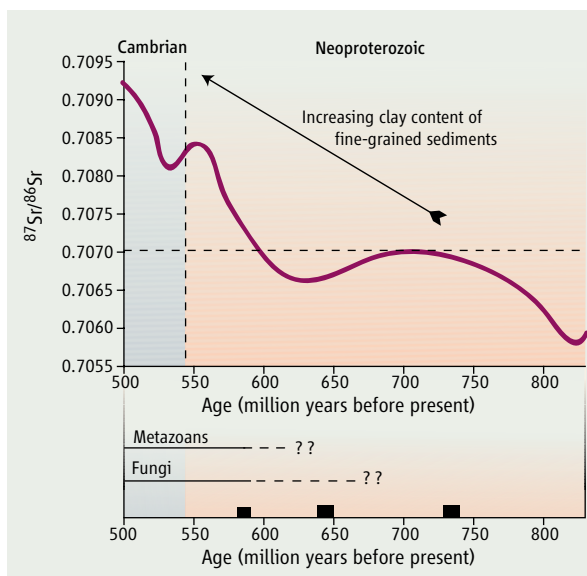
The author is in the Department of Earth and Atmospheric Sciences, Cornell University, Ithaca, NY 14853, USA. E-mail: lad9@cornell.edu

constraint on atmospheric oxygen levels. Many years ago Runnegar (5) used physiological modeling to demonstrate that unless these very early animals had unexpectedly sophisticated circulation systems, they would require oxygen levels not very different from that of the modern atmosphere.

We have no direct paleobarometer for atmospheric oxygen during the deep past, and so levels must be inferred indirectly. Evidence from carbon- and sulfur-isotope data (6–8) implies that oxygen levels rose substantially during the Ediacaran period (recently formally defined as the interval between the end of the Marinoan glaciation at about 635 million years ago and the base of the Cambrian period at 544 million years ago). If so, what was it about Earth history in this unusual period that led to higher oxygen levels, which may have both spurred and been driven by radical evolutionary diversification? Enhanced burial of organic carbon appears to be part of the answer. Photosynthesis produces

oxygen as a by-product of carbon fixation. Almost all of the oxygen is consumed by respiration, but some organic carbon is buried in sediments and so is protected from reoxygenation, allowing a corresponding quantity of O_2 to accumulate in the environment. If production of free oxygen exceeds the rate at which it is consumed by other sinks such as the oxidation of sulfur and iron and the destruction of “old” organic carbon present in ancient sediments as kerogen, then the partial pressure of oxygen in the atmosphere (pO_2) will rise. Simple enough, but this further begs the question as to “why?” What events may have tipped the balance of the carbon cycle toward increased sequestration of organic carbon in sediments and consequent accumulation of O_2 in the atmosphere?

Kennedy *et al.* propose a novel hypothesis that links a change in terrestrial weathering regimes, driven by the expansion of a primitive land biota, with enhanced burial of organic carbon. They note that, in modern sediments, most (90%) organic carbon is adsorbed to the surface of soil-formed (pedogenic) clay minerals, fine aluminosilicate particles with high reactive surface area produced by chemical weathering in soils. It has long been noted that Precambrian sediments appeared to be composed of less-weathered materials than younger sediments, suggesting a long-term shift in terrestrial weathering processes, but there had been no recent attempts to address this issue systematically. Kennedy *et al.* have now done so by measuring the ratio of pedogenic clays to “detrital” clays



A change in weathering. Evolution of the $^{87}\text{Sr}/^{86}\text{Sr}$ ratio in seawater during the Neoproterozoic and Cambrian periods. High ratios generally indicate greater weathering inputs to the oceans. Weathered clays have a high surface area and facilitate increased burial of organic carbon in marine sediments, which in turn could lead to more oxygen in the atmosphere, creating an environment suitable for the emergence of animals. Time lines at the bottom show the period over which metazoans and fungi emerged. The black rectangles indicate major Neoproterozoic glacial intervals.

(essentially mechanically finely ground rocks that have much less ability to sequester carbon) in sedimentary rocks from 775 to 525 million years ago. They found a marked increase in pedogenic clay content during this interval, suggesting that soil-forming processes evolved over the same time. The increased clay content should have facilitated the preservation of organic carbon in sediments, leading to enhanced oxygen production. The authors propose that the expansion of primitive soil biota was responsible for greater production of pedogenic clays. Today pedogenic processes leading to clay formation are greatly accelerated by plants, fungi, and other soil biota. The origins of terrestrial ecosystems are not well understood, but clearly extend into the Proterozoic. Molecular divergence data have suggested that ancestral fungi diverged about 1 billion years ago, and vascular plants nearly 700 million years ago (9), but no fossil examples had been recognized before the Ordovician period (~460 million years ago). The recent report of ancient fungi from the same Chinese sediments that contain the earliest evidence for metazoans (about 580 million years ago) greatly extends the terrestrial fossil record and supports the idea that there were land biota that could have enhanced weathering processes in the late Proterozoic (10).

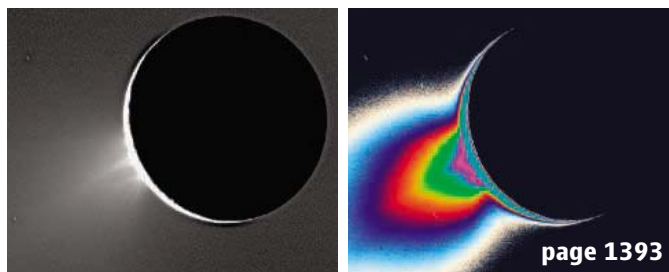
Additional evidence for a change in weathering processes may come from the record of the isotopic composition of strontium in the Neoproterozoic oceans, a period during which the $^{87}\text{Sr}/^{86}\text{Sr}$ ratio increased dramatically (see the

figure). The major cause was the formation of the Pan-African mountain ranges, which metamorphosed and uplifted crust through extensive regions of Africa, South America, and elsewhere. As with the Himalayan mountain formation, such disturbance led to an increased flux of strontium with elevated $^{87}\text{Sr}/^{86}\text{Sr}$ to the oceans (11). But there is another, less dramatic but equally important facet of seawater strontium history. Before the mid-Neoproterozoic, marine $^{87}\text{Sr}/^{86}\text{Sr}$ values never reached as high as 0.707, whereas afterward they almost never fell below that value. A gradually decreasing flux of strontium (with low $^{87}\text{Sr}/^{86}\text{Sr}$) from the mantle to the oceans is likely one factor, but Kennedy *et al.* suggest that $^{87}\text{Sr}/^{86}\text{Sr}$ ratios record a change in the style and intensity of continental weathering, as “modern” pedogenesis facilitated by land biota emerged. If continental collision events alone are responsible for imparting high $^{87}\text{Sr}/^{86}\text{Sr}$ ratios to the oceans, why haven’t we seen episodic fluctuations to high values before 600 million years ago, associated with known earlier collisions?

Like any novel idea, the scenario proposed by Kennedy *et al.* raises as many questions as it answers. It will be necessary to test how widespread the change in sedimentary clay mineralogy is, because most (but not all) of their data come from a single basin. Alternative explanations of the strontium-isotope history are certainly possible. Our knowledge about terrestrial environments and their inhabitants in the Proterozoic remains very limited. And finally, all inferences about Precambrian oxygen levels in the atmosphere remain just that—we have no good paleobarometer for pO_2 in the ancient past, although perhaps molecular fossils will one day provide better constraints, as they have for pCO_2 . But, Kennedy *et al.* pose an intriguing hypothesis that relates the advent of large eukaryotic organisms in the oceans to the impact of their eukaryotic cousins on terrestrial weathering processes. We can hope that time will tell if the spread of fungi on land helped set the stage for the spread of animals in the sea.

References

1. S. Xiao, Y. Zhang, A. H. Knoll, *Nature* **391**, 553 (1998).
2. D. Condon *et al.*, *Science* **308**, 95 (2005).
3. K. J. Peterson, N. J. Butterfield, *Proc. Natl. Acad. Sci. U.S.A.* **102**, 9547 (2005).
4. M. Kennedy, M. Droser, L. M. Mayer, D. Pevear, D. Mrofka, *Science* **311**, 1446 (2006); published online 2 February 2006 (10.1126/science.1118929).
5. B. Runnegar, *Alcheringa* **3-4**, 223 (1982).
6. D. E. Canfield, A. Teske, *Nature* **382**, 127 (1996).
7. L. A. Derry, A. J. Kaufman, S. B. Jacobsen, *Geochim. Cosmochim. Acta* **56**, 1317 (1992).
8. M. T. Hurtgen, M. A. Arthur, G. P. Halverson, *Geology* **33**, 41 (2005).
9. D. S. Heckman *et al.*, *Science* **293**, 1129 (2001).
10. X. Yuan, S. Xiao, T. N. Taylor, *Science* **308**, 1017 (2005).
11. J. M. Edmond, *Science* **258**, 1594 (1992).



Cassini at Enceladus

CONTENTS

Perspectives

- 1389 Enceladus: Cosmic Gymnast, Volatile Miniworld
J. S. Kargel
- 1391 Does Enceladus Govern Magnetospheric Dynamics at Saturn?
M. G. Kivelson

Research Articles

- 1393 Cassini Observes the Active South Pole of Enceladus
C. C. Porco et al.
- 1401 Cassini Encounters Enceladus: Background and the Discovery of a South Polar Hot Spot
J. R. Spencer et al.

Reports

- 1406 Identification of a Dynamic Atmosphere at Enceladus with the Cassini Magnetometer
M. K. Dougherty et al.
- 1409 The Interaction of the Atmosphere of Enceladus with Saturn's Plasma
R. L. Tokar et al.
- 1412 Enceladus' Varying Imprint on the Magnetosphere of Saturn
G. H. Jones et al.
- 1416 Cassini Dust Measurements at Enceladus and Implications for the Origin of the E Ring
F. Spahn et al.
- 1419 Cassini Ion and Neutral Mass Spectrometer: Enceladus Plume Composition and Structure
J. H. Waite Jr. et al.
- 1422 Enceladus' Water Vapor Plume
C. J. Hansen et al.
- 1425 Composition and Physical Properties of Enceladus' Surface
R. H. Brown et al.

INTRODUCTION

Tiger, Tiger, Burning Bright

The Cassini spacecraft has been touring Saturn's neighborhood since it entered orbit there on 1 July 2004. As well as interrogating the giant planet and its filigree rings, understanding the formation of Saturn's moons is one of the key goals of the mission. Saturn has 35 named moons in its family, as well as a plethora of smaller objects hidden in the rings. The variety of moons is staggering. Some consist of exposed rock; others are enveloped in thick ice. Some are pock-marked with billion-year-old craters; others varnished with fresh snow. Cassini's busy schedule included more than 20 encounters with Saturn's moons in the past year, offering but a sampling of these different worlds.

One of the most curious of all Saturn's moons is Enceladus. The sixth largest saturnian satellite—although at a mere 504 km across, its width is smaller than that of Arizona or Spain—Enceladus rides in the middle of Saturn's E ring, a wide and diffuse blue ring of fine particles. Because this ring lacks the bigger shards characteristic of ancient satellite smash-ups, astronomers have long suspected that the E-ring particles emanate from Enceladus itself.

Earlier Earth-based and Voyager space probe images revealed that Enceladus' surface is icy and complex. Old cratered terrains butt up against newly resurfaced smooth ice flows. So Cassini scientists hoped to see signs of recent activity and possibly ice volcanism. As the papers in this special issue show, their anticipation was rewarded. In three flybys, in February, March, and July 2005, Cassini trained its instruments on Enceladus. The first two cruises descended to about 1000 and 500 km above the moon's equator. Onboard cameras snapped images of lines of folded mountain ridges and cracked white ice plains streaked with dark green organic material. The magnetometer saw signs of ions leaking out from Enceladus' atmosphere, and it localized, in the second flyby, a strong outflow from the south pole. The trajectory of the third flyby on 14 July 2005 was then adjusted to fly through the emergent gas just 168 km above the south pole.

The flybys show that Enceladus' south polar landscape is still active today and is being resurfaced by cryovolcanism and fresh snowfall. Tidal forces have twisted and buckled the surface ice, producing long ridges and fractures. At infrared wavelengths, the south pole actually glows. An underground heat source lies beneath a surface grid of "tiger stripes": a parallel set of linear trenches stained with dark organic material. From these warm vents, water vapor, ice, and dust particles are lofted in a spectacular plume, like spray from a Yellowstone geyser. Ions are driven further into the atmosphere and out into the magnetosphere of Saturn itself and the E ring. The rate at which water is being blown out is enough to replenish not only the E ring but also oxygen throughout the whole saturnian system.

So is the mystery of Enceladus solved? Not at all. Finding such active geology on such a tiny moon is a big surprise. Neptune's Triton and Jupiter's Io have ice and sulfur volcanoes, respectively, but are larger bodies; Europa has experienced plate tectonics but no current activity is seen there. Yet tiny Enceladus produces a plume large enough to drench the whole Saturn system. The origin of Enceladus' internal heating is also still a major puzzle. To produce the plume, water needs to be boiled off or sublimated. Ammonia could act as antifreeze but was not detected by Cassini. Does liquid water, or locked-up ammonia, lie beneath the surface? We may need to wait for future missions to this enigmatic moon to find out for sure, but Enceladus is definitely on the map.

—JOANNE BAKER

PERSPECTIVE

Enceladus: Cosmic Gymnast, Volatile Miniworld

Jeffrey S. Kargel

The exploration of Saturn by the Cassini/Huygens mission has yielded a rich collection of data about the planet and its rings and moons, in particular its small satellite Enceladus and giant satellite Titan. Once believed too small to be active, Enceladus has been found to be one of the most geologically dynamic objects in the solar system. Among the surprises are a watery, gaseous plume; a south polar hot spot; and a surface marked by deep canyons and thick flows.

In Greek mythology, Enceladus was a giant, but for us it is a saturnian world so small that its diameter could fit within France or New Mexico. Enceladus is the subject of seven Reports and two Research Articles in this issue on key findings of Cassini's recent flybys (1–9). [In an accompanying Perspective, Kivelson (10) discusses implications of the findings for our understanding of the magnetosphere of Enceladus.] Observations suggest and theory permits partial melting, even a subsurface ocean, but only if Enceladus also is a well-flexed cosmic gymnast or possesses a special cold cosmic stew of volatiles.

Just a year ago, Cassini/Huygens revealed that Saturn's mega-moon, Titan, has river valleys, shorelines, and rounded pebbles shaped by liquid hydrocarbons (11). We can easily explain geologic activity on planet-size Titan. More enigmatic is why an object as small as Enceladus—now found to be among the most geologically active objects in the solar system—also could be so dynamic.

Enceladus spouts a watery, gassy plume (1–4) with water and gas fluxes similar to those of Yellowstone National Park's Old Faithful geyser. With low gravity ($1/86$ of Earth's), the plume spews thousands of kilometers into space from the geothermally heated south polar region (5). The possibility of a plume, now confirmed, has been discussed for a quarter-century since Voyager and Earth-based observations indicated a saturnian ring of ice spherules near Enceladus' orbit. Enceladus' plume (4) and those of Yellowstone are powered largely by gaseous carbon dioxide. Methane, nitrogen, and propane add to Enceladus' emissions (4). Dry ice and a CO₂-clathrate-like structure or amorphous equivalent, and traces of short-chain hydrocarbons, have been identified in surface water ice (6).

No satellite smaller than Enceladus is known to be still geologically active. Neptune's moon Triton, five times the diameter of Enceladus and almost 200 times as massive, has icy volcanic landscapes,

a nitrogen polar cap, and active nitrogen plumes (12). Jupiter's Europa—even bigger than Triton and possessing a liquid briny ocean (13) and a floating crust with shifting icy plates, domical intrusions (14), and erupted deposits of hydrated salts or acids and ice (15, 16)—has not yielded any proof of suspected current activity. Uranus' Miranda—slightly smaller than Enceladus—has gigantic ice canyons and ice volcanism, but activity ceased long ago (17).

Enceladus' sustained, continuing activity is indicated by (i) its active plume (1–4); (ii) a south polar hot spot (5); (iii) amorphous and crystalline ice possibly just hours to decades old in some places (6); (iv) a surface ripped by deep fractured canyons and possible folded ice mountains comparable to the Appalachians (18) (Fig. 1, A); and (v) variations in crater density caused by periodic resurfacing (18–20). Detailed stratigraphic analysis is needed to unravel the sequence and causes of geologic events. I suspect that planetary geologists will eventually settle on a model of shifting, glacier-like tectonic plates; this would finally make high-energy tidal heating unavoidable.

Enceladus' activity requires a heat engine and effective utilization of its heat (1, 5, 18, 21). A water-ice crustal model heated only by radioactive element decay has a basal temperature far short of all potential melting and clathrate dissociation transitions (Fig. 1D). Cranking up heat generation (e.g., tidal heating) or heat retention (e.g., the clathrate crustal model) are the only solutions, although reducing melting points (e.g., with added ammonia, methanol, sulfuric acid, or chloride salts) can help (Fig. 1D). Figure 1D shows thermal conductive models for radiogenic heating of a water-ice crust and of one made mainly of clathrate hydrates and for tidal heating of an ice crust. The models show that basal partial melting of a clathrate shell is plausible (Fig. 1E); so is an ice-covered, briny, gassy ocean (Fig. 1F).

Calculated from Enceladus' measured mass and density (1), the models have a rock core (radius 169.04 km, density 3000 kg m⁻³) and volatile crust 83.26 km thick (density 1010 kg m⁻³). The models use temperature-dependent thermal conductivities of water ice and clathrate

hydrate (22); pressure-dependent melting and clathrate dissociation; and assumed core heating by radioactive decay at 90% the rate per kilogram as Earth's average heat generation, or tidal heating in the floating shell sufficient to drive a regional heat flow of 0.25 W m⁻² (5).

Enceladus' methane, carbon dioxide, and nitrogen erupting with H₂O (4) gives a possible clue that effective heat retention is part of the heating mechanism. These gases would form thermally insulating clathrate hydrates (modified forms of water ice that contain apolar gas molecules within cages of H₂O) (22).

The water-dominated gas composition of Enceladus' plume (4) is consistent with low-pressure boiling of an erupted aqueous liquid (1, 2) that had become gas-saturated at depth (at least tens of bars pressure) with a mixture of clathrate-forming gases. Perhaps the source is a deep, gas-saturated ocean or a deep crustal pocket of water in equilibrium with CO₂-dominated, CH₄-N₂-bearing clathrates residing on the sea-floor above the rock core (Fig. 1, E and F).

The radiogenic heat production of Enceladus, about 280 MW, may be imparted to the icy shell from the core by melting 840 kg of ice per second, enough to supply the plume; 70 to 90% of this water probably refreezes at depth or falls back onto the surface after eruption. If this melting rate was sustained for 4 billion years, it could recycle Enceladus' entire ice mass. Tidal dissipation—seemingly needed to explain the south polar hot spot (5)—could help maintain a deep watery ocean.

Chemical heterogeneity, especially chemical and rheological layering, not only can increase tidal dissipation and heat flow, it can also help explain evidence for possible crustal folding (1, 18) and heterogeneous geological activity (23). Detection of NH₃ would validate a classical model of the solar nebula and saturnian system (24). It could also account for low-temperature activity on Enceladus (1, 18, 19, 21, 25, 26), including possible cryovolcanism (Fig. 1, A to C). However, NH₃ has not been identified on Enceladus or on any other saturnian icy satellite by Cassini (1, 4, 6), though some telescopic studies have revealed possible weak NH₃ absorptions. The gas-rich water plume might arise from dissociation of clathrate hydrates from which ammonia had been excluded by earlier clathrate formation (27).

If it turns out that NH₃ really is missing, Enceladus may have started with but then lost its NH₃, or hydrothermal circulation may have sequestered it in rocky ammonium minerals. Current volatile emissions—150 to 350 kg/s (2)—are sufficient to blow off more than one-sixth of Enceladus' mass if sustained for 4 billion years. Ammonia is more volatile than H₂O, and its aqueous solutions would erupt more readily than pure water; NH₃ would be depleted faster than H₂O. Though volatile, CH₄, N₂, CO, and CO₂ are readily sequestered into stable clathrates

Department of Hydrology and Water Resources, University of Arizona, Tucson, AZ 85721, USA. E-mail: kargel@hwr.arizona.edu

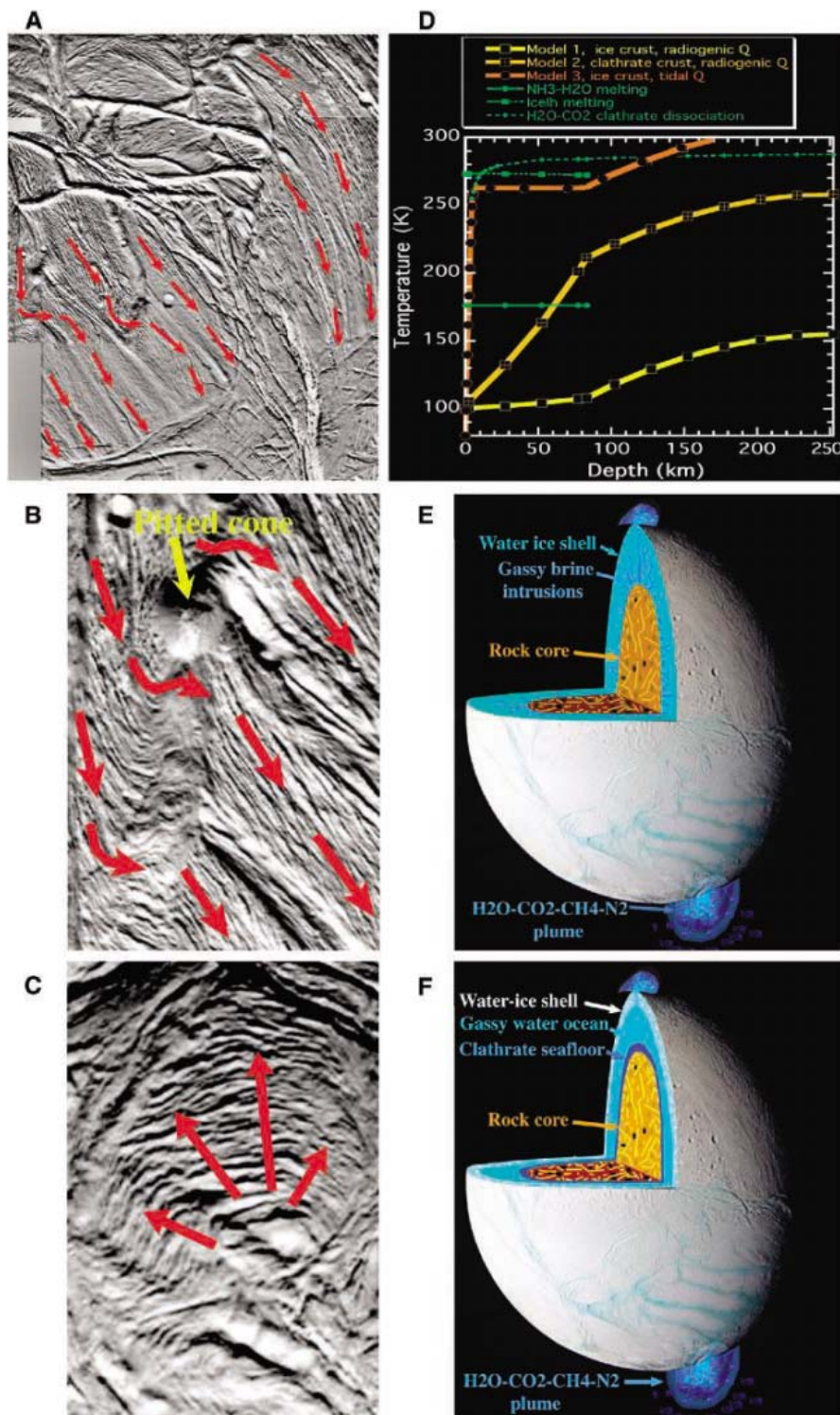


Fig. 1. Hilly, ridged, and grooved terrains on Enceladus. (A) Mosaic of Cassini images acquired 17 February 2005. The images suggest possible glacier-like flow or a thick, pasty cryovolcanic flow. (B) Prominent ridges and finer ridge-and-groove topography indicate crustal deformation, including possible flow diversion around a partly buried hill, which might also be a cryovolcanic cone (inferred flow direction toward lower right). (C) Another instance of a possible pasty cryovolcanic flow from a possible source in a low hilly area. (D) Thermal conductive models are described in the text. (E) Possible interior thermal model including a clathrate crust and radiogenic heating. The model could include basal melting, which might feed the plumes. (F) Possible interior thermal model relying on tidal heating and using a water-ice crust; CO₂ clathrate could exist at the bottom of the ocean, and dissolved gas in the ocean could help drive the water plumes.

(22). These gases are not as soluble in water as ammonia is; thus, an early H₂O + NH₃ + CH₄ + CO₂ ± N₂ ± CO system could evolve toward clathrate enrichment and depletion of NH₃.

Enceladus' active gas plume adds impetus to an alternative model of Triton's nitrogen plume, which had been viewed as a consequence of solid-state greenhouse heating of surficial ices. Clathrate decomposition now seems likelier.

Cassini observations of Enceladus also offer insights into Titan's interior. Both satellites have similar uncompressed densities and perhaps similar compositions. Missing on Enceladus is Titan's anoxic atmospheric photochemistry, which obscures its crust and mantle ices. The emission of methane in Enceladus' plume supports outgassing from Titan's interior to supply atmospheric methane (28). The Huygens studies of the isotopic composition of Titan's nitrogen have reinforced an earlier model proposing that the nitrogen was derived by photochemistry of a primordial NH₃ atmosphere (28). If NH₃ fails to turn up at Enceladus, it may be time to reconsider different nebula chemistry and accretion models and Titan atmospheric evolution. Waite *et al.* (2) make the striking observation that Enceladus' plume has a cometlike volatile composition, but so far sulfurous molecules have not been reported. Sulfur may be sequestered in the rocky core in the form of relatively involatile metal sulfides, or sulfur may have been lost by outgassing of supervolatile hydrogen sulfide.

Enceladus' highly reflective frost coating may have an analog in the bright surface of the solar system's recently discovered "10th planet" (29), suggesting that plume activity may also occur there. The "10th planet's" energy source could not be tidal, but its large size (larger than Pluto and Triton) would permit radiogenic heat sufficient to induce internal melting and volatile degassing despite having the solar system's record coldest surface temperatures.

There seem to be many geological and geophysical similarities and some differences between Enceladus and Jupiter's larger ice-crust oceanic moon, Europa. On Europa, small-scale diapiric upwellings are common; in contrast, Enceladus may operate with rarer episodes of large-scale crustal overturn, a process that can shed heat but does so as an energy miser compared to Europa. The existence of some terrains on Enceladus that are heavily cratered and presumably ancient and other terrains that are uncratered and still warm further suggests that Enceladus has operated with intense geologic activity in some regions, and very little activity elsewhere. According to adaptations of a model developed for Europa (23), this could be related to regional differences in the chemical composition, elasticity, and thermal conductivity of the crust.

Looking to the future of the Cassini mission, outstanding questions loom. Is there

evidence for plate tectonics? Where are the plumes' vents, where are the plumes' sources in the interior, and how are they driven? Does Enceladus host hydrated salts or acids, such as those found on Europa (15, 16)? Where is the ammonia, or is it truly absent? Is there a briny ocean, such as Europa's and other Galilean satellites' (13–15)?

If a wet domain exists at the bottom of Enceladus' icy crust, like a miniature European ocean, Cassini may help to confirm it. Might it be a habitat? Cassini cannot answer this question. Any life that existed could not be luxuriant and would have to deal with low temperatures, feeble metabolic energy, and perhaps a severe chemical environment (16). Nevertheless, we cannot discount the possibility that Enceladus might be life's distant outpost.

References and Notes

1. C. C. Porco *et al.*, *Science* **311**, 1393 (2006).
2. C. J. Hansen *et al.*, *Science* **311**, 1422 (2006).
3. F. Spahn *et al.*, *Science* **311**, 1416 (2006).
4. J. H. Waite Jr. *et al.*, *Science* **311**, 1419 (2006).
5. J. R. Spencer *et al.*, *Science* **311**, 1401 (2006).
6. R. H. Brown *et al.*, *Science* **311**, 1425 (2006).
7. M. K. Dougherty, *Science* **311**, 1406 (2006).
8. G. H. Jones *et al.*, *Science* **311**, 1412 (2006).
9. R. L. Tokar *et al.*, *Science* **311**, 1409 (2006).
10. M. G. Kivelson, *Science* **311**, 1391 (2006).
11. J.-P. Lebreton *et al.*, *Nature* **438**, 758 (2005).
12. S. K. Croft *et al.*, in *Neptune and Triton*, D. P. Cruikshank, Ed. (Univ. of Arizona Press, Tucson, 1996), p. 879.
13. M. G. Kivelson *et al.*, *Science* **289**, 1340 (2000).
14. R. T. Pappalardo *et al.*, *J. Geophys. Res.* **104**, 24105 (1999).
15. T. B. McCord *et al.*, *Science* **280**, 1242 (1998).
16. J. S. Kargel *et al.*, *Icarus* **148**, 226 (2000).
17. R. Greenberg *et al.*, in *Uranus*, J. T. Bergstrahl, E. D. Miner, M. S. Matthews, Eds. (Univ. of Arizona Press, Tucson, 1991), p. 410.
18. J. S. Kargel, S. Pozio, *Icarus* **119**, 385 (1996).
19. B. A. Smith *et al.*, *Science* **215**, 504 (1982).
20. J. B. Plescia, J. M. Boyce, *Nature* **301**, 666 (1983).
21. S. W. Squyres, R. T. Reynolds, P. M. Cassen, *Icarus* **53**, 319 (1983).
22. R. G. Ross, J. S. Kargel, in *Solar System Ices*, C. de Bergh, M. Festou, B. Schmitt, Eds. (Kluwer, Dordrecht, Netherlands, 1998), p. 33.
23. O. Prieto, J. S. Kargel, *Lunar Planet. Sci.* XXXIII, abstract 1726 (2002).
24. J. S. Lewis, *Icarus* **16**, 241 (1972).
25. D. J. Stevenson, *Nature* **298**, 142 (1982).
26. J. S. Kargel, *Icarus* **100**, 556 (1992).
27. O. Prieto-Ballesteros, J. S. Kargel, *Lunar Planet. Sci. Conf. XXXVII*, Abstract 1971 (2006).
28. J. I. Lunine, D. J. Stevenson, *Icarus* **70**, 61 (1987).
29. R. Irion, *Science* **311**, 589 (2006).
30. Fig. 1 source images: See <http://saturn.jpl.nasa.gov/home/>.

10.1126/science.1124495

PERSPECTIVE

Does Enceladus Govern Magnetospheric Dynamics at Saturn?

Margaret Galland Kivelson

Instruments on the Cassini spacecraft reveal that a heat source within Saturn's moon Enceladus powers a great plume of water ice particles and dust grains, a geyser that jets outward from the south polar regions and most likely serves as the dominant source of Saturn's E ring. The interaction of flowing magnetospheric plasma with the plume modifies the particle and field environment of Enceladus. The structure of Saturn's magnetosphere, the extended region of space threaded by magnetic-field lines linked to the planet, is shaped by the ion source at Enceladus, and magnetospheric dynamics may be affected by the rate at which fresh ions are created.

Early in 2005, the Cassini spacecraft passed Saturn's moon Enceladus, providing a wealth of new data on this curious satellite, as the mission teams report in this issue (1–9). A tiny moon (diameter ~500 km) with an exceptionally bright icy surface, Enceladus orbits Saturn at a distance of $4.89 R_S$ (where R_S is a Saturn radius = 60,268 km). A textbook on planetary sciences (10) published shortly before Cassini's arrival in the Saturn system describes it as "remarkable and enigmatic," conjectures that its interior may be partially liquid, and considers that it may be the source of particles forming the E ring. Cassini's recent discoveries of warm surface features near the south pole (7) and of an extended plume of water ice particles and dust (5, 6) provide insight into the enigma and begin to resolve the question of the source of the bright material on the surface, the E ring, and the torus

of neutral O and OH present in Saturn's inner magnetosphere (11, 12).

In an accompanying Perspective (13), Kargel discusses implications of the observations for our understanding of the interior and physical properties of Enceladus. The newest discoveries also provide critical insight into the processes that drive Saturn's magnetospheric dynamics.

In particular, the plume ejecta affect local properties of the magnetospheric plasma, such as mass density and flow patterns. A magnetized plasma flowing toward an electrically conducting moon or a moon surrounded by a cloud of ions will be slowed and diverted (14, 15). The local magnetospheric magnetic field, in turn, responds as if it were frozen into the flowing plasma; the field strength and plasma density increase in the regions of slowed flow. Much of the plasma avoids encounter with the moon; field lines bow out in response to the diversion of the flow. Because the plasma slows first near the moon and only with some delay at locations on field lines far above and below the moon, the interaction bends those field lines as if they were the strings of sling shots draped around projectiles. With this picture in mind and the

natural assumption that the moon is roughly spherical, one can predict the form of the magnetic perturbations along flyby trajectories in different parts of the interaction region. The first flyby (17 February 2005) occurred ~1259 km north of the moon, and indeed, the observed magnetic perturbations were consistent with the sling-shot analogy.

On the closer (~497 km) flyby of 9 March 2005, however, the field bent in a direction different from that anticipated for a compact quasi-spherical moon; as a result, the magnetometer team concluded that an extended atmosphere must be present, localized near the south pole. To test this inference, the altitude of the third flyby (14 July 2005) was decreased to ~168 km. This optimized pass enabled the remote sensing instruments (1, 3, 5, 7, 9) to detect not an atmosphere but a rather narrow plume jetting water vapor and dust particles (6) above the south polar regions. The plume originates in the region of heated and distinctively colored surface lineaments referred to as "tiger stripes" and is the source of a localized cloud of ions and electrons (4, 8) whose effects on the magnetic field forecast its presence. Slowing and diversion of the plasma flow began at a distance of 27 Enceladus radii (R_E) from the moon, consistent with a widely distributed source of neutral material (8).

The particulates that maintain Saturn's E-ring properties now can be fully identified. The trajectories and fluxes of dust particles in the plume appear adequate to maintain the E ring (6). The ice particles and water-group atoms and molecules supplement an E-ring source, and through charge exchange and impact ionization they continuously supply heavy ions to the inner magnetosphere. Tokar *et al.* (8) estimate a rate of mass loading (≥ 100 kg/s) compatible with earlier estimates based on Hubble Space Telescope observations (16).

It is also clear that not only Enceladus but also its plume absorb energetic particles that drift

Institute of Geophysics and Planetary Physics and Department of Earth and Space Sciences, University of California, Los Angeles, CA 90095-1567, USA. E-mail: mkivelson@igpp.ucla.edu

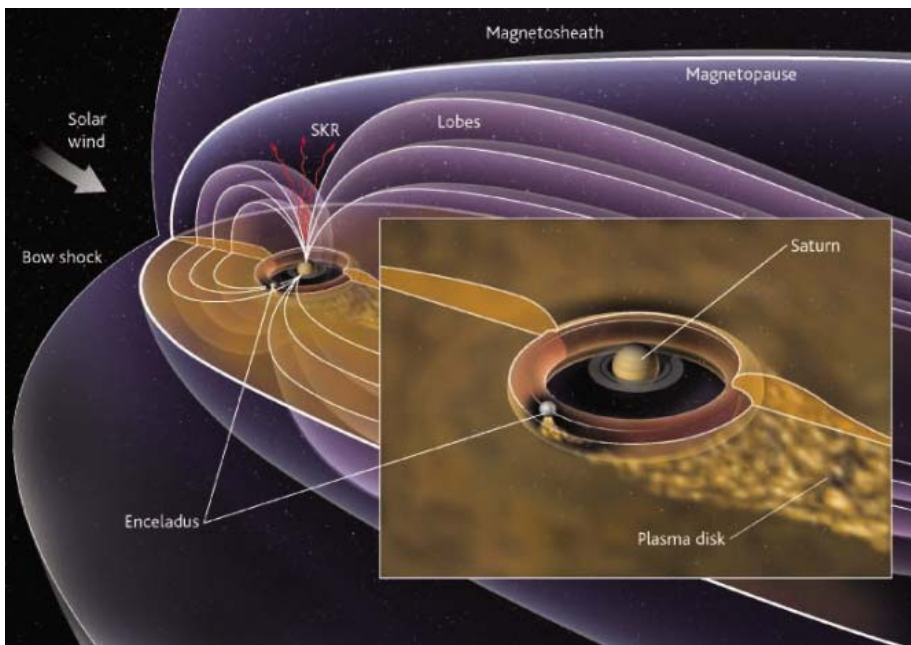


Fig. 1. Schematic of Saturn's magnetosphere showing the plume at Enceladus as the source of plasma and outflowing plasma on the night side in a region linked magnetically to a region of lower-than-average ionospheric conductance. Red arrows indicate kilometric radiation emitted from Saturn's polar region (SKR). Diagram is not to scale.

toward them. Changes in absorption signatures of energetic electrons from orbit to orbit suggest that the outgassing rate of the plume varies on time scales of days or weeks (4).

With the water ion source in the inner magnetosphere better understood, we can think about how this plasma contributes to magnetospheric structure and dynamics (Fig. 1). Electromagnetic forces accelerate the newly ionized material until it roughly corotates with Saturn, draining angular momentum from Saturn's ionosphere. This rotating plasma exerts centrifugal stress on its surroundings. Beyond $1.9 R_S$ from the spin axis, the stresses related to rotation dominate the gravitational force. If the integrated mass of ions on magnetic flux tubes crossing the equator of Saturn near the orbit of Enceladus exceeds the integrated mass of ions on flux tubes crossing further out, the system is unstable to flux tube interchange—a process in which mass-loaded flux tubes change places with less heavily loaded flux tubes (17). Mass is thus transported outward, possibly with little effect on the magnetic configuration. The process is analogous to that found in gravitationally bound atmospheres, wherein a cold dense element of gas embedded in a hot tenuous environment at fixed pressure falls toward the surface. The rotational interchange process, which spontaneously carries mass outward, is less often described in the magnetospheric context, but its signatures have been identified at Earth (18), Jupiter (19), and most recently at Saturn (20, 21), where they are found over a large range of radial distances.

Currents carried in the plasma establish the magnetic structure of the middle and outer magnetosphere. Beyond roughly $10 R_S$, the thermal energy density ($\propto p$) becomes greater than the magnetic energy density ($\propto B^2/\mu_0$), where B is the field magnitude, μ_0 is the permeability of vacuum, and p is the thermal pressure. Under these conditions, plasma currents cause the magnetic field to bulge out radially near the equator (referred to as ballooning) and the plasma expands outward, forming a plasma disk (22, 23). Probably the most puzzling aspect of magnetospheric dynamics is that the field configuration (23) and particle fluxes (24, 25) vary at the planetary rotation period, as does the radio emission in the kilometric band (26). There is, as yet, no consensus on how periodicity is imposed by the rotation of a nearly axially dipole field (27). The mechanism proposed by Espinosa *et al.* (28) requires a “camshaft”—some anomaly in the inner magnetosphere that launches outward-moving pulsed perturbations. (A camshaft is a structure that converts rotational motion into linear motion.) The high level of symmetry of Saturn's magnetic field, however, made it difficult to identify the form of the anomaly.

Cassini magnetometer data are consistent with the camshaft model, with the modulated rate of outflow of plasma from the inner magnetosphere possibly linked to varying rates of interchange and ballooning of the flux tubes linked to different positions around Saturn (29). Modulated transport would then impose periodicity on both plasma and field signatures despite the symmetry

of the internal magnetic field of Saturn. Aspects of this picture relate to the magnetic anomaly model introduced to describe some Jovian magnetospheric processes (30).

Variations of ionospheric conductance at fixed latitude could arise from high-order multipoles of the internal field (undetectable at spacecraft altitudes) or from nonuniform atmospheric structure. A complete account of the process would have to explain the source of periodicity and also the variability of the period of kilometric radio emissions (labeled as SKR in Fig. 1) over decades (31, 32). Although many of these specific ideas have not yet been tested, we can be sure that the dynamics of Saturn's magnetosphere are dominated by responses to plasma introduced by Enceladus.

References and Notes

1. R. H. Brown *et al.*, *Science* **311**, 1425 (2006).
2. M. K. Dougherty *et al.*, *Science* **311**, 1406 (2006).
3. C. J. Hansen *et al.*, *Science* **311**, 1422 (2006).
4. G. H. Jones *et al.*, *Science* **311**, 1412 (2006).
5. C. C. Porco *et al.*, *Science* **311**, 1393 (2006).
6. F. Spahn *et al.*, *Science* **311**, 1416 (2006).
7. J. R. Spencer *et al.*, *Science* **311**, 1401 (2006).
8. R. L. Tokar *et al.*, *Science* **311**, 1409 (2006).
9. J. H. Waite Jr. *et al.*, *Science* **311**, 1419 (2006).
10. I. dePater, J. J. Lissauer, *Planetary Sciences* (Cambridge Univ. Press, Cambridge, 2001).
11. D. E. Shemansky *et al.*, *Nature* **363**, 329 (1993).
12. A. Eviatar, J. D. Richardson, *Ann. Geophys.* **10**, 511 (1992).
13. J. S. Kargel, *Science* **311**, 1389 (2006).
14. F. M. Neubauer, *J. Geophys. Res.* **85**, 1171 (1980).
15. D. J. Southwood, M. G. Kivelson, R. J. Walker, J. A. Slavin, *J. Geophys. Res.* **85**, 5959 (1980).
16. S. Jurac *et al.*, *Geophys. Res. Lett.* **29**, 2172 (2002).
17. T. W. Hill, *Planet. Space Sci.* **24**, 1151 (1976).
18. D. J. Southwood *et al.*, *J. Geophys. Res.* **106**, 30109 (2001).
19. M. G. Kivelson *et al.*, *Geophys. Res. Lett.* **24**, 2127 (1997).
20. Leisner *et al.*, *Geophys. Res. Lett.* **32**, L14508, 10.1029/2005GL022652 (2005).
21. D. T. Young *et al.*, *Science* **307**, 1262 (2005).
22. J. E. P. Connerney, M. H. Acuna, N. F. Ness, *J. Geophys. Res.* **88**, 8779 (1983).
23. M. K. Dougherty *et al.*, *Science* **307**, 1266, 10.1126/science.1106098 (2005).
24. S. M. Krimigis *et al.*, *Science* **307**, 1270 (2005).
25. C. Paranicas *et al.*, *Geophys. Res. Lett.* **32**, L21101, 10.1029/2005GL023656 (2005).
26. M. L. Kaiser *et al.*, in *Saturn*, T. Gehrels, M. Shapley-Matthews, Eds. (Arizona Press, Tucson, AZ, 1984), pp. 378–415.
27. M. H. Acuna, J. E. P. Connerney, N. F. Ness, *J. Geophys. Res.* **88**, 8771 (1983).
28. S. A. Espinosa, M. K. Dougherty, D. J. Southwood, *J. Geophys. Res.* **108**, A2, 10.1029/2001JA005084 (2003).
29. D. J. Southwood, M. G. Kivelson, paper presented at the American Geophysical Union Fall Meeting, San Francisco, CA, 5 to 9 December 2005.
30. T. W. Hill, A. J. Dessler, C. K. Goertz, in *Physics of the Jovian Magnetosphere*, A. J. Dessler, Ed. (Cambridge Univ. Press, New York, 1983), pp. 353–394.
31. A. Lecacheux, P. H. M. Galopeau, M. Aubier, in *Planetary Radio Emissions IV*, H. Rucker, S. Bauer, A. Lecacheux, Eds. (Austrian Academy of Science, Vienna, 1997), pp. 313–325.
32. D. A. Gurnett *et al.*, *Science* **307**, 1255 (2005).
33. I thank D. J. Southwood for sharing insights into the dynamics of the Saturn's magnetosphere and M. K. Dougherty for permission to work with her team. I acknowledge support from NSF under grant ATM 02-05958.

10.1126/science.1124494

RESEARCH ARTICLE

Cassini Observes the Active South Pole of Enceladus

C. C. Porco,^{1*} P. Helfenstein,² P. C. Thomas,² A. P. Ingersoll,³ J. Wisdom,⁴ R. West,⁵ G. Neukum,⁶ T. Denk,⁶ R. Wagner,⁷ T. Roatsch,⁷ S. Kieffer,⁸ E. Turtle,⁹ A. McEwen,⁹ T. V. Johnson,⁵ J. Rathbun,¹⁰ J. Veverka,² D. Wilson,¹ J. Perry,⁹ J. Spitale,¹ A. Brahic,¹¹ J. A. Burns,² A. D. DelGenio,¹² L. Dones,¹³ C. D. Murray,¹⁴ S. Squyres²

Cassini has identified a geologically active province at the south pole of Saturn's moon Enceladus. In images acquired by the Imaging Science Subsystem (ISS), this region is circumscribed by a chain of folded ridges and troughs at $\sim 55^\circ\text{S}$ latitude. The terrain southward of this boundary is distinguished by its albedo and color contrasts, elevated temperatures, extreme geologic youth, and narrow tectonic rifts that exhibit coarse-grained ice and coincide with the hottest temperatures measured in the region. Jets of fine icy particles that supply Saturn's E ring emanate from this province, carried aloft by water vapor probably venting from subsurface reservoirs of liquid water. The shape of Enceladus suggests a possible intense heating epoch in the past by capture into a 1:4 secondary spin/orbit resonance.

Within 6 months of entering Saturn orbit on 1 July 2004 UTC, the Cassini spacecraft began a year of intense examination of the major icy satellites of Saturn. Between 15 December 2004 and 24 December 2005, Cassini executed 21 satellite flybys, including 7 flybys with closest approaches within 1500 km. Of all of these, the most eagerly anticipated were those of Enceladus.

At 504 km in diameter, Enceladus orbits between Mimas and Tethys. A mean motion resonance with Dione excites its orbital eccentricity of 0.0047. It has long been known to have peculiar surface properties, and its visual geometric albedo of 1.4 (1) makes it one of the brightest satellites in the solar system, with a reflectance spectrum dominated by pure water ice (2). Enceladus' association with the E ring, and the very narrow size distribution of particles constituting the E

ring, suggested possible present-day venting or geyser-like activity (3) and subsequent coating of the moon by E-ring particles. Voyager images also provided high-resolution (~ 1 km/pixel) coverage, primarily of the northern hemisphere of Enceladus, with some lower resolution observations extending downward to mid-southern latitudes, showing that its surface is divided into morphologically diverse geological provinces that document a long and complex history (4–6). Bowl-shaped craters dot the heavily cratered, oldest terrains; craters elsewhere showed evidence for viscous relaxation. Other regions displayed narrow linear ridges with kilometer-scale relief, as well as fractures overprinting other fractures. The youngest visible regions appeared smooth. Voyager coverage near the south polar region was sparse and poorly resolved.

Pre-Cassini studies of Enceladus' thermal history and interior structure focused on explaining the viscous relaxation and extensive resurfacing suggested by Voyager images (4). The goal of previous models was to investigate ways of producing, at some recent epoch, global interior temperatures at or close to the water ice melting point, allowing possible cryovolcanism, subsolidus convection, and near-surface viscous relaxation of impact structures. Post-Voyager thermal history studies concluded that it was impossible to reach the melting point of pure ice under the current physical conditions (5). However, the presence of ammonia, which can exist with water as a eutectic melt at absolute temperatures $T \sim 175$ K, was suggested as a means to lower the temperature (7) and melt the interior (5). Cryovolcanic activity driven by water-ammonia became a plausible resurfacing mechanism. Models invoking Enceladus' orbital evolution and the possibility of intense tidal heating in the past have also been examined [e.g., (8)]. On the basis of Voyager-era estimates of the shape of Enceladus,

a 1:3 spin/orbit resonance was postulated as being capable of producing sufficient present-day heat to melt the interior (9), although it required that Enceladus be undergoing a forced libration of several degrees amplitude.

Cassini flybys. Because of its uniqueness among saturnian moons, three very close Cassini encounters of Enceladus were executed in 2005 to gather information on its physical characteristics, magnetic and plasma environment, and geologic activity (if any). The first encounter on 17 February 2005 saw approach on the trailing hemisphere and brought the spacecraft within 1259 km over the Saturn-facing equatorial region of the moon during closest approach. This flyby resulted in the first detection, by the Cassini Magnetometer, of a tenuous atmosphere around Enceladus distorting Saturn's magnetic field lines (10), and confirmed [by the Visual and Infrared Mapping Spectrometer (VIMS)] a surface dominated by water, with simple organics and CO_2 coincident with prominent fractures seen in the south polar region (11). Surface NH_3 was not detected. Imaging Science Subsystem (ISS) images acquired during this flyby in both clear and spectral filters (12) revealed the "smooth" plains seen by Voyager to be finely fractured.

The second closest approach took place on 9 March 2005, at a distance of 497 km above the anti-Saturn equatorial region. The magnetic signature during this flyby confirmed a southerly atmospheric source of water-ion mass loading of the plasma around Enceladus.

The third flyby of Enceladus on 14 July 2005 was lowered to a close-approach distance of 168 km (well within Enceladus' Hill radius of ~ 950 km) to allow high-resolution investigation with both remote sensing and in situ instruments of the southern polar environment. Very high resolution images of the south polar terrains, as well as some extremely high resolution images acquired during this event (with image scales as fine as 4 m/pixel), revealed a landscape near the south pole littered with house-sized ice boulders, carved by tectonic features unique to Enceladus, and almost entirely free of impact craters. Several prominent, ~ 130 -km-long fractures dubbed "tiger stripes" were seen straddling the south pole; the region south of $\sim 55^\circ\text{S}$ latitude was circumscribed by an unusual continuous chain of sinuous fractures and ridges. The Cassini Composite Infrared Spectrometer (CIRS) found the south polar region to be anomalously warm (13); comparison of the thermal and imaging results revealed the highest graybody temperatures observed on Enceladus, between 114 and 157 K, to be coincident with the prominent tiger stripe fractures crossing the south pole (14).

The July encounter produced unequivocal evidence of a plume of water vapor and small icy particles emanating from the south polar region of Enceladus (15–18) (Fig. 1). Surprisingly, the Ion and Neutral Mass Spectrometer (INMS)

¹Cassini Imaging Central Laboratory for Operations, Space Science Institute, 4750 Walnut Street, Suite 205, Boulder, CO 80301, USA. ²Department of Astronomy, Cornell University, Ithaca, NY 14853, USA. ³Division of Geological and Planetary Sciences, California Institute of Technology, 150-21, Pasadena, CA 91125, USA. ⁴Department of Earth, Atmospheric, and Planetary Sciences, Massachusetts Institute of Technology, Cambridge, MA 02139, USA. ⁵Jet Propulsion Laboratory, California Institute of Technology, Pasadena, CA 91109, USA. ⁶Institut für Geologische Wissenschaften, Freie Universität, 12249 Berlin, Germany. ⁷Institute of Planetary Research, German Aerospace Center, Rutherfordstrasse 2, 12489 Berlin, Germany. ⁸Department of Geology, University of Illinois, Urbana, IL 61801, USA. ⁹Department of Planetary Sciences, University of Arizona, Tucson, AZ 85721, USA. ¹⁰Department of Physics, University of Redlands, 1200 East Colton Avenue, Redlands, CA 92373, USA. ¹¹Centre d'Etudes de Saclay, Université Paris 7, L'Orme des Merisiers, 91191 Gif-sur-Yvette Cedex, France. ¹²Goddard Institute for Space Studies, NASA, 2880 Broadway, New York, NY 10025, USA. ¹³Department of Space Studies, Southwest Research Institute, 1050 Walnut Street, Suite 400, Boulder, CO 80302, USA. ¹⁴Astronomy Unit, Queen Mary, University of London, London E1 4NS, UK.

*To whom correspondence should be addressed. E-mail: carolyn@ciclops.org

detected no gaseous NH_3 (16). On the basis of these findings, very high phase angle, high-resolution ISS imaging sequences were executed on 27 November 2005 specifically to examine the plume over the south pole.

We discuss here the results of analyses of ISS images of the south polar environment of Enceladus. Images taken as early as 16 January 2005, images acquired during the February and July 2005 flybys, and those taken in late November 2005 have yielded striking visual evidence of many narrow jets of fine icy particles emanating from the south polar terrain (SPT) feeding a large plume over the south pole. They have also yielded indications of extreme geologic youth in the SPT, morphological evidence of a change over time in surface stresses in the southern hemisphere, and possible evidence of an epoch of intense heating in the past. Moreover, recent Cassini imaging and spacecraft tracking data, as well as up-to-date dynamical modeling of the entire Saturnian satellite system, have substantially improved the accuracy of the Enceladus mass density, and therefore radiogenic heating estimates, since the Voyager flybys. Enceladus' interior is clearly warmer and more dissipative than most previous interior models have predicted. All these new results have motivated a re-evaluation of the past and present state of the moon's interior, with the seemingly unavoidable conclusion that the standard, spherically symmetric thermal models of Enceladus' interior do not apply.

South polar terrain. The SPT of Enceladus is distinguished by its tectonic patterns, youthful geology, and unusual albedo and color patterns. The region is disrupted by complex fracture patterns and separated from the rest of Enceladus by a continuous sinuous chain of scarps, parallel ridges, and troughs at $\sim 55^\circ\text{S}$ latitude and covers an area of about 70,000 km^2 (about 9% of Enceladus' surface; Fig. 2). This boundary is interrupted in several places by "Y-shaped" discontinuities (Fig. 2, A, B, and D) that taper northward. These features transition toward the equator to subparallel networks of north-south-trending rifts and cracks that are the youngest features on these terrains (Fig. 2, A and D). The south-facing openings of the Y-shaped discontinuities confine parallel chains of convex-northward curved ridges and troughs (Fig. 2, A, B, and D). ISS stereo images and oblique views of the confined fold belts show that they are hundreds of meters higher than surrounding terrain. These curved forms can best be interpreted as fold belts resulting from horizontal compression.

The interior of the SPT is characterized by a complex network of cross-cutting fractures. Most conspicuous is a family of roughly parallel lineaments that we informally term "tiger stripes" (Fig. 3A). ISS images show that the tiger stripes are linear depressions, typically about 500 m deep, 2 km wide, and 130 km in length, flanked

on both sides by prominent 100-m-high ridges (Fig. 2C; Fig. 3, B and C). Darker material extends a few kilometers to either side. They are spaced ~ 35 km apart and have similar shapes and orientations, with strike directions $\sim 45^\circ$ offset from the Saturn direction (longitude 0° ; Fig. 2A). In the anti-Saturn hemisphere (longitude 180°), tiger stripes often terminate in prominent hook-shaped bends, but in the sub-Saturn hemisphere, they progressively bifurcate into crudely dendritic patterns (Fig. 3C).

The spectrophotometry of the SPT is unusual on Enceladus. At low phase, the bright plains in between the tiger stripes are $\sim 10\%$ brighter than the average reflectivity of Enceladus (Fig. 3A); the contrast between these units and the tiger stripes is $\sim 20\%$ and the greatest seen on Enceladus. These distinct properties may be directly related to the geologic activity, present-day venting, and particle fallout ongoing in this region (see below).

ISS broadband spectra of all SPT materials (fig. S1A) are consistent with a composition of pure water ice. However, although the very bright interstripe plains show almost flat spectra, indicative of grain sizes on the order of tens of micrometers (19) (fig. S1B), the tiger stripes' spectra show stronger absorptions consistent with larger grain sizes of ~ 100 μm . ISS multispectral measurements alone do not indicate whether the coarse-grained ice consists of a surface deposit of ~ 100 - μm particles, boulders composed of coarse-grained ice crystals, relatively bare outcrops of solid ice, or some other morphology. Elsewhere on Enceladus we find coarse-grained icy material, also in association with pristine fractures, in rather limited areas on fracture walls. This too may be exposed solid ice. Narrow deposits of spectrally distinct icy material that often thread along the valley floors (Fig. 3B) may indicate icy blocks that have broken loose from fracture walls. The

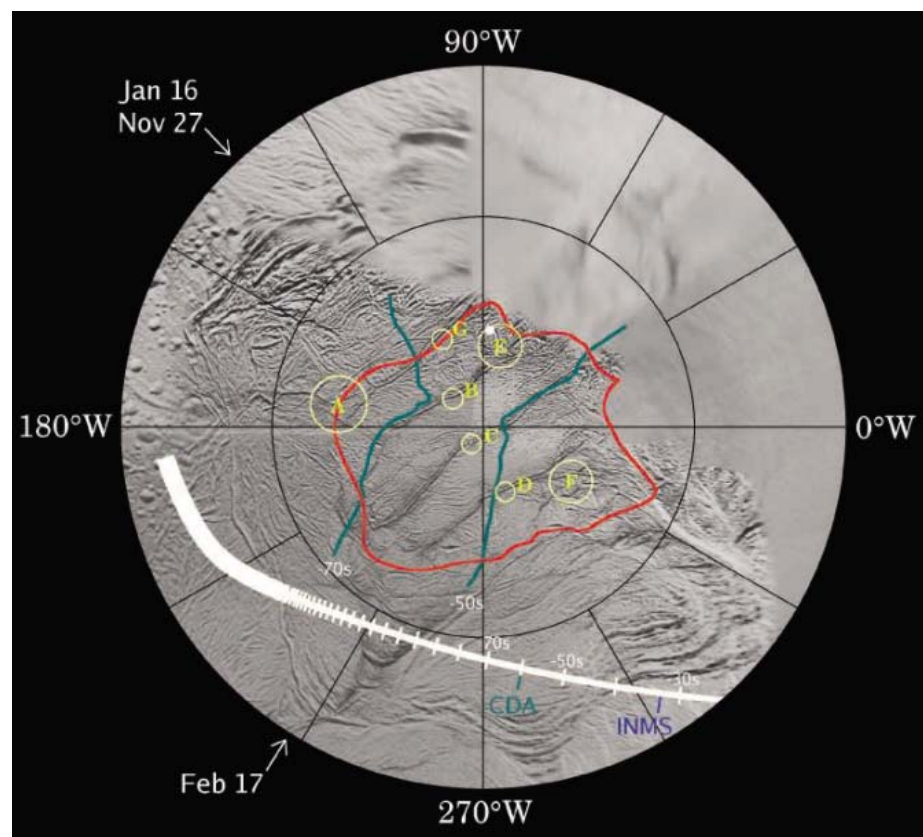


Fig. 1. Observations and model results from a suite of Cassini instruments projected onto a polar stereographic base map of the 30° to 90°S latitude portion of the southern hemisphere of Enceladus. The flight path of Cassini, marked by seconds from closest approach, during the 11 July 2005 flyby is indicated, along with the locations of the position of the spacecraft when the CDA particle (15) and INMS vapor (16) counts peaked. The spacecraft altitude at these positions was ~ 400 km and ~ 250 km, respectively. The contours enclosing the source regions of particles arriving at Cassini from within the SPT at -50 s and -70 s from closest approach, as modeled by the CDA experiment, are drawn in green. The single white dot is the intersection with the limb of the path of γ -Orionis seen from the UVIS experiment (17). The contour enclosing brightness temperatures hotter than 77 K as measured by CIRIS is shown in orange; the seven hottest measured locales, A through G, are shown in yellow (13). The "look" directions for the ISS plume observations on 16 January, 17 February, and 27 November are indicated by arrows.

tiger stripes have sharp relief and cross-cut all other fractures in their path. This, together with their color and coarse grain size, is evidence of geologic youth.

Most of Enceladus' bright surface (Fig. 3A) is likely derived from a covering of fine-grained regolith that has accumulated over time as a result of impact comminution, especially by high-velocity E-ring particles and perhaps sputtering redistribution. The absence of such a covering on the tiger stripes is consistent with the interpretation that the tiger stripe material was either emplaced too recently to have accumulated such

a regolith or has undergone thermal processing (such as thermal metamorphism of ice grains) or both. The high temperatures of the tiger stripes (13) strongly suggest that warm conditions and active venting may be responsible for their crystallinity and other spectrophotometric attributes.

The highest resolution images of the SPT, with nominal image scales of 38 and 3.8 m/pixel (Fig. 3, D and E), show a hummocky or block-covered surface between trough-like expressions of crossing fractures. The color within this region is a patchy mixture of bluish tiger stripe material and whiter ice, and may be a transitional unit. Most

blocks in this unit are between 20 and 50 m across; a few are as large as 100 m. The high fraction of the surface covered by the blocks, and the lack of any craters within tens of kilometers, suggests a formation mechanism other than crater ejecta, such as tectonic or seismic disruption of a highly fractured surface layer. Erosional mechanisms, such as sublimation and particle bombardment, may have further modified them.

The SPT that surrounds and predates the tiger stripes is morphologically and stratigraphically complex. Local patterns of fractures vary from straight orthogonal sets, some showing

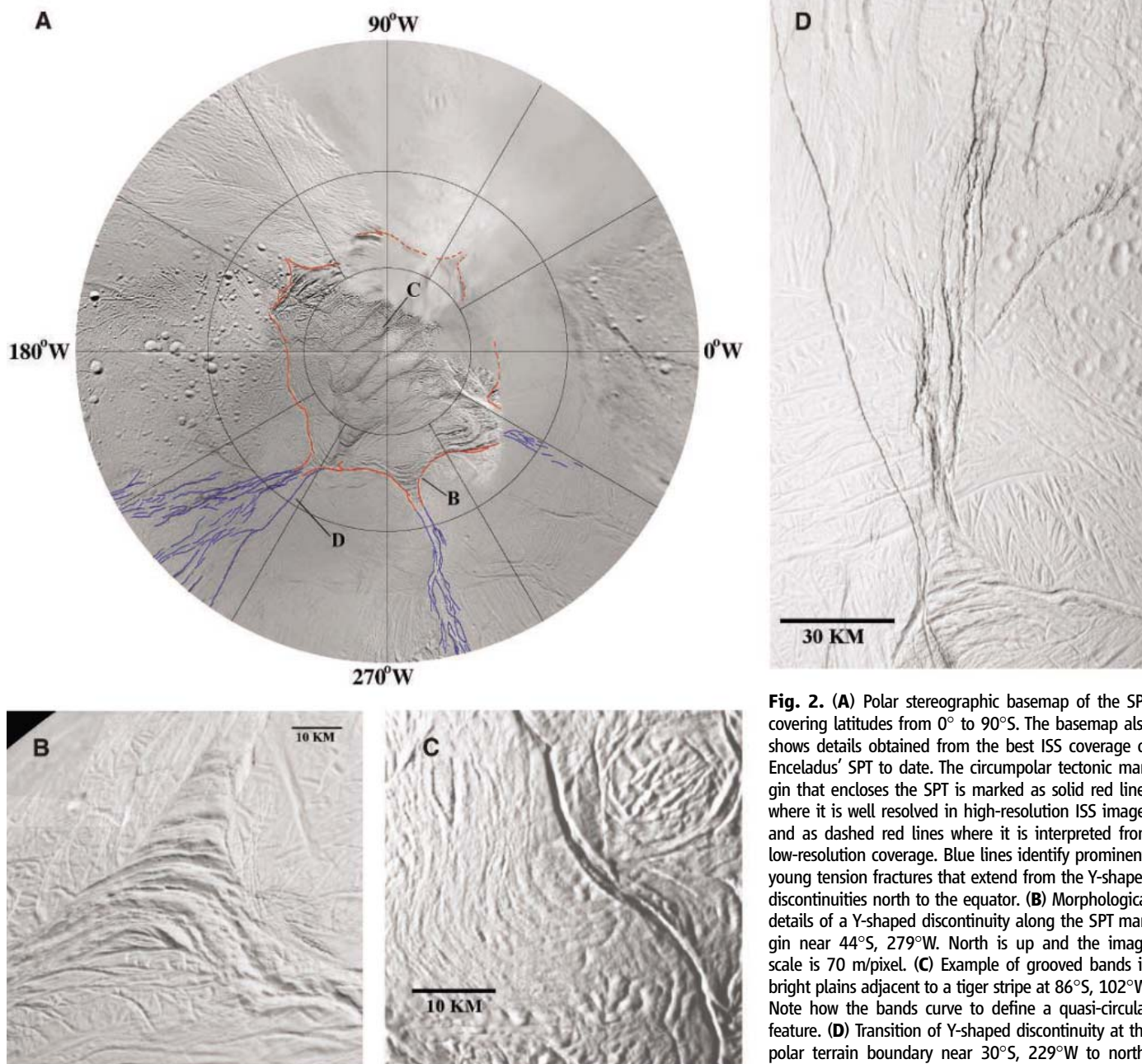


Fig. 2. (A) Polar stereographic basemap of the SPT covering latitudes from 0° to 90°S. The basemap also shows details obtained from the best ISS coverage of Enceladus' SPT to date. The circumpolar tectonic margin that encloses the SPT is marked as solid red lines where it is well resolved in high-resolution ISS images and as dashed red lines where it is interpreted from low-resolution coverage. Blue lines identify prominent, young tension fractures that extend from the Y-shaped discontinuities north to the equator. (B) Morphological details of a Y-shaped discontinuity along the SPT margin near 44°S, 279°W. North is up and the image scale is 70 m/pixel. (C) Example of grooved bands in bright plains adjacent to a tiger stripe at 86°S, 102°W. Note how the bands curve to define a quasi-circular feature. (D) Transition of Y-shaped discontinuity at the polar terrain boundary near 30°S, 229°W to north-south-trending fractures extending to the equator (blue lines in Fig. 3A).

apparent lateral shear offsets, to highly reticulated patterns of grooves and ridges. Grooved bands (Fig. 2C) with tens to 100 m of relief often curve parallel to bends in adjacent tiger stripes. However, in some locations, they deflect and arc to form quasi-circular patterns that may represent relaxed and degraded impact craters.

Alternatively, these quasi-circular patterns may be surface expressions of subsurface diapirs.

Cratering statistics. Crater counts on Enceladus were obtained from images acquired during the February, March, and July 2005 flybys. Of all saturnian satellites investigated so far [e.g., (20–22)], Enceladus has the largest range in crater

number density, implying a record of long-lasting, possibly still ongoing, geologic activity (Fig. 4). Heavily and moderately cratered regions are found outside the SPT, in places dissected by isolated or densely spaced sets of fractures and troughs, or ridges and grooved bands (Table 1). The lowest crater densities on Enceladus were measured in the SPT near the tiger stripes. Here, only a small number of craters occur, none larger than 1 km.

The cratering frequencies are roughly consistent with impacts of bodies in moderately eccentric planetocentric orbits (23–25). Scaling the impactor fluxes from Iapetus to Enceladus under two different flux scenarios (Table 1), and accounting for the derived age of the Iapetus surface (21), the derived absolute ages for terrains on Enceladus from crater counts strongly indicate geologic activity over a time span of more than 4 billion years up to the present. Ages within the SPT are possibly as young as 500,000 years or younger. The discrete ages of different terrains suggests that rather than being continuously active through geologic time, Enceladus experienced localized episodes of activity perhaps separated by much longer time periods of inactivity.

Shape and density. The shape of Enceladus has been determined from limb profiles in 23 narrow-angle images. The satellite is well represented by an ellipsoid with semi-axes 256.6 ± 0.5 , 251.4 ± 0.2 , and 248.3 ± 0.2 km. Knowledge of the mass of Enceladus has been improved over Voyager-era estimates by the use of astrometric measurements taken from Cassini as well as historical Earth-based, Hubble Space Telescope, and Voyager images, together with dynamical modeling of the bodies in the Saturn system and spacecraft tracking data from the Pioneer, Voyager, and Cassini missions (26). Adopting the most recent value derived from these methods [$GM = 7.2085 \pm 0.0068 \text{ km}^3 \text{ s}^{-2}$ (27), where GM is Newton's gravitational constant times the mass of Enceladus], and using the effective radius of 252.1 ± 0.2 km derived from ISS images, we compute a mean density for Enceladus of $1608.3 \pm 4.5 \text{ kg m}^{-3}$. Enceladus shows a total range of departures from the mean ellipsoid of ~ 2 km. Longitudinally averaged limb heights rise from 400 m below the reference ellipsoid at the south pole to 400 m above it at 50°S latitude. If Enceladus is homogeneous throughout, then its shape is close to that of an equilibrium ellipsoid (i.e., one with a hydrostatic shape controlled by gravity and spin). An object hydrostatically relaxed in synchronous spin at Enceladus' orbit would have a difference of long and short axes of 8.05 km (28), within our uncertainty of 0.6 km of the measured 8.3 km.

The intermediate (b) axis is too large for an exact equilibrium shape, and if homogeneous, Enceladus currently supports between 250 and 500 m of topography relative to an equipotential surface. We conclude that Enceladus' shape is consistent with relaxation of a homogeneous object of density 1608 kg m^{-3} at its current or-

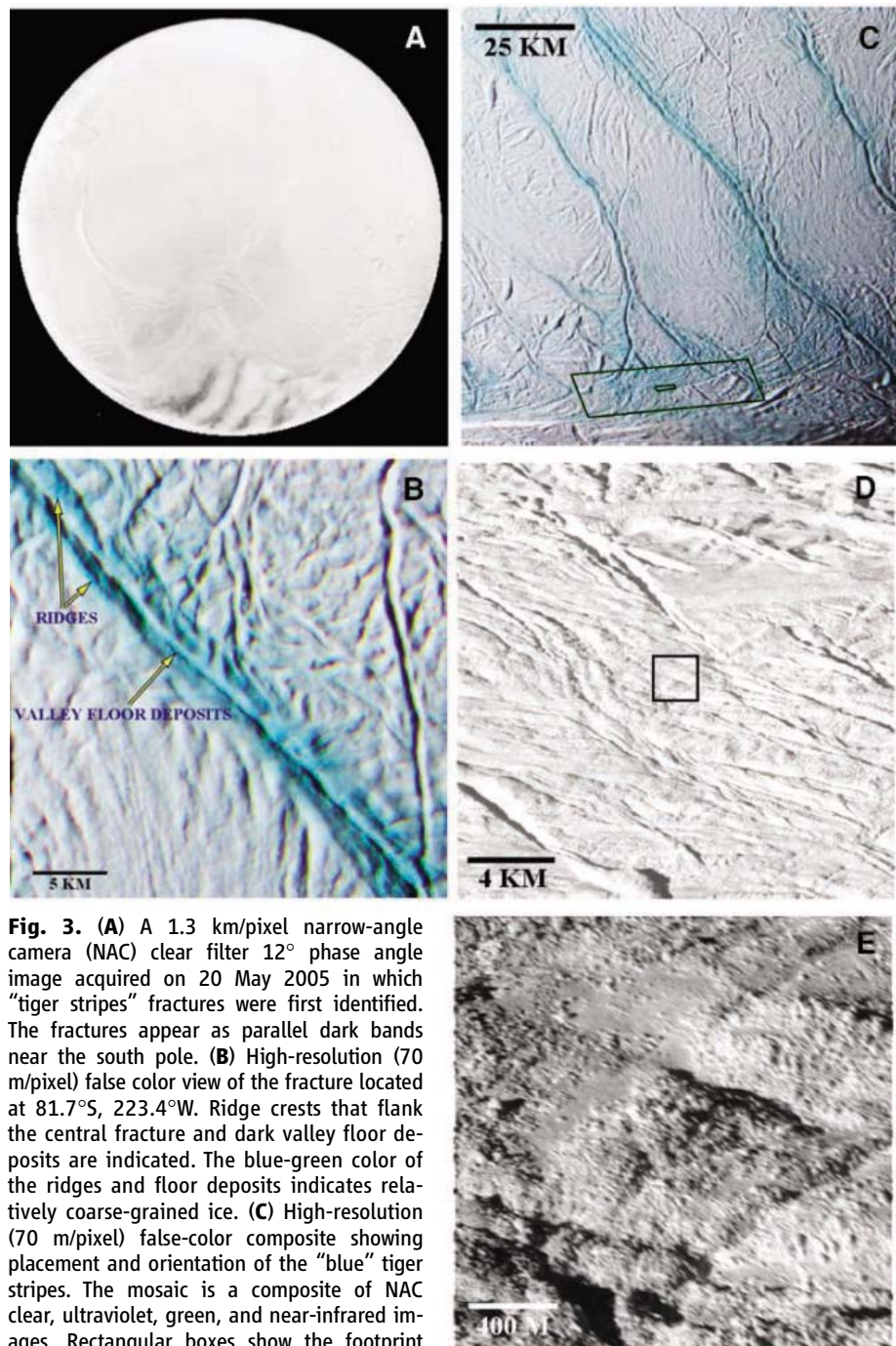


Fig. 3. (A) A 1.3 km/pixel narrow-angle camera (NAC) clear filter 12° phase angle image acquired on 20 May 2005 in which “tiger stripes” fractures were first identified. The fractures appear as parallel dark bands near the south pole. (B) High-resolution (70 m/pixel) false color view of the fracture located at 81.7°S , 223.4°W . Ridge crests that flank the central fracture and dark valley floor deposits are indicated. The blue-green color of the ridges and floor deposits indicates relatively coarse-grained ice. (C) High-resolution (70 m/pixel) false-color composite showing placement and orientation of the “blue” tiger stripes. The mosaic is a composite of NAC clear, ultraviolet, green, and near-infrared images. Rectangular boxes show the footprint locations of the 37 m/pixel wide-angle camera (WAC) (larger box) and 4 m/pixel NAC (smaller box) images shown in (D) and (E), respectively. (D) WAC 37 m/pixel image obtained at the distal edge of a tiger stripe [see (C)]. Central square shows location of co-aligned NAC 4 m/pixel image shown in (E). (E) Highest spatial scale (4 m/pixel) image ever obtained of Enceladus' surface. Image exhibits several pixels of smear from left to right because of spacecraft motion.

bitual distance. Models with thin ice crusts are also indistinguishable from hydrostatic shapes. A core of density 1700 kg m^{-3} requires an ice crust of thickness $\sim 10 \text{ km}$; a core density of 1800 kg m^{-3} requires a crust of $\sim 20 \text{ km}$. Within the uncertainties, both also support topography under 500 m and can be regarded as consistent with relaxation under current conditions (Table 2).

However, a fully differentiated Enceladus with a water-ice mantle and a core of density 2700 kg m^{-3} would exhibit a departure from a fully relaxed, hydrostatic shape of more than a kilometer. A differentiated body with such relief must have relaxed at a higher rotation rate than at present. If orbitally evolved, this would place its relaxation between 0.87 and 0.95 of Enceladus' current orbital distance. Denser, smaller cores would require shape equilibration even closer to Saturn. However, standard orbit evolution models indicate that the orbit of Enceladus could not have changed more than 5% , which suggests that it

mostly likely formed within 95% of its current location (29). Moreover, orbital evolution outward would push the shape of a warm body toward a less oblate, more hydrostatic form, inconsistent with the tectonic patterns seen on the surface (which suggest progression, at least in the southern hemisphere, to a more oblate shape; see below). Hence, whether homogeneous or not, Enceladus probably did not undergo substantial orbital evolution.

The shape of the moon is also important for ascertaining its rotation state. Table 2 gives the moments of inertia for all four interior models mentioned above. In all four cases, the moments yield a ratio of libration frequency to spin frequency $\epsilon = [3(B - A)/C]^{1/2} \sim 0.25$; this value raises the question of whether Enceladus is currently in a forced 1:4 secondary spin-orbit libration, or has been in the past (9). To search for present-day libration, we have obtained 1375 measurements of 190 control points in 129 im-

ages that span more than half of Enceladus' orbit with respect to periape and have fitted these with a model describing the 1:4 spin/orbit libration. No libration was detected. The uncertainties in the solution yield a libration amplitude upper limit of 1.5° . Limb-fitting results require the long axis to point within 5° of Saturn.

Particle plumes. Plumes emanating from the south polar region of Enceladus have been detected in ISS high phase angle images. One relatively large, near-surface plume was seen in images taken on 16 January 2005 at a phase angle of 148° (Fig. 5A). Near-surface plumes were again detected on 17 February 2005 at a phase angle of 153.3° ; a fainter, much more extended component is also visible at this phase angle (Fig. 5B, right). Finally, very high phase angle (161.4°) images were taken on 27 November 2005 (Fig. 6) and reveal many distinct near-surface jets, emanating from the surface in a variety of directions and supplying a much bigger, fainter plume towering over the south polar region by at least 435 km . The fact that these structures were seen at high rather than low phase angles indicates that they consist of fine, forward-scattering particles. The source regions of these jets inferred from triangulation appear to be consistent with the tiger stripes.

Absolute brightness measurements, and hence particle column densities (30), were obtained in the photometrically calibrated versions of the high-resolution November images over a range of heights and azimuths above the moon's south polar limb to determine the profile of particle number density with altitude, as well as the particle escape rate integrated over the extended plume. In all three image sequences—January, February, and November—the scale heights within $\sim 50 \text{ km}$ of the surface are $\sim 30 \text{ km}$; the fall-off becomes more gradual above that point. In the November images, the brightness profile up to one Enceladus radius above the surface fits a model in which the vertical velocity v has a Gaussian distribution [i.e., proportional to $\exp(-v^2/v_0^2)$]; the other velocity components are zero. The particles move vertically, perpendicular to the orbit plane, in the gravitational field of Enceladus; the tidal field of Saturn does not affect motions in this direction. The best fit gives a mean vertical velocity $v_0/\pi^{1/2} = 60 \text{ m s}^{-1}$. This is much less than the

Fig. 4. Cumulative crater size-frequency distributions of geologic units measured on Enceladus. The five sets of distributions correspond to the units listed in Table 1. Curve shown is the lunar highland distribution. The shape of the lunar curve is compatible with the measurements if crater diameters are shifted by about a factor of 5 to smaller values with respect to lunar conditions. Uppermost (oldest) distributions are from heavily cratered plains. Black (open) diamonds correspond to striated and folded plains within Sarandib Planitia. Black solid dots represent distributions measured in the SPT. The single dot is the estimation of a maximum crater age for the single 37 m/pixel WAC frame.

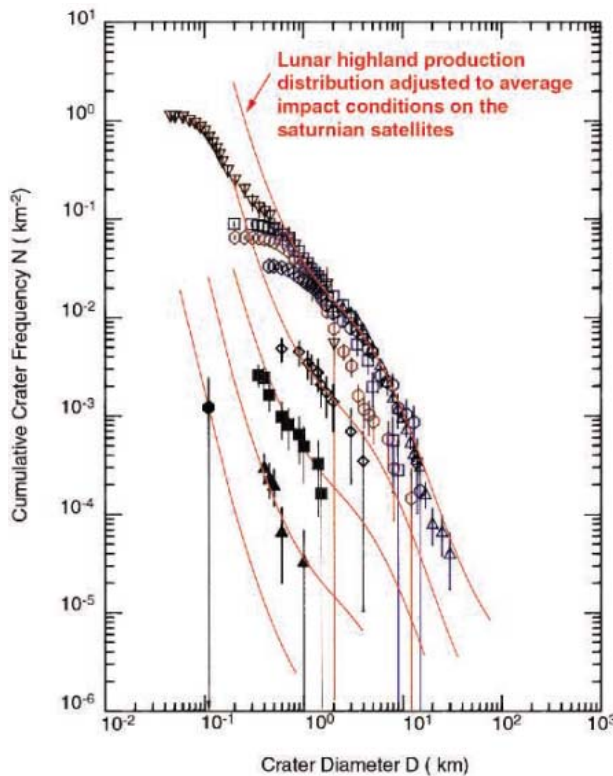


Table 1. Location of crater counting areas (geologic units) and crater frequency ratios (N -ratios, where N is cumulative crater frequency) of counts with respect to a hypothetical surface of age 4.4×10^9 years on Enceladus. Geologic units were identified and mapped at regional scales of $\sim 100 \text{ m/pixel}$;

a single WAC frame (37 m/pixel ; Fig. 3D) obtained during the July flyby was also measured. In areas II and III, no craters larger than $\sim 5 \text{ km}$ were found. The ages are derived for two scenarios: a lunar-like impact chronology with steep initial decay (23, 25, 43) and a constant-flux model of cometary impacts (44).

Geologic unit and location	N -ratio	Age (10^6 years) (lunar-like)	Age (10^6 years) (constant flux)
I. Heavily cratered plains (15° to 45°N , 340° to 360°W ; 20°N to 30°S , 160° to 210°W)	1/4.7	4200	1700
II. Striated and folded plains in Sarandib Planitia (15°N to 5°S , 305° to 320°W)	1/70	3750	170
III. Ridged and grooved plains in Samarkand Sulcus (55° to 65°S , 170° to 240°W)	1/1170	980	10
IV. South Polar Terrain ($>55^\circ\text{S}$, 160° to 320°W)	1/10,770	100	1
V. Single WAC frame within SPT 37 m/pixel (350°W , 75°S)	$<1/311,000$	<4	<0.5

escape speed (235 m s^{-1}), which implies that most of the particles are falling back to the surface.

Our model implies that only $\sim 1\%$ of the upward-moving particles escape to supply the E ring. For an assumed particle radius of $1 \mu\text{m}$, the inferred escape rate is $\sim 10^{13} \text{ s}^{-1}$, which is only twice the value estimated by the Cosmic Dust Analyzer (CDA), $5 \times 10^{12} \text{ s}^{-1}$, for particles with radii $r \geq 2 \mu\text{m}$ (15). The closeness of these two numbers is surprising because ISS, which is sensitive at high phase angles to particles as small as $0.1 \mu\text{m}$, is probably seeing a large population of particles smaller than $2 \mu\text{m}$ that CDA does not see. Our mass escape rate is $\sim 0.04 \text{ kg s}^{-1}$, 4% of that estimated to supply the E ring using pre-Cassini parameters for both the plasma environment and the E-ring optical depth (31). Cassini has found temporal variability in the neutrals and plasma environment around Saturn, so the E-ring supply rate is uncertain. Also, our estimate is uncertain, first because it relies on an assumed particle size distribution, and second because it is sensitive to the exponential tail of the velocity distribution. Future Cassini observations in an extended mission should allow better imaging of the extended plume and a more accurate measure of the escape rate. At the moment, we interpret these observations to indicate that the south polar jets are the primary source of the E ring. The fact that almost all of the observed particles in the jets and extended plume are falling back to the surface may explain the extreme brightness of the interstripe plains as being due to freshly fallen snow (Fig. 3A).

According to our model fit to the observations, the particles that escape to supply the E ring have mean velocities of $\langle v \rangle \sim 90 \text{ m s}^{-1}$ after they leave the gravity field of Enceladus. Particles injected vertically into Saturn's orbit from Enceladus' south pole with such velocities will have full vertical excursions (above and below the equatorial plane) on the order of $h \sim \langle v \rangle P / \pi$, where P is the orbital period (1.37 days) of Enceladus, or $h \sim 3400 \text{ km}$. This is comparable to the vertical extent of the E ring at the orbit of Enceladus, $\sim 5000 \text{ km}$, as measured in Cassini ISS images (32), and argues in favor of the south polar jets on Enceladus being the source of the E ring.

Plume dynamics. What do Cassini observations imply about the physical conditions within the jets and at their source? There are two basic

possibilities for the source of the jets: either sublimating ice, above or below ground, or underground reservoirs of boiling liquid erupting through vents in the tiger stripes. The former operates at temperatures below 273 K ; the latter operates above 273 K . We consider both in order.

The Ultraviolet Imaging Spectrograph (UVIS) observation of the occultation by Enceladus of γ -Orionis (17) returned an estimated horizontal column abundance of water vapor, within 30 km of the surface near 76°S (Fig. 1), of 1.5×10^{20} molecules m^{-2} . The mass of water vapor in the column is therefore $7.16 \times 10^{-6} \text{ kg m}^{-2}$. At an equivalent location of $\sim 15 \text{ km}$ above a latitude of 76°S in the high-resolution November ISS images, we measured a horizontal particle column abundance of $\sim 6 \times 10^8 \text{ m}^{-2}$, assuming an effective water-ice particle radius of $1 \mu\text{m}$ and a broad distribution of sizes (30). The mass of ice

in the column is therefore $\sim 3 \times 10^{-6} \text{ kg m}^{-2}$, which is comparable to the mass of water vapor, assuming the UVIS and ISS horizontal paths are the same. The large ice/gas ratio argues strongly against ice condensing out of vapor, as would be expected for the sublimating ice model: The entropy change when the vapor condenses is ~ 20 times the entropy change when the same amount of vapor expands, so only a small fraction of the vapor can condense during an adiabatic expansion.

The grains could be embedded in the ice from the start and get entrained in the flow, like the dust grains in a comet, but this seems unlikely. The grains in comets are refractory and eventually cover the comet's surface with a dark crust. In contrast, the surface of Enceladus is bright and is mostly water ice. In particular, the spectrum of the plains between the tiger stripes (fig. S1) indicates that the plume particles falling back onto the

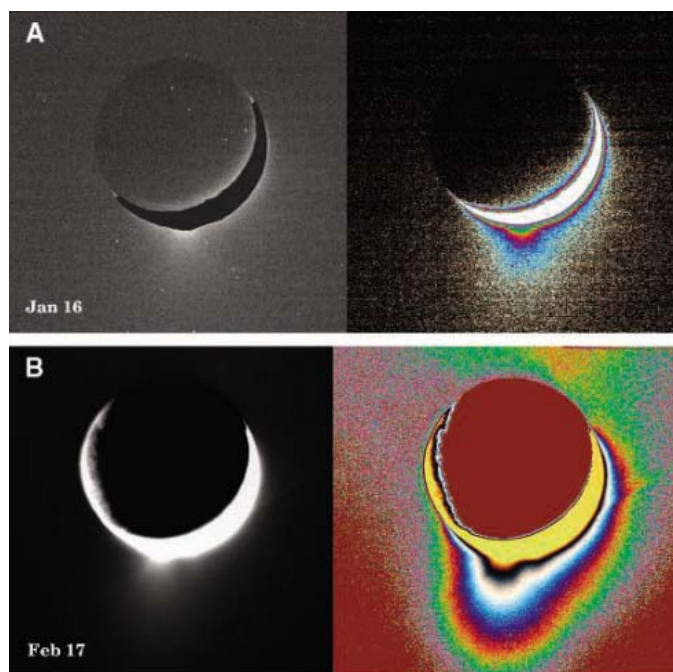


Fig. 5. False-color ISS NAC images of Enceladus' plumes (A) A NAC image taken in the IR1 filter (12) on 16 January 2005 at a phase angle of 148° with an image scale of $\sim 1.25 \text{ km/pixel}$, showing a plume extending below the southern limb. Its full width at half maximum (FWHM) brightness and an altitude of 25 km was $\sim 60 \text{ km}$. The subspacecraft latitude was -2.6° ; the view is toward 133°W longitude (Fig. 1) and broadside to the tiger stripes. (B) A NAC image taken in the IR1 filter (12) on 17 February 2005, at a phase angle of 153.3° with an image scale of 1.8 km/pixel . The subspacecraft latitude was $+0.6^\circ$; the view is toward 238°W longitude, along

the tiger stripes (Fig. 1). Two near-surface plumes can be seen extending below the southern limb: a large one [maybe the same as in (A)] with FWHM $\sim 60 \text{ km}$, and a smaller one, about one-third as bright as the main plume and separated from it by $\sim 100 \text{ km}$ ($\sim 23^\circ$ in the counterclockwise direction), with a FWHM of $\sim 30 \text{ km}$. A fainter and much more extended component can be seen in the enhanced, color-coded image on the right. A thin camera artifact, crossing diagonally across Enceladus, can also be seen.

Table 2. Moments and values of ϵ (the ratio of libration frequency to spin frequency, $[3(B - A)/C]^{1/2}$) for four different interior models. Moments are relative to MR^2 , where M is mass and R is the mean radius, about axes a , b ,

and c . Shape model radii are 256.6 ± 0.5 , 251.4 ± 0.2 , and $248.3 \pm 0.2 \text{ km}$. Uncertainties in model moments derive from ranges of shapes allowed by maximum change in a , b , and c .

Variable	Model 1 (homogeneous, 1608 kg m^{-3})	Model 2 (crust: 10.6 km ice , 930 kg m^{-3} ; core 1700 kg m^{-3})	Model 3 (crust: 20.5 km ice , 930 kg m^{-3} ; core 1800 kg m^{-3})	Model 4 (mantle 930 kg m^{-3} ; core 2700 kg m^{-3})
A	0.3919 ± 0.0005	0.3785 ± 0.0005	0.3666 ± 0.0005	0.3138 ± 0.0005
B	0.4002 ± 0.0001	0.3865 ± 0.0001	0.3744 ± 0.0001	0.3205 ± 0.0001
C	0.4050 ± 0.0005	0.3911 ± 0.0005	0.3789 ± 0.0005	0.3243 ± 0.0005
ϵ	0.249 ± 0.014	0.248 ± 0.016	0.248 ± 0.017	0.249 ± 0.017

surface must be water ice. It is conceivable that ice grains, originally embedded in the ice matrix, get entrained in the flow, but this too seems unlikely. If no other gases are present, sintering will fuse micrometer-sized ice grains together in less than an hour, even at pressures as low as 1 Pa (33). Once fused to the matrix, the particles can no longer be entrained. The presence of micrometer-sized particles in the plume argues against entrainment in the sublimating ice model, but further study is needed.

On the other hand, there is no problem forming particles from a boiling liquid. A liquid boils when the pressure drops below its saturation vapor pressure. The erupting mixture of vapor and liquid—or, in the case of Enceladus, vapor, liquid, and ice particles—is like a cold Yellowstone geyser (34). Ammonia-water mixtures, although liquid down to 175 K, are ruled out as sources because the almost pure ammonia composition of the vapor is inconsistent with the observations (16). Therefore, any boiling liquid/geysers must involve pure water at 273 K or above. (Ammonia-water mixtures may be circulating underground and thermally conducting heat to the surface, keeping the tiger stripes warm, but these fluids cannot be venting to the surface.)

The boiling liquid can produce a cloud of gas and ice if some of the liquid is carried along with the vapor and freezes as it expands out of the vent. An H₂O mixture at the triple point has a temperature $T = 273$ K and a vapor pressure $P_v = 612$ Pa, corresponding to a hydrostatic head of 7 m in the weak gravity of Enceladus. When capped by a layer of ice, liquid water at this depth and temperature is in equilibrium with ice grains and vapor; at greater and warmer depths, the liquid is stable. If this pressure is released (e.g.,

when a crack forms in the ice), bubbles of vapor form and the liquid freezes. The heat of fusion ($L_f = 6.0$ kJ/mol) goes into heat of vaporization ($L_v = 40.6$ kJ/mol), and the mole fraction X of the vapor rises from zero to $L_f/(L_f + L_v) = 0.13$. Although the mixture is then mostly ice, $1 - X = 0.87$ by mole, its volume per mole is 24,000 times that of liquid water. In contrast, the expansion in a Yellowstone geyser is only a factor of ~ 10 , and the water comes out as a frothy mixture.

When released from pressure, the source fluid will accelerate out of the vent as an ice/gas mixture. The geometry of the vent determines the angle of emergence and what fraction of the ice is in micrometer-sized particles. A gas expanding into vacuum reaches sonic speed, which for water vapor at 273 K is twice the escape velocity. Even water vapor at 200 K can accelerate micrometer-sized particles to escape velocity. Warmer, denser vapors can accelerate larger particles. Our inference, that most of the particles are falling back, implies that particles much larger than 1 μm are present. A boiling liquid at 273 K could produce copious amounts of large and small ice particles. The particles would retain the launch velocities and angles acquired in the conduit to form the collimated jets observed (Fig. 6A). There is no need to grow the particles from an escaping high-velocity gas or entrain them in the flow from the ice matrix. For these reasons, we favor the boiling liquid model over the sublimating ice model. On the basis of pressure arguments alone, the liquid chambers giving rise to Enceladus' geysers could be as close as 7 m to the surface.

Discussion. How to get liquid water close to the surface on Enceladus is a difficult question. Because previous interior thermal models for

Enceladus cannot explain the anomalous heating seen in the SPT, we cannot exclude the possibility that the processes producing the observed heating might result in local regions with even higher temperatures, leading to subsurface reservoirs of liquid water. In this model, heating large enough to raise the temperature to 273 K might be provided by very localized, near-surface tidal and/or librational frictional heating operating on and within the tiger stripe fractures, as has been suggested for Europa (35), although detailed models for Enceladus have not been investigated.

Our proposed models for plume sources imply large temperatures near the surface. Because warm water ice can deform relatively easily by viscous creep over short geological times, we have investigated the implications of such elevated near-surface temperatures for the observed small-scale topography (e.g., 100-m ridges bounding fractures 500 m deep) on the satellite's surface. We have applied models using rheologic parameters from a recent exploration of superplastic flow assuming grain boundary-sliding basal slip in ice under low stress (36) and considering a grain size of 100 μm , equal to that inferred for the tiger stripes. Assuming a background temperature of the SPT of ~ 95 K and liquid reservoirs at depths between 0.5 and 1 km for ammonia-water at 175 K and 1 to 2 km for water at 273 K (i.e., a large geothermal gradient), finite element modeling shows that ~ 1 -km topography would undergo measurable deformation on time scales of a few million to tens of millions of years. Very shallow liquid layers in regions outside the SPT are probably inconsistent with the retention of the observed topography there for the inferred lifetimes (from cratering statistics) of a billion years or more

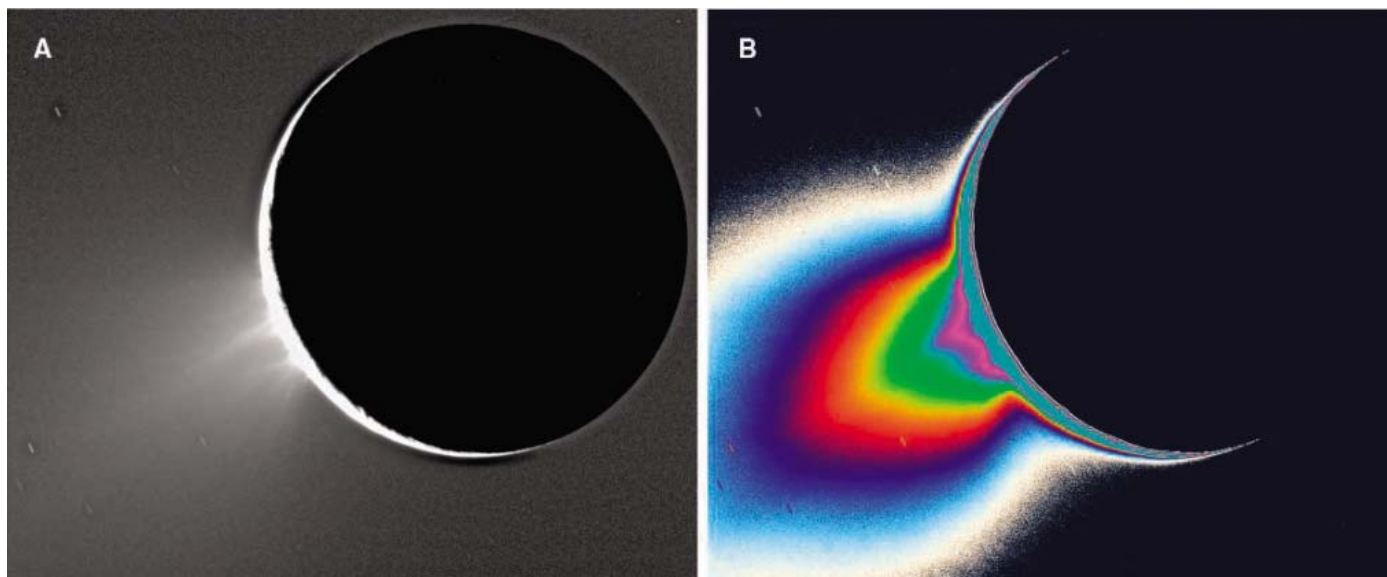


Fig. 6. (A) An ISS NAC clear-filter image (12) of Enceladus' near-surface plumes (which can be resolved into individual jets) taken on 27 November 2005 at a phase angle of 161.4° with an image scale of ~ 0.89 km/pixel. The subspacecraft latitude was $+0.9^\circ$; the view on this day was also

broadside to the tiger stripes (Fig. 1). The south pole is pointing toward the lower left. (B) A color-coded version of (A), in which faint light levels were assigned different colors to enhance visibility, shows the enormous extent of the fainter component above the south polar region.

(Table 1). Thus, Enceladus' subsurface structure may be globally heterogeneous, with some regions retaining a cold, thick upper crust for some time and the SPT being the only region where liquid may be close to the surface at the present time.

Tidal heating associated with the eccentricity of Enceladus' orbit, forced by its 2:1 mean motion resonance with Dione, has long been suspected (37). Using Cassini values for the mass (27), volume and mean density (this paper), and the current value of the orbital eccentricity $e = 0.0047$, we calculate a tidal heating rate of 1.2×10^{15} ergs s^{-1} for a homogeneous model and an assumed tidal dissipation parameter $Q = 20$: The lower the value of Q , the more dissipative the interior.

Enceladus' rotation state is important when considering possible heating inputs from the 1:4 secondary resonance librations. For Enceladus to be librating with an amplitude equal to the measured upper limit (1.5°), ϵ must equal 0.25005 for the current orbital eccentricity, well within the uncertainties of the measured ϵ for all homogeneous and differentiated models. This would yield a present-day heating rate due to secondary libration alone of 1.8×10^{15} ergs s^{-1} , again for $Q = 20$.

The Cassini value of mass density for Enceladus implies a rock fraction ($mass_{rock}/mass_{Enc}$) of 0.61. This higher rock fraction, plus the higher mass, compared to the values derived from Voyager data, imply an increase of a factor of 2.5 in the total rock mass over Voyager-based estimates. Thus, we can expect the present-day radiogenic heating rate to be equivalently higher, 3.2×10^{15} ergs s^{-1} , assuming chondritic long-lived radionuclide abundances (38). The present-day total heating rate on Enceladus from all aforementioned sources, assuming $Q = 20$, could be 4×10^{15} to 6×10^{15} ergs s^{-1} , or ~ 0.5 GW, about one-tenth the observed total power coming from the SPT (13). However, this heating rate might be significantly enhanced for more realistic viscoelastic models of the interior.

Previous models (5) have suggested that the present tidal heating from eccentricity forcing by the resonant perturbations of Dione alone, although not enough to initiate melting, might be sufficient to maintain as liquid a portion of an icy interior as near to the surface as 10 km, if the start of melting had occurred in a previous epoch and if the melting point were depressed by mixing a substantial amount of ammonia with water in the ice (8). Also, calculations (39) using the older heating estimates but differentiated interiors show that a mantle temperature of 210 K could be within 10 km of the surface for specific rheological parameterizations. The higher radiogenic heating indicated by Cassini results (2.5 times as much energy as used in pre-Cassini models) and the possibility of additional present-day librational heating suggest that some interior liquid is even more likely than in previous models, assuming ammonia is present, and may be possible within tens of kilometers of the surface in differentiated

models without invoking large amounts of ammonia. Although no instrument has positively detected ammonia, its existence cannot be ruled out: The derived upper limiting value to the ammonia abundance [0.5% in the plume vapor (16)] could still permit a geophysically important amount of ammonia at depth, although, as discussed above, an ammonia-water mixture cannot be venting to space. It is also possible, as mentioned above, that a pure-water interior heated preferentially on fractures as for Europa (35) might retain near-surface liquid water up to the present in localized regions. Consequently, it is plausible that Enceladus may be sufficiently heated today by some combination of the mechanisms mentioned above to explain the observed south polar venting, provided it underwent an early epoch of intense heating and, once heated, retained a low Q up through the present in some portion of the interior. Explaining the observed power output of 5 GW (13) is more challenging.

How was Enceladus initially heated? Previous suggestions (5) calling for a larger orbital eccentricity in the past to increase tidal heating are not attractive: Not only is considerable past orbital evolution not likely, but capture into the 2:1 mean motion Dione resonance through tidal evolution does not produce a past eccentricity larger than Enceladus' current value. If, instead, the moon was at one time in the 1:4 secondary libration resonance, as the observed value of $\epsilon \sim 0.25$ suggests, how did it get captured, and could heating from this mechanism have been sufficient for melting? Wisdom (9) discussed several scenarios for placing Enceladus in a spin-orbit secondary resonance. One possibility is an impact that initiated libration and allowed capture into the 1:4 resonance. An initial $\epsilon = 0.26$, with an associated libration amplitude of 22° , yields a heating rate 100 times that due to the forced eccentricity today for typical fully elastic models and the same temperature-independent $Q = 20$. For more realistic temperature-dependent viscoelastic models of the interior and a long residence time in this resonance, considerable initial heating may be possible, although detailed models have not yet been examined.

It is easy to see how strong heating from a large past libration could completely relax the body, reducing ϵ to < 0.26 , damping the libration, and thus terminating the spin-orbit secondary resonance, resulting in a hydrostatic shape. However, the uncertainties allow the possibility that the shape may be nonhydrostatic and ϵ may be as high as 0.26 (Table 2). A nonhydrostatic shape and a present-day $\epsilon \sim 0.26$ could be explained if Enceladus were in the 1:4 resonance in the past, and internal heating of the moon was insufficient to bring about full differentiation and hydrostatic equilibrium but still served to decrease Q , increase dissipation, and damp the resonance. Moreover, if this heating were nonuniform within the body, as Cassini ob-

servations show, the figure might have evolved in unusual ways, relaxing in some regions and not others, yet remaining overall close to its original figure and original ϵ despite the damping of the libration.

These changes in figure might have left discernible marks on the surface. The symmetry and distribution of young tectonic patterns, especially those associated with the SPT, suggest that Enceladus may have undergone large-scale changes of figure over time. The north-south-trending fractures and rifts that extend northward from the south polar Y-shaped discontinuities (Fig. 2D) appear to have formed in response to horizontal extensional stresses aligned along circles of latitude. Such parallel "hoop" stresses near equatorial latitudes could arise in response to an increase in flattening of the figure of Enceladus (40, 41).

Moreover, the appearance and symmetry of the SPT boundary at $\sim 55^\circ$ S latitude identify a change in the character of stresses associated with global deformation. Here, the change in orientation of the Y-shaped discontinuities, from north-south-trending nearer the equator to east-west-trending along the south polar margin, imply a change in principal tensile stresses that caused the fracturing, from strong tensile stresses parallel to the equator at equatorial latitudes to predominantly compressional stresses perpendicular to circles of latitude at the SPT boundary. The sinuous belts of ridges and troughs at the SPT margin were probably formed in response to horizontal compressive stresses perpendicular to circles of latitude. A transition in the character of horizontal stresses with increasing latitude is also expected to accompany an increase of flattening in Enceladus' figure (40, 41).

Two problems with this "figure flattening" interpretation are (i) the absence of similar circumpolar features and tectonic fractures in the north polar region, indicating that the putative alteration in shape was not global, and (ii) the lack of any plausible mechanism for increased flattening. We note that the observed asymmetric distribution of heat within the body may explain the surface expression of global stresses in one hemisphere and not the other. These are suggestions that remain to be investigated in detail. The tiger stripe fractures in the SPT, and their $\sim 45^\circ$ orientation with respect to the Saturn direction, suggest tidal deformation or some other process as another contributing factor in the tectonic patterns characterizing the SPT.

References and Notes

1. A. J. Verbiscer, R. G. French, C. A. McGhee, *Icarus* **173**, 66 (2005).
2. D. P. Cruikshank, *Icarus* **41**, 246 (1980).
3. K. D. Pang, C. C. Voge, J. W. Rhoads, J. M. Ajello, *J. Geophys. Res.* **89**, 9459 (1984).
4. B. A. Smith *et al.*, *Science* **212**, 163 (1981).
5. S. W. Squyres, R. T. Reynolds, P. M. Cassen, S. J. Peale, *Icarus* **53**, 319 (1983).

6. J. S. Kargel, S. Pozio, *Icarus* **119**, 385 (1996).
7. J. Lewis, *Icarus* **15**, 174 (1971).
8. S. J. Peale, *Annu. Rev. Astron. Astrophys.* **37**, 533 (1999).
9. J. Wisdom, *Astron. J.* **128**, 484 (2004).
10. M. K. Dougherty *et al.*, *Science* **311**, 1406 (2006).
11. R. H. Brown *et al.*, *Science* **311**, 1425 (2006).
12. C. C. Porco *et al.*, *Space Sci. Rev.* **115**, 363 (2004).
13. J. R. Spencer *et al.*, *Science* **311**, 1401 (2006).
14. ISS and CIRS are acknowledged in the codiscovery of the correlation between the hottest temperatures measured in the SPT and the tiger stripe fractures.
15. F. Spahn *et al.*, *Science* **311**, 1416 (2006).
16. J. H. Waite Jr. *et al.*, *Science* **311**, 1419 (2006).
17. C. J. Hansen *et al.*, *Science* **311**, 1422 (2006).
18. G. H. Jones *et al.*, *Science* **311**, 1412 (2006).
19. G. Hansen, personal communication.
20. C. C. Porco *et al.*, *Science* **307**, 1237 (2005).
21. G. Neukum *et al.*, *Lunar Planet. Sci. Conf. 36*, abstract 2034 [CD-ROM] (2005).
22. R. Wagner *et al.*, *Bull. Am. Astron. Soc.* **37**, 701 (2005).
23. G. Neukum, thesis, Ludwig-Maximilians-Universität München (1983).
24. G. P. Horedt, G. Neukum, *J. Geophys. Res.* **89**, 10405 (1984).
25. G. Neukum, *Adv. Space Res.* **5**, 107 (1985).
26. R. Ionascu, *Jet Propulsion Laboratory Interoffice Memorandum IOM 343J-05-017* (2 May 2005).
27. R. Jacobson and the Cassini Project Navigation team, personal communication.
28. S. F. Dermott, *Icarus* **37**, 575 (1979).
29. S. F. Dermott, P. C. Thomas, *Icarus* **109**, 241 (1994).
30. Brightness values were converted into particle densities with the use of an assumed analytical particle size distribution (42): $n(r) = \text{constant } r^{(1-3b)/b} \exp(-r/ab)$, where a is the effective radius (1.0 μm , appropriate for particles in the E ring) and $b = 0.25$. The quantity b is large enough to ensure a fair fraction of the particles are large enough (i.e., $>2 \mu\text{m}$) for CDA to detect. Horizontal (line-of-sight) column densities, N_{los} , were computed from the peak I/F by the relation $N_{\text{los}} = 4(I/F)/[A_{\text{sca}} \times P(\varphi)]$, where A_{sca} is the scattering cross section appropriate for the chosen particle size distribution, and $P(\varphi)$ is the phase function computed for Mie scatterers at phase angle φ . The scattering cross section used for the assumed particle size distribution and an effective observation wavelength of 569 nm was 3.12 square μm ; $P(\varphi = 161.4^\circ) = 6.688$.
31. A. Juhasz, M. Horanyi, *J. Geophys. Res.* **107**, A6 1066 (2002).
32. M. Hedman, personal communication.
33. J. Eluszkiewicz, J.-L. Moncet, *Icarus* **166**, 375 (2003).
34. S. W. Kieffer, in *The Satellites of Jupiter*, D. Morrison, Ed. (Univ. of Arizona Press, Tucson, AZ, 1982), pp. 647–723.
35. E. J. Gaidos, F. Nimmo, *Nature* **405**, 637 (2000).
36. D. L. Goldsby, D. L. Kohlstedt, *J. Geophys. Res.* **106**, 11017 (2001).
37. C. F. Yoder, *Nature* **279**, 767 (1979).
38. G. Schubert, T. Spohn, R. T. Reynolds, in *Satellites*, J. A. Burns, M. S. Matthews, Eds. (Univ. of Arizona Press, Tucson, AZ, 1986), pp. 224–292.
39. M. N. Ross, G. Schubert, *Icarus* **78**, 90 (1989).
40. P. Helfenstein, E. M. Parmentier, *Icarus* **53**, 415 (1983).
41. H. J. Melosh, *Icarus* **31**, 221 (1977).
42. J. E. Hansen, *J. Atmos. Sci.* **28**, 1400 (1971).
43. G. Neukum, B. A. Ivanov, W. K. Hartmann, *Space Sci. Rev.* **96**, 55 (2001).
44. K. Zahnle, P. Schenk, H. Levison, L. Dones, *Icarus* **163**, 263 (2003).
45. We acknowledge the financial support of NASA/JPL, the UK Particle Physics and Astronomy Research Council, the Deutsches Zentrum für Luft- und Raumfahrt (German Aerospace Center), and Université Paris VII Denis Diderot, Commissariat à l'Énergie Atomique, Astrophysique Interactions Multieschelle, France.

Supporting Online Material

www.sciencemag.org/cgi/content/full/311/5766/1393/DC1
Fig. S1

25 November 2005; accepted 21 February 2006
10.1126/science.1123013

RESEARCH ARTICLE

Cassini Encounters Enceladus: Background and the Discovery of a South Polar Hot Spot

J. R. Spencer,^{1*} J. C. Pearl,² M. Segura,² F. M. Flasar,² A. Mamoutkine,² P. Romani,²
B. J. Buratti,³ A. R. Hendrix,³ L. J. Spilker,³ R. M. C. Lopes³

The Cassini spacecraft completed three close flybys of Saturn's enigmatic moon Enceladus between February and July 2005. On the third and closest flyby, on 14 July 2005, multiple Cassini instruments detected evidence for ongoing endogenic activity in a region centered on Enceladus' south pole. The polar region is the source of a plume of gas and dust, which probably emanates from prominent warm troughs seen on the surface. Cassini's Composite Infrared Spectrometer (CIRS) detected 3 to 7 gigawatts of thermal emission from the south polar troughs at temperatures up to 145 kelvin or higher, making Enceladus only the third known solid planetary body—after Earth and Io—that is sufficiently geologically active for its internal heat to be detected by remote sensing. If the plume is generated by the sublimation of water ice and if the sublimation source is visible to CIRS, then sublimation temperatures of at least 180 kelvin are required.

Cassini-Huygens is a major international planetary mission that entered orbit around Saturn on 1 July 2004 for a nominal 4-year investigation of the planet, its satellites, rings, and magnetosphere. In 2005, Cassini made three flybys of the enigmatic satellite Enceladus, long suspected to be recently geologically active and the source of Saturn's tenuous, extended E ring. Results from multiple Cassini instruments on the third flyby on 14 July 2005 offer convincing proof that this small icy satellite is currently active, as described in this series of companion papers.

Enceladus. Discovered by William Herschel in 1789, Enceladus orbits close to Saturn at a

radius of 3.94 Saturn radii and thus is difficult to observe from Earth because of the scattered light of the planet and its rings. Enceladus' orbital period is 1.37 days. Telescopic infrared spectra indicate a surface composed of almost pure water ice (1), although a tentative detection of ammonia ice has been reported recently (2). The Voyager encounters with the satellite in 1981 established its radius (252.1 km) (3) and that its visual geometric albedo is startlingly high, consistent with fresh snow or ice, and higher than for any other known solar system body (4, 5). Voyager 2 also discovered that Enceladus was unique among Saturn's medium-sized icy satellites, be-

cause its surface includes sizable crater-free areas that have been resurfaced by endogenic forces (4) and were estimated to be <200 million years old (6). Other parts of the satellite are heavily cratered and perhaps nearly as old as the solar system, but the craters show considerable signs of internal modification. All regions of the satellite, regardless of age, exhibit uniformly high albedos, implying that the entire satellite is coated with a ubiquitous fresh material (7). Particle-orbit models have shown that Enceladus is probably the major source of the tenuous E ring (8), which is most dense at the satellite's orbit. The mechanism for the injection of material from the satellite into the E ring has been debated; volcanism (9), geysers (10), large impacts (11), and collisions between Enceladus and E-ring particles themselves (12) have all been proposed. Regardless of the means of transport, the micrometer-sized particles that make up the ring must be constantly replenished, because sputtering (10, 13) would destroy them on time scales much shorter than the age of the solar system.

The heat source for the extensive resurfacing on an object as small as Enceladus has always been difficult to explain, especially when compared to other saturnian satellites that show much less evidence of activity (14–16). The orbital eccentricity of Enceladus (0.0047, comparable to that of Io) is perhaps sufficient for substantial

¹Department of Space Studies, Southwest Research Institute, 1050 Walnut Street, Suite 400, Boulder, CO 80302, USA.

²NASA Goddard Spaceflight Center, Code 693, Greenbelt, MD 20771, USA. ³Jet Propulsion Laboratory, California Institute of Technology, 4800 Oak Grove Drive, Pasadena, CA 91109, USA.

*To whom correspondence should be addressed. E-mail: spencer@boulder.swri.edu

tidal heating given the right internal structure (16), but the absence of internal activity on nearby Mimas, which has an orbital eccentricity of 0.0202, makes this source problematic, too. The contrast with Mimas might be explained if Mimas is in a cold, elastic, nondissipative state, whereas Enceladus is in a self-maintaining warm, plastic, dissipative state (17). Resonantly excited rotational librations have recently been suggested as a possible alternative tidal heating mechanism (18, 19).

Cassini flybys. Cassini has observed Enceladus with multiple instruments including the Ultraviolet Imaging Spectrograph (UVIS), the visible-wavelength Imaging Science Subsystem (ISS), the Visual and Infrared Mapping Spectrometer (VIMS), the Composite Infrared Spectrometer (CIRS), the magnetometer (MAG), the Cosmic Dust Analyzer (CDA), the Cassini Plasma Spectrometer (CAPS), the Radio and Plasma Wave Science (RPWS) instrument, and the Ion and Neutral Mass Spectrometer (INMS). The first close Cassini flyby of Enceladus, on orbit 3 on 17 February 2005 at an altitude of 1258.6 km (Table 1), focused on the equatorial region centered near longitude 310°W. ISS revealed a world scarred by extensive tectonic activity (19), and VIMS spectra indicated that the surface composition was completely dominated by water ice (20). MAG data showed a draping of Saturn's magnetic field lines around the moon, which suggested the presence of an atmosphere (21). However, UVIS observations of a stellar occultation showed no sign of an atmosphere at low latitudes (22). During the second flyby, on orbit 4 at an altitude of 497.0 km on 9 March 2005, Cassini concentrated on the equatorial region of the hemisphere centered near 190°W. ISS images revealed complex networks of ridges and troughs coexisting with ancient cratered plains. MAG measured a signature in addition to the one seen in February, possibly indicating an induced or intrinsic magnetic field. Based on the MAG results, the Cassini Project decided to reduce the altitude of the 14 July 2005 encounter, on orbit 11, from 1000 km down to ~170 km.

On the 14 July flyby, the spacecraft approached the illuminated anti-Saturn hemisphere, which is centered on longitude 180°W, from the south. On approach, the remote sensing instruments (ISS, VIMS, UVIS, and CIRS) observed Enceladus beginning 8 hours before the closest approach, starting from a distance of 288,000 km. At 21 min before the closest approach, the spacecraft began the turn to point to the star γ -Orionis (Bellatrix), and at 4 min before the closest approach, Bellatrix was occulted by Enceladus; measurements of the occultation were performed by UVIS (22). As Enceladus passed in front of the star, the moon crossed through the boresights of the remote sensing instruments, providing a brief opportunity for remote sensing at very high spatial resolution. The subspacecraft point at the closest approach

was at 24°S, 326°W. After the occultation, at 3 min after the closest approach, the spacecraft began to turn back to Enceladus and resumed remote sensing of the nighttime surface at 31 min after the closest approach, continuing to 114 min. Throughout the inbound and outbound portions of the flyby and during the closest approach, the fields and particles instruments obtained valuable information on the plasma and particulate environment around Enceladus. In particular, INMS (23), CAPS,

RPWS (24), and CDA (25) obtained in situ measurements of the near-south polar environment.

Composite Infrared Spectrometer results. The CIRS instrument (26) used the three Enceladus encounters to investigate the satellite's thermal radiation, which provides clues to its surface properties and a means to detect possible endogenic activity. The only previous observations of Enceladus' thermal radiation were by Voyager 2 in 1981 (27), which derived a disk-

Table 1. Cassini Enceladus encounter geometries. Times are in universal time at the spacecraft.

Cassini orbit	Date	Time	Altitude at closest approach (km)	Approach geometry 2 hours before encounter	
				Subspacecraft latitude, longitude	Phase angle
3	17 February 2005	03:30	1258.6	309°W, 0°N	25
4	9 March 2005	09:08	497.0	191°W, 1°S	47
11	14 July 2005	19:55	168.2	186°W, 47°S	47

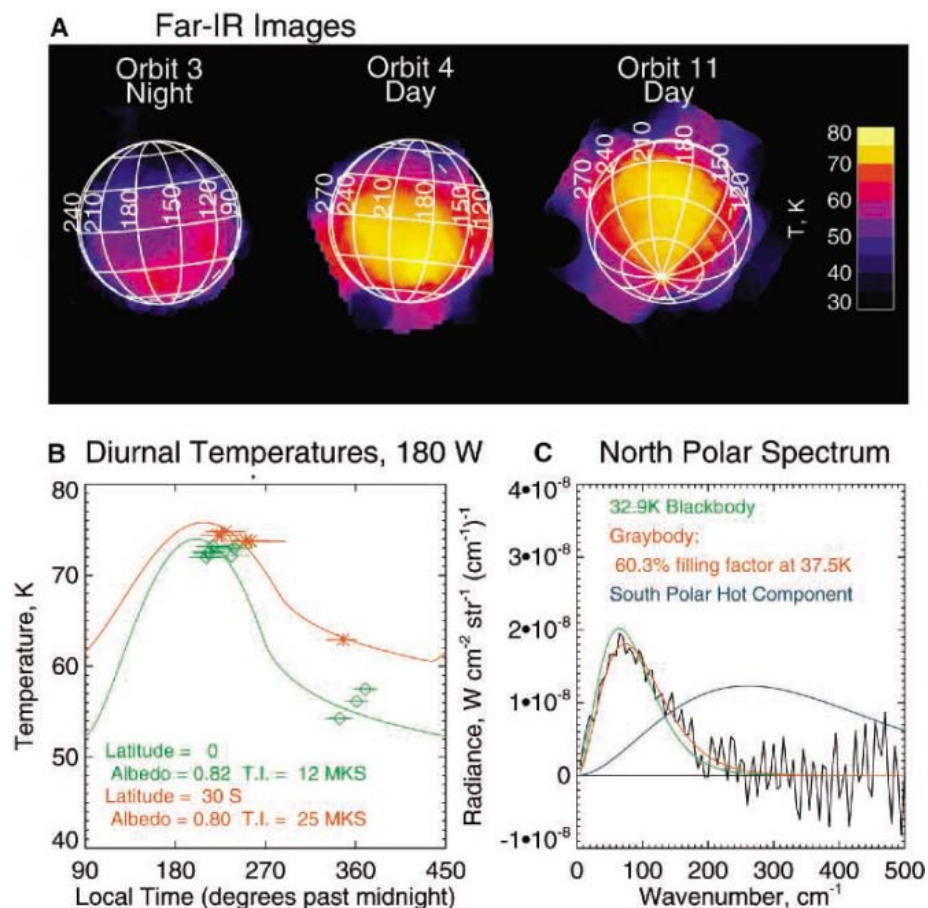


Fig. 1. Far-IR observations of Enceladus. (A) Far-IR brightness temperature images of the nighttime and daytime thermal emission from the anti-Saturn hemisphere of Enceladus (centered at longitude 180°W) from the three Cassini encounters. The apparent signal beyond the limb of Enceladus is an artifact of the low spatial resolution and the plotting technique. (B) Thermal model fits to the far-IR day and night brightness temperatures at longitude 180°W and two different latitudes, as measured on orbits 3 and 4, showing the large spatial variations in thermal inertia [TI, in m kg s (MKS units)]. Horizontal bars show the local time range of each observation. (C) Far-IR spectrum of the north pole, with best fit blackbody and graybody spectra, showing the lack of the high-temperature component seen at the south pole. The fine structure in this and all spectra shown is due to noise.

integrated 250-cm^{-1} brightness temperature (28) of 67 K at 37° phase angle with an inferred subsolar temperature of $75 \pm 3\text{ K}$, but provided little other information. CIRS consists of two Fourier transform spectrometers, which together measure thermal emission from 10 to 1400 cm^{-1} (wavelengths 1 mm to $7\text{ }\mu\text{m}$) at a selectable spectral resolution between 0.5 and 15.5 cm^{-1} . The far-infrared interferometer (10 to 600 cm^{-1}) has a 4-mrad field of view on the sky. The mid-infrared (IR) interferometer consists of two 1×10 arrays of 0.3-mrad pixels, which together span 600 to 1400 cm^{-1} .

Cassini's first two flybys of Enceladus, in February and March 2005, provided good views of the low-latitude regions on both sides of the satellite. Daytime thermal emission from the anti-Saturn side of the moon was mapped by the far-IR detector in March 2005, and the same region was seen at night in February 2005 (Fig. 1A). Most

spectra are well described by blackbody curves in the 50 to 600 cm^{-1} range, and we estimate surface temperature by least squares fitting of blackbody curves to the spectra. Comparison of daytime and nighttime temperatures for the same regions allows for the determination of bolometric albedo and thermal inertia (29) as a function of location on this hemisphere. Nighttime temperatures showed spatial variability, probably resulting from thermal inertia variations. Day and night temperatures near longitude 180°W can be matched by models with thermal inertias in the range 12 to $25\text{ J m}^{-2}\text{ s}^{-1/2}\text{ K}^{-1}$, averaged over the uppermost $\sim 1\text{ cm}$ of the surface layer, whereas bolometric albedo on this hemisphere is more constant, varying between 0.80 and 0.82 (Fig. 1B). These bolometric albedos are consistent with the estimate from Voyager photometry of 0.90 ± 0.10 (30), and subsolar temperatures near 76 K are also consistent with Voyager es-

timates (27). The thermal inertia is 100 times smaller than that of solid water ice (31), implying a highly unconsolidated surface.

The third flyby, on orbit 11 on 14 July 2005, provided the first good view of the south polar regions of Enceladus. Maps of the daytime thermal emission were obtained with both the mid-IR and far-IR detectors on approach. The low spatial resolution of the far-IR detector prevented good observations of the south polar region at long wavelengths (Fig. 1A), but the mid-IR detector was able to map the entire disk at a spatial resolution of 25 km over the 600 - to 800-cm^{-1} (12.5 to $16\text{ }\mu\text{m}$) spectral range, with useful signal at higher wave numbers in the warmest regions (Fig. 2, A and B). The equatorial regions showed 650-cm^{-1} brightness temperatures in the high 70 s K , consistent with models of passive solar heating based on the range of thermal inertias and albedos determined from the earlier flybys (Fig. 1). However, most of the polar region south of latitude 65°S showed higher brightness temperatures, reaching 85 K near the south pole. This temperature is surprisingly warm; the temperature at the south pole, which is in equilibrium with current insolation (i.e., assuming zero thermal inertia), is only 68 K for an albedo of 0.81 because of the highly oblique illumination there (solar elevation at the pole was only 23°). An implausibly low south polar albedo of 0.55 , 67% of the equatorial albedo, would be necessary to increase the equilibrium temperature to 85 K . The elevated temperatures are not due to seasonal effects; we modeled long-term seasonal variations in the south polar temperature due to changes in the subsolar latitude and heliocentric distance of Enceladus for a range of thermal inertias, and we found that at the current season (midway between the southern summer solstice and the fall equinox), the south polar temperature is lower still for nonzero thermal inertia. The region of elevated south polar temperatures corresponds closely to a geologically youthful region occupied by four prominent troughs (dubbed "tiger stripes") seen by the Cassini cameras (Fig. 2B) (19).

The spectrum of the south polar thermal emission yields evidence for even higher temperatures, making an origin from solar heating even less likely. We found that the south polar spectrum was not well fit by a single-temperature blackbody filling the field of view. After subtracting the expected background thermal emission from a solar-heated surface, assuming a model with an albedo of 0.81 and thermal inertia of $20\text{ J m}^{-2}\text{ s}^{-1/2}\text{ K}^{-1}$, the average spectrum of the $37,000\text{-km}^2$ region south of 65°S could be fitted perfectly, within the uncertainties, by a graybody (i.e., a blackbody multiplied by a wavelength-independent filling factor). The best fit graybody has a temperature of $133 \pm 12\text{ K}$ occupying $345^{+320}_{-160}\text{ km}^2$, where the superscript and subscript are the errors (Fig. 2C). We determined uncertainties in the fit parameters by a Monte Carlo technique. We first

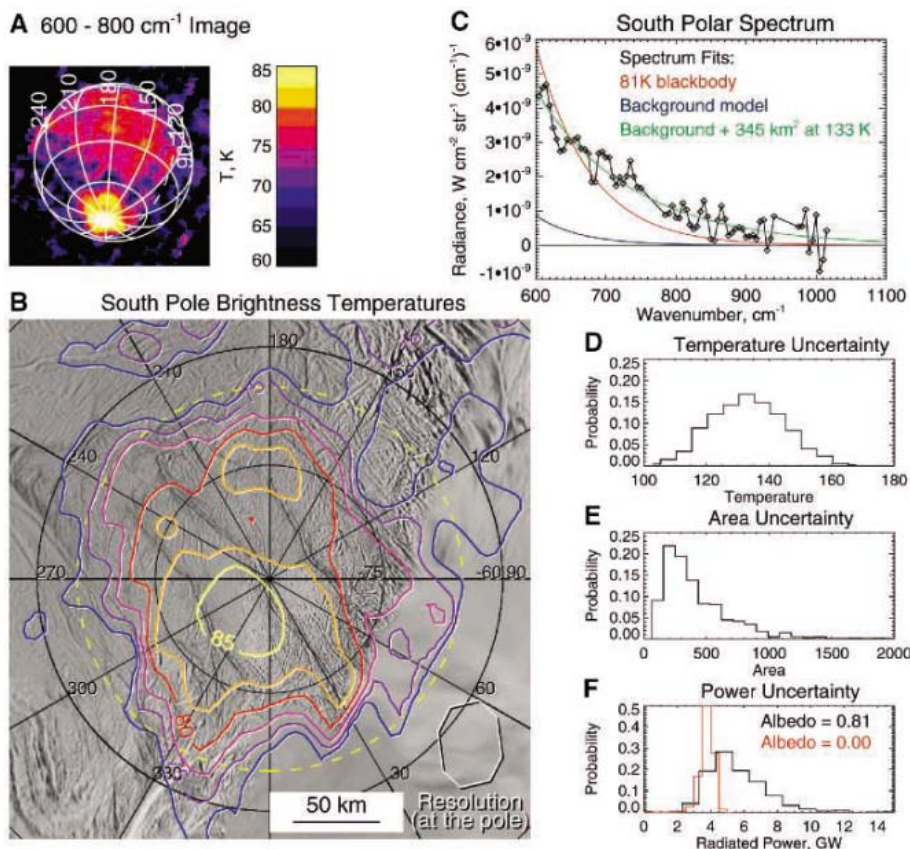


Fig. 2. (A) Mid-IR brightness temperature image of Enceladus from orbit 11, showing the prominent south polar hot spot. The dashed line is the terminator. (B) Brightness temperature contours derived from the observation in (A), superposed on an ISS base map (19), showing the spatial correlation of the hot material with the region containing the tiger stripe troughs. Spatial resolution (lower right) of the temperature map is about 50 km after projection and smoothing. The yellow dashed line shows the latitude boundary of the average spectrum shown in (C). (C) Thermal emission spectrum of the region south of latitude 65°S , compared with the best fit blackbody spectrum, which does not match the data, and the best fit graybody plus background model spectrum, which matches the data very well. (D to F). Probability distributions for the temperature (D), filling factor (E), and total radiated power (F) for the hot material in the south polar region, on the assumption of a single temperature for the hot material, derived by Monte Carlo techniques. The power distribution is shown for assumed hot material albedos of 0.81 and 0.00 .

determined noise levels (which are dominated by instrumental noise) from the scatter of the observed spectrum around the best fit model. We then added random noise at that level to the model, refitted the noisy model spectrum, and repeated this process many times to determine the probability distribution of fit parameters (Fig. 2, D and E). The probability distribution of fitted temperatures (Fig. 2D) suggests that maximum temperatures below 110 K are highly unlikely.

The spectral fits allow estimation of the total radiated power from the south polar region. After adjusting fitted temperatures for the thermal contribution expected from sunlight absorbed by the hot regions, and assuming that the hot sources have the same albedo (~0.81) as the rest of the surface, we derived a radiated nonsolar power of 5.8 ± 1.9 GW (Fig. 2F). Even if the hot sources have an albedo of 0.0 (highly unlikely but not formally ruled out, because the hot regions could be mixed with higher albedo regions on spatial scales too small to be resolved), the nonsolar power is still 3.9 GW. These estimates do not include the potential power contributions from the kinetic and latent heat of the south polar plume seen by other Cassini instruments (21–25), or any heat radiated at lower temperatures. For comparison, the total endogenic power radiated by Io is $\sim 10^5$ GW (32), and Enceladus' power generation per unit volume, assuming all the heat escapes from the south pole, is 3% that of Io. Assuming that the heat is generated below the surface, the average heat flow over the region south of 65°S is 0.25 W m^{-2} , compared with $\sim 2.5 \text{ W m}^{-2}$ for Io (32). The depth to melting or to ice warm and ductile enough to transport heat by convection, assuming pure solid H₂O ice and an ice conductivity of $3 \times 10^5 \text{ erg cm}^{-1} \text{ s}^{-1} \text{ K}^{-1}$ at the mean temperature of 180 K (33), is then only 2.5 km if the heat is generated below this level. In the hot regions at 124 K, heat flow is 13 W m^{-2} , and solid H₂O ice will approach the melting temperature at a depth of only 40 m. It is perhaps more likely that the heat is transported to the surface by advection of warm vapor rather than by conduction.

The relationship to the geological features becomes clearer in higher resolution CIRS observations obtained during the last 2.5 hours of the approach to Enceladus. In this period, CIRS did not perform contiguous scans of Enceladus, but instead rode along with the pointing determined by the ISS cameras as they obtained imaging mosaics of the moon, resulting in very scattered coverage with mid-IR spatial resolution as fine as 50 m near the closest approach (Fig. 3A). These higher resolution observations confirm that the thermal emission is highly localized and is associated with individual prominent tiger stripe troughs (19). The spatial correlation is not perfect, but discrepancies can perhaps be ascribed to pointing uncertainties. In some cases, the pointing uncertainties can be eliminated, because CIRS observations were obtained near-simultaneously with

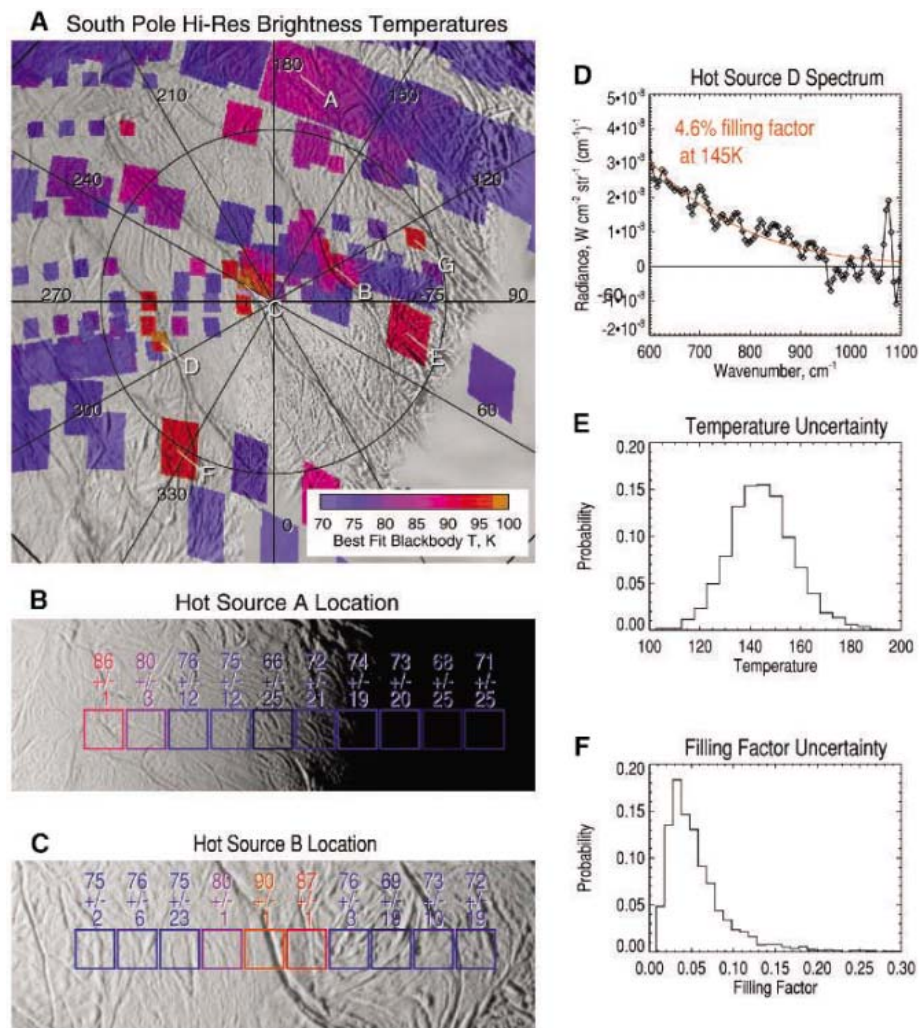


Fig. 3. (A) Color-coded south polar brightness temperatures at high spatial resolution, derived from the ISS ride-along CIRS observations, superposed on an ISS base map (19). This shows the correlation between high brightness temperatures and the individual tiger stripe troughs. Isolated colored rectangles represent observations taken during slews, and these have less reliable locations than other observations. The locations of the seven hot sources described in Table 2 and the rest of this figure are indicated. (B and C) Precise location of hot sources A and B relative to the topography as derived from simultaneous ISS images (19). Each box shows a single mid-IR field of view and its associated brightness temperature, with uncertainties. Field of view size is 17.5 km for source A and 6.0 km for source B. (D) The hottest individual CIRS spectrum (source D) and the best fit graybody spectrum. (E and F) Probability distribution of the temperature and filling factor for the spectrum of source D, assuming a single temperature.

Table 2. Selected discrete hot sources identified by CIRS.

Hot source designation	Latitude	Longitude	CIRS resolution (km)	Best fit graybody		
				Temperature	Filling factor	Width if linear
A	69°S	171°W	17.5	114 ± 22	0.063	1100 m
B	84°S	137°W	6.0	117 ± 16	0.092	550 m
C	87°S*	236°W*	5.8	135 ± 9	0.082	480 m
D	80°S*	289°W*	5.8	145 ± 14	0.046	250 m
E	78°S*	78°W*	13.6	133 ± 28	0.035	480 m
F	75°S*	328°W*	13.3	157 ± 24	0.017	230 m
G	76°S*	115°W*	6.0	127 ± 28	0.053	320 m

*Approximate location, no simultaneous imaging.

camera exposures, and because the ISS field of view includes the 1×10 -pixel CIRS mid-IR field of view. The location of the thermal emission observations relative to the geological features can then be determined very precisely (Fig. 3, B and C), confirming the association with the troughs, although there also seems to be some thermal emission from regions adjacent to the troughs. Table 2 describes the seven discrete hot sources that can be identified with greatest confidence in the ride-along observations, either because of simultaneous imaging or particularly strong thermal emission (Fig. 3A). We fitted blackbodies to the spectra of these sources after subtracting spectra of adjacent regions taken with the same CIRS detector, thus removing, to first order, the small contribution of thermal emission from the background and reducing calibration uncertainties. The association of the hot sources with linear features makes it likely that the hot sources are themselves linear, and Table 2 lists the inferred width of each source on the assumption that it is a linear feature extending across and beyond the CIRS field of view. The hot regions appear to be typically hundreds of meters wide. Some of the hottest individual spectra (sources C to G) were obtained during slews between ISS mosaic positions, and thus cannot be located so precisely, although they also appear to be close to the tiger stripe troughs. The brightest spectrum, D, requires a temperature of 145 ± 14 K, with temperatures below 120 K being highly unlikely (Fig. 3, D to F).

CIRS observed the north pole of Enceladus after the closest approach, and although mid-IR coverage is more limited than at the south pole, we can rule out a similar hot spot in the north. A far-IR integration of an 80-km-diameter region centered on the north pole, which has been in darkness since 1995, determined a best fit temperature of 32.9 ± 1.2 K (Fig. 1C). To be conservative, however, this should be considered an upper limit because of the possibility that scattered radiation from surrounding warmer regions contaminated the signal. The corresponding thermal inertia, averaged over the penetration depth of the seasonal thermal wave (about 1 m), is $<100 \text{ J m}^{-2} \text{ s}^{-1/2} \text{ K}^{-1}$. Any north polar hot component at the temperature of the south polar spot (133 K) would have to have less than 15% of the heat flow of the south polar spot in order to avoid detection in this integration. The lack of a north polar hot spot is consistent with the presence of heavily cratered terrain at the north pole (4, 6).

Discussion. It is likely that these warm troughs are the source of the dust and vapor plume seen by other Cassini instruments (21–25). From a stellar occultation measurement, UVIS detected a vapor plume above the south polar region (22) and determined an escape rate of 5×10^{27} to 10×10^{27} molecules per second. If we assume that the immediate origin of this plume is thermal sublimation of warm water ice (or the plume is in

vapor pressure equilibrium with surface ice at its source) and that this warm ice is visible to the CIRS instrument (rather than being hidden in deep fractures, for instance), we can constrain the temperature of the plume source using the observed thermal emission from the south pole. The mean south polar radiance at 900 cm^{-1} , about $5 \times 10^{-10} \text{ W cm}^{-2} \text{ str}^{-1} (\text{cm}^{-1})^{-1}$ (Fig. 2C), places an upper limit on the exposed area of a high-temperature plume source at a given temperature; thus, by using the vapor pressure curve for water ice (34), these results also place an upper limit to the sublimation rate from this source. The UVIS escape rate can be reconciled with the observed 900-cm^{-1} radiance only for plume source temperatures of 180 K or higher. A 180 K plume source would have an area of 28 km^2 , equivalent, for instance, to a 50-m width along each of the four $\sim 130\text{-km}$ -long tiger stripes (19), to produce the UVIS lower limit H_2O flux. 180 K is close to the 173 K temperature of a water/ammonia eutectic melt, a plausible cryovolcanic fluid within Enceladus (14), but the correspondence may be coincidental, because ammonia was not detected in the plume by the INMS instrument (23). The 345-km^2 area of the south polar warm material (Fig. 2B) is consistent with all the warm material being concentrated along the tiger stripes, with a mean width for the warm material of ~ 660 m, roughly consistent with the widths inferred from the high-resolution samples (Table 2).

The presence of these high temperatures at the south pole of Enceladus is surprising. As described above, the temperatures in many places are too high to be caused by simple re-radiation of sunlight absorbed at the surface. Very high subsurface temperatures can, in theory, be produced by subsurface trapping of solar radiation—the so-called solid-state greenhouse effect (35)—and might generate warm gases that could escape along fractures and form plumes, as has been proposed for Neptune's moon Triton (36). However, sufficiently large temperature enhancements have not been demonstrated in practice, and the association of the heat with obviously endogenic geological features (19) also makes a solar heating origin unlikely. An endogenic heat source is thus the most plausible explanation for the high temperatures. Maximum available power from radiogenic heat, assuming a chondritic composition for the nonice material in Enceladus, is about 0.1 GW (15), much smaller than observed. But tidal heating might generate 10 to 100 times more heat (37), which is comparable to the observed value. It is also possible that Enceladus is in an oscillatory state, as has been proposed for Io and Europa (38). In that case, its eccentricity and tidal heating rate may have recently been much higher, and perhaps the moon is still cooling down from that period.

The Cassini CIRS instrument has found that Enceladus is radiating at least several gigawatts of endogenic heat at temperatures of up to 145 K or

higher. Comparison with ISS images (39) shows that most or all of the heat is concentrated along surface troughs. These warm troughs are presumably the source of the vapor and dust plumes seen by other Cassini instruments.

References and Notes

1. D. P. Cruikshank, *Icarus* **41**, 246 (1980).
2. J. P. Emery, D. M. Burr, D. P. Cruikshank, R. H. Brown, J. B. Dalton, *Astron. Astrophys.* **435**, 353 (2005).
3. S. F. Dermott, P. C. Thomas, *Icarus* **109**, 241 (1994).
4. B. A. Smith *et al.*, *Science* **215**, 505 (1982).
5. A. J. Verbiscer, R. G. French, C. A. McGhee, *Icarus* **173**, 66 (2005).
6. J. S. Kargel, S. Pozio, *Icarus* **119**, 385 (1996).
7. B. J. Buratti, *Icarus* **75**, 113 (1988).
8. M. Horanyi, J. A. Burns, D. P. Hamilton, *Icarus* **97**, 248 (1992).
9. K. D. Pang, C. C. Voge, J. W. Rhoads, J. M. Ajello, *J. Geophys. Res.* **89**, 9459 (1984).
10. P. K. Haff, G. L. Siscoe, A. Eviatar, *Icarus* **56**, 426 (1983).
11. W. B. McKinnon, *Lunar Planet. Sci. Conf.* **14**, 487 (1983).
12. D. P. Hamilton, J. A. Burns, *Science* **264**, 550 (1994).
13. S. Jurak, R. E. Johnson, J. D. Richardson, *Icarus* **149**, 384 (2001).
14. S. W. Squyres, R. T. Reynolds, P. M. Cassen, *Icarus* **53**, 319 (1983).
15. G. Schubert, T. Spohn, R. T. Reynolds, in *Satellites*, J. Burns, M. Matthews, Eds., (Univ. of Arizona Press, Tucson, AZ, 1986), pp. 224–292.
16. M. N. Ross, G. Schubert, *Icarus* **78**, 90 (1989).
17. L. Czechowski, J. Leliwa-Kopystyński, *Planet. Space Sci.* **53**, 749 (2005).
18. J. Wisdom, *Astron. J.* **128**, 484 (2004).
19. C. C. Porco *et al.*, *Science* **311**, 1393 (2006).
20. R. H. Brown *et al.*, *Science* **311**, 1425 (2006).
21. M. K. Dougherty *et al.*, *Science* **311**, 1406 (2006).
22. C. J. Hansen *et al.*, *Science* **311**, 1422 (2006).
23. J. H. Waite Jr. *et al.*, *Science* **311**, 1419 (2006).
24. R. L. Tokar *et al.*, *Science* **311**, 1409 (2006).
25. F. Spahn *et al.*, *Science* **311**, 1416 (2006).
26. M. Flasar *et al.*, *Space Sci. Rev.* **115**, 169 (2004).
27. R. Hanel *et al.*, *Science* **215**, 544 (1982).
28. Brightness temperature is the temperature of a blackbody emitting the observed flux at the observed wavelength.
29. Thermal inertia, defined as $\sqrt{(k\rho c)}$, where k is the thermal conductivity, ρ is the density, and c is the specific heat, describes the ability of a surface to resist temperature changes caused by changes in insolation.
30. B. Buratti, J. Veverka, *Icarus* **58**, 254 (1984).
31. J. R. Spencer *et al.*, in *Pluto and Charon*, S. A. Stern, D. Tholen, Eds. (Univ. of Arizona Press, Tucson, AZ, 1997), pp. 435–473.
32. A. S. McEwen, L. P. Keszthelyi, R. Lopes, P. M. Schenk, J. R. Spencer, in *Jupiter, the Planet, Satellites, and Magnetosphere*, F. Bagenal, T. Dowling, W. McKinnon, Eds. (Cambridge Univ. Press, Cambridge, UK, 2004), pp. 307–328.
33. J. Klinger, *Science* **209**, 271 (1980).
34. C. E. Bryson, V. Czacarra, L. L. Levenson, *J. Chem. Eng. Dat.* **19**, 107 (1974).
35. D. L. Matson, R. H. Brown, *Icarus* **77**, 61 (1989).
36. R. H. Brown, R. L. Kirk, T. V. Johnson, L. A. Soderblom, *Science* **250**, 431 (1990).
37. L. Czechowski, paper presented at the 35th Committee on Space Research (COSPAR) Scientific Assembly, Paris, France, 18 July 2004.
38. H. Hussmann, T. Spohn, *Icarus* **171**, 391 (2004).
39. CIRS and ISS are acknowledged in the codiscovery of the correlation between the hot spots and the tiger stripe fractures.
40. We acknowledge the invaluable support of the entire Cassini science and engineering teams in making these observations possible. The work was supported by the NASA Cassini Project.

21 October 2005; accepted 5 January 2006
10.1126/science.1121661

REPORT

Identification of a Dynamic Atmosphere at Enceladus with the Cassini Magnetometer

M. K. Dougherty,^{1*} K. K. Khurana,² F. M. Neubauer,³ C. T. Russell,² J. Saur,³ J. S. Leisner,² M. E. Burton⁴

The Cassini magnetometer has detected the interaction of the magnetospheric plasma of Saturn with an atmospheric plume at the icy moon Enceladus. This unanticipated finding, made on a distant flyby, was subsequently confirmed during two follow-on flybys, one very close to Enceladus. The magnetometer data are consistent with local outgassing activity via a plume from the surface of the moon near its south pole, as confirmed by other Cassini instruments.

Interest has been high in Cassini's observation of Saturn's moon Enceladus because of its possible contribution to the material in the E ring. The first data were obtained during a flyby on 17 February 2005 (day 48) with a closest approach altitude of 1265 km. Magnetometer observations (*I*) from this flyby revealed clear perturbations of the magnetic field, indicating that the nearly corotating plasma flow from Saturn with its frozen-in magnetic field was slowing down near Enceladus and being deflected around it. In addition, enhanced ion cyclotron wave activity at the water group gyrofrequency during the flyby indicated that Enceladus is a major source of ions for the magnetospheric plasma. A second flyby on 9 March 2005 (day 68) at an altitude of 500 km

confirmed both the draping and ion cyclotron wave signatures, although clear differences between the two passes were observed. This discovery of substantial atmospheric/ion pickup acting as an obstacle to the flow of magnetospheric plasma around Enceladus led to a decision to decrease the altitude of the third Cassini flyby on 14 July 2005 (day 195) to 173 km, enabling a more detailed study of this exotic interaction by numerous onboard instruments (2–6). We describe the observations from these three flybys and offer an interpretation below.

The three Cassini flybys of Enceladus had distinct and complementary trajectories (Fig. 1). Data are shown according to the Enceladus Interaction Coordinate System (ENIS) aligned with the expected direction of the corotational flow (7). The first flyby was above Enceladus at about 4.7 Enceladus radii (R_E) on average above the orbital plane (8). The second flyby was below the moon at about 1.5 R_E , and the third flyby made a south-to-north cut as the spacecraft flew by at closest approach of about 0.7 R_E . On the last two flybys, Cassini moved inbound toward Saturn from upstream of Enceladus (as measured relative to the corotational flow),

whereas on the first flyby it moved outbound. All passes moved in the direction of corotation (i.e., with increasing *X* in the ENIS system).

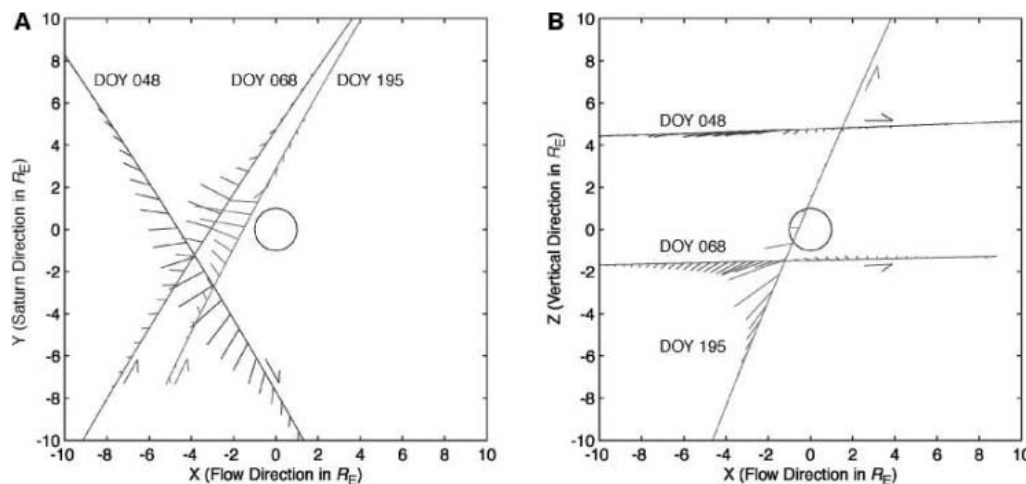
The magnetic field of Saturn at Enceladus is 325 nT due southward at the orbit of Enceladus. The perturbations that were observed during the three flybys are slight tilts of the field and a small compression of the southward field. It is most convenient for discussion to display only the perturbed field in the three directions (Fig. 1): B_X in the direction of the rotating planet, B_Y toward Saturn, and B_Z northward. The magnetic field perturbation on the first pass, day 48 of 2005, extends over a broad region from about 5 R_E inside Enceladus' orbit to about 8 R_E outside. The negative *X* component of the perturbed magnetic field is consistent with a slowdown of the flow below the spacecraft. The positive *Y* deflection of the field direction on the Saturn side and its negative *Y* deflection on the anti-Saturn side indicate that there is some deflection to the flow on either side of Enceladus. This signature indicates that the magnetospheric plasma that corotated with Saturn was slowed and deflected by an obstacle to the flow. Such an obstacle could be provided by an atmosphere in which ionization leads to mass loading of the magnetized plasma near Enceladus. At Enceladus one does not expect induction processes to be important because the background magnetic field has at most small deviations from axial symmetry. For a permanent dipole, a surface field on the order of ~1000 nT—as a result of remanent magnetization or a dynamo field—would be necessary to explain the first flyby observations. Neither scenario is plausible when taking into account the small size of Enceladus and its assumed internal structure and chemistry. Indeed, the second flyby observations were clearly inconsistent with the existence of a permanent dipole.

Hence, if we assume that an atmospheric interaction is occurring that caused the first flyby observations, then we may expect a scenario (Fig. 2) where Alfvén wings (9, 10) above and below the conducting obstacle are generated via cur-

¹Blackett Laboratory, Imperial College London, London SW7 2AZ, UK. ²Institute of Geophysics and Planetary Physics, University of California, Los Angeles, CA 90025, USA. ³Institute for Geophysics and Meteorology, Köln University, 50923 Köln, Germany. ⁴Jet Propulsion Laboratory, California Institute of Technology, Pasadena, CA 91109, USA.

*To whom correspondence should be addressed. E-mail: m.dougherty@imperial.ac.uk

Fig. 1. (A) The three flyby trajectories in the (*X*, *Y*) plane of the ENIS coordinate system, where *X* is along the direction of corotational flow and *Y* is positive toward Saturn; arrows denote the flyby direction. Overlain on the trajectories are the residuals of the magnetic field (after the background magnetic field has been removed from the data). The residuals are scaled such that 4.5 nT = 2 R_E . (B) The three flyby trajectories in the (*X*, *Z*) plane of the ENIS coordinate system, where *X* is along the direction of corotational flow and *Z* is along Saturn's spin axis; arrows denote the flyby direction. Data are displayed as in (A).



rents that are driven through the atmosphere by the motional electric field of the incident plasma combined with the electric conductivity of the atmosphere (which in turn results from elastic collisions or ion pickup). The pickup process is connected with mass loading and has a decelerating effect on the plasma. Initial modeling suggests that the current flowing in the pickup region is on the order of 10^5 A. Pickup is also the mechanism that excites ion cyclotron waves. The electromagnetic coupling interaction between Jupiter and its volcanic moon Io is a well-known example of this type of interaction between a large moving conductor and a magnetized plasma (11, 12), although at Io the currents linking the moon to Jupiter are up to 10 times as large. Ion mass loading decelerates the plasma as slow-moving, Enceladus-derived plasma is added to the faster moving magnetospheric plasma. Because the slowing is greatest where the mass loading is greatest, we would a priori expect the greatest slowing in Enceladus' orbital plane. Because the upstream field is directed southward, the B_x or along-flow component of the draped field will be negative in any plane above the mass-loading region and positive in any plane below that region (Fig. 2). In addition, above and upstream of the mass-loading region, draping will produce a positive B_y component on the Saturnward side and a negative perturbation on the side facing away from Saturn upstream of Enceladus as the flow is decelerated to the sides of Enceladus. Finally, the field would be compressed in front of the obstacle where the magnetized plasma flow has slowed. This compression would appear mainly in the B_z component. On the first flyby, with the Cassini spacecraft above Enceladus, we see a negative B_x as expected, with the change in the B_y perturbation (from negative on the negative Y side and positive on the positive Y side) indicating that the flow is being slowed and diverted around Enceladus. Moreover, the field is compressed, as expected from an upstream flyby.

The far-field signature of the Alfvén wing current system that was observed by Cassini (without actual penetration of the current-carrying wing) cannot provide detailed information about the size of the wing or the atmospheric source. Even for a strong atmospheric interaction, the necessary diameter of the atmospheric volume producing the perturbations is by necessity larger than the body of the satellite and needs to be at least on the order of $\sim 4 R_E$. A recent plasma model (13) predicts an even larger volume. This work suggests that a sputtering-produced atmosphere at Enceladus would not be sufficient to produce the observed magnetic field perturbations, and hence an additional atmospheric source must have been operating. A region of about $8 R_E$ is affected in front of and to the side of the moon, consistent with a large but weak interaction region. The magnetic field perturbations are also consistent with the

conductor/atmospheric volume being south of the spacecraft trajectory and downstream of it.

The second and third flyby data sets are not as easily explained by the simple guidelines used above. The second pass on day 68 is

below Enceladus (Fig. 1), and the region of strongly perturbed field is noticeably smaller and occurs inside of $\sim 3.5 R_E$. If the interaction was symmetric around Enceladus, so that the source of the slowdown was above the spacecraft,

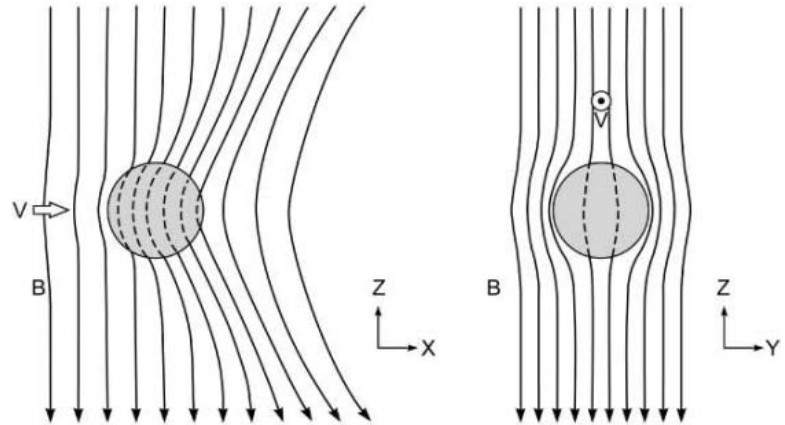


Fig. 2. A schematic showing the expected draping behavior of magnetic field lines, denoted by B in the vicinity of a large conducting obstacle. The left and right panels show the (X, Z) and (Y, Z) planes of the ENIS coordinate system, respectively. The inflowing corotating Saturn plasma (with velocity V) is slowed down with the field being draped around the obstacle. Field lines are dashed where they are moving through the conducting body.

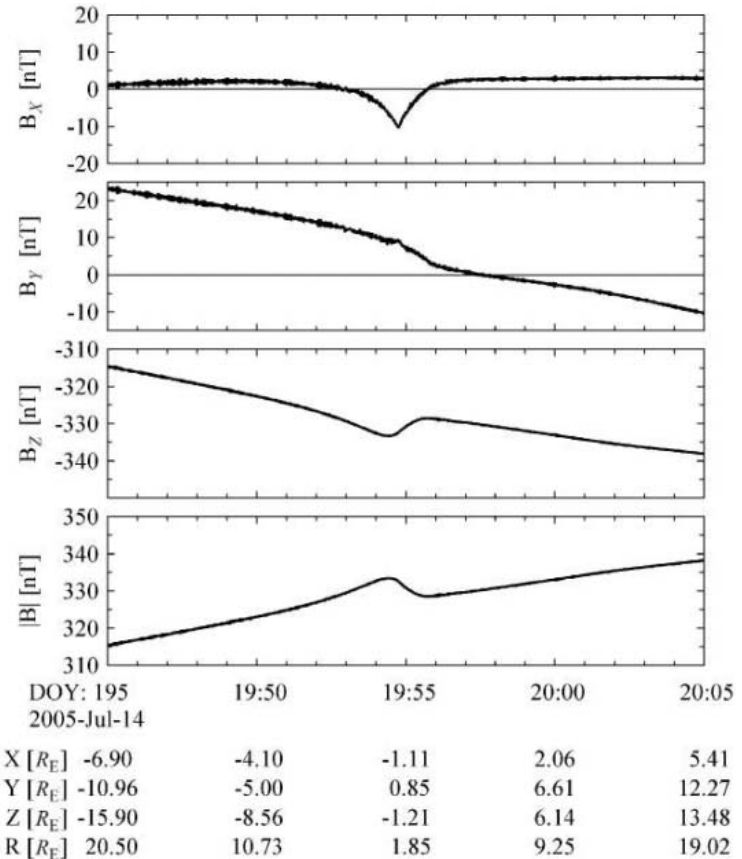


Fig. 3. Magnetic field data from the close flyby on day 195 in the ENIS coordinate system. The three components of the magnetic field and the absolute value of the field magnitude are shown. The clear perturbation in the magnetic field due to the interaction with Enceladus is clearly visible. Details of the spacecraft trajectory are listed beneath the plot; R is the radial distance of the Cassini spacecraft away from Enceladus.

then the perturbation vectors should be reversed relative to those of day 48. Outbound from about $Y = 3 R_E$, this is true. However, inbound before $Y = 0 R_E$, this is only partially true; B_Y appears to be in the direction for deflection around Enceladus above Cassini, but the B_X component is in the direction of slowdown below Cassini. Thus, the second flyby reveals a more complex picture. Because the major perturbation in the field appears to be in the negative B_X direction, the source is south of the spacecraft, even though the spacecraft itself is south of Enceladus. This implies the existence of a perhaps narrower pickup region extending southward, possibly due to an outgassing polar plume.

The implications of these findings, linked with the clear evidence from Voyager observations of endogenic geological activity (14) and speculations of outgassing or geyser-type activity, led to the decision to substantially decrease the altitude of the next Enceladus flyby. This took place on day 195 at 173 km. In the ENIS coordinate system, with the largest perturbation occurring in the B_X component, a sharp corner is seen in the minimum before closest approach (Fig. 3). These sharp gradients in the field suggest that the spacecraft may have crossed a current boundary during this time, perhaps even an entry into the atmospheric plume/ionosphere. The data on this encounter need to be visualized in three dimensions because the trajectory moves very rapidly in Z during the encounter. It can clearly be seen (Fig. 1) that the perturbation vectors are almost identical to those of day 68 despite the rapid motion in Z . The B_X perturbation is that of a slowdown in the flow below the spacecraft (while Cassini is in turn well below the orbital plane of Enceladus). Hence, the outgassing source must by necessity be at high southern latitudes well below the orbital plane. This is consistent with the realization that a neutral atmosphere at Enceladus is not strongly gravitationally bound for normal temperatures and will be even weaker for the high temperatures detected by observations (2, 3) in the tiger stripes (4) near the south pole. However, this is not the complete story, because the B_Y

perturbation is that of a deflection in Y around Enceladus but above Cassini. In other words, the perturbation in B_Y is 90° from what one would expect for a simple draping-type signature.

Ion cyclotron waves oscillating near the gyrofrequencies of water-group ions have been observed on nearly every Cassini orbit between 3.5 and $7 R_S$ (15). During the three close encounters of Enceladus, however, the waves changed in character as the spacecraft approached the moon. Near the orbit of Enceladus, the water-group waves nominally have amplitudes of ~ 0.25 nT. On each of the three flyby days, the wave amplitude began to increase above the background some $35 R_E$ away. On the first flyby, the amplitude rose to 0.72 nT at closest approach and continued increasing outbound from Enceladus. On the second flyby, the amplitude at closest approach was 0.34 nT; on the third flyby, the amplitude increased to a maximum of 0.55 nT but decreased to 0.32 nT at closest approach.

Because wave growth increases as pickup rate and background flow speed increase, the observed decrease on day 195 may result from a decrease in either the pickup rate or the velocity of the pickup. However, because we expect the pickup rate to monotonically increase as Enceladus is approached, we believe the decrease in wave amplitude signals a slowdown in the plasma flow near the moon. The subsolar latitude on Enceladus is about 20° S, but it has been shown (16) that charge exchange and electron impacts, not photoionization, would be the dominant forms of ionization (by two orders of magnitude). Therefore, any variation of wave amplitudes between the different flybys is more easily attributed to variations in the moon's neutral cloud morphology, the background plasma, and the spacecraft location relative to the flow than to any photoionization effects. The energy of an Enceladus pickup ion varies as the square of the relative velocities between the plasma and the neutrals, with about half of the energy of the pickup ion being available for wave generation (17). Thus, by measuring the electromagnetic energy flux of the ion cyclotron waves, we can estimate the energy flow into the picked-up

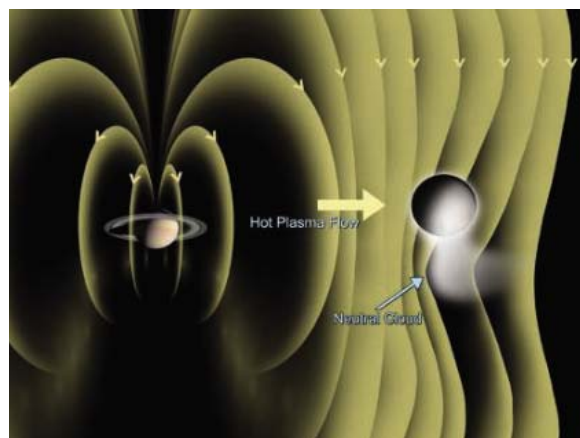
ions and hence the mass addition rate. For example, with the wave amplitude on the first flyby, the production rate near Enceladus can be estimated to be about 8 times the rate observed in the E ring far from the moon. This mass addition rate varies between flybys, both near and far from Enceladus.

The Cassini magnetometer data from the three recent flybys of Enceladus are consistent with the other Cassini instrument analyses of the existence of an outgassing plume near the south pole of the moon (Fig. 4). The magnetic field observations from the first flyby are most readily interpreted in terms of an atmospheric interaction in which ions are picked up and the flow is slowed down and deflected around Enceladus. In the second and third flybys, the major perturbations that are observed are compatible with a source south of the spacecraft; the narrower extent of the perturbed region is consistent with an outgassing plume close to the south pole of Enceladus, with neutrals being ejected radially away. The B_X signature is consistent in all three flybys but is more concentrated in extent in the second two flybys, as one might expect if the plume is expanding away from cracks in the surface of the moon. The B_Z perturbations simply reflect the compression in the magnetic field, with the field compressing so as to slow and deflect the flow. The B_Y perturbations in the latter two flybys are rather more difficult to interpret and will require detailed modeling work to better understand them.

The magnetic field measurements, together with the Ultraviolet Imaging Spectrograph occultation observations (5) from all three flybys, suggest appreciable temporal variations in the atmospheric plume on a time scale of months. The field results are consistent with the plume location obtained from other observations (2, 3, 6): The plume is emitted from the tiger stripes or cracks on the surface close to the south pole (4).

Initial numerical simulations based on (13) quantitatively confirm our qualitative conclusions. The simulations clearly indicate that the cause of the field perturbations is an atmospheric plume originating near the south pole of Enceladus. They also show that the neutral atmosphere that is generated is a dynamic one. Data from the first flyby require a spatially broadly distributed atmosphere on the scales of R_E , and because the flyby was well north of Enceladus itself, the observations were unable to place constraints on the latitudinal extent of the atmosphere. The last two flybys were much closer to Enceladus and hence could be much more constraining, indicating the source of the magnetic field perturbations to be an atmospheric plume near the south pole of Enceladus. In addition, observations made at the last two flybys are inconsistent with the broadly distributed neutral cloud and suggest the existence of a much narrower plume, confirming the dynamic nature of the atmosphere. The dynamic nature of the Enceladus neutral cloud is also consistent with the large variation of neutrals observed re-

Fig. 4. A schematic (where Saturn and Enceladus are not to scale) showing the corotating Saturn magnetic field and plasma being perturbed by the neutral cloud that is produced by a polar plume generated close to the south pole of Enceladus. This scenario fits the second two flyby observations.



motely (18). This substantial neutral source from Enceladus may go some way toward answering one of the outstanding questions regarding our understanding of Saturn's magnetosphere: What is the missing source of the large densities of water and its derivatives that are observed?

References and Notes

- M. K. Dougherty *et al.*, *Space Sci. Rev.* **114**, 331 (2004).
- J. R. Spencer *et al.*, *Science* **311**, 1401 (2006).
- R. H. Brown *et al.*, *Science* **311**, 1425 (2006).
- C. C. Porco *et al.*, *Science* **311**, 1393 (2006).
- C. J. Hansen *et al.*, *Science* **311**, 1422 (2006).
- J. H. Waite Jr. *et al.*, *Science* **311**, 1419 (2006).
- ENIS is defined with X in the direction of corotational flow; Y is positive toward Saturn and Z is along Saturn's spin axis.
- An Enceladus radius is defined as $R_E = 252.1$ km.
- S. D. Drell, H. M. Foley, M. A. Ruderman, *J. Geophys. Res.* **70**, 3131 (1965).
- F. M. Neubauer, *J. Geophys. Res.* **85**, 1171 (1980).
- J. W. Belcher, *Science* **238**, 170 (1987).
- M. G. Kivelson *et al.*, *J. Geophys. Res.* **106**, 26121 (2001).
- J. Saur, D. F. Strobel, *Astrophys. J.* **620**, L115 (2005).
- B. A. Smith *et al.*, *Science* **215**, 504 (1982).
- A Saturn radius is defined as $R_S = 60,268$ km.
- E. C. Sittler *et al.*, *J. Geophys. Res.* **109**, A01214 (2004).
- D. E. Huddleston, R. J. Strangeway, J. Warnecke, C. T. Russell, M. G. Kivelson, *J. Geophys. Res.* **103**, 19887 (1998).
- L. W. Esposito *et al.*, *Science* **307**, 1251 (2005); published online 16 December 2004 (10.1126/science.1105606).

5 October 2005; accepted 11 January 2006
10.1126/science.1120985

REPORT

The Interaction of the Atmosphere of Enceladus with Saturn's Plasma

R. L. Tokar,^{1*} R. E. Johnson,² T. W. Hill,³ D. H. Pontius,⁴ W. S. Kurth,⁵ F. J. Cray,⁶ D. T. Young,⁶ M. F. Thomsen,¹ D. B. Reisenfeld,⁷ A. J. Coates,⁸ G. R. Lewis,⁸ E. C. Sittler,⁹ D. A. Gurnett⁵

During the 14 July 2005 encounter of Cassini with Enceladus, the Cassini Plasma Spectrometer measured strong deflections in the corotating ion flow, commencing at least 27 Enceladus radii (27×252.1 kilometers) from Enceladus. The Cassini Radio and Plasma Wave Science instrument inferred little plasma density increase near Enceladus. These data are consistent with ion formation via charge exchange and pickup by Saturn's magnetic field. The charge exchange occurs between neutrals in the Enceladus atmosphere and corotating ions in Saturn's inner magnetosphere. Pickup ions are observed near Enceladus, and a total mass loading rate of about 100 kilograms per second (3×10^{27} H₂O molecules per second) is inferred.

Enceladus sits in an OH cloud, or torus, around Saturn that was originally detected by the Hubble Space Telescope (1). This cloud extends from about 3 to 8 Saturn radii [$1 R_S$ (Saturn's radius) = 60,268 km] with maximum concentration ($\sim 10^3$ cm⁻³) inferred near the orbit of Enceladus ($3.95 R_S$). The OH cloud is produced by dissociation of H₂O, and although the peak concentration suggested that the largest source of water molecules was in the region near the orbit of Enceladus, the nature of this source was unknown. Models indicate that the source region near $4 R_S$ must provide $\sim 80\%$ of the total OH source, estimated to be $\sim 0.4 \times 10^{28}$ to 1×10^{28} H₂O molecules s⁻¹ (2, 3).

On 14 July 2005, the Cassini spacecraft passed within 168.2 km of Enceladus, through the cloud of neutrals and plasma (Fig. 1). The orbital speed of Enceladus is 12.6 km s⁻¹, whereas the thermal plasma corotates with Saturn at 39 km s⁻¹ near Enceladus. Thus, the

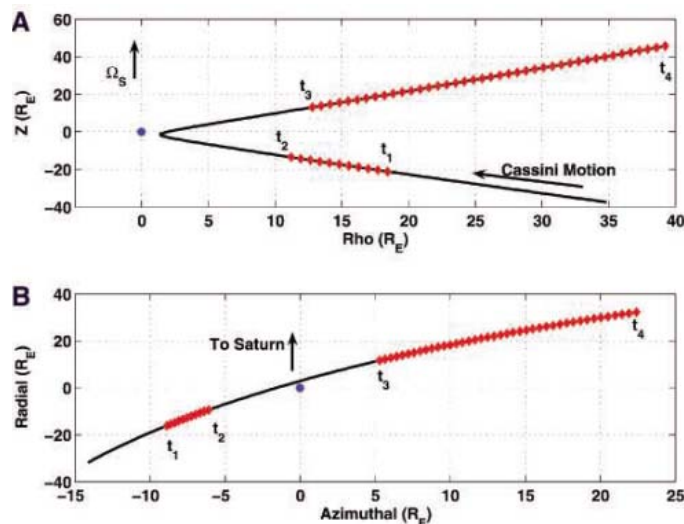
corotating plasma overtakes Enceladus, forming a corotational wake in the positive azimuthal direction at a speed of 26.4 km s⁻¹. Cassini passed upstream of this wake (Fig. 1B). A strong enhancement in the flux of plasma ions was detected by the Cassini Plasma Spectrometer (CAPS) (4) in two time intervals (Fig. 1) between $t_1 = 19:41$ UT and $t_2 = 19:46$ UT and between $t_3 = 20:04$ UT and $t_4 = 20:26$ UT.

Another Cassini instrument, the Radio and Plasma Wave Science (RPWS) instrument (5),

measured electric field fluctuations as a function of frequency and time during the Enceladus encounter (Fig. 2). We consider first the RPWS data and then return to the CAPS data. RPWS provides an estimate of the total electron density, N_e , at Cassini from the measured frequency of the upper hybrid resonance band (Fig. 2). This frequency is a known function of both the magnetic field strength (θ) and the total electron density. The emission observed near the upper hybrid resonance frequency is complex, with a smoothly varying narrowband emission at low frequencies and a more sporadic broadband extension to higher frequencies (Fig. 2). We assume that the narrowband relative maximum in the peak near the bottom of this complex line is the upper hybrid band and that the broadband extension to higher frequencies is a thermal plasma effect. The upper hybrid band indicates that the total electron density, shown approximately by the right-hand scale, smoothly increases from about 45 cm⁻³ at 19:30 UT to about 70 cm⁻³ at 20:04 UT. There is a short period close to Enceladus when the narrowband emission is not identifiable, likely due to dust particles hitting the spacecraft. During this time, it is not possible for RPWS to precisely determine the electron density, although there does not appear to be evidence for a substantial increase in the density ($> \sim 20\%$) at closest approach.

The study uses electron spectrometer, ELS, and ion mass spectrometer, IMS, data from CAPS

Fig. 1. Periods of CAPS-measured enhanced ion flux along the Cassini spacecraft trajectory during the close encounter of Enceladus on 14 July 2005. (A) An Enceladus-centered cylindrical coordinate system with the vertical axis in the direction of Saturn's spin axis and the horizontal axis the perpendicular distance from Enceladus ($1 R_E = 252.1$ km). (B) A projection into the equatorial plane with the radial coordinate positive toward Saturn and the azimuthal coordinate positive in the direction of corotation.



¹Space Science and Applications, Los Alamos National Laboratory, Los Alamos, NM 87545, USA. ²University of Virginia, Charlottesville, VA 22904, USA. ³Rice University, Houston, TX 77251, USA. ⁴Birmingham-Southern College, Birmingham, AL 35254, USA. ⁵University of Iowa, Iowa City, IA 52242, USA. ⁶Southwest Research Institute, San Antonio, TX 78228, USA. ⁷University of Montana, Missoula, MT 59812, USA. ⁸Mullard Space Science Laboratory, University College London, Holmbury St. Mary, Dorking, Surrey RH5 6NT, UK. ⁹NASA Goddard Space Flight Center, Greenbelt, MD 20771, USA.

*To whom correspondence should be addressed. E-mail: rlt@lanl.gov

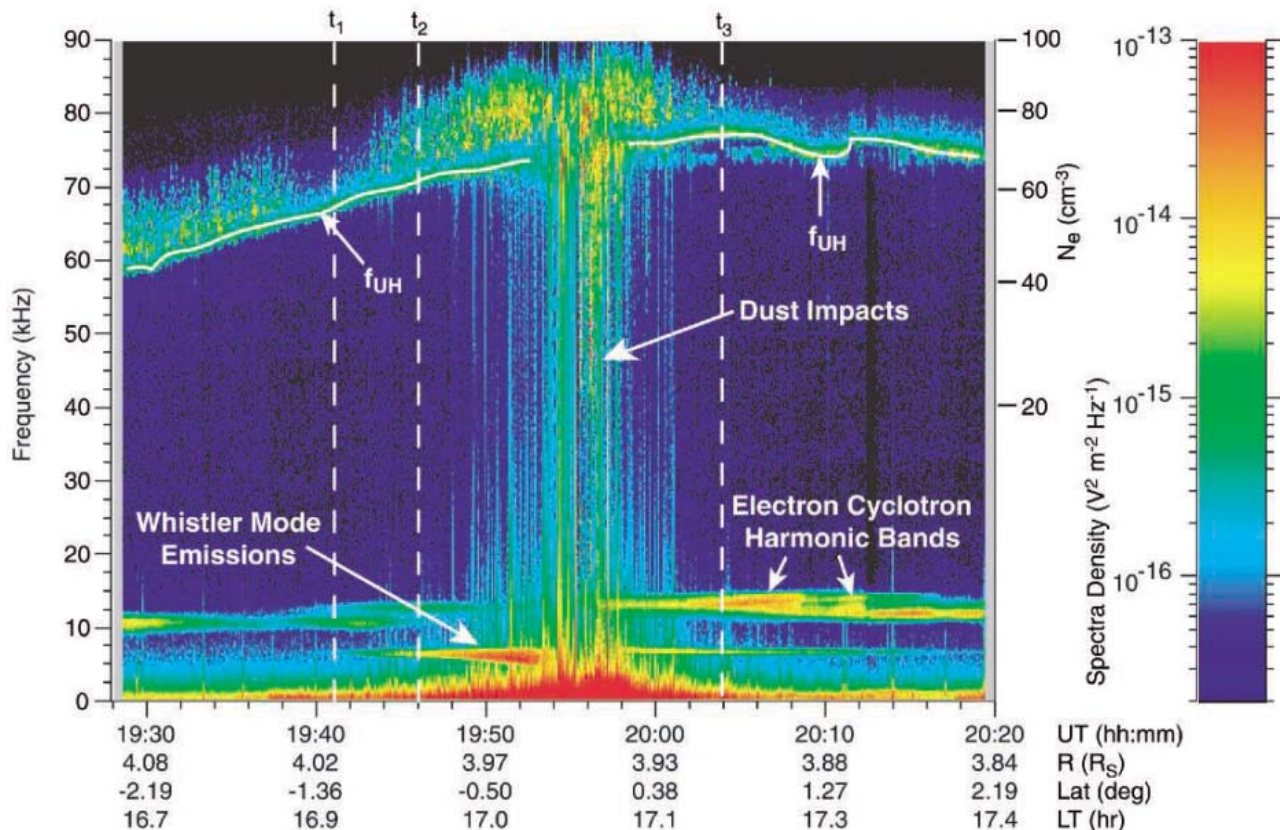


Fig. 2. Data from the Cassini RPWS instrument illustrating the electric field spectral density as a function of frequency and time on 14 July 2005. Upper hybrid, whistler mode, and electron cyclotron harmonic emissions are measured by RPWS, as is common in Saturn’s inner

magnetosphere. Closest approach to Enceladus occurs at 19:55 UT. The upper hybrid emission (f_{UH}) is a known function of the total electron density and magnetic field strength, yielding the electron density denoted in the upper right. LT is local time.

(4), with the penetrating radiation background removed (Fig. 3). Looking first at the electron counting rate as a function of energy and time, summed over the ELS field of view and uncorrected for spacecraft potential (Fig. 3A), two electron populations are visible: a “cold” (~2 to 3 eV) population with peak counts near A and a “hot” (~20 eV) population with peak counts near B. During the encounter with Enceladus, the spacecraft potential is less than the ELS minimum energy, making electron density and temperature extraction difficult. However, constraining the ELS data with the RPWS total electron density (Fig. 2), the spacecraft potential is ~-2 V, and the densities and the temperatures of cold and hot electron components are $N_c = 70.3 \text{ cm}^{-3}$ and $T_c = 1.35 \text{ eV}$ and $N_h = 0.2 \text{ cm}^{-3}$ and $T_h = 12.5 \text{ eV}$, respectively. During the time interval from 19:30 to 20:30 UT, N_c and T_c vary by ~40% and ~20% respectively.

Next we consider the IMS ion counting rate as a function of energy and time (Fig. 3B). Although enhanced ion flux is observed throughout the encounter, a slowing and deflection of the ion flow velocity is observed when CAPS viewing is favorable, before closest approach (between 19:41 and 19:46 UT) and also after closest approach (between 20:14 and 20:26 UT). The ion compo-

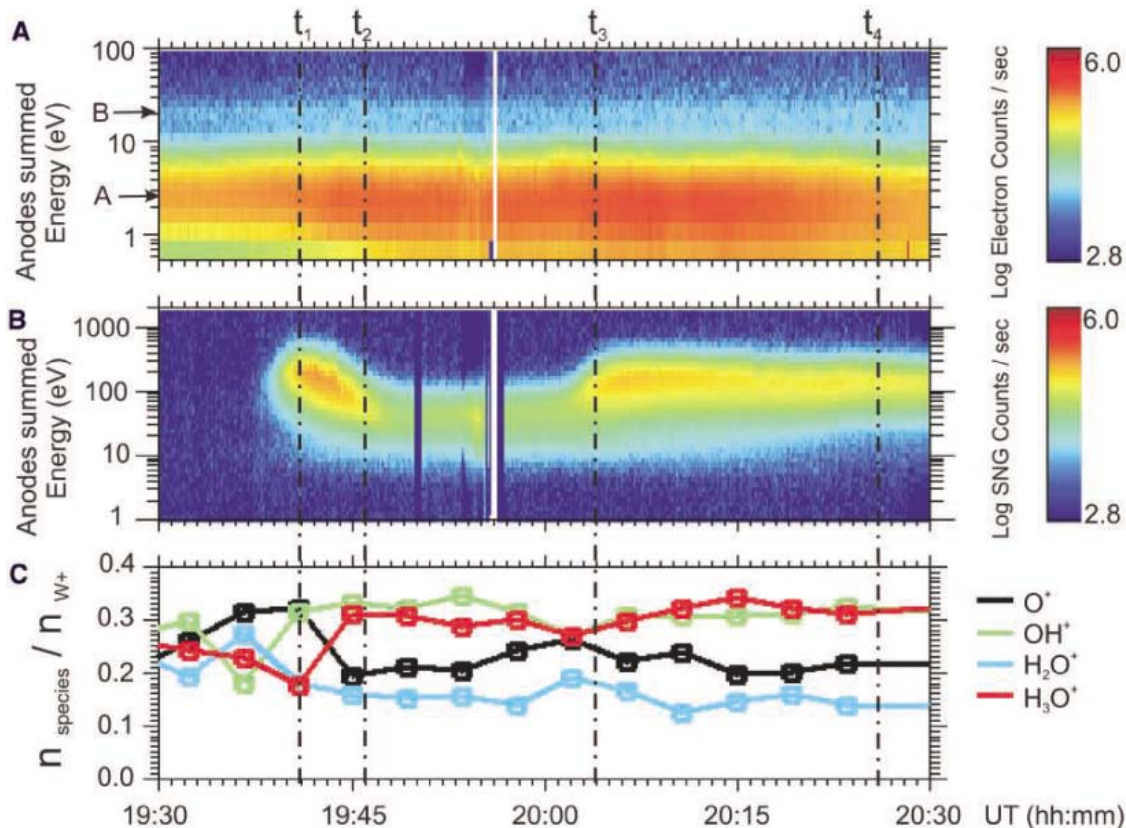
sition can be obtained by IMS time-of-flight techniques (Fig. 3C) throughout the encounter, with water group ions O^+ , OH^+ , H_2O^+ , and H_3O^+ detected.

To extract ion plasma moments, we used a forward model of IMS with the ions assumed to be O^+ and with phase space density a convected isotropic maxwellian. The free parameters in the model are ion temperature and two components of the ion flow velocity (radial and azimuthal). The ion temperature obtained from this procedure is ~35 eV away from Enceladus (at 19:41 and 20:26 UT) and decreases to ~15 eV closer to Enceladus (at 19:46 UT). The temperature away from Enceladus is consistent with previous CAPS results (7); the temperature further in is a rough estimate given the assumption of a single ion component (O^+) with isotropic phase space density. The ion flow velocity is constrained to lie in Saturn’s equatorial plane, and the total ion density is constrained to equal the RPWS total electron density (Fig. 2). In Fig. 4, the ion flow velocity (red vectors) is plotted on the Cassini trajectory (Fig. 1B). Also shown for reference is the ion flow velocity for rigid corotation and model flow streamlines discussed below. The measured flow is slowed and deflected from the corotation direction at least 27 Enceladus radii (R_E ; $1 R_E = 252.1 \text{ km}$) from the

moon (at the start of the inbound segment), and at a distance of $57 R_E$ (near the end of the outbound segment) the flow is mostly in the azimuthal direction with a smaller radial component.

Although viewing was not optimum, IMS also provided a direct observation of water group ion pickup near closest approach to Enceladus via a distinctive ion velocity-space distribution. In ion pickup, a newborn ion has the velocity of its parent neutral, but by virtue of its acquired electrical charge it experiences the electric field associated with the magnetospheric plasma flowing relative to the neutral-gas reference frame. The ion is accelerated by this electric field and by the ambient magnetic field such that it subsequently executes a cycloidal motion, which may be described as a circular gyration about a magnetic field line that is moving with the plasma flow velocity. In velocity space, the pickup ions exhibit a characteristic signature: a ring-shaped peak in phase space density centered on the local bulk flow velocity and with a radius equal to the flow speed at the point of ionization (Fig. 5). The ions detected by IMS are consistent with the distribution expected for pickup into plasma, flowing at 17.5 km s^{-1} with respect to the neutrals and subsequently slowing to 14 km s^{-1} at the observation point. This is well below the relative corotation-

Fig. 3. Data from the CAPS on 14 July 2005. **(A)** Electron counting data from ELS. Cold and hot electron components are detected with peak counts near A and B. **(B)** Ion counting data from IMS, with the slowing of the ion flow evident between t_1 and t_2 . **(C)** Individual water group (O^+ , OH^+ , H_2O^+ , H_3O^+) ion densities divided by the total water group ion density, obtained from IMS time-of-flight measurements. The reduced χ^2 for the composition fits averages to 8.5 for O^+ , 33.9 for OH^+ , 8.1 for H_2O^+ , and 8.0 for H_3O^+ . Thus the confidence in the fits is very good for all ions except OH^+ , for which it is fair. The uncertainty in the fit is dominated by the choice of model function, not statistics. The $1-\sigma$ relative uncertainties in the densities run between 2 and 3%.



al speed at Enceladus of 26.4 km s^{-1} and more characteristic of the strongly slowed and deflected flow in the near vicinity of the satellite. This distribution indicates that the ion pickup rate increases substantially near Enceladus.

The initial quantitative interpretation of the plasma flow velocity deflections (Fig. 4) uses a modified version of an electrodynamics model originally developed for Jupiter's moon Io (8). Compared with Io, plasma deflection at Enceladus occurs much farther from the moon, indicating an extended neutral gas cloud with mass loading distributed over a large volume. The mass-loading rate is taken to be proportional to the neutral density (9), assumed in the model to vary as the inverse square of distance from Enceladus. The model solutions (indicated by the green flow contours in Fig. 4) are determined by the ratio of total mass-loading rate to the Pedersen conductance assumed for Saturn's ionosphere. The latter quantity is not well constrained observationally, but scaling from the case of Jupiter (10) suggests a value of ~ 0.1 to 1 S. If we adopt the lower value, the measured flow deflections roughly imply a total mass-loading rate of $\sim 3 \times 10^{27} \text{ H}_2\text{O/s}$ ($\sim 100 \text{ kg/s}$), comparable to the rate that has been independently estimated (2, 3) to be required to supply the remotely observed OH cloud. A larger conductance (11) would imply a correspondingly larger mass-loading rate.

The RPWS data (Fig. 2) do not indicate a substantial increase in plasma density near

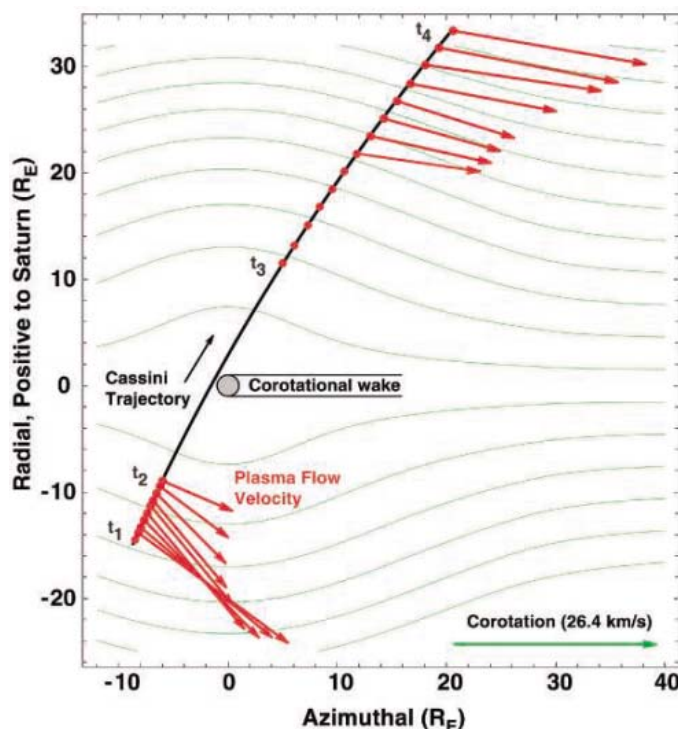
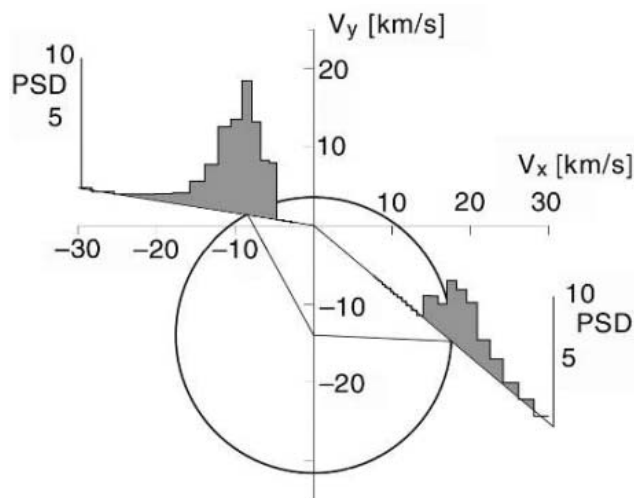


Fig. 4. Plot of the Cassini trajectory and ion flow velocities obtained from IMS (Fig. 3). IMS viewing in the radial direction is poor for about 10 min after t_3 . The plasma flow is slowed and deflected over a large volume extending more than $30 R_E$ from Enceladus. Model streamlines (green contours) indicate a total mass-loading rate of $\sim 100 \text{ kg s}^{-1}$ ($3 \times 10^{27} \text{ H}_2\text{O molecules s}^{-1}$) times $\Sigma/(0.1 \text{ S})$, where Σ is Saturn's ionospheric Pedersen conductance.

Enceladus, requiring that charge exchange be the dominant mass-loading process. Further support is obtained from the RPWS electron densities, ELS electron temperatures, and IMS ion flow speeds. These data indicate that the lifetime

of a water molecule to electron impact ionization near Enceladus is an order of magnitude larger than the charge exchange lifetime. In addition, the ultraviolet photoionization lifetime is two orders of magnitude larger than the charge exchange

Fig. 5. Ring velocity-space distribution observed by IMS near Enceladus. The plane of the figure represents a slice through the spacecraft-centered velocity-space distribution essentially perpendicular to the magnetic field and measured 114 s before closest approach (19:53:26 UT at 4.2 R_E). The V_x direction points toward Saturn and the V_y direction is in the azimuthal direction about Saturn, positive in the westward direction. Phase space density (PSD) is in units of $10^{-6} \text{ s}^3 \text{ m}^{-6}$. The circle shows the locus in velocity space that would be occupied



by ions that were picked up in a 17.5 km s^{-1} flow that is presently flowing at 14 km/s in the $-V_y$ direction relative to Cassini. The plots on the inclined baselines show the PSD in two different directions, at gyrophase angles of $\sim 165^\circ$ and $\sim -45^\circ$ relative to the V_x axis and at $\sim 110^\circ$ and 95° from the magnetic field direction. In both directions, the peaks in the PSD occur at a velocity consistent with the ring location as shown. This ring-type distribution constitutes direct evidence for ion pickup in the slower flows that characterize the near-Enceladus environment.

lifetime. Charge exchange is a process in which a fast ion captures an electron from a slow neutral in the vicinity of Enceladus. It produces, on average, a fast neutral and a slow ion. After such an interaction, the local ion density does not change, but the rotating fields pick up and accelerate the

ion, producing the observed mass loading. The charge exchange process described here produces an enormous expansion of the Enceladus cloud by creating the energetic neutrals (I_2) that are required to describe the large-scale OH cloud observed by the Hubble Space Telescope.

References and Notes

1. D. E. Shemansky *et al.*, *Nature* **363**, 329 (1993).
2. S. Jurac *et al.*, *Geophys. Res. Lett.* **29**, 2172 (2002).
3. J. D. Richardson, S. Jurac, *Geophys. Res. Lett.* **31**, 24803 (2004).
4. D. T. Young *et al.*, *Space Sci. Rev.* **114**, 1 (2004).
5. D. A. Gurnett *et al.*, *Space Sci. Rev.* **114**, 395 (2004).
6. M. K. Dougherty *et al.*, *Science* **311**, 1406 (2006).
7. E. C. Sittler *et al.*, *Geophys. Res. Lett.* **32**, L14507 (2005).
8. T. W. Hill, D. H. Pontius Jr., *J. Geophys. Res.* **103**, 19879 (1998).
9. J. H. Waite Jr. *et al.*, *Science* **311**, 1419 (2006).
10. D. F. Strobel, S. K. Atreya, in *Physics of the Jovian Magnetosphere*, A. J. Dessler, Ed. (Cambridge Univ. Press, New York, 1983), pp. 51–67.
11. L. E. Moore, M. Mendillo, I. C. F. Mueller-Wodarg, D. L. Murr, *Icarus* **172**, 503 (2004).
12. R. E. Johnson, M. Liu, E. C. Sittler Jr., *Geophys. Res. Lett.*, in press.
13. We wish to thank the large number of scientists and engineers on the CAPS and RPWS teams who made the results reported here possible, particularly L. K. Gilbert for help in the production of Fig. 3 and M. Dougherty of the Cassini magnetometer (MAG) team for graciously providing MAG data. The work at Los Alamos was performed under the auspices of the U.S. Department of Energy. The work of U.S. coauthors was supported by Jet Propulsion Laboratory contract 1243218 with Southwest Research Institute and contract 961152 with the University of Iowa. Work in the United Kingdom was supported by the Particle Physics and Astronomy Research Council. Cassini is managed by the Jet Propulsion Laboratory for NASA.

6 October 2005; accepted 21 November 2005
 10.1126/science.1121061

REPORT

Enceladus' Varying Imprint on the Magnetosphere of Saturn

G. H. Jones,^{1*} E. Roussos,¹ N. Krupp,¹ C. Paranicas,² J. Woch,¹ A. Lagg,¹ D. G. Mitchell,² S. M. Krimigis,² M. K. Dougherty³

The bombardment of Saturn's moon Enceladus by >20-kiloelectron volt magnetospheric particles causes particle flux depletions in regions magnetically connected to its orbit. Irrespective of magnetospheric activity, proton depletions are persistent, whereas electron depletions are quickly erased by magnetospheric processes. Observations of these signatures by Cassini's Magnetospheric Imaging Instrument allow remote monitoring of Enceladus' gas and dust environments. This reveals substantial outgassing variability at the moon and suggests increased dust concentrations at its Lagrange points. The characteristics of the particle depletions additionally provide key radial diffusion coefficients for energetic electrons and an independent measure of the inner magnetosphere's rotation velocity.

The importance of interactions between the Kronian magnetosphere and the Enceladus/E-ring system is becoming increasingly apparent. Saturn's inner magnetosphere is awash

with ionized components of water (I) that probably originate at the E-ring (2) and, as recently confirmed, ultimately at Enceladus itself (3, 4). This material substantially alters the inner Kronian magnetosphere, being analogous in several respects to the volcanic material from Io that shapes Jupiter's magnetosphere. Previous observations of the Enceladus-magnetosphere interaction region by Pioneer 11 and Voyager 2 (5), at 3.950 Saturn radii (R_S) from the planet (6), totaled four crossings of saturnian magnetic field lines that intersect Enceladus' orbit, i.e., the moon's L-shell.

During July 2004 to October 2005, Cassini performed 30 such L-shell crossings, providing a wealth of information on the magnetospheric effects of the moon and the E-ring core through the Low Energy Magnetospheric Measurement System (LEMMS) (7) of the Magnetospheric Imaging Instrument (MIMI). LEMMS uses semiconductor detectors to measure ion and electron fluxes in the energy ranges of 20 keV to 60 MeV and 20 keV to 5 MeV, respectively, usually at a 5.65-s resolution. As well as being ion sources, Enceladus and the E-ring are important sinks for saturnian radiation-belt particles. Brown and collaborators (8) consider the consequences of energetic-particle bombardment for the moon's surface chemistry. Here, we report expanded observations of the reciprocal processes: Enceladus' effect on the energetic-particle population and the remote sensing of substantial variability in its outgassing rate. The latter's changing effect on energetic particles may have important implications for the inferred age of the moon's radiation-weathered surface.

Within the radiation belts, low-energy magnetospheric plasma corotates almost rigidly with Saturn (I). Within the LEMMS energy range, gradient and curvature drifts are pronounced: Positive ions drift azimuthally in the sense of corotation, and electrons in the opposite direction. Low-energy electrons counterdrift slowly enough to maintain a net motion in the corotation direc-

¹Max Planck Institut für Sonnensystemforschung, Max-Planck-Str. 2, 37191 Katlenburg-Lindau, Germany. ²Applied Physics Laboratory, The Johns Hopkins University, 11100 Johns Hopkins Road, Laurel, MD 20723–6099, USA. ³The Blackett Laboratory, Imperial College London, London SW7 2BW, UK.

*To whom correspondence should be addressed. E-mail: jones@mps.mpg.de

tion. However, electrons above the 1.082-MeV resonant energy (9) drift rapidly enough to flow past Enceladus in the direction opposing the moon's motion (Fig. 1). When swept up by Enceladus, ions and low-energy electrons therefore form a wake downstream in the corotation flow, leading the moon's orbital motion, whereas electrons above the resonant energy form a wake upstream, trailing the orbital motion. At all energies, these wakes, termed microsignatures, continue drifting in the same L-shell and direction and at the same velocity as the predepletion plasma. Because microsignatures are primarily refilled by radial diffusion, their longevity mainly depends on the diffusion rate, with contributions to the signatures' erosion coming from other magnetospheric processes such as injection events, energy dispersion, and pitch-angle diffusion.

Electron microsignatures are expected to be sharp and deep near an electromagnetically inert moon, with radial extents equaling the moon's diameter. Radial diffusion should broaden and flatten these features with increasing longitudinal separation. High-energy electron signatures agree very well with this picture (Fig. 2). Low-energy microsignatures, however, vary considerably with distance from Enceladus, both in profile and depth; several processes could be responsible. Saturn's magnetic field drapes around the enceladian atmosphere (10). Low-energy electrons sensitive to magnetic field perturbations can be guided around the moon, evading absorption. This forms a narrower, less evacuated wake, possibly asymmetrical due to nonisotropic material outflow from Enceladus. Extended clouds of expelled ice particles and neutral gas would also obstruct electrons. Waves generated by the pickup of fresh ions originating at Enceladus and the E-ring would also increase pitch-angle diffusion rates considerably. We suggest that the electron signatures' breadth and variable depths signify changes on time scales of days or weeks in Enceladus' ionosphere, the E-ring itself, or the ring's neutral gas torus. This variability is consistent with other Cassini observations (11) and ground-based E-ring observations (12). Whatever the immediate reason for the signatures' changes, variability in the Enceladian vents is probably their ultimate cause.

No downstream electron microsignatures have been seen at separations greater than $\sim 80^\circ$, indicating large diffusion coefficients at these energies or considerable evasion of flux absorption through ionospheric flow deflection. Tethys microsignatures persist over greater longitude ranges (13, 14). One possible reason for this difference is the extensive Enceladus/E-ring neutral gas torus, which could diminish the relative depth of the moon's own microsignature through electron collisions with neutral species. No ion microsignatures were observed, which is explainable by their shallowness: 0.1- to 1-MeV ions have only a 13 to 18% probability of collision with Enceladus (15). Upstream energetic electron microsigna-

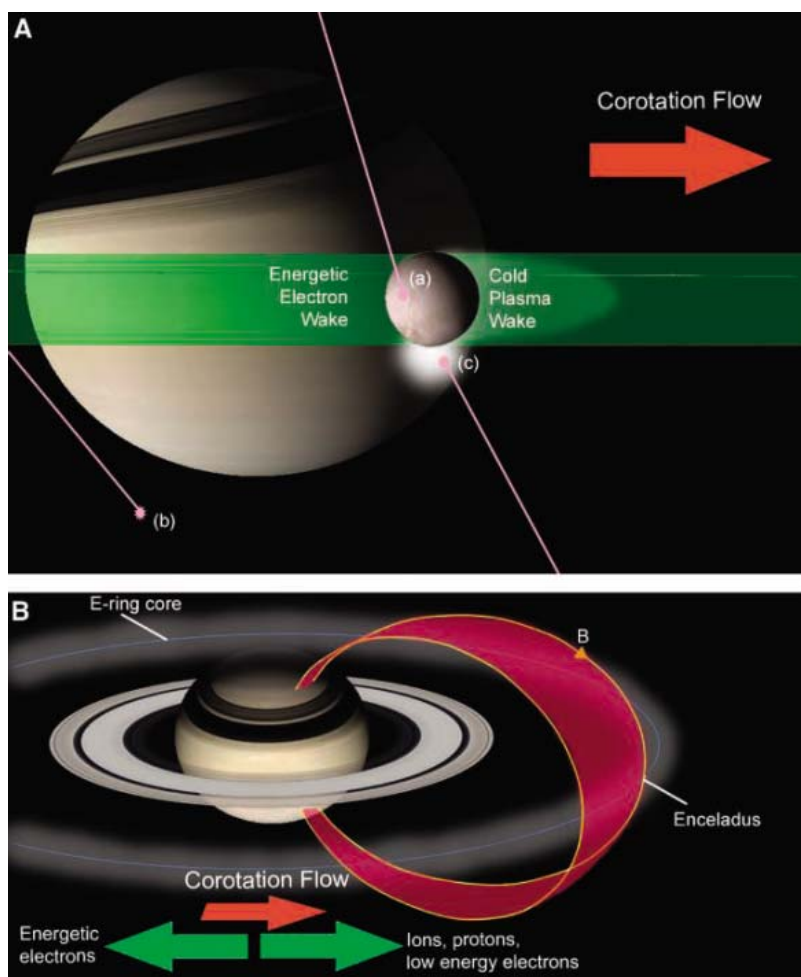


Fig. 1. An overview of the particle-moon interactions, looking toward Saturn at the orbit of Enceladus, and a broader view providing context. **(A)** High-energy particles can be lost from the magnetosphere through collisions with the moon's surface (a), with scattering E-ring dust particles (b), and with neutral gas originating at Enceladus or outgassed from E-ring particles (c). Because the corotating plasma's angular velocity (red arrow; 38.6 km s^{-1}) exceeds that of Enceladus (12 km s^{-1}), this material continuously overtakes the moon (27). **(B)** The bounce motion of trapped particles allows microsignature observations all along magnetic field lines that pass close to Enceladus. Displayed in red is a portion of the volume occupied by energetic electron microsignatures, upstream of the moon in the corotation flow.

tures, including those of the close flybys on days 48, 68, and 195 of 2005 (4), consistently behave as if Enceladus is insulating and atmosphere free. These electrons may have sufficient energy to penetrate the ionospheric obstacle.

Electrons above the resonant energy are therefore lost in a predictable, steady way, whereas outgassing levels apparently influence lower energy electron signatures. All the close flybys to date have been upstream of Enceladus; an appraisal of the atmosphere's influence on the structure of low-energy electron wakes requires future close downstream passes.

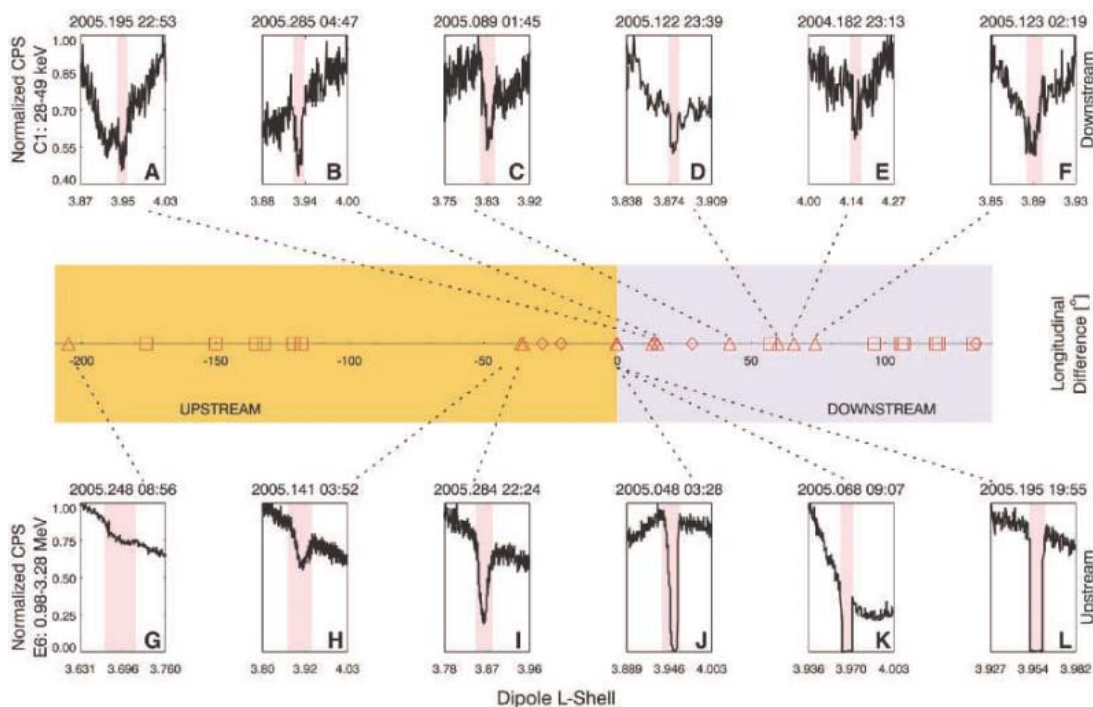
The close-flyby data (Fig. 3), combined with observations of numerous upstream microsignatures, offer a resource to calculate energetic electron radial diffusion coefficients, D_{LL} (16). LEMMS data reveal a narrow energy range (Fig.

3C) within the microsignature where the flux transitions from $\sim 20\%$ of the surrounding value to near zero. The latter region is the actual energetic electron wake, and the partial decrease marks a reduction in penetrating radiation, i.e., background flux (13). The transition therefore denotes the electron resonant energy, which we find to be $0.75 \pm 0.03 \text{ MeV}$ for 90° pitch angles; the value for rigid corotation is 1.082 MeV.

The resonant energy yields, through a previously unused technique (17), a cold plasma corotation angular velocity, Ω (18), of $(1.39 \pm 0.03) \times 10^{-4} \text{ rad s}^{-1}$. This is $85 \pm 2\%$ of the planetary rotation angular velocity (19), the difference almost undoubtedly being due to mass loading of the magnetosphere by ionized neutral gas. The inferred corotation frequency agrees with theory (20), Voyager studies (21), and other

CASSINI AT ENCELADUS

Fig. 2. Electron micros-signatures of Enceladus (in normalized counts per second, CPS) observed during Cassini's first 14 months at Saturn. (A to F) Low-energy micros-signatures, downstream of Enceladus in the corotational flow. (G to L) Upstream micros-signatures, above the resonant energy, with (J) to (L) showing the three close flybys. The center panel shows each event's longitudinal separation from Enceladus. Triangles denote observed micros-signatures, diamonds show crossings where data gaps or spacecraft rotations preclude interpretation, and squares denote periods during which no micros-signature was observed in the available data. In the latter cases, a micros-signature may possibly have been present but could not be observed due to inappropriate LEMMS pitch-angle coverage. The



depths and radial extents of downstream micros-signatures are not in accord with their longitudinal separations. Several micros-signatures, e.g., (A), are flanked by a broad flux decrease. (A), which has the broadest observed width (~16,000 km), was observed when Enceladus was definitely outgassing (3). The lack of identified micros-signatures

between (G) and (H) is probably due to the low fluxes involved; magnetospheric perturbations can easily mask such weak signatures. All events except (E) were located closer to Saturn than expected. This inward electron drift is consistent with flow diversion within a magnetic pileup region (28).

Cassini results (22). Using this Ω value and the method of (23) yields $D_{LL} = (2.0 \pm 0.5) \times 10^{-8} R_S^2 s^{-1}$ for energies of 0.98 to 3.28 MeV. This value is fully consistent, at least in radial extent, with the signature observed by Voyager 2 when 20° upstream of Enceladus (5) and is equivalent to a 1.5-MeV wake refilling in 14.5 to 15.5 hours.

The above method only sets an upper D_{LL} limit for low-energy electrons, because Enceladus and the E-ring are a complex combined obstacle for these particles, with large variations in profiles responding to changes at both the moon and ring. Using the cleanest signatures (Fig. 2, B and C), we find this upper limit to be $(9.0 \pm 0.2) \times 10^{-9} R_S^2 s^{-1}$. The locations of these signatures suggest a maximum observed wake lifetime of ~5 hours for 20- to 100-keV electrons. If radial diffusion alone refilled these signatures, they should survive for ~16 to 20 hours. Another process, probably ion pickup-related pitch-angle diffusion, therefore increases the refilling rate.

Enceladus' micros-signatures are time- and longitude-dependent. The moon's longitude- and time-averaged effects on particles' radial distribution, termed macrosignatures, are also detected. Flux decreases in >13-MeV ions near Enceladus' L-shell are observed equally well all around the moon's orbit (Fig. 4). The macrosignature's radial breadth initially suggests that an obstacle more extended than Enceladus is presented to the high-energy protons; ring material is an established

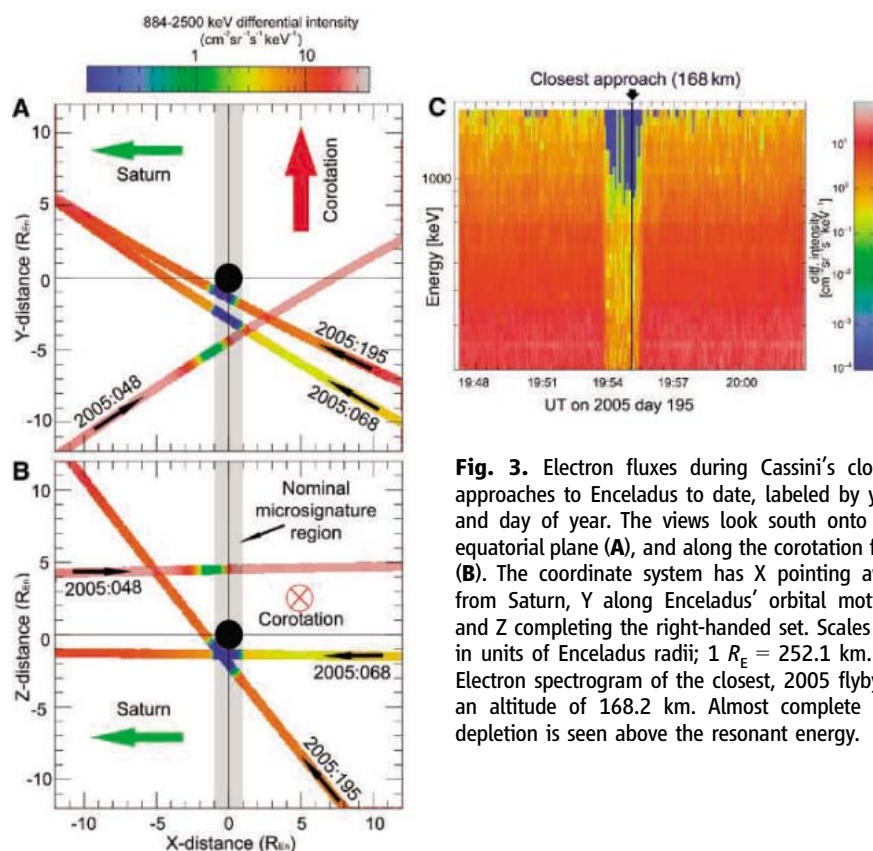


Fig. 3. Electron fluxes during Cassini's closest approaches to Enceladus to date, labeled by year and day of year. The views look south onto the equatorial plane (A), and along the corotation flow (B). The coordinate system has X pointing away from Saturn, Y along Enceladus' orbital motion, and Z completing the right-handed set. Scales are in units of Enceladus radii; $1 R_E = 252.1$ km. (C) Electron spectrogram of the closest, 2005 flyby at an altitude of 168.2 km. Almost complete flux depletion is seen above the resonant energy.

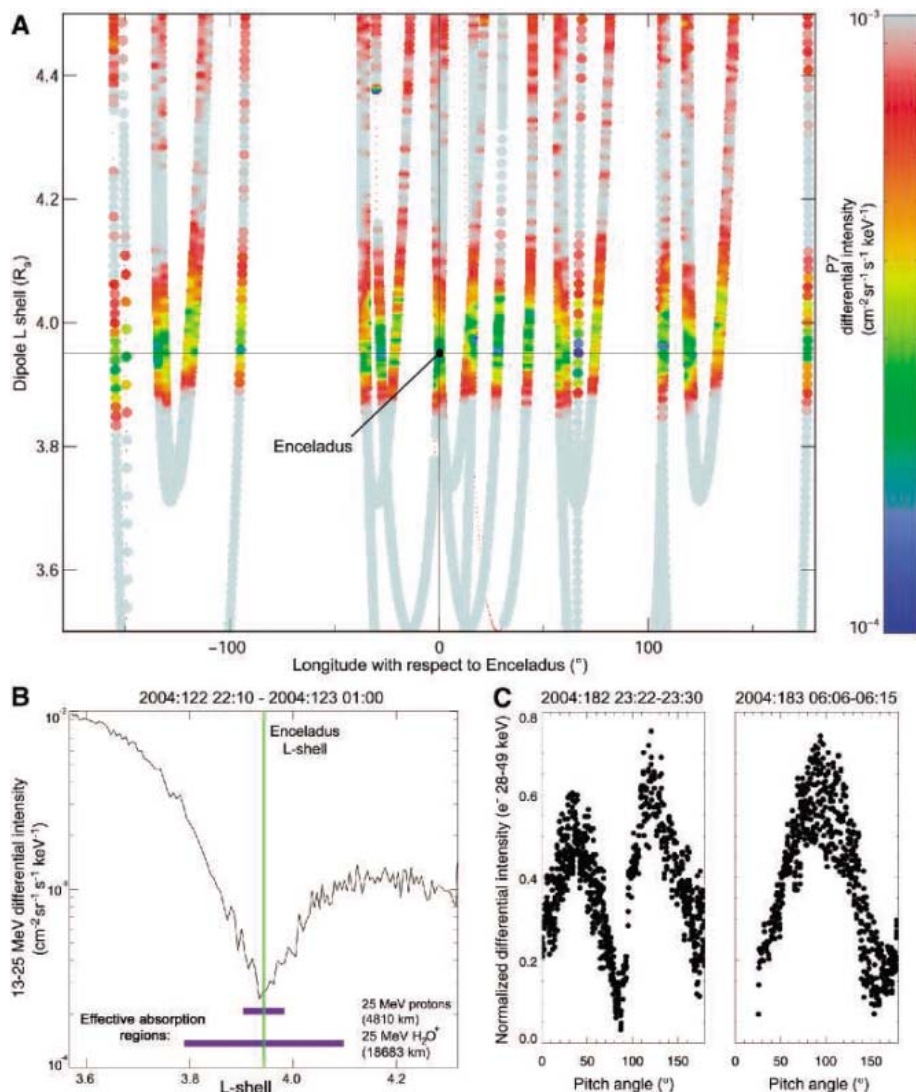


Fig. 4. High-energy proton macrosignatures and the E-ring's variable effects on electron pitch-angle distributions. **(A)** MIMI proton fluxes (13 to 25 MeV) on crossing Enceladus' L-shell, mapped onto the equatorial plane. The trajectories are plotted in a frame rotating about Saturn with Enceladus. **(B)** A typical energetic proton macrosignature profile, covering a radial distance of $\sim 0.7 R_S$. The edge-to-edge effective absorption region equals the satellite diameter plus four ion gyroradii. This region is shown for 25-MeV protons and H_2O^+ ions (blue bars). **(C)** Smoothed low-energy electron pitch-angle distributions at 66.0° ahead of and 150.8° behind Enceladus.

sink for energetic particles [e.g., (24)]. However, it should be noted that at these energies, the ions' large gyroradii may, at least partially, be responsible for the wide macrosignatures, i.e., particles whose guiding centers of gyration pass far from Enceladus can still strike the moon. For a macrosignature to be as persistently deep as observed all around Enceladus' orbit, the proton wakes' refilling rate must be slower than the particles' rate of reencounter with the moon. Because ion gradient and curvature drifts are in the corotation direction, moon revisit periods are ~ 1 hour for 10-MeV protons and ~ 16 hours for the cold plasma, explaining why no low-energy ion macrosignature is observed.

Larger E-ring particles may concentrate near the stable Lagrange points, 60° in longitude from Enceladus. Before Saturn orbit insertion, Cassini crossed Enceladus' L-shell at 66.0° from the moon (Fig. 4C) and observed an electron pitch-angle distribution consistent with particle absorption by dust and/or by neutral gas originating at the dust, as predicted (25). The L-shell was recrossed a few hours later at 150.8° behind the moon, but showed no 90° pitch-angle depletion. Confinement of the Lagrange point depletion to a narrow pitch-angle range suggests that it was primarily caused by dust, not by Enceladus itself. This great variation in particle behavior suggests that the density number of E-ring dust at Enceladus' orbit

varies azimuthally. The Lagrange points may be particularly dense regions (26). The large variability in the downstream electron microsignatures suggests that dust may play a major role in their formation. Indeed, their profiles suggest that they decay within a few tens of degrees; Voyager 2 saw no microsignature when only 30° downstream (5). E-ring dust and the associated gas torus may occasionally sustain and enhance the microsignature profiles by decreasing the electron diffusion rates and providing additional sinks for the electrons that remain in the moon's wake.

References and Notes

1. S. M. Krimigis *et al.*, *Science* **307**, 1270 (2005).
2. S. Jurac, R. E. Johnson, J. D. Richardson, *Icarus* **149**, 384 (2001).
3. F. Spahn *et al.*, *Science* **311**, 1416 (2006).
4. J. R. Spencer *et al.*, *Science* **311**, 1401 (2006).
5. J. F. Carbary, S. M. Krimigis, W.-H. Ip, *J. Geophys. Res.* **88**, A11, 8947 (1983).
6. $1 R_S = 60,268$ km.
7. S. M. Krimigis *et al.*, *Space Sci. Rev.* **114**, 233 (2004).
8. R. H. Brown *et al.*, *Science* **311**, 1425 (2006).
9. M. F. Thomsen, J. A. Van Allen, *J. Geophys. Res.* **85**, A11, 5831 (1980).
10. M. K. Dougherty *et al.*, *Science* **311**, 1406 (2006).
11. L. W. Esposito *et al.*, *Science* **307**, 1251 (2005).
12. C. Roddier, F. Roddier, J. E. Graves, M. J. Northcott, *Icarus* **136**, 50 (1998).
13. C. Paranicas *et al.*, *Geophys. Res. Lett.* **32**, L21011 (2005).
14. E. Roussos *et al.*, *Geophys. Res. Lett.* **32**, L24107 (2005).
15. C. Paranicas, A. F. Cheng, *Icarus* **125**, 380 (1997).
16. The rate at which magnetospheric particles diffuse radially is parameterized by the coefficient D_{\perp} . The latter's value was estimated by fitting a one-dimensional diffusion equation (23) to the LEMMS observations.
17. At the resonant energy, the moon's Keplerian orbital frequency equals the sum of the energetic particles' frequencies of corotation, gradient, and curvature drifts. The corotation frequency can be derived by substituting all the other, known values.
18. Ω is the angular velocity of the cold plasma that revolves around Saturn approximately in step with the planet's rotation (9). $\Omega = 1.637 \times 10^{-4}$ rad s^{-1} for rigid corotation with Saturn.
19. D. A. Gurnett *et al.*, *Science* **307**, 1255 (2005).
20. J. Saur, B. H. Mauk, A. Kabiner, F. M. Neubauer, *J. Geophys. Res.* **109**, A05217 (2004).
21. H. S. Bridge *et al.*, *Science* **212**, 217 (1981).
22. B. H. Mauk *et al.*, *Geophys. Res. Lett.* **32**, L14505 (2005).
23. J. A. Van Allen, M. F. Thomsen, B. A. Randall, *J. Geophys. Res.* **85**, 5709 (1980).
24. J. A. Van Allen, *J. Geophys. Res.* **88**, A9, 6911 (1983).
25. M. F. Thomsen, J. A. Van Allen, *Geophys. Res. Lett.* **6**, 11, 893 (1979).
26. We note that similar 90° pitch-angle depletions are sometimes observed at Tethys's orbit (14).
27. R. L. Tokar *et al.*, *Science* **311**, 1409 (2006).
28. C. Paranicas, R. W. McEntire, A. F. Cheng, A. Lagg, D. J. Williams, *J. Geophys. Res.* **105**, A7, 16005 (1999).
29. We thank M. Kusterer (The Johns Hopkins University Applied Physics Laboratory, JHUAPL), N. Achilleos, and S. Kellogg (Imperial College London) for data reduction. MIMI/LEMMS was in part financed by the German Bundesministerium für Bildung und Forschung through the German Aerospace Center (DLR) under contract 50 OH 0103 and by the Max Planck Gesellschaft. The work at JHUAPL was supported by NASA under contract NAS5-97271 with The Johns Hopkins University.

5 October 2005; accepted 5 January 2006
10.1126/science.1121101

REPORT

Cassini Dust Measurements at Enceladus and Implications for the Origin of the E Ring

Frank Spahn,¹ Jürgen Schmidt,^{1*} Nicole Albers,¹ Marcel Hörning,¹ Martin Makuch,¹ Martin Seiß,¹ Sascha Kempf,² Ralf Srama,² Valeri Dikarev,^{2,3} Stefan Helfert,² Georg Moragas-Klostermeyer,² Alexander V. Krivov,³ Miodrag Sremčević,⁵ Anthony J. Tuzzolino,⁶ Thanasis Economou,⁶ Eberhard Grün^{2,4}

During Cassini's close flyby of Enceladus on 14 July 2005, the High Rate Detector of the Cosmic Dust Analyzer registered micron-sized dust particles enveloping this satellite. The dust impact rate peaked about 1 minute before the closest approach of the spacecraft to the moon. This asymmetric signature is consistent with a locally enhanced dust production in the south polar region of Enceladus. Other Cassini experiments revealed evidence for geophysical activities near Enceladus' south pole: a high surface temperature and a release of water gas. Production or release of dust particles related to these processes may provide the dominant source of Saturn's E ring.

The tenuous E ring is the outermost and largest ring in the saturnian system, consisting of particles with a peak size between 0.3 and 3 μm (1). The highest density of the E ring and its smallest vertical extent are both observed close to the orbit of Enceladus (1, 2), which favors this moon as the main source of that faint ring. In situ dust measurements at Enceladus with the dust detector aboard the Cassini spacecraft offer the unique opportunity to learn about this satellite and about dust-production processes at its surface and, ultimately, to shed light on the origin of the E ring.

We report on measurements carried out with the High Rate Detector (HRD) of the Cosmic Dust Analyzer (CDA) during the flyby of Enceladus on 14 July 2005. The detector consists of two thin (28 μm and 6 μm) polyvinylidene fluoride sensors with cross sections of 50 cm^2 and 10 cm^2 (3). Here, we focus on the data collected by the 50- cm^2 sensor, which is sensitive for particles with a radius larger than 2 μm . An impacting hypervelocity grain changes the polarization in the sensor volume, resulting in a short, sharp pulse enabling the detector to register up to 10^4 dust impacts s^{-1} (4).

During the flyby, a significant increase in the count rate of dust particles was recorded about 10 min before to about 10 min after the

closest approach of the spacecraft to the moon (Fig. 1). The peak count rate was 4 particles s^{-1} at 1 min before the closest approach. Similarly, the Cassini Ion and Neutral Mass Spectrometer (INMS) (5) detected water gas, also at a peak rate before the closest approach, albeit with a somewhat smaller offset of 30 s. This gas plume was also seen by the Ultraviolet Imaging Spectrograph (UVIS) (6) and, indirectly at an earlier flyby, by the magnetometer (7). The time difference between the rate peaks points to a decoupling of gas and dust shortly after both components are released from the satellite surface (8). A gas and dust source near the south pole is compatible with these premature maxima of the rates, because the spacecraft approached the moon from the south and came closest to Enceladus at a latitude of $\sim 25^\circ\text{S}$ [figure 1 of (5, 9)]. In contrast, a dust cloud generated by micrometeoroid impacts, as was observed by the Galileo mission around the jovian moons (10), would lead to a peak rate directly at the closest approach.

The observed particle count rate constrains the production rate of particles at Enceladus, while the time offset of its maximum from the closest approach can be used to locate those regions on the moon's surface from which the particles originate. Comparing the data to theoretical models of dust production, we can estimate the relative contributions of alternative mechanisms of particle creation, yielding implications for the dominant source of the E-ring particles. Besides geophysical processes (11, 12), micrometeoroid bombardment has been proposed as a particle-creation process (13). Two families of micrometeoroids are relevant at Enceladus, namely E-ring particles and in-

terplanetary dust particles. The typically large velocities of such projectiles relative to the moon, from a few to tens of kilometers per second, make the impacts energetic enough to abundantly produce ejecta at the moon's surface and create a dust cloud (10, 14). However, the detection of an anomalously high temperature (9) in the south polar region of Enceladus near elongated cracked fractures (15) (dubbed "tiger stripes") lends new support to the idea of E-ring dust particles created by cryovolcanism (ice volcanoes).

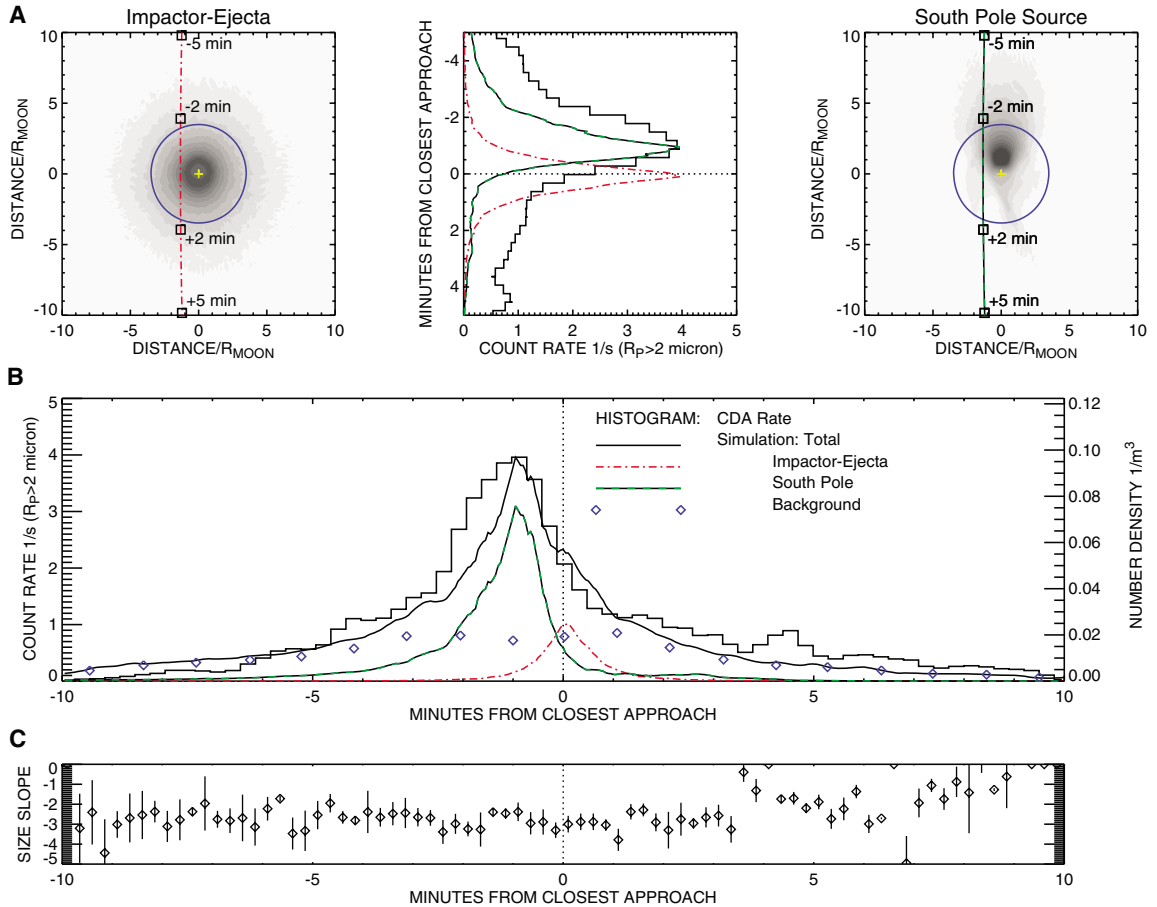
We have modeled the distributions of dust in the vicinity of Enceladus for cases of isotropic ejection of grains from the entire surface and for a localized dust source at the south pole of the moon (Fig. 1). These two cases correspond to the particle production by the impactor-ejecta mechanism and by geological processes at the south pole, respectively. Because the spacecraft's trajectory near the closest approach (168.2 km above the surface) lies well inside the Hill sphere (16) of gravitational influence of the moon [$r_h \sim 948$ km, compared with a radius of 252.1 km (15)], an analytical model for the dust cloud developed in (17), based on the two-body approximation, should give an adequate estimate (18). However, to account for the full three-body dynamics near the Hill scale, we have numerically simulated the dust configuration around the satellite for both source models. In the simulations, particle paths are integrated subject to Saturn's and Enceladus' gravity (18, 19). In both simulations, 1 million particles are launched from the satellite's surface, with starting conditions that are plausible for particles created in an impactor-ejecta process (20, 21). To simulate the impactor-ejecta source, the starting positions are chosen uniformly over the entire surface of the moon. The localized source is simulated with starting positions distributed uniformly in a circular area of an angular diameter of 30° centered at the south pole, which is on the order of the size of the hot region (9). The motion of the particles governed by the gravity of the planet and the satellite does not depend on the particles' mass or radius; thus, grains with different radii need not be distinguished in the simulations. Therefore, the size distribution in the model dust cloud near the moon derives from the particle size distribution assumed for the particle-creation process.

In the simulations, the impactor-ejecta process is found to generate a highly symmetric dust configuration in the vicinity of the satellite, as expected, so that the HRD on a flyby through this cloud would observe a maximal count rate directly at the closest approach (Fig. 1A). In contrast, the simulated dust ejection from the south pole source reproduces well the observed maximal count rate 1 min before the closest approach.

¹Institut für Physik, Universität Potsdam, Am Neuen Palais 10, Haus 19, D-14469 Potsdam, Germany. ²Max Planck Institut für Kernphysik, Saupfercheckweg 1, 69117 Heidelberg, Germany. ³Astrophysikalisches Institut, Friedrich Schiller Universität, 07745 Jena, Germany. ⁴Hawaii Institute of Geophysics and Planetology, University of Hawaii, Honolulu, HI 96822, USA. ⁵Laboratory for Atmospheric and Space Physics, University of Colorado, Boulder, CO 80303, USA. ⁶Laboratory for Astrophysics and Space Research, University of Chicago, Chicago, IL 60637, USA.

*Corresponding author: jschmidt@agnld.uni-potsdam.de

Fig. 1. Comparison of the CDA data to simulations. **(A)** Particle density in the plane of Cassini's trajectory estimated from simulations, darker shades referring to a higher density. The impactor-ejecta process (left) leads to a more symmetric dust cloud, whereas a localized source at the south pole of the moon (right) shows a strong asymmetry. Circles denote the intersection of the plane with the Hill sphere of gravitational influence, and the normal projection of the moon's center (not in that plane) is marked by a cross symbol. Cassini's trajectory is plotted as a dash-dotted or dashed line, respectively. The central plot shows the count rates predicted by the simulations computed along the actual spacecraft trajectory, both normalized to the peak rate of the data shown in histogram mode. **(B)** The sum of the rates derived from the two simulations and the simulated E-ring background, normalized to the observed peak rate. The maximal strength of the impactor-ejecta process relative to that of the south pole source is chosen in a way that no secondary peak develops in the combined rate near the closest approach. **(C)** The slopes of the differential size distribution $n(R_p) \propto R_p^\alpha$ versus time to the closest approach. The increase of α for $t > 4$ min is due to a maneuver of Cassini and the related change in the instrument's boresight.



Fitting combinations of both contributions with a consistent E-ring particle background to the data, and requiring that no second peak develops in the rate at the closest approach, we can estimate the maximal strength of the impactor-ejecta dust creation at Enceladus relative to that of the south pole source (Fig. 1B). From this fit (HRD data for $R_p > 2 \mu\text{m}$), we can infer the rate of particles larger than $2 \mu\text{m}$ emitted by the south pole source and escaping the moon's gravity to amount to 5×10^{12} particles s^{-1} , whereas the impactor-ejecta mechanism would produce at most 10^{12} such particles s^{-1} . These numbers correspond to an escaping mass of at least 0.2 kg s^{-1} , assuming $R_p = 2 \mu\text{m}$ for all grains. For an extended size distribution, this rate may extend to kilograms per second. The E-ring particle background, which is naturally contained in the HRD data, has been simulated, following the motion of particles subject to gravity and perturbation forces (18, 19), until they are lost in collisions with Enceladus, other E-ring moons, or the main rings. A self-consistent combination of the simulated dust populations is in reasonable agreement with the observed HRD rate (Fig. 1B).

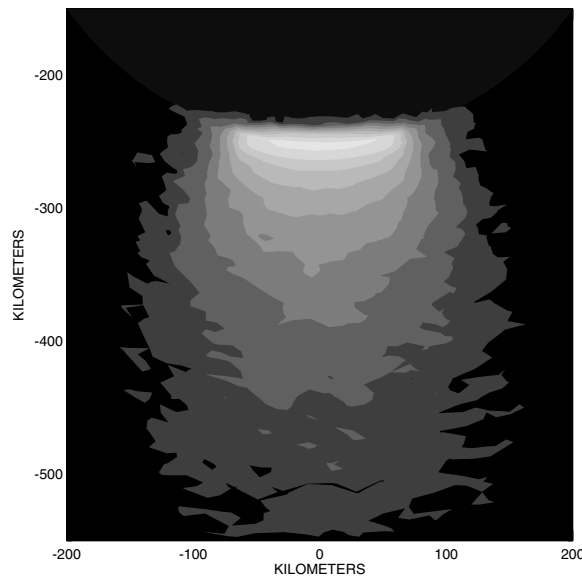


Fig. 2. Side view of a simulated dust plume at Enceladus' south pole. Contours of equal column particle density are shown in a Cartesian frame fixed at the center of the moon. The brightest contour denotes 10^7 particles per m^2 , the column density dropping by one-half from level to level.

A differential particle size distribution inferred from the data of both HRD sensors fits to a power law $n(R_p) \propto R_p^\alpha$ with a slope $\alpha \sim -3$ that remains almost constant during the flyby (Fig. 1C). This near constance of the exponent indicates that the dynamics of larger grains is

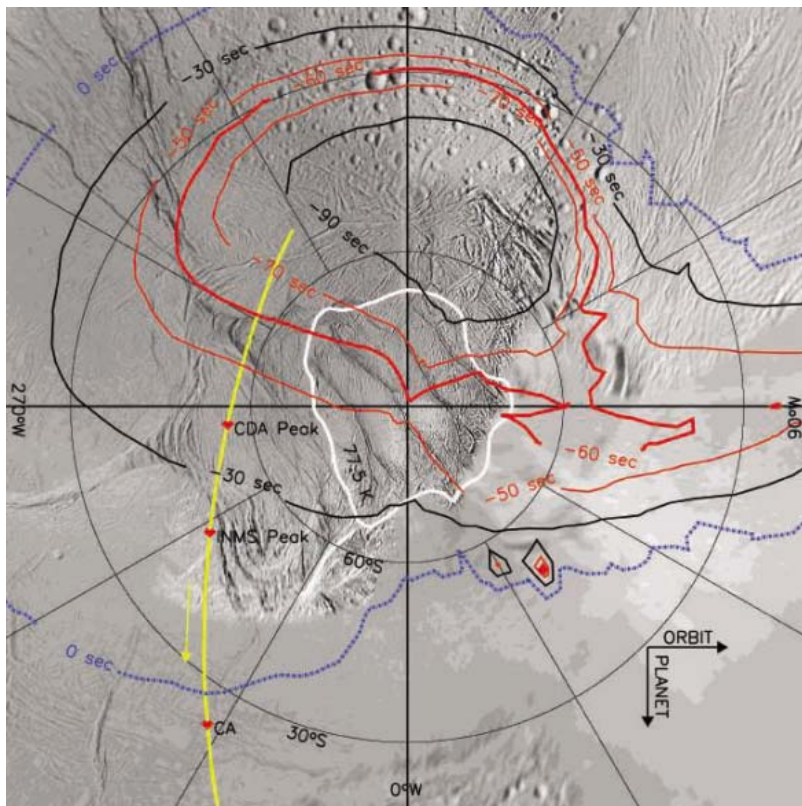


Fig. 3. Results of a series of simulations where the position of the source is varied systematically over the moon's surface. For each simulation, the particle count rate along the Cassini trajectory is computed. The contours of equal time offsets of the maximal count rate from the closest approach are plotted over a base map of Enceladus' south pole (15). The thick red line marks the contour of a -60-s offset of the maximal count rate, which was about the value observed by the CDA. Other contours correspond to offsets of -90, -70, -50, -30, and 0 s. The white line around the pole denotes the 77.5-K isotherm from the Composite Infrared Spectrometer (9). Cassini's ground track is shown in yellow, and the times of rate maxima of the CDA (-50 s) and INMS (-30 s) (5), as well as the closest approach (CA), are marked.

dominated by gravity. Such a power law is expected for an impactor-ejecta particle formation scenario (20). On the other hand, we showed that the south pole source should be the dominant source of particles. A possible explanation would be that the particles are formed in meteoroid impacts and lifted by south polar gas venting. However, an effective acceleration of grains in the gas plume seems implausible for the gas densities inferred from UVIS (6, 15).

A side view of the dust configuration from the simulation of the south pole source is shown in Fig. 2, where the absolute numbers are fixed by HRD data at the closest approach. A similarly strong stratification of the dust density is evident in images of the dust plume (15). In the simulation, the stratification results basically from the power-law distribution of particle starting velocities (21).

To investigate the influence of the particle source location on the rate profile measured by HRD, we performed a series of about 2600 simulations, where the source position was systematically varied over the moon's surface.

Here, we used 50,000 particles per simulation, employing for simplicity the initial conditions for the impactor-ejecta mechanism (20). For each source, we determined the time offset of the peak count rate to the closest approach for this flyby. In this way, we obtained a contour map of offset times over the moon's surface, which is plotted over an Image Science Subsystem base map (15) of the geologically active south pole region in Fig. 3. It was found that only a small part of the total surface of Enceladus can have sources that would match the actually observed offset of -1 min. Interestingly, the region of the tiger stripes (covering latitudes > 70°S) is indeed compatible with the data, yielding offsets from -50 to -70 s.

On the basis of simulations of the dust environment around Enceladus, we conclude that the Cassini CDA data of the Enceladus flyby on 14 July are compatible with a dust source in the south polar region of the moon. A particle ejection mechanism caused by hypervelocity micrometeoroid impacts alone cannot explain the data. New in situ measurements of Enceladus' dust

cloud will be obtained during a flyby in 2008 at an altitude of only 100 km over 69°N.

References and Notes

1. P. D. Nicholson *et al.*, *Science* **272**, 509 (1996).
2. M. R. Showalter, J. N. Cuzzi, S. M. Larson, *Icarus* **94**, 451 (1991).
3. R. Srama *et al.*, *Space Sci. Rev.* **114**, 465 (2004).
4. This property of the HRD becomes crucial in regions of high particle density (parts of the E ring and in the vicinity of its source satellites) where the impact ionization detector of the CDA is saturated.
5. J. H. Waite Jr. *et al.*, *Science* **311**, 1419 (2006).
6. C. J. Hansen *et al.*, *Science* **311**, 1422 (2006).
7. M. K. Dougherty *et al.*, *Science* **311**, 1406 (2006).
8. Early decoupling of gas and dust is in accordance with the reported low gas densities [Knudsen regime (5)] found in the gas plume (6), making molecule-dust collisions unlikely during the time (tens of minutes) from ejection to the impact of the grain at the HRD.
9. J. R. Spencer *et al.*, *Science* **311**, 1401 (2006).
10. H. Krüger, A. V. Krivov, D. P. Hamilton, E. Grün, *Nature* **399**, 558 (1999).
11. P. K. Haff, G. L. Siscoe, A. Eviatar, *Icarus* **56**, 426 (1983).
12. J. S. Kargel, S. Pozio, *Icarus* **119**, 385 (1996).
13. J. E. Colwell, *Icarus* **106**, 536 (1993).
14. M. Sremčević, A. V. Krivov, H. Krüger, F. Spahn, *Planet. Space Sci.* **53**, 625 (2005).
15. C. C. Porco *et al.*, *Science* **311**, 1393 (2006).
16. Within the Hill sphere, the satellite's gravity dominates Saturn's gravity. The Hill radius is defined in terms of the masses of Saturn M_s and Enceladus M_e , and of the distance a_e between them, as $r_h = a_e^3 \sqrt{M_e/3(M_s + M_e)}$.
17. M. Sremčević, A. V. Krivov, F. Spahn, *Planet. Space Sci.* **51**, 455 (2003).
18. Materials and methods are available as supporting material on Science Online.
19. Perturbation forces (Saturn's oblateness, Lorentz force, and radiative forces) are crucial for the long-term dynamics of the particle and the configuration of the E ring (22-26). They can be neglected for the simulation of dust in the vicinity of Enceladus.
20. A. V. Krivov, M. Sremčević, F. Spahn, V. V. Dikarev, K. V. Kholshevnikov, *Planet. Space Sci.* **51**, 251 (2003).
21. Initial velocities follow a cumulative power law $N(>v) \propto v^{-2}$, $0.15 v_{esc} < v < 2 v_{esc}$, where $v_{esc} \sim 239 \text{ m s}^{-1}$ is Enceladus' escape velocity. Starting directions are uniformly distributed in a cone of semi-opening angle of 25° normal to the surface at the starting location.
22. M. Horányi, J. A. Burns, D. P. Hamilton, *Icarus* **97**, 248 (1992).
23. D. P. Hamilton, J. A. Burns, *Science* **264**, 550 (1994).
24. V. V. Dikarev, *Astron. Astrophys.* **346**, 1011 (1999).
25. F. Spahn, K.-U. Thiesenshusen, J. Colwell, R. Srama, E. Grün, *J. Geophys. Res.* **104**, 24111 (1999).
26. A. Juhász, M. Horányi, *Geophys. Res. Lett.* **31**, 19703 (2004).
27. We thank T. V. Johnson for comments on the manuscript. The Potsdam group was supported by Deutsche Forschungsgemeinschaft grants Sp 384/16, Sp 384/17, and Sp 384/18; Deutsches Zentrum für Luft und Raumfahrt (DLR) grant 500H0003; and the Studienstiftung des deutschen Volkes. The group at the Max Planck Institut für Kernphysik was supported by the Max Planck Society and by DLR under grant 5000H9802. The work in Chicago was supported by Jet Propulsion Laboratory contract 96 11 70, and M. Sremčević is funded by the Cassini UVIS project.

Supporting Online Material
www.sciencemag.org/cgi/content/full/311/5766/1416/DC1
 Materials and Methods
 Figs. S1 to S7
 References

14 October 2005; accepted 19 January 2006
 10.1126/science.1121375

REPORT

Cassini Ion and Neutral Mass Spectrometer: Enceladus Plume Composition and Structure

J. Hunter Waite Jr.,¹ Michael R. Combi,¹ Wing-Huen Ip,² Thomas E. Cravens,³ Ralph L. McNutt Jr.,⁴ Wayne Kasprzak,⁵ Roger Yelle,⁶ Janet Luhmann,⁷ Hasso Niemann,⁵ David Gell,¹ Brian Magee,¹ Greg Fletcher,¹ Jonathan Lunine,^{6,8} Wei-Ling Tseng²

The Cassini spacecraft passed within 168.2 kilometers of the surface above the southern hemisphere at 19:55:22 universal time coordinated on 14 July 2005 during its closest approach to Enceladus. Before and after this time, a substantial atmospheric plume and coma were observed, detectable in the Ion and Neutral Mass Spectrometer (INMS) data set out to a distance of over 4000 kilometers from Enceladus. INMS data indicate that the atmospheric plume and coma are dominated by water, with significant amounts of carbon dioxide, an unidentified species with a mass-to-charge ratio of 28 daltons (either carbon monoxide or molecular nitrogen), and methane. Trace quantities (<1%) of acetylene and propane also appear to be present. Ammonia is present at a level that does not exceed 0.5%. The radial and angular distributions of the gas density near the closest approach, as well as other independent evidence, suggest a significant contribution to the plume from a source centered near the south polar cap, as distinct from a separately measured more uniform and possibly global source observed on the outbound leg of the flyby.

The INMS instrument on the Cassini spacecraft, pointing within 60° of the direction of motion of the spacecraft and traveling with a relative velocity of ~8 km s⁻¹ to Enceladus, was able for the first time to investigate the composition and spatial distribution of gases in the plume and coma surrounding Enceladus (Fig. 1). Previous close flybys of Enceladus (<4000 km) by the Cassini spacecraft have all been carried out with INMS pointed in the anti-ram direction of motion of the spacecraft, thereby precluding possible measurements of any neutral gases associated with Enceladus.

The Cassini INMS is a dual-ion source quadrupole mass spectrometer covering the mass-to-charge ranges 0.5 to 8.5 and 11.5 to 99.5 daltons (1, 2). The dual-source design combines classic closed- and open-ionization source configurations that measure inert species and reactive species and ions, respectively. The primary data reported in this paper were ob-

tained with the closed source. In the closed source, the neutral gas flows into a spherical antechamber where it thermally accommodates with the walls before flowing through a transfer tube to an electron ionization source and is ionized by electron impact at 70 eV. The high flyby velocity of the Cassini spacecraft with respect to Enceladus (~8 km s⁻¹) produces a dynamic pressure enhancement in the antechamber that increases sensitivity (1, 2), but at a reduced level because of the 60° orientation of the sensor with respect to the ram direction of the spacecraft's motion.

The spectrum displayed in Fig. 2 indicates a mass scan covering the range 1 to 99 daltons. The individual mass spectra that were used to form the spectrum were acquired every 4.6 s for the time period when the spacecraft was closer than 500 km to the surface of Enceladus. The spectra have been added to enhance the signal-to-noise ratio. The background subtraction for ingress and egress data are treated separately to account for changes observed well before and well after the Enceladus flyby. The primary constituents H₂O, CO₂, N₂ or CO, and CH₄ are evident from the primary mass peaks at 18, 44, 28, and 16 daltons, respectively. Mass peaks are also measured for the minor atmospheric species (C₂H₂ and C₃H₈). Other species that could be present at a level <0.5% include NH₃ and HCN.

The responses of all of the measurable product channels of the primary constituents of interest were determined during the flight unit

and engineering unit calibrations (with the exception of H₂O, NH₃, and HCN, which were obtained from National Institute of Standards and Technology tabulations). These responses were subsequently used in the deconvolution of the spectra. Because of the nature of the electron-beam ionization source, the signal in each mass bin is a combination of the signals from the ionization or dissociative ionization of several constituents. Spacecraft velocity and attitude are used to compute the ram flow enhancement. From these data, a matrix is constructed relating instrumental response for various mass channels to the atmospheric composition. Inversion of this matrix with suitable numerical methods (3) yields abundances for a range of constituents. The measurements (and matrix elements) are weighted by the reciprocal measurement error.

The best fit to the atmospheric composition based on the mass deconvolution (according to a reduced chi-squared metric) gives 91 ± 3% H₂O, 3.2 ± 0.6% CO₂, 4 ± 1% N₂ or CO (depending on the identity of the mass peak at 28 daltons), and 1.6 ± 0.4% CH₄, where the error estimates are the larger of the fit range or the 1σ statistical error of the fit and do not include systematic errors from factors such as calibration, which may be as high as 20% (Table 1). Statistically meaningful residuals in the mass ranges 14 to 17 and 26 to 27 daltons suggest that there may also be trace quantities (<~1%) of ammonia, acetylene, hydrogen cyanide, and propane.

The signal-to-noise ratio in the mass-18 channel (predominantly the H₂O signature) is sufficient within 4000 km of Enceladus to investigate how the water vapor density varies along the track of the spacecraft (Fig. 3). In Fig. 3, we also compare the water vapor density with the density of dust particles greater than 2 μm in size inferred from the Cassini Cosmic Dust Analyzer (CDA) (4). There is noticeable asymmetry with respect to the closest approach in both data sets and a reasonable correlation between them, but with an offset of 32 s. Furthermore, water vapor density variations well above the level of expected statistical variation suggest spatial and/or temporal structure of the outgassing source. Moreover, the spatial variability and the asymmetry of the water vapor and dust distributions with respect to closest approach (Fig. 3) suggest an association with the southern thermal hot spot (5, 6).

The mass spectrum obtained by INMS can be used to understand the origin and evolution of the interior of Enceladus. The inferred surface pressure of the atmosphere (properly an exosphere) lies between 10⁻¹ and 10⁻⁴ nanobars, such that collisions and subsequent gas-phase chemical reactions play a minor role within the atmospheric plume. Furthermore, the ionization and dissociation time constants (hours at a

¹Department of Atmospheric, Oceanic, and Space Sciences, University of Michigan, Ann Arbor, MI 48109, USA.

²Institutes of Astronomy and Space Science, National Central University, Chung Li 32054, Taiwan. ³Department of Physics and Astronomy, University of Kansas, Lawrence, KS 66045, USA. ⁴Applied Physics Laboratory, Johns Hopkins University, Laurel, MD 20723, USA. ⁵NASA Goddard Space Flight Center, Greenbelt, MD 20771, USA.

⁶Lunar and Planetary Laboratory, University of Arizona, Tucson, AZ 85721, USA. ⁷Space Science Laboratory, University of California, Berkeley, CA 94720, USA. ⁸Istituto di Fisica dello Spazio Interplanetario, Via del Fosso del Cavaliere 100, 00133 Rome, Italy.

Fig. 1. View of Enceladus showing surface features and the Cassini ground track during the flyby on 14 July 2005. The south polar hot spot is shown in red, amidst the surface feature known as the tiger stripes. The spacecraft trajectory is shown in yellow. The colors of the points along the trajectory represent Cassini's closest approach to Enceladus (purple), the closest approach to the southern polar hot spot (red), the point along the track where INMS saw the maximum water vapor density (black), and the point along the track where the CDA saw the peak in dust particle density (green). The direction of motion of the spacecraft (ram direction) is represented by the arrowhead on the trajectory. SC, spacecraft.

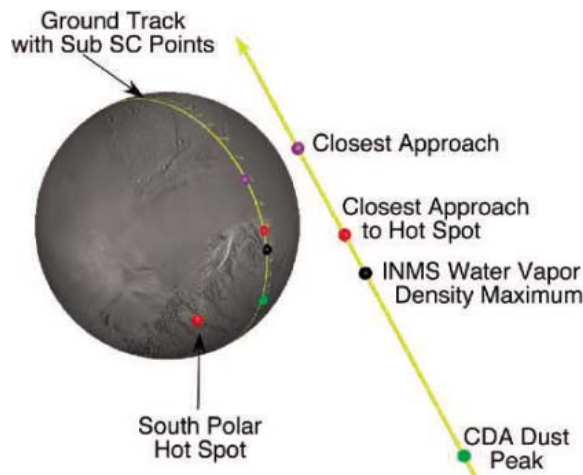
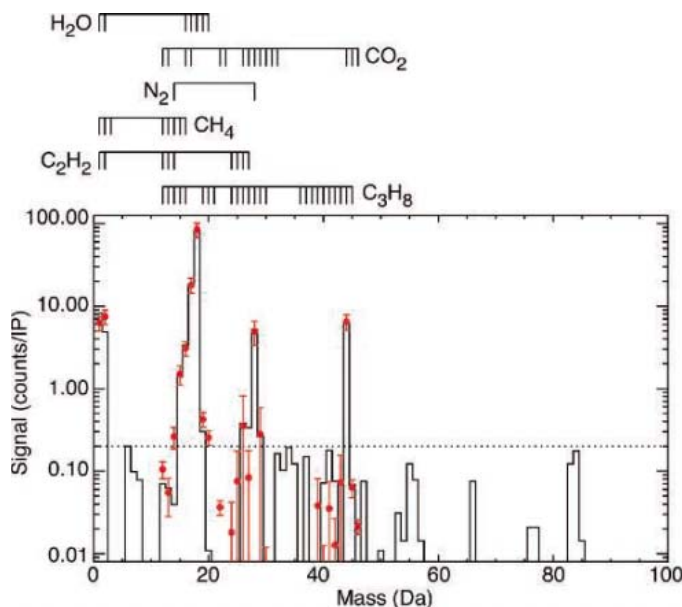


Fig. 2. Average mass spectrum for altitudes below 500 km. The solid black line indicates the measured average spectrum and the red symbols represent the reconstructed spectrum. The error bars displayed are the larger of the 20% calibration uncertainty or the 1σ statistical uncertainty. The dotted line is indicative of the 1σ noise level. The dissociative ionization products produced by the electron ionization source for each constituent are shown above the figure. Da, daltons; IP, integration period.



minimum) are orders of magnitude longer than the inferred transport time from the surface to the point of measurement (~ 6 min). Therefore, the outgassing products measured by INMS are presumed to have been produced in aqueous and/or solid phases or in a high-pressure gas channel within Enceladus before outgassing or sputtering took place. Furthermore, the nonspherical density variations of the plume and coma suggest that the observed composition is an accurate representation of the gas composition that occurs at the site of local outgassing from the south polar hot spot (Table 1). This suggestion of a close association between surface and plume composition is reinforced by the strong correlation between the surface composition derived from data collected by the Cassini Visual and Infrared Mapping Spectrometer (VIMS) within the tiger stripes associated with the south polar

hot spot (7) and the plume composition measured by INMS 250 km above the boundary of the south polar region (6). VIMS measured predominantly water ice, with an admixture of carbon dioxide (very similar to the findings of INMS), and an organic signature from a light hydrocarbon. Furthermore, from the VIMS data we infer an upper limit for a CO mixing ratio of 0.5% (8). Similarly, the Cassini Ultraviolet Imaging Spectrograph (UVIS) observations set an upper limit of 2% for the CO mixing ratio (9, 10). When considered together, the VIMS and UVIS observations suggest, although not conclusively, that the INMS peak at mass 28 is most likely produced by N_2 . Follow-up observations are needed to verify this.

The presence of N_2 and little, if any, NH_3 ($<0.5\%$) is notable, because ever since the discovery of large crater-free areas on Enceladus

Table 1. Composition of the gas plume and coma associated with Enceladus. The minimum and maximum values represent the range of values associated with adopting different compositional mixtures. The standard deviation represents the largest statistical uncertainty associated with the fit of each constituent.

Species	Minimum	Maximum	SD
H_2O	0.9070	0.9150	0.0300
CO_2	0.0314	0.0326	0.0060
Mass 28 (CO or N_2)	0.0329	0.0427	0.0100
CH_4	0.0163	0.0168	0.0040

by Voyager imaging, ammonia has been a preferred substance for lowering the melting point of water ice and increasing its buoyancy so as to aid or enable resurfacing (11). Ammonia was reported to have been detected as a very weak hydrate feature in one ground-based near-infrared spectroscopic observation of Enceladus (12) but not in another (13). Our failure to detect ammonia suggests either that it is not involved in the subsurface mechanisms that created the plume or that aqueous chemistry within the interior source regions of the plume effectively converts NH_3 to N_2 before it can be exposed to or ejected from the surface. We can, however, virtually rule out chemical complexing of some or all of the NH_3 with the walls of the INMS antechamber, a phenomenon seen in laboratory studies of ammonia (14) but unlikely here on the basis of our careful analysis of the background changes after the flyby. With respect to the identification of the molecular nitrogen, we cannot completely rule out the mass-28 species being CO rather than N_2 , in which case the outgassing observed from the plume would have a composition that is remarkably close to that of comets, as inferred from multiple cometary observations [tables 1 and 2 in (15)]. Thus, further study both of the identity of the mass-28 peak and of possible loss mechanisms that might make NH_3 difficult to observe are warranted.

The radial and angular density distributions of water vapor are also important in understanding the nature of the processes responsible for the outgassing. The fit to the functional form $\ln(\text{density})$ versus $1/(\text{distance to the center of Enceladus})^x$ for the combined ingress and egress data set gives a best fit of $x = 1.5 \pm 0.1$ (supporting online material text). However, asymmetries in this fit inbound ($x = 2.0$) versus outbound ($x = 1.1$) and irregularities near the closest approach, as well as evidence from other Cassini investigations (4–7, 10), suggest an asymmetric gas distribution organized around a source centered near the “warm” (5, 6) south polar cap. To understand this asymmetry, we used a direct-simulation Monte Carlo model developed originally for comets (16, 17) to

Fig. 3. Plot of the INMS water density and CDA dust density as a function of time along the orbital trajectory. CDA measurements represent particles larger than 2 μm in grain size. Shifting the INMS density data -32 s from the closest approach (CA) maximizes the Pearson correlation coefficient (~ 0.85) between INMS-derived water densities and CDA-derived dust densities. The light green shading indicates the estimated timing uncertainty in the dust peak, the gray shading indicates the estimated uncertainty in the water vapor peak, and the dark green shading indicates the overlap.

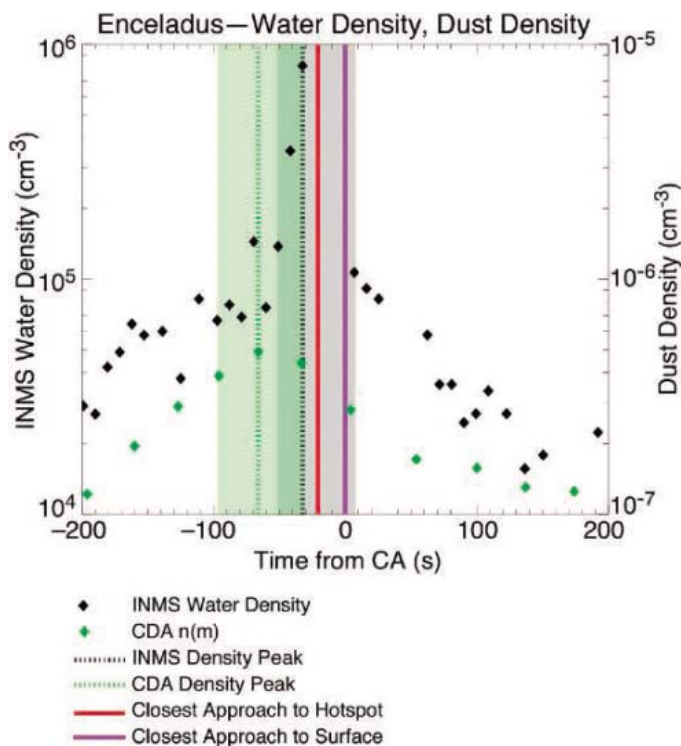
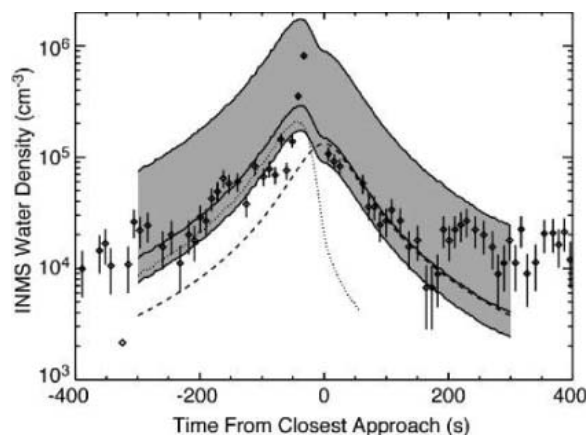


Fig. 4. Comparison of model results to INMS density data near its closest approach to Enceladus. The diamonds show the INMS-measured water density with the 1σ uncertainties indicated by the vertical lines. The dotted line corresponds to the south polar source model covering latitudes from -90° to -82° . The dashed line corresponds to a spherical global, possibly sputtered source. The solid line corresponds to the sum of these two sources. The gray area denotes the density range.



which we have added the effect of the weak gravitational field. The water molecules are introduced into the model from (5, 6) the south polar source and (1) a uniform surface (possibly sputtering) source. Several source characterizations were attempted, varying the relative upward speed from the source at the surface, the size of the south polar source (4° to 15° from the pole), the temperature, and the source strengths. The uniform source is a simple spherical outflow model with a density of $n = S/(4\pi v R_E^2)$, where S is the total global source rate, v is the average upward molecular velocity, and R_E is the distance from the center of Enceladus.

Figure 4 shows the results of modeling the INMS response to the plume and coma of Enceladus in the time period of 400 s before and

after the closest approach, which corresponds to 1700 km from the center of Enceladus. The source rate from the model's uniform component (the dashed line) is $S_1 \approx 1.2 \times 10^{26}$ molecules s^{-1} , assuming a speed of about 400 m s^{-1} . The model's south polar plume extends to a latitude of -82° and has a thermal speed distribution for the water sublimation temperature of 190 K and a source rate of $S_2 \approx 1.7 \times 10^{26}$ molecules s^{-1} (18). Varying the temperature from 140 K (average temperature of the tiger stripes region) to 270 K (suggested in some subsurface heating scenarios) introduces a range of 20% to the source strength. A small third "jet" source with a half-cone angle width of 3° and a source strength of only $\sim 5 \times 10^{23}$ molecules s^{-1} could explain the peak; however, the deviation of these two points from the model

is of the same magnitude as several other points and may simply result from temporal or spatial irregularities in the emission from the surface. The total H_2O production rate from Enceladus ($S = S_1 + S_2$) is $S \approx 1.5 \times 10^{26}$ to 4.5×10^{26} molecules s^{-1} , and the total gas production rate $S_{\text{gas}} \approx 1.7 \times 10^{26}$ to 5.0×10^{26} molecules s^{-1} , assuming the gas is 90% H_2O from INMS measurements.

The INMS measurements corresponding to egress times larger than 250 s after the closest approach show an extended plateau that does not continue the downward trend of the models. The region within 2000 km from the center of Enceladus only takes about 1 to 2 hours to populate. If these larger values in the extended region are caused by temporal variations in the source rate of water from Enceladus, as has been seen in Cassini UVIS measurements of atomic oxygen (19), then source rates up to a factor of 6 or more than the modeled values could occur. The lower INMS measurements (compared with the nominal model in Fig. 4) indicate source rates of a factor of 0.6 below the nominal model values. The bounds of the minimum and maximum model indicate a highly variable source rate that varies on time scales of less than 1 hour over a wide range from 1×10^{26} s^{-1} to 3×10^{27} s^{-1} . The density range is shown as the broad gray area in Fig. 4. The larger values in this range are more indicative of the broad distribution seen at large distances from Enceladus and are comparable to the source rates required to account for the water source of OH in the whole circum-saturnian region. The density peak seen near the closest approach could result from the start of a new high-source rate episode. Notably, the high level and irregularity of the source rate indicated by the egress data, 250 to 400 s after the closest approach, are far to the north and cannot be traced directly back to the south polar plume. Therefore, it is likely that the south polar plume and the uniform source are both highly variable.

The special role of Enceladus in supplying water vapor and its related neutral and ionized constituents to the magnetosphere of Saturn has been recognized since the observations by the Hubble Space Telescope (HST) of a substantial OH torus (20). These results led to model-based estimates of the source strengths of the various icy moons and rings necessary to reproduce the observed spatial variations. In particular, Jurac *et al.* (21) concluded that about 80% of the required water vapor must come from Enceladus and the E-ring region, implying that the production from Enceladus was $\sim 3.75 \times 10^{27}$ molecules s^{-1} or 93 kg s^{-1} , which could be consistent with the higher set of INMS measurements at larger radial distances (~ 2000 km), especially after the closest approach. This could mean that the water source rate from

Enceladus might vary markedly by nearly an order of magnitude on time scales of hours (19). Jurac *et al.* (21) also suggested that impacts by E-ring particles, a possible source, would be insufficient to produce this amount. Nevertheless, Roddier *et al.* (22) had imaged a transient feature with HST that could have been interpreted as a large, impact-produced vapor cloud. The fresh deposits on Enceladus' surface suggested by its high albedo also reinforced the idea that E-ring grains are constantly being swept up, along with any larger objects that may be present. Sputtering of ice by energetic O⁺ ions as a source required more surface area than could be accounted for by the combination of Enceladus and the expected E-ring grains. In a subsequent paper, Jurac and Richardson (23) concluded that the source rate for the observed water needed to be three times larger and that its production mechanism remained unclear. The discovery by Cassini of an unexpected venting of water vapor from the south pole of Enceladus, of approximately the right amount, may provide a solution to this mystery.

References and Notes

- J. H. Waite *et al.*, *Space Sci. Rev.* **114**, 113 (2005).
- W. K. Kasprzak *et al.*, *Proc. SPIE* **2803**, 129 (1996).
- W. H. Press, B. P. Flannery, S. A. Teukolsky, W. T. Vetterling, *Numerical Recipes* (Cambridge Univ. Press, Cambridge, 1986).
- F. Spahn *et al.*, *Science* **311**, 1416 (2006).
- J. R. Spencer *et al.*, *Science* **311**, 1401 (2006).
- C. C. Porco *et al.*, *Science* **311**, 1393 (2006).
- R. H. Brown *et al.*, *Science* **311**, 1425 (2006).
- The VIMS-derived mixing ratio is based on the absence of CO absorption features in the gas column between the surface above the south polar cap and the spacecraft (10^{14} cm⁻²), divided by the column density of water acquired by UVIS during a stellar occultation (1.5×10^{16} cm⁻²) (10).
- The absence of CO ultraviolet absorption bands in the UVIS occultation data sets an upper limit for CO abundance at 2% of the water density for a measured water column of 1.5×10^{16} cm⁻² (10).
- C. J. Hansen *et al.*, *Science* **311**, 1422 (2006).
- S. W. Squyres, R. T. Reynolds, P. M. Cassen, S. J. Peale, *Icarus* **53**, 319 (1983).
- J. P. Emery, D. M. Burr, D. P. Cruikshank, R. H. Brown, J. B. Dalton, *Astron. Astrophys.* **435**, 353 (2005).
- D. P. Cruikshank *et al.*, *Icarus* **175**, 268 (2005).
- S. Boone, M. F. Nicol, in *LPSC 21 Proc.* (Lunar and Planetary Institute, Houston, TX, 1991), pp. 603–610.
- D. C. Bockelee-Morvan, J. Crovisier, M. J. Mumma, H. A. Weaver, in *Comets II*, M. C. Festou, H. U. Keller, H. A. Weaver, Eds. (Univ. Arizona Press, Tucson, AZ, 2004), pp. 391–423.
- The observed asymmetries and the coincidence of water vapor, CO₂, and dust appearing to emanate from the south polar tiger stripes region of Enceladus indicate a possible cometary activity analog. Our analysis of the composition and plume shape suggests the temperature below the surface at the source of the water vapor must be somewhere in the range of at least ~190 to 273 K, the temperatures required for the sublimation of ice. If dust particles have been ejected from the cracks in the surface by the action of the flow of water molecules, then it is likely that the confined volume below the surface must be rather small so as to yield sufficiently high gas densities to achieve substantial dust entrainment (24). If the observed dust particles are ice condensates from the gas plumes emanating from the cracks, as has also been suggested for comets (25), then gas densities must also be quite high. In an expanding cometary coma, the number density of water molecules in which dust is effectively accelerated by the gas flow is greater than about 10^8 cm⁻³. Near the nucleus, where the dust acceleration is the largest, gas densities are larger than 10^{11} cm⁻³ for a moderately bright comet like 1P/Halley or 1996 B2 (Hyakutake) (25). Taken together, this implies that the water flow exits from relatively small fissures in the surface [such as the tiger stripes (2 by 120 km) (6) themselves compared with the size of the general emitting region] and that the flow is already accelerated to rather large speeds and is correspondingly cooled below the reservoir temperature [in excess of 190 K (26)] when it passes through the surface. The fissures must also be large enough to allow at least semicollisional gas flow below the surface (i.e., the fissure's bore size must be larger than the mean free path between molecules). If the fissures are too small, then molecules will stick to the cold surfaces and never exit, sealing off the crack. Even the average temperature observed by the Composite Infrared Spectrometer of 140 K is far below the sublimation temperature so that most molecules striking the surface would stick. Such recondensation is a common feature included in porous subsurface cometary nucleus models (27).
- M. R. Combi, *Icarus* **123**, 207 (1996).
- The source strength inferred from the model allows us to estimate a surface density that can be compared to the UVIS observations (10) if we assume a thermal escape speed and an area of the outgassing. ISS (6) indicates that the tiger stripes region of ice crystal and dust generation presents 1 to 3% of the area of the polar cap at southern latitudes greater than 82°. If we assume that the gas production and dust and ice generation regions coincide, and if we further assume a thermal speed for the water vapor of 400 m s⁻¹, we derive an inferred near-surface density based on the extended plume measured by INMS of 1×10^9 to 5×10^9 cm⁻³. On the other hand, UVIS (10) reports a water column density of 1.5×10^{16} cm⁻² and infers a scale length of 80 km, which leads to a near-surface density of 1.9×10^9 cm⁻³. This value is within the range inferred by INMS.
- L. W. Esposito *et al.*, *Science* **307**, 1251 (2005).
- D. E. Shemansky, P. Matherson, D. T. Hall, T. M. Tripp, *Nature* **363**, 329 (1993).
- S. Jurac *et al.*, *Geophys. Res. Lett.* **29**, 2172 (2002).
- C. Roddier, F. Roddier, J. E. Graves, M. J. Northcott, *Icarus* **136**, 50 (1998).
- S. Jurac, J. D. Richardson, *J. Geophys. Res.* **110**, 10.1029/2004JA010635 (2005).
- R. V. Yelle, L. A. Soderblom, J. R. Jokipii, *Icarus* **167**, 30 (2004).
- T. Yamamoto, O. Ashihara, *Astron. Astrophys.* **152**, L17 (1985).
- M. R. Combi, W. M. Harris, W. H. Smyth, in *Comets II*, M. C. Festou, H. U. Keller, H. A. Weaver, Eds. (Univ. Arizona Press, Tucson, AZ, 2004), pp. 523–552.
- B. Davidsson, Y. Skorov, *Icarus* **168**, 163 (2004).
- The Cassini INMS investigation is supported by contract number 1228303 from the NASA Jet Propulsion Laboratory. M.R.C. was supported by grant NAG5-12822 from the NASA Planetary Atmospheres Program. W.-H.I. was supported by grant NSC 94-2111-M-008-033.

Supporting Online Material

www.sciencemag.org/cgi/content/full/311/5766/1419/DC1

SOM Text

Fig. S1

Table S1

12 October 2005; accepted 12 December 2005

10.1126/science.1121290

REPORT

Enceladus' Water Vapor Plume

Candice J. Hansen,^{1*} L. Esposito,² A. I. F. Stewart,² J. Colwell,² A. Hendrix,¹ W. Pryor,⁴ D. Shemansky,³ R. West¹

The Cassini spacecraft flew close to Saturn's small moon Enceladus three times in 2005. Cassini's UltraViolet Imaging Spectrograph observed stellar occultations on two flybys and confirmed the existence, composition, and regionally confined nature of a water vapor plume in the south polar region of Enceladus. This plume provides an adequate amount of water to resupply losses from Saturn's E ring and to be the dominant source of the neutral OH and atomic oxygen that fill the Saturnian system.

The youthful geologic appearance of Enceladus (1) and the correlation of the peak density of Saturn's E ring with the orbit of Enceladus (2) have long led scientists to speculate that Enceladus is the source of the ring (2–5). The narrow size distribution of particles in

the E ring suggests a liquid or vapor origin, in contrast to the broad range of particle sizes that would be generated by impacts (2). To test the hypothesis that Enceladus has geologic activity supplying the E ring as well as neutral species in Saturn's magnetosphere, the Cassini Ultraviolet Imaging Spec-

trograph (UVIS) team planned stellar occultation observations on Cassini's first and third close flybys of Enceladus to search for the presence of a tenuous atmosphere (6). The detection, by the Cassini Magnetometer team (7), of draped field lines consistent with the presence of an atmosphere gave further impetus to the second occultation observation. Because of Enceladus' small size and weak gravity (~12 cm/s²), any sputtered or sublimated atmosphere will be lost (8); thus, if a tenuous atmosphere were to be detected, it would have to come from some sort of geologic activity. We now know that

¹Jet Propulsion Laboratory/California Institute of Technology, 4800 Oak Grove Drive, Pasadena, CA 91109, USA.

²Laboratory for Air and Space Physics (LASP), University of Colorado, Boulder, CO 80303, USA. ³Space Environment Technologies, 320 North Halstead, Suite 170, Pasadena, CA 91107, USA. ⁴Central Arizona College, Coolidge, AZ 85228, USA.

*To whom correspondence should be addressed. E-mail: Candice.j.Hansen@jpl.nasa.gov

this is the case, and we report here on the results established by the occultations observed by UVIS.

Observations of stellar occultations are a sensitive method for looking for the presence of tenuous atmospheres (9), particularly at ultraviolet wavelengths, where many gases have strong absorptions. The Cassini UVIS has four optical channels: the high-speed photometer (HSP), the extreme ultraviolet (EUV) spectrograph, the far ultraviolet (FUV) spectrograph, and the hydrogen/deuterium absorption cell (6). The HSP and FUV were used to observe the occultations. The HSP is sensitive to 1100 to 1900 Å and is read out once per 2 ms. The FUV also covers the range from 1100 to 1900 Å and was configured with 512 spectral bins (1.56 Å resolution) for the July occultation observation. The FUV integration time was 5 s.

The star lambda Scorpii (Shaula) was occulted by Enceladus on 17 February 2005, the first of three close Enceladus flybys (Fig. 1A). A second occultation, of the star gamma Orionis (Bellatrix), was observed on the third and closest flyby on 14 July 2005 (Fig. 1, B to D). Only the gamma Orionis ingress showed the attenuation of starlight due to the presence of an absorbing gas. No detectable change of signal was detected by the HSP or FUV on the lambda Scorpii occultation before or after the star's signal was blocked by Enceladus. Detection and nondetections and ingress and egress locations are summarized in Table 1.

In the HSP and FUV data for the gamma Orionis occultation ingress, which occurred at -76° latitude, the signal was attenuated as the star passed behind Enceladus' plume (Fig. 2). The starlight started to decrease at ~ 24 s before ingress, at a ray altitude of ~ 155 km. The signal of the star was lost completely at UTC 19:54:56, when the star crossed behind the hard limb. The HSP has a finite recovery time on bright stars such as gamma Orionis, so it is not possible to separate a weak atmospheric signal from the instrument response on egress. For egress measurements, we summed the FUV spectral pixels, but the temporal resolution is lower than the HSP data because of the longer integration time. No detectable change of signal was seen in FUV data on the egress of gamma Orionis. Clearly, the gas detected at the ingress of the gamma Orionis occultation is not globally distributed. These data are consistent with a plume of gas over the southern pole.

The presence of an absorbing gas shows up in the FUV spectrum as relatively narrow features at short wavelengths and a broad shallow absorption from ~ 1450 to 1800 Å as compared to the unocculted spectrum (Fig. 3). Time record 33, the last full 5-s integration before ingress, shows the deepest absorption. The ray altitude above Enceladus' surface corresponding to time record 33 ranged from 30 to 7 km.

The average unocculted star spectrum (I_0) was computed from 25 time records summed over three spatial rows (the instrument pointing drifted slightly over the course of the occultation).

The ratio of time record 33 (I) to I_0 shows the spectrum of the absorbing gas (Fig. 4). We fit the spectrum to water by computing $I = I_0 \exp(-n \times \sigma)$ for water, where σ is the cross section as a function of wavelength (I_0) and n is the column density. Figure 4 compares a water spectrum with column density $n = 1.5 \times 10^{16} \text{ cm}^{-2}$ to the I/I_0 spectrum for time record 33. This column density represents the integrated effect of water vapor along the ray path from the spacecraft to the star through the atmosphere. Statistical analysis of smoothed data shows that the water vapor absorption exceeds 2σ beginning with time record 29. The slight mismatch at short wavelengths may be due to using absorption cross sections that were

measured at room temperature [the absorption cross sections at longer wavelengths, which dominate our fit, are not as affected by temperature (I/I)] and/or imprecise simulation of the instrument response at these wavelengths.

A molecule not apparent in the FUV absorption spectrum is CO. The Cassini Ion Neutral Mass Spectrometer detected a constituent with a mass of 28 atomic mass units, which could be N_2 or CO (12). The Cassini UVIS observation, however, sets an upper limit of $< 1.3 \times 10^{14} \text{ cm}^{-2}$ from the absence of CO absorption bands (13) at 1544, 1510, 1477, and 1447 Å, assuming that a 10% dip in the signal is required for positive identification of an absorption feature.

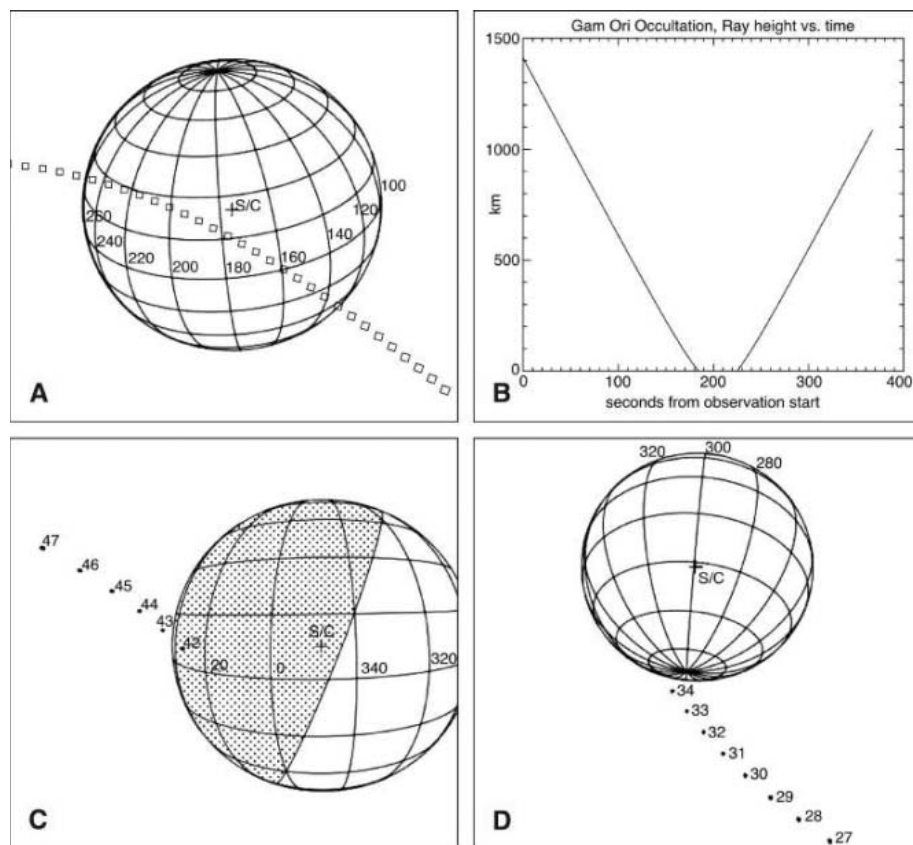


Fig. 1. (A) The path followed by the star lambda Scorpii as it was occulted by Enceladus, the first occultation observed by UVIS. The second stellar occultation observed was that of the star gamma Orionis. The altitude of the ray between UVIS and the star relative to the surface of Enceladus is given in kilometers as a function of time in (B). The path of gamma Orionis goes from right to left as a function of time in (C) and (D). (C) Egress of gamma Orionis. (D) Ingress of gamma Orionis. The UVIS field of view is plotted every 5 s. The number over the field of view is the time record number of the data set.

Table 1. Occultation geometry summary.

Occultation date		Occultation intercept latitude	Occultation intercept longitude (west)	Atmosphere detected?
17 February 2005	Ingress	15	300	No
	Egress	-31	141	No
14 July 2005	Ingress	-76	86	Yes
	Egress	-0.20	28	No

Fig. 2. The signal of the star plotted versus time for the two occultations observed by UVIS. The left panel shows the steep drop in the FUV count rate as the star lambda Scorpii went behind Enceladus, then reemerged. Similarly, the right panel shows the FUV data from the gamma Orionis occultation. The gradual drop of the signal during ingress is due to the starlight being attenuated by Enceladus' plume. Small steps in the signal on both stars' ingress and egress correspond to the records in which the star was not in the FUV field of view (coming in and/or out of occultation) for the full 5-s integration.

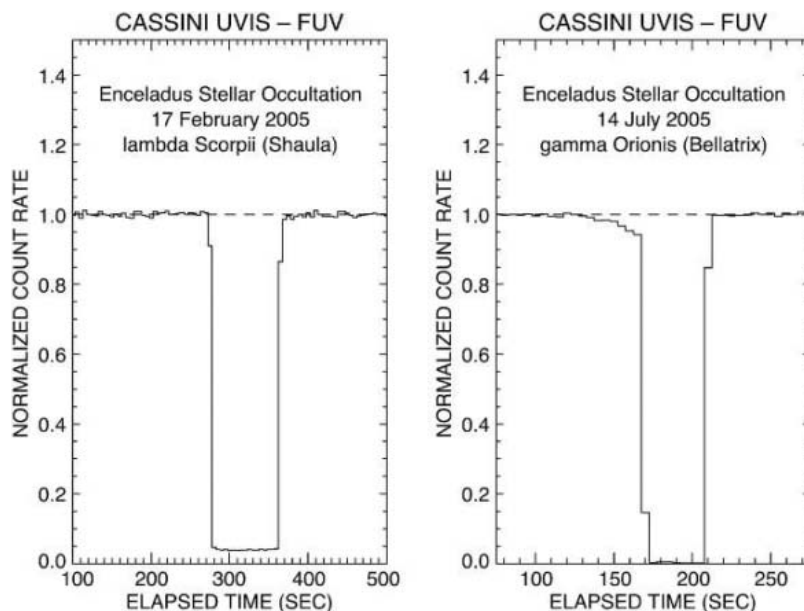


Fig. 3. Smoothed FUV spectra for the unocculted star signal (blue) compared to the signal coming through the plume (red).

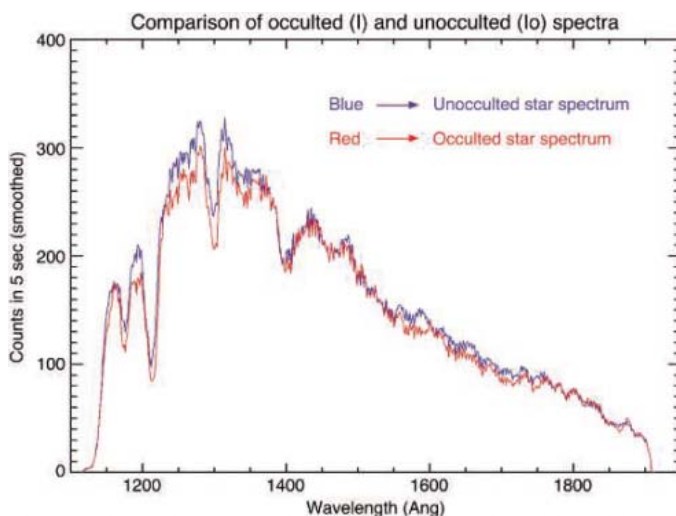
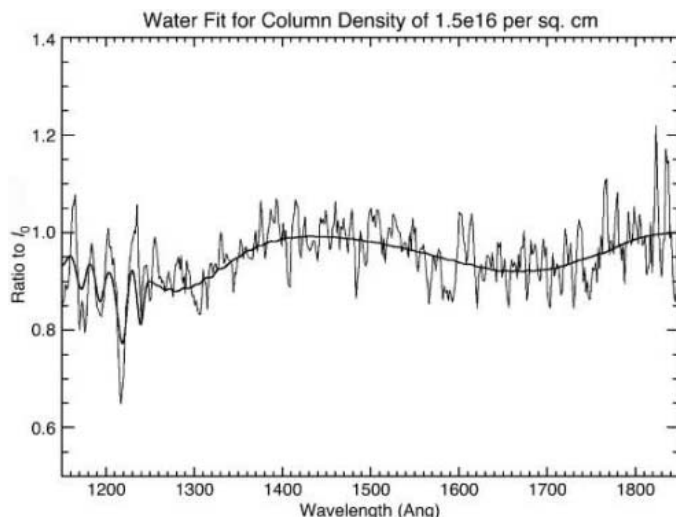


Fig. 4. An average unocculted star spectrum (I_0) was computed from 25 time records. The ratio of time record 33 (I) to I_0 is shown (thin line). A water spectrum with column density $n = 1.5 \times 10^{16} \text{ cm}^{-2}$ divided by I_0 is compared (thick line).

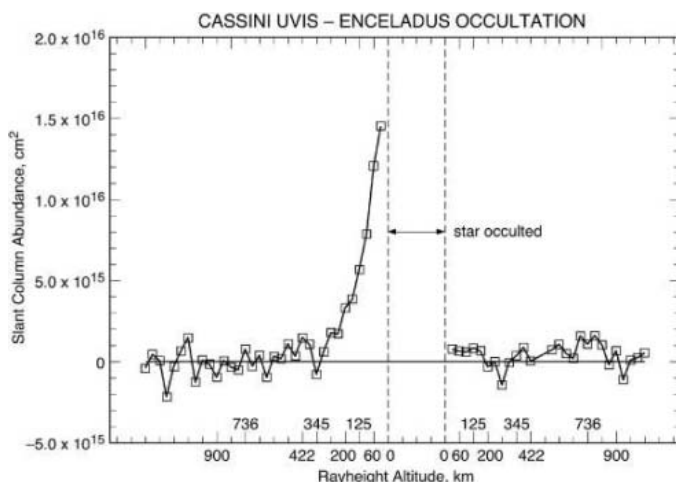


Looking at the slant column abundance of the water vapor versus altitude (Fig. 5), the attenuation of the star signal during the gamma Orionis ingress is best fit with an exponential decline with altitude. The best fit scale length, L , is 80 km. (Because this is an escaping atmosphere, this scale is not the same as the scale height for a gravitationally bound atmosphere.) Time records 27 and 28 appear to show the presence of water, although not yet at a 2σ confidence level.

The rate of water loss from Enceladus, S , is given by the product of the molecular abundance $N (= n/h)$, the plume area h^2 , and the velocity v , as follows: $S = N \times h^2 \times v = n \times h \times v$. We estimate the linear dimension of the plume, h , as the measured scale length $L = 80 \text{ km}$. The observed column density along the path to the star is $n = 1.5 \times 10^{16} \text{ cm}^{-2}$. If we assume that the density corresponds to vapor that is in vapor pressure equilibrium with a warm ice source, then the temperature (T) of the ice is $\sim 145 \text{ K}$. A lower limit for the velocity is the thermal velocity at $T = 145 \text{ K}$, which gives $v = 41,200 \text{ cm/s}$. Note that v is well above the $24,000 \text{ cm/s}$ escape velocity. The flux is thus at least $S = 5 \times 10^{27}$ molecules/s. Under these simple assumptions, the amount of water escaping from Enceladus is $\sim 150 \text{ kg/s}$. Alternatively, h can be estimated from the horizontal dimension of the plume crossed by the star during the course of the occultation, $\sim 175 \text{ km}$. Analysis by the Cassini Composite Infrared Spectrometer team of their thermal data indicates that temperatures could be as high as 180 K (14). At 180 K , the thermal velocity v is $46,000 \text{ cm/s}$. Using $h = 175 \text{ km}$ and $v = 46,000 \text{ cm/s}$ gives $S > 1 \times 10^{28}$ molecules/s, which is approximately 350 kg/s .

Saturn's E ring, composed of water ice grains that are primarily 0.3 to $3 \mu\text{m}$ in size (15), ex-

Fig. 5. Water abundance shown as a function of time (ticks are every 10 s), labeled with the ray height in kilometers at a few representative times.



tends from about three to at least eight Saturn radii, with a peak density at Enceladus' orbit (2). Analysis by Jurac *et al.* (16) concluded that the lifetimes of 1- μm grains are <50 years, because water molecules are sputtered from the grains' surfaces by the plasma trapped in Saturn's magnetosphere. A source of water is needed to maintain the E ring.

Saturn's system is filled with neutral products from the electron- and photodissociation of H_2O molecules: Hubble Space Telescope observations detected neutral OH (17), and UVIS detected neutral atomic oxygen throughout Saturn's system (18) as the Cassini spacecraft approached Saturn. Most H_2O molecules dissociate to $\text{H} + \text{OH}$, with more O coming from the subsequent dissociation of OH. Neutrals are lost from the system because of charge exchange and collisions with ions. From measured O and OH abundances and theoretical estimates of the loss processes of all water products from the system, various investigators have estimated H_2O supply rates necessary to maintain a steady state as $>2 \times 10^{27}$ H_2O molecules/s (17), possibly as high as 3.75×10^{27} (19) or 10^{28} H_2O molecules/s (20, 21). Potential H_2O sources identified by these investigators included sputtering and collisions; however, the rates of these processes are not sufficient to replace the lost neutrals (19). The source for resupplying the E ring and replacing the neutrals remained a mystery until the discovery of the water vapor plume coming from Enceladus.

The inferred source rate of H_2O in the present observation is of the same order as the earlier estimated loss rates for O and OH. If Enceladus is responsible for the majority of water product gas in the magnetosphere, this implies eruptive activity over at least the past 15 years. The escape flux of water from Enceladus' plume calculated from our measurement of the column density may or may not represent a steady state, because the observation history is confined to a single flyby. Based simply on source magnitude, however, it is probable that Enceladus is the dominant source of the observed neutrals in the Saturn system.

If Enceladus is a significant source for maintaining the E ring, it implies that grain particles are part of the mix of matter in the plume. If Enceladus' plume has a comet-like dust-to-gas ratio, then the mass of water coming from Enceladus, >150 kg/s, is more than sufficient to compensate for the estimated loss rate of the E ring of 1 kg/s (22). The polar plume at Enceladus is clearly an unusual and important geophysical phenomenon.

References and Notes

1. B. A. Smith *et al.*, *Science* **215**, 504 (1982).
2. M. R. Showalter, J. N. Cuzzi, S. M. Larson, *Icarus* **94**, 451 (1991).

3. R. J. Terrile, A. Cook, *Lunar Planet. Sci.* **12** (suppl. A), 10 (1981).
4. B. J. Buratti, *Icarus* **75**, 113 (1988).
5. M. Horanyi, J. A. Burns, D. P. Hamilton, *Icarus* **97**, 248 (1992).
6. L. Esposito *et al.*, *Space Sci. Rev.* **115**, 299 (2004).
7. M. K. Dougherty *et al.*, *Science* **311**, 1406 (2006).
8. J. Saur, D. F. Strobel, *Astrophys. J.* **620**, L115 (2005).
9. G. R. Smith, D. M. Hunten, *Rev. Geophys.* **28**, 117 (1990).
10. W. F. Chan, G. Cooper, C. E. Brion, *Chem. Phys.* **178**, 387 (1993).
11. R. Harrelvelt, M. C. Hemert, *J. Chem. Phys.* **114**, 9453 (2001).
12. J. H. Waite Jr. *et al.*, *Science* **311**, 1419 (2006).
13. M. Eidsberg, F. Rostas, J. Breton, B. Thieblemont, *J. Chem. Phys.* **96**, 5585 (1992).
14. J. R. Spencer *et al.*, *Science* **311**, 1401 (2006).
15. P. D. Nicholson *et al.*, *Science* **272**, 509 (1996).
16. S. Jurac, R. E. Johnson, J. D. Richardson, *Icarus* **149**, 384 (2001).
17. D. P. Shemansky Matheson, D. T. Hall, H.-Y. Hu, T. M. Tripp, *Nature* **363**, 329 (1993).
18. L. W. Esposito *et al.*, *Science* **307**, 1251 (2005).
19. S. Jurac *et al.*, *Geophys. Res. Lett.* **29**, 2172 (2002).
20. S. Jurac, J. D. Richardson, *J. Geophys. Res.* **110**, A09220 (2005).
21. D. Shemansky *et al.*, paper presented at the meeting of the Committee on Space Research, Paris, France, 18 July 2004.
22. A. Juhasz, M. Horanyi, *J. Geophys. Res.* **107**, 1066 (2002).
23. This work was partially supported by the Jet Propulsion Laboratory, California Institute of Technology, under a contract with NASA. We thank N. Strange for his efforts in ensuring that the gamma Orionis occultation was included in the design of Cassini's trajectory past Enceladus.

Supporting Online Material

www.sciencemag.org/cgi/content/full/311/5766/1422/DC1
Fig. S1

12 October 2005; accepted 20 January 2006
10.1126/science.1121254

REPORT

Composition and Physical Properties of Enceladus' Surface

Robert H. Brown,¹ Roger N. Clark,² Bonnie J. Buratti,³ Dale P. Cruikshank,⁴ Jason W. Barnes,¹ Rachel M. E. Mastrapa,⁴ J. Bauer,³ S. Newman,³ T. Momary,³ K. H. Baines,³ G. Bellucci,⁵ F. Capaccioni,⁶ P. Cerroni,⁶ M. Combes,⁷ A. Coradini,⁶ P. Drossart,⁷ V. Formisano,⁵ R. Jaumann,⁸ Y. Langevin,⁹ D. L. Matson,³ T. B. McCord,¹⁰ R. M. Nelson,³ P. D. Nicholson,¹¹ B. Sicardy,⁷ C. Sotin¹²

Observations of Saturn's satellite Enceladus using Cassini's Visual and Infrared Mapping Spectrometer instrument were obtained during three flybys of Enceladus in 2005. Enceladus' surface is composed mostly of nearly pure water ice except near its south pole, where there are light organics, CO_2 , and amorphous and crystalline water ice, particularly in the region dubbed the "tiger stripes." An upper limit of 5 precipitable nanometers is derived for CO in the atmospheric column above Enceladus, and 2% for NH_3 in global surface deposits. Upper limits of 140 kelvin (for a filled pixel) are derived for the temperatures in the tiger stripes.

Saturn's sixth largest satellite, Enceladus, orbits the planet within the extended E ring at a distance of 238,040 km, or ~ 4 Saturn radii. Enceladus has an equatorial diameter of 504.2 km and a surface that consists of a composite of moderately cratered terrain and large expanses with no craters (1). Internal activity has

resulted in several episodes of resurfacing, ridge building, folding, and faulting (2, 3). Near-infrared spectroscopy of Enceladus from Earth-based telescopes (4–6) has revealed partially crystalline H_2O ice, consistent with Enceladus' unusually high reflectance. At wavelength 0.8 μm , the geometric albedo slightly exceeds 1.0 (5).

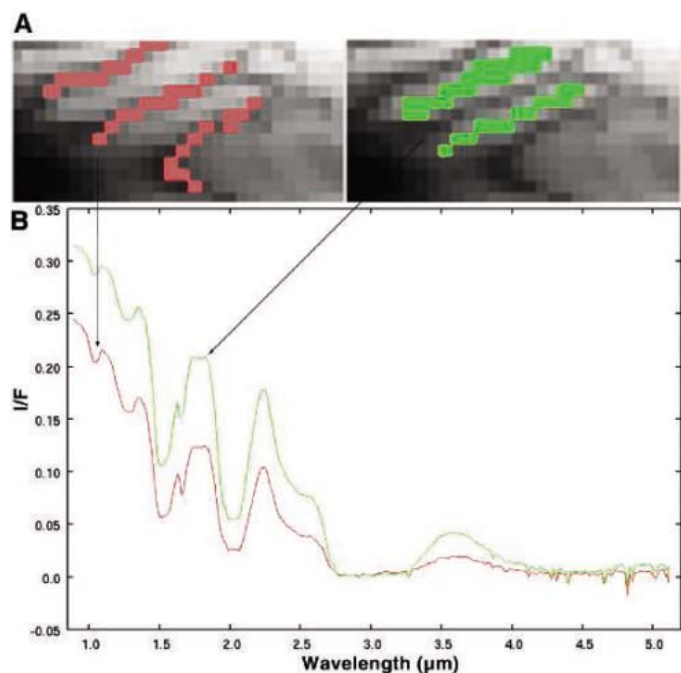
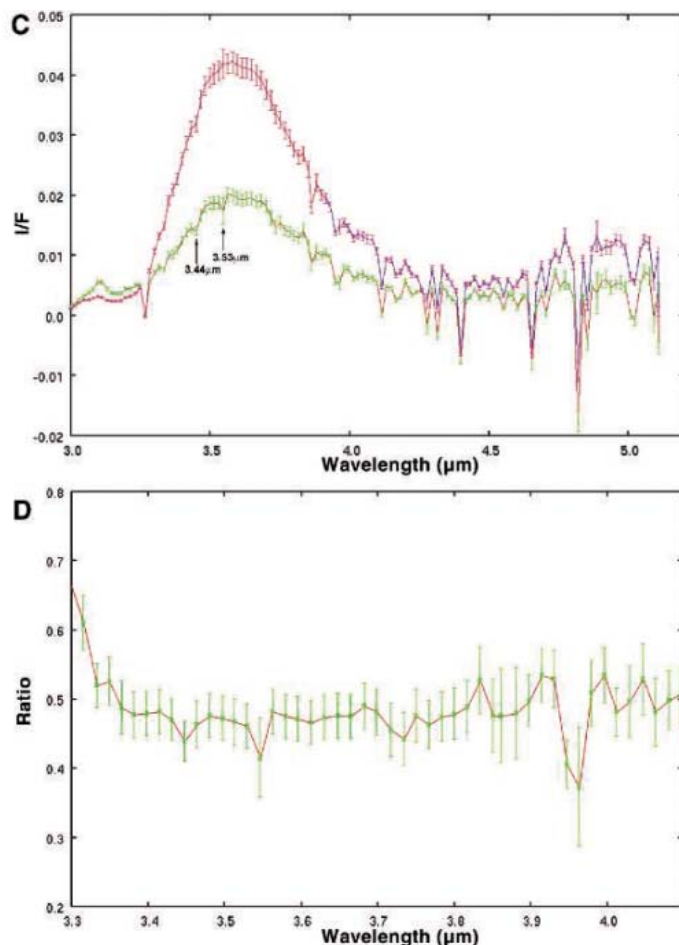


Fig. 1. Spectra of Enceladus in the region of the tiger stripes and from nearby regions. **(A)** A VIMS image of part of the tiger stripes region. The color-coded pixels indicate the areas from which the two averaged spectra in **(B)** are taken. The image is comprised of 28 by 14 pixels taken in the high-resolution mode of the VIMS infrared channel, whose footprint on Enceladus is 5 by 10 km for a total dimension of 140 by 140 km (in this mode, the VIMS pixels are rectangular and the image has been rendered with the use of square pixels). The frame is centered at roughly -80° latitude and 130° longitude. **(B)** The spectra of emergent intensity to incident flux (I/F) for the two regions in **(A)**. They were obtained by averaging all of the individual spectra in the tiger stripes and in the nearby areas [see **(A)**]. **(C)** A more detailed graph of the ratio of the two spectra in **(C)** in the 3.0- to 5.1- μm spectral region. **(D)** A more detailed graph of the ratio of the two spectra in **(C)** in the 3.3- to 4.1- μm spectral region. The 1σ error bars in **(D)** result primarily from level shifts in the two spectra, a result of the tiger stripes being noticeably darker than the sur-



rounding regions. The actual uncertainty in the spectra is better represented by the point-to-point scatter. We attribute the absorptions near 3.44 and 3.53 μm in the ratio spectrum in **(C)** to short-chain organics. There are other features in the ratio spectrum that may be real and are, as yet, unidentified. No spectra shown have units. They are simple numerical ratios.

Some telescopic spectra show a weak absorption at 2.2 to 2.4 μm , suggesting the presence of NH_3 or NH_3 hydrate (4, 6), whereas other spectra of similar quality do not (5). The spread in time of the spectra (1995 to 2003) and the change from an equatorial to a more south polar view of Enceladus over that interval suggest the possibility of short-term changes in the surface reflectance. Results of the magnetometer investigation

on Cassini gave early indications of a substantial atmosphere on Enceladus (7), which led to a lowering of the altitude of the 14 July flyby. The 14 July flyby led to the discovery of a plume of material emanating from the south polar region of Enceladus, most likely from the tiger stripes (the tiger stripes are a complex of volcanically active fissures of likely tectonic origin several hundred kilometers long, concentrated very near the south pole of Enceladus) (1, 8–10). Areas within the tiger stripes are substantially hotter than would be expected if only passively heated by sunlight (8).

Here, we report near-infrared spectra of spatially resolved regions on Enceladus, which we obtained using the Visible and Infrared Mapping Spectrometer (VIMS) (11) during the three Cassini flybys of this satellite in 2005 (17 February, 9 March, and 14 July 2005). In total, 207 VIMS cubes of Enceladus were obtained.

The VIMS is an imaging spectrometer operating in the wavelength region 0.35 to 5.1 μm

in 352 channels, with a nominal pixel size of 0.5 mrad and a maximum spatial format of 64 by 64 pixels. The data entity from the instrument is called a “cube” and can be thought of as a stack of 352 images, measuring 64 by 64 pixels and ordered by increasing wavelength.

The analysis of the VIMS data for Enceladus described here is in three general areas: the composition of surface and the size of the ice grains in the near surface, the degree of crystallinity of the near surface, and the temperature of the surface. Although the analysis extends to the entire surface of Enceladus covered by the observations during the three flybys, we focus on the south polar region of Enceladus and particularly on the area of the tiger stripes because they are so unusual.

Our analysis of the spectrum of Enceladus shows that its surface is almost completely dominated by water ice (Fig. 1) with a weak coloring agent in the ultraviolet-visible spectral region and with some minority constituents in specific areas. Globally, the typical water-ice grain size is 50 to

¹Lunar and Planetary Laboratory, University of Arizona, Tucson, AZ 85721, USA. ²U.S. Geological Survey, Denver, CO 80225, USA. ³Jet Propulsion Laboratory, California Institute of Technology, Pasadena, CA 91109, USA. ⁴NASA Ames Research Center, Moffett Field, CA 94035, USA. ⁵Instituto di Fisica dello Spazio Interplanetario, 0133 Rome, Italy. ⁶Instituto di Astrofisica Spaziale, 0133 Rome, Italy. ⁷Observatoire de Paris-Meudon, 92195 Meudon Cedex, France. ⁸Deutsches Zentrum fuer Luft und Raumfahrt, 12489 Berlin, Germany. ⁹Institute d’Astrophysique Spatiale, Universite de Paris, 91405 Orsay Cedex, France. ¹⁰Department of Earth and Space Sciences, University of Washington, Seattle, WA 98195, USA. ¹¹Department of Astronomy, Cornell University, Ithaca, NY 14853, USA. ¹²University of Nantes, 44072 Nantes Cedex, France.

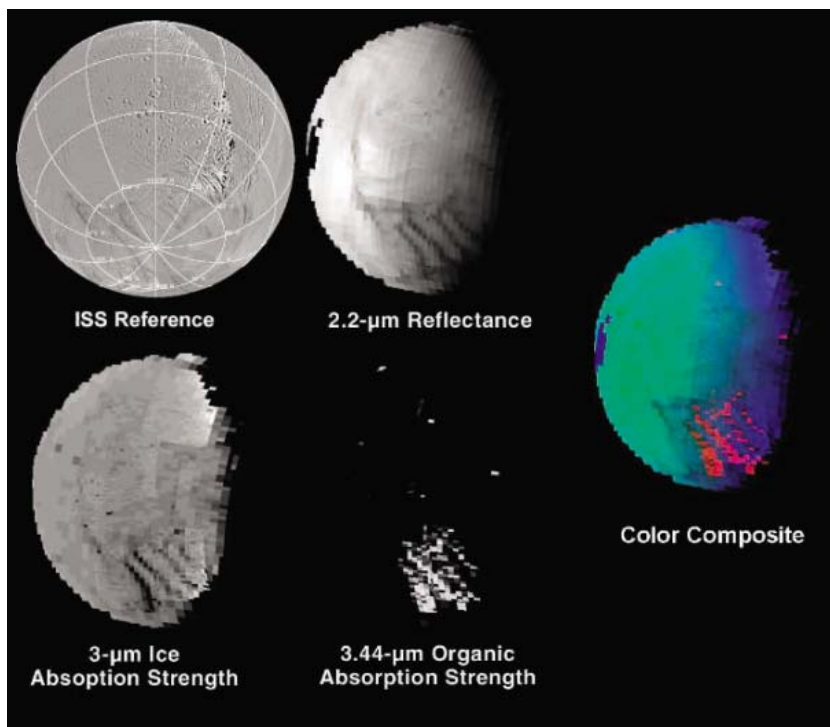


Fig. 2. A compositional map of Enceladus. This map was produced by stacking red, green, and blue images coded as follows: The red image maps the strength of the 3.44- μm organic absorption to red intensity, the green image maps the 2.2- μm continuum reflectance to green intensity, and the blue image maps the intensity of the 3- μm water-ice absorption to blue intensity. The images are stacked as a red-green-blue triplet. Note the correlation of the organic signature with the tiger stripes and the presence of stronger water-ice absorptions there as well. ISS, visible-wavelength Imaging Science Subsystem.

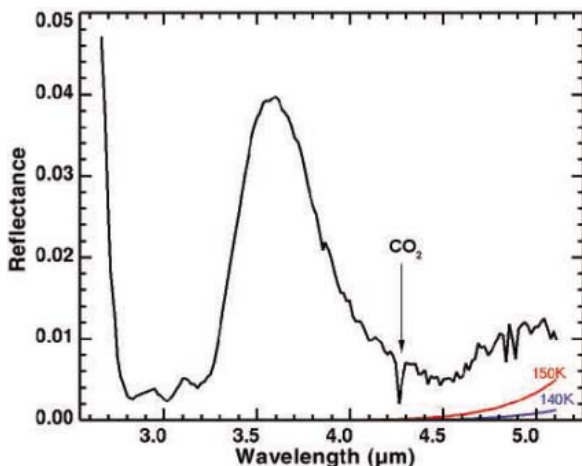


Fig. 3. Average spectrum of the tiger stripes. Note the strong CO_2 absorption near 4.26 μm . The curves labeled 140 and 150 K are the apparent reflectance that would result for a surface that had a 0.0 actual reflectance at those two temperatures.

150 μm , but grain sizes increase to 100 to 300 μm in the tiger stripes region (Figs. 1 and 2).

We found traces of free CO_2 ice, trapped CO_2 (either as a liquid or gaseous inclusion), and simple organics in the tiger stripes. Whereas the organic signatures map geologic features (Fig. 2), the close approach data for 14 July have anomalous noise that obscures spectral features with wavelengths longer than 4 μm . CO and CO_2 are molecules that we would expect to find in icy bodies formed in the Saturn system (12–17). Indeed, we

found free CO_2 ice in small amounts globally and in higher concentrations near Enceladus' south polar regions, but we found no CO.

In data taken well before the closest approach on 14 July 2005, we found in the tiger stripes region a strong signature of CO_2 with an absorption-band depth of 74%. The center wavelength of the CO_2 absorption in the tiger stripes region indicates that the CO_2 is not free ice, but rather complexed, most likely with water ice (Fig. 3). There is no evidence in our

data for free CO_2 ice in the tiger stripes. This is perhaps not surprising because the temperatures seen there by the Cassini Composite Infrared Spectrometer (CIRS) instrument (8) would cause solid CO_2 to rapidly migrate northward of the tiger stripes region to areas with colder temperatures. Some free CO_2 is indeed seen northward of the tiger stripes region in our data. Furthermore, that there is such a high abundance of complexed CO_2 in the tiger stripes suggests active replenishment, probably from ongoing geophysical activity in the region (1, 8–10).

No signature of CO ice, gas, clathrate, or any other physical form was seen in our data. Based on the data taken about 1 hour before the closest approach, an upper limit of 5 precipitable nanometers (corresponding to a column density of roughly 10^{14} molecules/ cm^2) can be placed on the amount of CO in the atmospheric column above the tiger stripes.

Another cosmochemically important compound is NH_3 . The role of NH_3 in solar system chemistry and geophysics has been extensively studied, and its role in Enceladus' geophysical activity has been widely hypothesized (3, 18–22). Unfortunately, no features due to NH_3 or its various hydrates were identified on Enceladus. To derive plausible upper limits for the abundance of NH_3 on Enceladus, we considered models of NH_3 plus water-ice mixtures. For NH_3 grain sizes similar to that of the water ice, we derived an upper limit of $\sim 1\%$. If the NH_3 -ice grains on Enceladus are larger than the water-ice grains, our modeling admits upper limits of $\sim 3\%$. NH_3 has its strongest absorptions near strong water-ice absorptions, thus reducing the sensitivity of models where NH_3 is intimately mixed with water. It is possible that small areas of pure NH_3 exist if they subtend less than 10% of a VIMS pixel, but considering all of this, the likely global upper limit to NH_3 on the surface of Enceladus is 2%. It should be noted, however, that as for CO_2 , temperatures in the area of the tiger stripes may be high enough to cause free NH_3 ice to migrate northward to areas of lower temperatures.

There are many other apparent spectral features in the VIMS data for Enceladus that require further study before an accurate assessment of their importance can be made. Of possible particular importance is a downturn in wavelengths longer than 5 μm and a possible 5.0- μm feature in the global average spectrum of Enceladus.

Disk-integrated spectra of Enceladus indicate that the water ice in Enceladus' equatorial and mid- to high-latitude regions is primarily crystalline (4, 6). Nevertheless, amorphous water ice should exist on the satellite (4). Amorphous water ice forms when it is condensed directly from the vapor to a solid at temperatures below about 100 K. If amorphous water ice is heated to 150 K, it irreversibly and exothermally

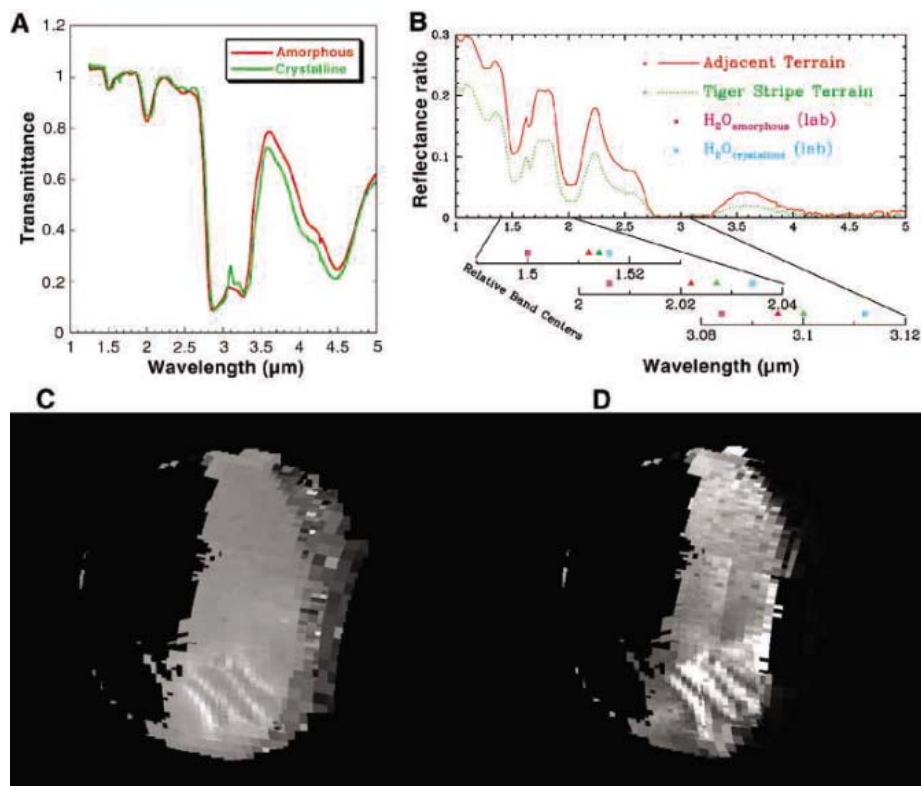


Fig. 4. (A) Spectra of crystalline and amorphous ice showing the 1.6- μm absorption band and the 3.1- μm Fresnel peak, both characteristic of crystalline ice (4). (B) Co-added spectra of the tiger stripes and the south polar region between the tiger stripes. Below the graph are the band positions for the main absorption bands at 1.5 and 2.0 μm and the Fresnel peak at 3.1 μm for the tiger stripes, the region between the tiger stripes, and amorphous and crystalline ice. The region with spectral characteristics most similar to crystalline ice is the tiger stripes. (C) A ratio of the 1.2- μm continuum to the 1.65- μm crystalline ice absorption band, showing that the tiger stripes have the deepest absorption at 1.65- μm and thus have the highest abundance of crystalline ice. (D) A ratio of the 1.2- μm continuum to the 3.1- μm Fresnel peak characteristic of crystalline water ice. The peak is highest in the tiger stripes, which is consistent with a high degree of crystallinity. The dark regions in the left part of the mosaics in (C) and (D) are due to saturated data.

converts on time scales of minutes to hours to crystalline water ice. The conversion can only be reversed by disruption of the crystal structure by bombardment of high-energy particles (23)—a process primarily limited by dose rather than by the energy spectrum of the incident particles (24). Examples of such a process can be seen on the Galilean satellites (23, 25, 26).

Enceladus orbits in the inner regions of Saturn's magnetosphere, where the particle flux is quite high. Furthermore, Enceladus may have its own magnetic field (7), which could increase the particle flux at its poles; because of this possibility, looking for amorphous ice near Enceladus' poles would be prudent.

Differences in their spectra can be exploited to search for crystalline and amorphous water ice on Enceladus (Fig. 4). The two most obvious indicators are the 1.65- μm absorption band and the 3.1- μm Fresnel reflection peak, both of which are much more prominent in crystalline ice. In addition, the central wavelengths of the absorp-

tion bands vary substantially between amorphous and crystalline water ice because of the reduced hydrogen bonding in amorphous water ice compared with that in crystalline ice (Fig. 4B). Our analysis indicates that, in a local sense (that is, confining our analysis to the south polar regions of Enceladus), crystalline ice is most abundant in the tiger stripes, whereas amorphous ice is most abundant in the south polar regions outside the tiger stripes. This is shown in the global ratio of the 1.2- μm reflectance to the 1.65- μm absorption band (Fig. 4C) and in the ratio of the 1.2- μm reflectance to the 3.1- μm peak (Fig. 4D), except that the tiger stripes are darker because the crystalline ice is brighter at 3.1 μm .

Laboratory experiments show that crystalline ice at temperatures below 100 K rapidly converts to amorphous ice in the presence of high-energy particles (24) and recrystallizes very quickly when heated to ~ 140 to 150 K (23). For geologically active, relatively hot areas such as those near Enceladus' south pole, it would be

difficult, if not impossible, to determine the time that these materials have been exposed to magnetospheric bombardment—i.e., their age. If, on the other hand, areas with a high degree of crystallinity exist in the coldest areas in the south polar region of Enceladus, they would be young, perhaps as young as a few decades (24). Further study of our data and additional observations of Enceladus' south polar region are required to address the question of age.

Despite the unambiguous detection of anomalously hot areas on Enceladus by the Cassini CIRS instrument (8), VIMS did not detect thermal emission from within the tiger stripes, mostly because the cutoff wavelength of the instrument is 5.1 μm . Co-adding spectra of the stripes to improve the signal-to-noise ratio allows us to place a robust 3σ upper limit at 140 K on the average temperature of VIMS tiger stripes pixels (27). Alternatively, a swath within the stripes can neither be wider than 135 m at the ammonia-water eutectic temperature of 173 K nor wider than ~ 20 cm at the water triple point 273 K.

References

1. C. C. Porco *et al.*, *Science* **311**, 1393 (2006).
2. W. B. McKinnon, *Rev. Geophys.* **25**, 260 (1987).
3. J. S. Kargel, S. Pozio, *Icarus* **119**, 385 (1996).
4. W. M. Grundy, M. W. Buie, J. A. Stansberry, J. R. Spencer, B. Schmitt, *Icarus* **142**, 536 (1999).
5. D. P. Cruikshank *et al.*, *Icarus* **175**, 268 (2005).
6. J. P. Emery, D. M. Burr, D. P. Cruikshank, R. H. Brown, J. B. Dalton, *Astron. Astrophys.* **435**, 353 (2005).
7. M. K. Dougherty *et al.*, *Science* **311**, 1406 (2006).
8. J. R. Spencer *et al.*, *Science* **311**, 1401 (2006).
9. C. J. Hansen *et al.*, *Science* **311**, 1422 (2006).
10. J. H. Waite Jr. *et al.*, *Science* **311**, 1419 (2006).
11. R. H. Brown *et al.*, *Space Sci. Rev.* **115**, 111 (2005).
12. J. S. Lewis, *Icarus* **15**, 174 (1971).
13. J. S. Lewis, *Science* **172**, 1127 (1971).
14. J. S. Lewis, *Sci. Am.* **230**, 51 (1974).
15. J. S. Lewis, *Annu. Rev. Phys. Chem.* **24**, 339 (1973).
16. J. S. Lewis, R. G. Prinn, *Astrophys. J.* **238**, 357 (1980).
17. J. S. Lewis, *Science* **186**, 440 (1974).
18. D. J. Stevenson, in *Uranus and Neptune*, NASA Conference Publication 2330, J. Bergstrahl, Ed. (NASA Scientific and Technical Information Branch, Washington, DC 1984), pp. 405–424.
19. D. J. Stevenson, *Nature* **298**, 142 (1982).
20. S. W. Squyres, R. T. Reynolds, P. M. Cassen, S. J. Peale, *Icarus* **53**, 319 (1983).
21. J. S. Kargel, *Earth Moon Planets* **67**, 101 (1995).
22. R. G. Prinn, B. Fegley, *Astrophys. J.* **249**, 308 (1981).
23. G. B. Hansen, T. B. McCord, *J. Geophys. Res. Planets* **109**, 1012 (2004).
24. G. Strazzulla, G. A. Baratta, G. Leto, G. Foti, *Europhys. Lett.* **18**, 517 (1992).
25. M. G. Kivelson *et al.*, *Nature* **384**, 537 (1996).
26. G. Schubert, K. K. Zhang, M. G. Kivelson, J. D. Anderson, *Nature* **384**, 544 (1996).
27. To establish upper limits on temperature, we used a Levenberg-Marquardt algorithm to fit the co-added tiger stripes spectrum to the spectrum of the interstripe region with the use of a multiplicative albedo-surrogate scaling factor and surface temperature as free parameters. The best fit temperature is indistinguishable from 0 K. We then increased the temperature of either the full pixel or a linear swath through the pixel until the quality of the fit degraded to the 3σ level and used that value for the upper limit.

Diffusive Separation of the Lower Atmosphere

Yosuke Adachi,* Kenji Kawamura, Laurence Armi, Ralph F. Keeling†

In 1826, John Dalton suggested that the composition of Earth's atmosphere could potentially change with elevation because of the separation of heavy and light molecules in Earth's gravitational field (*1*). Subsequent measurements, however, found convincing evidence of separation only above 100-km elevation, reinforcing the view that any separation effect is overwhelmed by turbulent mixing at lower elevations (*2, 3*). Here we show, by using precise measurements of the Ar/N₂ ratio, that a detectable separation effect can also occur in near-surface layers, although temperature gradients rather than gravity appear to be the main driving force.

On the nights of 25–26 February and 15–16 April 2005, we sampled air in Borrego Sink [33.22°N, 116.32°W, ~140 m above sea level (ASL)], which is a ~2-km² depression in the center of a wide desert plain, rimmed by 500- to 1500-m mountains to the north, west, and south. Samples were collected at three heights as shown in Fig. 1. On both nights, elevated Ar/N₂ ratios were observed near the surface, relative to air aloft and relative to background air (*4–6*) measured at Scripps Pier in La Jolla, CA. On 15–16 April, the Ar enrichment was much greater, ~100 per meg (1000 per meg = 1 per mil) at 4 m, and this coincided with clearer skies, lower surface winds (<~0.2 m s⁻¹ at 2 m), and greater diurnal temperature range (27°C), compared with 25–26 February (0.3 to 2.5 m s⁻¹, 14°C range). Within 3.5 hours after sunset on 15 April, a temperature inversion of 10°C had formed between the surface and 10-m elevation, and a complete cessation of surface turbulence was indicated based on a Richardson number criterion.

The two contributors that drive diffusive separation are gravity and tem-

perature; the heavier molecules diffuse toward the center of Earth's gravitational field and the cold end of a temperature gradient. Within a nocturnal surface inversion layer, both of these processes will tend to cause an accumulation of Ar near the ground. In topographic low points such as the Borrego Sink, where cold air accumulates as it flows down slope at night, the Ar-enriched surface layer will deepen due to convergence and associated uplift.

These processes can be represented in a simple model consisting of the one-dimensional diffusion equation (*7*).

$$\frac{\partial C}{\partial t} = \frac{\partial}{\partial z} \left[D \left(\frac{\partial C}{\partial z} + 10^6 \frac{\Delta M g}{RT} + \Omega \frac{dT}{dz} \right) \right] - W \frac{\partial C}{\partial z}$$

Here, *C* is δ(Ar/N₂), *t* is time, *z* is height, *D* is molecular diffusivity, Δ*M* is the molar mass difference between Ar and N₂, *g* is gravitational acceleration, *R* is the gas constant, *T* is temperature, Ω is the thermal diffusion sensitivity,

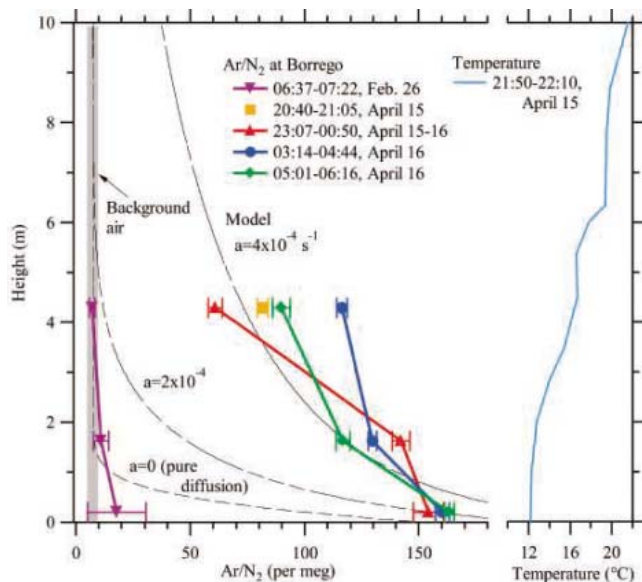


Fig. 1. Ar/N₂ ratios of air samples expressed as δ (per meg) = [(Ar/N₂)_s / (Ar/N₂)₀ - 1] × 10⁶ where (Ar/N₂)_s and (Ar/N₂)₀ are the molar ratio of the sample and an arbitrary laboratory reference, respectively. Shown are averages of 3 to 6 flask replicates, with the estimated standard error based on replicate agreement. Also shown are numerical solutions to the one-dimensional model for an elapsed time of 3 hours and the temperature profile at 22:00 on 15 April. The model assumes $dT/dz = 1^\circ\text{C m}^{-1}$ and $\Omega = 243$ per meg $^\circ\text{C}^{-1}$. Times are given in local standard time. See (*5*) for analysis procedures; an aspirated radiation shield was used to avoid thermal separation at the intake (*6*).

and $W = az$ (uplifting speed), where *a* (measured in s⁻¹) is the convergence. The model is run with an initial condition corresponding to a well-mixed atmosphere at sunset and yields reasonable agreement with the observations at the two higher sampling heights on 15–16 April after an elapsed time of 3 hours using $a \sim 4 \times 10^{-4} \text{ s}^{-1}$. The latter corresponds to $W = 0.16 \text{ cm s}^{-1}$ at 4 m, which seems plausible given the conditions on 15–16 April. For a given value of Ω (constant at a given temperature), the relative magnitude of the thermal and gravimetric contributions depends on the temperature gradient dT/dz . On 15–16 April, gravity contributed ~17% to the total separation.

The model overpredicts the Ar/N₂ gradient below 2 m, which may be because of small-scale turbulence generated by the sampling itself, or because of the model's neglecting near-surface shear. The model also predicts that Ar/N₂ ratios should increase continuously through the night, whereas the observations indicate that a quasi-steady state was achieved by ~3 hours after sunset. The steady state could be explained if the accumulation in the sink were balanced by horizontal advection, once the pool of cold air in the sink deepened sufficiently. Indeed, on the east of Borrego Sink is an opening that leads to the Borrego Sink Wash and lower elevations, where the cold, Ar-enriched air presumably drains. Because of its simplicity, the model doesn't capture such details of the three-dimensional velocity field. The model's principal value is to illustrate the plausibility of obtaining signals of the general magnitude observed.

We have observed a tendency for Ar to accumulate in a topological low spot under a strong nocturnal inversion and low winds. We expect this tendency occurs for other heavy constituents such as Kr and Xe and, although not previously reported, this must be a general feature of the atmosphere.

References and Notes

1. J. Dalton, *Philos. Trans. R. Soc. London* **116**, 174 (1826).
2. B. A. Mirtov, *Gaseous Composition of the Atmosphere and its Analysis* (Israel Program for Scientific Translation, Jerusalem, Israel, 1964).
3. R. H. Bieri, M. Koide, E. A. Martell, T. G. Scholz, *J. Geophys. Res.* **75**, 6731 (1970).
4. M. Battle *et al.*, *Geophys. Res. Lett.* **30**, 1786 (2003).
5. R. F. Keeling *et al.*, *Tellus B* **56**, 322 (2004).
6. T. W. Blaine, thesis, University of California, San Diego (2005).
7. J. P. Severinghaus, A. Grachev, M. Battle, *Geochim. Geophys. Geosyst.* **2**, 2000GC000146 (2001).
8. We thank J. Severinghaus and two anonymous reviewers for suggestions. Support for this work came from NSF (grant 03-30093), NOAA Office of Global Programs, and the Comer Science and Education Foundation.

13 October 2005; accepted 23 January 2006
10.1126/science.1121312

Scripps Institution of Oceanography, 9500 Gilman Drive, La Jolla, CA 92093-0244, USA.

*Present address: Department of Applied Chemistry, Keio University, Yokohama 223-8522, Japan.

†To whom correspondence should be addressed. E-mail: rkeeling@ucsd.edu

Structure of the Hydrophilic Domain of Respiratory Complex I from *Thermus thermophilus*

Leonid A. Sazanov* and Philip Hinchliffe

Respiratory complex I plays a central role in cellular energy production in bacteria and mitochondria. Its dysfunction is implicated in many human neurodegenerative diseases, as well as in aging. The crystal structure of the hydrophilic domain (peripheral arm) of complex I from *Thermus thermophilus* has been solved at 3.3 angstrom resolution. This subcomplex consists of eight subunits and contains all the redox centers of the enzyme, including nine iron-sulfur clusters. The primary electron acceptor, flavin-mononucleotide, is within electron transfer distance of cluster N3, leading to the main redox pathway, and of the distal cluster N1a, a possible antioxidant. The structure reveals new aspects of the mechanism and evolution of the enzyme. The terminal cluster N2 is coordinated, uniquely, by two consecutive cysteines. The novel subunit Nqo15 has a similar fold to the mitochondrial iron chaperone frataxin, and it may be involved in iron-sulfur cluster regeneration in the complex.

Complex I [dihyronicotinamide adenine dinucleotide (NADH)–ubiquinone oxidoreductase, EC 1.6.5.3] is the first enzyme of the mitochondrial and bacterial respiratory chains. It catalyzes the transfer of two electrons from NADH to quinone, coupled to the translocation of about four protons across the membrane, helping to provide the proton-motive force required for the synthesis of adenosine triphosphate (ATP) (1, 2). The mitochondrial enzyme contains 46 different subunits (3) and is one of the largest known membrane protein complexes. The prokaryotic enzyme is simpler and has 14 subunits with a combined molecular mass of about 550 kD. Analogs of all subunits of bacterial complex I (also referred to as NDH-1) are found in the mitochondrial enzyme (1), and they contain equivalent redox components (2). Mitochondrial and bacterial enzymes have a characteristic L-shaped structure, with the hydrophobic arm embedded in the membrane and the hydrophilic peripheral arm protruding into the mitochondrial matrix or the bacterial cytoplasm (4–6). Thus, NDH-1 is a “minimal” model of complex I. Until now, its atomic structure and the mechanism of electron transfer have not been known. Because of its central role in respiration, mutations in subunits of complex I can lead to many human neurodegenerative diseases (7). Also, complex I has been suggested to be a major source of reactive oxygen species (ROS) in mitochondria, which can damage mitochondrial DNA and may be one of the causes of aging (8).

The hydrophilic domain of complex I contains the NADH-binding site, the flavin-mononucleotide (FMN), and eight or nine iron-sulfur (Fe-S) clusters (2, 9), whereas the proton-pumping machinery is probably in the membrane arm. FMN accepts two electrons simultaneously (as a hydride) from NADH and transfers them one at a time to one-electron carriers, the Fe-S clusters. These subsequently reduce membrane-embedded quinone to quinol in two one-electron steps. In models of the subunit arrangement (10–13), subunits Nqo1 to 3 form the dehydrogenase domain, and subunits Nqo4 to 6 and Nqo9 connect it to the membrane arm (*Thermus* nomenclature is used throughout, with bovine mitochondrial nomenclature shown in parentheses in section headings). Fe-S clusters identified by electron paramagnetic resonance spectroscopy (EPR) include the binuclear clusters N1a and N1b, and the tetranuclear clusters N2, N3, N4, N5, N6a, and N6b (2, 9). Complex I from *Thermus thermophilus* and from some other bacteria contains the additional tetranuclear cluster N7 (14). At pH 7, the two-electron midpoint redox potential of NADH is about –320 mV, of ubiquinone +110 mV (*Thermus* uses menaquinone, –80 mV), and of FMN about –340 mV. The one-electron potential of cluster N1a is about –370 mV and of cluster N2 about –100 mV, and all the other clusters appear to be isopotential at about –250 mV (2, 9). It is likely that cluster N3 accepts electrons from FMN, whereas the high-potential cluster N2 reduces the quinone at the interface with the membrane domain (1, 2, 9).

We have solved the crystal structure of the hydrophilic domain (peripheral arm) of complex I from *T. thermophilus* HB-8. This subcomplex consists of seven known hydrophilic subunits (Nqo1 to 6 and Nqo9) and a previously un-

known subunit, which we have identified as part of the complex and named Nqo15 (15, 16). The domain contains all the redox centers and represents more than half the molecular mass of the entire complex (280 out of 520 kD).

Structure Determination and Overall Architecture

Two heavy atom derivatives were useful in providing phase information [in addition to previous Fe-edge data (15)], so that, after density modification, the resolution could be extended to 3.3 Å (17). Side chains became clearly visible (fig. S1), and the atomic model was built into the electron density. The model was refined to $R_{\text{cryst}} = 26.5\%$ and $R_{\text{free}} = 29.8\%$, with good stereochemistry (table S1). Some N- and C-terminal residues, as well as a few external loops, were not observed in the density and so were not modeled (17). The current model contains 2333 residues (out of 2510 predicted from the sequences), 9 Fe-S clusters, and 1 FMN molecule.

In the overview of the structure shown in Fig. 1A, the peripheral arm of complex I is a Y-shaped assembly about 140 Å high. One uppermost tip of the molecule is formed by the subunits Nqo1 and Nqo2, and the other by the C-terminal domain of Nqo3. The main stem is formed by the N-terminal domain of Nqo3 and the connecting subunits. Its lower part consists of subunits Nqo4 and Nqo6 (which coordinates the terminal Fe-S cluster N2), and it forms an interface with the membrane domain. The overall arrangement of subunits and clusters is consistent with our previous interpretation, apart from the assignment of clusters N4 and N5 in subunit Nqo3 (15), which are now reversed (Fig. 1B). The FMN is coordinated by subunit Nqo1 at the deep end of a solvent-exposed cavity containing an apparent NADH-binding site. FMN is within 14 Å, the maximum distance for physiological electron transfer (18), of both tetranuclear cluster N3 and binuclear cluster N1a. Thus, electrons can be transferred effectively from the flavin to cluster N3 and then, as judged by shortest edge-to-edge distances (Fig. 1B), through a series of five isopotential clusters to the terminal cluster N2, located next to the likely quinone-binding site. This pathway, NADH-FMN-N3-N1b-N4-N5-N6a-N6b-N2-quinone, is likely to be the main route for electron transfer within the enzyme. Cluster N7, in subunit Nqo3, is too far from the other clusters to accept electrons effectively. As proposed (15), binuclear cluster N1a may act as an antioxidant.

At the interface with the membrane domain, subunit Nqo6 contains a rigid (as judged from B-factors) N-terminal α helix H1 (Fig. 1A), involved in crystal contacts. This amphipathic helix protrudes about 25 Å from the complex and has a relatively polar upper surface and a

Medical Research Council Dunn Human Nutrition Unit, Wellcome Trust/MRC Building, Hills Road, Cambridge CB2 2XY, U.K.

*To whom correspondence should be addressed. E-mail: sazanov@mrc-dunn.cam.ac.uk

hydrophobic lower surface. It is, therefore, likely to extend into the surface region of the membrane domain. This interpretation is consistent also with the fit of the structure into a low resolution model of the intact *Escherichia coli* complex I, obtained by cryo-electron microscopy (19). Thus, helix H1 can help in the orientation of the model relative to the intact complex; the membrane domain is likely to extend in the direction of the N terminus of this helix (to the right in Fig. 1A). Extensive intersubunit contacts are present in the structure (table S2) and are listed in (17).

Protein Subunits and Redox Centers

Subunit Nqo1 (51 kD). This subunit contains the NADH-binding site, the primary electron acceptor FMN, cluster N3, and as a whole, it has no significant sequence similarity to any proteins of known structure. The subunit can be separated roughly into four domains (Fig. 2A): an N-terminal domain (residues 7 to 72, *Thermus* numbering throughout) ending with a glycine-rich loop, followed by a Rossman-fold domain (73 to 240), a ubiquitin-like domain (241 to 335) and a C-terminal four-helical bundle containing cluster N3 (336 to 438).

The N-terminal domain wraps around the Rossman-fold domain on the surface of the complex and contains three short α helices. Searches with SSM [secondary structure matching (20)] and DALI (21) at the European Bio-

informatics Institute servers did not reveal significant structural analogs of this domain. Below and in (17), alignments performed with SSM are listed, although DALI was used for the initial searches. The N-terminal domain ends with a glycine-rich loop (residues 62 to 72) that was previously suggested to be involved in binding the adenosine diphosphate (ADP) moiety of NADH, as part of a Rossman nucleotide-binding fold (1). Indeed, the Rossman fold-like domain is found after this loop, but it is not a classical Rossman fold and it appears to bind FMN, and presumably NADH as well, in a novel mode. Instead of a six-stranded parallel β sheet with a 6, 5, 4, 1, 2, 3 order of strands (22), there are only four strands in the order 4, 1, 2, 3, flanked by α helices (Fig. 2A).

In a classical Rossman fold, the loop between the first strand and nascent helix is glycine rich and binds one of the nucleotide phosphate groups. However, in Nqo1, this loop (residues 93 to 102) does not contain glycine; it is mostly shielded from the solvent and interacts with the buried edge of the isoalloxazine ring of FMN. Flavin is bound at the deep end of a solvent-exposed cavity [previously called channel 1 (15)], which contains an apparent binding site for NADH (Fig. 3A). FMN interacts mostly with strand four of the parallel β sheet and with loops emerging from strands one and three. It is held in place by a hydrogen-bonding network

(17) and interacts mainly with residues from a previously predicted flavin-binding domain [residues 175 to 220 (1)], but also with residues among those previously suggested to bind NADH [64 to 70 and 90 to 100 (1)].

The FMN cavity can accommodate one NADH molecule comfortably, as indicated by manual docking (not shown on figure), and the residues likely to interact with NADH are shown in Fig. 3A. The invariant residues Glu⁹⁷ and Tyr¹⁸⁰ are exposed to the solvent at the deep end of the cavity and can interact with the nicotinamide carboxamide. Residues 66 to 69 from the glycine-rich loop can bind the phosphate groups of the substrate. Consistently, our preliminary data obtained from NADH-containing crystals (at about 5 Å resolution), show a strong additional electron density in this area. The invariant Glu¹⁸⁵ (and/or Glu¹⁸⁴) can make hydrogen bonds to the ribose of the adenosine moiety, similar to the aspartate residue conserved in other dehydrogenases (22). Notably, the aromatic rings of Phe⁷⁸ and Phe²⁰⁵, near the entrance to the cavity, are nearly parallel and about 8.5 Å apart. These residues are well positioned to coordinate the adenine ring between side chains, by aromatic stacking interactions. If NADH binds as proposed, its nicotinamide ring will be adjacent to the isoalloxazine ring of FMN, which allows hydride transfer. Similar elements of NAD(P)(H) binding are found in other nucleotide-binding proteins, but in different structural environments. All the residues involved in binding FMN and NADH are strongly conserved, which suggests that the binding pocket is conserved. Thus, in complex I, uniquely, a Rossman-fold domain has evolved to bind both FMN and NADH, by the addition of an extra glycine-rich loop at the N terminus.

The subsequent ubiquitin-like domain has a structural role, but it may also be involved in degradation of complex I, as the domain is exposed at the surface near the tip of the molecule (17). Finally, the C-terminal domain coordinates cluster N3 and consists of a four-helix bundle. Although this fold is quite common [fold a.24 in SCOP (23)], it has not been observed previously to bind Fe-S clusters. The [4Fe-4S] cluster is coordinated in the cubane geometry by Cys³⁵⁴, Cys³⁵⁶, and Cys³⁵⁹ from the loop between the first and second helices of the bundle and by Cys⁴⁰⁰ from the loop between the third and fourth helices (fig. S2A).

Subunit Nqo2 (24 kD). This subunit can be divided into two domains: an N-terminal four-helical bundle (residues 3 to 75) (17) and a thioredoxin-like C-terminal domain (residues 76 to 180) (Fig. 2B). The N-terminal domain is involved in interactions with subunits Nqo1 and Nqo3. The C-terminal domain coordinates the binuclear cluster N1a and consists of a mixed β sheet flanked by two α helices. It is very similar to the thioredoxin-like [2Fe-2S] ferredoxin from *Aquifex aeolicus* [Protein Data Bank

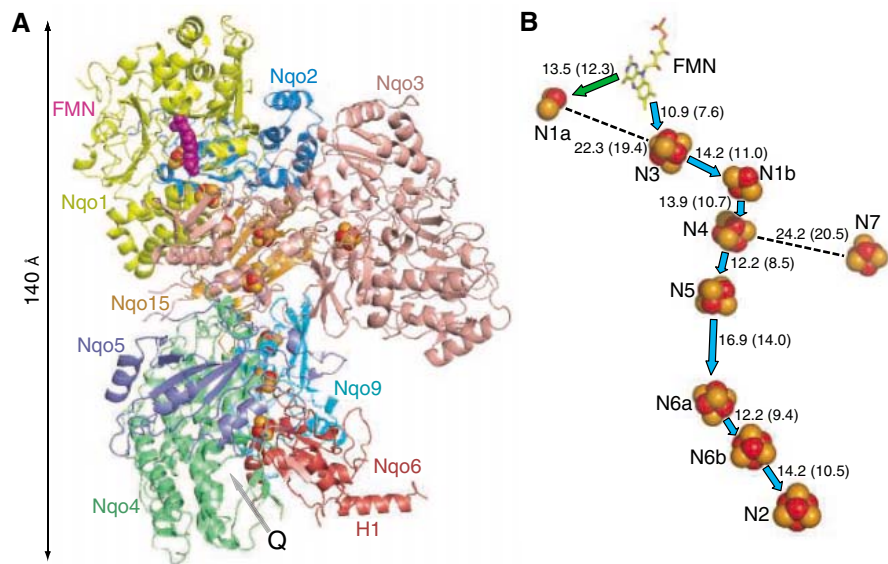


Fig. 1. Architecture of the hydrophilic domain of *T. thermophilus* complex I. **(A)** Side view, with the membrane arm likely to be beneath and extending to the right, in the direction of helix H1. Each subunit is colored differently; FMN is shown as magenta spheres, metal sites as red spheres for Fe atoms and yellow spheres for S atoms. A possible quinone-binding site (Q) is indicated by an arrow. **(B)** Arrangement of redox centers. The overall orientation is similar to that in (A), tilted to provide an improved view of the FMN and the clusters. Cluster N1a is in subunit Nqo2; N3 and FMN in Nqo1; N1b, N4, N5, and N7 in Nqo3; N6a/b in Nqo9; and N2 in Nqo6. The main pathway of electron transfer is indicated by blue arrows, and a diversion to cluster N1a by a green arrow. The distances between the centers given in angstroms were calculated both center-to-center and edge-to-edge (shown in parentheses). Clusters N3 and N4 are separated by 17.6 Å (13.8 Å edge-to-edge), and clusters N1b and N5 by 19.2 Å (16.7 Å edge-to-edge).

(PDB) identifier 1f37 (24), root mean square deviation (RMSD) = 1.7 Å over 80 C_α atoms, with 19% sequence identity, including cluster-ligating cysteines]. This similarity was noted previously from sequence comparisons (25). The stability of the fold is enhanced by a disulfide link between Cys¹⁴⁴ from the last β strand and Cys¹⁷² from a surface-exposed loop.

Cluster N1a is coordinated by cysteines 83, 88, 124, and 128. The cluster is only about 12 Å from the isoalloxazine ring, and so can accept electrons from FMN, but cannot pass them on directly to the nearest cluster N3, which is 19 Å away. Polar residues in the environment of this and other clusters are listed in (17). Such residues, located near the clusters, could help adjust redox potentials (26, 27). N1a appears to have a more hydrophobic environment than other clusters, which may explain its low midpoint potential.

Subunit Nqo3 (75 kD). This is the largest subunit in complex I, comprising two main parts, an N-terminal [FeFe]-hydrogenase-like domain (residues 1 to 240) and a domain similar to molybdopterin-containing enzymes (residues 241 to 767, subdomains I to IV) (Fig. 2C).

As predicted from sequence similarities (1, 25), the N-terminal domain of Nqo3 is similar to the N-terminal domain of [FeFe]-hydrogenases; residues 1 to 240 align with an RMSD = 2.0 Å and 23% sequence identity over 177 C_α atoms, with residues 1 to 206 from [FeFe]-hydrogenase [PDB 1feh (28)]. The coordination of clusters N1b, N4, and N5 within Nqo3 (fig. S2C) is similar (in its ligands and the distances between clusters) to the coordination of clusters FS2, FS4B, and FS4C, respectively, in the [FeFe]-hydrogenase (28). In Nqo3, binuclear cluster N1b is coordinated in a [2Fe-2S] ferredoxin-like fold (28) by cysteines 34, 45, 48, and 83. Tetranuclear cluster N4 is coordinated in a 2 × [4Fe-4S] ferredoxin-like fold (28) by cysteines 181, 184, 187, and 230 (fig. S2C). In [FeFe]-hydrogenases, this fold contains an additional tetranuclear cluster FS4A, which is absent from complex I, although the fold is conserved.

The tetranuclear cluster N5 is coordinated by Cys¹¹⁹, Cys¹²², Cys¹²⁸, and His¹¹⁵ from a loop between two α helices (Fig. 3B). Similar to the [FeFe]-hydrogenase, the N^ε atom of His¹¹⁵ is a ligand for iron from cluster N5, in contrast to other known examples where N^δ is the coordi-

nating ligand (28). It has been discussed that the histidine ligand may tune the midpoint potential (28). In complex I, cluster N5 belongs to the equipotential group of clusters, but its EPR properties are unusual, as it exhibits very fast spin relaxation and exists in a mixed high-spin ground state (29). Cluster FS0 in nitrate reductase A is also ligated by three cysteines and one histidine (26) and has a fast spin relaxation and an unusual high-spin ground state (30). Thus, it is likely that the unusual properties of cluster N5 are due to its histidine ligation. Several polar residues are within hydrogen-bonding distances to the cluster [Fig. 3B and (17)]. Such an environment in the protein interior may indicate that cluster N5 is not simply a “stepping stone” in the electron transfer pathway, but that it could have an additional role in the mechanism of complex I.

Contrary to predictions (25), the C-terminal domain of Nqo3 (residues 241 to 767) does not have any structural similarity to the C-terminal active-site domain of [FeFe]-hydrogenases. However, it is clearly similar to a family of molybdenum (molybdopterin guanine dinucleotide, MGD) cofactor-containing enzymes.

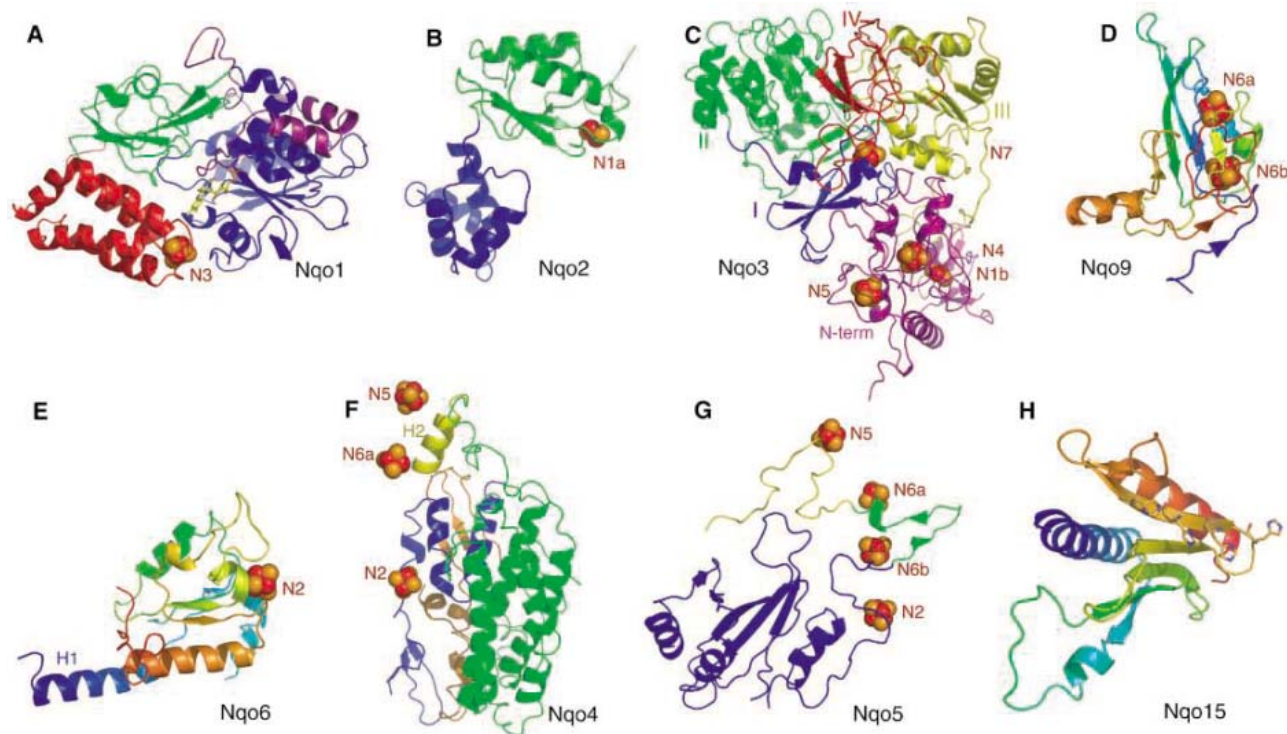


Fig. 2. The folds of individual subunits. Fe-S centers are shown as red spheres for Fe atoms and yellow spheres for S atoms, with cluster names in red. Subunits are not drawn to the same scale. (A) Nqo1. Its N-terminal domain is in purple, a Rossman-fold domain in blue, an ubiquitin-like domain in green, and the C-terminal helical bundle, coordinating cluster N3, in red. FMN is shown in stick representation. (B) Nqo2. The N-terminal helical bundle is shown in blue, the thioredoxin-like domain coordinating cluster N1a in green. (C) Nqo3. The N-terminal [FeFe]-hydrogenase-like domain coordinating clusters N1b, N4, and N5 is magenta, subdomains of the C-terminal molybdoenzyme-like domain are shown in I (coordinating cluster N7), blue; II, green; III, yellow; and IV,

red. (D) Nqo9, coordinating clusters N6a and N6b, is shown in rainbow representation, colored blue to red from N to C terminus. (E) Nqo6, coordinating cluster N2, is shown in rainbow representation, with helix H1 indicated. (F) Nqo4. The N-terminal αβ domain is shown in blue, the α-helical bundle in green, the extended helix H2 in yellow, and the C-terminal αβ domain in orange. Clusters are shown for orientation only. (G) Nqo5. The N-terminal αβ domain interacting with Nqo4 is shown in blue, the domain interacting with Nqo9 in green, and the C-terminal loop interacting with Nqo3 in yellow. Clusters are shown for orientation only. (H) Nqo15, shown in rainbow representation. The histidines exposed inside the putative iron storage cavity are shown.

For example, residues 241 to 767 of Nqo3 superimpose with nitrate reductase [PDB 2nap (31), RMSD = 2.7 Å and 18% sequence identity over 428 C_α atoms]. The alignments include the position and Cys ligands of cluster N7, matching the analogous [4Fe-4S] cluster in molybdopterin-containing enzymes. Weak sequence homology with molybdopterin-containing enzymes in this region was noted previously (32).

The C-terminal domain of Nqo3 can be separated into four subdomains similar to those of nitrate reductase (31): They are domains I (residues 241 to 308), II (309 to 373 and 540 to 670), III (374 to 539), and IV (671 to 767). Domain I coordinates cluster N7, in a mostly hydrophobic environment. The related domains II and III each resemble a Rossman fold and consist mostly of a parallel five-stranded β sheet flanked by helices on each side. These two domains face each other, with the edges of β sheets creating a cavity in the middle. In nitrate reductase, this cavity is occupied by the MGD cofactor. In Nqo3, the cavity is capped

by domain IV, which is connected to domain II by a long, isolated β strand-type segment (residues 673 to 691), running over the surface of the protein. Domain IV has a mostly irregular structure, with one antiparallel β sheet. Its analog in nitrate reductase also acts as a lid for the MGD cavity. However, complex I does not contain a molybdenum cofactor. The NAD⁺-reducing formate dehydrogenase complex from *Ralstonia eutropha* includes an MGD-containing analog of the full-length Nqo3 (subunit FdsA), as well as analogs of Nqo1 and Nqo2 (33). This and similar enzymes could share a common ancestor with complex I, and it appears that the C-terminal part of Nqo3 evolved from an MGD-containing ancestor, after losing the molybdenum cofactor. However, cluster N7, which is too far away from the main redox chain to participate in electron transfer, has been retained in *T. thermophilus* and some other bacteria, probably because it confers structural stability on the fold in domain I. Sequence similarities indicate that the fold of the Nqo3 subunit is conserved in other species,

although most prokaryotes and all eukaryotes have lost cluster N7.

The functional role of the C-terminal domain of Nqo3 is unclear. Upon reduction with NADH, a large conformational change in *E. coli* complex I (and specifically in Nqo3) to an “open,” expanded conformation was observed (34). It is conceivable that, in an open conformation, the lid formed by domain IV moves, which provides access to the cavity between domains II and III. The B-factors show that the C-terminal part of Nqo3 is one of the most flexible areas of the complex. In the structure described here (presumably the oxidized “closed” conformation), there is a small cavity in the protein surface near His⁵⁹¹, corresponding to the edge of the MGD cavity in nitrate reductase. No effectors are known to bind in this area. The Nqo3 cavity is too far from the main redox chain for electron transfer, and there is no obvious second NAD(H)-binding site elsewhere in the structure. Therefore, the suggestion that complex I has two different catalytic binding sites for NAD(H), with the second site operating during reverse electron flow (35), is inconsistent with the structure. Observed kinetic differences (35) may be due to conformational changes in complex I. However, because the former MGD-binding site is present, it is conceivable that NAD(H) or another effector binds to Nqo3 in a regulatory role, especially in an “open” conformation.

Subunit Nqo9 (TYKY). This subunit coordinates the tetranuclear clusters N6a and N6b, which follow cluster N5 in the redox chain. As predicted from sequence comparisons (1), the fold (Fig. 2D) is similar to that of the 2 × [4Fe-4S] ferredoxin family (17). The clusters are linked by short α helices, so that cluster N6a is coordinated by cysteines 53, 56, 59, and 108, and cluster N6b is coordinated by cysteines 63, 98, 101, and 104 (fig. S2D), with several polar residues nearby (17). We propose that this naming convention should be used for all N6a/b clusters in complex I from other species. Residues at the N and C termini of Nqo9 (not in the ferredoxin fold) are involved in contacts with other subunits, mainly Nqo6. Overall, the role of this subunit appears to provide a “connecting chain” of two clusters between cluster N5 and the terminal cluster N2, and to stabilize the structure of the complex by interacting with other subunits (Fig. 1 and table S2).

Subunits Nqo4 (49 kD) and Nqo6 (PSST). As expected from their similarity to subunits of [NiFe]-hydrogenases, these subunits interact extensively; hence, they are discussed together. Subunit Nqo6 superimposes with the N-terminal part (coordinating the proximal cluster) of the small subunit of the [NiFe]-hydrogenase from *Desulfovibrio gigas* [PDB 2frv (36), RMSD = 2.8 Å and 24% sequence identity over 102 C_α atoms]. The fold consists of a parallel β sheet flanked by α helices, resembling a flavodoxin (36). Notably, the extended N-terminal helix

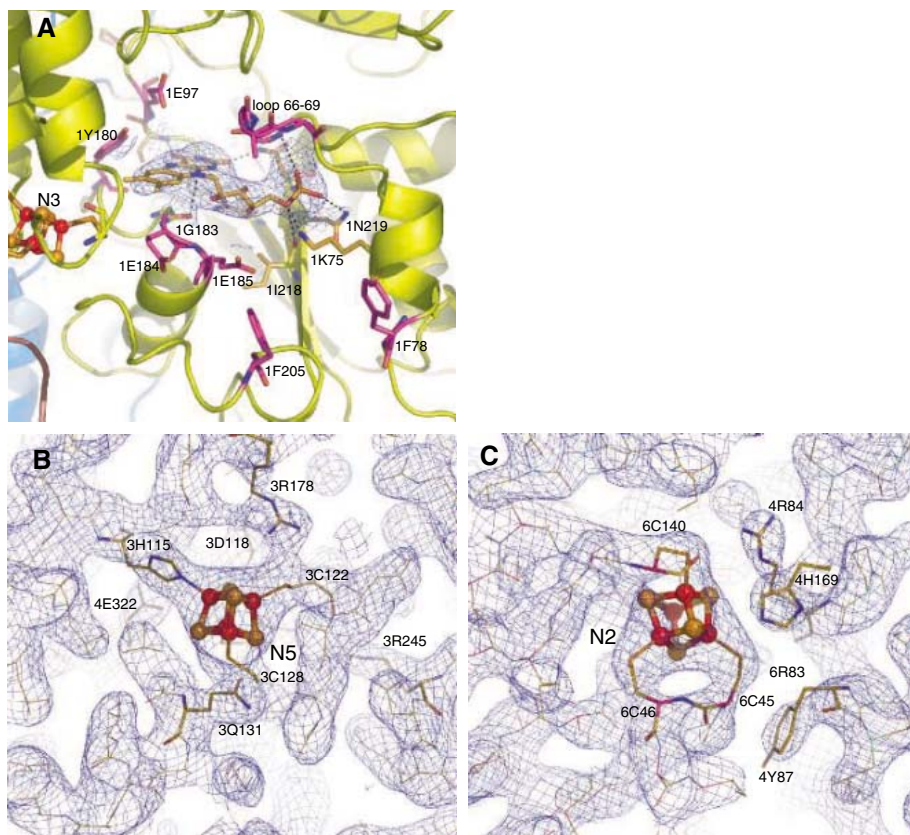


Fig. 3. The environments of the FMN-binding site and of selected Fe-S clusters. **(A)** The binding site for FMN and NADH, viewed from the solvent-exposed side. Residues involved in FMN binding are shown in stick representation with carbon in yellow and hydrogen bonds as dotted lines. Residues likely to be involved in NADH binding are shown in stick representation, with carbon in magenta. Prefixes to residue names indicate the subunit number. Cluster N3 is visible to the left. Subunits are colored as in Fig. 1. A σ_A -weighted $2F_{\text{obs}} - F_{\text{calc}}$ map contoured at 1σ is shown around the FMN. **(B)** Cluster N5 and **(C)** cluster N2. Cluster ligands and polar residues nearby are shown. The backbones of subunits are colored as in Fig. 1. Electron density is from a σ_A -weighted $2F_{\text{obs}} - F_{\text{calc}}$ map contoured at 1σ . Clusters are shown as spheres of 0.3 van der Waals radius.

H1 found in Nqo6 (Figs. 1 and 2E) is absent from the hydrogenase. The fold at the interface of Nqo6 and Nqo4 and the relative positions of these subunits are similar to the arrangement of small and large subunits in the hydrogenase. Similar to the proximal cluster in the hydrogenase, cluster N2 is coordinated only within Nqo6, but is at the interface with Nqo4. One of the four cysteine ligands of the hydrogenase proximal cluster is not conserved in complex I, which has instead two invariant adjacent cysteines, ${}_6\text{Cys}^{45}$ and ${}_6\text{Cys}^{46}$ (the prefix indicates subunit number). As there is no previous example in the PDB of an Fe-S cluster coordinated by two consecutive cysteines, it has been proposed that the fourth ligand may be provided by Nqo4, although mutagenesis indicated otherwise (37). Cluster N2 is coordinated by ${}_6\text{Cys}^{45}$ and ${}_6\text{Cys}^{46}$, which are in the first turn of a helix, connected through a β strand to helix H1. The coordination is completed by ${}_6\text{Cys}^{111}$ and ${}_6\text{Cys}^{140}$ (Fig. 3C). The Chi-1 angles of ${}_6\text{Cys}^{45}$ and ${}_6\text{Cys}^{46}$ deviate from optimal values, and the experimental electron density connecting these ligands with cluster N2 is noticeably lower than for other cysteines, which may reflect a suboptimal geometry and associated higher mobility.

Cluster N2 has also probably the most polar environment of all complex I clusters. It is hydrogen-bonded with the conserved residues ${}_4\text{Arg}^{84}$ and ${}_4\text{His}^{169}$ (similar to Arg^{63} and His^{219}

in the hydrogenase) and is about 4 Å from ${}_6\text{Arg}^{83}$. Five backbone amides are also within NH-S hydrogen bond distance. It has been suggested that an increase in the number of such bonds and interactions with backbone amide dipoles (27), as well as interactions with polar head groups (26), leads to higher redox potentials. Most other clusters in the structure are involved in two to four interactions with backbone amides. The combined effect of interactions with the backbone and with polar head groups could account for the high redox potential of N2 relative to other clusters. Mutations of ${}_4\text{Arg}^{84}$ and ${}_4\text{His}^{169}$ analogs led to an apparent loss of cluster N2 with retention of activity (38). In view of the structure, it is more likely that the cluster was retained, but with the redox potential lowered below the detection level. N2 is only 8 Å from the membrane domain interface, but is, as are all the clusters, shielded from the solvent.

Subunit Nqo4 superimposes with the large subunit of the [NiFe]-hydrogenase [PDB 2frv (36), RMSD = 2.2 Å and 18% sequence identity over 280 C_α atoms]. The alignment includes N- and C-terminal $\alpha\beta$ -type domains (residues 35 to 106 and 334 to 409, respectively) and a very long four-helix bundle (residues 107 to 320, Fig. 2F). A few short helices, a β sheet, and less regular segments in the hydrogenase are absent from Nqo4. Some of

these areas are occupied by subunit Nqo5, without structural similarity to the hydrogenase. The location of a Ni-binding site in the hydrogenase is conserved in complex I, adjacent to cluster N2 and partly exposed toward an elongated cavity at the interface with the membrane domain, in the cleft between subunits Nqo4 and Nqo6 (Fig. 4, A and B). Judging from this location, this cavity is probably the binding site for a quinone, consistent with the observation that a semiquinone species forms within 12 Å of cluster N2 (39). Mutations of analogs of the conserved residues ${}_4\text{Asp}^{401}$ and ${}_4\text{Val}^{403}$, which face the cavity, lead to resistance to quinone-like inhibitors (38, 40). The hydroxyl of invariant ${}_4\text{Tyr}^{87}$ also faces the cavity, and is 8 Å from cluster N2 and 6 Å from the sulfur atom of its ligand ${}_6\text{Cys}^{45}$ (Fig. 3C). Mutation of this tyrosine in *Yarrowia lipolytica* completely abolished the activity (38). Therefore, the quinone head group is likely to interact with these residues and, possibly, also with exposed ${}_4\text{Arg}^{42}$ and ${}_4\text{Arg}^{350}$. Most of the other residues lining the cavity are hydrophobic, which allows it to accommodate part of the isoprenoid tail, although most of the tail is probably in the membrane domain. Thus, the structure confirms suggestions that the quinone-binding site evolved from the Ni-containing active center of the hydrogenase (38).

The interface with the membrane domain is mostly hydrophobic near helix H1 of Nqo6, but comprises a mixture of hydrophobic and acidic residues in the area of subunit Nqo4 (Fig. 4B). This suggests that binding of the peripheral arm of complex I to the membrane domain may involve both hydrophobic and polar interactions.

Notably, helix H2 (residues 321 to 333), which is absent from the hydrogenase, is extended far outside the main body of Nqo4, approaching clusters N5 and N6a (Fig. 2F). The sequence in this region is highly conserved, including the invariant residues ${}_4\text{Glu}^{322}$ and ${}_4\text{His}^{327}$, which interact (17) with clusters N5 and N6a, respectively (Fig. 3B and fig. S2D). Mutation of ${}_4\text{His}^{327}$ led to a 50% loss of activity, indicating an important functional role for this unusually arranged helix (38).

Subunit Nqo5 (30 kD). The N-terminal domain of this subunit (residues 1 to 153) wraps around Nqo4 on one side, and the subunit interacts also with Nqo9 via a two-stranded β sheet (residues 154 to 171) and with Nqo3 via an extended C-terminal loop (residues 172 to 196) (Figs. 1A and 2G; table S2). The main fold consists of a five-stranded mixed β sheet (interacting with a β sheet in Nqo4), flanked on the outside by α helices. One possible role for Nqo5 appears to be in the stabilization of the complex. Mutation in *Yarrowia* of the invariant ${}_4\text{Arg}^{409}$, which in *Thermus* is involved in a salt bridge with the invariant ${}_5\text{Asp}^{120}$, led to destabilization of the enzyme (41).

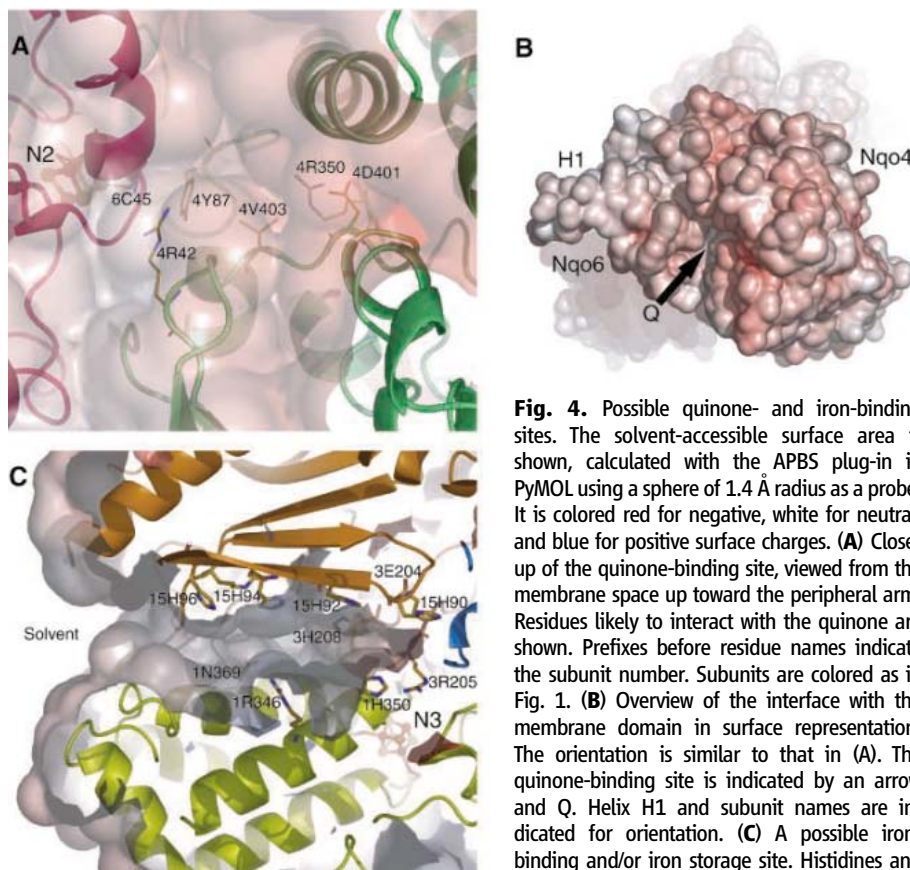


Fig. 4. Possible quinone- and iron-binding sites. The solvent-accessible surface area is shown, calculated with the APBS plug-in in PyMOL using a sphere of 1.4 Å radius as a probe. It is colored red for negative, white for neutral, and blue for positive surface charges. (A) Close-up of the quinone-binding site, viewed from the membrane space up toward the peripheral arm. Residues likely to interact with the quinone are shown. Prefixes before residue names indicate the subunit number. Subunits are colored as in Fig. 1. (B) Overview of the interface with the membrane domain in surface representation. The orientation is similar to that in (A). The quinone-binding site is indicated by an arrow and Q. Helix H1 and subunit names are indicated for orientation. (C) A possible iron-binding and/or iron storage site. Histidines and other polar residues lining the cavity are shown.

Subunit Nqo15. This 129-residue protein [National Center for Biotechnology Information (NCBI) GenInfo (GI) identifier 55771878] is the first subunit of bacterial complex I identified in addition to the 14 conserved subunits (16). Nqo15 is bound to the side of the complex near the N terminus of Nqo3, where it interacts with subunits Nqo3, Nqo2, Nqo1, Nqo9, and Nqo4 (Fig. 1A and table S2). Without Nqo15, this region would be rather narrow compared with the rest of the structure. Thus, one of its probable functions is to stabilize the complex. Unexpectedly, the fold of Nqo15 was found to be similar to the unique fold of the frataxin family (Fig. 2H). Despite the low sequence similarity, Nqo15 superimposes very well with the *E. coli* frataxin homolog CyaY [PDB 1ew4 (42), RMSD = 2.5 Å, 13% sequence identity over 88 C α atoms] and with human frataxin [PDB 1ekg (43), RMSD = 3.3 Å, 11% sequence identity over 96 C α atoms]. The fold consists of a large, twisted, six-stranded antiparallel β sheet, flanked on one side by N- and C-terminal α helices.

Mitochondrial matrix frataxin and its homologs in bacteria are thought to be iron chaperones, participating in the storage of iron and in the maturation of Fe-S and heme-containing proteins (43, 44). Frataxin deficiency in humans leads to Friedreich's ataxia, a severe neurodegenerative disorder. Frataxin serves as an iron donor to aconitase, converting an inactive 3Fe-4S cluster to an active 4Fe-4S cluster (44).

Nqo15 interacts with complex I mainly through the exposed face of its β sheet. Between this β sheet and the rest of the complex there is a hydrophilic channel [with an elliptical cross section of about 7 Å by 15 Å, previously named channel 2 (15)] leading from the solvent to within about 10 Å of cluster N3, at its deep end, and cluster N1a, at its side. Remarkably, this cavity is lined with six exposed histidine residues, four of them provided by Nqo15 [histidines 90, 92, 94, and 96 (Fig. 2H)], as well as $_1\text{His}^{350}$ and $_3\text{His}^{208}$ (Fig. 4C). At the deep end of the channel, in an area with negative surface charge, there is a possible binding pocket for iron (as suggested by similarity to frataxin), formed by $_{15}\text{His}^{92}$, $_3\text{His}^{208}$, and $_3\text{Glu}^{204}$. Additionally, $_1\text{His}^{350}$ and $_{15}\text{His}^{90}$ would only require a side-chain rotation to contribute to metal binding. Remaining Nqo15 histidines 94 and 96 are in a good position to serve as anchors that guide iron into the binding site. Thus, another possible role for Nqo15 is the storage of iron. It could be used for the reconstitution of the nearby Fe-S clusters N3 and N1a, if iron is lost from them. No electron density for bound metal was observed in the cavity, possibly because Fe is lost during purification. Binding of frataxin to its target proteins is mediated by iron (45), consistent with our proposal for an iron-binding site at the interface between Nqo15 and the rest of complex I. Also, frataxin is suggested to bind to its partners via the conserved exposed face of the

β sheet (42), similar to Nqo15. Therefore, Nqo15 may represent the first example of a frataxin-like protein permanently bound to its target.

No other frataxin analogs were found in *T. thermophilus*, and analogs of Nqo15 were found only in close relatives, *Deinococcus geothermalis* and *Deinococcus radiodurans*. The permanent attachment of an Nqo15-like protein to complex I may be unique to thermophiles and may be a consequence of their harsh environment.

Functional Implications

One of the most puzzling questions about complex I is why it contains so many Fe-S clusters. Evolution of the complex from many smaller building blocks is probably part of the answer, as the structure shows. One of the clusters, N7, is not conserved and is likely to be an evolutionary remnant. However, the number of conserved clusters retained appears to be in excess of the minimum number needed just to connect the NADH- and quinone-binding sites. Electron transfer could, in principle, proceed between clusters N3 and N4 (edge-to-edge distance 13.8 Å), without N1b participation. Additional reasons for complexity may lie in the mechanism of the enzyme.

Complex I flavin, after reduction by NADH to FMNH $_2$, releases two electrons in two steps with one-electron redox potentials (at pH 7.0) of about -300 mV (FMNH $_2$ /flavosemiquinone) and of about -390 mV (flavosemiquinone/oxidized flavin) (46). Electrons can be transferred effectively to the nearest cluster N3 (potential -250 mV) and along the cluster chain to membrane-embedded quinone (Fig. 1B). Under steady-state NADH oxidation, the Fe-S clusters in complex I are almost fully reduced, and the rate-limiting step is likely the oxidation of N2 by quinone (47). When cluster N3 is reduced, electron transfer from flavosemiquinone (potential -390 mV) to cluster N1a (potential -370 mV) is thermodynamically favorable. As soon as N3 is reoxidized during quinone reduction, electrons from N1a can proceed via FMN into the main cluster chain. A pair of electrons from FMN may thus be donated nearly simultaneously to clusters N3 and N1a, and the flavosemiquinone radical may be short-lived. Cluster N1a is shielded from the solvent (fig. S2B), whereas FMN is exposed (Fig. 3A), and flavosemiquinone, as well as FMNH $_2$, can generate ROS by reduction of oxygen (48). Therefore, such temporary storage of electrons by N1a is likely to minimize ROS production during turnover of complex I. Apart from Fe-S cluster ligands, $_1\text{Cys}^{182}$ is the only other conserved cysteine in complex I, and it has been identified as the site of the oxidative attack and as a redox-sensitive thiol (49). It is only 6 Å from the FMN, consistent with flavin serving as a source of ROS.

Considering the coupling between electron transfer and proton translocation, two

main modes of coupling have been proposed: direct (redox-driven, e.g., Q-cycle variations) or indirect (through conformational changes) (1, 2, 34, 50, 51). Some features of the structure support direct coupling. There is a clear electron transfer pathway from FMN to cluster N2. Polar residues, found in the vicinity of nearly all clusters, may adjust redox potentials for optimal rates. The unique coordination of cluster N2 by two consecutive cysteines is conserved in complex I and is likely to be important for the mechanism. The midpoint potential of N2 is pH-dependent, indicating that its reduction is coupled to proton binding (2, 9). This may be due to the polar environment of the cluster, in particular $_4\text{His}^{169}$. However, the unusual coordination of the cluster may allow its direct protonation, coupled to reduction. In this respect, N2 may resemble [3Fe-4S] clusters or redox-active [4Fe-4S] clusters, coordinated by only three cysteines, which can be directly protonated (52). The invariant $_4\text{Tyr}^{87}$ can interact with one of the two consecutive N2 ligands, $_6\text{Cys}^{45}$, as well as with the quinone (Figs. 3C and 4A). This arrangement could facilitate electron transfer and possibly proton transfer or coupling. As most elements would be needed for any NADH to quinone pathway, these features do not support the direct mechanism exclusively.

However, some elements of the structure can be interpreted as pointing to long-range conformational interactions. Notably, the conserved helix H2 extends away from Nqo4 to clusters N5 and N6a, and it interacts with them through polar residues (Fig. 2F and fig. S2D). One role of such an unusual arrangement could be to provide a way of communicating the redox state of these clusters to Nqo4 and further on to the membrane domain, possibly through conformational changes. In addition, the distance between clusters N5 and N6a is the longest in the redox chain (Fig. 1B), which may reflect a transfer-controlling step. Cluster N2 is linked through one β strand to the rigid helix H1, which is likely to extend on the membrane domain surface toward antiporter-like subunits Nqo12 to 14 (11). This helix could also provide a connection between the clusters and the proton-pumping machinery, possibly as a kind of "lever." As the conformation of Nqo3 is changed when enzyme reduction takes place (34), its large C-terminal domain could participate in a conformational mechanism. The very long redox chain of complex I may help to coordinate large-scale conformational changes (34, 51). As four protons are moved across the membrane in each catalytic cycle, a combination of direct and indirect mechanisms could operate in complex I.

References and Notes

1. J. E. Walker, *Q. Rev. Biophys.* **25**, 253 (1992).
2. T. Yagi, A. Matsuno-Yagi, *Biochemistry* **42**, 2266 (2003).
3. J. Carroll, I. M. Fearnsley, R. J. Shannon, J. Hirst, J. E. Walker, *Mol. Cell. Proteomics* **2**, 117 (2003).

4. N. Grigorieff, *J. Mol. Biol.* **277**, 1033 (1998).
5. G. Peng *et al.*, *Biochemistry* **42**, 3032 (2003).
6. V. Guenebaut, A. Schlitt, H. Weiss, K. Leonard, T. Friedrich, *J. Mol. Biol.* **276**, 105 (1998).
7. A. H. Schapira, *Biochim. Biophys. Acta* **1364**, 261 (1998).
8. R. S. Balaban, S. Nemoto, T. Finkel, *Cell* **120**, 483 (2005).
9. T. Ohnishi, *Biochim. Biophys. Acta* **1364**, 186 (1998).
10. M. Finel, J. M. Skehel, S. P. Albracht, I. M. Fearnley, J. E. Walker, *Biochemistry* **31**, 11425 (1992).
11. P. J. Holt, D. J. Morgan, L. A. Sazanov, *J. Biol. Chem.* **278**, 43114 (2003).
12. T. Friedrich, D. Scheide, *FEBS Lett.* **479**, 1 (2000).
13. H. Leif, V. D. Sled, T. Ohnishi, H. Weiss, T. Friedrich, *Eur. J. Biochem.* **230**, 538 (1995).
14. E. Nakamaru-Ogiso, T. Yano, T. Yagi, T. Ohnishi, *J. Biol. Chem.* **280**, 301 (2005).
15. P. Hinchliffe, L. A. Sazanov, *Science* **309**, 771 (2005).
16. P. Hinchliffe, J. Carroll, L. A. Sazanov, in preparation.
17. Materials and methods are available as supporting material on Science Online.
18. C. C. Page, C. C. Moser, X. Chen, P. L. Dutton, *Nature* **402**, 47 (1999).
19. D. J. Morgan, L. A. Sazanov, unpublished data.
20. E. Krissinel, K. Henrick, *Acta Crystallogr. D Biol. Crystallogr.* **60**, 2256 (2004).
21. L. Holm, C. Sander, *Science* **273**, 595 (1996).
22. A. M. Lesk, *Curr. Opin. Struct. Biol.* **5**, 775 (1995).
23. A. G. Murzin, S. E. Brenner, T. Hubbard, C. Chothia, *J. Mol. Biol.* **247**, 536 (1995).
24. A. P. Yeh *et al.*, *J. Mol. Biol.* **300**, 587 (2000).
25. P. M. Vignais, B. Billoud, J. Meyer, *FEMS Microbiol. Rev.* **25**, 455 (2001).
26. M. G. Bertero *et al.*, *Nat. Struct. Biol.* **10**, 681 (2003).
27. G. Fritz *et al.*, *Proc. Natl. Acad. Sci. U.S.A.* **99**, 1836 (2002).
28. J. W. Peters, W. N. Lanzilotta, B. J. Lemon, L. C. Seefeldt, *Science* **282**, 1853 (1998).
29. T. Yano *et al.*, *J. Biol. Chem.* **278**, 15514 (2003).
30. R. A. Rothery *et al.*, *Biochemistry* **43**, 5324 (2004).
31. J. M. Dias *et al.*, *Struct. Fold. Design* **7**, 65 (1999).
32. M. Finel, *Biochim. Biophys. Acta* **1364**, 112 (1998).
33. J. I. Oh, B. Bowien, *J. Biol. Chem.* **273**, 26349 (1998).
34. A. A. Mamedova, P. J. Holt, J. Carroll, L. A. Sazanov, *J. Biol. Chem.* **279**, 23830 (2004).
35. V. G. Grivennikova, R. Roth, N. V. Zakharova, C. Hagerhall, A. D. Vinogradov, *Biochim. Biophys. Acta* **1607**, 79 (2003).
36. A. Volbeda *et al.*, *Nature* **373**, 580 (1995).
37. D. Flemming, A. Schlitt, V. Spehr, T. Bischof, T. Friedrich, *J. Biol. Chem.* **278**, 47602 (2003).
38. N. Kashani-Poor, K. Zwicker, S. Kerscher, U. Brandt, *J. Biol. Chem.* **276**, 24082 (2001).
39. T. Yano, W. R. Dunham, T. Ohnishi, *Biochemistry* **44**, 1744 (2005).
40. E. Darrouzet, J. P. Issartel, J. Lunardi, A. Dupuis, *FEBS Lett.* **431**, 34 (1998).
41. L. Grgic, K. Zwicker, N. Kashani-Poor, S. Kerscher, U. Brandt, *J. Biol. Chem.* **279**, 21193 (2004).
42. S. J. Cho *et al.*, *Proc. Natl. Acad. Sci. U.S.A.* **97**, 8932 (2000).
43. S. Dhe-Paganon, R. Shigeta, Y. I. Chi, M. Ristow, S. E. Shoelson, *J. Biol. Chem.* **275**, 30753 (2000).
44. A.-L. Bulteau *et al.*, *Science* **305**, 242 (2004).
45. T. Yoon, J. A. Cowan, *J. Biol. Chem.* **279**, 25943 (2004).
46. V. D. Sled, N. I. Rudnitsky, Y. Hatefi, T. Ohnishi, *Biochemistry* **33**, 10069 (1994).
47. A. B. Kotlyar, V. D. Sled, D. S. Burbaev, I. A. Moroz, A. D. Vinogradov, *FEBS Lett.* **264**, 17 (1990).
48. A. P. Kudin, N. Y. Bimpong-Buta, S. Vielhaber, C. E. Elger, W. S. Kunz, *J. Biol. Chem.* **279**, 4127 (2004).
49. Y. R. Chen, C. L. Chen, L. Zhang, K. B. Green-Church, J. L. Zweier, *J. Biol. Chem.* **280**, 37339 (2005).
50. T. Friedrich, *J. Bioenerg. Biomembr.* **33**, 169 (2001).
51. G. Belogradov, Y. Hatefi, *Biochemistry* **33**, 4571 (1994).
52. J. L. C. Duff, J. L. J. Breton, J. N. Butt, F. A. Armstrong, A. J. Thomson, *J. Am. Chem. Soc.* **118**, 8593 (1996).
53. This work was funded by the Medical Research Council. We thank J. E. Walker, A. G. W. Leslie, and A. G. Murzin for helpful discussions of the manuscript; the European Synchrotron Radiation Facility for provision of synchrotron radiation facilities; and the staff of beamlines ID23 and ID29 for assistance. The coordinates and the structure factors have been deposited in the Protein Data Bank (accession code 2FUG).

Supporting Online Material

www.sciencemag.org/cgi/content/full/1123809/DC1

Materials and Methods

SOM Text

Figs. S1 and S2

Tables S1 and S2

References

13 December 2005; accepted 30 January 2006

Published online 9 February 2006;

10.1126/science.1123809

Include this information when citing this paper.

REPORTS

Ultrafast Interfacial Proton-Coupled Electron Transfer

Bin Li,¹ Jin Zhao,¹ Ken Onda,¹ Kenneth D. Jordan,² Jinlong Yang,³ Hrvoje Petek^{1*}

The coupling of electron and nuclear motions in ultrafast charge transfer at molecule-semiconductor interfaces is central to many phenomena, including catalysis, photocatalysis, and molecular electronics. By using femtosecond laser excitation, we transferred electrons from a rutile titanium dioxide (110) surface into a CH₃OH overlayer state that is 2.3 ± 0.2 electron volts above the Fermi level. The redistributed charge was stabilized within 30 femtoseconds by the inertial motion of substrate ions (polaron formation) and, more slowly, by adsorbate molecules (solvation). According to a pronounced deuterium isotope effect (CH₃OD), this motion of heavy atoms transforms the reverse charge transfer from a purely electronic process (nonadiabatic) to a correlated response of electrons and protons.

Titanium dioxide (TiO₂) is a large-band gap semiconductor with important applications in photocatalysis and solar energy conversion (1–5). Electron-hole pair excitation within semiconductors such as TiO₂ can initiate photocatalytic reactions in chemisorbed molecular overlayers through interfacial charge transfer. In response to charge injection into a molecular overlayer, the interfacial lattice

ions and molecules will undergo inertial motion to minimize the free energy (dielectric screening) or even chemical reactions, which are in competition with the charge population decay by reverse transfer into the semiconductor. Of particular interest as a source of abundant clean energy and for environmental remediation is the activation of bonds that contain hydrogen atoms through the coupling of electrons and protons, which can catalyze disproportionation of H₂O into H₂ and O₂ (1–3).

Excess electrons in molecular overlayers on metal oxide surfaces are strongly attracted to the dangling hydrogen atoms of surface-bound -OH groups and on coadsorbed protic solvent molecules that are not engaged in

strong hydrogen bonds (6, 7). The injection of electrons into the molecular overlayer can even release hydrogen atoms from the existing hydrogen bonds to create new dangling hydrogen atom centers. Such correlated dynamics of electrons and protons are fundamentally important in chemistry and biology. They can drive photocatalytic reactions as well as modulate charge transport at the semiconductor/protic solvent interfaces, and they are known to play a role in photosynthesis, respiration, and transport through biological membranes (8–13).

In a recent time-resolved two-photon photoemission (TR-2PP) study of H₂O/TiO₂(110) surfaces, we discovered an excited electronic state 2.4 ± 0.1 eV above the Fermi level E_F. This state attains the maximum intensity when -OH species, which are formed by the dissociation of H₂O at defect sites on TiO₂(110), coexist with chemisorbed H₂O at ~1-monolayer (ML) coverage. On the basis of chemical evidence and density functional theory (DFT) calculations, we assigned this resonance to partially hydrated, or “wet,” electron states. Electrons injected into the molecular overlayer are delocalized over several hydrogen atoms associated with -OH groups and neighboring water molecules. The injected electrons decay into the conduction band of TiO₂ through reverse charge transfer in less than 15 fs, faster than the dielectric response of the interface can stabilize them (6, 7).

¹Department of Physics and Astronomy, ²Department of Chemistry, University of Pittsburgh, Pittsburgh, PA 15260, USA. ³Hefei National Laboratory for Physical Sciences at Microscale, University of Science and Technology of China, Hefei, Anhui 230026, China.

*To whom correspondence should be addressed. E-mail: petek@pitt.edu

Here we provide further insight into the decay of interfacial electrons through correlated motion of both heavy and light (hydrogen/deuterium) atoms by using the model system of $\text{CH}_3\text{OH}/\text{TiO}_2(110)$. Methanol is the simplest protic organic adsorbate—with well-known liquid and interfacial electron solvation, adsorption, and photochemical properties (14–21)—which acts as a hole trap in photocatalysis (22). We find that CH_3OH stabilizes wet electrons more effectively than H_2O does, allowing their progressive energy relaxation through inertial polaron formation and diffusive solvation to be observed on femtosecond to picosecond time scales. A pronounced deuterium isotope effect after a prompt inertial response suggests that the dielectric screening transforms the reverse charge transfer process from the nonadiabatic regime, where state occupations switch between electronic surfaces, to the proton-coupled regime, where the electron transfer is correlated with proton motions.

TR-2PP measurements on $\text{CH}_3\text{OH}/\text{TiO}_2(110)$ surfaces were performed according to the procedures for $\text{H}_2\text{O}/\text{TiO}_2$ (6, 23, 24). 2PP through a transiently occupied wet electron state (Fig. 1) was induced with 10-fs pulses from the second harmonic of a Ti:sapphire laser (3.05 eV photon energy). 2PP spectra, recorded by scanning a hemispherical electron energy analyzer, are dominated by the transiently occupied wet electron state (24). Two-pulse correlation (2PC) measurements were used to record the energy and population decay of the wet electron state. The 2PP signal was acquired simultaneously at seven photoelectron energies while scanning the delay between identical pump-probe pulses (25). The reduced TiO_2 surface was prepared by standard ultrahigh-vacuum methods with a controlled density of surface-bridging oxygen-atom (O_b) (Fig. 2) vacancies (23). After purification, either high-purity CH_3OH or CH_3OD gas was deposited onto the TiO_2 surface at 100 K. The coverage of ~ 1 ML corresponding to adsorption of one methanol molecule at each terminal five-coordinate Ti_{5c}^{4+} site (20) was attained by exposure to ~ 1.2 Langmuir ($1 \text{ L} = 1.33 \times 10^{-6} \text{ mbar}\cdot\text{s}$), according to the procedure established in (24). Other coverages are referenced to this coverage, assuming a constant adsorption probability. For the comparison of results for CH_3OH and CH_3OD , the work function provided an independent measure of coverage (23).

Upon adsorption, CH_3OH is deprotonated at O_b vacancy sites to form methoxy CH_3O^- and hydroxy $-\text{OH}$ species incorporated into the bridging rows. After titrating the O_b vacancies, additional first-monolayer CH_3OH molecules bind with their O atoms to the Ti_{5c}^{4+} sites. Partial deprotonation at Ti_{5c}^{4+} sites to form additional bridging $-\text{OH}$ groups creates higher $-\text{OH}$ coverage than those obtained for H_2O -covered surfaces (Fig. 2) (20, 21).

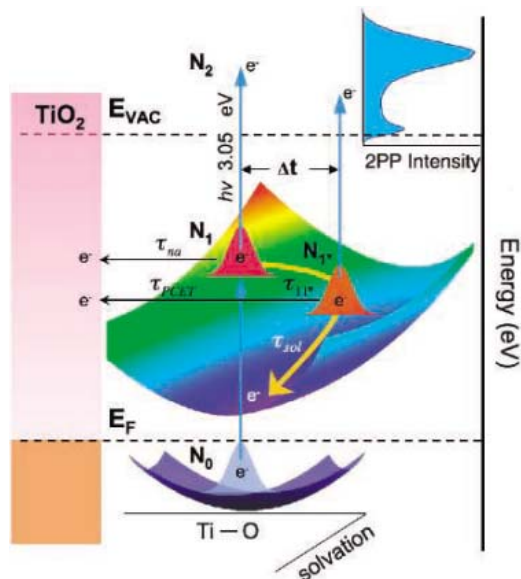


Fig. 1. Schematic diagram for the 2PP excitation at the $\text{CH}_3\text{OH}/\text{TiO}_2$ interface. The photoinduced charge transfer from the partially reduced $\text{Ti}_{5c}^{4+\delta}$ sites (N_0) to the CH_3OH overlayer (N_1) initiates the coupled electron-nuclear dynamics. The redistribution of charge elicits a dielectric response involving fast Ti–O bond stretching (polaron formation) along with slower adsorbate reorganization (solvation) to relax the initially prepared N_1 to a quasi-stable N_{1^*} state. Simultaneously, the population decay by reverse charge transfer evolves from the nonadiabatic (τ_{na}) to the proton-coupled (τ_{PCET}) regimes. The 2PP spectra (shown for 1-ML CH_3OH) and the pump-probe 2PC measurements obtained by further excitation of electrons to continuum states (N_2) above the vacuum level E_{VAC} record the intermediate state electronic structure and dynamics.

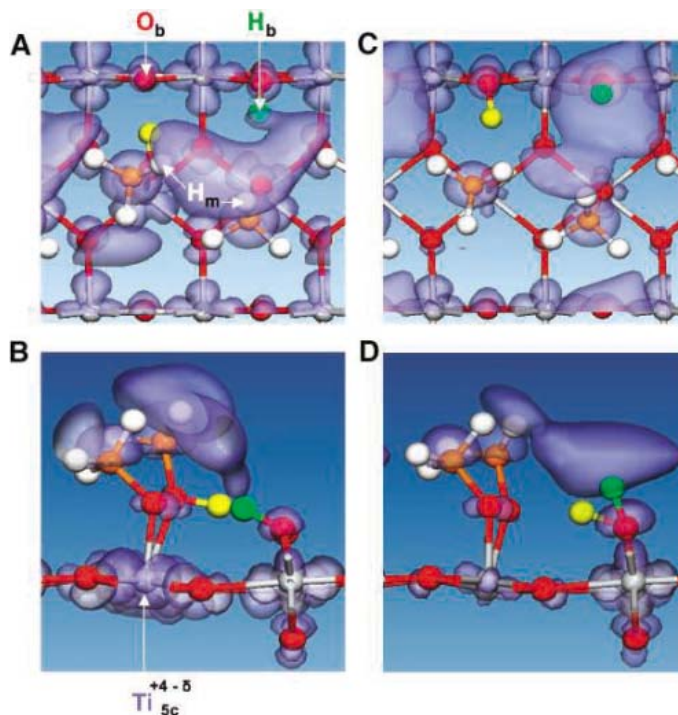


Fig. 2. (A and B) Top and side views, respectively, of the optimized geometry of the ground state and the associated lowest energy (2.5 eV) unoccupied adsorbate localized orbital of 50% deprotonated CH_3OH at 1-ML coverage on $\text{TiO}_2(110)$ from DFT calculations (26). Ti, blue; O, red; C, orange; and H, white; atoms remain essentially fixed, whereas the H atoms of the bridging $-\text{OH}$ (green) and methanol $-\text{OH}$ (yellow) undergo a substantial change in the excited state structural optimization. Arrows indicate the bridging oxygen O_b , terminal five-coordinate titanium Ti_{5c} rows, and methyl H_m atoms. The translucent structures indicate the unoccupied orbital distribution of the wet electron state. (C and D) The top and side views, respectively, of the optimized geometry when an electron is added to the unoccupied state. The structural changes from (A) and (B) to (C) and (D) mainly consist of rotation of the bridging $-\text{OH}$ toward the surface normal configuration and proton transfer from the CH_3OH to the proximate O_b site. Simultaneously, the wet electron distribution descends toward the surface from the methyl groups to the bridging $-\text{OH}$.

On reduced $\text{TiO}_2(110)$ surfaces, the excess surface charge introduced by O_b vacancies or hydrogen atoms is delocalized over several $\text{Ti}_{5c}^{4+\delta}$ sites in a band ~ 0.7 eV below E_F (7). Excitation with 3.05-eV light induces charge transfer from the $\text{Ti}_{5c}^{4+\delta}$ donor to a CH_3OH overlayer acceptor state at 2.3 ± 0.2 eV above E_F (Fig. 1). In (24),

we reported on the CH_3OH coverage, sample temperature, and parallel momentum dependence of this wet electron state. Here we present the excited state energy relaxation and population-decay dynamics instigated by the correlated motion of the injected charge and the heavy and light atoms at the interface.

The resonance at 2.3 ± 0.2 eV attains the maximum intensity at 1 ML CH_3OH coverage. It is similar to the wet electron resonance on $\text{H}_2\text{O}/\text{TiO}_2$ (6, 7, 24) in its dependence on the surface -OH concentration, the parent molecule coverage, and its energy relative to E_F , implying related electronic structures of the excess electrons. To better characterize the molecular and electronic structure of $\text{CH}_3\text{OH}/\text{TiO}_2$ surfaces, we performed DFT calculations (26–29). The CH_3OH structure where 50% of molecules are deprotonated (Fig. 2, A and B) was calculated to have lower total ground state energy than the 0 and 100% deprotonated structures. Nevertheless, independent of the degree of deprotonation, the calculations give similar spatial distributions and energies of 2.5 ± 0.1 eV above E_F for the lowest energy unoccupied overlayer state at the ground state geometry. By contrast to the $\text{H}_2\text{O}/\text{TiO}_2$ system, the unoccupied density of states resides mostly on the H_m atoms of CH_3 , where m denotes methyl, because hydrogen bonding consumes all of the dangling hydrogen atoms in the ground state (Fig. 2, A and B). The aliphatic hydrogen atoms of alcohols are known to participate in electron solvation in liquid methanol (16–18).

An overview of the electron injection, energy relaxation, and population decay dynamics for CH_3OH and CH_3OD overlayers is evident from plots of 2PP intensity spanning 2PC records at 14 different energies for several coverages (Fig. 3). By contrast to $\text{H}_2\text{O}/\text{TiO}_2$ (6), the solvated electron dynamics for $\text{CH}_3\text{OH}/\text{TiO}_2$ strongly depend on the coverage, with lifetimes extending to the picosecond range for ≥ 3 -ML CH_3OH (30). The data in Fig. 3 show the following trends: (i) At low coverages (≤ 1 ML), the resonance decays in <30 fs, independent of energy or isotopic substitution. (ii) Above 1-ML coverage, both the excited state population and its energy decay with fast and slow components. (iii) Only the slow decay components depend strongly on the CH_3OH coverage. (iv) The slow population decay shows a pronounced deuterium isotope effect.

To extract quantitative rates for the electron energy and population relaxation, we simulated the 2PC measurements with a model based on the optical Bloch equations (25, 31). Two-photon absorption probability was calculated for a transient intermediate state that evolves through the coupling of the electronic and nuclear degrees of freedom (Fig. 1). The signal corresponding to the photoexcited state N_1 (resonance peak at zero delay) decays with isotope- or coverage-independent single exponential kinetics with a total rate $1/\tau_1 = 1/\tau_{\text{na}} + 1/\tau_{11^*}$ (τ_{na} represents the nonadiabatic reverse charge transfer into the conduction band of TiO_2). Simultaneously, N_1 decays in energy by ~ 0.1 eV on a time scale τ_{11^*} of 30 to 40 fs to a quasi-stationary screened N_{1^*} state. Based on the energy/time scales for polaron formation through the excitation of ~ 24 -THz longitudinal

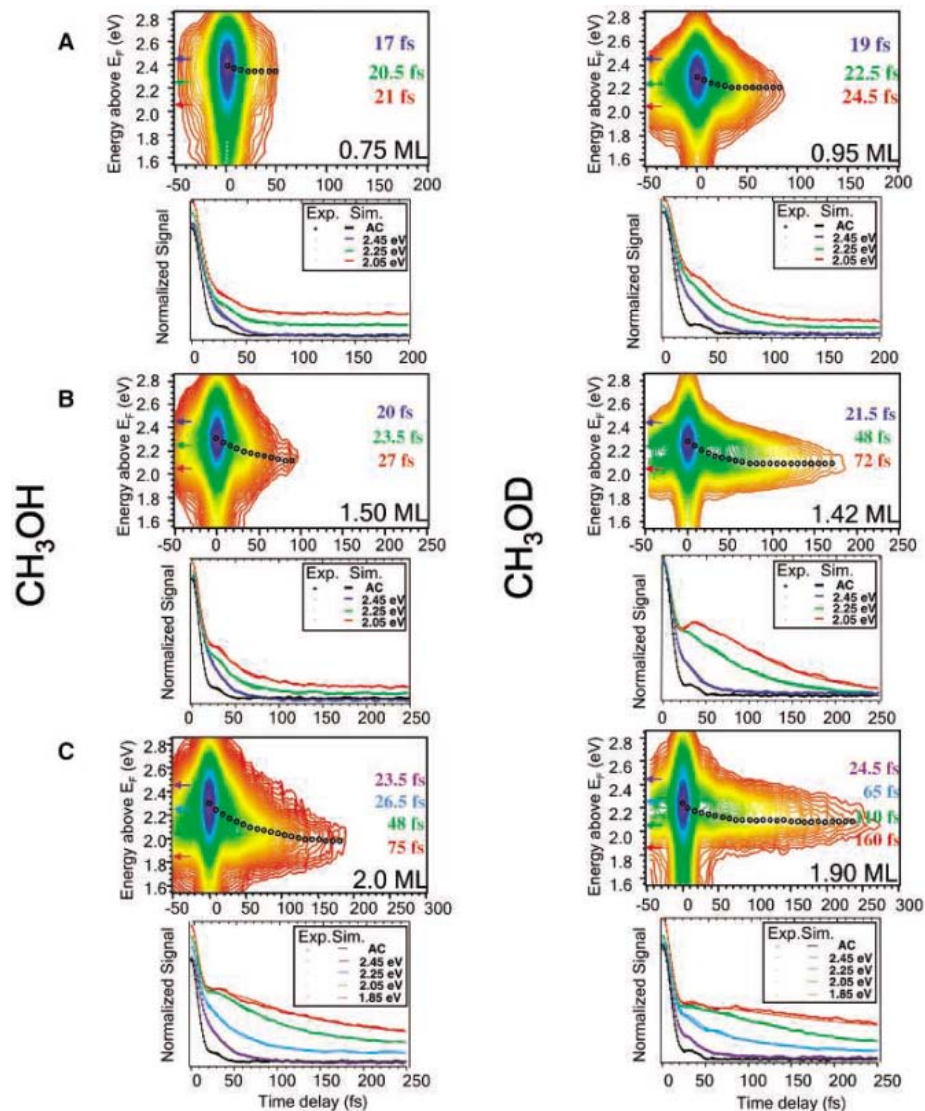


Fig. 3. (A to C) The top panels show three-dimensional (3D) plots of the energy and population dynamics of the wet electron state on CH_3OH and $\text{CH}_3\text{OD}/\text{TiO}_2(110)$ surfaces for <1 - to 2-ML coverages that show the strong dependence of the wet electron state dynamics on the methanol coverage and D isotope substitution. The 3D plots are constructed from 2PC measurements taken at 0.1-eV intervals. The black circles indicate the change in the resonance maximum with time. The bottom panels show the original 2PC measurements used to construct the 3D plots at several characteristic energies indicated by the color-coded arrows in (A) to (C) and their simulation (solid lines) according to the model described in Fig. 1 and the text.

Ti-O -stretching optical phonons of TiO_2 (32), we attribute the fast energy relaxation τ_{11^*} from N_1 to N_{1^*} to the lattice ions screening the charge distribution created by the photoinduced transfer from the $\text{Ti}_{\text{sc}}^{4+\delta}$ sites to the CH_3OH overlayer. Such electron-lattice correlation in TiO_2 is evident in both the electronic structure of O_b atom vacancy defects and the transient photoconductivity of TiO_2 (32). This inertial dielectric response stabilizes N_{1^*} with respect to the reverse charge transfer.

The dynamics of N_{1^*} are most apparent below the CH_3OH resonance (e.g., 2.05 eV) (Fig. 3B, bottom). A rise time τ_1 and a population and energy decay on a slower (coverage- and

isotope-dependent) time scale τ_{1^*} characterize the 2PC signal at this energy. Based on a TR-2PP study of $\text{CH}_3\text{OH}/\text{Ag}(111)$ (19), we attribute the slow energy relaxation to the diffusive solvation of the injected charge by CH_3OH molecules with a time constant τ_{sol} .

The deuterium isotope effect on the population relaxation of N_{1^*} cannot be explained by a purely electronic process such as the inelastic electron scattering (25). Rather, it is indicative of proton-coupled electron transfer (PCET), which plays an important role in homogeneous photocatalysis (9, 10). Including a PCET contribution τ_{PCET} , the total decay rate of N_{1^*} at a fixed energy is given by $1/\tau_{1^*} = 1/\tau_{\text{PCET}} +$

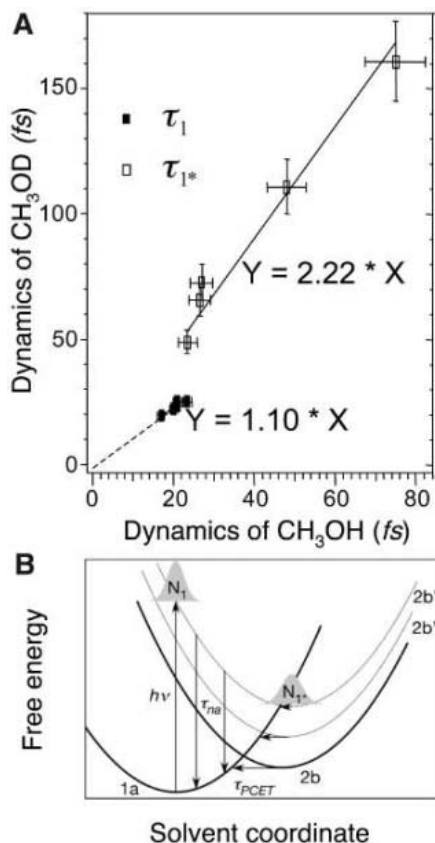


Fig. 4. (A) The τ_1 and τ_{1^*} lifetimes determined for comparable coverage and observation energy for the $\text{CH}_3\text{OH}/\text{TiO}_2(110)$ (abscissa) and $\text{CH}_3\text{OD}/\text{TiO}_2(110)$ (ordinate) surfaces. The significant departure of the slope for τ_{1^*} from 1.0 indicates a rate limited by proton dynamics such as is evident in Fig. 2. (B) Schematic free energy surfaces for the PCET plotted against a generalized solvent coordinate (33). The solid lines represent surfaces for an electron and a proton before (1a) and after (2b) photoinduced transfer; the dotted lines (2b'' and 2b') represent manifold 2b surfaces with different degrees of proton vibrational excitation. The wave packet excited near the equilibrium ground state structure (N_1 state) evolves through the inertial dielectric response toward the 2b manifold minima (N_{1^*} state). The nonadiabatic electronic decay (down arrows) most likely occurs before crossings of the 1a manifold with the 2b manifold. The PCET is most probable at surface crossings between the 1a and 2b manifolds (horizontal arrows).

$1/\tau_{\text{sol}}$. Thus, the intermediate state populations evolve according to

$$N_1(t) = N_1^0 e^{-\frac{t}{\tau_1}} \quad (1)$$

and

$$N_{1^*}(t) = N_1^0 e^{-\frac{t}{\tau_{1^*}}} + \alpha \frac{N_1^0}{\tau_{1^*}} \frac{\tau_1 \tau_{1^*}}{\tau_1 - \tau_{1^*}} \times \left(e^{-\frac{t}{\tau_1}} - e^{-\frac{t}{\tau_{1^*}}} \right) \quad (2)$$

where N_1^0 and $N_{1^*}^0$ are the initial amplitudes and α is a free parameter required to simulate dynamics of a continuum of intermediate states with a two-state model. In addition, the coherent component in 2PP is added to the incoherent one given by eqs. 1 and 2, and their sum is convoluted with the pulse autocorrelation (25, 31). The simulations agree well with the experimental 2PC scans (Fig. 3, A to C, bottom).

In Fig. 4A, we plot the parameters τ_1 and τ_{1^*} for CH_3OD against those for CH_3OH , extracted from data from comparable coverage and measurement energy. The best fit lines through the experimental τ_1 and τ_{1^*} lifetimes with slopes of 1.1 and 2.2 quantify the D/H isotope effect. The substantial increase of the slope for N_{1^*} from unity indicates an appreciable isotope effect. The magnitude of isotope effect depends on whether the proton kinetic energy or the tunneling limits the charge transfer rates. The observed slope of 2.2, which is substantially larger than the maximum isotope effect for the inertial proton motion of $\sqrt{m_D/m_H} \sim 1.4$, where m_D and m_H are the masses of D and H atoms, respectively, such as observed in electron hydration in liquid H_2O (11), implies that it is determined by either proton tunneling or vibrational zero-point energy differences (33). Based on the liquid CH_3OH studies, we do not expect an isotope effect on the diffusive solvation dynamics (11, 15).

Photoinduced electron transfer under highly nonequilibrium conditions, such as in the dye-sensitized charge injection or the wet electron population decay into TiO_2 , cannot be described by quasi-equilibrium models such as the Marcus-Jortner theory (8, 34, 35). In Fig. 4B we propose a scenario for how the inertial structural changes associated with the dielectric response of the interface control the wet electron dynamics. The free energy surfaces for the proton and electron transfer are plotted in Fig. 4B against a generalized solvent coordinate representing the multi-dimensional dielectric response of the interface to both the electron and proton displacements (33). Photoexcitation occurs “vertically,” that is, faster than the proton or solvent response, from the donor surface 1a shown in Fig. 4B (electron at the $\text{Ti}_{5c}^{4-\delta}$ sites and proton at its ground state geometry) to a manifold of acceptor surfaces 2b, 2b', 2b'', etc. This manifold represents the excited state where an electron is in the CH_3OH overlayer and a proton is displaced with respect to the ground state (Fig. 2, C and D), with different degrees of excitation of an internal proton vibration (2b', 2b'', etc.). Because at the instant of excitation, a proton in the excited state is strongly displaced along these internal coordinates, the optical transition terminates on a distribution of vibrationally excited free-energy surfaces. The wave packet created on the 2b manifold evolves toward the surface minimum through the inertial dielectric response. In competition with the dielectric

relaxation, the excited state population decays by nonadiabatic processes, which change the state occupation (vertical transitions), and by PCET processes, which exchange the proton and electron between the acceptor and donor states (horizontal transitions) (34). Exothermic non-adiabatic transitions occur before the wave packet propagates to crossings of the 1a manifold with the 2b manifold. By contrast, PCET is most probable at crossings between 1a and 2b manifolds, where the activation energy (solvent reorganization) is minimum. As the excited state evolves toward the equilibrium structure of wet electron state, the transition from non-adiabatic to PCET-dominated population decay is revealed by the emergence of the deuterium isotope effect.

To gain further insight into the PCET process, the structure of $\text{CH}_3\text{OH}/\text{TiO}_2$ was optimized in a DFT calculation with an excess electron added to the molecular overlayer (36, 37). We cut a single layer of TiO_2 from a three-layer slab of the optimized ground state structure (Fig. 2, A and B), added an electron to the lowest energy virtual orbital associated with the H_m atoms, and optimized the overlayer structure, while keeping all the surface atoms except O_b fixed (38). The optimized structure was attained after substantial displacement of hydrogen atoms of the -OH groups on the surface and of the CH_3OH molecules (Fig. 2, C and D), with concomitant shift of the electron distribution from H_m to H_b atoms. By following the hydrogen atom positions along the optimization path, we found that the stabilization energy of 0.5 eV is gained through the rotation of the bridging -OH to the vertical orientation (0.35 eV) and through the transfer of a proton from CH_3OH to its neighboring O_b site (0.15 eV). The hydrogen atom motion during the structural relaxation drives wet electrons from the H_m sites (which are isolated from the surface by carbon atoms) to H_b sites, (which are closer to the surface and more strongly coupled to the conduction band) (6).

The DFT calculations provide insight into PCET dynamics that could account for the D isotope effect observed at >1-ML coverages. Additional interactions, such as the binding of second-monolayer CH_3OH molecules through a hydrogen bond with O_b atoms, can hinder and possibly impose a barrier for the proton motion in Fig. 2.

Our studies elucidate how the dielectric response of a protic-solvent/metal-oxide interface controls the electron transfer and solvation in a photocatalytic system. Presolvated electrons, such as those observed for $\text{CH}_3\text{OH}/\text{TiO}_2$, are potent reagents that have been implicated in the photocatalytic decomposition of halocarbons, which are relevant to chemical remediation and the destruction of Earth's ozone layer (39). Conditions exist to support similar wet electron states on all oxide surfaces in contact with protic solvents. However, details of the electronic structure and dynamics most likely

depend on the specific molecular-scale solvent-substrate interactions.

References and Notes

1. A. Fujishima, K. Honda, *Nature* **238**, 37 (1972).
2. M. Grätzel, *Nature* **414**, 338 (2001).
3. M. A. Fox, M. T. Dulay, *Chem. Rev.* **93**, 341 (1993).
4. R. Wang *et al.*, *Nature* **388**, 431 (1997).
5. P. V. Kamat, *Chem. Rev.* **93**, 267 (1993).
6. K. Onda *et al.*, *Science* **308**, 1154 (2005).
7. J. Zhao, B. Li, K. D. Jordan, J. Yang, H. Petek, in preparation.
8. H. Tributsch, L. Pohlmann, *Science* **279**, 1891 (1998).
9. R. I. Cukier, D. G. Nocera, *Annu. Rev. Phys. Chem.* **49**, 337 (1998).
10. S. Hammes-Schiffer, *Acc. Chem. Res.* **34**, 273 (2001).
11. M. S. Pshenichnikov, A. Baltuska, D. A. Wiersma, *Chem. Phys. Lett.* **389**, 171 (2004).
12. C. Tanner, C. Manca, S. Leutwyler, *Science* **302**, 1736 (2003).
13. J. Lin, I. A. Balabin, D. N. Beratan, *Science* **310**, 1311 (2005).
14. X. Shi, F. H. Long, H. Lu, K. B. Eisenthal, *J. Phys. Chem.* **99**, 6917 (1995).
15. H. Shirota, K. Yoshihara, N. A. Smith, S. Lin, S. R. Meech, *Chem. Phys. Lett.* **281**, 27 (1997).
16. M. J. Tauber, C. M. Stuart, R. A. Mathies, *J. Am. Chem. Soc.* **126**, 3414 (2004).
17. P. Minary, L. Turi, P. J. Rossky, *J. Chem. Phys.* **110**, 10953 (1999).
18. L. Turi, *J. Chem. Phys.* **110**, 10364 (1999).
19. S. H. Liu *et al.*, *J. Phys. Chem. B* **106**, 12908 (2002).
20. M. A. Henderson, S. O. Tapia, M. E. Castro, *Fara. Disc.* **114**, 313 (1999).
21. S. P. Bates, M. J. Gillan, G. Kresse, *J. Phys. Chem. B* **102**, 2017 (1998).
22. T. Kawai, T. Sakata, *J. Chem. Soc. Chem. Commun.* **694** (1980).
23. K. Onda, B. Li, H. Petek, *Phys. Rev. B* **70**, 045415 (2004).
24. K. Onda, B. Li, J. Zhao, H. Petek, *Surf. Sci.* **593**, 32 (2005).
25. H. Petek, S. Ogawa, *Prog. Surf. Sci.* **56**, 239 (1997).
26. The calculations were carried out by using the generalized gradient approximation (GGA) based on DFT. At the GGA level, we choose the Perdew-Burke-Ernzerhof functional (27, 28), together with the double numerical atomic orbitals augmented by polarization functions (DNP), as the basis functions and the density functional semi-core pseudopotential (DSPP). Self-consistent field procedures were done with a convergence criterion of 10^{-6} atomic units (au) on the energy and electron density. Geometry optimizations were performed with a convergence criterion of 10^{-3} au on the gradient, 10^{-3} au on the displacement, and 10^{-5} au on the energy. All the calculations were carried out using the molecular simulation package DMOL3 [DMOL3 is a DFT-based package with atomic basis distributed by Accelrys (29)].
27. J. P. Perdew, K. Burke, M. Ernzerhof, *Phys. Rev. Lett.* **78**, 1396 (1997).
28. J. P. Perdew, K. Burke, M. Ernzerhof, *Phys. Rev. Lett.* **77**, 3865 (1996).
29. B. Delley, *J. Chem. Phys.* **92**, 508 (1990).
30. B. Li, K. Onda, H. Petek, data not shown.
31. M. J. Weida, S. Ogawa, H. Nagano, H. Petek, *J. Opt. Soc. Am. B* **17**, 1443 (2000).
32. E. Hendry, F. Wang, J. Shan, T. F. Heinz, M. Bonn, *Phys. Rev. B* **69**, 081101 (2004).
33. H. Decornez, S. Hammes-Schiffer, *J. Phys. Chem. A* **104**, 9370 (2000).
34. W. Stier, O. V. Prezhdo, *J. Phys. Chem. B* **106**, 8047 (2002).
35. L. G. C. Rego, V. S. Batista, *J. Am. Chem. Soc.* **125**, 7989 (2003).
36. R. Monnier, J. P. Perdew, D. C. Langreth, J. W. Wilkins, *Phys. Rev. B* **18**, 656 (1978).
37. R. O. Jones, O. Gunnarsson, *Rev. Mod. Phys.* **61**, 689 (1989).
38. The excited state prepared in the experiment corresponds to an electron in the CH₃OH overlayer and a hole remaining at the TiO₂ surface. By adding an electron to the CH₃OH orbital to simulate the excited state, we make an assumption that the hole is screened and the excitonic effects can be ignored. Calculations where the ground state is optimized with an extra electron (the true ground state of our excited state) gave the essentially identical structure to those in Fig. 2, A and B. The success of the excited state optimization procedure relies on the molecular overlayer state being sufficiently decoupled from the surface to not decay into the conduction band of TiO₂.
39. Q. B. Lu, T. E. Madey, *Phys. Rev. Lett.* **82**, 4122 (1999).
40. This work was supported by the Department of Defense Multidisciplinary University Research Initiative program under Grant DAAD19-01-1-0619, by the New Energy Development Organization of Japan "Molecular Wire" project, by the National Science Foundation of China (grants 20533030 and 50121202), and by NSF grant CHE-0518253. The apparatus for TR-2PP has been developed with support from NSF grant DMR-0116034. We thank J. T. Yates Jr. for the donation of the CH₃OD sample.

3 November 2005; accepted 31 January 2006
10.1126/science.1122190

Observation of Feshbach Resonances in the $F + H_2 \rightarrow HF + H$ Reaction

Minghui Qiu,^{1,3*} Zefeng Ren,^{1*} Li Che,¹ Dongxu Dai,¹ Steve A. Harich,¹ Xiuyan Wang,¹ Xueming Yang,^{1†} Chuanxiu Xu,⁴ Daiqian Xie,^{4†} Magnus Gustafsson,^{5,6} Rex T. Skodje,^{5,6} Zhigang Sun,^{1,2,7} Dong H. Zhang^{1,2,7†}

Reaction resonances, or transiently stabilized transition-state structures, have proven highly challenging to capture experimentally. Here, we used the highly sensitive H atom Rydberg tagging time-of-flight method to conduct a crossed molecular beam scattering study of the $F + H_2 \rightarrow HF + H$ reaction with full quantum-state resolution. Pronounced forward-scattered HF products in the $v' = 2$ vibrational state were clearly observed at a collision energy of 0.52 kcal/mol; this was attributed to both the ground and the first excited Feshbach resonances trapped in the peculiar $HF(v' = 3)-H'$ vibrationally adiabatic potential, with substantial enhancement by constructive interference between the two resonances.

Dynamical resonance in chemical reactions (1) has attracted great attention from both experimentalists and theoreticians (2–5) over the past 30 years. In general, the transition state is an energy maximum along the reaction coordinate, and so it does not persist as a discrete structure. However, in special cases, a reaction complex in the transition-state region can be transiently trapped in vibrationally adiabatic wells along the reaction coordinate. A transiently trapped state along the reaction coordinate in the transition-state region is normally called a dynamical resonance or a Feshbach resonance. Dynamical resonance (or reaction resonance) thus constitutes an extremely sensitive probe of the potential energy surface (PES) of a chemical reaction.

The most well-studied example for dynamical resonance is the $F + H_2 \rightarrow HF + H$ reaction, which is also known to be the main pumping step for the HF chemical laser. Theoretical predictions of a reaction resonance in the $F + H_2$ reaction were first made in the 1970s (6–9). In a landmark crossed-beams experiment on the $F + H_2$ reaction in the collision energy range of 0.7 to 3.4 kcal/mol by Lee and co-workers (10, 11), a forward-scattering peak for the $HF(v' = 3)$ product was clearly observed and was attributed to a reaction resonance. Later theoretical studies using both the quasi-classical trajectory method (12) and the quantum mechanical scattering method (13) on the Stark-Werner PES (SW-PES) (14), however, did not confirm this conjecture. In a recent study of the

$F + HD \rightarrow HF + D$ reaction, a step in the excitation function around 0.5 kcal/mol was unambiguously observed (15). Concurrent theoretical analysis based on the SW-PES showed that this step is due to a H-F-D(003) resonance. Neumark and co-workers also probed the transition state of the $F + H_2$ reaction by negative ion photodetachment spectroscopy (16). Full quantum mechanical calculations based on the SW-PES led to nearly quantitative agreement with the FH_2^- photoelectron spectrum (16). The nature of the resonances observed in the FH_2^- photoelectron spectrum was analyzed by Russell and Manolopoulos (17).

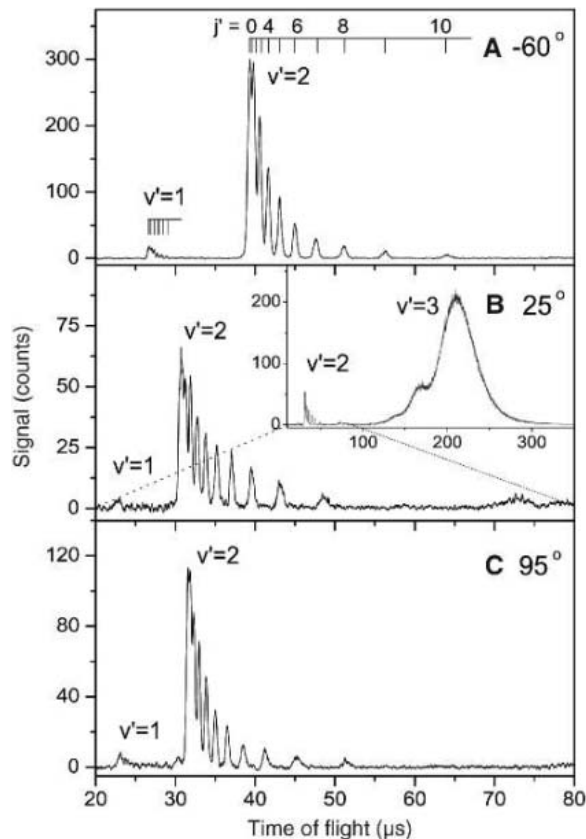
Despite more recent experimental studies on this system (18, 19), a definitive detection of reaction resonances in the $F + H_2$ reaction in a scattering experiment still remains elusive. Moreover, serious questions have been raised about the SW-PES that predicts the resonances, such as

¹State Key Laboratory of Molecular Reaction Dynamics, ²Center for Theoretical and Computational Chemistry, Dalian Institute of Chemical Physics, Chinese Academy of Sciences, Dalian, Liaoning 116023, P. R. China. ³Department of Physics, Dalian Jiaotong University, Dalian, P. R. China. ⁴Institute of Theoretical and Computational Chemistry, Department of Chemistry, Nanjing University, Nanjing, Jiangsu 210093, P. R. China. ⁵Institute of Atomic and Molecular Sciences, Academia Sinica, P.O. Box 23-166, Taipei, Taiwan. ⁶Department of Chemistry and Biochemistry, University of Colorado, Boulder, CO 80309, USA. ⁷Department of Computational Science, National University of Singapore, Singapore 119260.

*These authors contributed equally to this work.

†To whom correspondence should be addressed. E-mail: xmyang@dicp.ac.cn, dqxie@nju.edu.cn, zhangdh@dicp.ac.cn

Fig. 1. TOF spectra of the H atom product from the $F(^2P_{3/2}) + H_2(j = 0)$ reaction at the collision energy of 0.52 kcal/mol. TOF spectra at three laboratory angles are shown: (A) $\Theta_L = -60^\circ$, (B) $\Theta_L = 25^\circ$, and (C) $\Theta_L = 95^\circ$, which correspond roughly to the forward-, sideways-, and backward-scattering directions for the $HF(v' = 2)$ product in the center-of-mass frame, respectively. Only $HF(v' = 1, 2, 3)$ products are observed here. The inset in (B) also shows the formation of $HF(v' = 3)$, which is much more abundant than $HF(v' = 2)$ at this scattering angle.



the delayed appearance of the $HF(v' = 3)$, the inclusion of spin-orbit interaction, and the assignment of the resonances (20). On the basis of modifications of the SW-PES at the exit channel, a new PES (SWMHS-PES) was recently developed for the $F + H_2$ reaction (20). The picture of reaction resonances at low collision energies on the SWMHS-PES is substantially different from that on the SW-PES. Clearly, a consensus physical picture of reaction resonances in this benchmark system has not yet emerged.

In an effort to resolve the controversy, we have carried out a full quantum-state resolved crossed-beam scattering study on the $F + H_2$ reaction, with the use of the high-resolution and highly sensitive H-atom Rydberg tagging method (21). State-to-state scattering studies have recently provided great insights into the dynamics of elementary chemical reactions (22–25). We also modeled the reaction in a full quantum scattering study, based on a highly accurate PES constructed for this purpose, which includes the spin-orbit interaction with small empirical corrections (26). Because the F^* atom in the first electronic excited state $^2P_{1/2}$ is about 400 cm^{-1} higher in energy than the ground state $F(^2P_{3/2})$, the resolution (about 1% in energy, or roughly 20 cm^{-1} at the translational energy $E_t = 2000 \text{ cm}^{-1}$) in this work can easily distinguish the $F(^2P_{3/2})$ and $F^*(^2P_{1/2})$ reactions. All the main signals observed and analyzed here were attributed to the ground-state F atom reaction.

Time-of-flight (TOF) spectra of the H atom products from the $F + H_2$ reaction were measured at many laboratory angles at 5° intervals, with the collision energy fixed at 0.52 kcal/mol (Fig. 1). The main structures in these TOF spectra can be clearly assigned to the HF product ro-vibrational states from the ground-state $F(^2P_{3/2})$ reaction with $H_2(j = 0)$. The spectra were then converted to the center-of-mass frame, using a standard Jacobian transformation, to obtain the product kinetic energy distributions. During the conversion, detection efficiencies of the H atom product at different laboratory angles and different velocities were simulated and included. The kinetic energy distributions obtained experimentally in the laboratory frame were fitted by simply adjusting the relative populations of the ro-vibrational states of the HF product. From these fittings, relative population distributions of the HF product at each ro-vibrational state were determined at 36 laboratory angles at the collision energy of 0.52 kcal/mol. Quantum-state distributions of the HF product in the center-of-mass frame ($\Theta_{cm} = 0^\circ$ to 180°) were then determined by a polynomial fit to the above results, and from these distributions, full ro-vibrational state-resolved differential cross section (DCS) values were determined (Fig. 2A).

At this collision energy, all $HF(v' = 1, 2, 3)$ products were observed. The observation of the $HF(v' = 3)$ product (the middle sharp peak in Fig. 2A) suggests that the $HF(v' = 3)$ product appears as soon as the collision energy reaches

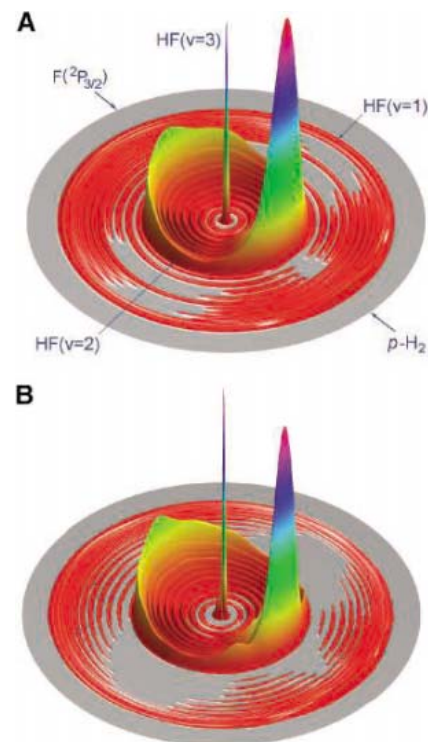


Fig. 2. Experimental (A) and theoretical (B) 3D contour plots for the product translational energy and angle distributions for the $F(^2P_{3/2}) + H_2(j = 0)$ reaction at the collision energy of 0.52 kcal/mol. The different circles represent different HF product ro-vibrational states. The forward-scattering direction for HF is defined along the F atom beam direction.

this channel's threshold. This result is consistent with previous experimental results at higher collision energies and is considerably different from the result predicted by the SW-PES, in which the $HF(v' = 3)$ product does not appear below collision energies of 1 kcal/mol. Another intriguing observation from this experiment is the pronounced forward-scattering peak (referenced to the F beam) for the $HF(v' = 2)$ product, which was not observed previously because of the experimental difficulty in accessing the low collision energy region and in measuring the DCS for this reaction. The forward-scattered product is potentially an important probe of reaction resonances, because forward reactive scattering could relate closely to the time delay caused by resonance-state trapping (4, 23).

We also carried out a careful measurement of the DCS collision energy dependence for the $HF(v' = 2)$ product in the forward-scattering direction. The detector was fixed in the forward direction at different collision energies, and the measurement was repeated 10 times at different collision energies to reduce experimental error, which was estimated to be about 10%. The data in the collision energy range of 0.2 to 0.9 kcal/mol show a peak for the forward-scattered $HF(v = 2)$ product at the collision energy of 0.52 kcal/mol (Fig. 3A).

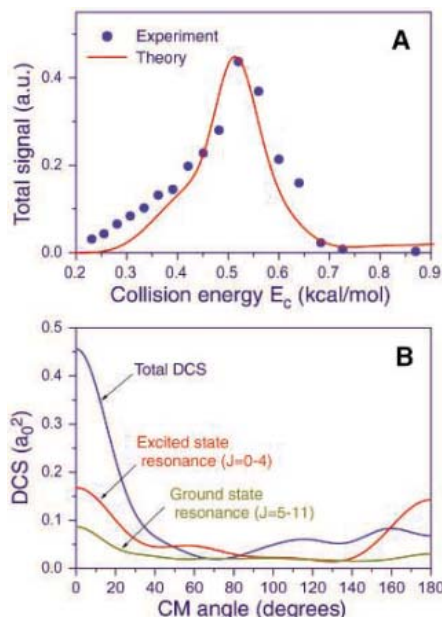


Fig. 3. (A) Collision energy–dependent DCS for the forward-scattering HF($v' = 2$) product. A resonance-like peak is clearly observed at the collision energy of 0.52 kcal/mol. The solid circles are the experimental data, and the solid line is the calculated theoretical result. (B) The total DCS of the HF($v' = 2$) product and the DCS contributions to the HF($v' = 2$) product from both the ground and the excited resonance partial waves at 0.52 kcal/mol.

To interpret these data, we constructed a highly accurate PES for the $F(P_{3/2}) + H_2$ reaction. We used the internally contracted multireference configuration interaction method (27, 28) with the Davidson correction (icMRCI + Q) (29) and the augmented correlation-consistent valence 5-zeta (aug-cc-pv5z) basis set of Dunning (30). [For a detailed description of the PES construction, see (26).] The static barrier for the reaction was calculated to be 2.33 kcal/mol. On the basis of this PES, fully converged quantum scattering calculations were carried out for the $F(P_{3/2}) + H_2(j = 0)$ reaction at collision energies up to 1.5 kcal/mol using the ABC code (31). All the theoretical results shown here are convoluted with the experimental collision energy spread. The calculations support predominantly forward-scattered HF($v' = 2$) products at a collision energy of 0.52 kcal/mol. The overall agreement between the theoretical and experimental data is very good (Fig. 2), which is remarkable given that the DCS varies rapidly around 0.52 kcal/mol. Thus, the new PES is clearly accurate from the dynamical point of view. We also compared theoretical and experimental DCSs at other collision energies, and the agreement is also generally good. Theoretical results show that the HF($v' = 3$) product (the middle sharp peak in Fig. 2B) is already abundant at 0.52 kcal/mol, in good agreement with the current experimental observation. This

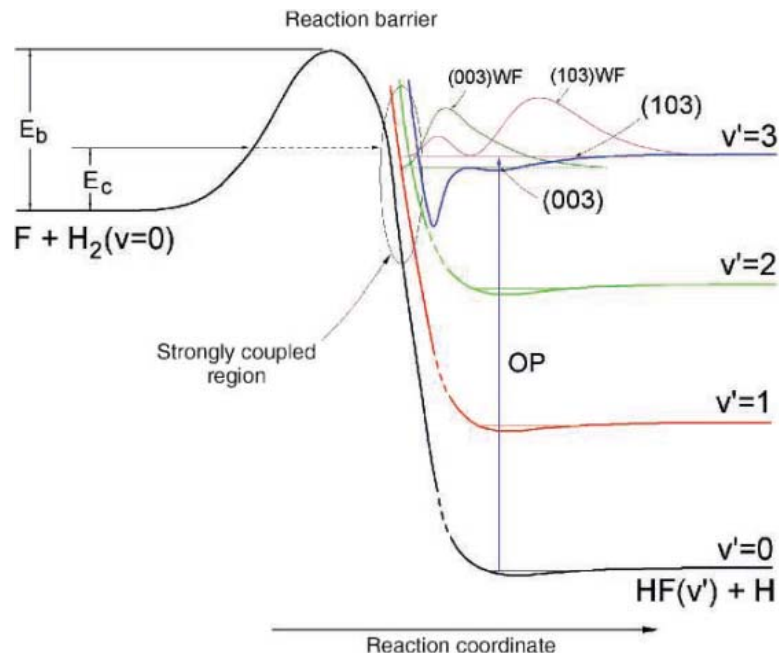


Fig. 4. Schematic diagram showing the resonance-mediated reaction mechanism for the $F + H_2$ reaction with two resonance states trapped in the peculiar HF($v' = 3$)–H' VAP well. The 1D wave functions of the two resonance states are also shown. The (003) state is the ground resonance state; the (103) resonance is the first excited resonance state. Calculated van der Waals states for the lower VAPs are also shown. OP, overtone pumping; E_b , barrier height; E_c , collision energy.

agreement shows clear progress from simulations based on previous potential energy surfaces.

We also calculated the collision energy dependence for the forward-scattering HF($v' = 2$) product (Fig. 3A), and the result mirrors the experimental result. It is obvious that the theoretical result is very similar to the experimental data, with a clear narrow peak precisely at 0.52 kcal/mol. Small empirical corrections, which scaled the ab initio calculated energies so that the asymptotic energetics matched the correct experimental values, rendered the theoretically predicted resonance peak in almost perfect agreement with the current experimental result. With these corrections, the predicted DCS is also in excellent agreement with the experimental DCS at the same collision energies.

The nature of the narrow resonant peak for the forward-scattered HF($v' = 2$) product is very intriguing. The energy-dependent reaction probability (32) (fig. S1) for the total angular momentum $J = 0$ exhibits two distinctive peaks, at 0.26 and 0.46 kcal/mol, that correspond to two reaction resonance states: the ground and the excited resonance states. Partial wave analysis shows that about 65% of the reaction cross section at 0.52 kcal/mol comes from the excited resonance with contributions from the $J = 0$ to 4 partial waves, whereas the other 35% is due to the ground resonance with contributions from $J = 5$ to 11 (32) (figs. S2 and S3). Figure 3B shows the total DCS and the DCS contributions from both the ground and the excited resonance partial waves at 0.52 kcal/mol. Clearly, the excited resonance plays a major role in the

HF($v' = 2$) forward scattering, but the ground resonance is also important. More interestingly, it seems that the partial waves from both resonances interfere constructively, making the forward-scattering HF($v' = 2$) peak much more pronounced than the mere summation of the DCS contributions from the ground and the excited resonances. The narrow peak for the HF($v' = 2$) forward scattering at the collision energy of 0.52 kcal/mol (Fig. 3A) is thus directly related to the constructive quantum interference between the two reaction resonance pathways.

From the converged time-dependent wave packet calculations, the exact scattering wave functions at 0.26 and 0.46 kcal/mol for $J = 0$ are extracted. The three-dimensional (3D) scattering wave function at the collision energy of 0.26 kcal/mol shows the existence of three nodes along the H-F coordinate (correlating to the HF product) in the HF–H' complex with no node along the reaction coordinate (32) (fig. S4). The projection of the $J = 0$ scattering wave function at 0.26 kcal/mol to the HF vibrational states shows that the main character in this wave function is HF($v' = 3$) with the outgoing waves mostly on HF($v' = 2$) (32) (fig. S5). This implies that the resonance state at 0.26 kcal/mol is the ground resonance state, (003), trapped in the HF($v' = 3$)–H' vibrational adiabatic potential (VAP) well. The 3D scattering wave function for $J = 0$ at the collision energy of 0.46 kcal/mol shows the existence of three nodes along the H-F coordinate (correlating to the HF product) in the HF–H' complex with one node along the

reaction coordinate (32) (fig. S4). The projection of the $J = 0$ scattering wave function at 0.46 kcal/mol to the HF vibrational states shows the main character in this wave function is predominantly HF($v' = 3$) with the outgoing waves also mostly on HF($v' = 2$) (32) (fig. S5). This suggests that the resonance state at 0.46 kcal/mol is the excited reaction resonance state trapped in the HF($v' = 3$)-H' VAP well. This resonance state can be assigned to the (103) resonance state with one-quantum vibration along the reaction coordinate, zero-quantum vibration on the bending motion (or hindered rotation), and three-quanta vibration along the HF stretching.

Figure 4 shows the resonance-mediated reaction mechanism. The HF($v' = 3$)-H' VAP on the new PES is very peculiar with a deeper vibrational adiabatic well close to the reaction barrier and a shallow van der Waals (vdW) well, which is similar to the picture on the SW-PES (33) and different from that on the SWMHS-PES (20). The 1D wave function for the ground resonance state in Fig. 4 shows that this state is mainly trapped in the inner deeper well of the HF($v' = 3$)-H' VAP with a considerable vdW character, whereas the excited resonance wave function is mainly a vdW resonance. The main character of the ground resonance state is similar to that of the observed resonance in the F-H-D reaction (15), but with some difference because of the vdW character in the F-H-H case. Because of the vdW characters, these two resonance states could likely be accessed via overtone pumping from the HF($v' = 0$)-H' vdW well. The above analysis also suggests

that the vdW interaction can affect the reaction dynamics in a substantial way (17, 34).

References and Notes

- G. C. Schatz, *Science* **288**, 1599 (2000).
- A. Kuppermann, in *Potential Energy Surfaces and Dynamical Calculations*, D. Truhlar, Ed. (Plenum, New York, 1981), pp. 375–420.
- Y. T. Lee, *Science* **236**, 793 (1987).
- K. Liu, *Annu. Rev. Phys. Chem.* **52**, 139 (2001).
- F. Fernandez-Alonso, R. N. Zare, *Annu. Rev. Phys. Chem.* **53**, 67 (2002).
- G. C. Schatz, J. M. Bowman, A. Kuppermann, *J. Chem. Phys.* **58**, 4023 (1973).
- G. C. Schatz, J. M. Bowman, A. Kuppermann, *J. Chem. Phys.* **63**, 674 (1975).
- G. C. Schatz, J. M. Bowman, A. Kuppermann, *J. Chem. Phys.* **63**, 685 (1975).
- S.-F. Wu, B. R. Johnson, R. D. Levine, *Mol. Phys.* **25**, 839 (1973).
- D. M. Neumark, A. M. Wodtke, G. N. Robinson, C. C. Hayden, Y. T. Lee, *Phys. Rev. Lett.* **53**, 226 (1984).
- D. M. Neumark, A. M. Wodtke, G. N. Robinson, C. C. Hayden, Y. T. Lee, *J. Chem. Phys.* **82**, 3045 (1985).
- F. J. Aoiz *et al.*, *Chem. Phys.* **223**, 215 (1994).
- J.-F. Castillo, D. E. Manolopoulos, K. Stark, H.-J. Werner, *J. Chem. Phys.* **104**, 6531 (1996).
- K. Stark, H.-J. Werner, *J. Chem. Phys.* **104**, 6515 (1996).
- R. T. Skodje *et al.*, *Phys. Rev. Lett.* **85**, 1206 (2000).
- D. E. Manolopoulos *et al.*, *Science* **262**, 1852 (1993).
- C. L. Russell, D. E. Manolopoulos, *Chem. Phys. Lett.* **256**, 465 (1996).
- L. Y. Rusin, M. B. Sevryuk, J. P. Toennies, *J. Chem. Phys.* **122**, 134314 (2005).
- S. A. Nizkorodov, W. W. Harper, W. B. Chapman, B. W. Blackmon, D. J. Nesbitt, *J. Chem. Phys.* **111**, 8404 (1999).
- M. Hayes, M. Gustafsson, A. M. Mebel, R. T. Skodje, *Chem. Phys.* **308**, 259 (2005).
- L. Schnieder, K. Seekamp-Rahn, E. Wrede, K. H. Welge, *J. Chem. Phys.* **107**, 6175 (1997).
- X. Liu, J. J. Lin, S. A. Harich, G. C. Schatz, X. Yang, *Science* **289**, 1536 (2000).
- S. A. Harich *et al.*, *Nature* **419**, 281 (2002).
- D. Dai *et al.*, *Science* **300**, 1730 (2003).
- B. R. Strazisar, C. Lin, H. F. Davis, *Science* **290**, 958 (2000).
- See supporting material on Science Online.
- H.-J. Werner, P. J. Knowles, *J. Chem. Phys.* **89**, 5803 (1988).
- P. J. Knowles, H.-J. Werner, *Chem. Phys. Lett.* **145**, 514 (1988).
- S. R. Langhoff, E. R. Davidson, *Int. J. Quantum Chem.* **8**, 61 (1974).
- T. H. Dunning, *J. Chem. Phys.* **90**, 1007 (1989).
- D. Skouteris, J. F. Castillo, D. E. Manolopoulos, *Comput. Phys. Commun.* **133**, 128 (2000).
- See fig. S1 for the $J = 0$ reaction probability, fig. S2 for the partial wave decomposition of the HF($v' = 2$) forward-scattering peak at the collision energy of 0.52 kcal/mol, fig. S4 for the 3D scattering wave functions at 0.26 and 0.46 kcal/mol for $J = 0$ from converged time-dependent wave packet calculations, and fig. S5 for projection of $J = 0$ scattering wave function at the collision energy of 0.26 kcal/mol (corresponding to the ground resonance state) to HF vibrational states and at 0.46 kcal/mol (corresponding to the excited resonance state).
- S. D. Chao, R. T. Skodje, *J. Chem. Phys.* **113**, 3487 (2000).
- T. Xie, D. Wang, J. M. Bowman, D. E. Manolopoulos, *J. Chem. Phys.* **116**, 7461 (2002).
- Supported mainly by the Chinese Academy of Sciences, the Ministry of Science and Technology, and the National Natural Science Foundation of China. M.G. and R.T.S. acknowledge the support of Academia Sinica. We thank K. Liu for many insightful discussions, and C. Zhou, W. Dong, and X. Wang for their help during the experiment.

Supporting Online Material

www.sciencemag.org/cgi/content/full/311/5766/1440/DC1

Materials and Methods

Figs. S1 to S5

References

5 December 2005; accepted 3 January 2006

10.1126/science.1123452

Signatures of H₂CO Photodissociation from Two Electronic States

H. M. Yin,¹ S. H. Kable,^{1*} X. Zhang,² J. M. Bowman^{2*}

Even in small molecules, the influence of electronic state on rotational and vibrational product energies is not well understood. Here, we use experiments and theory to address this issue in photodissociation of formaldehyde, H₂CO, to the radical products H + HCO. These products result from dissociation from the singlet ground electronic state or the first excited triplet state (T_1) of H₂CO. Fluorescence spectra reveal a sudden decrease in the HCO rotational energy with increasing photolysis energy accompanied by substantial HCO vibrational excitation. Calculations of the rotational distribution using an ab initio potential energy surface for the T_1 state are in very good agreement with experiment and strongly support dominance of the T_1 state in the dynamics at the higher photolysis energies.

The study of reaction dynamics of small molecules has contributed greatly to our understanding of molecular reactivity—an understanding that now allows us to follow and even control reactions from precise quantum states of a reactant to the quantum states of the products. However, even for molecules as small as four atoms, the influence of different electronic states on the product state distributions is not well understood. Here we examine this issue for the otherwise very well studied

photodissociation of the tetra-atomic formaldehyde molecule (H₂CO).

Formaldehyde is found in the troposphere as a result of air pollution. It decomposes via photodissociation due to absorption of actinic solar radiation (I). Although this process might seem to represent a simple chemical reaction, there are at least six different photochemical and photophysical pathways that could occur after absorption of a near-ultraviolet photon excites H₂CO to its lowest excited singlet elec-

tronic state (Fig. 1). These processes include fluorescent relaxation; internal conversion to a vibrationally excited electronic ground state (S_0), which in turn results in dissociation to radical or molecular products; or intersystem crossing to a triplet electronic state, also followed by dissociation to radical products.

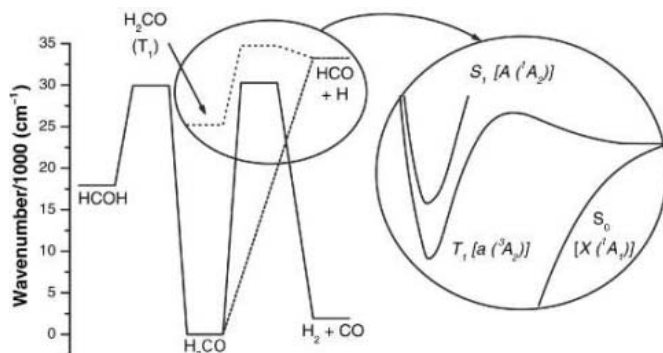
The fluorescence and S_0 dissociative pathways to the radical and molecular products have a long history, with much of the pioneering work done by Moore and Weisshaar (2). Knowledge of the respective branching ratios (or quantum yields) is vital to atmospheric modeling. An alternative route to molecular products from S_0 , via a “roaming atom” mechanism (3), was reported in 2004 (4). An isomerization pathway on S_0 has been predicted (5, 6) but not observed experimentally.

Reaction via the triplet channel has also long been suspected, although its precise threshold energy and probability are not well established.

¹School of Chemistry, University of Sydney, Sydney, NSW 2006, Australia. ²Department of Chemistry and Cherry L. Emerson Center for Scientific Computation, Emory University, Atlanta, GA 30322, USA.

*To whom correspondence should be addressed. E-mail: s.kable@chem.usyd.edu.au (S.H.K.), jmbowma@emory.edu (J.M.B.)

Fig. 1. Relevant potential energy slices of H_2CO producing the radical $\text{H} + \text{HCO}$ products. Energies are based on ab initio calculations and do not include zero-point energy (6).



Although the singlet and triplet channels both produce $\text{H} + \text{HCO}$ product, the fundamental reaction dynamics are very different. The pathway on the S_0 potential energy surface (PES) is barrierless. Experiments have shown that the dynamical signature of this pathway is a set of products whose energy is distributed statistically throughout all available degrees of freedom (7, 8). The translational energy of the fragments is modest, again in keeping with the notion that the reaction on a bound PES is dynamically slow and energy is distributed among all available degrees of freedom. Recently, a quasi-classical trajectory (QCT) study of this reaction on the S_0 PES found qualitative agreement with the experimental results, i.e., that the HCO rotational energy distribution is very broad and translation is modest (9).

As the excess energy is increased, early experiments in which the H-atom recoil energy was measured showed a change in the translational energy distribution from relatively low and statistical to significant and inverted (10). This finding was attributed to the opening of the triplet pathway, which has a barrier to the production of $\text{H} + \text{HCO}$ (Fig. 1). The H-atom experiments placed the height of the triplet barrier between 1020 and 2100 cm^{-1} above the thermochemical threshold. More recent H-atom Rydberg-tagging experiments (11, 12) revealed vibrational and partial rotational resolution in the partner HCO fragment. These experiments, which were carried out with 40 different initial energies spanning 1400 cm^{-1} , revealed great complexity in the translational “spectra.” Even nearby rotational and vibrational levels of formaldehyde showed quite different translational energy distributions. Some states produced vibrationally excited HCO, whereas others showed little vibrational excitation. Some showed large excitation of K_a rotational states, but others were rotationally cold. These results were interpreted as a competing interplay of dynamics on the S_0 and T_1 surfaces. Specifically, the S_0 channel was expected to continue yielding products in a statistical distribution of internal states, and therefore with substantial rotational and vibrational excitation. The T_1 channel, in contrast, was expected to give product state distributions reflective of more impulsive dynamics, because the reaction proceeds

over a distinct transition state of $\sim 2000 \text{ cm}^{-1}$ relative to $\text{H} + \text{HCO}$ (at its minimum). In this context, most of the exit channel energy would be partitioned into translational energy, predominantly in the H atom, whereas internal HCO degrees of freedom would be much less excited.

Here we probe in detail the dissociation dynamics of formaldehyde at energies straddling the triplet barrier. Experimentally, we have chosen initial states whose excess energies (820 to 2600 cm^{-1}) span a greater range than uncertainty of the estimates of the triplet barrier height. The energies of the lower lying states are far below the triplet barrier and, hence, any HCO product must arise predominantly from the S_0 channel. Tunneling on the T_1 PES is of course possible at these lower energies; however, this would be a minor contributor to radical products. Conversely, at the highest excitation energies, the triplet barrier should be exceeded according to both the best experimental and theoretical estimates (6, 10, 13). Several state energies lying within the uncertainty range of the barrier height were also examined.

For the calculations, we chose energies in a similar range and analyzed the HCO vibrational and rotational state populations obtained from trajectories done separately on the S_0 or T_1 PESs. The calculations and experiments agree semiquantitatively but do not accord with previous expectations. This result leads us to reappraise the role of the triplet surface in formaldehyde photochemistry and to recharacterize the dynamical signature of reaction via this pathway.

The experimental setup for producing and detecting HCO from the photolysis of H_2CO has been described previously (7, 8). H_2CO was excited into specific vibrational and rotational states (ν, J, K_a, K_c) in the first excited singlet state ($S_1, ^1A_2$). The production of HCO via S_0 or T_1 channels is monitored by using laser-induced fluorescence (LIF) excitation spectroscopy of the $\text{HCO } \text{B} \leftarrow \text{X}$ transition. The spectrum is complex but fully assigned (14), allowing the determination of product state distributions with full resolution of vibrational and rotational states.

Figure 2 shows two excitation (or action) spectra of H_2CO , obtained by monitoring either LIF or production of HCO ($\nu = 0$) (photofragment excitation or phofex). The spectra are

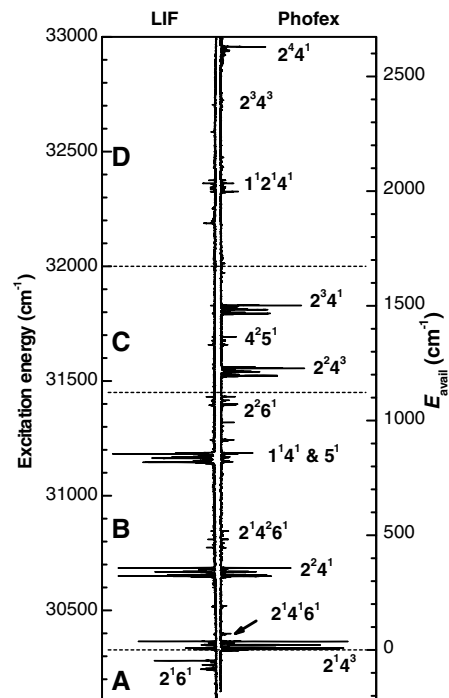


Fig. 2. Laser-induced fluorescence (LIF, left) and photofragment excitation (Phofex, right) spectra of H_2CO . Region A: H_2CO is bound and hence no structure is seen in the phofex spectrum. Region B: H_2CO is unbound on the S_0 surface but bound on the T_1 surface. Region C: H_2CO is within the uncertainty limits of the T_1 barrier height. Region D: H_2CO is unbound on both S_0 and T_1 surfaces. The state labels refer to excitation of the vibrational modes of H_2CO in the S_1 state, e.g., $2^2 4^1$ indicates two vibrational quanta in the CO stretch (mode 2) plus one quantum of excitation in a bending vibration (mode 4).

sorted by photolysis energy into four distinct regions, denoted A, B, C, and D. In region A, at the bottom of the figure, H_2CO has insufficient energy to dissociate into $\text{H} + \text{HCO}$. Consequently, there is no signal in the phofex spectrum, although the signature of excited H_2CO (the $2^1 6^1$ level near 30,220 cm^{-1}) shows up clearly in the fluorescence spectrum. The boundary between regions A and B is therefore the C-H bond energy, which is known accurately to be $30,327.6 \pm 0.9 \text{ cm}^{-1}$ (7, 15).

HCO fragments are produced throughout regions B to D. In Region B, the S_0 channel should dominate, according to the best experimental and theoretical estimates of the triplet barrier height. Although the threshold for dissociation on S_0 has been exceeded, both LIF and phofex spectra show nearly identical structure throughout region B. There is little fluorescence signal in regions C and D. Region C spans approximately the current uncertainty limits for the height of the triplet barrier. Region D lies above the uncertainty limits, and therefore the HCO fragments observed in the phofex spectrum may arise from either the S_0 or T_1 surfaces.

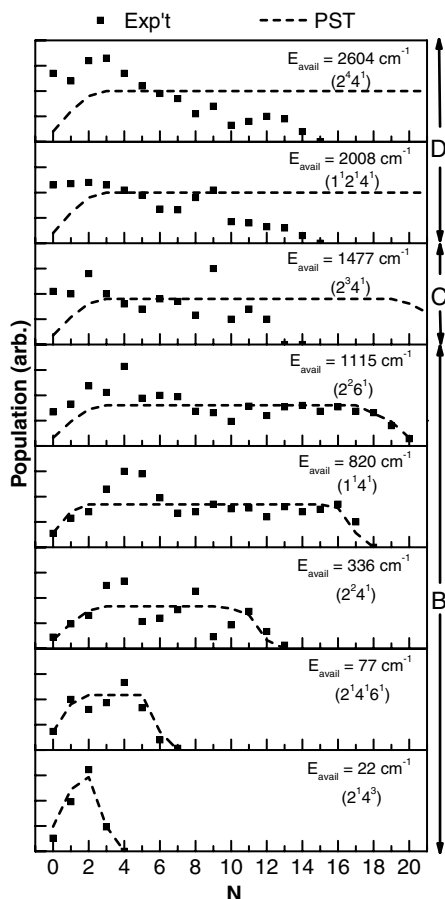


Fig. 3. Rotational state distributions of the HCO fragment following dissociation of H₂CO. Regions B to D correspond to those in Fig. 2. The distributions reflect dynamics for HCO production from the S_0 and T_1 states that are completely different. The distributions in region B are well modeled by phase space theory, whereas those in region D are in excellent agreement with QCT trajectory calculations on an ab initio T_1 surface in this work. The data in this figure cover ~ 2600 cm⁻¹ of excess energy and show the distribution over the N rotational quantum number of HCO for $K_a = 0$ and $\nu = 0$.

The internal energy distributions of the HCO fragments following excitation of eight H₂CO states throughout regions B to D are shown in Fig. 3. The data spanning region B show a consistent progression: All rotational states are fairly equally populated, and the population extends to the kinematic limit (i.e., the limit set by conservation of energy, linear momentum, and angular momentum). The experimental data in region B are represented reasonably well by phase space theory (dashed lines in Fig. 3). Phase space theory is a statistical theory, which assigns equal probability to formation of each product state, weighted with the appropriate degeneracies and subject to the kinematic constraints just noted. The details of these specific calculations for formaldehyde have been reported previously (7, 8).

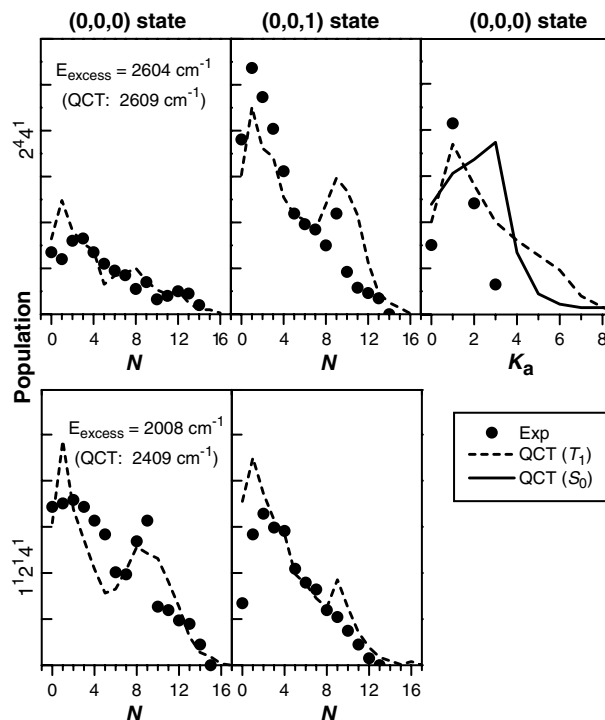


Fig. 4. Comparison between experimental and QCT results for two initial states of H₂CO (2^44^1 and $1^12^14^1$), which should lie above the triplet barrier. The left column shows the HCO population distribution over the N rotational states for $K_a = 0$ and $\nu = 0$. The middle column shows the same distribution for the $(0,0,1)$ vibrational state. The right column shows the distribution over the K_a states (integrated over N) for $\nu = 0$. The experimental data were not available for the $1^12^14^1$ state due to the low signal. The close agreement indicates that the T_1 surface dominates the reaction for these specific levels.

At excitation energies greater than 1200 cm⁻¹, the distributions change markedly. They now peak at very low angular momentum and do not access nearly as high-lying N -states as were seen in region B. They are also much less sensitive to the initial energy than the region B distributions. This sudden change in the distributions at these energies, which are close to the top and above the barrier on the T_1 PES, strongly points to the growing importance of the T_1 channel. Prevailing wisdom suggests that reaction over the triplet barrier should produce rotationally and vibrationally cold HCO fragments (12). Although the present rotational data are consistent with this suggestion, our spectra show considerable vibrational excitation in the HCO products (Fig. 4), even in region D (where the triplet pathway is clearly accessible). Within the excited vibrational states, rotational excitation also remains well below the energetic limit.

To explore the origin of this discrepancy between previous expectations and the present results, we carried out QCT calculations using the techniques described previously (4, 9). These QCT calculations were done on a new ab initio-based PES that describes the T_1 minimum, saddle point, and asymptotic region for the H + HCO products. The calculations were done at the CCSD(T) level of theory with the aug-cc-pVTZ basis set (16), implemented in MOLPRO (17). At each total energy $\sim 10,000$ trajectories were calculated, with initial conditions obtained at the saddle point as described in (9, 18). Final rovibrational states of the HCO product were obtained by the histogram binning method, as done previously (9).

The experimental and QCT rotational distributions (Fig. 4) are in almost quantitative agreement in several key respects. First, the rotational (N , $K_a = 0$) distributions are very cold, peaking at $N < 3$ and only extending to about $N = 13$, in marked contrast to the distributions obtained at lower excitation energy. For example, following excitation of 2^26^1 , where the excess energy, E_{excess} , is 1000 to 1200 cm⁻¹ less, all rotational states up to $\sim N = 20$ are substantially populated. Second, the rotational distributions are almost invariant with energy over the range $E_{\text{excess}} = 1200$ to 2600 cm⁻¹. Again, this feature contrasts starkly with states at lower energy, for which the distributions over N and K_a vary strongly with E_{excess} . Third, substantial population is found in vibrationally excited HCO, almost as soon as the barrier is overcome in the QCT calculations, and in all experiments for $E_{\text{excess}} > 1200$ cm⁻¹. It is important to note that there is only a single normalizing scale factor used for each of the 2^44^1 and $1^12^14^1$ distributions, so the close agreement between the experimental and theoretical vibrational populations, evidenced in Fig. 4, shows that the QCT calculations are capturing the essential nature of the reaction semiquantitatively. Fourth, the form of the rotational distribution is almost invariant with vibrational state (for at least $\nu = 0$ and 1). Fifth, Fig. 4 also shows the population distribution over the K_a states of HCO for excitation into the 2^44^1 state. At this energy, the QCT calculations on the T_1 surface produce a rotational distribution that is peaked at $K_a = 1$, whereas on the S_0 PES, at the same energy, the distribution peaks at $K_a = 4$. The experimental

K_a distributions (also in Fig. 4) are slightly colder than the QCT calculations predict. However, they also peak at $K_a = 1$ and more closely resemble the QCT results on the T_1 surface than those calculated on S_0 .

These five observations, common to both experiment and theory, appear contradictory to expectations. In particular, the very low rotational excitation accompanied by the consistently high vibrational excitation seems inconsistent with a reaction proceeding over a barrier. The important coordinate in this analysis is the HCO angle. At the T_1 transition state, this angle is much closer to free HCO than it is to the equilibrium bond angle on the T_1 surface (13, 19). Therefore, this barrier might also be termed "late." This insight has been used previously (12) to infer that vibrationally excited HCO must arise from the S_0 channel, whereas distributions that are vibrationally and rotationally cold would indicate evolution of the reaction on the T_1 surface. Our experimental and QCT results call this assumption into question. In the QCT results, the reaction is guaranteed to evolve on the T_1 surface. Even so, the population in excited vibrational levels is substantial. This result can be explained in part by a sudden treatment of dynamics, which is appropriate for a barrier-dominated reaction. The CO bond length is roughly 0.015 Å longer at the saddle point than in HCO (19), and so vibrational excitation of the CO stretch is certainly plausible as a result. In addition, the T_1 saddle point geometry is nonplanar, with the departing H atom nearly perpendicular to the HCO plane. This geometry is probably the least efficient configuration for rotational excitation of the HCO fragment and may explain qualitatively why so little rotational excitation is seen.

In the experiments, both S_0 and T_1 states can contribute to the true population distributions. The agreement between the experimental and QCT distributions in Fig. 4 suggests very strongly that when formaldehyde is excited to these specific states, the triplet channel dominates. Clearly, population in excited vibrational states is not a fingerprint for the S_0 pathway. The most robust dynamical signature of the singlet channel is population in very high N and K_a states. The dynamical signature of the T_1 channel is high vibrational excitation coupled with very low rotational excitation.

The dynamical signatures of most of the formaldehyde chemical pathways have thus now been identified. Reaction on S_0 leads to statistical HCO, or to rotationally hot CO and vibrationally cold H_2 , via the direct dissociation over the molecular channel saddle point; alternatively, rotationally cold CO and vibrationally hot H_2 can emerge via the roaming atom mechanism. Reaction on T_1 yields rotationally cold but vibrationally hot HCO. However, several notable issues remain to be addressed. One concerns the possibility of tunneling through the T_1 barrier. Experiment finds that

in region C, which is somewhat below the classical barrier height, the HCO rotational and vibrational distributions are similar to those in region D (above the barrier) rather than B (well below the barrier), suggesting that tunneling is present. Another, more general, issue is the electronic/nuclear coupling among the three electronic states, S_1 , T_1 , and S_0 , which is clearly the next frontier to be explored.

References and Notes

- G. P. Brasseur, J. L. Orlando, G. S. Tyndall, *Atmospheric Chemistry and Global Change* (Oxford Univ. Press, Oxford, 1999).
- C. B. Moore, J. C. Weishaar, *Annu. Rev. Phys. Chem.* **34**, 525 (1983).
- The "roaming atom" channel involves trajectories that start out as a simple C-H bond cleavage; however, the H atom fails to escape because part of the available energy is tied up in other degrees of freedom (principally other HCO vibrations). The loosely bound H atom can roam around the periphery of the HCO moiety, where it encounters the other H atom, then behaves like an abstraction reaction and departs as H_2 . This pathway involves a different region of the PES and results in completely different reaction dynamics (the CO is rotationally cold and the H_2 is vibrationally excited) than for the direct dissociation of the molecular products (an asymmetric planar transition state).
- D. Townsend *et al.*, *Science* **306**, 1158 (2004).
- M. J. H. Kemper, C. H. Hoeks, H. M. Buck, *J. Chem. Phys.* **74**, 5744 (1981).
- X. Zhang, S. Zou, L. B. Harding, J. M. Bowman, *J. Phys. Chem. A* **108**, 8980 (2004).
- A. C. Terentis, S. E. Waugh, G. F. Metha, S. H. Kable, *J. Chem. Phys.* **108**, 3187 (1998).
- H.-M. Yin, K. Nauta, S. H. Kable, *J. Chem. Phys.* **122**, 194312 (2005).
- X. Zhang, J. L. Rheinecker, J. M. Bowman, *J. Chem. Phys.* **122**, 114313 (2005).

- M.-C. Chuang, M. F. Foltz, C. B. Moore, *J. Chem. Phys.* **87**, 3855 (1987).
- M. J. Dulligan, M. F. Tuchler, J. Zhang, A. Kolessov, C. Wittig, *Chem. Phys. Lett.* **276**, 84 (1997).
- L. R. Valachovic *et al.*, *J. Chem. Phys.* **112**, 2752 (2000).
- Y. Yamaguchi, S. S. Wesolowski, T. J. van Huis, H. F. Schaefer III, *J. Chem. Phys.* **108**, 5281 (2002).
- S. H. Lee, I. C. Chen, *J. Chem. Phys.* **103**, 104 (1995).
- A. C. Terentis, S. H. Kable, *Chem. Phys. Lett.* **258**, 626 (1996).
- The potential surface is a fit to roughly 20,000 UCCSD(T)/aug-cc-pVTZ energies spanning the T_1 global minimum, the saddle point to the radical products, and the region beyond into the H + HCO channel. The energies were fit using the expression given in (4) and the root mean square fitting error is 95 cm^{-1} (0.27 kcal/mol) for energies up to 28 kcal/mol above the T_1 minimum, which is ~ 8 kcal/mol above the T_1 saddle point energy of the radical product channel. The electronic barrier to dissociation, H + HCO(e), is 2068 cm^{-1} (5.9 kcal/mol), which is quite close to the best ab initio value of 2130 cm^{-1} reported in (14).
- MOLPRO is a package of ab initio programs written by H.-J. Werner and P. J. Knowles, with contributions from J. Almlöf, R. D. Amos, A. Berning, D. L. Cooper, M. J. O. Deegan, A. J. Dobson, F. Eckert, S. T. Elbert, C. Hampel, R. Lindh, A. W. Lloyd, W. Meyer, A. Nicklass, K. Peterson, R. Pitzer, A. J. Stone, P. R. Taylor, M. E. Mura, P. Pulay, M. Schutz, H. Stoll, and T. Thorsteinsson.
- Y.-T. Chang, C. Minichino, W. H. Miller, *J. Chem. Phys.* **96**, 4341 (1992).
- J. M. Bowman, X. Zhang, *Phys. Chem. Chem. Phys.* **8**, 1 (2006).
- S.H.K. and H.M.Y. thank the Australian Research Council for funding their research, and S. Rowling and A. Buell for assistance in the experiment and analysis. J.M.B. and X.Z. thank the U.S. Department of Energy (grant DE-FG02-97ER14782) for financial support and P. Zhang for useful discussions about the electronic structure calculations.

5 December 2005; accepted 6 January 2006
10.1126/science.1123397

Late Precambrian Oxygenation; Inception of the Clay Mineral Factory

Martin Kennedy,^{1*} Mary Droser,¹ Lawrence M. Mayer,² David Pevear,¹ David Mrofka¹

An enigmatic stepwise increase in oxygen in the late Precambrian is widely considered a prerequisite for the expansion of animal life. Accumulation of oxygen requires organic matter burial in sediments, which is largely controlled by the sheltering or preservational effects of detrital clay minerals in modern marine continental margin depocenters. Here, we show mineralogical and geochemical evidence for an increase in clay mineral deposition in the Neoproterozoic that immediately predated the first metazoans. Today most clay minerals originate in biologically active soils, so initial expansion of a primitive land biota would greatly enhance production of pedogenic clay minerals (the "clay mineral factory"), leading to increased marine burial of organic carbon via mineral surface preservation.

Geochemical and physical evidence suggests that a stepwise increase in oxygen occurred around 1.1 to 0.54 billion years ago (Ga) (1–5) and was a necessary precondition to support the physiological needs of large metazoans (6–8). Whereas the dominant supply of free oxygen to the atmosphere is oxygenic photosynthesis, which began by at least 2.8 Ga (9), the changes in the earth system facilitating a rise in oxygen in the latest Precambrian remain controversial. Photosynthetic oxygen stays in the atmosphere and ocean unless it is consumed by

oxidation of organic matter or other reducing agents at the Earth's surface. The stepwise pattern of oxygen increase implies the modification or activation of a mechanism that became a permanent part of the oxygen and carbon cycles, one that should be important and apparent in modern

¹Department of Earth Science, University of California Riverside, Riverside, CA 92521, USA. ²Darling Marine Center, University of Maine, Walpole ME 04573, USA.

*To whom correspondence should be addressed. E-mail: martink@mail.ucr.edu

organic carbon burial but absent in the Precambrian. Although many hypotheses have been offered to explain the late Precambrian rise of oxygen (1, 4, 8), the irreversible and stepwise pattern argues against processes that are episodic, reversible, or equally active before and after the rise of oxygen, such as tectonics. Here, we offer a paradigm for organic carbon burial in Precambrian marine sediments based on clay minerals, the major cause of carbon preservation and burial in the modern system that we believe was initiated during the latest Precambrian.

Studies of modern marine systems over the past 10 years give a new understanding of how organic carbon enters the sedimentary record. Rather than the conventional model of particles of organic matter rapidly buried in sediment and preserved, the bulk of organic carbon deposited in continental margin sediments is dispersed among or bound to clay minerals (phyllosilicates), as indicated by strong correlations with surface area, data from physical separations, and microscopy (10–14). By contrast, discrete, unbound particulate organic matter comprises <10% of total organic carbon (TOC) (11, 13, 15). The spatial correlation of TOC with clay mineral concentration is likely a result of a sheltering and preservative effect that phyllosilicate surfaces provide to organic matter, and laboratory experiments show that mineral association powerfully enhances preservation of labile carbon compounds (15). Whatever the exact mechanism of protection, studies of both modern and ancient (16) sediments indicate the first order importance of clays as a means of concentrating, accompanying, or preserving organic carbon (11, 13, 14).

Elemental and mineralogical trends indicate long-term changes in shale composition from the Precambrian to the Phanerozoic that could have important implications for an increase in clay production. There is a progressive decline in the K_2O/Al_2O_3 of shale (17, 18) in the Russian and the North American platforms. Loss of K relative to Al is expected with a shift from tektosilicate-dominated (feldspar and quartz) shales and siltstones, with minor amounts of illite-mica-chlorite accessory clays, to smectite- and kaolinite-dominated claystones [summarized in (18, 19); this trend is also influenced by burial diagenesis]. This chemical shift is consistent with a mineralogical shift from mica-illite and chlorite toward smectite, mixed layer smectite-illite, and kaolinite assemblages (19) typical of pedogenic clay minerals (PCM). Simultaneously, incompletely weathered arkose and greywacke become less abundant (18, 20), giving way to chemically mature orthoquartzite (21) (Fig. 1B).

On the basis of these data, we hypothesize secular change in the mineralogy of fine-grained marine sediments (shale and mudstone) from mechanically weathered micas and tektosilicates of high-temperature origin to a more phyllosilicate-rich pedogenic assemblage that should be associated with an enhanced preservation of organic carbon in the sedimentary reservoir in

the mode of modern sediments discussed above. The absence of a working Precambrian “clay factory” should be evident in the rock record, because PCM comprise an important sink of ions produced by weathering and, with recycled clays, make up >60% of Phanerozoic shale, the most common rock type at the Earth’s surface (19).

To determine whether a secular change in clay abundance occurred during the latest Precambrian, we investigated a prominent passive-margin succession spanning the 850 to 530 million years ago (Ma) transition in Australia. This succession was selected because it exhibited (i) a thick interval (>10 km) of passive-margin, shelfal, fine-grained, marine sediments, a majority of which are shales and mudstones (22) typical of depositional environments in which modern mudstones accumulate, and (ii) sufficient exposure to sample the finest-grained lithologies. Although the Australian section provides one of the most complete successions globally (it houses the stratotype section and point defining the Ediacaran Period) and is an ideal test of our hypothesis, we also studied successions in south China and Baltica. To avoid pitfalls of averaging, we sampled the finest-grained intervals within each succession (15 formations total) (table S1) to test the hypothesis.

We found a striking increase in the x-ray diffraction (XRD) peak ratio of total phyllosili-

cate (clay minerals and micas) to quartz through the Neoproterozoic (Fig. 2) (23), supporting the hypothesis that clay formation increased radically at the end of the Proterozoic. We suggest that this trend most likely represents a secular change in PCM formation, delivery, and abundance rather than local, effects, diagenesis, or tectonically influenced trends, because it (i) occurs in multiple margins with different geologic histories, (ii) spans a broader range of time than any single process capable of influencing grain-size trends (i.e., sea level change, deltaic deposition, glaciation, etc.), and (iii) is robust across multiple depositional sequences (cycles of deepening) capable of concentrating the finest-grained fraction available. Additionally, there are no shale diagenetic mechanisms we are aware of that could account for such a strong shift from tektosilicates to octahedrally bound Al in phyllosilicates in (pH neutral) marine sediments.

Because clay minerals deposited in marine sediments are sensitive records of continental paleoenvironments (24), a secular change in clay mineral abundance at the end of the Precambrian may have important implications for terrestrial soils. Unlike other detrital grains such as quartz or feldspar, most clay minerals are not produced by simple mechanical reduction of parent rock and should not be confused with mechanical reduction in grain size of any silicate to clay size

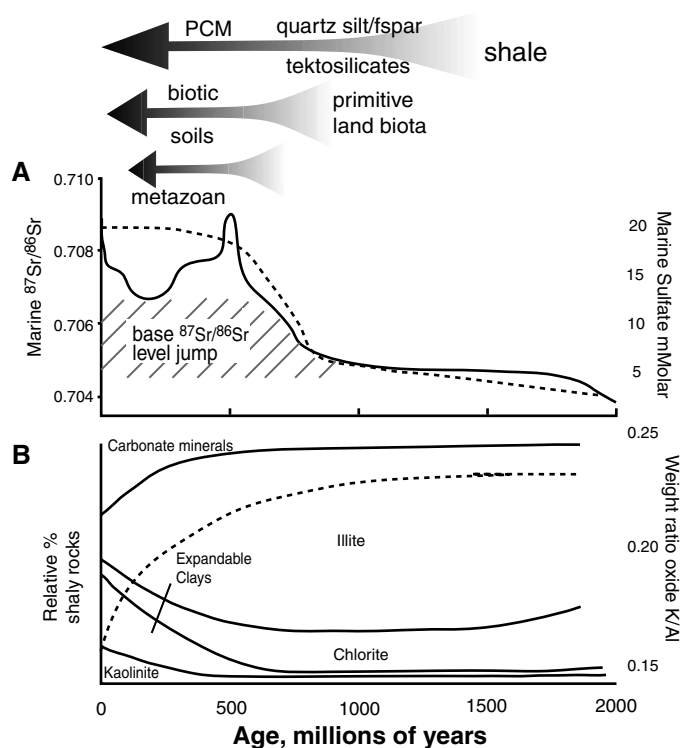


Fig. 1. (A) Solid line represents generalized $^{87}Sr/^{86}Sr$ seawater evolution from carbonate sediments [from (26)]. Minimum $^{87}Sr/^{86}Sr$ for a given age show a stepwise increase in $^{87}Sr/^{86}Sr$, suggested here to result from an increase in chemical weathering resulting from the advent of biogenic soils. Dashed line represents the rise in concentration of dissolved marine sulfate [from (2)], which coincides with general rise in atmospheric oxygen (2). (B) Solid lines and left axis record the increase in expandable clays and kaolinite (PCM) into the Phanerozoic relative to illite, mica, and chlorite within shale from (19), reflecting illitization as well as

enhanced chemical weathering and PCM production associated with biotic soils. The right axis and dashed line records K_2O/Al_2O_3 of shale from the North American and the Russian platforms compiled by (18), showing a shift toward PCM production from mechanically produced lithologies (mica, illite, and feldspar). Also see (17). Elemental data from our sample suite (table S1) show a positive relation between K and Al content ($r = 0.614$), suggesting postdepositional illitization is the dominant control on K/Al, but not necessarily on total clay, in the samples we studied.

(<2 μm). PCM rarely form by solid-state transformation of another mineral but rather precipitate as phyllosilicate crystals from cation-rich soil solutions that are in equilibrium with the ambient environment. Likewise, there is little evidence for large-scale conversion of tectosilicates (dominantly feldspars) to clay minerals in fine-grained sediments, and hydrothermal clay formation produces different clay mineral suites than those found in shales (19, 24, 25). The latitudinal mineralogical zoning of detrital clay minerals in modern marine sediments is consistent with increasing chemical weathering intensity with decreasing latitude, indicating the importance of this terrestrial contribution to marine clay deposition (24).

The lower clay mineral abundance in the earlier sections indicates a reduced continental chemical weathering intensity. This dilution does not, however, preclude the formation of clay minerals and their concentration in local depositional environments throughout the Proterozoic; such clay formation commonly occurs by weathering of volcanic sediments, and clay can be concentrated by sedimentary processes. However, it is not representative of the dominant mode of shale formation, and so these deposits should be rare. The increased phyllosilicates with time identify a new or enhanced source of PCM and increased clay sedimentation (apparent in Cambrian mudstones and through the Phanerozoic), whereas the increasing range of values indicates the effects on the growing clay flux by varying amounts of silt dilution. TOC (without considering sedimentation rate) does not record carbon burial flux; however,

TOC values (table S1) are at least consistent with our hypothesis, showing a commensurate rise with PCM even after thermal alteration.

Enhanced continental chemical weathering implied by PCM formation is also recorded in the step to more radiogenic $^{87}\text{Sr}/^{86}\text{Sr}$ values within Neoproterozoic seawater (26) (Fig. 1). Because the marine $^{87}\text{Sr}/^{86}\text{Sr}$ record provides a globally integrated measure of chemical weathering, it corroborates the secular origin for the clay mineral trend (Fig. 2). Seawater Sr isotopic composition derives from continental weathering and hydrothermal or mantle sources, whose contributions can be estimated because continental runoff is much richer in ^{87}Sr than hydrothermal sources. The Sr isotope record offers an important corroboration of the hypothesis because the seawater values can only be influenced by chemically weathered ions and will not change with variations in fluxes of mechanically weathered material (assuming constant hydrothermal contribution). Further, because minerals such as feldspar and mica derived from mechanical weathering of igneous and metamorphic rocks are strongly enriched in ^{87}Sr as well as K, an enhanced rate of chemical weathering and ion liberation to solution (and PCM formation) should increase $^{87}\text{Sr}/^{86}\text{Sr}$ in marine carbonates.

Two patterns of change mark the marine Sr isotopic record (Fig. 1): (i) a long-term (billion year) plateau with a major step at 0.7 Ga, establishing markedly more radiogenic marine values, and (ii) a shorter-term (~ 100 My) rise and fall in values coincident with the Cambrian Pan-African and the Tertiary Himalayan orogen-

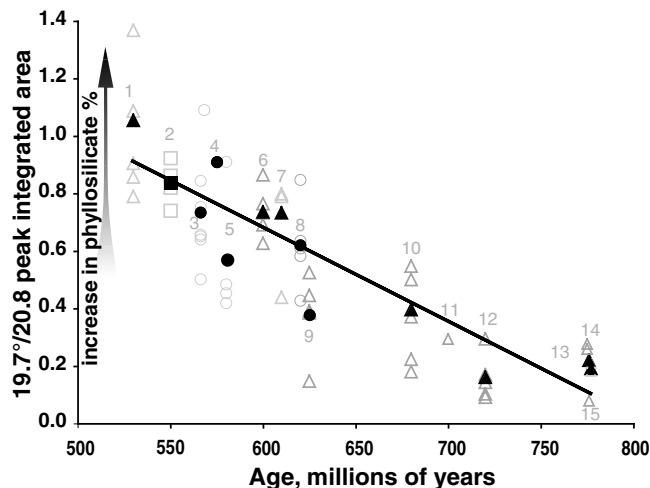
ic events. Here we focus on the long-term, step-like rise of marine $^{87}\text{Sr}/^{86}\text{Sr}$ from 0.705 during the early Neoproterozoic to 0.707, which begins in the late Neoproterozoic and subsequently comprises the lowest value through the Phanerozoic. We suggest that this new plateau results from an irreversible change in chemical weathering regime in parallel with a secular rise in clay mineral abundance.

What might have caused such a change in continental weathering? In the Phanerozoic, biotic soils promote production of PCM by providing organic matter that mechanically stabilizes soil profiles, retains cations and water, and increases fluid residence time (24, 27). Whereas minor amounts of clay formation are possible directly on rock surfaces, the difficulties of retaining and concentrating leached ions are substantial, so that rock surfaces do not produce clay minerals as well as biotic soils. The biotic soil-forming environment for clay minerals can be likened to the carbonate "factory" within the carbonate system. In the absence of a clay mineral-forming mechanism before the late Precambrian, clay minerals deposited in marine sediments were probably not substantial until the evolution and colonization of the terrestrial environment by some form of a primitive land biota.

The transience of terrestrial environments (especially soils) prevents the geological record from preserving reliable evidence of the transformation from an abiotic to a biotic surface. However, physical and geochemical data suggest a primitive land biota by at least 1 Ga (27, 28, 29). Molecular evidence suggests mosses, fungi, and liverworts by ~ 700 Ma (30) and a fossil marine fungi/lichen record by 600 Ma (31) [fungi markedly enhance weathering (32)]. Carbon isotopes of Neoproterozoic karst suggest that soil biomass was sufficient to impart a Phanerozoic-like meteoric isotopic signal to diagenetic carbonate (31). Thus although we cannot specifically identify the transitional states of a land biota, there is ample evidence for these transitions during the Proterozoic. Furthermore, modern microbial crusts stabilize soil profiles, retain water, enhance weathering rates, drive chemical differentiation, and provide chemically adsorptive organic matter (32–34). Thus, the advent of soils sufficiently biotic for clay formation likely predated complex terrestrial ecosystems (33, 35).

One hypothesis for late Precambrian rise of oxygen calls on enhanced burial of organic matter associated with increased tectonic activity between 1.1 and 0.8 Ga (4). This hypothesis uses the positive relation between sedimentation rate and organic matter burial flux observed in modern sedimentary systems, which likely results from the scaling of clay mineral flux with total sedimentation rate (13). Our hypothesis changes the emphasis from temporal changes in quantity of deposition to changes in its quality, that is, its clay mineral abundance. The Neogene Bengal fan illustrates a variation on this theme.

Fig. 2. Secular changes in the relative amounts of phyllosilicate and quartz determined by using the Schultz ratio (16, 23, 25, 38) for Neoproterozoic to Cambrian mudstones. Samples represent the finest-grained units that were at least 5 m thick from three locations: South Australia (triangles), Baltica (circles), and south China (squares). These data show an increase in the proportion of phyllosilicates relative to quartz with decreasing age. Because of the stability of quartz, its abundance serves as a crude



standard indicating the amount of tectosilicates either present (Schultz ratio low) or once present, now clay minerals (Schultz ratio high) in a shale of average chemical composition. Gray symbols are the range of values from a specific unit (all samples analyzed), whereas the solid figure is the average value for a given unit. Units studied include the following: 1, Oraparinna Shale; 2, Doushantuo Formation; 3, Birri Formation; 4, Ekre Shale; 5, Innerelva Member and Stappogiedde Formation; 6, Bunyeroo Formation; 7, Brachina Formation; 8, Nyborg Formation; 9, Reynella Member and Elatina Formation; 10, Enorama Shale; 11, Tarcowie Siltstone; 12, Tapley Hill Formation; 13, Mintaro Shale; 14, Saddleworth Formation; and 15, Woolshed Flat Shale. Age assignments are approximate, and correlations between basins have their basis in the assumed age of 630 Ma for the Marinoan (lower Varanger) glacial and 740 Ma for the Sturtian glacial. Sample locations, data, methods (including elemental data), and stratigraphic references can be found in table S1.

Onset of the monsoon in the Miocene drove an increase in chemical weathering in the Ganges-Brahmaputra watersheds, resulting in a shift from mechanical weathering (tektosilicates, plus mica, illite, and chlorite) to chemical weathering (secondary detrital PCM; smectite, kaolinite) (36). The later PCM mineral assemblage resulted in an ~fourfold increase in organic loading and substantially increased the organic carbon burial flux (36).

The global change that promoted the rise of animals by 0.6 Ga (37) remains one of the most important yet least understood events in the geobiologic record. Here we adopt a non-uniformitarian approach by identifying an important component of the modern system that was largely absent or ineffective in the Precambrian and changed in an irreversible manner sometime during the Neoproterozoic. The modern ocean buries 1.6×10^{14} g C/year, of which 86% (1.38×10^{14} g C/year) is buried in ocean margins (11), where OC concentration and hence burial flux is linearly proportional to clay content. Applying this burial rate throughout the Phanerozoic and assuming that the peak ratios in Fig. 2 are proportional to clay content, then the clay-driven increase in OC burial that developed during 730 to 500 Ma (Fig. 2) ramped from 0.21×10^{14} to 1.38×10^{14} g C/year. The resulting sixfold increase in oxygen retention would have greatly influenced biogeochemical cycling of redox sensitive elements such as Fe^{+2} and S^{2-} (2, 3, 5) and ultimately increased the oxygen concentration of the atmosphere. The evolutionary innovation and expansion of land biota could permanently increase weathering intensity and PCM formation, establishing a new level of organic carbon burial and oxygen accumulation.

References and Notes

- L. A. Derry, A. J. Kaufman, S. B. Jacobsen, *Geochim. Cosmochim. Acta* **56**, 1317 (1992).
- L. C. Kah, T. W. Lyons, T. D. Frank, *Nature* **431**, 834 (2004).
- D. E. Canfield, A. Teske, *Nature* **382**, 127 (1996).
- D. J. Des Marais, H. Strauss, R. E. Summons, J. M. Hayes, *Nature* **359**, 605 (1992).
- S. T. Brennan, T. K. Lowenstein, J. Horita, *Geology* **32**, 473 (2004).
- P. Cloud, *Paleobiology* **2**, 351 (1976).
- B. Runnegar, *Alcheringa* **6**, 223 (1982).
- A. H. Knoll, *Life on a Young Planet* (Princeton Univ. Press, Princeton, NJ, 2003), p. 247.
- J. Brooks, G. A. Logan, R. Buick, R. E. Summons, *Science* **285**, 1033 (1999).
- R. G. Keil, E. Tsamakis, C. B. Fuh, J. C. Giddings, J. I. Hedges, *Geochim. Cosmochim. Acta* **58**, 879 (1994).
- J. I. Hedges, R. G. Keil, *Mar. Chem.* **49**, 81 (1995).
- L. M. Mayer, L. L. Schick, K. R. Hardy, R. Wagai, J. McCarthy, *Geochim. Cosmochim. Acta* **68**, 3863 (2004).
- L. M. Mayer, *Geochim. Cosmochim. Acta* **58**, 1271 (1994).
- B. Ransom, K. Dongseon, M. Kastner, S. Wainwright, *Geochim. Cosmochim. Acta* **62**, 1329 (1998).
- R. G. Keil, D. B. Montlucon, F. G. Prahl, J. I. Hedges, *Nature* **370**, 549 (1994).
- M. J. Kennedy, D. R. Pevear, R. J. Hill, *Science* **295**, 657 (2002).
- R. Cox, D. R. Lowe, R. L. Cullers, *Geochim. Cosmochim. Acta* **59**, 2919 (1995).
- R. M. Garrels, F. T. Mackenzie, *Evolution of Sedimentary Rocks* (Norton, New York, 1971), p. 397.
- C. E. Weaver, *Clays, Muds and Shales* (Developments in Sedimentology, Elsevier, New York, 1989), p. 819.
- A. B. Ronov, *Geokhimiya* **8**, 715 (1964).
- R. H. Dott Jr., *J. Geol.* **111**, 387 (2003).
- W. V. Preiss, *Bull. Geol. Surv. S. Australia* **53**, 438 (1987).
- The Schultz ratio is an uncalibrated, dimensionless number that specifically indicates the relative amount of total phyllosilicates versus quartz by using the x-ray peak intensities for the sum of all phyllosilicates (020 peak, $19.8^\circ 2\theta$, Cu K α radiation) and quartz (100 peak, $20.8^\circ 2\theta$) on random powder mounts. For a granite or clean sandstone, this number would be <0.2. For mudstones and pelitic metamorphics (clay shales, mudstones, slates, and mica schists), it typically is between 0.2 and 2.0. Sediment derived from fine grinding of granite to clay size does not change the Schultz ratio unless dissolution and reprecipitation as a clay mineral has occurred. It is an indicator of available clay minerals in the provenance area, both recycled, and newly formed by soil processes. Later clay diagenesis (such as illitization) does not change the Schultz ratio because it typically converts one phyllosilicate to another.
- H. Chamley, *Clay Sedimentology* (Springer, Berlin, 1989), p. 623.
- L. G. Schultz, *U. S. Geol. Surv. Tech. Rep. No. 391C* (1964).
- G. Shields, J. Veizer, *Geochem. Geophys. Geosystems* **3**, 1 (2002).
- G. J. Retallack, *Soils of the Past, an Introduction to Pedology* (Blackwell Science, Oxford, ed. second, 2001), p. 404.
- A. R. Prave, *Geology* **30**, 811 (2002).
- R. J. Horodyski, L. P. Knauth, *Science* **263**, 494 (1994).
- D. S. Heckman et al., *Science* **293**, 1129 (2001).
- X. Yuan, S. Xiao, T. N. Taylor, *Science* **308**, 1017 (2005).
- A. Neaman, J. Chorover, S. L. Brantley, *Am. J. Sci.* **305**, 147 (2005).
- S. E. Campbell, *Origins Life* **9**, 335 (1979).
- J. F. Banfield, W. W. Barker, S. A. Welch, A. Taunton, J. V. Smith, *Proc. Natl. Acad. Sci. U.S.A.* **96**, 3404 (1999).
- J. A. Raven, D. Edwards, *J. Exp. Bot.* **52**, 381 (2001).
- C. France-Lanord, L. A. Derry, *Nature* **390**, 65 (1997).
- A. H. Knoll, S. B. Carroll, *Science* **284**, 2129 (1999).
- F. L. Lynch, *Clays Clay Miner.* **45**, 618 (1997).
- We thank S. Jensen, T. Bristow, G. Jiang, J. Gehling, and M. Fuller for help in the field. This work was sponsored by NASA grant NWG04G42G and NSF-EAR grants 0223198 and 0345207.

Supporting Online Material

www.sciencemag.org/cgi/content/full/1118929/DC1

Materials and Methods

Table S1

References and Notes

16 August 2005; accepted 13 December 2005

Published online 2 February 2006;

10.1126/science.1118929

Include this information when citing this paper.

The Last Deglaciation of the Southeastern Sector of the Scandinavian Ice Sheet

V. R. Rinterknecht,^{1*} P. U. Clark,¹ G. M. Raisbeck,² F. Yiou,² A. Bitinas,³ E. J. Brook,¹ L. Marks,⁴ V. Zelčs,⁵ J.-P. Lunkka,⁶ I. E. Pavlovskaya,⁷ J. A. Piotrowski,⁸ A. Raukas⁹

The Scandinavian Ice Sheet (SIS) was an important component of the global ice sheet system during the last glaciation, but the timing of its growth to or retreat from its maximum extent remains poorly known. We used 115 cosmogenic beryllium-10 ages and 70 radiocarbon ages to constrain the timing of three substantial ice-margin fluctuations of the SIS between 25,000 and 12,000 years before the present. The age of initial deglaciation indicates that the SIS may have contributed to an abrupt rise in global sea level. Subsequent ice-margin fluctuations identify opposite mass-balance responses to North Atlantic climate change, indicating differing ice-sheet sensitivities to mean climate state.

At its maximum extent, the Scandinavian Ice Sheet (SIS) merged with the Barents Ice Sheet (BIS) and Kara Ice Sheet to form a Eurasian ice sheet complex that was the second largest of the former Northern Hemisphere ice sheets (1–3). Such a large ice mass would have influenced climate on scales ranging from regional to hemispheric and may have affected the formation of North Atlantic deep-water through releases of meltwater and icebergs. Simulations with climate models suggest that the mass balance of the SIS was particularly sensitive to changes in North Atlantic climate because of its location immediately downwind of the North Atlantic Ocean (4). Finally, the SIS deformed the underlying crust, and the record of postglacial isostatic recovery can be inverted to reveal geophysical properties of the lithosphere and mantle (5, 6).

Isolating the relative contributions of the SIS to changes in global sea level, climate, and the solid Earth requires that the chronology of its growth and decay be well constrained. Ice-

¹Department of Geosciences, Oregon State University, Corvallis, OR 97331, USA. ²Centre de Spectrométrie Nucléaire et de Spectrométrie de Masse, 91405 Orsay, France. ³Geological Survey of Lithuania, LT-03123 Vilnius, Lithuania. ⁴Polish Geological Institute, 00-975 Warsaw, Poland. ⁵Department of Geography and Earth Sciences, University of Latvia, Riga, LV-1586, Latvia. ⁶Institute of Geosciences, University of Oulu, Post Office Box 3000, Linnanmaa 90014, Finland. ⁷National Academy of Sciences of Belarus, Institute of Geological Sciences, 220141 Minsk, Belarus. ⁸Department of Earth Sciences, University of Aarhus, DK-8000 Aarhus, Denmark. ⁹Institute of Geology, Tallinn University of Technology, 10143 Tallinn, Estonia.

*Present address: Lamont-Doherty Earth Observatory, Columbia University, Palisades, NY 10964, USA.

†To whom correspondence should be addressed. E-mail: vincent@ldeo.columbia.edu

rafted debris (IRD) in marine cores often provide well-dated records of ice-sheet variability (7, 8), but the linkages between the physics of ice sheets and the formation of an IRD signal have not been clearly established. Prominent end moraines deposited by the southern SIS margin across northern Europe provide a direct record of ice-margin fluctuations, but the paucity of organic material for radiocarbon dating in this region has prevented the development of more than a general understanding of the timing of these fluctuations (9). We measured cosmogenic ^{10}Be concentrations in samples associated with six main moraines (10) deposited by the southeastern SIS in Poland, Belarus, Lithuania, Latvia, Estonia, and Finland (Fig. 1) that firmly establish the chronology of the southern SIS margin since 25,000 years before the present (25 kyr B.P.).

Boulder exposure ages were calculated from $^{10}\text{Be}/^9\text{Be}$ ratios measured by accelerator mass spectrometry (table S1) (10). We present the moraine age as either the mean exposure ^{10}Be age or the error-weighted mean exposure ^{10}Be age, and the uncertainty as the larger of the standard deviation of the mean exposure ages or the error-weighted mean of the analytical uncertainty (10). Outliers exist in the exposure-age populations of all but one of the SIS moraines (Fig. 2). We attribute the anomalously old ages (generally ≥ 30 ^{10}Be kyr) to incomplete erosion of boulder surfaces that had previously been exposed to secondary cosmic rays, resulting in ^{10}Be inheritance. Exposure ages that are clearly too young (generally ≤ 10 ^{10}Be kyr) may reflect post-depositional exhumation or movement or unrecognized erosion of boulder surfaces. Accordingly, we removed these outliers and then further reduced the data set by using Chauvenet's criterion (11) to reject outliers from the sample population of a given moraine, reducing our measured data set from 138 to 111 ^{10}Be ages (10). We then combined previously published ^{10}Be data on four samples from the Salpausselkä I moraine in Finland (12) with data on our nine samples from that moraine (13).

By combining our new ^{10}Be data with 70 new and existing limiting radiocarbon ages on interstadial or postglacial organic matter (table S2), we developed a comprehensive chronology of the southeastern margin of the SIS that identifies three ice-margin fluctuations between 25,000 and 12,000 calendar (cal) yr B.P. (Fig. 3A). Calibrated radiocarbon ages indicate that after a long interstadial, the SIS margin advanced into the Baltic lowlands after $24,900 \pm 370$ cal yr B.P. (14) and reached its maximum extent marked by the Last Glacial Maximum (LGM) Moraine after $20,980 \pm 270$ cal yr B.P. (15) (Fig. 3A). We interpret the cosmogenic ages on surface boulders from moraines to represent the final time of moraine formation. Our 10 ^{10}Be ages from the LGM Moraine in Belarus and Lithuania (Fig. 2A) thus suggest that the SIS margin began to retreat from its

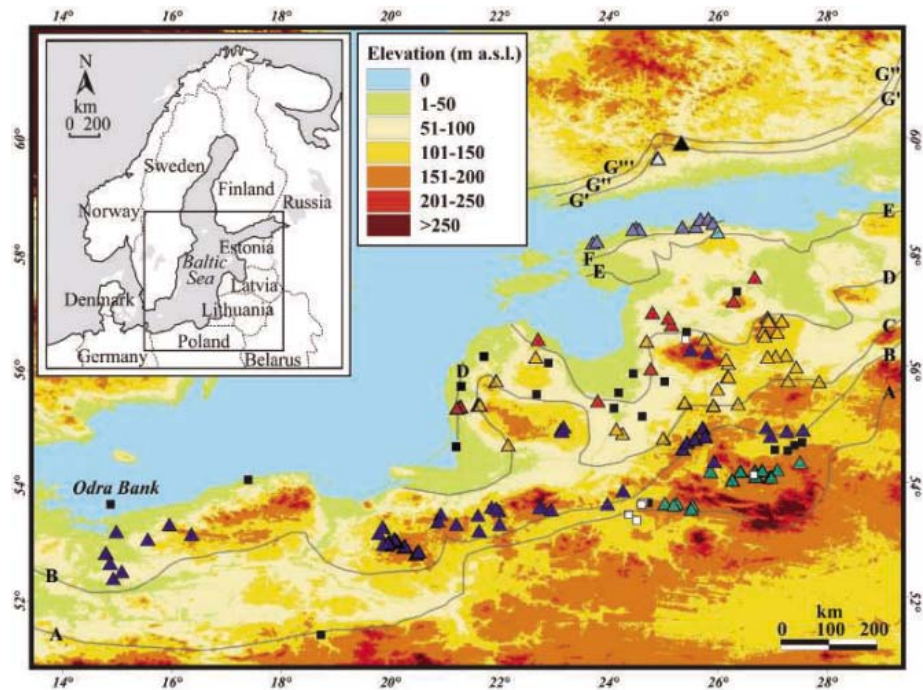


Fig. 1. Digital elevation model of the sampling area (adapted from <http://lpdaac.usgs.gov>). The main ice-marginal positions are outlined in gray (21). a.s.l., above sea level. (A) LGM Moraine. (B) Pomeranian Moraine. (C) Middle Lithuanian Moraine. (D) North Lithuanian Moraine. (E) Pandivere Moraine. (F) Palivere Moraine. (G) Salpausselkä I Moraine. (G') Salpausselkä II Moraine. (G'') Salpausselkä III Moraine. ^{10}Be sites are indicated as follows: LGM Moraine (green-blue triangles), Pomeranian Moraine (dark blue triangles), Middle Lithuanian Moraine (orange triangles), North Lithuanian Moraine (red triangles), Pandivere Moraine (light blue triangle), Palivere Moraine (purple triangles), Salpausselkä I Moraine (gray triangle represents nine samples) (13), Salpausselkä I Moraine (black triangle represents four samples) (12). ^{14}C sites are indicated as follows: this study (white squares), previous studies (black squares).

maximum limit at $19,000 \pm 1600$ ^{10}Be years (Fig. 3A).

Radiocarbon ages on peat from the Odra Bank of the Baltic coast (16), 20 km north of the Polish coast (Fig. 1), indicate that the ice margin retreated north of this site before $16,760 \pm 360$ cal yr B.P., in good agreement with our new radiocarbon age for interstadial sediments in Lithuania ($16,470 \pm 230$ cal yr B.P.; laboratory number AA-53595) (Fig. 3A and table S2). The younger age at Odra Bank indicates that the site remained unglaciated until after $15,520 \pm 430$ cal yr B.P., when ice subsequently readvanced to the Pomeranian Moraine. A similar age for ice recession ($\sim 15,400$ cal yr B.P.) had previously been inferred from radiocarbon dating of organic deposits at the Raunis site, Latvia (15), which became a key constraint in interpretations of SIS marginal history (9). Subsequent investigations, however, demonstrated that these deposits are thoroughly penetrated by recent rootlets (17, 18), pointing to possible radiocarbon contamination.

Forty-two ^{10}Be ages from the Pomeranian Moraine have a mean age of $14,600 \pm 300$ ^{10}Be years (Fig. 2B), which is significantly younger than the previous moraine-age estimate of $\sim 18,000$ cal yr B.P. (19–21). Combined with the Odra Bank radiocarbon ages, these data

identify a significant post-LGM fluctuation of the SIS margin, with readvance from north of the Baltic coast to within 50 to 100 km of the LGM Moraine after $\sim 15,500$ cal yr B.P. and a subsequent retreat beginning at $\sim 14,600$ ^{10}Be years (Fig. 3A). The ^{10}Be ages from three younger Baltic recessional moraines and one boulder from the Pandivere Moraine indicate a relatively slow retreat of the SIS margin from the Pomeranian Moraine to a position south of the Baltic coast by $\sim 13,000$ ^{10}Be years (Figs. 2, C to F, and 3A). With the exception of two radiocarbon ages from Poland [the Gardno site (23, 24)] and two radiocarbon ages from Latvia [the Progress site (17, 18)], our 92 ^{10}Be ages dating ice retreat from the Pomeranian Moraine to the south coast of the Baltic Sea are in excellent agreement with 23 ^{14}C ages on postglacial organic material that provide minimum ages for deglaciation of the same region (Fig. 3A and table S2).

The third and youngest fluctuation of the southern SIS occurred after ice-margin retreat several tens of kilometers north of what is now the Salpausselkä I Moraine before it readvanced to deposit that moraine (Fig. 3A) (25). When we combine our ^{10}Be data from the Salpausselkä I Moraine with those of Tschudi *et al.* (12) and use an integrated production rate to account for

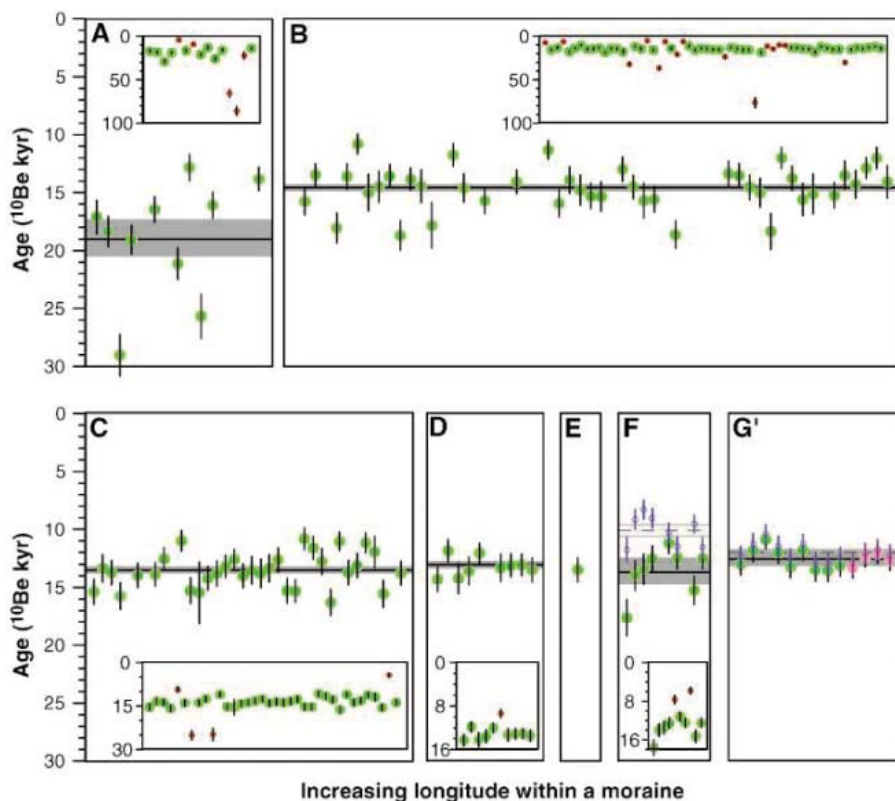


Fig. 2. Single ^{10}Be exposure ages (green and red symbols). **(A)** LGM Moraine [mean age = 19.0 ± 1.6 ^{10}Be thousand years ago (ka), $n = 10$ samples]. **(B)** Pomeranian Moraine (mean age = 14.6 ± 0.3 ^{10}Be ka, $n = 42$). **(C)** Middle Lithuanian Moraine (mean age = 13.6 ± 0.3 ^{10}Be ka, $n = 32$). **(D)** North Lithuanian Moraine (error-weighted mean age = 13.1 ± 0.3 ^{10}Be ka, $n = 9$). **(E)** Pandivere Moraine (13.1 ± 1.1 ^{10}Be ka, $n = 1$). **(F)** Palivere Moraine (mean age = 13.6 ± 1.2 ^{10}Be ka, $n = 8$). **(G')** Salpausselkä I Moraine (error-weighted mean age = 12.5 ± 0.7 ^{10}Be ka, $n = 13$). ^{10}Be exposure ages are ordered within a moraine using the sample longitudes (west to east). Insets in **(A)** to **(D)** and **(F)** correspond to the full data set. Green symbols are ^{10}Be exposure ages used in the moraine age calculation. Red symbols are outliers not included in the moraine age. Error bars for single ^{10}Be exposure ages correspond to 1σ analytical uncertainty only. The black horizontal lines identify the mean age or the error-weighted mean age for each moraine. Shaded gray bands correspond to 1σ uncertainty (the standard deviation of the mean exposure age or error-weighted mean of the analytical uncertainties combined when necessary with uncertainties associated with water submergence and/or uplift assumptions). Pink symbols in **(G')** are the ^{10}Be data from Tschudi *et al.* (12), recalculated using our corrected production rate and erosion and uplift assumptions (13). Open symbols in **(F)** and **(G')** correspond to ^{10}Be samples uncorrected for estimated water submergence and/or isostatic uplift (10). The black dashed line corresponds to the moraine mean age in **(F)** (10.1 ± 0.5 ^{10}Be ka, $n = 8$), and to the moraine error-weighted mean age in **(G')** (12.0 ± 0.2 ^{10}Be ka, $n = 13$) for these uncorrected ages.

isostatic uplift of the region (10), we find that ice retreat from the moraine began at $12,500 \pm 700$ ^{10}Be years (13) (Figs. 2G' and 3A).

Our new chronology for the southern SIS margin has several important implications for understanding the response of the SIS to climate change and its contribution to global sea level change. Our constraints on the timing of the southern SIS at its last maximum extent (~ 21 cal kyr B.P. to 19.0 ^{10}Be kyr) are in good agreement with ages constraining a major advance of the western SIS margin (26) and the maximum extent of the BIS margin (27, 28). Because the SIS and BIS coalesced at their maximum extent, this agreement indicates the expansion of much of the Eurasian ice sheet

complex to its full glacial extent during the interval of relative climate stability and low sea level of the LGM (19.0 to 23.0 kyr B.P.).

Within dating uncertainties, our new ages suggest that the onset of deglaciation of the southern SIS margin at ~ 19.0 ^{10}Be kyr may be synchronous with a rapid sea-level rise of 10 to 15 m at ~ 19.0 cal kyr B.P. that abruptly terminated the LGM lowstand (29) (Fig. 3B). Clark *et al.* (30) inferred that the source of this event originated from one or more of the Northern Hemisphere ice sheets. Our dating of the retreat of the southern SIS margin at this time provides direct evidence that the SIS may have contributed to this abrupt sea-level event. The abruptness of the sea-level event in the ab-

sence of any associated abrupt warming (Fig. 3, B and C) points to an instability of the SIS that caused it to partially collapse, although the gradual warming that preceded the event suggests the possibility of a nonlinear response of the ice sheet to that warming (31). Such a response may have induced fast flow (32) and drawdown of the low-sloping Baltic Sea ice stream (21), causing retreat of the southeastern SIS margin.

This phase of early deglaciation was followed by a 3 to 4 kyr interval of restricted SIS margin extent that coincides with a reduction of the Atlantic meridional overturning circulation induced by the 19-kyr sea-level event and subsequent Heinrich event 1 (H1) (Fig. 3D) (30, 33), with the attendant loss of ocean heat transport to the North Atlantic region causing the Oldest Dryas cold interval (Fig. 3C). Why did the southern SIS margin remain retracted during this cold interval? We suggest that the southward expansion of the polar front in the North Atlantic associated with H1 (34), with an attendant increase in sea ice coverage, caused moisture starvation of the SIS (4), thus preventing its margin from readvancing. Evidence in support of this hydrologic response comes from proxy records that indicate that extreme aridity over Europe accompanied cold temperatures during Heinrich events (35).

We attribute the subsequent readvance of the southern SIS margin to the Pomeranian Moraine to the initial warming that occurred in the North Atlantic region after H1 but before the large and abrupt warming marking the onset of the Bølling-Allerød (Fig. 3, A and C). In particular, a more positive SIS mass balance and attendant ice-margin readvance are expected outcomes of such a warming as a consequence of the precipitation-temperature feedback, which is most effective under cold climates (36). Pollen records support the idea that this atmospheric hydrologic response occurred in showing a rapid shift from semiarid to temperate taxa over parts of southern Europe starting at ~ 16 cal kyr B.P. (35).

The large-scale recession of the southern SIS margin beginning at $14,600 \pm 300$ ^{10}Be years, marking the start of the final retreat of the SIS from the Baltic lowlands, appears to represent a response to the abrupt onset of the Bølling-Allerød warm interval at ~ 14.6 cal kyr B.P. In this case, the warming to near-interglacial temperatures associated with the Bølling-Allerød interval (Fig. 3C) would have overwhelmed the precipitation-temperature feedback and caused a negative mass balance over the ice sheet (36). The ages of the three post-Pomeranian moraines (Figs. 1 and 2C, D, and F) suggest that the receding margin must have paused briefly during the Bølling-Allerød warm interval to construct each of them. Although the precise age of these events cannot be resolved by our dating, the most likely explanation for their occurrence is an ice-margin response to the three centennial-

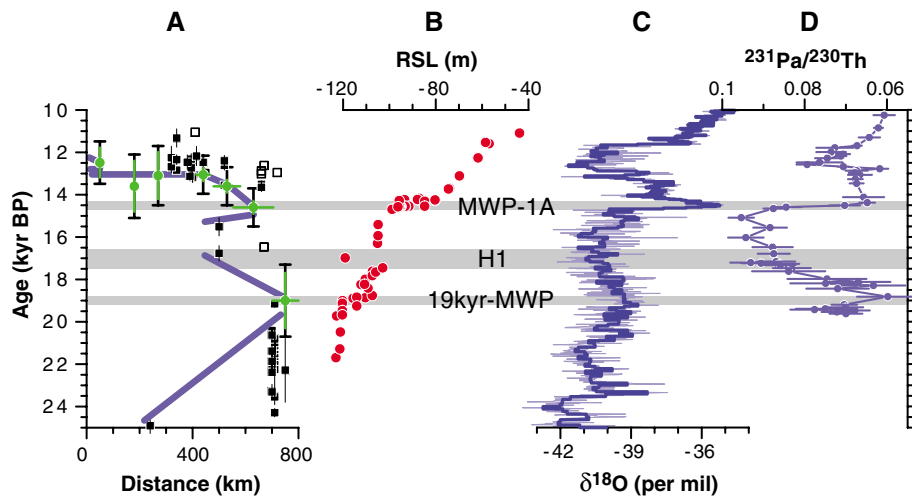


Fig. 3. (A) Time-distance diagram showing fluctuations of the southern margin of the SIS as constrained by our mean or error-weighted mean ¹⁰Be ages (green circles) (table S1) and calibrated radiocarbon ages (white squares, this study; black squares, previous studies) (table S2). The smallest (green) vertical error bar for each moraine age corresponds to the error as described in (10). The largest (black) vertical error bar for each moraine age includes the uncertainty in the ¹⁰Be production rate (6%) for comparison with other records. Horizontal uncertainties shown for our ¹⁰Be data identify the spatial north-south distance over which samples from each moraine were collected. We calibrated radiocarbon ages younger than 21,381 ¹⁴C yr B.P. using IntCal04 (39); we calibrated older radiocarbon ages using the Cariaco Basin calibration curve (40). We excluded four samples (Gd-6117, Gd-4776, TA-129, and TA-129A; table S2) from this data set because they are probably redeposited or contaminated. (B) Records of far-field relative sea-level (RSL) change during the last deglaciation (29, 41, 42). (C) δ¹⁸O record from the Greenland Ice Sheet Project 2 ice core (43, 44). (D) Sedimentary ²³¹Pa/²³⁰Th record from North Atlantic core OCE326-GGC5, a proxy for the Atlantic meridional overturning circulation (33).

scale cold events that occurred during the Bølling-Allerød warm interval (Fig. 3C). The short distance (~100 km) separating the Pomeranian and Middle Lithuanian Moraines along the climatically sensitive southern SIS margin is also important in indicating a negligible contribution of the SIS to global sea level rise in response to Bølling-Allerød warming.

Our new ¹⁰Be ages confirm the Younger Dryas age of the Salpausselkä I Moraine (25) and support the varve chronology (37) in showing that the southern SIS margin subsequently began to retreat to the Salpausselkä II Moraine during the Younger Dryas. The presence of the three Younger Dryas moraines may reflect small climate changes during the Younger Dryas affecting SIS mass balance. Alternatively, the small ice-margin retreat may indicate a dynamic response associated with a drawdown of ice through the Gulf of Bothnia. In any event, in contrast to the preceding Pomeranian readvance, which occurred in response to a small warming during a cold climate, the readvance to the Salpausselkä I Moraine occurred in response to a large Younger Dryas cooling during a warm climate. We attribute these opposite responses to the importance of the precipitation-temperature feedback in controlling mass balance only during cold climates (36). Similar opposing mass balance changes are projected for the two remaining ice sheets in response to future global warming, with a negative mass

balance simulated for the warm-climate Greenland Ice Sheet and a positive mass balance simulated for the cold-climate Antarctic Ice Sheet (38).

References and Notes

- G. H. Denton, T. J. Hughes, *The Last Great Ice Sheets* (Wiley, New York, 1981).
- P. U. Clark, A. C. Mix, *Quat. Sci. Rev.* **21**, 1 (2002).
- J. I. Svendsen *et al.*, *Quat. Sci. Rev.* **23**, 1229 (2004).
- S. W. Hostetler, P. U. Clark, P. J. Bartlein, A. C. Mix, N. J. Pisias, *J. Geophys. Res.* **104**, 3947 (1999).
- K. Lambeck, C. Smither, P. Johnston, *Geophys. J. Int.* **134**, 102 (1998).
- G. A. Milne *et al.*, *Science* **291**, 2381 (2001).
- G. C. Bond, R. Lotti, *Science* **267**, 1005 (1995).
- K. H. Baumann *et al.*, *Quat. Res.* **43**, 185 (1995).
- J. Ehlers, P. L. Gibbard, in *Quaternary Glaciations—Extent and Chronology, Part I: Europe*, (Elsevier, Amsterdam, Netherlands, 2004).
- Materials and methods are available as supporting material on Science Online.
- J. R. Taylor, *An Introduction to Error Analysis*, (University Science Books, Sausalito, CA, 1997).
- S. Tschudi, S. Ivy-Ochs, C. Schlüchter, P. W. Kubik, H. Rainio, *Boreas* **29**, 287 (2000).
- V. R. Rinterknecht *et al.*, *Quat. Sci. Rev.* **23**, 2283 (2004).
- A. Liiva, E. Ilves, J. M. Punning, *Radiocarbon* **8**, 430 (1966).
- A. A. Velichko, M. A. Faustova, *Quat. Sci. Rev.* **5**, 447 (1986).
- R. Kramarska, *Geol. Quart.* **42**, 277 (1998).
- A. Dreimanis, V. Zelčs, in *Glacial Deposits in North-East Europe*, J. Ehlers, S. Kozarski, P. Gibbard, Eds. (A. A. Balkema, Rotterdam, Netherlands, 1995), pp. 105–113.
- Previous work inferred that a till representing ice readvance overlies organic beds at the Raunis, Latvia, site (15). Dreimanis and Zelčs (17), however, question the evidence for ice readvance, the stratigraphic context of the dated unit, and the reliability of the radiocarbon dates. Further work on this site and others (the Progress site) is required to confirm their stratigraphic and geochronologic integrity.
- J. Ehlers, L. Eissmann, L. Lippstreu, H.-J. Stephan, S. Wansa, in (9), pp. 135–146.
- Our mean ¹⁰Be age for the Pomeranian Moraine in eastern Europe requires a revision to the longstanding correlation, by way of northern Germany, with the SIS margin in Denmark (19, 21). However, our age is in excellent agreement with the well-dated timing of retreat from the western Swedish coast (22).
- G. S. Boulton, P. Dongelmanns, M. Punkari, M. Broadgate, in (9), pp. 441–460.
- J. Lundqvist, B. Wohlfarth, *Quat. Sci. Rev.* **20**, 1127 (2001).
- K. Rotnicki, R. K. Borkowka, *Prace Państwowe Instytutu Geologicznego* **149**, 84 (1995).
- The two dated samples (23), recovered from cores, are on “organic intercalations” in glacial lake clay and “organogenic infillings” in alluvial fan sediments. In the absence of further details on the dated material, we speculate that these dates may conflict with the age of deglaciation suggested by our ¹⁰Be ages as well as the majority of other radiocarbon ages from the Baltic lowlands (table S2) because of contamination. However, these ages are similar to those from the Odra Bank (16) and our new radiocarbon age from Lithuania (AA-53595) (table S2) that date an interval of ice retreat, suggesting that the dated material may be reworked organic matter deposited during this interstadial event.
- H. Rainio, in *Glacial Deposits in North-East Europe*, J. Ehlers, S. Kozarski, P. Gibbard, Eds. (A. A. Balkema, Rotterdam, Netherlands, 1995), pp. 57–66.
- J. Mangerud, in (9), pp. 271–294.
- J. Y. Landvik *et al.*, *Quat. Sci. Rev.* **17**, 43 (1998).
- E. Larsen *et al.*, *Boreas* **28**, 115 (1999).
- Y. Yokoyama, K. Lambeck, P. De Deckker, P. Johnston, L. K. Fifield, *Nature* **406**, 713 (2000).
- P. U. Clark, A. M. McCabe, A. C. Mix, A. J. Weaver, *Science* **304**, 1141 (2004).
- H. J. Zwally *et al.*, *Science* **297**, 218 (2002).
- J. A. Piotrowski, J. Kraus, *J. Glaciol.* **43**, 495 (1997).
- J. F. McManus, R. Francois, J. M. Gherardi, L. D. Keigwin, S. Brown-Leger, *Nature* **428**, 834 (2004).
- E. Bard, F. Rostek, J.-L. Turon, S. Gendreau, *Science* **289**, 1321 (2000).
- N. Combournieu Nebout *et al.*, *Geology* **30**, 863 (2002).
- H. Le-Treut, M. Ghil, *J. Geophys. Res.* **88**, 5167 (1983).
- M. Saarnisto, T. Saarinen, *Global Planet. Change* **31**, 387 (2001).
- P. Huybrechts, J. Gregory, I. Janssens, M. Wild, *Global Planet. Change* **42**, 83 (2004).
- P. J. Reimer *et al.*, *Radiocarbon* **46**, 1029 (2004).
- K. Hughen *et al.*, *Science* **303**, 202 (2004).
- E. Bard, B. Hamelin, R. G. Fairbanks, A. Zindler, *Nature* **345**, 405 (1990).
- T. K. S. Hanebuth, P. M. Grootes, *Science* **288**, 1033 (2000).
- P. M. Grootes, M. Stuiver, J. W. C. White, S. Johnsen, J. Jouzel, *Nature* **366**, 552 (1993).
- M. Stuiver, P. M. Grootes, *Quat. Res.* **53**, 277 (2000).
- This work was supported by the NSF Paleoclimate Program (E.J.B. and P.U.C.) and the French Institut National de Physique Nucléaire et de Physique de Particules and Institut National des Sciences de l’Univers. We thank S. Tschudi for providing data from the Salpausselkä I Moraine and S. Hostetler, J. Licciardi, J. Mangerud, and anonymous reviewers for comments.

Supporting Online Material

www.sciencemag.org/cgi/content/full/311/5766/1449/DC1
Materials and Methods
Tables S1 and S2
References

28 September 2005; accepted 9 February 2006
10.1126/science.1120702

Exposed Water Ice Deposits on the Surface of Comet 9P/Tempel 1

J. M. Sunshine,^{1*} M. F. A'Hearn,² O. Groussin,² J.-Y. Li,² M. J. S. Belton,³ W. A. Delamere,⁴ J. Kissel,⁵ K. P. Klaasen,⁶ L. A. McFadden,² K. J. Meech,⁷ H. J. Melosh,⁸ P. H. Schultz,⁹ P. C. Thomas,¹⁰ J. Veverka,¹⁰ D. K. Yeomans,⁶ I. C. Busko,¹¹ M. Desnoyer,¹⁰ T. L. Farnham,² L. M. Feaga,² D. L. Hampton,¹² D. J. Lindler,¹³ C. M. Lisse,¹⁴ D. D. Wellnitz²

We report the direct detection of solid water ice deposits exposed on the surface of comet 9P/Tempel 1, as observed by the Deep Impact mission. Three anomalously colored areas are shown to include water ice on the basis of their near-infrared spectra, which include diagnostic water ice absorptions at wavelengths of 1.5 and 2.0 micrometers. These absorptions are well modeled as a mixture of nearby non-ice regions and 3 to 6% water ice particles 10 to 50 micrometers in diameter. These particle sizes are larger than those ejected during the impact experiment, which suggests that the surface deposits are loose aggregates. The total area of exposed water ice is substantially less than that required to support the observed ambient outgassing from the comet, which likely has additional source regions below the surface.

Before the successful impact experiment with comet 9P/Tempel 1, NASA's Deep Impact mission collected high spatial resolution data of the cometary surface from two visible-color imagers and a near-infrared (near-IR) spectrometer (1). These instruments, particularly the spectrometer, were designed to detect likely cometary materials including water ice, which has major absorptions at wavelengths of 1.5, 2.0, and 3.0 μm (2, 3). Here, we report on the successful detection and mapping of water ice deposits on the surface of 9P/Tempel 1, thus fulfilling one of the major science objectives of the mission.

As comets approach the Sun, they release volatiles. This ambient outgassing produces a gas- and dust-rich coma that obscures the cometary nucleus. Thus, very few observations of bare cometary nuclei exist. Previous cometary missions, notably the Deep Space 1 (DS1) mission to comet 19P/Borrelly (4), have searched for evidence of volatiles on cometary surfaces. DS1 included a near-IR spectrometer with a spatial resolution of 160 m across the nucleus, yet no evidence of absorptions due to water ice in the 1.3- to 2.6- μm region was found (5). The limited ground-based observations of possibly bare cometary nuclei similarly lack absorptions due to water ice (6–10).

¹Science Applications International Corporation (SAIC), Chantilly, VA 20151, USA. ²University of Maryland, College Park, MD 20742, USA. ³Belton Space Exploration Initiatives, Tucson, AZ 85716, USA. ⁴Delamere Support Services, Boulder, CO 80301, USA. ⁵Max Planck Institute for Solar System Research, Katlenburg-Lindau D37191, Germany. ⁶Jet Propulsion Laboratory, Pasadena, CA 91109, USA. ⁷University of Hawaii, Honolulu, HI 96822, USA. ⁸University of Arizona, Tucson, AZ 85721, USA. ⁹Brown University, Providence, RI 02412, USA. ¹⁰Cornell University, Ithaca, NY 14853, USA. ¹¹Space Telescope Science Institute, Baltimore, MD 21218, USA. ¹²Ball Aerospace & Technology Corporation, Boulder, CO 80301, USA. ¹³Sigma Scientific, Greenbelt, MD 20771, USA. ¹⁴Applied Physics Laboratory, Johns Hopkins University, Laurel, MD 20723, USA.

*To whom correspondence should be addressed. E-mail: sunshinej@saic.com

Water ice has, however, been spectrally identified in near-IR telescopic data of the surfaces of Kuiper Belt objects (KBOs) and centaurs (11, 12), the presumed source region for comets (13). In addition, recent Cassini Visual and Infrared Mapping Spectrometer near-IR spectra (14) of the saturnian satellite Phoebe, likely a captured KBO (15), include strong absorptions due to the ubiquitous presence of water ice (16), as previously observed in disk-averaged telescopic observations (17). These results, coupled with the considerable production rates of H₂O and water ice crystals observed in cometary comae, are strong evidence for the presence of water ice in comets

(18–20). However, water ice has not previously been directly detected on the surface of a comet.

The possible presence of volatiles on the surface of 9P/Tempel 1 was first inferred from albedo differences correlated to morphology. Small, relatively bright regions (~30% brighter than surrounding areas) are present in visible-spectrum images (e.g., Fig. 1, A and D). To support more quantitative analysis, we spatially coregistered and rescaled the calibrated intensity/solar flux (I/F) color images to match the clear filter (broad band centered at 650 nm) image for both the Medium- and High-Resolution Imagers (MRI and HRI) onboard Deep Impact. Because the color differences were very subtle, the color image sets were then normalized to those at 750 nm and to a large uniform area of the nucleus; this allowed evaluation of the relative color variations across the nucleus (Fig. 2).

IR spectral scans of the nucleus calibrated to radiance units (21) were assembled into data cubes, which provided inherently spatially coregistered images at 512 wavelengths from 1.05 to 4.8 μm . Each spectrum was independently fit with a blackbody function from 3.0 to 4.4 μm , which was then subtracted to remove the thermal component. As such, a temperature map across the nucleus was also created (1). The spectra were divided by the solar radiance to produce I/F spectra and then normalized to unity at 2.0 μm , yielding relative reflectance spectra.

Color variations on the nucleus can be identified in ratios of image pairs. For HRI, the 450

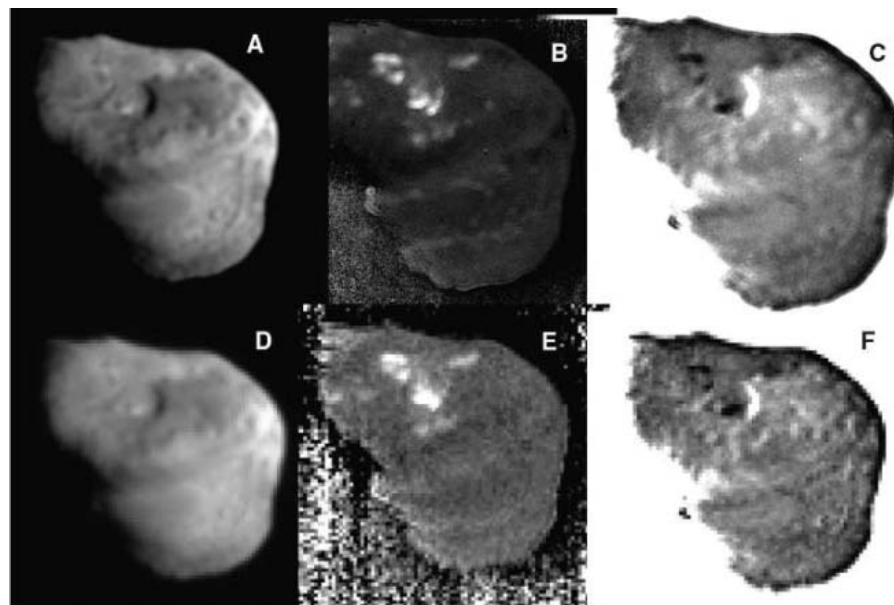


Fig. 1. (A) HRI 750-nm image (16 m/pixel). (B) HRI 450 nm/750 nm image showing areas (brighter) that have relatively higher reflectance at shorter wavelengths. (C) HRI 950 nm/750 nm image showing areas (darker) with relatively lower reflectance at longer wavelengths. Similar results are shown for MRI images (82 m/pixel): (D) 750 nm, (E) 387 nm/750 nm, and (F) 750 nm/950 nm.

nm/750 nm image includes three anomalously bright areas (higher reflectance at 450 nm than at 750 nm) in the top half of the nucleus (Fig. 1B). These same areas are atypically dark in the 950 nm/750 nm image (lower reflectance at 950 nm than at 750 nm) (Fig. 1C). Areas on the nucleus with 450 nm/750 nm ratios of >1.13 and with 950 nm/750 nm ratios of <0.98 were mapped (Fig. 2A) and their average spectral properties calculated (Fig. 2B). Although the MRI color filters are at different wavelengths and narrower than those of the HRI (3), nearly identical results were found from similar processing of the MRI data (Fig. 2, C and D). After correction for emission angle effects, we calculated the total area of these anomalously colored regions to be 0.49 km^2 from HRI and 0.55 km^2 from MRI, corresponding to $\sim 0.5\%$ of the nominal surface area of the nucleus [113 km^2 , assuming a mean radius of 3 km (J)].

To determine the origin of the anomalous colors of these areas, we examined high spectral resolution IR spectra. Relative to typical nucleus spectra, all three regions included distinct 1.5- and 2.0- μm absorptions diagnostic of water ice. These absorptions were clearly seen in spectra from three different IR nucleus scans (200 m/pixel, 160 m/pixel, and 120 m/pixel). Spectra from the highest resolution IR nucleus scan of the three different water ice-rich regions were plotted relative to a broad smooth region of the nucleus and normalized to unity at 2.0 μm (Fig. 2F). A map of 2.0- μm absorption

band strength (Fig. 2E) shows that this absorption correlates very well with the higher spatial resolution maps of anomalous regions seen in the visible data. It is therefore clear that the anomalous color regions are due to the presence of water ice.

The water ice regions are shown overlaying the derived temperature map in Fig. 3. At least two of the ice-rich areas (yellow circles 1 and 2) occur in local cold regions of the nucleus; the third is near a local cold region. However, the scale of the temperature map (120 m/pixel) is insufficient to separate the effects of the topographic variations from any possible effects due to ice. Stereo imaging shows that the largest area of ice (circle 1) is in a depression $80 \pm 20 \text{ m}$ below the surrounding areas. Nonetheless, the temperature derived for the water ice regions varies from 285 to 295 K ($\pm 8 \text{ K}$). These temperatures are significantly above $\sim 200 \text{ K}$, the free sublimation temperature of water ice at a distance of 1.5 AU from the Sun and an incidence angle of 55° [as calculated from (22)]. Thus, the temperatures measured indicate that pure water ice cannot fill a complete IR pixel.

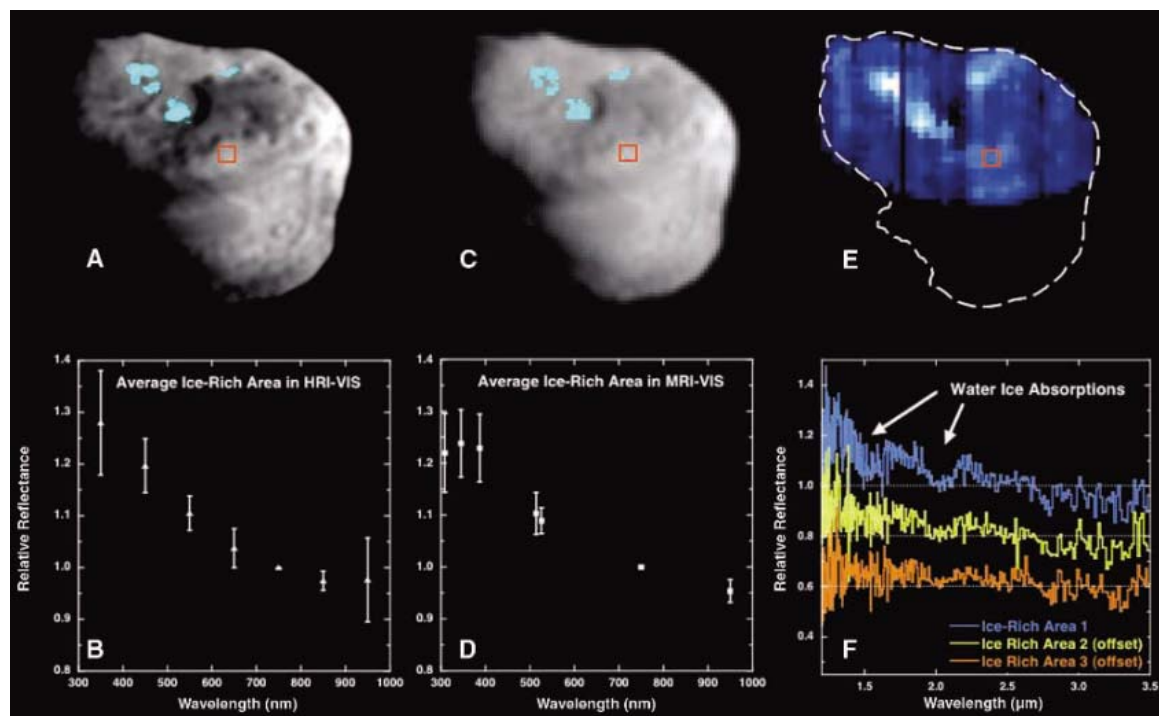
If we consider the case where water ice is intimately mixed with as much as 99% dark (0.04 albedo) material, the aggregated temperature would be only 230 K, still far below the $280 \pm 8 \text{ K}$ minimum measured temperature. Therefore, at the resolution of 120 m/pixel, the cold water ice component has a negligible effect on the thermal flux. Thus, if sublimation is

to be prevented, the surface exposures of water ice (whether or not it is intimately mixed with a dark non-ice component) cannot be in thermal equilibrium with any non-ice component (nominally at $\sim 300 \text{ K}$ at 1.5 AU and 55° incidence angle).

If the water ice and non-ice nuclear components are thermally decoupled, they must also be physically separated at the same scale (in this case, at the macroscopic scale of 120 m/pixel). The measured reflectance at 120 m/pixel can therefore be modeled as a simple linear (i.e., aerial) combination of the spectra of its components. Using optical constants (23) and scattering theory (24), we calculated spectra of pure ice components of various grain sizes. The water ice-rich spectra were then modeled as linear combinations of theoretical ice spectra of various grain sizes and an average non-ice IR spectrum of the nearby nucleus (Fig. 4B).

The relative intensities of ice absorptions at 1.5, 2.0, and 3.0 μm change as a function of particle size (25). In spectra of larger grain sizes, absorptions at longer wavelengths saturate (i.e., they have near zero reflectance). Because absorptions at 3.0 μm are nearly absent in the spectra of the ice-rich regions of the nucleus, their particle size cannot be less than 5 μm (Fig. 4A). At the other extreme, particles larger than 50 μm reflect relatively more at shorter wavelengths and do not match the observed ice-rich spectrum (Fig. 4A). Thus, modeling of the ice-rich nucleus spectrum as a mixture of water ice and non-ice constrains the

Fig. 2. Maps and spectra of ice-rich areas relative to non-ice regions of the nucleus. (A and B) HRI visible data (16 m/pixel). (C and D) MRI visible data (82 m/pixel). (E and F) IR data (120 m/pixel). Note that the IR scan at the highest resolution only covers the upper half of the nucleus, as shown. The ice-rich areas are mapped in the visible images as combinations of high 450 nm/750 nm relative reflectance (387 nm/750 nm for MRI) and low 950 nm/750 nm relative reflectance and in the IR images by the strength of absorptions at 2.0 μm . The visible spectra are normalized to unity at 750 nm, whereas the IR spectra are normalized at 2.0 μm . All data



are normalized to the same broad smooth area of the nucleus (indicated by the red boxes) to facilitate detection of these subtle variations. Each of the three ice-rich regions (see Fig. 3) have IR spectra that include distinct absorptions due to water ice.

ice component to be $6 \pm 3\%$ with particles that are $30 \pm 20 \mu\text{m}$ in size (Fig. 4B).

The combination of high spatial resolution color images and IR spectra has allowed us to unambiguously detect water ice on the surface of a comet. The relatively ice-rich regions on 9P/Tempel 1 are not uniformly distributed on the surface, but instead are restricted to three distinct regions that are both relatively low in elevation and relatively cold. Water ice absorptions are not exposed on other regions of the nucleus that include scarps and other morphologic indicators of erosion (*I*). In addition, the upper region of the nucleus, where all observed water ice deposits are located, is potentially a source for several natural outbursts observed before impact (*I*).

There is ample morphologic evidence that the surface of 9P/Tempel 1 has been extensively processed since its formation (*I*). In addition, analysis of thermal data reveals that the water ice is thermally (and thus physically) decoupled from the non-ice nuclear components on a macroscopic scale. Taken together, these obser-

vations suggest that the exposed water ice regions are not primary [for example, forming mantles around silicates, as proposed by the aggregated interstellar material model of (26)]. It is also possible that the water ice has recondensed from recent activity. Finally, the surface water ice particle sizes ($30 \pm 20 \mu\text{m}$) are greater than the size range of the ejecta (0.5 to $5 \mu\text{m}$) inferred from various measurements after impact (*I*, 27, 28). This suggests that the surface deposits are in fact loose aggregates of smaller particles that are easily fractured during ejection, one of the interpretations offered by A'Hearn *et al.* (*I*).

The ambient outgassing of 9P/Tempel 1 is $\sim 6 \times 10^{27}$ H_2O molecules s^{-1} measured before impact (28), which is consistent with values from previous apparitions (29). The free sublimation temperature of water ice calculated above (~ 200 K) would produce water sublimation at a rate of $\sim 4.5 \times 10^{21}$ molecules $\text{m}^{-2} \text{s}^{-1}$. A surface area of 1.3 km^2 of 100% water ice is therefore required to account for the ambient outgassing of water, consistent with previous

results (30, 31). The observed 0.5 km^2 of 6% water ice, equivalent to $\sim 0.03 \text{ km}^2$ of pure water ice, is considerably less than this value. Thus, although they may be associated with natural outbursts, the water ice deposits we detected on the surface of 9P/Tempel 1 are not the dominant sources of outgassing. Therefore, if we assume that the distribution of ice on the unobserved parts of the nucleus is broadly similar to the observed distribution, the ambient outgassing observed for 9P/Tempel 1 likely has extensive subsurface sources.

References and Notes

- M. F. A'Hearn *et al.*, *Science* **310**, 258 (2005); published online 8 September 2005 (10.1126/science.1118923).
- J. M. Sunshine *et al.*, *Space Sci. Rev.* **117**, 269 (2005).
- D. L. Hampton *et al.*, *Space Sci. Rev.* **117**, 43 (2005).
- R. M. Nelson, M. D. Rayman, H. A. Weaver, *Icarus* **167**, 1 (2004).
- L. A. Soderblom *et al.*, *Icarus* **167**, 100 (2004).
- J. Licandro *et al.*, *Earth Moon Planets* **90**, 495 (2002).
- J. Licandro, H. Campins, C. Hergenrother, L. M. Lara, *Astron. Astrophys.* **398**, L45 (2003).
- H. Campins, J. Licandro, J. Guerra, M. Chamberlain, E. Pantin, *Bull. Am. Astron. Soc.* **35**, 1011 (2003).
- P. A. Abell *et al.*, *Icarus* **179**, 174 (2005).
- C. Delahodde, O. R. Hainaut, J. Romin-Martin, P. L. Lamy, *Asteroids, Comets, and Meteorites*, Berlin, 29 July to 2 August 2002, abstract 20.08.
- M. A. Barucci, D. P. Cruikshank, S. Mottola, M. Lazzarin, in *Asteroids III*, W. F. Bottke, A. Cellino, P. Paolicchi, R. P. Binzel, Eds. (Univ. of Arizona Press, Tucson, AZ, 2002), pp. 273–288.
- M. A. Barucci, A. Doressoundiran, D. P. Cruikshank, in *Comets II*, M. Festou, H. U. Keller, H. A. Weaver, Eds. (Univ. of Arizona Press, Tucson, AZ, 2004), pp. 647–658 and references therein.
- M. J. Duncan, M. H. F. Levison, *Science* **276**, 1670 (1997).
- R. H. Brown *et al.*, *Space Sci. Rev.* **115**, 111 (2004).
- T. V. Johnson, J. I. Lunine, *Nature* **435**, 69 (2005).
- R. N. Clark *et al.*, *Nature* **435**, 66 (2005).
- T. C. Owen *et al.*, *Icarus* **139**, 379 (1999).
- M. S. Hanner, *Icarus* **47**, 342 (1981).
- J. K. Davies *et al.*, *Icarus* **127**, 238 (1997).
- H. Kawakita *et al.*, *Astrophys. J.* **601**, L191 (2004).
- The IR spectrometer is calibrated to an absolute radiance precision of $\pm 10\%$.
- F. P. Fanale, J. R. Salvail, *Icarus* **60**, 476 (1984).
- S. G. Warren, *Appl. Opt.* **23**, 1206 (1984).
- B. W. Hapke, *Reflectance and Emittance Spectroscopy* (Cambridge Univ. Press, New York, 1993).
- R. N. Clark, *J. Geophys. Res.* **86**, 3087 (1981).
- J. M. Greenberg, in *Comets*, L. L. Wilkening, Ed. (Univ. of Arizona Press, Tucson, AZ, 1982), pp. 131–163.
- S. Sugita *et al.*, *Science* **310**, 274 (2005); published online 15 September 2005 (10.1126/science.1119091).
- D. G. Schleicher, K. L. Barnes, N. L. Baugh, *Astron. J.* **131**, 1138 (2006).
- L. M. Lisse *et al.*, *Space Sci. Rev.* **117**, 161 (2005).
- M. F. A'Hearn, R. L. Millis, D. G. Schleicher, D. J. Osip, P. V. Birch, *Icarus* **118**, 223 (1995).
- J. J. Cowan, M. F. A'Hearn, *Moon Planets* **21**, 155 (1979).
- Supported by NASA through the Discovery Program's Deep Impact mission. We are extremely grateful for the personal efforts and professional excellence of numerous engineers and supporting scientists who were critical to the successful development and execution of the Deep Impact mission. We also thank T. Roush for making his Hapke code and optical constants available.

Fig. 3. Temperature map of the upper half of the nucleus derived from IR spectra (with 2 K contour intervals from 280 to 330 K; 120 m/pixel). Three ice-rich regions (yellow circles) are located near locally cold regions with temperatures of ~ 285 , 290, and 295 K, respectively.

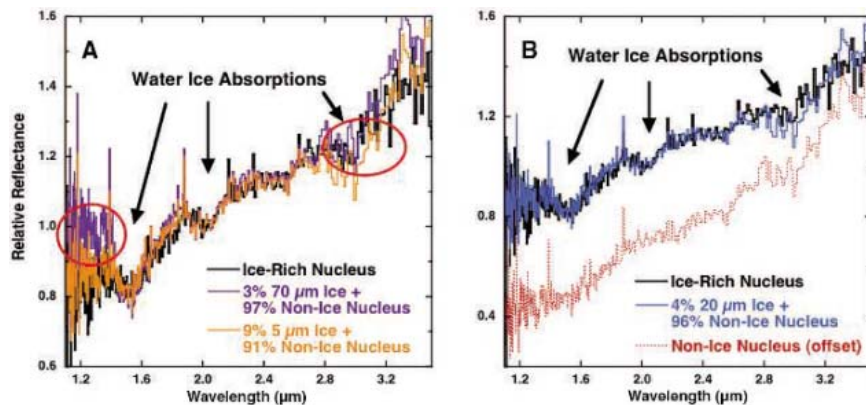
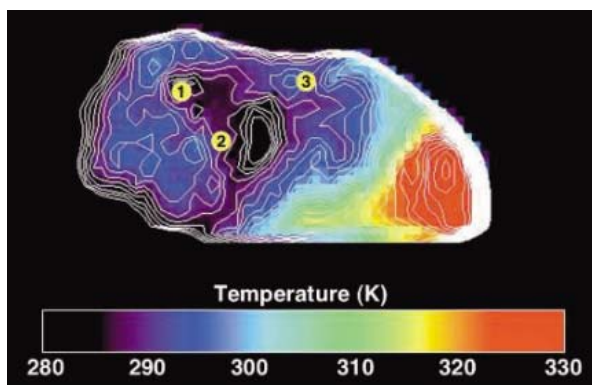


Fig. 4. Results of modeling of linear combinations of IR spectra of non-ice regions of the nucleus and calculated spectra of various particle sizes of water ice derived from optical constants. (A) The ice-rich nucleus spectrum (black), when modeled as a mixture of non-ice nucleus [see (B)] and a calculated spectrum of 70- μm water ice particles (purple), does not match at short wavelengths, whereas a mixture with 3- μm water ice particles (orange) produces a poor match at long wavelengths. (B) The same ice-rich spectrum (black) is well modeled with 30- μm water ice particles (blue) and a nearby non-ice nucleus spectrum (red; offset by -0.3 for clarity). Modeling indicates that the ice regions contain $6 \pm 3\%$ ice with particles $30 \pm 20 \mu\text{m}$ in size.

9 December 2005; accepted 26 January 2006

Published online 2 February 2006;

10.1126/science.1123632

Include this information when citing this paper.

Laonastes and the “Lazarus Effect” in Recent Mammals

Mary R. Dawson,^{1*} Laurent Marivaux,² Chuan-kui Li,³ K. Christopher Beard,¹ Grégoire Métais¹

The living Laotian rodent *Laonastes aenigmamus*, first described in early 2005, has been interpreted as the sole member of the new family Laonastidae on the basis of its distinctive morphology and apparent phylogenetic isolation from other living rodents. Here we show that *Laonastes* is actually a surviving member of the otherwise extinct rodent family Diatomyidae, known from early Oligocene to late Miocene sites in Pakistan, India, Thailand, China, and Japan. *Laonastes* is a particularly striking example of the “Lazarus effect” in Recent mammals, whereby a taxon that was formerly thought to be extinct is rediscovered in the extant biota, in this case after a temporal gap of roughly 11 million years.

In recent years, tropical southeast Asia has been recognized as an important “hot spot” for modern biological diversity (1). The latest addition to the mammalian biota of this hot spot is the rodent *Laonastes aenigmamus*, recently described by scientists working on a biodiversity survey in Laos (2). Initial investigations of its morphological and molecular affinities established that *Laonastes* is phylogenetically divergent from other living rodents, which led to its classification in the new family Laonastidae. Current knowledge of *Laonastes*, known locally as the khanyou, is based on whole specimens that were purchased in local markets and individual bones collected from owl pellets and cave deposits. Although living individuals have yet to be observed by biologists, *Laonastes* seems to be nocturnal in its activity pattern and is thought to inhabit karstic terrain. It has a vaguely squirrel-like appearance, with an elongated head, pelage ranging from black to grizzled, and a long hairy tail. Its jaws and dentition are highly distinctive, having an enlarged hystricomorphous infraorbital foramen, lacking development of the coronoid process on the mandible, and having distinctly bilophodont cheek teeth. The postcranial skeleton, on the other hand, is generalized, suggesting a scampering mode of locomotion.

Although initial phylogenetic results indicated that *Laonastes* pertains to an ancient phylogenetically isolated lineage of rodents, morphological comparisons with fossil rodents have not been undertaken previously. Our familiarity with the fossil record of Asian rodents led us to make extensive com-

parisons between *Laonastes* and the otherwise extinct Diatomyidae, known from early Oligocene to late Miocene strata in Pakistan, India, Thailand, China, and Japan (3–10). Three fossil genera—*Fallomus*, *Diatomys*, and *Willmus*—are currently recognized in the Diatomyidae. *Fallomus* is known from isolated teeth and fragments of jaws from the Oligocene and early Miocene of Pakistan, India, and Thailand (4, 7, 8), whereas the poorly documented *Willmus* is known from two isolated teeth from the late Miocene of Pakistan (10). *Diatomys*, on the other hand, is better known and more widely distributed, having Miocene records in Shandong and Jiangsu provinces in eastern China, Kyushu Island in Japan, northern Pakistan, and the Lamphun district of Thailand (3, 5).

Diatomys shantungensis was originally described from the late early Miocene Shanwang Series of Shandong Province, China, based on two relatively complete (but laterally compressed) partial skeletons (3). The well-preserved dentitions of these specimens show that the cheek teeth in each jaw quadrant include one premolar and three molars displaying a simple transversely bilophodont occlusal pattern. Details of cranial and mandibular anatomy were difficult to interpret because of the lateral compression of the fossils. However, *Diatomys* was originally thought to have an unenlarged infraorbital foramen (the sciuriform condition) and a sciurognathous lower jaw. Its postcranial skeleton lacks any obvious morphological adaptations for either leaping or burrowing.

In June 2005, a new and less compressed specimen of *D. shantungensis* was discovered from the type locality in Shandong Province. The new specimen, IVPP V12692, complete with whiskers and traces of pelage (Fig. 1, A to C), clarifies aspects of the cranial and mandibular anatomy of *Diatomys* that were either missing or obscured by postmortem deformation in previously described specimens of this species. IVPP V12692 shows that the infraorbital foramen of *Diatomys* is very large; hence, *Diatomys* resembles

Laonastes (Fig. 1D) in having the hystricomorphous condition. IVPP V12692 also shows that the mandible lacks a coronoid process and has a relatively low condyle; the masseteric fossa extends forward to a level below p4; an anteroposterior ridge, the linea obliqua, separates dorsal and ventral portions of the masseteric fossa; the angular process is in the same vertical plane as the incisor (the sciurognathous condition); the angular process extends posteriorly as far as the condylar process; the ventral side of the angular process is very slightly inflected; and the incisor root is short, extending posteriorly to a level below m2. Thus, the new specimen demonstrates that the mandibles of *Diatomys* and *Laonastes* are virtually identical in sharing the following derived characters: absence of a coronoid process, masseteric fossa extending forward to below p4, masseteric fossa subdivided into dorsal and ventral sections, condyle low but higher than tooth row, and shortened incisor.

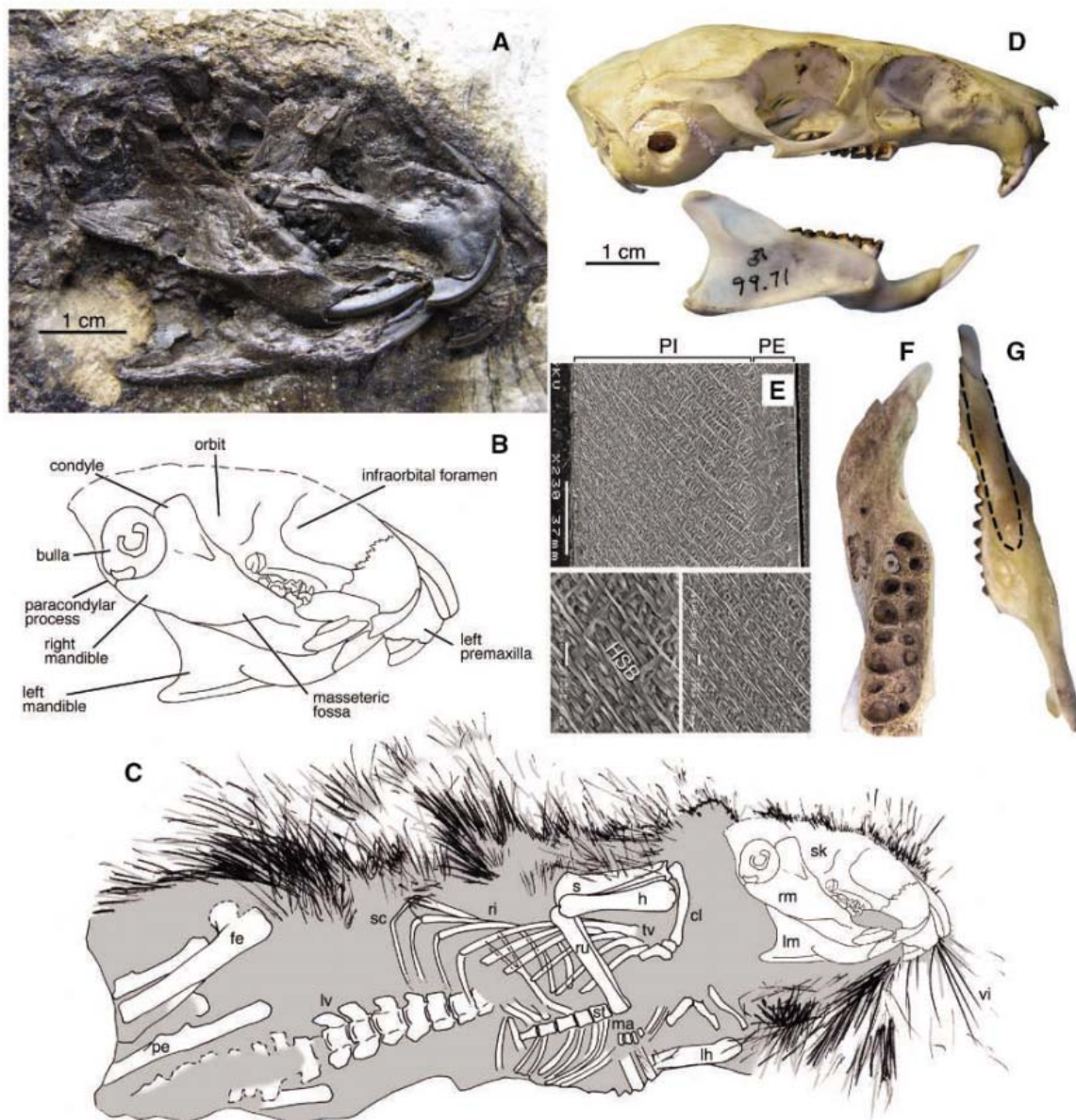
Laonastes was originally described as having a hystricognathous mandible (2). A reexamination of pertinent specimens shows that *Laonastes* actually has a sciurognathous mandible like that of *Diatomys* (Fig. 1, D and G). Another characteristic of hystricognathous rodents was also attributed to *Laonastes* in the original description: a groove for passage of the pars reflexa of the masseter superficialis muscle to its insertion on the medial surface of the angle. Reexamination of specimens of *Laonastes* revealed no space for this groove in its sciurognathous jaw.

Only heavily worn teeth of *Laonastes* are currently available for investigation. Nevertheless, the cheek teeth of *Laonastes* are clearly bilophodont, a condition that also characterizes *Diatomys*. The acquisition of bilophodonty occurred within Diatomyidae, because Oligocene species of *Fallomus* have cusped cheek teeth showing derivation of the bilophodont pattern from a more generalized rodent dental morphology (4, 7, 8). The cheek teeth of *Laonastes* have elongated crowns that have been described as hypsodont. A highly unusual aspect of the dentition that *Laonastes* shares with fossil diatomyids is the presence of supernumerary roots on the cheek teeth. In *Laonastes*, the upper cheek teeth each have three roots, but their size and disposition are unusual for rodents. The upper cheek teeth of *Laonastes* bear an enlarged U-shaped anterior root and two posterior roots, whereas the lower dentition shows that three roots are present on p4 and four occur on m1-3 (Fig. 1F). In *Diatomys*, the upper molars each have four roots, whereas the number of roots supporting the lower dentition is identical to that of *Laonastes* (3, 5). Molars of *Fallomus* exhibit some variation in the number of

¹Section of Vertebrate Paleontology, Carnegie Museum of Natural History, 4400 Forbes Avenue, Pittsburgh, PA 15213, USA. ²Laboratoire de Paléontologie, Institut des Sciences de l'Évolution, Case Courrier 064, Université Montpellier II, place Eugène Bataillon, F-34095 Montpellier Cedex 05, France. ³Institute of Vertebrate Paleontology and Paleoanthropology, Post Office Box 643, Beijing 100044, People's Republic of China.

*To whom correspondence should be addressed. E-mail: dawsonm@carnegiemnh.org

Fig. 1. Morphological characters of *Diatomys* and *Laonastes*. (A and B) Right side of skull and (C) articulated skeleton of *D. shantungensis* (IVPP V12692) from the early Miocene, Shandong Province, China. Abbreviations on the skeleton are as follows: cl, clavicle; fe, femur; h, right humerus; lh, left humerus; lv, lumbar vertebrae; ma, manus; pe, pelvis; ri, ribs; ru, right ulna; s, scapula; sc, sternal cartilage; sk, skull; st, sternum; tv, thoracic vertebrae; and vi, vibrissae. (D to G) *L. aenigmamus*. (D) Right lateral view of skull and mandible of specimen BMNH 1999.71. (E) Scanning electron photomicrographs of lower incisor enamel of BMNH 1998.407, showing the multiserial condition. (Top) Longitudinal section including the total enamel thickness (~310 μm) with moderately thin radial enamel of the portio externa (PE) and thick (80%) portio interna (PI) with HSBs; the straight HSBs are inclined at about 50° to the enamel-dentine junction at right; scale bar, 100 μm . (Bottom) Details of the PI, showing decussating HSBs with three to four prisms per band and the well-marked transition zone between adjacent decussating HSBs; a thin interprismatic matrix (IPM) never surrounds the prisms but appears as inter-row sheets running at a high angle ($\geq 80^\circ$, nearly rectangular) to the prism direction and never anastomoses between the prisms; scale bars, 10 μm . The pattern of the



IPM typifies a derived multiserial subtype III. (F) Occlusal view of left mandible of BMNH 1998.408, showing three roots of p4 and four roots of lower molars. (G) Ventral view of sciurognathous left mandible of BMNH 1999.71, with a dashed line showing the position of the lower incisor.

roots, but they typically have four (7). This proliferation of roots is derived among rodents, in which the primitive condition has three roots on P4-M3 (including two buccal roots and one larger lingual root) and two roots (one anterior and one posterior) on p4-m3. Given that four roots support the upper cheek teeth of *Diatomys* and *Fallomus*, the enlarged U-shaped anterior root on the upper cheek teeth of *Laonastes* probably resulted from the coalescence of the two anterior roots that occur in fossil diatomyids.

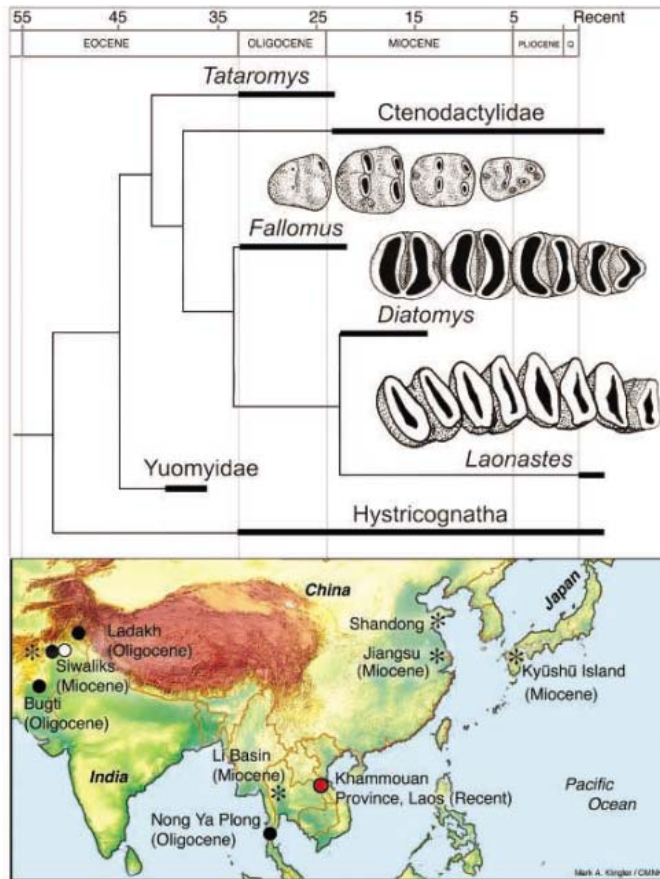
The microstructure of incisor enamel in *Fallomus* and *Diatomys* is multiserial, a condition that also characterizes ctenodactylid, pedetid, and hystricognath rodents (5, 8). Al-

though the original description of *Laonastes* failed to consider this character, our analysis of incisor enamel microstructure in *Laonastes* revealed the presence of multiserial enamel in this taxon as well (Fig. 1E). Incisor enamel microstructure in *Laonastes* is very similar to that of *Diatomys* in having the same number of prisms per Hunter-Schreger band (HSB) and in showing the same degree of complexity of the interprismatic matrix (inter-row sheets running at a high angle to the prism direction and a well-marked transition zone between adjacent decussating HSBs). It differs, however, in showing the HSBs to be much more inclined ($>50^\circ$) to the enamel-dentine junction than is the case in *Diatomys*

(25° to 30°), a difference that is not unexpected given the large temporal gap between these genera.

Other skeletal similarities between extinct diatomyids and *Laonastes* can be added to those of the mandible and dentition. *Laonastes* has a separate neurovascular canal within the orbit. This feature is not interpretable in available specimens of *D. shantungensis*, but the Oligocene *Fallomus* also has a separate neurovascular canal, demonstrating early establishment of this character in diatomyids (7). *Diatomys* and *Laonastes* are the same size, with head and body length spanning roughly 250 mm, followed by a long tail composed of 20 to 25 caudal vertebrae.

Fig. 2. Simplified phylogeny (see supporting online material) showing temporal and geographic distributions of diatomyids. **(Top)** Suggested relationships of diatomyids within Rodentia, showing occlusal views of right p4-m3 (anterior end to right) of *Fallomys*, *Diatomys*, and *Laonastes*. **(Bottom)** Geographic distribution of *Fallomys* (black circles), *Diatomys* (asterisks), *Willmus* (white circle), and *Laonastes* (red circle).



Diatomys and *Laonastes* also share the following postcranial characters: the humerus has a reduced deltoid ridge and a wide distal end and lacks an entepicondylar foramen; the lesser trochanter of the femur is mostly posterior in position; and the astragalus has a sharp medial keel, wide body, and short neck (2, 3, 5). Our phylogenetic analysis of morphological data from various living and extinct rodents identifies *Laonastes* as a member of Diatomyidae, being more closely related to *Diatomys* than the latter is to *Fallomys* (Fig. 2 and supporting online material). We therefore synonymize Laonastidae with Diatomyidae (11).

The discovery of the living diatomyid rodent *Laonastes* offers a rare opportunity to compare phylogenetic results that were derived independently from neontological and paleontological data sets. To date, phylogenetic analyses of genetic data from *Laonastes* have yielded conflicting results, but a combined analysis of mitochondrial data from 12S ribosomal RNA and cytochrome b places *Laonastes* as a basal member of Hystricognathi (2). Further molecular analyses should be undertaken, especially in light of the antiquity of the phylogenetic branching events postulated here for this rodent. A recent analysis of morphological data recognized diatomyids as one of several extinct outgroups of living Hystricognathi (12). Of these

outgroups, it is striking that the diatomyids continued to evolve in Asia, while the ctenodactylids became extinct in southern Asia but evolved subsequently in Africa. Given the diversity of extinct Asian rodents that apparently lie near the base of the modern radiation of Hystricognathi, *Laonastes* strengthens paleobiogeographic hypotheses proposing that this group of mainly African and South American extant rodents originated in Asia (6).

The “Lazarus effect” refers to the re-appearance of taxa after a lengthy hiatus in the fossil record (13, 14). The discovery of living examples of taxa that were previously thought to be extinct is a very special case of the Lazarus effect, one that has only rarely been documented among mammals and other vertebrates. With the exception of microbiotheriid marsupials (15), all fossil mammal taxa that were subsequently found to be alive have been Pleistocene in age and congeneric with their modern counterparts (16). Uniquely among placental mammals, *Laonastes* pertains to a clade (Diatomyidae) that was formerly believed to have been extinct for more than 11 million years. Diatomyids join tree shrews, flying lemurs, and tarsiers as examples of ancient and formerly wider-ranging mammalian taxa that are currently living with relictual distributions in southeast Asia.

From a paleontological and phylogenetic perspective, efforts to conserve *Laonastes*, the sole survivor of a morphologically distinctive family of rodents with deep evolutionary roots in Asia, should be given the highest priority. If it can be preserved, the Paleogene zoo that survives today in southeast Asia can offer invaluable insights regarding past and present biodiversity.

References and Notes

1. N. Myers, R. A. Mittermeier, C. G. Mittermeier, G. A. B. da Fonseca, J. Kent, *Nature* **403**, 853 (2000).
2. P. D. Jenkins, C. W. Kilpatrick, M. F. Robinson, R. J. Timmins, *Syst. Biodivers.* **2**, 419 (2005).
3. C.-k. Li, *Vert. Palasiatica* **12**, 43 (1974).
4. L. J. Flynn, L. L. Jacobs, I. U. Cheema, *Am. Mus. Novit.* **2841**, 1 (1986).
5. P. Mein, L. Ginsburg, *Geodiversitas* **19**, 783 (1997).
6. L. Marivaux, M. Vianey-Liaud, J.-L. Welcomme, J.-J. Jaeger, *Zool. Scr.* **31**, 225 (2002).
7. L. Marivaux, J.-L. Welcomme, *J. Vert. Paleontol.* **23**, 420 (2003).
8. L. Marivaux, Y. Chaimanee, C. Yamee, P. Srisuk, J.-J. Jaeger, *Geodiversitas* **26**, 493 (2004).
9. L. J. Flynn, *Himalayan Geol.* **21**, 39 (2000).
10. L. J. Flynn, M. E. Morgan, *Palaont. Electron.* **8.1.17A**, 1 (2005).
11. Synonymy: Diatomyidae (5) [including Laonastidae (2)]. Current content: type genus *Diatomys* (3), *Fallomys* (4), *Willmus* (10), and *Laonastes* (2). Range: early Oligocene to Recent, Asia. Diagnosis: rodents having hystricomorphous infraorbital foramen and sciurognathous mandible; mandible lacking coronoid process, condyle low but higher than cheek teeth, and masseteric fossa extending forward to below p4; dental formula 1/1, 0/0, 1/1, 3/3, with relatively large terminal teeth; upper incisor lacking groove; incisor enamel multiserial; supernumerary roots on cheek teeth; molar pattern varies from cuspsate in early diatomyids to bilophodont; postcranial skeleton generalized. Differs from Ctenodactylidae in having large P4/4, supernumerary roots on cheek teeth, and a bilophodont occlusal pattern lacking loph/lophid connection between trigon/talon and trigonid/talonid; hypoconulids on lower cheek teeth are reduced to absent. Differs from bilophodont Geomyoidea in having hystricomorphous skull, multiserial incisor enamel, and large P4/4. Differs from bilophodont Pedetidae in having long, low skull and long lower jaw with low condyle, and lacking postcranial characters associated with bipedal locomotion.
12. L. Marivaux, M. Vianey-Liaud, J.-J. Jaeger, *Zool. J. Linn. Soc.* **142**, 105 (2004).
13. D. Jablonski, in *Dynamics of Extinction*, D. K. Elliott, Ed. (Wiley-Interscience, New York, 1986), pp. 183–229.
14. E. Fara, *Geol. J.* **36**, 291 (2001).
15. L. G. Marshall, *Fieldiana Geol.* **10**, 1 (1982).
16. R. M. Wetzel, R. E. Dubos, R. L. Martin, P. Myers, *Science* **189**, 379 (1975).
17. We thank P. Jenkins, D. Hills, and J. Hooker for access to specimens; Z. Qiu for making available the new specimen of *Diatomys*; Z. Luo, J. Wible, and three anonymous reviewers for helpful discussions; and M. Klingler for graphics. Financial support from NSF, CNRS, and the Singer-Polignac Foundation is gratefully acknowledged.

Supporting Online Material

www.sciencemag.org/cgi/content/full/311/5766/1456/DC1
 Materials and Methods
 SOM Text
 Fig. S1
 References

21 December 2005; accepted 27 January 2006
 10.1126/science.1124187

Opposing Effects of Native and Exotic Herbivores on Plant Invasions

John D. Parker,* Deron E. Burkepile, Mark E. Hay†

Exotic species are widely assumed to thrive because they lack natural enemies in their new ranges. However, a meta-analysis of 63 manipulative field studies including more than 100 exotic plant species revealed that native herbivores suppressed exotic plants, whereas exotic herbivores facilitated both the abundance and species richness of exotic plants. Both outcomes suggest that plants are especially susceptible to novel, generalist herbivores that they have not been selected to resist. Thus, native herbivores provide biotic resistance to plant invasions, but the widespread replacement of native with exotic herbivores eliminates this ecosystem service, facilitates plant invasions, and triggers an invasional “meltdown.”

Invasive exotic species threaten native biodiversity (1), alter ecosystem structure and function (2), and annually cost up to \$120 billion in the United States alone (3). Determining the ecological traits and interactions that affect invasion success are therefore critical for predicting, preventing, and mitigating the negative effects of biological invasions. The leading hypothesis for why some exotic species become superabundant in their new ranges is the enemy release hypothesis, proposing that exotic species thrive because they lack coevolved enemies in their new ranges (4–9). However, introduced ranges contain evolutionarily novel enemies that exotic invaders may not be adapted to deter (10, 11), and the biotic resistance hypothesis suggests that resistance by native enemies in the new range will limit the establishment or spread of most invaders (4–6). Regardless of the mechanisms involved, invasions by exotic species are increasingly common, and it has been hypothesized that positive feedbacks among this increasing number of exotic species can facilitate additional invasions and lead to an invasional “meltdown” (12). Such meltdowns might be exacerbated by humans introducing exotic species into, and harvesting native species from, native ecosystems, potentially both lowering the capacity for biotic resistance and increasing the potential for positive feedbacks among exotic species.

Exotic plants are often assumed to gain enemy release because herbivores will selectively attack native over exotic plants (7). However, this may be more applicable for specialist enemies that require host-specific feeding cues than for generalist consumers that view most plants as foods unless deterred by plant defenses. The distinction between generalist and specialist herbivores is especially crit-

ical because generalists often have larger impacts on plant community structure than specialists do (13, 14); they commonly consume exotic plants in preference to native plants in laboratory feeding assays (15); and their effects on plant invasions have been historically overlooked (7). Rarely, however, have experimental exclusions of generalist herbivores been used to test whether these herbivores alter the abundance of exotic plants in natural communities. Instead, most tests of enemy release and biotic resistance have focused on correlative response variables that may not translate into demographic impacts (e.g., the number of native enemy species attacking an exotic species rather than the damage inflicted) (8, 9), or on a few “model” species (16, 17) that may not be typical of exotic species in general.

We tested the effects of herbivores on exotic plant invasions using meta-analysis to examine 63 published studies that experimentally excluded herbivores and monitored the success of more than 100 exotic plant species. Most ($n = 35$) of the studies we found monitored herbivore effects on entire plant communities rather than on plant invasions per se and thus avoided potential bias due to focusing on particular species. For these studies, we evaluated how herbivores affected the relative abundance of exotic plants (the fraction of the total plant community that was non-native) and the absolute abundance (e.g., plant biomass and cover) and species richness of both native and exotic plants (18). An additional 28 studies monitored herbivore effects only on specific species of exotic plants. These studies were used to assess native herbivore impacts on the establishment of exotic plants and to broaden our analysis by examining an additional 29 exotic plant species not included in the community-wide investigations. We did not include studies reporting enemy diversity or leaf damage alone because these indirect estimates may not translate to impacts on plant demography (19). Studies were drawn from a range of biomes (grasslands, scrublands, forests, deserts, freshwater and saltwater marshes, and lake bottoms) and herbivores (native bison,

elk, deer, antelope, waterfowl, wallabies, rabbits, rodents, land crabs, fishes, mollusks, and insects; and exotic cattle, horses, deer, sheep, goats, rabbits, rodents, fishes, mollusks, and insects) (18).

In studies assessing herbivore effects on entire plant communities, native and exotic herbivores had opposing effects on the relative abundance of exotic plants. Native herbivores strongly suppressed, whereas exotic herbivores strongly enhanced, the relative abundance of exotic plants (Fig. 1). Native herbivores decreased the relative abundance of exotic plants by 28% (log response ratios correspond to a decrease in the relative abundance of exotic plants from $36.6 \pm 5.5\%$ in the exclusion treatments to $26.5 \pm 5.2\%$ in the grazed communities; mean \pm SE), consistent with the biotic resistance hypothesis. In contrast, exotic herbivores increased the relative abundance of exotic plants by 65% (from $24.3 \pm 3.8\%$ in the exclusion treatments to $40.2 \pm 4.9\%$ in the grazed communities), consistent with the invasional meltdown hypothesis. Overall, the relative abundance of exotic plants was 52% higher in communities grazed by exotic herbivores ($40.2 \pm 4.9\%$) than in communities grazed by native herbivores ($26.5 \pm 5.2\%$).

An assessment of absolute, as opposed to relative, abundance also demonstrated that native and exotic herbivores had strongly opposing effects on native versus exotic plants. Native herbivores suppressed the abundance of exotic plants, whereas exotic herbivores suppressed the abundance of native plants (Fig. 2, A and B). Grazing by exotic herbivores also

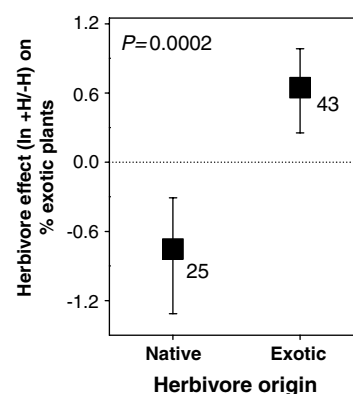


Fig. 1. Effects of native and exotic herbivores on the relative abundance (% of total plant cover or biomass) of exotic plants from 35 studies involving 68 experiments. Negative numbers indicate a decrease, and positive numbers an increase, in the relative abundance of exotic plants in the presence versus absence of herbivores. Numbers to the right of symbols are the number of experiments contributing to the mean. Points show means \pm bias-corrected 95% confidence intervals. Effects are significant when the 95% confidence interval does not cross zero; P value tests difference in effects of native versus exotic herbivores.

School of Biology, Georgia Institute of Technology, Atlanta, GA 30332, USA.

*Present address: Department of Ecology and Evolutionary Biology, Cornell University, Ithaca, NY 14853, USA. E-mail: jdp52@cornell.edu

†To whom correspondence should be addressed. E-mail: mark.hay@biology.gatech.edu

increased the species richness of exotic plants (Fig. 2D), whereas native herbivores had no detectable effect on the species richness of either native or exotic plants (Fig. 2C). Thus, native herbivores limited the abundance of exotic plants but not the likelihood of colonization by new species. In contrast, exotic herbivores promoted exotic plant dominance and richness by disproportionately reducing the abundance of native species. Although these results could be confounded if experiments on native versus exotic herbivores differed systematically in variables such as productivity, grazing rate, etc., that could affect herbivore impact (20, 21), we found no evidence of such bias (18). Moreover, the general patterns we found were not driven by any one, common herbivore type; if we removed the studies with herbivores that were common and that had strong impacts (e.g., cattle, waterfowl), these general patterns persisted and remained significant (18).

Most previous assessments of release from herbivores have focused on effects of native invertebrate herbivory on exotic plant size or growth (6, 7). In contrast, our analyses of native herbivores focused primarily on the impacts of vertebrates (24 of 25 experiments). We hypothesized that vertebrate herbivores would have larger effects than invertebrates by virtue of their larger size, enhanced mobility, broader diets, and propensity to kill plants rather than suppress plant growth (13, 22). To test this hypothesis, we analyzed the impacts of native vertebrate and invertebrate herbivores on survivorship of exotic plant species. Native vertebrate herbivores had a three- to fivefold larger

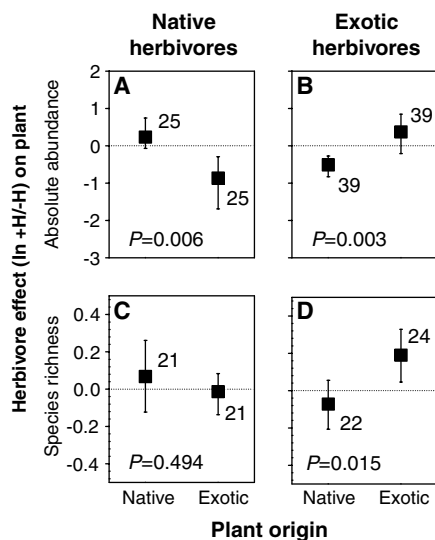


Fig. 2. Effects of native (left) and exotic herbivores (right) on the absolute abundance (A and B) and the species richness (C and D) of native and exotic plants. *P* values test differences between herbivore effects on native and exotic plants for each contrast. Other analyses as in Fig. 1.

impact on exotic plant survival than did native invertebrate herbivores (18). This suggests that studies focused on native invertebrate herbivores alone may find small effects on plant invasions (7, 11) because smaller and more specialized invertebrate herbivores have relatively modest impacts on plant survival.

Most exotic plants are noninvasive residents of their new communities (23), and the mean patterns shown in Figs. 1 and 2 could hide important biotic signals if noninvasive exotic plants were strongly suppressed by native herbivores but invasive exotic plants were not. Such a pattern could mean that the enemy release hypothesis would be valid for the small subset of species that become aggressive invaders. We thus asked whether herbivores had weaker impacts on plants that were more widely listed as invasive throughout the United States (8). However, neither native nor exotic herbivores had weaker effects on plants that were broadly considered invasive across the United States (Fig. 3). This pattern also held when we categorized plants as invasive even if they were listed as noxious by only a single U.S. state or natural resource agency (18). Thus, whether noxiousness was considered a continuous or categorical variable, and whether we considered agricultural or natural area invaders, noxious exotic plants were no less affected by herbivores than were noninvasive exotic plants.

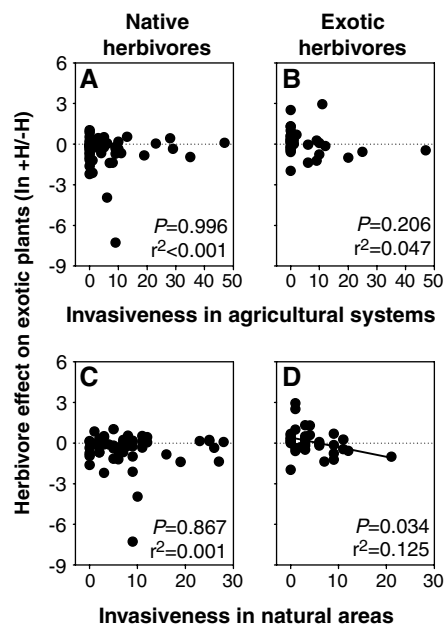


Fig. 3. Mean effects of native herbivores (A and C) and exotic herbivores (B and D) on exotic plant species as a function of the number of states or natural resource agencies within the United States listing each species as noxious in agricultural (A and B) or natural areas (C and D), respectively. Statistical analysis was by linear least-squares regression.

Historically, exotic species were thought to thrive by escaping their coevolved, specialist enemies (4, 5), and little attention was paid to the consequences of gaining evolutionarily novel, generalist enemies in their new ranges. Evolutionary logic, however, suggests that exotic plants may be less adapted than native plants for repelling native herbivores (10). In fact, native, generalist herbivores preferentially attack exotic over native plants in the laboratory (15) and they suppress the abundance of exotic plants in the field (Figs. 1 and 2A). Similarly, exotic herbivores are novel enemies to native plants, and exotic herbivores selectively suppress the abundance of native plants in the field (Fig. 2B). The evolutionary logic for exotic herbivores suppressing native but not exotic plants makes sense only if many of the exotic plants are from the same home range and thus potentially adapted to the exotic herbivore. This was the case for our data set. Of the 41 exotic plant species for which native ranges were known, 88% originated from the same region of the same continent as the exotic herbivores used in that study (18). Thus, by negatively affecting evolutionarily naïve, native plants, exotic herbivores promoted the relative abundance and species richness of coadapted exotic plants from the same native range.

In recent centuries, weeds of European descent have left a global legacy of European ecological imperialism (24). Despite ample opportunity, comparatively fewer New World species have managed to invade the Old World (24, 25). For more than a century, naturalists have been mystified by the “invisible barrier...preventing passage Eastward though allowing it Westward” and by “this total want of reciprocity in migration” (24, p. 166). Our analyses suggest that anthropogenic alteration of herbivore communities has facilitated exotic plant invasions. When Europeans initially colonized North and South America, Australia, and New Zealand, they largely extirpated native bison, elk, kangaroos, prairie dogs, moas, and tortoises and replaced them with introduced cattle, pigs, horses, sheep, goats, rabbits, and other exotic herbivores from Eurasia (12, 24, 26). Thus, a source of biotic resistance to plant invasions (native herbivores, Figs. 1 and 2A) was replaced with species that promote further invasions (exotic herbivores, Figs. 1 and 2, B and D). Consequently, exotic generalist herbivores decimated naïve, New World plants and paved the way for invasions of Old World plants that were adapted to these herbivores (25, 27). Thus, exotic plants may thrive not by escaping their native enemies, but by following them. These findings have considerable implications for ecosystem conservation, suggesting that eradication of exotic herbivores and restoration of native generalist herbivores could mitigate exotic plant invasions and avoid problems associated with introductions of non-native herbivores for biocontrol (28).

References and Notes

- D. S. Wilcove, D. Rothstein, J. Dubow, A. Phillips, E. Losos, *Bioscience* **48**, 607 (1998).
- R. N. Mack *et al.*, *Ecol. Appl.* **10**, 689 (2000).
- D. Pimentel, R. Zuniga, D. Morrison, *Ecol. Econ.* **52**, 273 (2005).
- C. R. Darwin, *The Origin of Species* (Literary Classics, New York, 1859).
- C. S. Elton, *The Ecology of Invasions by Animals and Plants* (Univ. of Chicago Press, Chicago, IL, 1958).
- J. L. Maron, M. Vila, *Oikos* **95**, 361 (2001).
- R. M. Keane, M. J. Crawley, *Trends Ecol. Evol.* **17**, 164 (2002).
- C. E. Mitchell, A. G. Power, *Nature* **421**, 625 (2003).
- M. E. Torchin, K. D. Lafferty, A. P. Dobson, V. J. McKenzie, A. M. Kuris, *Nature* **421**, 628 (2003).
- H. M. T. Hokkanen, D. Pimentel, *Can. Entomol.* **121**, 829 (1989).
- R. I. Colautti, A. Ricciardi, I. A. Grigorovich, H. J. MacIsaac, *Ecol. Lett.* **7**, 721 (2004).
- D. Simberloff, B. Von Holle, *Biol. Invasions* **1**, 21 (1999).
- M. J. Crawley, in *Insect-Plant Interactions*, E. A. Bernays, Ed. (CRC Press, Boca Raton, FL, 1989), vol. 1, pp. 45–71.
- D. Lodge, G. Cronin, E. van Donk, A. Froelich, in *The Structuring Role of Submerged Macrophytes in Lakes*, E. Jeppesen, M. Sondergaard, M. Sondergaard, K. Christoffersen, Eds. (Springer, New York, 1998), pp. 149–174.
- J. D. Parker, M. E. Hay, *Ecol. Lett.* **8**, 959 (2005).
- L. M. Wolfe, *Am. Nat.* **160**, 705 (2002).
- S. J. DeWalt, J. S. Denslow, K. Ickes, *Ecology* **85**, 471 (2004).
- Materials and methods are available as supporting material on Science Online.
- E. Siemann, W. E. Rogers, *Ecology* **84**, 1489 (2003).
- J. M. Chase, M. A. Leibold, A. L. Downing, J. B. Shurin, *Ecology* **81**, 2485 (2000).
- T. J. Stohlgren, L. D. Schell, B. Vanden Heuvel, *Ecol. Appl.* **9**, 45 (1999).
- M. Hay, P. Steinberg, in *Herbivores: Their Interactions with Secondary Metabolites. Evolutionary and Ecological Processes*, G. Rosenthal, M. Berenbaum, Eds. (Academic Press, San Diego, 1992), pp. 371–413.
- M. Williamson, A. Fitter, *Ecology* **77**, 1661 (1996).
- A. W. Crosby, *Ecological Imperialism: The Biological Expansion of Europe, 900–1900* (Cambridge Univ. Press, Cambridge, UK, 1986), p. 368.
- M. J. Crawley, P. H. Harvey, A. Purvis, *Philos. Trans. R. Soc. London Ser. B* **351**, 1251 (1996).
- M. Holmgren, *Biol. Invasions* **4**, 25 (2002).
- R. N. Mack, J. N. Thompson, *Am. Nat.* **119**, 757 (1982).
- S. M. Louda, D. Kendall, J. Connor, D. Simberloff, *Science* **277**, 1088 (1997).
- Supported by the NSF, the National Park Service, and the Harry and Linda Teasley endowment to Georgia Tech.

Supporting Online Material

www.sciencemag.org/cgi/content/full/311/5766/1459/DC1
Materials and Methods
Tables S1 and S2
References and Notes

17 October 2005; accepted 31 January 2006
10.1126/science.1121407

A Major Ecosystem Shift in the Northern Bering Sea

Jacqueline M. Grebmeier,^{1*} James E. Overland,² Sue E. Moore,³ Ed V. Farley,⁴ Eddy C. Carmack,⁵ Lee W. Cooper,¹ Karen E. Frey,⁶ John H. Helle,⁴ Fiona A. McLaughlin,⁵ S. Lyn McNutt⁷

Until recently, northern Bering Sea ecosystems were characterized by extensive seasonal sea ice cover, high water column and sediment carbon production, and tight pelagic-benthic coupling of organic production. Here, we show that these ecosystems are shifting away from these characteristics. Changes in biological communities are contemporaneous with shifts in regional atmospheric and hydrographic forcing. In the past decade, geographic displacement of marine mammal population distributions has coincided with a reduction of benthic prey populations, an increase in pelagic fish, a reduction in sea ice, and an increase in air and ocean temperatures. These changes now observed on the shallow shelf of the northern Bering Sea should be expected to affect a much broader portion of the Pacific-influenced sector of the Arctic Ocean.

The northern Bering Sea, despite its seasonal ice cover (Fig. 1A), supports some of the highest benthic faunal biomass densities in the world's oceans (1, 2). Over most of the Bering Sea shelf, zooplankton grazing and microbial processing in the water column have a small impact on pelagic retention, and therefore a large fraction of usable carbon settles to the benthos (3). However, in the southern (subarctic) region of the Bering Sea, the resulting benthic biomass is largely consumed by upper

trophic level demersal fish and epifaunal invertebrates, whose northern distribution is limited by the presence of near-freezing bottom temperatures (4, 5). The location of this temperature-determined subarctic-Arctic boundary is thus

the primary agent determining ecosystem variability. In the absence of demersal fish and predatory invertebrates, benthic-feeding seabirds and marine mammals become the primary consumers in the northern (Arctic) region of the Bering Sea (6, 7).

A change from arctic to subarctic conditions is under way in the northern Bering Sea, with an attendant northward shift of the pelagic-dominated marine ecosystem that was previously limited to the southeastern Bering Sea (8). The ice-dominated, shallow ecosystem favoring benthic communities and bottom-feeding sea ducks, such as spectacled eiders (*Somateria fuscgeri*), and marine mammals, including walrus (*Odobenus rosmarus*) and gray whales (*Eschrichtius robustus*), is being replaced by one dominated more by pelagic fish. Such shifts clearly affect both subsistence harvests and commercial fisheries. Yupik hunters of St. Lawrence Island, for example, have observed an increase in warm winds in winter and the replacement of stable pan and pack ice with brash and thin ice, changes that affect their ability to

¹Marine Biogeochemistry and Ecology Group, Department of Ecology and Evolutionary Biology, 10515 Research Drive, Building A, Suite 100, University of Tennessee, Knoxville, TN 37932, USA. ²Pacific Marine Environmental Laboratory, National Oceanic and Atmospheric Administration (NOAA), Seattle, WA 98115, USA. ³Alaska Fisheries Science Center, NOAA, 7600 Sand Point Way NE, Seattle, WA 98115, USA. ⁴Auke Bay Laboratory, Alaska Fisheries Science Center, National Marine Fisheries Service, NOAA, 11305 Glacier Highway, Juneau, AK 99801, USA. ⁵Institute of Ocean Sciences, Fisheries and Oceans Canada, 9860 West Saanich Road, Sidney, BC V8L 4B2, Canada. ⁶Department of Geography, University of California, Los Angeles, CA 90095, USA. ⁷Geophysical Institute, University of Alaska Fairbanks, Fairbanks, AK 99775, USA.

*To whom correspondence should be addressed. E-mail: jgrebmei@utk.edu

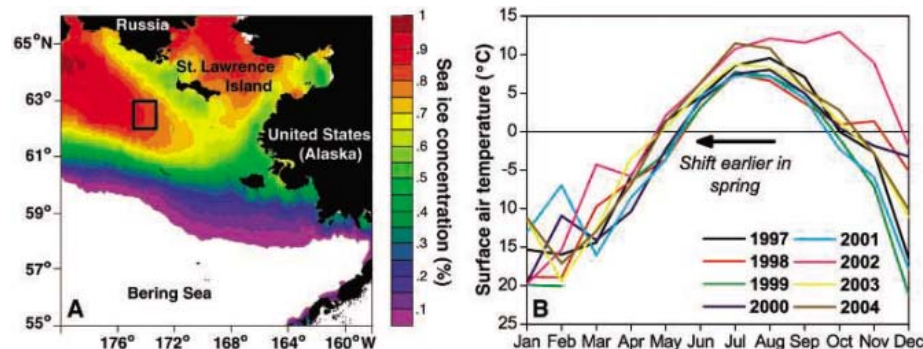


Fig. 1. (A) Location map (box indicates location of time-series biological sites) and average April sea ice concentration (1 corresponds to 100%, and 0.1 corresponds to 10%) in the northern Bering Sea from 2000 to 2004. Ice concentrations are based on microwave satellite instruments, Defense Meteorological Satellites Program SSM/I (12, 16). **(B)** Monthly averaged surface air temperature measured at Savoonga (63.68°N, 170.5°W) on St. Lawrence Island over the years 1997 to 2004. Note the interannual variability in the timing of melt onset (~3 weeks) based on date air temperature rises above 0°C (13).

hunt and fish along with fundamental changes in animal behavior (9).

A critical feature that affects benthic predators in the northern Bering Sea is a recurrent subsurface cold pool (<0°C) extending southward of St. Lawrence Island. This feature forms as a result of ice formation in the winter and subsequent trapping of this cold water in place as sea ice melts and surface water warms in spring and summer (10) (Fig. 2). Higher air temperatures and lower winter ice cover, however, result in a contraction of the summertime extent of the cold pool and an associated increase in mean seawater temperature (4). In the northern Bering Sea, our measurements of temperatures within the cold pool obtained over 12 years (1988 to 2005) suggest, after factoring out seasonal variation, that bottom water temperatures are increasing (Fig. 2, bottom, and tables S1 and S2) (11, 12). This warming trend is comparable to increases in atmosphere and ocean temperatures that were observed in the southeastern Bering Sea after 1977, changes that led to an ecosystem reorganization that favored pelagic over benthic predators (8). Likewise, data collected on St. Lawrence Island from 1997 to 2004 show an increase in air temperatures over time with the onset of ice melt occurring earlier (~3 weeks) (Fig. 1B) (13). These temperature trends directly affect the ecosystem changes we report here.

Clement *et al.* (14) compared late winter sea ice extent and duration in 1999 and in 2001 and found that ice was thinner and retreated earlier in 2001, which supports the Yupik observations of declining ice conditions (9). The Clement *et al.* study was an initial indication of what a recent time-series sea ice data analysis showed to be a

continued decline from 2002 to the present for Arctic sea ice in the western Amerasian Arctic (15). Similarly, sea ice concentrations for the northern Bering Sea in April, averaged for the years 2000 to 2004 by using satellite-derived passive microwave measurements, show ice concentrations below 0.7 (70%) in the region between the Alaska coastline and St. Lawrence Island (Fig. 1A) (12, 16). These data support an increasing trend in open water documented by an analysis of the 24-year (1979 to 2002) satellite-derived time series of ice cover in the Chirikov Basin north of St. Lawrence Island (17). Thus, satellite, field, and Yupik traditional ecological observations support the conclusion that the northern Bering Sea has had lower ice concentrations in the past decade, with declines similar to those observed in the southeastern portion of the Bering Sea (8).

Sediment oxygen uptake is an indicator of carbon supply to the benthos, and time series data from 1988 to 2004 collected in March to September southwest of St. Lawrence Island show a decline from ~40 mmol O₂ m⁻² day⁻¹ in 1988 to sustained values of ~12 mmol O₂ m⁻² day⁻¹ for 1998 to 2004 (Fig. 3A and table S2) (5, 11, 18). Measurements of benthic standing stock show a decrease from about 40 g C m⁻² to 20 g C m⁻² over the same time period (Fig. 3B and table S2) (5, 11). In the past, benthic trophic efficiencies in the northern Bering Sea have been high (up to 50%) (19), reflecting tight pelagic-benthic coupling, and therefore support high benthic standing stocks (20). However, these data suggest that the prey base for benthic-feeding gray whales, walrus, and sea ducks is declining in the northern Bering Sea. One possible explanation for this is that these

apex predators have exceeded the carrying capacity for this system. An alternative hypothesis is that ecosystem change and declining productivity are reducing food supply to benthic prey, thus affecting apex predators (3, 5, 21). A comparison of surveys from 2002 with those from 1981 to 1985 shows that gray whales have responded by relocating their primary foraging area northward, from the Chirikov Basin adjacent to the north shore of St. Lawrence Island to north of Bering Strait (7). Additional evidence that gray whales are traveling north and extending their residence times in Arctic waters includes the surprising detection of gray whale calls during an over-winter (2003 and 2004) deployment of autonomous hydrophones near Barrow, Alaska (22). These data come from the first ever deployment of acoustic recorders mounted on moorings deployed during the Western Arctic Shelf-Basin Interactions (SBI) global change project in 2003 and 2004 (22, 23). Local subsistence hunters in Barrow, Alaska, continue to report more numerous gray whales than in any time previously. Bivalve populations, used as prey items by diving sea duck populations, including the threatened spectacled eider, are also in decline (6, 21).

Native hunters have observed changes in walrus behavior in response to changes in sea

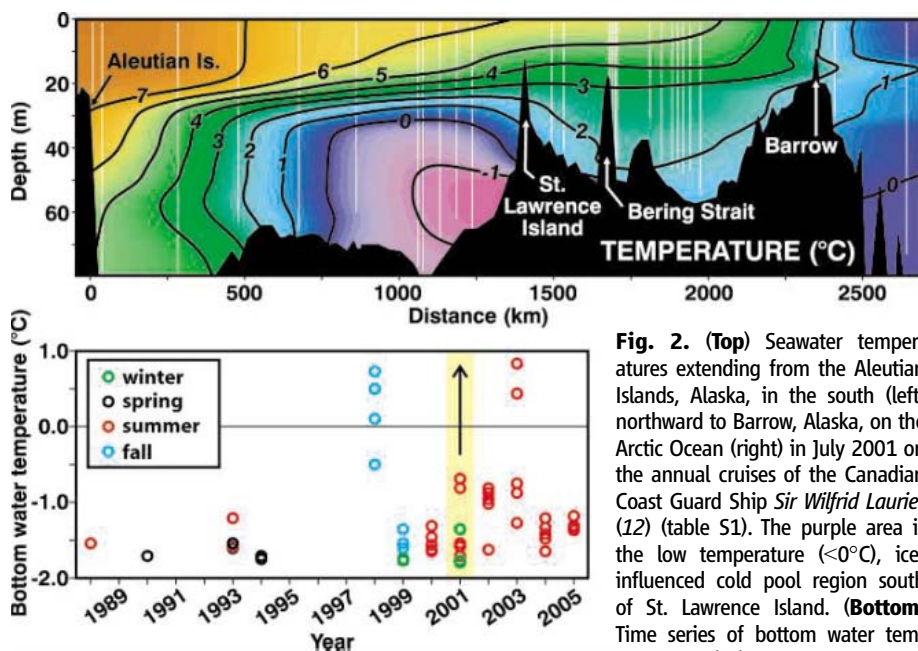


Fig. 2. (Top) Seawater temperatures extending from the Aleutian Islands, Alaska, in the south (left) northward to Barrow, Alaska, on the Arctic Ocean (right) in July 2001 on the annual cruises of the Canadian Coast Guard Ship *Sir Wilfrid Laurier* (12) (table S1). The purple area is the low temperature (<0°C), ice-influenced cold pool region south of St. Lawrence Island. **(Bottom)** Time series of bottom water temperatures (°C) in the cold pool

south of St. Lawrence Island occupied at different seasons from 1988 to 2005 (12) (table S2). The yellow highlighted area indicates data collected in 2001 that corresponds to the top graph.

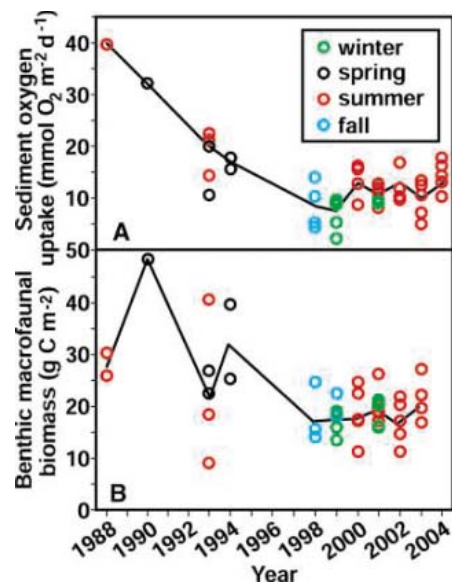


Fig. 3. Time series measurements (1988 to 2004) of (A) total sediment oxygen uptake (mmol O₂ m⁻² day⁻¹) and (B) benthic macrofaunal biomass (g C m⁻²) at stations occupied southwest of St. Lawrence Island in the northern Bering Sea over four seasons (see small box in Fig. 1A for station locations). Color coding indicates the seasonal measurements: winter (March and April), spring (May and June), summer (July and August), and fall (September). Each point represents the mean of two sediment cores (133 cm²) for sediment oxygen uptake and four 0.1 m² van Veen grabs for the benthic macrofaunal biomass (12) (table S2). Trend lines are drawn through the mean of these station values for each year.

ice cover (24). Walrus prefer broken ice floes, and when the ice melts or moves away early walrus go with it, taking them too far away to hunt (25). Reduced sea ice in the late 1990s caused walrus to swim farther between feeding areas; when the ice retreated far to the north in the Chukchi Sea, the animals suffered (24). Field observations during the SBI field program in 2004 documented separated walrus pups coincident with unusually warm surface water being advected northward into the Arctic Basin (water temperature > 10°C) (26).

Other examples of ecosystem change are becoming evident. Fish population surveys of the eastern Bering Sea shelf by the Alaska Fisheries Science Center in late summer and early fall from 2002 to 2004 found large numbers of juvenile pollock (*Theragra chalcogramma*) in the northern Bering Sea just south of St. Lawrence Island in 2004, possibly in response to warm ocean temperatures. Northward range extensions of pelagic fish species include major increases in the number of juvenile pink salmon (*Oncorhynchus gorbusha*) in the northern Bering Sea, which feed on pollock (27). Local observations indicate that pink salmon are now colonizing rivers that drain into the Arctic Ocean north of Bering Strait (28).

A proximate cause for the shift in the climate of the Bering Sea is the decrease in the strong positive phase of the Arctic Oscillation (AO), beginning in 1996 (29), and the subsequent establishment of a multiyear period of weaker northerly winds over the Pacific Arctic (30). A positive AO (also referred to as a northern annular mode) reflects an increase in the strength of the polar vortex winds and a decrease in sea-level pressure over the central Arctic. A strong polar vortex generally acts as a barrier to northward propagation of storms in the Pacific sector. In contrast to the AO pattern, the composite 1000-hPa geopotential height anomaly field for March to May during 2000 to 2005 (Fig. 4A) (31) shows low height anomalies over the Siberian Peninsula and high height anomalies over Alaska, with a strong gradient between

these centers. This structure corresponds to wind reversals, including stronger southerly winds over the northern Bering Sea, and thus to a weakening of climatologically dominant northerly wind regime. Each of the years individually is similar to the composite, as are the height anomaly fields in 1996 and 1997. Near-surface air temperatures for 2000 to 2005 had warm anomalies (~3°C) over eastern Siberia and the northern Bering Sea (Fig. 4B) (31); direct observations from coastal weather stations show anomalies of the same magnitude. The region of warm temperatures is associated with minimum ice cover north of eastern Siberia in these years (15), warming of permafrost (32), as well as increases in the 1000- to 500-hPa thickness field over the region. Although the reason for the year-to-year persistence of the weak northerly wind field over the northern Bering Sea in spring is unknown and includes influences from the atmospheric general circulation, some of the multiyear persistence might be associated with regional feedbacks from the surface to the atmosphere from the loss in Arctic sea ice in the marine environment (15) and tundra on land (33, 34) over the past decade. Recent warming in the Arctic has allowed shrubs and the treeline to move northward into regions previously occupied by Arctic tundra (33). As the terrestrial plant type changes, warmer temperatures interact with the land, resulting in more exposure to sunlight and a loss of snow cover, which reduces the albedo effect and provides a positive feedback for continued land warming (34). Similarly, a loss of sea ice reduces surface ocean reflectivity and allows for surface ocean warming, which acts as a positive feedback for continued sea ice melt.

Although a shift back to cold climate conditions is possible because of large climate variability in high latitudes, the northern Bering Sea is part of a larger climate system (30) and thus likely to follow global patterns of diminished sea ice cover. It is difficult to envision rapid removal of the heat already gained by the ocean

in recent years from diminished sea ice. These observations support a continued trend toward more subarctic ecosystem conditions in the northern Bering Sea, which may have profound impacts on Arctic marine mammal and diving seabird populations as well as commercial and subsistence fisheries.

References and Notes

1. J. M. Grebmeier, W. O. Smith Jr., R. J. Conover, in *Arctic Oceanography: Marginal Ice Zones and Continental Shelves*, W. O. Smith Jr., J. M. Grebmeier, Eds. (American Geophysical Union, Washington, DC, 1995), pp. 231–261.
2. R. C. Highsmith, K. O. Coyle, *Nature* **344**, 862 (1990).
3. J. R. Lovorn *et al.*, *Mar. Ecol. Prog. Ser.* **291**, 135 (2005).
4. T. Yllie-Echeverria, W. S. Wooster, *Fish. Oceanogr.* **7**, 159 (1998).
5. J. M. Grebmeier, K. H. Dunton, in *Impacts of Changes in Sea Ice and Other Environmental Parameters in the Arctic*, H. P. Huntington, Ed., Marine Mammal Commission Workshop, Girdwood, AK, 15 to 17 February 2000 (Marine Mammal Commission, Bethesda, MD, 2000), pp. 80–93, (www.mmc.gov/reports/workshop/seaice.html).
6. J. R. Lovorn, S. E. Richman, J. M. Grebmeier, L. W. Cooper, *Polar Biol.* **26**, 259 (2003).
7. S. E. Moore, J. M. Grebmeier, J. R. Davis, *Can. J. Zool.* **81**, 734 (2003).
8. J. E. Overland, P. J. Stabeno, *Eos* **85**, 309 (2004).
9. I. Krupnik, in *The Earth Is Faster Now*, I. Krupnik, D. Jolly, Eds. (Article Research Consortium of the United States, Fairbanks, AK, 2002), pp. 156–197.
10. J. D. Schumacher, K. Aagaard, C. H. Pease, R. B. Tripp, *J. Geophys. Res.* **88**, 2723 (1983).
11. J. M. Grebmeier, L. W. Cooper, *J. Geophys. Res.* **100**, 4439 (1995).
12. Materials and methods are available as supporting material on Science Online.
13. Data are available from the U.S. National Climate Data Center (NCDC) via <http://lwf.ncdc.noaa.gov/oa/climate/climatedata.html>.
14. J. L. Clement, L. W. Cooper, J. M. Grebmeier, *J. Geophys. Res.* **109**, C03022 (2004).
15. J. C. Stroeve *et al.*, *Geophys. Res. Lett.* **32**, L04501 (2005).
16. The Special Sensor Microwave Imager (SSM/I) sea ice data are available from the U.S. National Snow and Ice Data Center via <ftp://sidacs.colorado.edu>.
17. S. E. Moore, K. L. Laird, *Ecol. Appl.*, in press.
18. L. W. Cooper *et al.*, *Mar. Ecol. Prog. Ser.* **291**, 13 (2002).
19. J. M. Grebmeier, H. M. Feder, C. P. McRoy, *Mar. Ecol. Prog. Ser.* **51**, 253 (1989).
20. J. M. Grebmeier, J. P. Barry, in *Polynyas: Windows into Polar Oceans*, W. O. Smith, D. Barber, Eds., in press.
21. J. M. Grebmeier, L. W. Cooper, abstr. SS2.02 in *Arctic Climate Impact Assessment, Extended Abstracts* (Arctic Monitoring and Assessment Programme, Reykjavik, Iceland, 2004).
22. S. E. Moore, K. M. Stafford, D. K. Mellinger, J. A. Hildebrand, *BioScience* **56**, 49 (2006).
23. J. M. Grebmeier, H. R. Harvey, *Deep-Sea Res.* **52**, 3109 (2005).
24. C. Pungowiyi, in *Impacts of Changes in Sea Ice and Other Environmental Parameters in the Arctic*, H. P. Huntington, Ed., Marine Mammal Commission Workshop, Girdwood, AK, 15 to 17 February 2000 (Marine Mammal Commission, Bethesda, MD, 2000), pp. 18–20 (www.mmc.gov/reports/workshop/seaice.html).
25. G. C. Ray, G. L. Hufford, *Rapp. P.-V. Reun. Cons. Int. Explor. Mer* **188**, 22 (1989).
26. L. W. Cooper *et al.*, *Aquat. Mammals*, in press.
27. For further information, please see www.afsc.noaa.gov/abl/oc/basis.htm.
28. C. Lean, personal communication.
29. D. W. J. Thompson, J. M. Wallace, *Geophys. Res. Lett.* **25**, 1297 (1998).

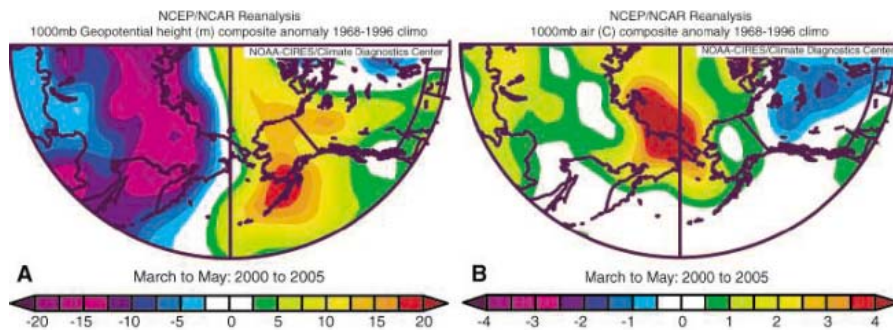


Fig. 4. (A) Anomalies of low geopotential heights over the eastern Siberian Peninsula and high heights over Alaska with a strong gradient between these centers for 2000 to 2005, which corresponds to strong southerly wind anomalies over the northern Bering Sea. (B) The same multiyear spring period shows a major near-surface temperature anomaly over eastern Siberia and the northern Bering Sea on the order of 3°C (31).

30. J. E. Overland, M. Wang, *Geophys. Res. Lett.* **32**, L23808 (2005).
31. Fields of atmospheric variables are from the National Center for Environmental Prediction Reanalysis project and are available through the U.S. Climate Diagnostics Center (www.cdc.noaa.gov).
32. T. E. Osterkamp, V. E. Romanovsky, *Permafrost Periglacial Proc.* **10**, 17 (1999).
33. M. Sturm, C. Racine, K. Tape, *Nature* **411**, 546 (2001).
34. F. S. Chapin III *et al.*, *Science* **310**, 657 (2005); published online 22 September 2005 (10.1126/science.1117368).
35. We thank A. Balsom, R. Brown, R. Pirtle-Levy (University of Tennessee Knoxville), B. van Hardenberg (Institute of Ocean Sciences, Canada), and M. Spillane (Pacific Marine Environmental Laboratory) for technical support and analytical assistance. We appreciate discussions with J. Loworn, P. Stabeno, and T. Whitlege on various aspects of this study. Funded by the NSF (grant OPP-9910319 to L. Cooper and J. Grebmeier), Cooperative Institute for Arctic Research/NOAA cooperative agreement NA17RJ1224 with the University of Alaska (UAF 04-0048 to J. Grebmeier), NOAA funds to J. Overland, and NASA Earth Science

Enterprise Program Office support (NAGS-12411 to J. Overland and L. McNutt). This is Pacific Marine Environmental Laboratory contribution no. 2860.

Supporting Online Material

www.sciencemag.org/cgi/content/full/311/5766/1461/DC1
Material and Methods
Tables S1 and S2
References

14 October 2005; accepted 3 February 2006
10.1126/science.1121365

Structure and Mechanism of the Lantibiotic Cyclase Involved in Nisin Biosynthesis

Bo Li,^{1*} John Paul J. Yu,^{3*} Joseph S. Brunzelle,⁴ Gert N. Moll,⁵ Wilfred A. van der Donk,^{1,2†} Satish K. Nair^{1,3†}

Nisin is a posttranslationally modified antimicrobial peptide that is widely used as a food preservative. It contains five cyclic thioethers of varying sizes that are installed by a single enzyme, NisC. Reported here are the *in vitro* reconstitution of the cyclization process and the x-ray crystal structure of the NisC enzyme. The structure reveals similarities in fold and substrate activation with mammalian farnesyl transferases, suggesting that human homologs of NisC posttranslationally modify a cysteine of a protein substrate.

The accelerated appearance of pathogenic bacteria that are resistant to the existing battery of antibiotics is a growing global health concern. This problem has prompted efforts toward the development of effective antibiotics with limited avenues for bacterial drug resistance. Attractive candidates are compounds with multiple modes of action, making resistance more difficult to develop. One example is nisin, a ribosomally synthesized and posttranslationally modified antimicrobial peptide that, despite worldwide use for decades in the food industry, has not induced widespread resistance (1). Nisin is highly effective [minimum inhibitory concentrations (MICs) on nM scales] against a range of Gram-positive bacteria, including food-borne pathogens. It exerts its biocidal activity through both pore formation in the membrane and the disruption of cell wall biosynthesis by binding to lipid II, which is an essential intermediate in peptidoglycan biogenesis (2, 3). The targeted affinity for the bacterial cell wall increases the efficacy of nisin by several orders of magnitude compared with other pore-forming molecules, such

as the eukaryotic peptide magainin. In a third independent biological activity, nisin inhibits the outgrowth of bacterial spores (4). Although the biosynthetic gene cluster of nisin was sequenced in 1989 (5), to date, *in vitro* reconstitution of its biosynthesis and that of other class I lantibiotics has been unsuccessful. Furthermore, no structural information is available to provide insights into the molecular mechanism of biosynthesis. We present here the *in vitro* enzymatic synthesis of nisin A and the crystal structure of the cyclase enzyme that introduces the characteristic thioether rings that are essential for biological activity. The bacterial enzyme bears structural similarities with the β subunit of mammalian farnesyl transferases, and it appears to use an unusual integral protein module, similar in motif to Src homology 2 (SH2) and Gyf domains, for substrate binding.

Nisin contains five thioether cross-links formed by the addition of cysteine residues to dehydroalanine (Dha) and dehydrobutyryne (Dhb) residues that originate from serine and threonine, respectively (Fig. 1A). These thioether structures are called lanthionines and methyllanthionines and are found in lantibiotics, a group of posttranslationally modified peptide antibiotics (6). The size of these rings in nisin varies from four amino acids for the B, D, and E rings to seven amino acids for the C ring. The cyclase enzyme NisC is believed to be responsible for the formation of all rings, but its activity or that of its homologs has not been demonstrated, and these proteins have no

sequence homology with any other functionally characterized proteins in the Swiss-Prot database.

We cloned *nisC* from *Lactococcus lactis* [American type culture collection (ATCC) accession number 11454] and developed a high-level heterologous expression system in *Escherichia coli*. The substrate was obtained from an engineered *L. lactis* strain that secretes dehydrated prenisin peptide (7, 8). This strain contains a plasmid that harbors the *nisA* gene, which codes for the precursor peptide (prepeptide); the *nisB* gene, which produces the dehydratase that acts on the serine and threonine residues; and the *nisT* gene, which encodes the transporter that secretes the modified peptide (6, 8). Cells were grown on minimal media, and the secreted dehydrated prepeptide was precipitated from the spent medium with trichloroacetic acid and desalted. Analysis with mass spectrometry and gel electrophoresis shows the expected molecular mass (Fig. 1B) and an estimated purity of >85%. Treatment of the dehydrated prenisin with the thiol modifying agent p-hydroxymercuribenzoic acid (PHMB) (9) after reduction of any disulfides with tris(carboxyethyl) phosphine (TCEP) demonstrates the presence of five free thiols (Fig. 1C). This treatment indicates that nisin is not present in this sample, because it would not have free thiols and should remain unmodified: No such peak is observed. Conversely, when the dehydrated peptide was treated with NisC followed by reduction with TCEP and reaction with PHMB, the product mixture showed a clear peak at 5715 daltons, which is associated with a peptide that is devoid of free cysteines as a result of five cyclizations (Fig. 1D). The removal of the leader peptide was achieved by treatment of the NisC product with substoichiometric concentrations of trypsin, resulting in a bioactive compound as shown by a clear zone of inhibition when spotted on a lawn of bacteria of the indicator strain *L. lactis* NZ9000 (fig. S1). When either NisC or trypsin treatment was omitted, no bioactivity was observed, corroborating the conclusion from Fig. 1, C and D, that cyclization is catalyzed by NisC.

Mass spectrometric analysis of the product of successive NisC and trypsin action showed the expected peak for mature nisin (Fig. 1E). No peaks were observed for proteolysis after Lys¹²

¹Department of Biochemistry, ²Department of Chemistry, ³Center for Biophysics and Computational Biology, University of Illinois at Urbana-Champaign, 600 South Mathews Avenue, Urbana, IL 61801, USA. ⁴Life Sciences Collaborative Access Team, Argonne National Labs, Argonne, IL, 60439, USA. ⁵BiOMaDe Technology Foundation, Groningen, Netherlands.

*These authors contributed equally to this work.

†To whom correspondence should be addressed. E-mail: vddonk@uiuc.edu (W.A.V.); s-nair@life.uiuc.edu (S.K.N)

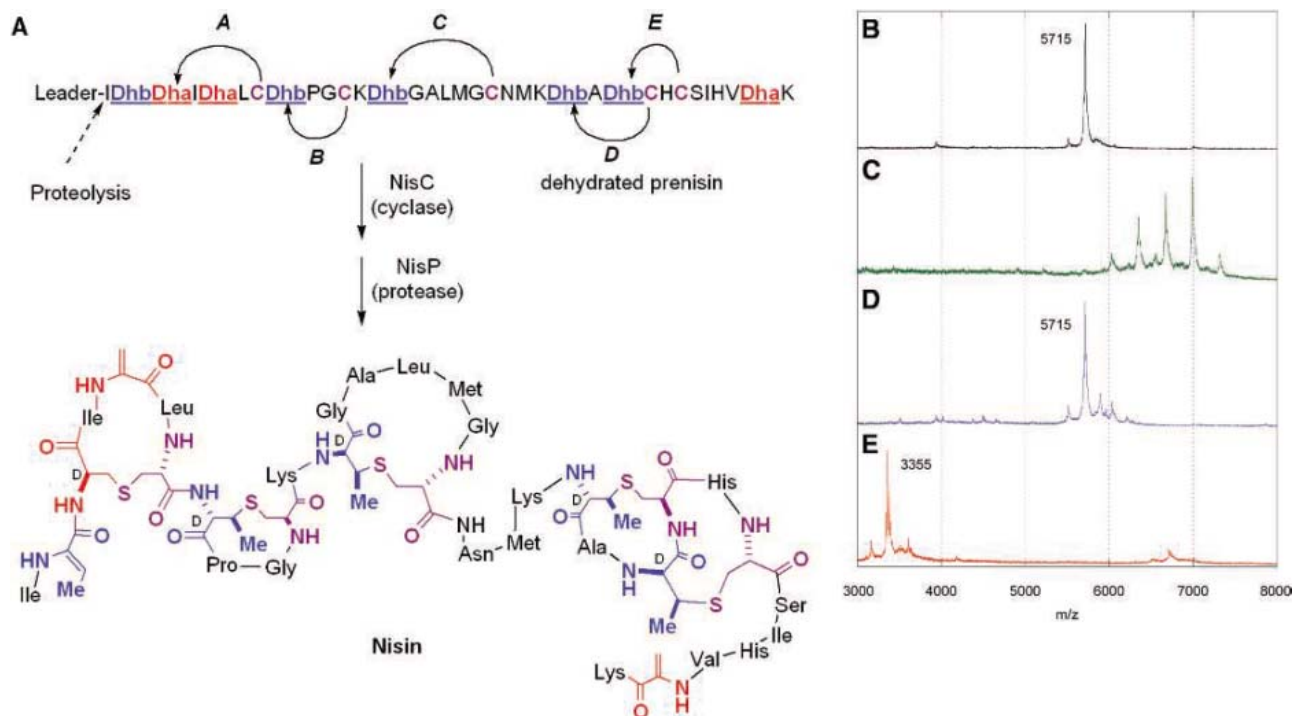
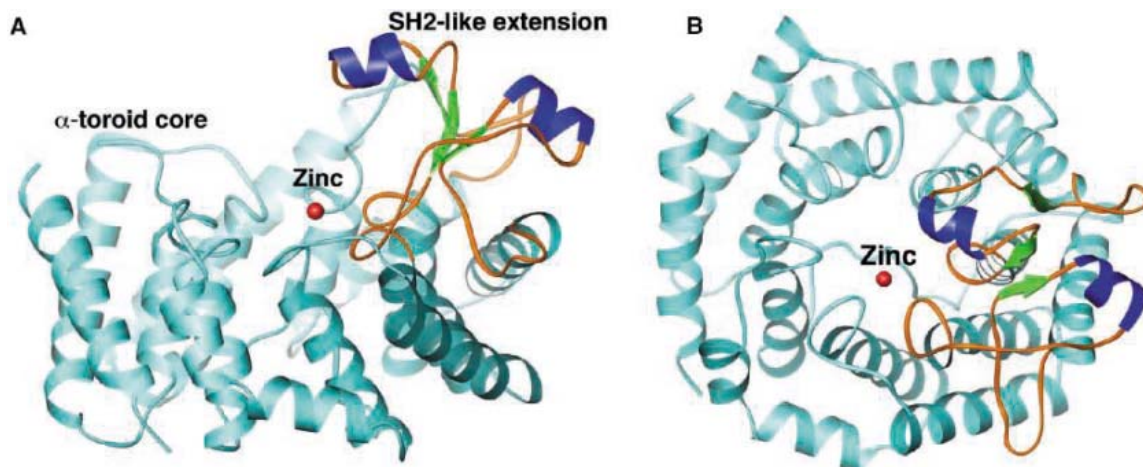


Fig. 1. The posttranslational maturation process of nisin. (A) The prepeptide NisA is ribosomally synthesized, followed by dehydration of Ser and Thr residues to provide dehydroalanine (Dha, red) and Z-dehydrobutyryne (Dhb, blue) residues. NisC then catalyzes the conjugate addition of Cys residues in a regio- and stereoselective manner to five of the Dha and Dhb residues to generate five cyclic thioethers, one lanthionine, and four methylanthionines. The stereochemistry of the cyclization introduces the *D*-configuration at the newly formed stereogenic centers. After cyclization is complete, the leader peptide is proteolytically removed by the protease NisP. The sequence of the leader peptide is MSTKDFNLDLVSVKKDSGASPR (35). Matrix-assisted laser desorption

ionization–time-of-flight (MALDI-TOF) mass spectra of (B) dehydrated prenisin, m/z 5715 ($M + H^+$), where M is the compound's mass and H^+ is a proton, and (C) dehydrated prenisin treated with TCEP and PHMB. The expected five adducts to the Cys residues (7) are observed, 6032 [$M + H^+ + 320$, 1 arylmercury adduct (HgAr)], 6353 ($M + H^+ + 640$, 2 HgAr), 6675 ($M + H^+ + 960$, 3 HgAr), 6997 ($M + H^+ + 1280$, 4 HgAr), and 7318 ($M + H^+ + 1600$, 5 HgAr). (D) Dehydrated prenisin treated with NisC and subsequently with TCEP and PHMB. The main peak no longer contains free thiols: 5715 ($M + H^+$) (calculated 5715). (E) Dehydrated prenisin treated with NisC and subsequently with trypsin. The observed peak corresponds to mature nisin: calculated, 3354; found, 3355 ($M + H^+$).

Fig. 2. (A) A view perpendicular to the α,α barrel, showing the disposition of the zinc ion and the extended domain. (B) View down the spindle axis of the toroid showing the relative positions of seven sets of α helices. The catalytic zinc ion is located near the center of the toroid adjacent to the extended domain. The figures were created with Ribbons software (33).



and Lys²². Similarly, no proteolysis occurs after these residues in dehydrated prenisin, presumably because of the structure of the adjacent posttranslationally modified amino acids. This result allows the use of trypsin to selectively remove the leader peptide from both cyclized and uncyclized peptide. After cleavage of the leader peptide from the dehydrated peptide,

NisC was unable to convert the dehydrated peptide into a bioactive substance (fig. S1), suggesting that the leader peptide fulfills a recognition role for NisC binding. This finding is consistent with published yeast two-hybrid results (10). Furthermore, whereas the overall conversion of lantibiotic prepeptides to the mature products has been shown to require

adenosine triphosphate (ATP) (11, 12), this co-factor is not essential for the cyclization reaction, because bioactivity was observed regardless of whether ATP was added to the enzyme assay. Indeed, we observed no ATP binding domains in the structure of NisC. SpaC, the cyclase enzyme from *Bacillus subtilis* involved in the biosynthesis of subtilin, which is a lantibiotic

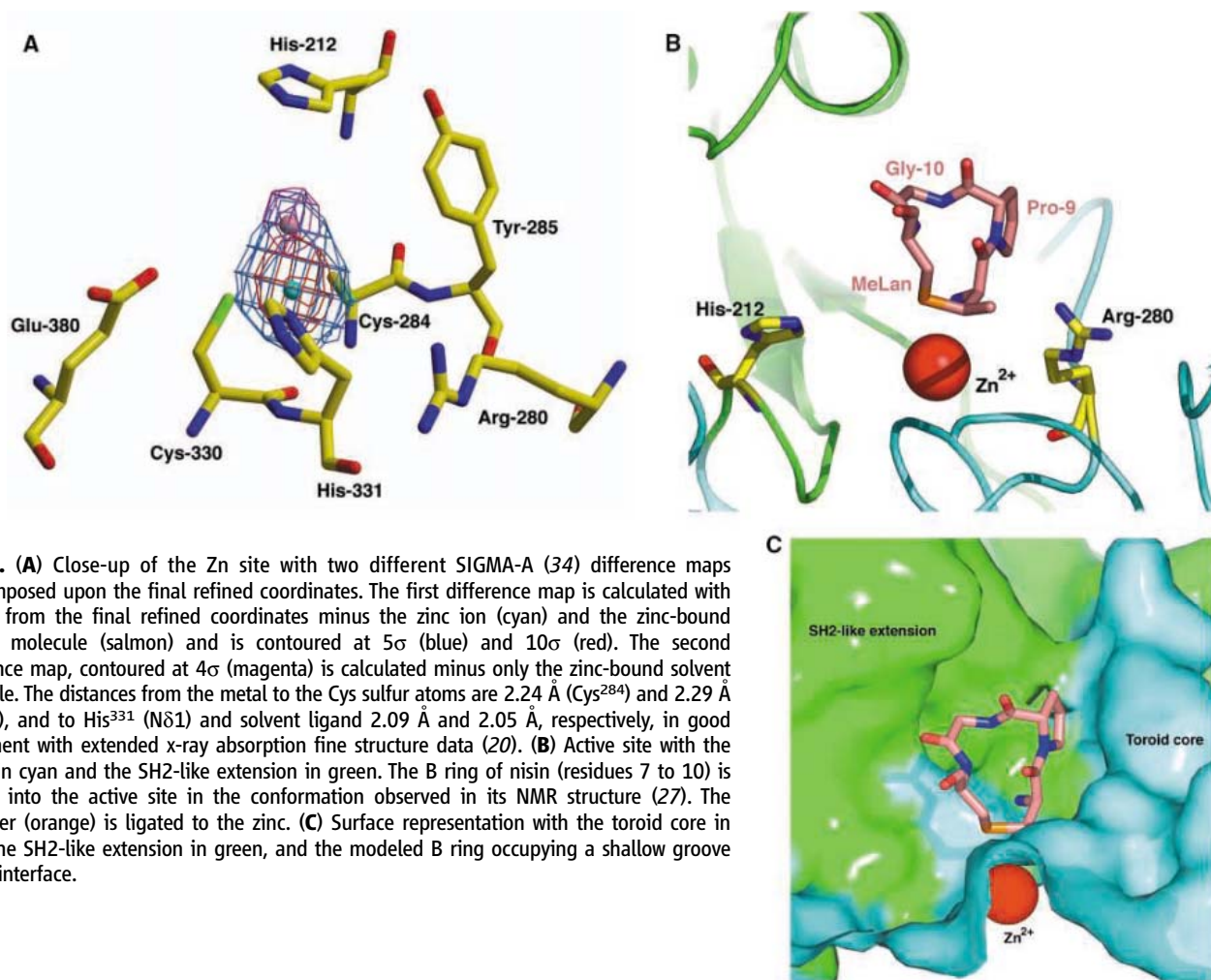


Fig. 3. (A) Close-up of the Zn site with two different SIGMA-A (34) difference maps superimposed upon the final refined coordinates. The first difference map is calculated with phases from the final refined coordinates minus the zinc ion (cyan) and the zinc-bound solvent molecule (salmon) and is contoured at 5σ (blue) and 10σ (red). The second difference map, contoured at 4σ (magenta) is calculated minus only the zinc-bound solvent molecule. The distances from the metal to the Cys sulfur atoms are 2.24 Å (Cys²⁸⁴) and 2.29 Å (Cys³³⁰), and to His³³¹ (N δ 1) and solvent ligand 2.09 Å and 2.05 Å, respectively, in good agreement with extended x-ray absorption fine structure data (20). (B) Active site with the toroid in cyan and the SH2-like extension in green. The B ring of nisin (residues 7 to 10) is docked into the active site in the conformation observed in its NMR structure (27). The thioether (orange) is ligated to the zinc. (C) Surface representation with the toroid core in cyan, the SH2-like extension in green, and the modeled B ring occupying a shallow groove at the interface.

with 67% sequence identity with nisin (fig. S2), also converted the dehydrated prenisin into nisin, albeit less efficiently (fig. S1). SpaC and NisC have only 31% sequence identity. These results show that lantibiotic synthesis is modular, with dehydration and cyclization occurring independently, which is promising for protein engineering of either activity.

The crystal structure of NisC was determined by multiple isomorphous replacements with anomalous scattering, solvent flattening, and phase combination (7). The structure of the native enzyme has been refined to a resolution of 2.5 Å ($R_{\text{free}} = 24.2\%$; see table S1). A higher resolution data set has also been collected from crystals grown in the presence of lead acetate, and this structure has been refined to 2.2 Å ($R_{\text{free}} = 23.3\%$). The two structures are essentially identical except for the presence of residual lead ions in the latter structure. The overall fold has a di-domain architecture composed largely of α helices, with an extended domain defined by a short stretch of α helices and β sheets (Fig. 2A). The core structure consists of 14 α helices folded into two layers of a toroid (Fig. 2B). The inner layer consists of seven helices (α_2 , α_4 , α_6 , α_8 , α_{10} ,

α_{12} , and α_{14}) that are arranged as a barrel. Likewise, the outer layer consists of seven helices (α_1 , α_3 , α_5 , α_7 , α_9 , α_{11} , and α_{13}) with short loops interconnecting the two layers. The extended domain adjacent to the α,α barrel is composed of noncontiguous elements. The first sheet-helix-sheet motif is an extension between helices α_7 and α_8 , and the second helix and sheet are an extension between helices α_9 and α_{10} . These extensions form a structure of three twisted, antiparallel β strands flanked by two short α helices (Fig. 2A) and are similar to eukaryotic multiprotein interaction modules such as the Gyf and SH2 domains (fig. S3). However, there is no evidence that this region has functional similarities to either Gyf or SH2 domains (7).

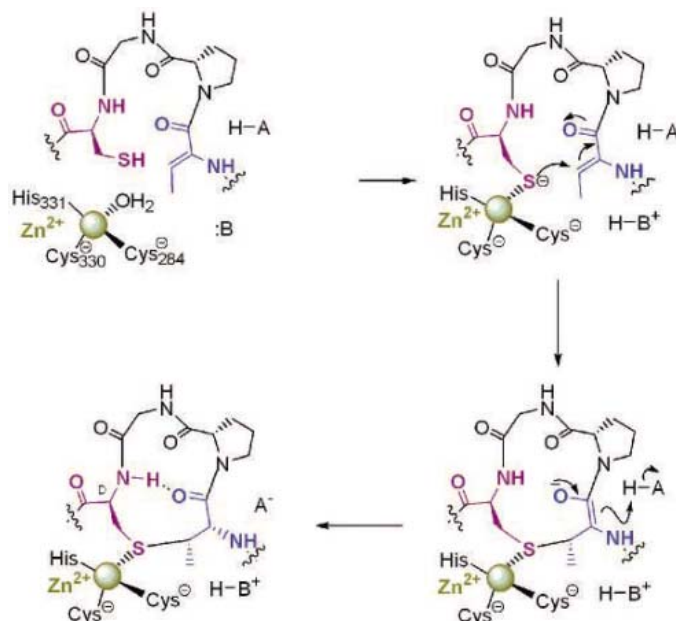
Despite the lack of any appreciable sequence similarity, the α -toroidal core structure is topologically similar to bacterial cellulases (13, 14), endoglucanase (15), terpenoid cyclases (16–18), and the β subunit of protein farnesyl transferase (19). Similarly to the structure of farnesyl transferase, a single zinc ion is situated at the top face of the α,α barrel in NisC (Fig. 2A). The topology between the two zinc enzymes is somewhat different, because the NisC toroid is

composed of seven sets of α helices, but the farnesyl transferase β subunit contains six sets of helices. In addition, the helices that constitute the outer layer of the NisC barrel are longer than those seen in farnesyl transferase, resulting in a tighter stacking between the outer and inner cores.

The conserved protein residues Cys²⁸⁴, Cys³³⁰, and His³³¹ bind the zinc ion, consistent with spectroscopic studies (20), with well-defined electron density assigned to a water molecule completing a tetrahedral coordination geometry (Fig. 3A). This type of coordination is reminiscent of other zinc proteins that catalyze alkylations of thiol substrates such as the Ada protein (21), vitamin B₁₂-dependent Met synthase (22), and B₁₂-independent Met synthase (23, 24). Although the ligand sets, structures, and sequences of these proteins differ, they have in common a net negative charge of the metal site upon coordination of a thiolate substrate (26), which, in the case of NisC, is intramolecular.

Two other residues that are conserved among the LanC cyclases, His²¹² and Arg²⁸⁰, are also located in the shallow bowl that is sandwiched between the top of the α -toroid core

Fig. 4. Proposed mechanism for the cyclization reaction catalyzed by NisC illustrated for the formation of the B ring of nisin. Upon binding of the dehydrated peptide, the sulfur of a Cys residue targeted for cyclization displaces the water from the Zn^{2+} ion and is deprotonated by an active site base or water. Coordination of cysteine to Zn in farnesyl transferase lowers its pK_a to 6.4 (25); hence, a protein-derived base is not absolutely required. Attack of the thiolate onto the β carbon of Dhb generates an enolate intermediate that is protonated to provide the D-configuration at the α carbon. Because the stereochemistry of the addition is anti, the active site base that deprotonates Cys must be different from the acid that protonates the enolate. Arg²⁸⁰ might activate a water molecule or could fulfill a different role such as activation of the carbonyl of Dha/Dhb.



and the extended domain (Fig. 3, A and B). These residues are likely involved in the acid-base chemistry of the reaction, which entails deprotonation of the Cys residue and protonation of the enolate intermediate generated by conjugate addition to the β carbon of Dha/Dhb (Fig. 4). Arg is not often found as an active site general acid/base because of its high pK_a (where K_a is the acid dissociation constant), and its role may be to position and activate a water molecule. The observed stereochemistry resulting from Cys addition to Z-Dhb to produce 2S,3S,6R-3-methylanthionine requires an anti-addition mechanism, consistent with the location of His²¹² and Arg²⁸⁰. Modeling of the B ring of nisin, which adopts a well-structured β turn in the nuclear magnetic resonance (NMR) structure of nisin (27), into the active site with the thioether sulfur coordinated to the metal places His²¹² and Arg²⁸⁰ on opposite faces of the methylanthionine ring (Fig. 3, B and C).

In the cocrystal structures of farnesyltransferase bound to a farnesyl diphosphate (FPP) or an FPP analog (28, 29), the isoprenoid is housed within a deep hydrophobic cavity in the center of the β subunit. At the analogous position, NisC has a cavity that is shallower, because the side chains of Leu²¹⁰ and Trp²⁸³ pack to fill the cavity adjacent to the zinc ion. The shallowness of the cavity and its solvent exposure allows NisC to generate thioether rings varying from four to seven amino acids. The regioselectivity of the cyclization is likely governed by processive directionality (30). The structure suggests a possible binding site for the leader sequence of dehydrated prenisin. Residues to

one side of the zinc site of NisC define an extensive binding groove lined with hydrophobic (Ile¹⁴³, Leu²⁶², Phe²⁷⁸, and Tyr²⁸⁵) as well as charged residues (Glu¹⁴⁴ and Asp²⁶⁰) and a number of backbone carbonyls. The acidic residues create a negatively charged channel that may interact with the cationic leader peptide containing three Lys and one Arg. One side of this groove is created by the α -toroidal base, whereas the extended region flanks the other side.

The structure of NisC provides insights into the LanC-like proteins (LANCL) found in a wide range of organisms that do not produce lantibiotics, such as *Drosophila melanogaster*, *Xenopus laevis*, *Arabidopsis thaliana* (31), and some mammals. These proteins have 20 to 25% sequence identity with NisC, including the conserved Zn ligands and the putative active site base (fig. S4). They are also predicted to contain the extended domain identified in NisC. LANCL-1 is recruited to the Maurer's cleft in human erythrocytes during development of *Plasmodium falciparum* and interacts with the parasite protein PfSBP1 (32), but the physiological function of the LANCL proteins is currently unknown. On the basis of the structural similarity of NisC with farnesyl transferase and the conservation of the metal ligands and peptide binding domain, the LANCL proteins likely carry out the posttranslational modification of a Cys residue of a currently unknown substrate protein.

References and Notes

- J. Delves-Broughton, P. Blackburn, R. J. Evans, J. Hugenholz, *Antonie Van Leeuwenhoek* **69**, 193 (1996).
- E. Breukink *et al.*, *Science* **286**, 2361 (1999).

- S. T. Hsu *et al.*, *Nat. Struct. Mol. Biol.* **11**, 963 (2004).
- W. C. Chan *et al.*, *Appl. Environ. Microbiol.* **62**, 2966 (1996).
- C. Kaletta, K. D. Entian, *J. Bacteriol.* **171**, 1597 (1989).
- C. Chatterjee, M. Paul, L. Xie, W. A. van der Donk, *Chem. Rev.* **105**, 633 (2005).
- Materials and methods are available as supporting material on Science Online.
- A. Kuipers *et al.*, *J. Biol. Chem.* **279**, 22176 (2004).
- K. E. Pitts, A. O. Summers, *Biochemistry* **41**, 10287 (2002).
- K. Siegers, S. Heinzmann, K.-D. Entian, *J. Biol. Chem.* **271**, 12294 (1996).
- L. Xie *et al.*, *Science* **303**, 679 (2004).
- C. Chatterjee *et al.*, *J. Am. Chem. Soc.* **127**, 15332 (2005).
- A. Aleshin, A. Golubev, L. M. Firsov, R. B. Honzatko, *J. Biol. Chem.* **267**, 19291 (1992).
- J. Sakon, D. Irwin, D. B. Wilson, P. A. Karplus, *Nat. Struct. Biol.* **4**, 810 (1997).
- P. M. Alzari, H. Souchon, R. Dominguez, *Structure* **4**, 265 (1996).
- C. A. Lesburg, G. Zhai, D. Cane, D. W. Christianson, *Science* **277**, 1820 (1997).
- C. M. Starks, K. Back, J. Chappell, J. P. Noel, *Science* **277**, 1815 (1997).
- K. U. Wendt, K. Poralla, G. E. Schulz, *Science* **277**, 1811 (1997).
- H. W. Park, S. R. Boduluri, J. F. Moomaw, P. J. Casey, L. S. Beese, *Science* **275**, 1800 (1997).
- N. M. Okeley, M. Paul, J. P. Stasser, N. Blackburn, W. A. van der Donk, *Biochemistry* **42**, 13613 (2003).
- L. C. Myers, M. P. Terranova, A. E. Ferentz, G. Wagner, G. L. Verdine, *Science* **261**, 1164 (1993).
- J. C. Evans *et al.*, *Proc. Natl. Acad. Sci. U.S.A.* **101**, 3729 (2004).
- R. Pejchal, M. L. Ludwig, *PLoS Biol.* **3**, e31 (2005).
- J. L. Ferrer, S. Ravel, M. Robert, R. Dumas, *J. Biol. Chem.* **279**, 44235 (2004).
- K. E. Hightower, C. A. Fierke, *Curr. Opin. Chem. Biol.* **3**, 176 (1999).
- J. J. Wilker, S. J. Lippard, *J. Am. Chem. Soc.* **117**, 8682 (1995).
- H. W. van den Hooven *et al.*, *Eur. J. Biochem.* **235**, 382 (1996).
- S. Long, P. J. Casey, L. S. Beese, *Biochemistry* **37**, 9612 (1998).
- S. B. Long, P. J. Casey, L. S. Beese, *Structure* **8**, 209 (2000).
- Y. Zhu, M. Gieselmann, H. Zhou, O. Averin, W. A. van der Donk, *Org. Biomol. Chem.* **1**, 3304 (2003).
- H. Bauer, H. Mayer, A. Marchler-Bauer, U. Salzer, R. Prohaska, *Biochem. Biophys. Res. Commun.* **275**, 69 (2000).
- T. Blisnick, L. Vincensini, J. C. Barale, A. Namane, C. Braun Breton, *Mol. Biochem. Parasitol.* **141**, 39 (2005).
- M. Carson, *Methods Enzymol.* **277**, 646 (1997).
- R. J. Read, *Acta Crystallogr.* **A42**, 140 (1986).
- Single-letter abbreviations for the amino acid residues are as follows: A, Ala; C, Cys; D, Asp; E, Glu; F, Phe; G, Gly; H, His; I, Ile; K, Lys; L, Leu; M, Met; N, Asn; P, Pro; Q, Gln; R, Arg; S, Ser; T, Thr; V, Val; W, Trp; and Y, Tyr.
- The structures have been deposited in the Protein Data Bank with the following accession codes: 2G02 (native NisC) and 2G0D (NisC with lead). This work was supported by the NIH (grant GM58822 to W.A.V.) and by the University of Illinois. J.J.Y. was supported by the Molecular Biophysics Training Grant (NIH) and by a National Research Service Award from the National Institute on Drug Abuse. We thank E. de Boef (BiOMaDe) for technical assistance and R. Matthews for helpful discussions.

Supporting Online Material

www.sciencemag.org/cgi/content/full/311/5766/1464/DC1

Materials and Methods

Figs. S1 to S4

Table S1

References

17 October 2005; accepted 5 January 2006
10.1126/science.1121422

Engineering Cooperativity in Biomotor-Protein Assemblies

Michael R. Diehl,^{1*} Kechun Zhang,¹ Heun Jin Lee,² David A. Tirrell¹

A biosynthetic approach was developed to control and probe cooperativity in multiunit biomotor assemblies by linking molecular motors to artificial protein scaffolds. This approach provides precise control over spatial and elastic coupling between motors. Cooperative interactions between monomeric kinesin-1 motors attached to protein scaffolds enhance hydrolysis activity and microtubule gliding velocity. However, these interactions are not influenced by changes in the elastic properties of the scaffold, distinguishing multimotor transport from that powered by unorganized monomeric motors. These results highlight the role of supramolecular architecture in determining mechanisms of collective transport.

Protein cooperativity allows systems of biomotor assemblies to operate with greater determinism and efficiency and often provides physiological functionality that cannot be achieved by single molecules (1–9). For example, cooperation between RNA polymerase molecules can result in increased rates of transcription (2), and increased transport velocities have been observed with groups of monomeric kinesin motors (3, 4) and with multimotor assemblies comprising dimeric kinesins and dyneins (5). In the latter case, assemblies traveled in vivo with velocities up to 10 times as high as those observed in vitro. This result implies the presence of intermotor interactions in vivo that are not reproduced in in vitro assays. Although models of biomotor cooperativity (1, 6) can explain generic aspects of multimotor transport and predict new modes of transport such as spontaneous oscillations (7–11), the molecular details that give rise to these cooperative effects remain elusive.

Many systems of motors are arranged in highly organized and hierarchical architectures

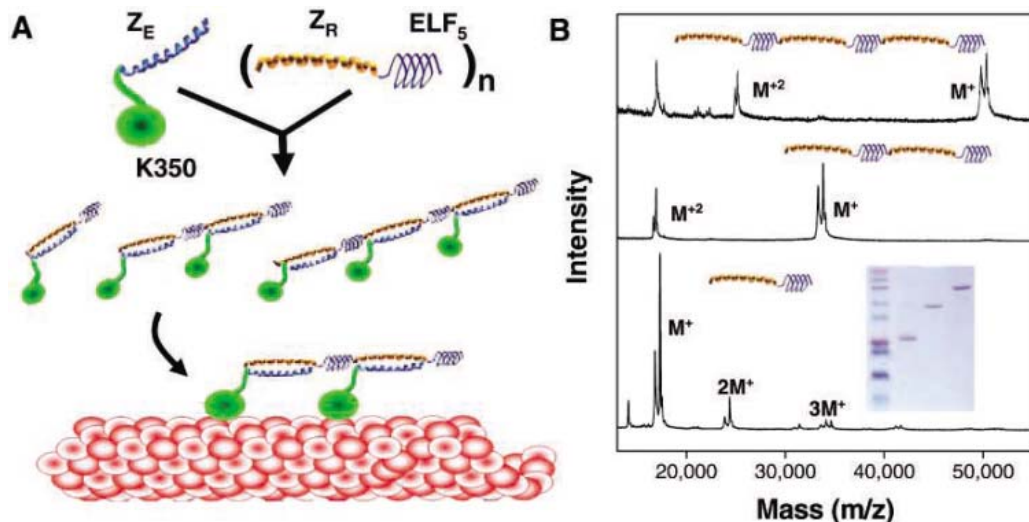
in vivo (12, 13), but it is not clear how features such as the mechanical compliance of motor-motor linkages and intermotor spacing influence collective dynamics. Because the mechanochemistry of biomotors is strongly dependent on strain [and hence on the mechanical coupling between motors (14, 15)], developing a more complete picture of collective motility requires a better understanding of the relations between architecture and function in multimotor assemblies.

To investigate the influence of supramolecular architecture on biomotor cooperativity, we have engineered a model multimotor system that allows us to precisely regulate intermotor coupling. We have synthesized a series of modular polymeric scaffolds (Fig. 1) in which molecular properties such as length, sequence, and secondary structure are specified by artificial genes that encode alternating rigid and elastic protein motifs (16). The rigid block is comprised of strongly associated acidic and basic leucine zipper domains that anchor motor proteins at specific distances

along the polymer backbone. Based on amino acid sequences developed by Vinson *et al.* (17), these zippers form strong heterodimeric complexes ($K_D \sim 10^{-15}$ M) and much weaker homodimers ($K_D \sim 10^{-6}$ to 10^{-3} M). The artificial protein scaffolds incorporate the basic zipper (Z_R) into the polymer backbone, whereas the complementary acidic zipper (Z_E) is fused to the C terminus of a truncated kinesin-1 motor (designated K350- Z_E). The flexible polymer block is derived from the elastomeric poly(VPGV _{α} G) structural motif of the protein elastin (EL) and confers well-characterized mechanical compliance on the assembly (18–20). Every fifth α -valine (V_α) residue is replaced by a phenylalanine (F) residue in the EL sequence used here, yielding the designation ELF. This substitution provides a means to control the thermoresponsive behavior of the polymers, as discussed in more detail below. Variation in the number of diblock repeats in the polymer provides discrete control over the number of coupled motors, which in the present series of experiments ranges from one to three. The C terminus of each scaffold is labeled with biotin to allow the motor assemblies to be tethered to streptavidin-coated surfaces.

The monomeric kinesin-1 construct contains a Z_E -fusion to the motor's catalytic domain and neck linker. Monomeric truncations of kinesin-1 that contain the neck linker are nonprocessive

Fig. 1. Engineered multimotor assemblies. **(A)** Schematic representation of the synthesis of the engineered multimotor assemblies. As a complex, the zippers (Z_E and Z_R) form a rigid linker approximately 6.5-nm long (assuming 6.3 heptad repeats in a zipper and 1.03 nm per heptad) (31). The length of the flexible ELF block can be approximated by assuming a β -spiral conformation. In this conformational state, elastin proteins possess a spiral pitch of 1 nm, where each turn contains three VPGV _{α} G pentapeptide units. Repeating this ELF motif, (VPGVG)₂VPGFG(VPGVG)₂, five times gives a length of 8 nm for the ELF₅ domain. Considering that four amino acids (KASK) form linkers between adjacent Z_R -ELF₅ diblock units, the total intermotor spacing set by the polymer is approximately 16 nm when bound to a microtubule (shown in red). **(B)** Matrix-assisted laser desorption/ionization mass spectra of polymer scaffolds containing one, two, and three repeats of the Z_R -ELF₅ diblock. The



splitting of the main peaks ($M+$) is due to a 525-Da shift in mass that arises from biotin functionalization at the C-terminal cysteine positions of the polymers. A tris-tricine gel of all three polymers is shown in the inset.

¹Division of Chemistry and Chemical Engineering, California Institute of Technology, Pasadena, CA 91125, USA.

²Department of Applied Physics, California Institute of Technology, Pasadena, CA 91125, USA.

*Present address: Department of Bioengineering and Department of Chemistry, Rice University, Houston, TX.

†To whom correspondence should be addressed. E-mail: diehl@rice.edu

and maintain plus-end directionality (21). As a result, the motions of individual K350-Z_E motors along microtubules can be described by Brownian diffusion models (22, 23). When anchored to the Z_R blocks of the artificial protein scaffolds (Z_R-ELF₅)_n, motors are separated by approximately 16 nm, or two microtubule lattice sites (Fig. 1).

To examine the consequences of clustering multiple motors, we measured the microtubule-stimulated adenosine triphosphatase (ATPase) rates of the polymer-motor complexes (Fig. 2A). Motor assemblies were preformed in solution by incubating the (Z_R-ELF₅)_n polymers and K350-Z_E motors (16, 24). When assembled on dimeric (Z_R-ELF₅)₂ and trimeric (Z_R-ELF₅)₃ scaffolds, the K350-Z_E motors exhibit roughly a 60% increase in the maximum microtubule-stimulated ATPase rate (k_{cat}) accompanied by a decrease by a factor of 2.6 to 3.1 in the Michaelis-Menten constant ($K_{0.5\text{MT}}$) when compared with complexes formed on monomeric (Z_R-ELF₅) scaffolds (Fig. 2). Similar results were obtained by using either microtubule affinity-purified or Ni-NTA (nickel

nitrilotriacetic acid)-purified K350-Z_E motors (Table 1).

Whereas the apparent bimolecular reaction rate ($k_{\text{cat}}/K_{0.5\text{MT}}$) of the monomeric motor complex falls within values predicted for diffusion-limited reactions (20 to 30 $\mu\text{M}^{-1} \text{s}^{-1}$) (25), the dimeric and trimeric complexes exhibit an increase by a factor of 4 or more in $k_{\text{cat}}/K_{0.5\text{MT}}$. This result suggests that the multiprotein complexes are processive. However, $k_{\text{cat}}/K_{0.5\text{MT}}$ values are smaller than those of native kinesin ($\geq 1000 \mu\text{M}^{-1} \text{s}^{-1}$) (26), implying (as expected) a distinct transport mechanism.

In microtubule gliding assays (16), microtubule velocities of two- and three-headed motors are about twice that of the monomer constructs (Fig. 2B). In these experiments, polymer and motor concentrations were chosen to ensure that the coverslip surface was saturated with motor assemblies. In each case, microtubules exhibited smooth gliding motions across the surface. Thus, microtubule gliding is occurring in a regime where transport is characterized by multiprotein suppression of individual motor fluctuations and is independent of the

number of motors involved in motility (6, 27). As a result, multimotor complexes must use an additional mechanism that enhances the velocity-determining step of the K350-Z_E motors. This mechanism should be linked to the enhanced ATPase activity observed in solution phase experiments and is likely the result of specific motor-motor coupling that occurs when several motors are anchored along a single polymer chain. Interestingly, trimeric multimotor complexes produced gliding velocities similar to those of dimeric assemblies.

Insight into the nature of the intermotor coupling in the multimotor assemblies can be gained by tuning the elastic properties of the scaffold's ELF motif. Elastin-like polypeptides (ELPs) undergo a phase transition in which hydrophobic folding of the chain drives a condensation process, forming a denser viscoelastic phase when the temperature is raised above the lower critical solution temperature (LCST) of the protein (18). Single-molecule atomic force microscopy pulling experiments demonstrate that the LCST transition results in a decrease in polymer length (28).

In concentrated polymer solutions, the condensation of ELPs can be monitored by measuring changes in turbidity with temperature (Fig. 3A). The transition temperature of the polymers increases with decreasing polymer length (29). In temperature-dependent microtubule gliding assays (Fig. 3B) (16), elastin condensation results in a decreased microtubule velocity. Similar behavior is observed when a stoichiometric excess of the (Z_R-ELF₅)₂ polymer is used to produce longer monomeric motors. In each case, the microtubule gliding velocity increases with increasing temperature in accordance with a standard Arrhenius-like temperature dependence above and below the transition. However, the condensation of the ELF units is accompanied by a decrease in the slope, yielding 20 to 30% lower activation barriers above the LCST (Table 1).

The attenuation of microtubule velocity upon condensation of the ELF domains when transport is powered by monomeric complexes can be explained by previous models of co-operating motors. These models predict enhancements of multimotor efficiency, velocity, and force generation when motor anchorages are stiff (1, 3). The observed decreases in both the velocities and activation barriers of micro-

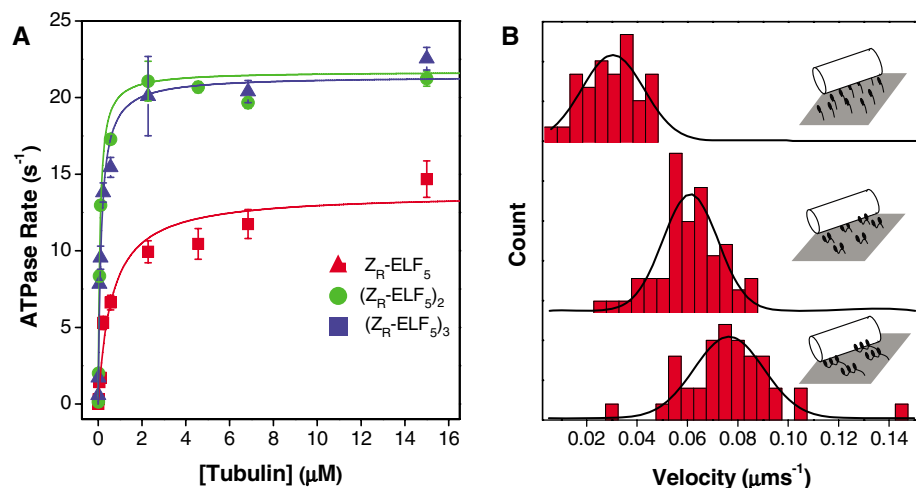


Fig. 2. Enhancement of ATPase activity and motility when multiple K350-Z_E motors are coupled to (Z_R-ELF₅)_n polymer scaffolds. **(A)** Microtubule-dependent ATPase activity of [K350-Z_E]_n/(Z_R-ELF₅)_n assemblies. The multimotor assemblies, [K350-Z_E]₂/(Z_R-ELF₅)₂ and [K350-Z_E]₃/(Z_R-ELF₅)₃, exhibit a 52% to 67% increase in the maximum ATPase rate (k_{cat}) compared with [K350-Z_E]₁/(Z_R-ELF₅)₁. The lines are Michaelis-Menten fits yielding $K_{0.5\text{MT}}$ (0.62 ± 0.20 ; 0.08 ± 0.01 ; 0.14 ± 0.20) and k_{cat} (13.7 ± 1.0 ; 21.7 ± 0.8 ; 21.4 ± 0.7) values for the monomer, dimer, and trimer complexes, respectively. **(B)** Velocity histograms for microtubules gliding over films prepared using preassembled motor/polymer complexes at 17°C for monomeric (top), dimeric (middle), and trimeric (bottom) complexes.

Table 1. Summary of kinetics and temperature-dependent gliding assays.

Assembly	MT Affinity-purified K350-Z _E			Ni-NTA purified K350-Z _E		
	$K_{0.5\text{MT}}^*$ (μM)	k_{cat}^* (s^{-1})	$k_{\text{cat}}/K_{0.5\text{MT}}^*$ ($\mu\text{M}^{-1} \text{s}^{-1}$)	$V \dagger$ (nm s^{-1})	ΔE (T < TC) (kJ mol^{-1})	ΔE (T > TC) (kJ mol^{-1})
[K350-Z _E] ₁ /(Z _R -ELF ₅) ₁	0.75 ± 0.30	15.4 ± 2.3	20	29 ± 22	150	105
[K350-Z _E] ₂ /(Z _R -ELF ₅) ₂ ‡	—	—	—	—	163	133
[K350-Z _E] ₂ /(Z _R -ELF ₅) ₂	0.29 ± 0.08	23.4 ± 1.7	81	61 ± 22	—58—	—
[K350-Z _E] ₃ /(Z _R -ELF ₅) ₃	0.24 ± 0.04	25.7 ± 0.9	104	76 ± 27	—69—	—

*Measured at 20°C

†MT gliding at 17°C

‡Monomeric complex using dimeric polymer

tubule transport are consistent with these theories if the simultaneous decrease in ELF length and stiffening of the mechanical linkage to the cover slip are taken into account. In microtubule gliding assays, the decrease in polymer length influences transport by producing a monomeric motor with a shorter “lever arm” and, consequently, a smaller working stroke.

Multimotor assemblies consisting of fully functionalized dimeric $[K350Z_E]_2/(Z_R-ELF_5)_2$ and trimeric $[K350Z_E]_3/(Z_R-ELF_5)_3$ complexes exhibit simple Arrhenius-like temperature dependence throughout the ELF phase transition region (Fig. 3C). The activation barriers obtained from these measurements are substantially lower than those of the monomeric motor assemblies (Table 1). Here, the insensitivity of multimotor transport to ELF condensation suggests a mechanism that relies on processes distinct from those that dominate transport driven by teams of unorganized monomeric complexes. One explanation for the difference is that mechanochemical coupling between neighboring motors is enhanced by the stiffening of the ELF linkages, compensating for a decrease in motor working distance. However, this possibility requires that these

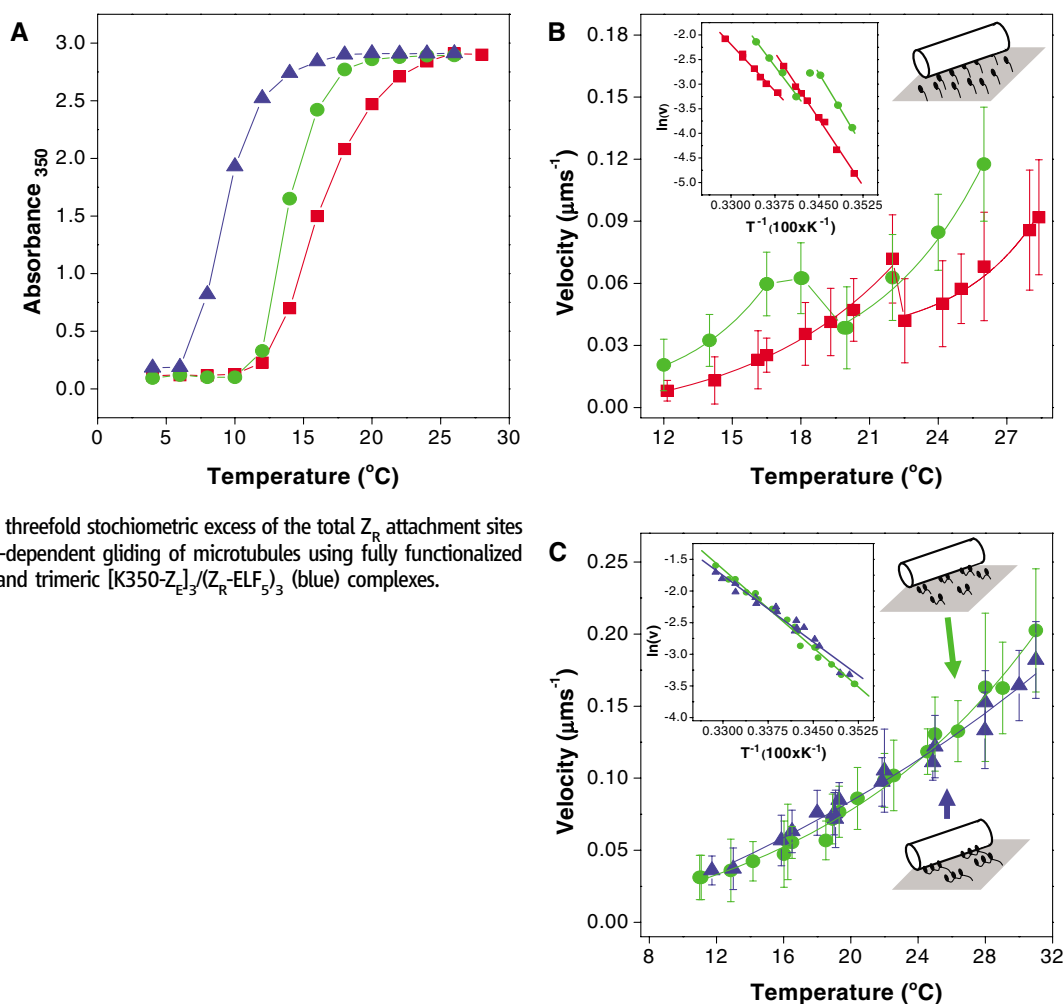
two competing factors are in near-perfect balance for both dimeric and trimeric assemblies. Alternatively, the velocity determining step of multimotor transport may not be dependent on the motions of lever arms that contain the ELF linkers as structural elements. Instead, engineered assemblies may use a multi-step mechanism that is rate-limited by other mechanical processes, such as motions where the motor’s neck linkers alone serve as lever arms or a diffusive search by a motor domain for its next binding site.

Although models involving diffusion-to-capture processes and/or conformational changes in neck linkers have been used to describe the stepping mechanics of kinesins (30), the results reported here indicate that the artificial proteins provide a structural framework that allows motors to push and pull on one another to enhance activity. Such cooperative interactions should lead to “inchworm-like” stepping motions that are influenced by weak mechanochemical coupling and, possibly, by coordinated displacements along the microtubule. The mechanism of movement should be influenced by architectural features of the assembly, including the large intermotor distance, the flexibility of the ELF linkages, the ability of

an assembly to bind multiple microtubule sites, and the asymmetric anchoring to the surface at one end of the scaffold. These features create a structural framework where motors are attached to the microtubule and to the surface through different mechanical linkages and where strain is unequally distributed across the motors in an assembly. These factors should constrain the mechanism of multimotor transport by determining the local reference frame for the displacement of a motor within an assembly and should influence cooperative interactions by tuning both the strain-dependent detachment of, and the mechanochemical coupling between, neighboring motors. Although further experiments to investigate the details of multimotor transport are underway, the results described here clearly demonstrate that controlling the supramolecular architecture of multimotor assemblies provides a means to reconfigure mechanisms of collective biomotor transport.

Fig. 3. Influence of the condensation of the ELF domain of the polymers on multimotor motility.

(A) Solution-phase LCST behavior of $[Z_E]_n/(Z_R-ELF_5)_n$ complexes measured in motility buffer (at equal Z_R-ELF_5 concentration: 2 mM). Condensation of the ELF domain produces an increase in turbidity of the solution as the temperature rises. (B) and (C) Temperature-dependent microtubule gliding velocities of monomeric (B) and multimeric (C) polymer/motor complexes. (B) Monomeric complexes were formed using either the Z_R-ELF_5 (red) or the dimeric $(Z_R-ELF_5)_2$ (green) polymers. Monomeric assemblies were prepared from the dimeric $(Z_R-ELF_5)_2$ polymers by using a threefold stoichiometric excess of the total Z_R attachment sites relative to the motor. (C) Temperature-dependent gliding of microtubules using fully functionalized dimeric $[K350Z_E]_2/(Z_R-ELF_5)_2$ (green) and trimeric $[K350Z_E]_3/(Z_R-ELF_5)_3$ (blue) complexes.



References and Notes

1. F. Julicher, A. Ajdari, J. Prost, *Rev. Mod. Phys.* **69**, 1269 (1997).
2. V. Epshtein, E. Nudler, *Science* **300**, 801 (2003).
3. Y. Okada, N. Hirokawa, *Nature* **424**, 574 (2003).

4. D. R. Klopfenstein, M. Tomishige, N. Stuurman, R. D. Vale, *Cell* **109**, 347 (2002).
5. C. Kural *et al.*, *Science* **308**, 1469 (2005).
6. S. Leibler, D. A. Huse, *J. Cell Biol.* **121**, 1357 (1993).
7. S. A. Endow, H. Higuchi, *Nature* **406**, 913 (2000).
8. M. Badoual, F. Julicher, J. Prost, *Proc. Natl. Acad. Sci. U.S.A.* **99**, 6696 (2002).
9. F. Jülicher, J. Prost, *Phys. Rev. Lett.* **78**, 4510 (1997).
10. S. Camalet, F. Julicher, J. Prost, *J. Phys. Rev. Lett.* **82**, 1590 (1999).
11. S. Camalet, T. Duke, F. Julicher, J. Prost, *Proc. Natl. Acad. Sci. U.S.A.* **97**, 3183 (2000).
12. S. A. Burgess, *J. Mol. Biol.* **250**, 52 (1995).
13. S. P. Gross, Y. Guo, J. E. Martinez, M. A. Welte, *Curr. Biol.* **13**, 1660 (2003).
14. T. Duke, *Philos. Trans. R. Soc. Lond. B Biol. Sci.* **355**, 529 (2000).
15. A. Vilfan, E. Frey, F. Schwabl, *Eur. Phys. J. B* **3**, 535 (1998).
16. Materials and methods are available as supporting material on Science Online.
17. J. R. Moll, S. B. Ruvinov, I. Pastan, C. Vinson, *Protein Sci.* **10**, 649 (2001).
18. D. W. Urry, *J. Phys. Chem. B* **101**, 11007 (1997).
19. D. W. Urry *et al.*, *Philos. Trans. R. Soc. Lond. B Biol. Sci.* **357**, 169 (2002).
20. Polymer flexibility can be estimated by calculating the elastic spring constant (κ) of a single ELF₅ linker using data from single molecule force-extension measurements. These experiments yield persistence lengths (L_p) for elastins of ~ 0.4 nm in the low force regime. Assuming a wormlike chain model for the polymer at low extension, κ can be estimated from $\kappa = 3k_b/72L_pL_c$, where L_c is the contour length of the polymer, k_b is the Boltzman constant, and T is temperature. A single ELF₅ linker contains ~ 125 amino acids, yielding $L_c = 36.35$ nm, assuming 0.29 nm per residue, and $\kappa = 0.4$ pN/nm.
21. R. B. Case, D. W. Pierce, N. Hom-Booher, C. L. Hart, R. D. Vale, *Cell* **90**, 959 (1997).
22. Y. Inoue, A. H. Iwane, T. Miyai, E. Muto, T. Yanagida, *Biophys. J.* **81**, 2838 (2001).
23. Y. Okada, N. Hirokawa, *Science* **283**, 1152 (1999).
24. Polymer-motor assemblies were formed by making a master mix of K350-Z_E and (Z_R-ELF₅)_n polymers and incubating for at least 20 min at 4°C before addition to the reaction. Concentrations of polymer solutions were determined from their A₂₈₀ values, using an extinction coefficient of 1480 cm⁻¹ mol⁻¹ for each Z_R-ELF₅ repeat in the polymers. The fidelity of the assembly process was examined for the trimeric [K350-Z_E]₃/(Z_R-ELF₅)_n complex using selectively radiolabeled proteins and multichannel scintillation counting. In these experiments, a K350-Z_E motor was radiolabeled with ³⁵S (77,104 cpm/nmol) by expressing the motor in 1 liter of LB medium supplemented with L-[³⁵S]cysteine (5 mCi). Similarly, a ³H labeled (Z_R-ELF₅)₃ polymer (33,046 cpm/nmol) was prepared by expression in 0.1 L of LB medium supplemented with L-[3,4(n)-³H]valine (2.5 mCi). After purification, the polymer was functionalized with a PEO-biotinmaleimide (Pierce) using standard maleimide labeling protocols. Then, radiolabeled polymers and motors were mixed in a 1:1.5 ratio with respect to the Z_R sites of the polymer and the motor. After incubation, the [motor]/(polymer) complex was selectively bound to a neutravidin resin. Excess motor was washed from the resin, and the sample, including the resin, was transferred to a scintillation vial. Comparison of the signals from ³⁵S and ³H channels yielded a motor/polymer ratio of 2.9 ± 0.4. Control experiments were performed with the polymers omitted from solution; results indicated nonspecific binding of the K350-Z_E motors to the resin did not influence our measurements.
25. D. D. Hackney, *Biophys. J.* **68**, 267s (1995).
26. D. D. Hackney, *Nature* **377**, 448 (1995).
27. W. O. Hancock, J. Howard, *J. Cell Biol.* **140**, 1395 (1998).
28. J. Hyun, W.-K. Lee, N. Nath, A. Chilkoti, S. Zauscher, *J. Am. Chem. Soc.* **126**, 7330 (2004).
29. D. E. Meyer, A. Chilkoti, *Biomacromolecules* **5**, 846 (2004).
30. N. J. Carter, R. A. Cross, *Nature* **435**, 308 (2005).
31. F. H. C. Crick, *Acta Crystallogr.* **6**, 689 (1953).
32. We thank A. J. Link and I. Fushman their help during the early stages of this project; L. Wade and D. Pearson for use of the temperature controller; and P. Wiggins, R. Bao, T. Squires, and S. Quake for valuable discussions. This work was supported by the Beckman Foundation through a Beckman Senior Research Fellowship (to M.R.D.) and by a grant from the National Science Foundation.

Supporting Online Material

www.sciencemag.org/cgi/content/full/311/5766/1468/DC1

Materials and Methods

Table S1

References

2 November 2005; accepted 6 February 2006

10.1126/science.1122125

Progressive Disruption of Cellular Protein Folding in Models of Polyglutamine Diseases

Tali Gidalevitz,* Anat Ben-Zvi,* Kim H. Ho, Heather R. Brignull, Richard I. Morimoto†

Numerous human diseases are associated with the chronic expression of misfolded and aggregation-prone proteins. The expansion of polyglutamine residues in unrelated proteins is associated with the early onset of neurodegenerative disease. To understand how the presence of misfolded proteins leads to cellular dysfunction, we employed *Caenorhabditis elegans* polyglutamine aggregation models. Here, we find that polyglutamine expansions disrupted the global balance of protein folding quality control, resulting in the loss of function of diverse metastable proteins with destabilizing temperature-sensitive mutations. In turn, these proteins, although innocuous under normal physiological conditions, enhanced the aggregation of polyglutamine proteins. Thus, weak folding mutations throughout the genome can function as modifiers of polyglutamine phenotypes and toxicity.

Although many results from in vitro and in vivo models that express mutant Huntingtin, α -synuclein, tau, superoxide dismutase-1, amyloid- β peptide, or prion proteins are consistent with the proposal that non-native species can form toxic folding intermediates, oligomers, and aggregates (1–5), distinct mechanisms for toxicity have been

proposed for each. These mechanisms range from specific protein-protein interactions to disruption of various cellular processes, including transcription (6, 7), protein folding (8, 9), protein clearance (10–13), energy metabolism (14), activation of apoptotic pathways (15), and others. This has led us to consider how the expression of a single aggregation-prone protein could have such pleiotropic effects and whether a more general mechanism could explain the many common features of protein conformation diseases. Moreover, because each cell and tissue contains various metastable polymorphic proteins (16), could the chronic expression of an

aggregation-prone protein have global consequences on homeostasis and thus affect folding or stability of proteins that harbor folding defects?

To test this hypothesis, we took a genetic approach using diverse *Caenorhabditis elegans* temperature-sensitive (ts) mutations to examine whether the functionality of the respective protein at the permissive condition was affected by expression of aggregation-prone polyglutamine (polyQ) expansions. Because many ts mutant proteins are highly dependent on the cellular folding environment (17–19), they represent highly sensitive indicators of a disruption in protein homeostasis. We employed transgenic *C. elegans* lines expressing different-length polyQ-YFP (yellow fluorescent protein) or CFP (cyan fluorescent protein) from integrated arrays in muscle (polyQm) (20, 21) or neuronal (polyQn) (22) cells. Both models show polyQ-length-dependent aggregation and toxicity.

Animals expressing ts mutant UNC-15 (*C. elegans* homolog of a muscle paramyosin) were crossed to *C. elegans* polyQm strains, and phenotypes at permissive and restrictive conditions were examined in double homozygotes. At the restrictive temperature, this ts mutation disrupts thick filament formation and leads to embryonic and early larval lethality and slow movement in adults (23). Expression of polyQ proteins alone in a wild-type background did not result in these embryonic and larval phenotypes. In contrast, more than 40% of embryos coexpressing mutant paramyosin and Q40m [paramyosin(ts)+Q40m] failed to hatch or

Department of Biochemistry, Molecular Biology, and Cell Biology, Rice Institute for Biomedical Research, Northwestern University, Evanston, IL 60208, USA.

*These authors contributed equally to this work.

†To whom correspondence should be addressed. E-mail: r-morimoto@northwestern.edu

move at the permissive temperature (Fig. 1, A and C). This effect was polyQ-length-dependent, because coexpression of Q35m or Q24m with paramyosin(ts) resulted in 27% or 5% unhatched embryos, respectively (Fig. 1C). The morphology of affected paramyosin(ts)+Q40m and paramyosin(ts)+Q35m embryos at 15°C (Fig. 1A) was similar to paramyosin(ts) at 25°C (Fig. 1B). Examination of muscle structure in paramyosin(ts)+Q40m embryos at 15°C revealed a disrupted pattern of actin staining, similar to the pattern in paramyosin(ts) embryos at 25°C but not at 15°C (fig. S1) or in wild-type animals (24). Thus, expression of an aggregation-prone polyQ protein is sufficient to cause a paramyosin ts mutation to exhibit its mutant phenotype at the permissive condition.

We next addressed whether this effect of polyQ expansions extended to neuronal cells, which are often affected in conformational diseases. Animals expressing a ts mutation in the neuronal protein dynamin-1 [dynamin(ts) animals] become paralyzed at the restrictive temperature (28°C) but have normal motility at the permissive temperature (20°C) (25). Pan-neuronal expression of Q40 in dynamin(ts) animals resulted in severe impairment of mobility (Fig. 1D) at the permissive temperature. No phenotypes were observed in animals co-expressing the nonaggregating Q19n. Thus, expression of polyglutamine expansions phenocopies temperature-sensitive mutations in muscle and neuronal cells at permissive conditions, and this genetic interaction reflects the aggregation propensity of polyQ expansions.

To ask whether these observations were applicable to other ts mutations, we tested the genetic interaction of Q40m and Q24m proteins with a wide range of characterized ts mutations (Table 1). Strains expressing ts mutant proteins UNC-54, UNC-52, LET-60 (*C. elegans* homologs of myosin, perlecan, and ras-1, respectively), or UNC-45 together with Q24m or Q40m were scored for specific ts phenotypes (26) at the permissive temperature. For all lines generated, the ts mutant phenotype was exposed at permissive conditions in the presence of the aggregation-prone Q40m but not by nonaggregating Q24m (Table 1). Thus, the chronic expression of an aggregation-prone polyQ protein interferes with the function of multiple structurally and functionally unrelated proteins.

To test whether interaction between polyQ expansions and ts mutant proteins was cell autonomous, we took advantage of tissue-specific phenotypes caused by expression of ras(ts) protein at the restrictive temperature: an embryonic lethality/larval development phenotype (Let/Lva), a defect in osmoregulation (Osm) likely reflecting neuronal dysfunction, and a multivulva phenotype (Muv) resulting from dysfunction in the hypodermis (27). We scored these phenotypes upon expression of polyQ in neuronal or muscle cells. PolyQ expansions in

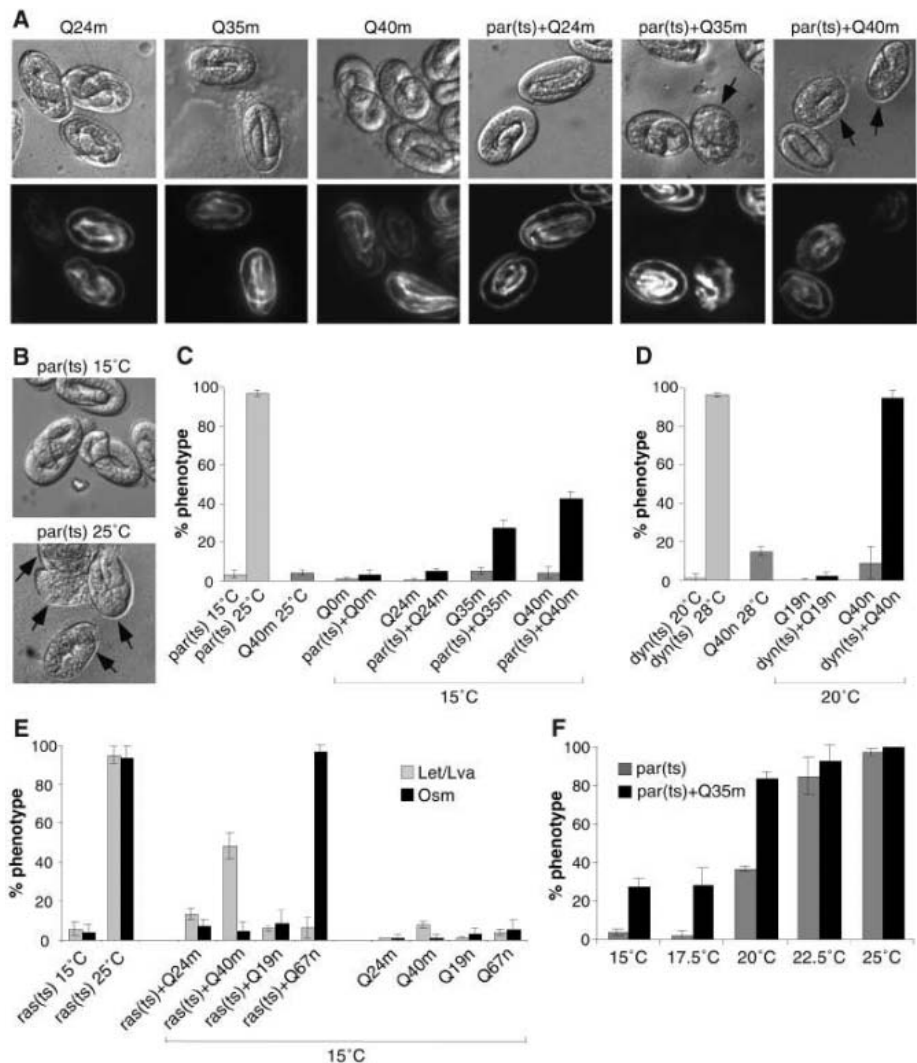


Fig. 1. Aggregation-prone proteins expose temperature-sensitive phenotypes of paramyosin(ts) (A to C, and F), dynamin(ts) (D), and ras(ts) (E) mutants at permissive temperatures. (A) Differential interference contrast (DIC) and fluorescence images of age-synchronized 3-fold embryos at 15°C. Fluorescence shows expression of polyQm (muscle)-YFP proteins (Q0m, Q24m, Q35m, and Q40m) from the unc-54 promoter. Arrows indicate embryos with abnormal body shape. (B) DIC images of age-synchronized 3-fold paramyosin(ts) embryos at indicated temperatures. Arrows as in (A). (C) Percentage of unhatched embryos and paralyzed L1 larvae. Data are the mean \pm SD, \geq 380 embryos per data point. (D) Percentage of uncoordinated age-synchronized young adult animals. Expression of polyQn (neuronal)-YFP proteins (Q19n, Q40n) is from the F25B3.3 promoter. Data are the mean \pm SD, \geq 80 animals per data point. (E) Percentage of animals exhibiting either Osm (black) or the combined Let/Lva (gray) phenotypes. Expression of Q67n is from the F25B3.3 promoter. Data are the mean \pm SD, \geq 70 synchronized adults for Osm and \geq 270 embryos for Let/Lva. ras(ts)+Q40m denotes ras(ts) animals heterozygous for Q40m. (F) Synergistic effect of elevated temperature and polyQ expansions on paramyosin(ts). Percentage of unhatched embryos and paralyzed L1 larvae for paramyosin(ts) (gray) and paramyosin(ts)+Q35m (black) at indicated temperatures. Data are the mean \pm SD, \geq 300 embryos for each data point.

neurons led to exposure of the Osm phenotype in ras(ts) animals at the permissive temperature but had no effect on the Let/Lva phenotype (Fig. 1E). Conversely, heterozygous expression of Q40m in muscle cells of ras(ts) animals caused 48% penetrance of Let/Lva phenotype but did not expose the neuronal Osm phenotype (Fig. 1E). Double homozygous ras(ts)+Q40m animals could not be scored, as they did not

reach mature adulthood (Table 1) (26). Neither neuronal nor muscle cell expression of polyQ expansions caused the hypodermal Muv phenotype (24). A similar control was performed with paramyosin(ts), which was not affected by polyQ expansions in neurons (Q67n) (24). Likewise, polyQ expansions did not affect Unc phenotypes that did not involve ts proteins (caused either by RNAi or gene deletion) (24).

Table 1. PolyQ expansions affect the functionality of unrelated ts mutant proteins. Specific phenotype of each ts mutation alone or in polyQm background was scored at indicated temperatures (26). Data are the mean \pm SD for at least the indicated number (*n*) of animals for each phenotype scored. *See (26).

Proteins expressed	TS allele	Phenotype scored (<i>n</i> value)	Animals displaying phenotype (%)			
			15°C	25°C	15°C	
					Q24	Q40
PolyQm	–	Slow movement (<i>n</i> > 300)			6.0 \pm 5.3	4.6 \pm 4.2
myosin(ts)	e1301		5.6 \pm 2.6	84.7 \pm 13.5		
myosin(ts)+Qm	e1301				11.2 \pm 6.7	51.9 \pm 19.3
myosin(ts)	e1157		5 \pm 4	98.7 \pm 1.4		
myosin(ts)+Qm	e1157				5.9 \pm 1.5	55 \pm 6
PolyQm	–	Abnormal body shape			0	0
perlecan(ts)	su250	(stiff paralysis) (<i>n</i> > 100)	1 \pm 1.2	97.6 \pm 2.2		
perlecan(ts)+Qm	su250				0.8 \pm 1.1	48.4 \pm 6.5
PolyQm	–	Egg-laying defect (<i>n</i> > 85)			0	0
UNC-45(ts)	e286		8.4 \pm 2.1	93.8 \pm 4.9		
UNC-45(ts)+Qm	e286				5.1 \pm 7.3	87.7 \pm 8.1
PolyQm	–	Embryonic lethality + larval			1 \pm 0.15	7.9 \pm 1.8
ras(ts)	ga89	development arrest (<i>n</i> > 270)	5.6 \pm 3.4	95.2 \pm 4.3		
ras(ts)+Qm	ga89				13.3 \pm 3	100*

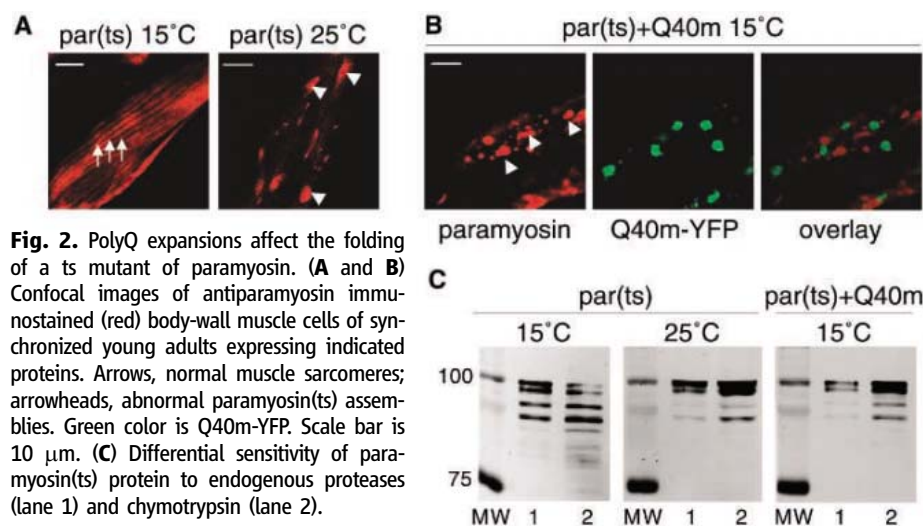


Fig. 2. PolyQ expansions affect the folding of a ts mutant of paramyosin. (A and B) Confocal images of antiparamyosin immunostained (red) body-wall muscle cells of synchronized young adults expressing indicated proteins. Arrows, normal muscle sarcomeres; arrowheads, abnormal paramyosin(ts) assemblies. Green color is Q40m-YFP. Scale bar is 10 μ m. (C) Differential sensitivity of paramyosin(ts) protein to endogenous proteases (lane 1) and chymotrypsin (lane 2).

Thus, the effect of polyQ expansions on mutant ts proteins reflects specific genetic interactions within the same cell type and does not result from decreased fitness of the organism.

To understand the nature of this interaction, we examined the localization of paramyosin(ts) protein coexpressed with Q40m. The L799F mutation affects coiled-coil interactions in paramyosin and at restrictive temperature results in mislocalization to paracrystalline assemblies instead of muscle sarcomeres (Fig. 2A) (23). Paramyosin(ts) protein coexpressed with Q40m at permissive conditions assembled into abnormal paracrystalline structures, distinct from the Q40m aggregates (Fig. 2B), and exhibited altered protease sensitivity (Fig. 2C). Thus, expression of Q40m uncovers the protein folding defect in paramyosin(ts) mutant. In view of this, the differential penetrance of ts phenotypes (Table 1) may reflect the sensitivity of

each ts mutation to disruption of the folding environment.

Aggregation-prone proteins may thus exert their destabilizing effects by placing a stress on the folding capacity of the cell. If so, the elevated temperature and the presence of aggregation-prone protein may synergize in their destabilizing effects on ts mutants. Expression of an intermediate length (Q35m) expansion shifted the temperature at which paramyosin(ts) was fully inactivated (Fig. 1F). Next, we asked whether the difference in penetrance from 48% to 100% Let/Lva phenotype of ras(ts) animals in the heterozygous and homozygous Q40m backgrounds (Table 1 and Fig. 1E) could be explained by differences in aggregation of Q40m. Heterozygous Q40m animals consistently showed later onset of aggregation and lower numbers of aggregates than homozygous animals (Fig. 3, A, B, and E). If the levels of polyQ affect the

folding of the ts protein, does the misfolding of the ts protein, in turn, intensify misfolding of polyQ? Q40m aggregation in paramyosin(ts) and ras(ts) backgrounds was enhanced dramatically (Fig. 3, C to E). In contrast, loss of function mutations not associated with expression of ts proteins (for example in paramyosin or perlecan) did not enhance aggregation (24). From a genetic perspective, temperature-sensitive mutations in proteins unrelated to cellular folding or clearance pathways behaved as modifiers of polyQ aggregation. Thus, a positive feedback mechanism exists to enhance the disruption of cellular folding homeostasis.

The appearance of misfolded protein in the cell normally activates a stress response that increases protein refolding and turnover and thus rebalances the folding environment (28, 29). In contrast, our results point to the unexpected sensitivity of cellular folding homeostasis to the chronic expression of misfolded proteins under physiological conditions. It is possible that the low flux of misfolded protein in conformational diseases may alone lack the capacity to activate the homeostatic stress response. This suggests that the stress response fails to compensate for the chronic expression of misfolded proteins in human disease.

One potential interpretation of our results is that the protein folding capacity of the cell, integrated at a systems level, is a reflection of expressed protein polymorphisms and random mutations (16), which in themselves do not lead to disease because of the balance achieved by folding and clearance mechanisms. However, these proteins may misfold and in turn contribute to the progressive disruption of the folding environment when this balance becomes overwhelmed, e.g., by the expression of an aggregation-prone protein in conformational diseases. Our data identify the presence of mar-

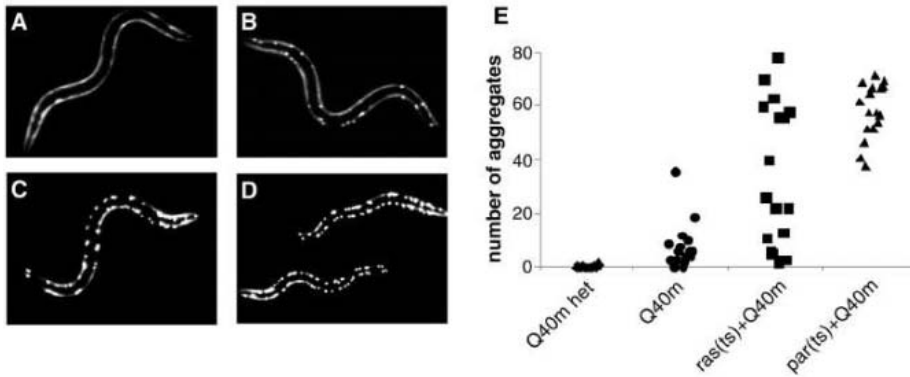
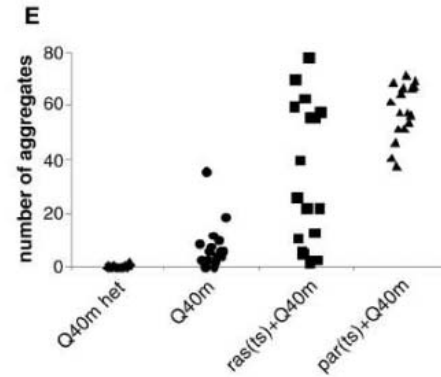


Fig. 3. Progressive disruption of cellular folding capacity by misfolded proteins. (A to D) Fluorescent images of representative L2 larvae at the permissive temperature of heterozygous (A) or homozygous (B) Q40m, *ras(ts)+Q40m* (C), and *paramyosin(ts)+Q40m* (D) strains. (E) Number of visible aggregates in L2 larvae expressing indicated proteins. *ras(ts)+Q40m* in (C) and (E) denotes the fluorescent progeny of an F2 *ras(ts)* animal expressing Q40m; these progeny could be either homozygous or heterozygous for Q40m.

ginally stable or folding-defective proteins in the genetic background of conformational diseases as potent extrinsic factors that modify aggregation and toxicity. Given the prevalence of polymorphisms in the human genome (30), they could contribute to variability of disease onset and progression (31). This interpretation also provides a mechanistic basis to the notion that the late onset of protein misfolding diseases may be due to gradual accumulation of damaged proteins (32), resulting in a compromise in folding capacity. Indeed, in a screen for regulators of polyQ aggregation in *C. elegans*, we identified nearly 200 genes whose diverse functions have the potential to affect protein homeostasis (21). Cellular degeneration in diseases of protein conformation is unlikely to be due to a single defect. Thus, the many toxic effects on various cellular processes attributed to misfolded proteins (6–15) could in fact be an integral part of the global disruption of protein homeostasis identified in this work.

References and Notes

1. S. W. Davies *et al.*, *Cell* **90**, 537 (1997).
2. M. DiFiglia *et al.*, *Science* **277**, 1990 (1997).
3. R. Kaye *et al.*, *Science* **300**, 486 (2003).
4. M. Tanaka, P. Chien, N. Naber, R. Cooke, J. S. Weissman, *Nature* **428**, 323 (2004).
5. J. F. Gusella, M. E. MacDonald, *Nat. Rev. Neurosci.* **1**, 109 (2000).
6. M. K. Perez *et al.*, *J. Cell Biol.* **143**, 1457 (1998).
7. A. McCampbell *et al.*, *Hum. Mol. Genet.* **9**, 2197 (2000).
8. P. J. Muchowski *et al.*, *Proc. Natl. Acad. Sci. U.S.A.* **97**, 7841 (2000).
9. S. Kim, E. A. A. Nollen, K. Kitagawa, V. P. Bindokas, R. I. Morimoto, *Nat. Cell Biol.* **4**, 826 (2002).
10. K. Ii, H. Ito, K. Tanaka, A. Hirano, *J. Neuropathol. Exp. Neurol.* **56**, 125 (1997).
11. C. J. Cummings *et al.*, *Nat. Genet.* **19**, 148 (1998).
12. N. F. Bence, R. M. Sampat, R. R. Kopito, *Science* **292**, 1552 (2001).
13. C. I. Holmberg, K. E. Staniszewski, K. N. Mensah, A. Matouschek, R. I. Morimoto, *EMBO J.* **23**, 4307 (2004).
14. M. Gu *et al.*, *Ann. Neurol.* **39**, 385 (1996).
15. V. L. Gabai, A. B. Meriin, J. A. Yaglom, V. Z. Volloch, M. Y. Sherman, *FEBS Lett.* **438**, 1 (1998).
16. S. L. Rutherford, S. Lindquist, *Nature* **396**, 336 (1998).



17. T. K. Van Dyk, A. A. Gatenby, R. A. LaRossa, *Nature* **342**, 451 (1989).
18. C. R. Brown, L. Q. Hong-Brown, W. J. Welch, *J. Clin. Invest.* **99**, 1432 (1997).
19. C. B. Pedersen *et al.*, *J. Biol. Chem.* **278**, 47449 (2003).
20. J. F. Morley, H. R. Brignull, J. J. Weyers, R. I. Morimoto, *Proc. Natl. Acad. Sci. U.S.A.* **99**, 10417 (2002).
21. E. A. Nollen *et al.*, *Proc. Natl. Acad. Sci. U.S.A.* **101**, 6403 (2004).
22. H. R. Brignull, S. Tang, R. I. Morimoto, in preparation.
23. K. Gengyo-Ando, H. Kagawa, *J. Mol. Biol.* **219**, 429 (1991).
24. Gidalevitz *et al.*, unpublished data.
25. S. G. Clark, D. L. Shurland, E. M. Meyerowitz, C. I. Bargmann, A. M. van der Bliek, *Proc. Natl. Acad. Sci. U.S.A.* **94**, 10438 (1997).

26. Materials and methods are available as supporting material on Science Online.
27. D. M. Eisenmann, S. K. Kim, *Genetics* **146**, 553 (1997).
28. S. A. Goff, A. L. Goldberg, *Cell* **41**, 587 (1985).
29. R. I. Morimoto, *Genes Dev.* **12**, 3788 (1998).
30. International SNP Map Working Group, *Nature* **409**, 928 (2001).
31. U.S.-Venezuela Collaborative Research Project, N. S. Wexler, *Proc. Natl. Acad. Sci. U.S.A.* **101**, 3498 (2004).
32. C. N. Oliver, B. W. Ahn, E. J. Moerman, S. Goldstein, E. R. Stadtman, *J. Biol. Chem.* **262**, 5488 (1987).
33. T.G. was supported by NIH Training Grant T32 HL076139 and by an Individual NRSA F32 GM075583-01; A.B.-Z. was supported by an EMBO Long-Term Fellowship, the Parkinson Foundation, and the Hereditary Disease Foundation; and H.R.B. was supported by National Institute of General Medical Sciences (NIGMS) Molecular Biology of Disease Training Grant T32 GM08061. R.I.M. was supported by grants from the NIH (NIGMS, National Institute of Neurological Disorders and Stroke, and National Institute on Aging), the Huntington Disease Society of America Coalition for the Cure, the ALS Association, and the Daniel F. and Ada L. Rice Foundation. Some nematode strains used in this work were provided by the Caenorhabditis Genetics Center, which is funded by the NIH National Center for Research Resources (NCRR). We thank J. West and members of the Morimoto laboratory for their discussion and comments on the manuscript and F. Moore for reagents.

Supporting Online Material

www.sciencemag.org/cgi/content/full/1124514/DC1

Materials and Methods

Fig. S1

References

3 January 2006; accepted 16 January 2006

Published online 9 February 2006;

10.1126/science.1124514

Include this information when citing this paper.

The Global Impact of Scaling Up HIV/AIDS Prevention Programs in Low- and Middle-Income Countries

John Stover,¹ Stefano Bertozzi,² Juan-Pablo Gutierrez,² Neff Walker,³ Karen A. Stanecki,⁴ Robert Greener,⁴ Eleanor Gouws,⁴ Catherine Hankins,⁴ Geoff P. Garnett,⁵ Joshua A. Salomon,⁶ J. Ties Boerma,⁷ Paul De Lay,⁴ Peter D. Ghys^{4*}

A strong, global commitment to expanded prevention programs targeted at sexual transmission and transmission among injecting drug users, started now, could avert 28 million new HIV infections between 2005 and 2015. This figure is more than half of the new infections that might otherwise occur during that period in 125 low- and middle-income countries. Although preventing these new infections would require investing about U.S.\$122 billion over this period, it would reduce future needs for treatment and care. Our analysis suggests that it will cost about U.S.\$3900 to prevent each new infection, but that this will produce a savings of U.S.\$4700 in forgone treatment and care costs. Thus, greater spending on prevention now would not only prevent more than half the new infections that would occur from 2005 to 2015 but would actually produce a net financial saving as future costs for treatment and care are averted.

Much has changed in the global response to the AIDS epidemic since the late 1990s. Access to treatment and care in the developing world was limited by costs, by the complexity of early treatment

regimens, and by a perceived lack of capacity to implement treatment programs even if drug costs were greatly reduced. The pioneering work of Brazil in providing broad access to antiretroviral therapy proved that, with political

will, middle-income countries could overcome these limitations (1). In 2001 when governments convened a special session of the United Nations General Assembly, they adopted a new set of commitments on AIDS that included access to effective care and treatment. In preparation for the special session, estimates were made of the resources required for an expanded response to the epidemic, including costs for core prevention and care and treatment activities (2). The impact of these interventions, at the anticipated costs, on the number of new adult infections was estimated subsequently (3). In response, significant financial resources have been mobilized by both donors and the affected governments and communities (4). A recent analysis has explored the interactions of prevention and treatment and care in sub-Saharan Africa (5), and an update and extension of the UNAIDS resource needs estimates was completed in 2005 (4). Increases in funding have produced expansions in prevention services and treatment and care services, but much of the recent advocacy and press attention has focused specifically on the need for antiretroviral therapy. Others have argued that, in the absence of curative therapy, effective prevention is the best way to prevent the premature death of the millions of people being infected with HIV each year (6). Here, we estimate the global net cost of prevention activities in the context of the new global commitment to provide care and treatment for adults and children.

We estimate the costs of an expanded prevention program, including 15 specific interventions, in 125 low- and middle-income countries, calculate the impact in terms of infections averted, and estimate the gross and net cost per infection averted during 2005–2015. Briefly, the total resource needs and corresponding targets for scaling up a range of prevention interventions targeting sexual transmission and transmission among injecting drug users are based on the resource needs estimates prepared by the Joint United Nations Programme on HIV/AIDS (UNAIDS) during 2005 (4). To calculate averted infections, we first project HIV prevalence in each country under current prevention efforts based on country-specific models used by UNAIDS and the World Health Organization (WHO) to develop estimates for 2005. Treatment scale-up is added

to these baseline scenarios, rising from current levels to 80% coverage of those in need for antiretroviral treatment (ART) for adults and children and for cotrimoxazole prophylaxis for children, as well as to 80% of pregnant women attending antenatal clinics for prevention of mother-to-child transmission (PMTCT) interventions in all regions by 2010, and with this coverage remaining at 80% through 2015. To estimate the impact of prevention programs, the changes in behavior resulting from exposure to prevention interventions are estimated using impact data from intervention studies, the impact of these behavior changes on incidence is modeled using two different simulation models, and the consequences of the incidence changes are projected using the Spectrum software package. The average cost per case averted is calculated by dividing the total prevention costs (expressed in constant 2004 prices) over the period 2005–2015 by the number of cases averted over the same period.

The forgone treatment and care costs per averted infection are then calculated. The costs of averted treatment and care are consistent with the 2005 UNAIDS resource needs estimates (4). Estimated costs of care and treatment are based on these estimates (a detailed description of the methodology and tools is provided in the supporting online material). Lifetime costs for each AIDS case are calculated on the assumption that the median number of years of ART treatment is 7.5 years in all countries. The net present value of the expected lifetime treatment costs

is calculated for the year in which the infection is prevented, on the basis of a discount rate of 5% and an average of 7 years from infection to onset of ART treatment. Sensitivity analyses are conducted for both the cost of averting an infection (by lowering the effectiveness of interventions) and the lifetime cost of treatment and care of these infections (by modifying the average survival to 5 and 10 years, respectively).

At current levels of implementation of prevention programs, the annual number of global infections is expected to increase from 4.8 million in 2005 to 5.9 million in 2015. Over this period, the total number of new infections is estimated to be 62.3 million, 7.9 million in children and 54.4 million in adults (fig. S1).

An estimated 31.1 million new infections (or 50%) between 2005 and 2015 would be averted by implementing the comprehensive prevention package examined here, 3.1 million in children and 28 million in adults. The number of averted infections would vary across regions, with 19.5 million in sub-Saharan Africa, 8.9 million in Asia, 0.7 million in North Africa and the Middle East, 0.7 in Eastern Europe, and 1.3 million in Latin America and the Caribbean (Table 1). The total cost of implementing this package during 2005–2015 would be U.S.\$122 billion (see fig. S4 for the distribution of resources by region). UNAIDS has projected that about U.S.\$27 billion is already programmed or promised for the period 2005 to 2007. About one-third of this amount is expected to come from local governments and out-of-pocket expenditures, with most of the rest from inter-

Table 1. Number of new infections and infections averted during 2005–2015 by applying the full prevention and treatment and care package, by region.

	10 ³ number of infections				10 ³ Infections averted	
	Current effort		Expanded prevention		Adults	Children
	Adults	Children	Adults	Children		
Sub-Saharan Africa	31,726	6,889	15,069	4,181	16,657	2,708
Asia	16,637	688	8,237	383	8,400	305
North Africa/Middle East	1,160	114	475	68	685	46
Eastern Europe	2,510	47	1,807	32	703	15
Latin America and Caribbean	2,397	144	861	65	1,536	79
Total	54,430	7,882	26,449	4,729	27,981	3,153

Table 2. Costs for prevention and averted future treatment and care, 2005–2015, by region.

	Cost for prevention per infection averted (U.S.\$)	Lifetime treatment cost (net present value U.S.\$)	Savings per infection averted (U.S.\$)
Sub-Saharan Africa	2,109	3,469	1,360
Asia	7,417	5,602	-1,815
North Africa/Middle East	2,756	6,822	4,066
Eastern Europe	9,148	11,203	2,055
Latin America and Caribbean	5,045	12,330	7,285
Global	3,923	4,707	784

¹Futures Group/Constella, Glastonbury, CT 06033, USA.

²National Institute of Public Health (INSP), Cuernavaca 62508, and Centro de Investigación y Docencia Económicas (CIDE), Mexico City 01210, Mexico. ³United Nations Children's Fund (UNICEF), New York, NY 10017, USA.

⁴Joint United Nations Programme on HIV/AIDS (UNAIDS), Geneva CH-1211, Switzerland. ⁵Imperial College, London SW7 2AZ, UK. ⁶Harvard University, Boston, MA 02138, USA. ⁷World Health Organization, 1211 Geneva 27, Switzerland.

*To whom correspondence should be addressed. E-mail: ghysp@unaids.org

national donors through bilateral and multi-lateral mechanisms (4).

In addition to the health benefits described above, the implementation of a comprehensive global prevention approach would significantly reduce the number of people requiring antiretroviral therapy in the future. The weighted global average (considering country-specific costs, intervention coverage, treatment package, and epidemiology) is a cost for prevention activities of U.S.\$3900 per infection averted (adults and children combined), which avoids an expenditure for treatment and care with a net present value of U.S.\$4700 and results in savings of U.S.\$780 per infection averted. The costs by region are presented in Table 2. Sensitivity analyses assuming lower prevention effectiveness indicate that there continue to be net savings in all regions except Asia and Eastern Europe (table S7). Sensitivity analyses assuming a life expectancy of 5 years on treatment indicate that there would still be net savings in all regions except in Asia and Eastern Europe. If one assumes a life expectancy of 10 years after treatment initiation, an even larger savings would accrue in all regions compared with the baseline estimates.

Compared with estimates of adult infections that would have been averted in adults for 2001–2010 if implementation had ramped up in 2001 (3), the current analyses indicate that an important window of opportunity was missed by not adequately scaling up prevention services in 2001–2005. Indeed, the latest evidence regarding coverage of prevention services shows only limited implementation of prevention services by 2003 (7). Previous analyses have shown that in sub-Saharan Africa, the number of people in need of treatment in future years could be drastically reduced if comprehensive prevention programs were implemented (5). Our estimates suggest that scale-up of prevention programs would not only be highly cost effective, but would even be cost saving in most regions. Because of the commitment to provision of universal access to antiretroviral care, averting future treatment needs could free resources to prevent more infections. The unit costs of prevention and treatment vary significantly by region, as do the dynamics of the epidemic, which leads to different net costs for different regions. Even in those regions where net costs are positive, the cost per disability-adjusted life year is well below average gross domestic product (GDP) per capita; highly cost effective by almost any standard (8).

Estimates of cost of prevention interventions per infection averted in this analysis at about \$3900 are considerably higher than estimates in the earlier analysis at around \$1000 (3). Part of the explanation is that time has been lost by not scaling up as called for in the United Nations General Assembly Special Session (UNGASS) Declaration of Commitment on HIV/AIDS,

while the number of new infections was growing rapidly between 2001 and 2010. That growth is predicted to be less steep in 2005–2015. Also, baseline estimates are lower than before because of newly available surveillance data. In addition, estimates of the unit costs of prevention are higher than they were in 2001 as a result of extensive consultations with country experts. There may be more cost-effective combinations of preventive interventions than the ones considered here, especially those interventions that are targeted at the major modes of transmission (9). Although the interventions and targets defined in the 2005 global resource needs estimation exercise used in our analyses are ambitious, individual countries are encouraged to set targets that are consistent with past scale-up rates, taking into account current infrastructure, capacity, and resources, as well as foreseeable financing. New preventive technologies may become available in 2005–2015, including male circumcision (10), microbicides, or vaccines. These would lead to additional reductions in the number of new infections.

Our estimates of future cost savings are conservative, given that they do not include savings in programming and infrastructure and human capacity costs, related to the reduced treatment needs. They also exclude savings in lost productivity due to illness and premature death, along with costs of orphanhood, including orphan support costs and reduced investment in their human capital. Finally, they also do not include an increase in prevention effectiveness as treatment programs scale-up (5).

As in any modeling exercise, there are uncertainties around various model inputs. The greatest degree of uncertainty in the estimates reported here regards the likely effectiveness of the array of prevention interventions when implemented at scale. These uncertainties are addressed only partially through sensitivity analysis. For very few interventions, such as PMTCT, do reliable data exist on prevention effectiveness at full scale. For most of the interventions, we made use of the limited data available with highly variable estimates of effectiveness—some of which include zero. Currently available data do not indicate whether there will be economies of scale and scope, or diseconomies as interventions are extended to populations that are more difficult to reach.

The scale-up rates were set by a Policy Steering Committee organized by UNAIDS and composed of representatives of civil society, UN organizations, major donors, and technical experts (4). As with all international goals, these are intended to be ambitious but achievable. A slower scale-up of prevention would provide fewer total benefits, although the cost per infection averted would be about the same. A slower scale-up in treatment coverage would postpone fewer deaths and reduce the savings derived from prevention.

Given the magnitude of the problem and the high level of uncertainty regarding comparative effectiveness of interventions, it is imperative that roll-out of large-scale prevention programs incorporate rigorous prospective evaluations of their effectiveness. Further limitations are that the model does not estimate the effects of expansion of reproductive health services for women that would reduce fertility. However, previous models have shown synergistic effects when prevention of pregnancy in HIV-positive women is introduced (11).

Even with these limitations, the insights from the current analyses are important to inform the necessary long-term planning of investments for health and development in low- and middle income countries. Resources for treatment and care will largely be funded by the same sources as resources for prevention programs, i.e., mostly by national health ministries and international donors. Our analyses suggest that both national governments and donor countries would be well advised to ensure that prevention programs are scaled up as soon as possible, because early investment in prevention will both prevent a greater proportion of future infections and reduce future costs for treatment and care by more than the cost of the prevention programs.

References and Notes

1. J. R. P. Marins *et al.*, *AIDS* **17**, 1675 (2003).
2. B. Schwartländer *et al.*, *Science* **292**, 2434 (2001).
3. J. Stover *et al.*, *Lancet* **360**, 73 (2002).
4. UNAIDS, "Resource needs for an expanded response to AIDS in low- and middle-income countries" (UNAIDS, Geneva, August 2005).
5. J. A. Salomon *et al.*, *PLoS Med.* **2**, e16 (2005).
6. E. Marseille, P. B. Hofmann, J. G. Kahn, *Lancet* **359**, 1851 (2002).
7. USAID, UNAIDS, WHO, UNICEF, POLICY Project, "Coverage of selected services for HIV/AIDS prevention, care, and support in low and middle income countries in 2003" (POLICY Project, Washington, DC, June 2004).
8. S. Bertozzi *et al.*, in *Disease Control Priorities in Developing Countries* (Oxford Univ. Press, ed. 2, Oxford, in press).
9. E. Pisani *et al.*, *BMJ* **326**, 1384 (2003).
10. B. Auvert *et al.*, *PLoS Med.* **2**, e298 (2005).
11. J. Stover, N. Fuchs, D. Halperin, A. Gibbons, D. Gillespie, "Adding family planning to PMTCT sites increases the benefits of PMTCT" (USAID Issue Brief, Population and Reproductive Health, Agency for International Development, Washington, DC, October 2003); (www.info.usaid.gov/our_work/global_health/pop/publications/docs/familypmtct.html).
12. We thank D. Evans, T. Adams, T. Tan-Torres, B. Johns, and P. Zurn for their contributions to the resource needs model. We also thank the many individuals and organizations that have supported the 2005 UNAIDS resource needs estimation exercise.

Supporting Online Material

www.sciencemag.org/cgi/content/full/1121176/DC1

Materials and Methods

Figs. S1 to S4

Tables S1 to S7

References

11 October 2005; accepted 20 January 2006

Published online 2 February 2006;

10.1126/science.1121176

Include this information when citing this paper.

Combinatorial Effects of Odorant Mixes in Olfactory Cortex

Zihua Zou* and Linda B. Buck†

In mammals, each odorant is detected by a combination of different odorant receptors. Signals from different types of receptors are segregated in the nose and the olfactory bulb, but appear to be combined in individual neurons in the olfactory cortex. Here, we report that binary odorant mixes stimulate cortical neurons that are not stimulated by their individual component odorants. We propose that cortical neurons require combinations of receptor inputs for activation and that merging the receptor codes of two odorants provides novel combinations of receptor inputs that stimulate neurons beyond those activated by the single odorants. These findings may explain why odorant mixtures can elicit novel odor percepts in humans.

Odor detection is mediated by odorant receptors (ORs) (1, 2), which are located on olfactory sensory neurons in the nasal olfactory epithelium (OE). Signals generated in these neurons in response to odorants are transmitted to the olfactory bulb (OB) of the brain, which in turn transmits signals to the olfactory cortex (OC) (3–5). ORs comprise a diverse family of receptors that number ~1000 in mice (6–8). Different odorants are detected by different, but sometimes partially overlapping, combinations of ORs (9, 10). Each sensory neuron expresses a single allele (11) of one OR gene (9). Neurons with the same OR are dispersed in the OE (12, 13). However, their axons synapse in a few OR-specific glomeruli in the OB. The result is a stereotyped map of OR inputs in which signals from different ORs are segregated in different glomeruli and their associated mitral cell relay neurons (14–16). In the OC, the axons of OB mitral cells carrying input from a given OR synapse with specific clusters of pyramidal neurons. The result is a stereotyped map of OR inputs distinctly different from that in the OB (17). Inputs from different ORs are mapped onto partially overlapping clusters of pyramidal neurons, and individual neurons appear to receive signals derived from multiple different ORs (17).

The arrangement of OR inputs in the OC raises the intriguing possibility that single cortical neurons can integrate signals from different ORs that detect the same odorant (the odorant's "receptor code") and, thus, perform an initial step in the reconstruction of an odor image from its deconstructed features. This could derive from a scenario in which the OC neuron not only receives combinatorial OR inputs, but actually requires coincident inputs from more

than one OR for its activation. One prediction of this model is that a binary mix of odorants would activate OC neurons beyond those activated by its component odorants. In the simplest version of this model, odorants A and B are each detected by two ORs (1+2 and 3+4, respectively) and the activation of a cortical neuron requires simultaneous inputs from two ORs. Neurons activated by odorant A or B alone receive combined signals from ORs 1+2 or 3+4, respectively. However, a mix of odorants A and B, in addition, stimulates neurons that receive signals from other pairs of the four ORs, such as ORs 1+3 or 2+4.

To test this model, we compared the responses of mouse OC neurons to binary mixtures of odorants versus their individual components. We did this using *Arc* catFISH (cellular compartment analysis of temporal activity by fluorescence in situ hybridization), a technique that allows visualization of neuronal responses to two different experiences (18). The immediate early gene *Arc* (*arg3.1*) is induced by depolarization in hippocampal neurons and appears in visual cortex in response to natural, retina-

dependent sensory input (19–21). On induction, *Arc* mRNA is seen first only in the nucleus and later only in the cytoplasm (18). By appropriate temporal spacing of different stimuli, the subcellular location of *Arc* mRNA can be used to distinguish responses of individual neurons to those stimuli.

In initial experiments, we asked whether exposure to odorants induces *Arc* mRNA expression in the mouse OC (22). As in hippocampus and visual cortex, *Arc* expression could be induced in the OC by depolarization and implicates *N*-methyl-D-aspartate (NMDA) glutamate receptors involved in excitatory synaptic transmission (19, 20). Unanesthetized, unrestrained mice were exposed to the odorant eugenol for 1 min and their brains removed after 5, 15, or 30 min. Tissue sections collected from the brains were subjected to fluorescence in situ hybridization (FISH) with an *Arc* cRNA probe, and the sections were then counterstained with 4',6'-diamidino-2-phenylindole (DAPI) to reveal the locations of neuronal nuclei. We focused on one major OC area, the anterior piriform cortex (APC) (5). The hybridized sections showed fluorescent *Arc* mRNA signal in a subset of APC neurons in layers II and III, the locations of pyramidal neurons that receive direct synaptic input from the OB (5). Similar to observations with hippocampal neurons (18), *Arc* mRNA signal was seen at one or two bright spots in the nucleus 5 min after odorant exposure, and subsequently appeared in the cytoplasm, where it was seen exclusively in most *Arc*⁺ neurons after 30 min (Fig. 1, A to C).

To further characterize odorant-induced *Arc* expression in the OC, we analyzed the subcellular patterning of *Arc* mRNA in coronal sections at 70- μ m intervals spanning the APC. Similar to odorant-induced patterns of c-Fos⁺ neurons in the APC (23, 24), *Arc*⁺ neurons were highly distributed along the anterior-posterior

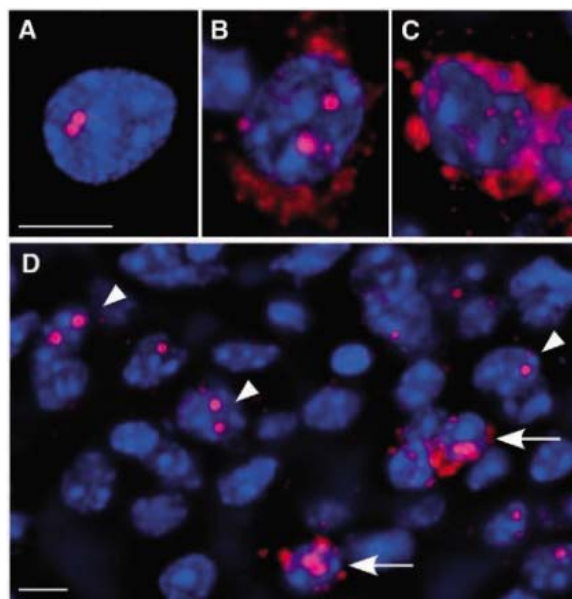


Fig. 1. Dynamic subcellular localization of *Arc* mRNA in olfactory cortex. An *Arc* cRNA probe (red) was hybridized to cortical sections 5 (A), 15 (B), or 30 (C) minutes after exposure to eugenol and cell nuclei were visualized with DAPI (blue). In most labeled neurons, *Arc* mRNA was first seen at one to two intranuclear spots (A) and then appeared in the cytoplasm (B), where it was found exclusively after 30 min (C). Exposure to two odorants administered first separately (at -30 min), and then as a binary mix (at -5 min), resulted in many neurons with only nuclear *Arc* signal (arrowheads) in the vicinity of neurons with both nuclear and cytoplasmic *Arc* signal (arrows) (D). Scale bar, 5 μ m.

Howard Hughes Medical Institute and Division of Basic Sciences, Fred Hutchinson Cancer Research Center, 1100 Fairview Avenue North, Seattle, WA 98109, USA.

*Present address: Department of Neuroscience and Cell Biology, The University of Texas Medical Branch, 301 University Boulevard, Galveston, TX 77555-0620, USA.

†To whom correspondence should be addressed. E-mail: lbuck@fhcrc.org

length of the APC (Fig. 2A), and the number of *Arc*⁺ neurons varied among cortices, with 1431 ± 565 and 666 ± 310 *Arc*⁺ neurons detected 5 and 30 min after odorant exposure, respectively (Table 1). However, the percentages of neurons with *Arc* mRNA in different subcellular compartments were similar among cortices (three cortices from two mice per condition) (Table 1). Five minutes after exposure to eugenol, the majority of *Arc*⁺ neurons ($81 \pm 3\%$) had *Arc* mRNA only in the nucleus whereas, after 30 min, most ($87 \pm 2\%$) had *Arc* signal only in the cytoplasm (Table 1).

We next used the temporal patterning of *Arc* mRNA expression to compare the responses of individual OC neurons to binary mixtures of odorants versus their component odorants. At -30 min (30 min before brain removal), mice ($n = 6$) were exposed sequentially to two different odorants, spaced one minute apart, and then at -5 min, they were exposed to a mixture of the two odorants. Control mice ($n = 6$) were exposed to the same odorant mixes at -30 and -5 min. We tested three binary mixes of odorants ("odor pairs") with diverse structures: (i) eugenol (clove) and dimethyl pyrazine (chocolate, nuts), (ii) methenyl methyl ether (citrus)

and methylamine (fishy), and (iii) vanillin (vanilla) and ethyl butyrate (apple). A 10-fold increase in odorant concentration can recruit additional ORs into an odor response (9) and increase the number of OC neurons induced to express *c-Fos* (23). Although the odorants in each binary mix had dissimilar structures, we could not exclude the possibility that some ORs might nonetheless recognize both odorants in a mix. To exclude the possibility that an odorant mix might thereby double the odorant concentration at some ORs, with one exception (odor pair 1, number 1 in Table 1), we doubled the concentration of each odorant when odorants were given separately rather than as a mix.

In mice exposed to an odorant mix twice, the majority of *Arc*⁺ APC neurons had *Arc* mRNA in both the nucleus and cytoplasm, indicating that they had responded to both exposures to the mix (mix-mix, Table 1). These neurons constituted $79 \pm 3\%$ of all *Arc*⁺ neurons for odor pair 1, $77 \pm 5\%$ for odor pair 2, and $79 \pm 5\%$ for odor pair 3 ($n = 3$ to 4 cortices from two mice per odor pair). For each odor pair, a small percentage of labeled neurons had *Arc* mRNA in only the nucleus (9 to

13%) or cytoplasm (9 to 14%) (Table 1). These percentages were slightly higher than those seen in mice exposed once to eugenol at -30 min (2 to 8% nuclear *Arc* signal only) or -5 min (4 to 9% cytoplasmic *Arc* signal only), which suggests that a small percentage of neurons responded to one exposure to the mix, but not the other.

Strikingly different results were obtained when animals were exposed to two odorants separately at -30 min and then as a mix at -5 min (sep-mix, Table 1). In these mice, many neurons contained *Arc* mRNA in both the nucleus and cytoplasm, which indicated that they had responded to an odorant mix, as well as to one (or both) of its individual components. However, in sharp contrast to when odorants were delivered twice as a mix, there were also many neurons that had *Arc* mRNA only in the nucleus, which indicated that they had responded to an odorant mix, but not to either of its component odorants alone. In these animals, 33 to 37% of *Arc*⁺ neurons had only nuclear *Arc* signal compared with 9 to 13% in animals given an odorant mix twice. The percentage of APC neurons with *Arc* mRNA in only the nucleus averaged $33 \pm 2\%$ for odor pair 1, $35 \pm 4\%$ for odor pair 2, and $37 \pm 1\%$ for odor pair 3 ($n =$ three to four cortices from two mice per odor pair). Thus, for each odor pair, about one-third of neurons that responded to the mix failed to respond to either of the single odorants in the mix.

In mice exposed to odorant mixtures by either exposure protocol, *Arc*⁺ neurons were highly distributed along the anterior-posterior length of the APC (Fig. 2B). This was the case for neurons with *Arc* mRNA in both the nucleus and cytoplasm, as well as for neurons with *Arc* signal only in the nucleus. Most neurons with only nuclear *Arc* signal were located in the vicinity of neurons with both nuclear and cytoplasmic *Arc* signal (Fig. 1D). Given that cortical neurons that receive input from the same OR are found in distinct clusters and inputs from different ORs can partially overlap (17), it is possible that neighboring cells with different subcellular patterns of *Arc* mRNA receive input from different, but partially overlapping sets of ORs.

To more accurately assess the populations of OC neurons responsive to odorants in these studies, we took into account data obtained from control animals exposed twice (at -30 and -5 min) to odorant solvents alone [dimethyl sulfoxide (DMSO) for odor pairs 1 and 3 and water for odor pair 2] (Table 1). We first subtracted the average numbers of neurons with different subcellular patterns of *Arc* mRNA in the controls from the corresponding numbers in the odorant-exposed animals. We then used the resulting net values for each experiment to calculate the percentage of neurons stimulated by the second odorant exposure, but not the first (net N only/N

Fig. 2. Distribution of *Arc*⁺ neurons after odorant exposure. These graphs show the number of neurons with *Arc* mRNA in the nucleus alone (red), nucleus and cytoplasm (blue), or cytoplasm alone (green) at 70- μ m intervals along the anterior-posterior length of the APC in individual mice. **(A)** Five min after exposure to eugenol (left), most *Arc*⁺ neurons contained only nuclear *Arc* mRNA, but 30 min after exposure (right) most contained only cytoplasmic *Arc* signal. **(B)** In mice exposed to a binary odorant mix twice (at -30 and -5 min) (left), neurons with both nuclear and cytoplasmic *Arc* mRNA predominated, but when two odorants were first given separately and then as a mix (right), many neurons had *Arc* mRNA in only the nucleus.

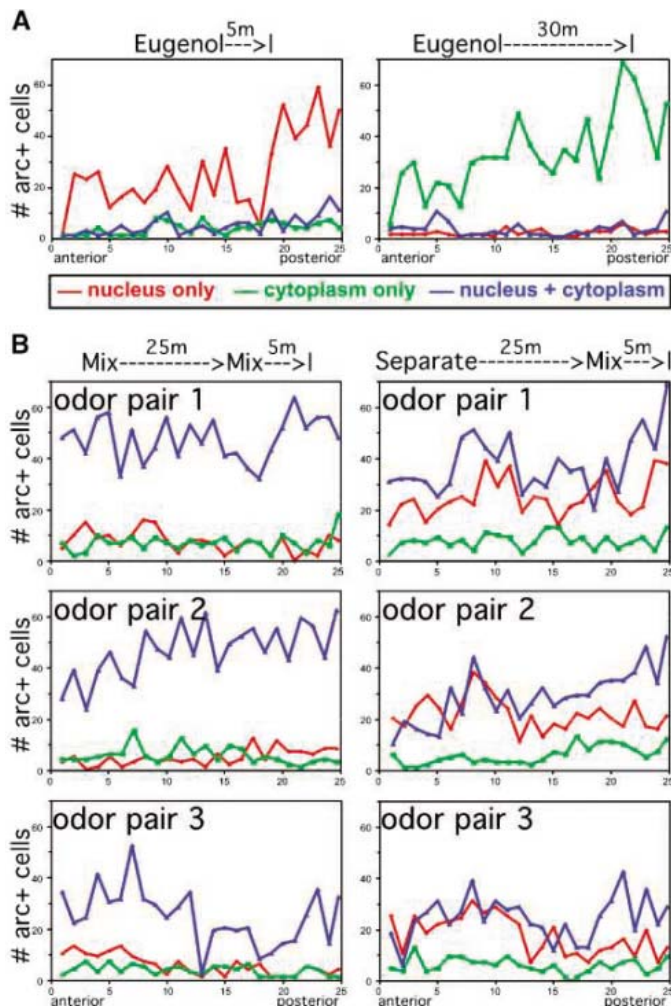
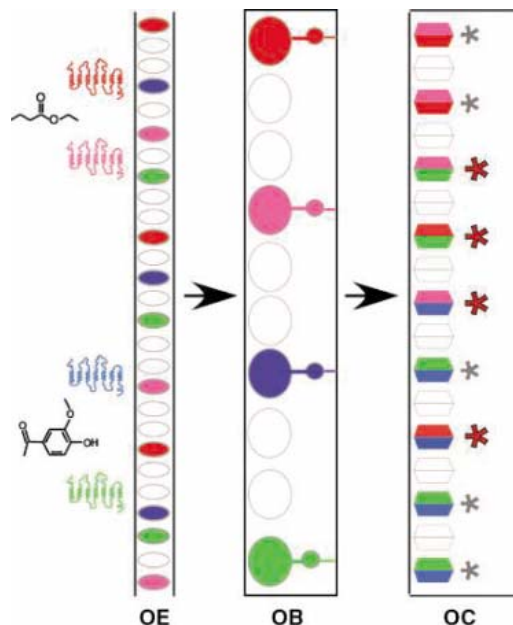


Table 1. Number of *Arc*⁺ neurons in olfactory cortex. Average \pm SD is indicated.

	N only (%)	C only (%)	N + C (%)	Total	Net N/N total, %	Net C/C total, %
Eugenol						
5 min						
1	618 (78)	72 (9)	103 (13)	793		
2	1537 (82)	75 (4)	255 (14)	1867		
3	1358 (83)	64 (4)	211 (13)	1633		
	1171 \pm 487 (81 \pm 3)	70 \pm 6 (6 \pm 3)	190 \pm 78 (13 \pm 1)	1431 \pm 565		
30 min						
1	7 (2)	286 (88)	33 (10)	326		
2	60 (8)	628 (85)	52 (7)	740		
3	38 (4)	822 (88)	73 (8)	933		
	35 \pm 27 (5 \pm 3)	577 \pm 271 (87 \pm 2)	53 \pm 20 (8 \pm 2)	666 \pm 310		
Odor pair 1						
mix-mix						
1	104 (7)	179 (11)	1289 (82)	1572		
2	160 (11)	161 (11)	1114 (78)	1435		
3	187 (12)	174 (11)	1193 (77)	1554		
	150 \pm 43 (10 \pm 3)	171 \pm 9 (11 \pm 0)	1199 \pm 87 (79 \pm 3)	1520 \pm 74	8	10
sep-mix						
1	662 (32)	205 (10)	1220 (58)	2087		
2	661 (32)	233 (11)	1174 (57)	2068		
3	599 (35)	184 (11)	913 (54)	1696		
	641 \pm 36 (33 \pm 2)	207 \pm 25 (11 \pm 1)	1102 \pm 166 (56 \pm 2)	1950 \pm 220	36	13
Odor pair 2						
mix-mix						
1	97 (10)	182 (19)	701 (72)	980		
2	113 (8)	130 (10)	1091 (82)	1334		
3	114 (9)	153 (12)	987 (79)	1254		
	108 \pm 9 (9 \pm 1)	155 \pm 26 (14 \pm 5)	910 \pm 202 (77 \pm 5)	1173 \pm 186	10	10
sep-mix						
1	463 (34)	195 (14)	715 (52)	1373		
2	519 (39)	120 (9)	696 (52)	1335		
3	432 (32)	68 (5)	851 (63)	1351		
	471 \pm 44 (35 \pm 4)	128 \pm 64 (9 \pm 5)	754 \pm 85 (56 \pm 6)	1353 \pm 19	39	9
Odor pair 3						
mix-mix						
1	117 (15)	63 (8)	588 (77)	768		
2	110 (20)	38 (7)	408 (73)	556		
3	68 (9)	75 (10)	603 (81)	746		
4	50 (7)	64 (9)	581 (84)	695		
	86 \pm 32 (13 \pm 6)	60 \pm 16 (9 \pm 1)	545 \pm 92 (79 \pm 5)	691 \pm 95	7	3
sep-mix						
1	355 (37)	100 (10)	504 (53)	959		
2	261 (37)	72 (10)	368 (52)	701		
3	546 (36)	90 (6)	868 (58)	1504		
4	516 (36)	65 (5)	850 (59)	1431		
	420 \pm 135 (37 \pm 1)	82 \pm 16 (8 \pm 3)	648 \pm 251 (56 \pm 4)	1149 \pm 384	38	5
DMSO						
1	36 (26)	57 (41)	47 (34)	140		
2	55 (39)	53 (37)	34 (24)	142		
3	63 (38)	43 (26)	59 (36)	165		
4	45 (38)	38 (32)	36 (36)	119		
	50 \pm 12 (35 \pm 6)	48 \pm 9 (34 \pm 6)	44 \pm 11 (31 \pm 5)	142 \pm 19		
Water						
1	2 (2)	95 (79)	24 (19)	121		
2	4 (4)	81 (84)	11 (11)	96		
3	0 (0)	8 (100)	0 (0)	8		
4	0 (0)	18 (72)	7 (28)	25		
	2 \pm 2 (3 \pm 2)	53 \pm 44 (84 \pm 12)	11 \pm 10 (17 \pm 12)	66 \pm 54		

Fig. 3. OR inputs and odor responses in the olfactory system. Inputs from different ORs are segregated in both the olfactory epithelium (OE) and olfactory bulb (OB), but are combined in single neurons in the olfactory cortex (OC). In this simple model, activation of an OC neuron requires input from two ORs. Two odorants are recognized by different pairs of ORs and activate OC neurons that receive input from those OR pairs. Mixing of the two odorants produces additional pairs of OR inputs that stimulate OC neurons that are not activated by either odorant alone.



total), and the percentage stimulated by the first odorant exposure, but not the second (net C only/C total).

In animals given an odorant mix twice, only 7 to 10% of neurons responded to the second exposure, but not the first (Table 1, net N only/N total). In sharp contrast, in animals exposed to odorants first separately and then as a mix, 36 to 39% of neurons that responded to the odorant mix at -5 min did not respond to its component odorants at -30 min. Compared with animals given an odorant mix twice, this percentage increased by 28% (4.5-fold) for odor pair 1, 29% (3.9-fold) for odor pair 2, and 31% (5.4-fold) for odor pair 3. Thus, for each odor pair, about 30% of cortical neurons that responded to the binary odorant mix did not respond to either of the single odorants in the mix.

Interestingly, the converse was not seen. Only a small percentage of neurons responded to the first odorant exposure, but not the second (Table 1, net C only/C total), regardless of whether the first exposure was to odorants delivered separately (5 to 13%) or as a mix (3 to 10%). The percentage changed little when the first odorant exposure was to separate odorants rather than their binary mix (1.3-, 0.9-, and 1.7-fold for odor pairs, 1, 2, and 3, respectively). This indicates that most OC neurons that responded to a single odorant also responded to an odorant mix containing that odorant. Nonetheless, the slight differences seen for odor pairs 1 and 3 in the two exposure protocols suggest that a small percentage of neurons responsive to the individual components of these mixes might have been suppressed when the single components were mixed (mixture suppression). The extent to which this occurs could vary among combinations of odorants. Mixture suppression has

previously been reported in the OB (25) and OC (26), as well as the OE (27).

In summary, these studies show that binary odorant mixes stimulate many cortical neurons beyond those that respond to their individual component odorants. About 30% of OC neurons that responded to a binary odorant mix were not stimulated by either of the single odorants in the mix. It was not possible to examine *Arc* expression in OB mitral cells in these studies, because the mitral cells were intermingled with numerous granule cell interneurons constitutively expressing *Arc*. However, the present findings in the OC contrast sharply with electrophysiological studies of the mammalian OB, which show that most or all mitral cells responsive to an odorant mix also respond to one component of the mix (25, 28). This is also the case for binary odorant mixes in fish, even though each fish mitral cell is connected to several glomeruli rather than one as in mammals (29, 30). With combinations of large numbers of odorants, more complex interactions may (30) or may not (28) occur in the OB, such as mixture suppression resulting from interneuron-mediated lateral inhibition among mitral cells (30).

The present findings indicate that the OC has an integrative capacity that is lacking from the OB. Signals from different ORs are segregated in different neurons in the nose and bulb, but individual pyramidal neurons in the OC appear to receive combined inputs from different ORs (17). Given that each odorant is detected by a combination of ORs (its receptor code) (9, 10), a straightforward explanation for the present results is that the activation of an OC pyramidal neuron requires input from more than one OR (Fig. 3). In this model, neurons stimulated by an odorant mix, but not its individual components, are those that receive novel combinations

of OR inputs that result from merging the receptor codes of two odorants. This would represent a synthetic operation in which the deconstructed features of an odorant, which are carried by different OR inputs, begin to be reconstructed at the level of individual cortical neurons in order to generate a unique odor perception. Synthetic operations could also derive from excitatory association fibers that interlink OC pyramidal neurons and provide a source of disynaptic excitatory input from the OB (31, 32). In this scheme, a neuron might be activated solely by the combined excitatory inputs from other OC neurons responsive to different components of an odorant mix.

Interestingly, these findings provide a potential explanation for certain odor mixture effects in humans. Humans have only a limited capacity to detect individual odorants in an odorant mix (33). With binary odorant mixes, individual components may be detected, but lose a described quality, such as "strawberry." Moreover, mixing two odorants can elicit a novel odor perception. For example, in certain proportions, a binary mix of eugenol (clove) and phenylethyl alcohol (rose) is perceived as "carnation," a distinctly different scent (34). The present studies suggest that these mixture effects may be due to the novel cortical representations that result from mixing odorants. Given that most natural odors derive from complex blends of odorants, it is quite possible that they emerge from cortical representations that bear only a remote resemblance to those of their component odorants.

References and Notes

1. L. Buck, R. Axel, *Cell* **65**, 175 (1991).
2. P. Mombaerts, *Nat. Rev. Neurosci.* **5**, 263 (2004).
3. E. Kandel, J. Schwartz, T. Jessell, *Principles of Neural Science* (McGraw-Hill, New York, 2000).
4. G. M. Shepherd, W. R. Chen, C. A. Greer, in *The Synaptic Organization of the Brain*, G. M. Shepherd, Ed. (Oxford Univ. Press, New York, 2004), pp. 165–216.
5. K. R. Neville, L. B. Haberly, in *The Synaptic Organization of the Brain*, G. M. Shepherd, Ed. (Oxford Univ. Press, New York, 2004), pp. 415–454.
6. X. Zhang, S. Firestein, *Nat. Neurosci.* **5**, 124 (2002).
7. J. M. Young, B. J. Trask, *Hum. Mol. Genet.* **11**, 1153 (2002).
8. P. A. Godfrey, B. Malnic, L. B. Buck, *Proc. Natl. Acad. Sci. U.S.A.* **101**, 2156 (2004).
9. B. Malnic, J. Hirono, T. Sato, L. B. Buck, *Cell* **96**, 713 (1999).
10. K. Kajija et al., *J. Neurosci.* **21**, 6018 (2001).
11. A. Chess, I. Simon, H. Cedar, R. Axel, *Cell* **78**, 823 (1994).
12. K. J. Ressler, S. L. Sullivan, L. B. Buck, *Cell* **73**, 597 (1993).
13. R. Vassar, J. Ngai, R. Axel, *Cell* **74**, 309 (1993).
14. K. J. Ressler, S. L. Sullivan, L. B. Buck, *Cell* **79**, 1245 (1994).
15. R. Vassar et al., *Cell* **79**, 981 (1994).
16. P. Mombaerts et al., *Cell* **87**, 675 (1996).
17. Z. Zou, L. F. Horowitz, J. P. Montmayeur, S. Snapper, L. B. Buck, *Nature* **414**, 173 (2001).
18. J. F. Guzowski, B. L. McNaughton, C. A. Barnes, P. F. Worley, *Nat. Neurosci.* **2**, 1120 (1999).
19. G. L. Lyford et al., *Neuron* **14**, 433 (1995).
20. W. Link et al., *Proc. Natl. Acad. Sci. U.S.A.* **92**, 5734 (1995).

21. Y. Tagawa, P. O. Kanold, M. Majdan, C. J. Shatz, *Nat. Neurosci.* **8**, 380 (2005).
22. See supporting data on Science Online.
23. Z. Zou, F. Li, L. B. Buck, *Proc. Natl. Acad. Sci. U.S.A.* **102**, 7724 (2005).
24. K. R. Illig, L. B. Haberly, *J. Comp. Neurol.* **457**, 361 (2003).
25. P. Giraudet, F. Berthommier, M. Chaput, *J. Neurophysiol.* **88**, 829 (2002).
26. D. A. Wilson, *J. Neurophysiol.* **90**, 65 (2003).
27. P. Duchamp-Viret, A. Duchamp, M. A. Chaput, *Eur. J. Neurosci.* **18**, 2690 (2003).
28. D.-Y. Lin, S. Z. Zhang, E. Block, L. C. Katz, *Nature* **434**, 470 (2005).
29. J. Kang, J. Caprio, *J. Neurophysiol.* **74**, 1435 (1995).
30. R. Tabor, E. Yaksi, J. M. Weislogel, R. W. Friedrich, *J. Neurosci.* **24**, 6611 (2004).
31. L. B. Haberly, *Chem. Senses* **26**, 551 (2001).
32. D. A. Wilson, *Chem. Senses* **26**, 577 (2001).
33. D. G. Laing, G. W. Francis, *Physiol. Behav.* **46**, 809 (1989).
34. C. Margot, personal communication.
35. We thank R. Childs and K. Wilson for expert technical assistance and members of the Buck laboratory for helpful discussions. We also thank D. Laing and C. Margot for information on odorant mixture effects in humans, and International Flavors and Fragrances, Inc., for odor chemicals. This project was supported by the Howard Hughes

Medical Institute and by grants from the NIH (National Institute on Deafness and Other Communication Disorders) and the Department of Defense (Army Research Office).

Supporting Online Material

www.sciencemag.org/cgi/content/full/311/5766/1477/DC1
Materials and Methods
References

9 January 2006; accepted 1 February 2006
10.1126/science.1124755

Genome-Wide Prediction of *C. elegans* Genetic Interactions

Weiwei Zhong and Paul W. Sternberg*

To obtain a global view of functional interactions among genes in a metazoan genome, we computationally integrated interactome data, gene expression data, phenotype data, and functional annotation data from three model organisms—*Saccharomyces cerevisiae*, *Caenorhabditis elegans*, and *Drosophila melanogaster*—and predicted genome-wide genetic interactions in *C. elegans*. The resulting genetic interaction network (consisting of 18,183 interactions) provides a framework for system-level understanding of gene functions. We experimentally tested the predicted interactions for two human disease-related genes and identified 14 new modifiers.

An essential part of understanding how a genome specifies the properties of an organism is elucidating interactions among its genes. Such interactions include protein-protein physical interactions as well as gene-gene and protein-gene interactions. One method to identify genetic interactions is by modifier screens (e.g., synthetic lethal screens). However, this process requires easily detectable phenotypes. Metazoan biological processes often involve phenotypes too complex to score in large-scale screens, and thus candidate genes are often tested. Unfortunately, a genome of 20,000 genes has as many as 200 million pairwise combinations, posing a formidable challenge.

Relative to randomly paired genes, functionally interacting genes are more likely to have similar expression patterns and phenotypes; thus, statistically combining these genetic features might lead to reliable predictions of functional interactions. Several such computational approaches have been applied to *S. cerevisiae* (1–5). In metazoans, which have more genes and more complex genetic interactions, network constructions have focused on either protein-protein interactions (6) or a specific biological process (7, 8), and thus they represent a subset of all genetic interactions. Unlike yeast data sets, most metazoan genetic data sets are incomplete (9). For example, only

292 *C. elegans* genes have complete annotations of anatomical expression, phenotype, and biological process in Gene Ontology (GO) (10) [WormBase WS140 (11)]. We therefore decided to incorporate information from multiple organisms. As gene functions are often conserved at the molecular level, we reasoned that if two genes possess features indicating a genetic interaction, their orthologous genes are also likely to be functionally linked. Pooling information across species might enable detection of interactions even if the genetic data for one organism are incomplete.

Data sets from different sources have different intrinsic error rates and different predictive strengths. A solid statistical model is thus essential for producing reliable predictions. Two types of methods, unions and Bayesian networks, have been used to integrate heterogeneous data [e.g., (1, 3)]. Bayesian network models are preferable to unions because they weight data sets according to their reliability (3), but current methods often assume that data sets are independent [naïve Bayesian network, e.g., (3, 6)]. We thus used logistic regression, a classical method for predicting binary outcomes (interaction versus no interaction), which provides performance comparable to that of naïve Bayesian networks (fig. S2) but relaxes the requirement of data independency, as it uses a weighted sum for data integration (9).

To calibrate the parameters of the computational system, we constructed a training set for *C. elegans* genetic interactions. Our positives were 1816 genetic interaction pairs curated from the literature (11) and 2878 physical interaction

pairs identified by yeast two-hybrid screens (12). Yeast two-hybrid data may not be as accurate as results of small-scale interaction studies in the literature. Also, two-hybrid data describe physical rather than genetic interactions, which include both direct and indirect interactions. We included the two-hybrid data in our training set because they greatly increased the size of our training set and provided unbiased coverage (the literature-curated data were often biased toward evolutionarily conserved genetic interactions).

Negatives for metazoan genetic interactions are more difficult to define. Proteins with different subcellular localizations have been used as negatives for physical interactions (3, 6); however, genetic interactions (for example, cell signaling pathways) do not require two gene products to colocalize. Genes annotated to function in different pathways have been used as negatives for yeast genetic interactions (3, 6), but in metazoans, knowledge of interactions is so limited that if two genes are not annotated to function in the same pathway, their relation should be considered unknown rather than non-interacting. We reasoned that two genes are less likely to be an interacting pair if a double mutant of these genes exists and there is no reported interaction. We thus took from WormBase 3296 pairs of linked cis markers used in genetic mapping experiments as our negatives. Although it is possible that these cis markers may interact in processes not examined during the mapping experiments, the probability that cis marker pairs are interacting genes should be lower than for other gene pairs.

Our computational algorithm started by mapping orthologous genes with the use of InParanoid (13). We then searched each *C. elegans* gene pair as well as its orthologous pairs in *D. melanogaster* and *S. cerevisiae* for five features: identical anatomical expression, phenotype, function annotation (e.g., biological process in GO), microarray coexpression, and the presence of interlogs (i.e., whether the *D. melanogaster* or *S. cerevisiae* orthologous gene pairs interact genetically or physically). We used likelihood ratios (3, 4) to assign a weighted score to each feature. The likelihood ratio is defined as

$$L = \frac{P(v|pos)}{P(v|neg)} \quad (1)$$

Howard Hughes Medical Institute and Division of Biology, California Institute of Technology, Pasadena, CA 91125, USA.

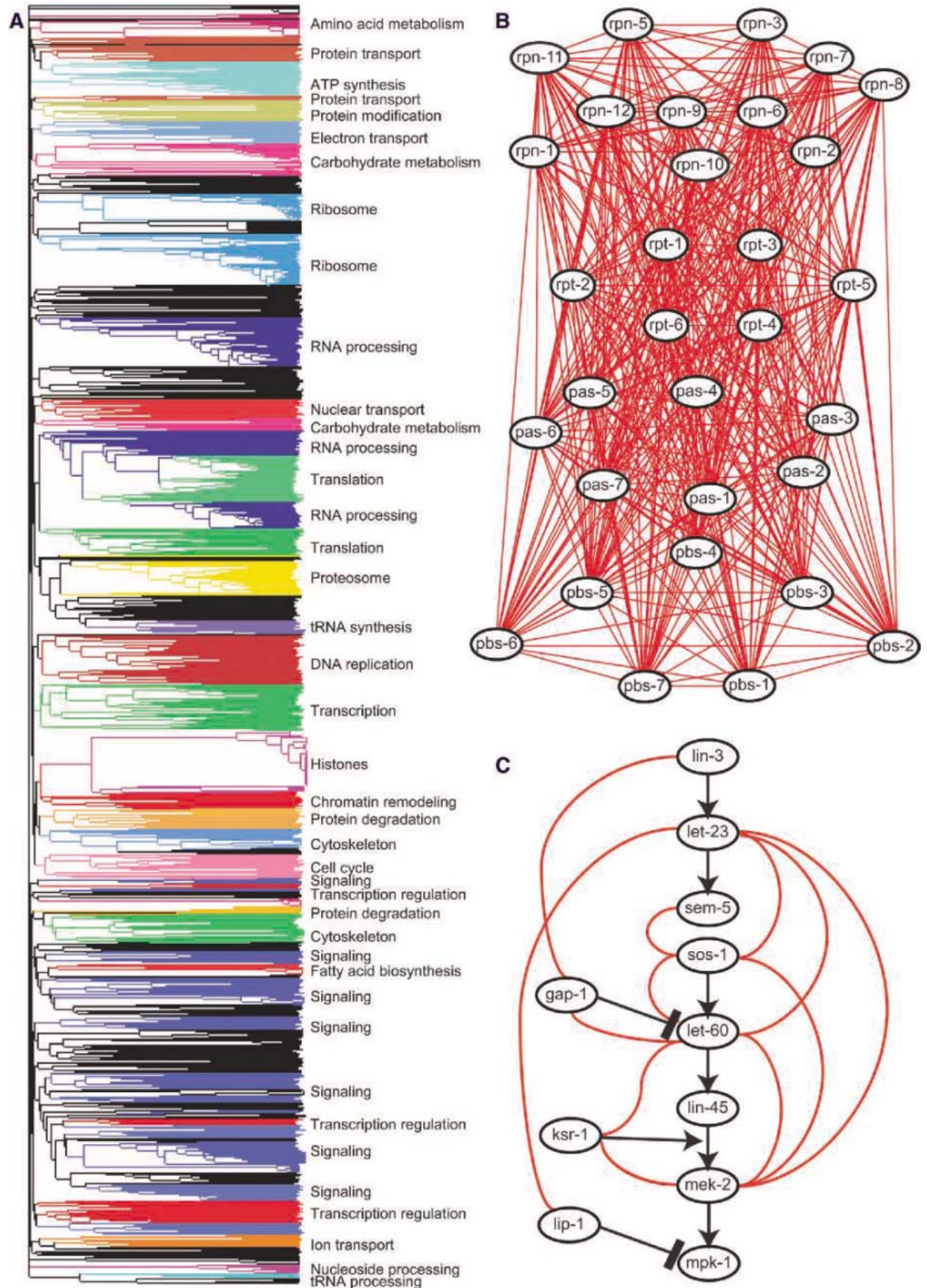
*To whom correspondence should be addressed. E-mail: pws@caltech.edu

where $P(v|pos)$ and $P(v|neg)$ are frequencies of gene pairs having the feature v (such as having a similar yeast phenotype) in the positives (pos) and the negatives (neg), respec-

tively. A value of L greater than 1 indicates that the feature is enriched in interacting gene pairs, with higher scores indicating stronger predictive power of the feature. Gene pairs with stronger

Pearson correlations (closer to 1) in microarray results get higher L -scores than pairs with weaker expression correlations; gene pairs that share specific expression, phenotype, or function an-

Fig. 1. Predicted genetic interactions. **(A)** Tree representation of genes clustered on the basis of their distances in the predicted network. Clusters were manually inspected. A cluster is colored and annotated if genes in the cluster share a common function; clusters with no common function and clusters with unknown functions are black. **(B and C)** Local views of the proteasome complex (B) and the epidermal growth factor receptor–ras–MAPK pathway (C). Red lines indicate predicted interactions (cutoff 0.9). Black lines indicate known genetic interactions, with arrows for activation and bars for inhibition.



notations get higher L -scores than pairs that share general annotations or share no annotations (fig. S1). Scores were integrated to estimate the overall probability of the two *C. elegans* genes interacting by

$$\ln \frac{p}{1-p} = c + \sum_{i=1}^n a_i \ln L_i \quad (2)$$

where L_i is the likelihood ratio for the i th predictor, c and a_i are constants determined by fitting of the training set with the software R (www.R-project.org), and p is the final output score that varies between 0 and 1, with 1 indicating a genetically interacting pair and 0 indicating no interaction.

We applied a threshold of 0.9, which exceeds the maximum contribution that any single feature can achieve [see also (9)]. The resulting genetic interaction network consists of 2254 genes and 18,183 interactions. To explore the predicted network at a system level, we clustered the genes on the basis of their interaction partners (14). The clusters revealed a modular network organization; most clusters correlated with protein complexes or biological processes (Fig. 1A). Some functional modules (e.g., the signaling module) contained several clusters, consistent with multiple pathways.

Close to 90% of the genes in the network were in one connected component.

To evaluate the performance of the computational system, we compared our predictions with known interactions to investigate the false negative rate. Our system predicted 414 interactions among the 31 proteasome components (Fig. 1B) and many interactions between the mitogen-activated protein kinase (MAPK) signaling pathway genes (Fig. 1C). Two genes, *lin-45* and *mpk-1*, were not connected to the pathway. These false negatives are due to incomplete annotation and incorrect ortholog mapping. For example, *lin-45* has only a sterile phenotype and a neuronal expression annotated in WormBase, although richer phenotype information exists. Also, InParanoid failed to identify orthologs of the two genes in either fly or yeast. Such false negatives will be automatically eliminated when model databases accumulate sufficient data and with better ortholog mappings.

To estimate the false positive rate, we examined all predicted interactors of *let-60/ras*, a component of the MAPK pathway. Of 87 predicted interactions for *let-60*, 12 are consistent with our training set, and 5 have been reported in the literature (9) although not included in our training set. To uncover novel interactions, we

tested 49 of the 70 predictions by RNA interference (RNAi) on a *let-60* gain-of-function mutant, *let-60(n1046)* (15). *let-60(n1046)* animals have a multivulva (Muv) phenotype (Fig. 2A) caused by excess induction of vulval precursor cells (VPCs) (average of 4.3 induced VPCs versus 3.0 for wild type). RNAi against 12 candidate genes significantly affected VPC induction in *let-60* animals (Fig. 2B). Only one candidate, *cdc-42*, affected VPC induction in wild-type animals (table S3), indicating that the observed changes in the *let-60* animals were results of genetic interactions.

As a control, we examined interactions of *let-60(n1046)* with 26 randomly selected, low-scoring genes (<0.6) that, like the high-score candidates, have annotated genetic data and have yeast and fly orthologs. Only one such gene significantly affected *let-60(n1046)* VPC induction ($P = 0.04$) (Fig. 2C), consistent with the expected false positive rate.

We next experimentally tested the predictions for another essential gene, the inositol-1,4,5-trisphosphate (IP_3) receptor gene *itr-1*. There is no known genetic/physical interlog of *itr-1* with any gene in either fly or yeast, nor are the *C. elegans* data sufficient to predict *itr-1* interactions. All 16 *itr-1* interaction predictions relied on combining several weak predictors

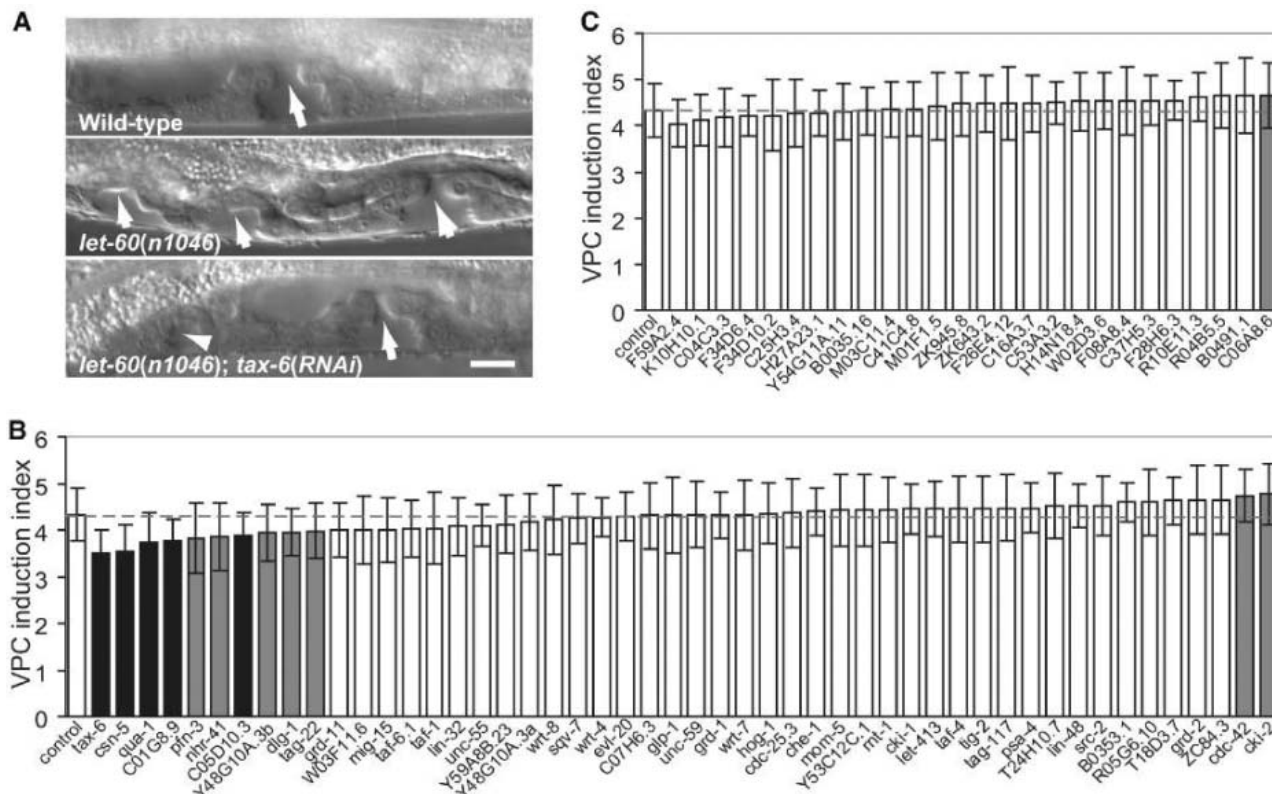


Fig. 2. *let-60* genetic interactions. (A) Nomarski images of the developing vulvae of wild-type, *let-60(n1046)*, and *let-60(n1046); tax-6(RNAi)* L4 larvae, showing different degrees of VPC induction. Arrows indicate vulval invaginations. Scale bar, 10 μ m. (B and C) VPC induction index of *let-60(n1046)* animals in response to RNAi of predicted interacting genes (B) and randomly selected low-

score genes (C). Bars and error bars represent means and SD, respectively; $n \geq 20$ for each data point. Gray horizontal dashed lines indicate the average induction index under control conditions (RNAi with vector-alone bacteria). Data sets that have significant differences from controls are in black ($P < 0.01$) or gray ($P < 0.05$) based on Student's t test (two-tailed, unequal variance).

(9). Although not in the training set, 4 of 16 predicted *itr-1* interactions can be confirmed by published results (9). Of the remaining 12, we had RNAi clones against six genes, and we tested them on the weak loss-of-function mutant *itr-1(sa73)* (16). *itr-1(sa73)* animals have slow pharyngeal pumping (17) (181 ± 12 pumps per minute versus 212 ± 18 for wild type, $n > 20$). Because RNAi against several candidates affected pumping rates in both the wild-type strain and the *itr-1(sa73)* strain, we used normalized rates [the ratio of the *itr-1(sa73)* and wild-type rates] to distinguish genetic interactions from additive effects. The ratio will be ~ 0.85 ($181/212$) if the RNAi has the same effect on both strains. RNAi of two genes, *egl-19* and *ccb-1*, significantly suppressed the *itr-1(sa73)* pumping defect ($P < 0.001$, Fig. 3A). By contrast, RNAi of nine randomly selected low-score genes did not affect *itr-1(sa73)* pumping (Fig. 3A). We confirmed the *egl-19* and *itr-1* interaction by performing *itr-1* RNAi on *egl-19* mutants. An *egl-19* gain-of-function mutant, *egl-19(n2368)*, showed a much stronger phenotype in response to *itr-1* RNAi relative to a weak loss-of-function mutant, *egl-19(n582)*. *itr-1* RNAi caused sterility, constipation, and reduced body size in all animals (Fig. 3B), but *egl-19(n2368); itr-1(RNAi)* animals became completely para-

lyzed (Fig. 3B), with a slower pharyngeal pumping rate than that of the *itr-1(RNAi)* or *egl-19(n582); itr-1(RNAi)* animals (Fig. 3C).

We thus verified 29/87 of the predicted *let-60* interactions and 6/16 of the predicted *itr-1* interactions. Excluding untested predictions, the prediction accuracy is 44% (29/66) for *let-60* and 60% (6/10) for *itr-1*. The actual prediction accuracy should be higher because not all genes are sensitive to RNAi and only one phenotype and one mutant allele were examined.

Our data are publicly available at <http://tenaya.caltech.edu:8000/predict>. Users can search for predicted interactions for any gene and see the evidence (fig. S6). The system serves as a cross-species genetic data search engine (fig. S7). Unlike manual searches of multiple databases, our computational approach provides statistical analysis to combine weak evidence and prioritize results, as well as fast and systematic data mining.

Our newly discovered genetic interactions may also have biological implications. For example, *tax-6* encodes the A-subunit of calcineurin, an upstream regulator of heterotrimeric guanine nucleotide-binding protein (G protein) signaling (18), and could regulate *let-60* activity in VPC induction through the G_q pathway, which is known to promote VPC induction (19). ITR-1 responds to the second messenger

IP_3 to induce intracellular Ca^{2+} release. *egl-19* and *ccb-1* both encode L-type voltage-gated Ca^{2+} channels. The surprising antagonistic effect of *itr-1* and these genes suggests that they have different sites of action in pharyngeal pumping regulation: *itr-1* may mainly function in muscle or excitatory neurons, whereas *egl-19* and *ccb-1* may be required for inhibitory neuron function.

Both *let-60* and *itr-1* have been the subject of a number of modifier screens [e.g., (20, 21)] conducted at low resolution to discover qualitative differences (e.g., Muv suppressed to wild type). Our quantitative analysis allowed us to detect interactions that would likely be missed by such screens. Quantitative assays are labor-intensive enough to be impractical for genome-wide screens. By computationally prioritizing candidates, it becomes feasible to effectively discover genetic interactions.

References and Notes

1. E. M. Marcotte, M. Pellegrini, M. J. Thompson, T. O. Yeates, D. Eisenberg, *Nature* **402**, 83 (1999).
2. O. G. Troyanskaya, K. Dolinski, A. B. Owen, R. B. Altman, D. Botstein, *Proc. Natl. Acad. Sci. U.S.A.* **100**, 8348 (2003).
3. R. Jansen *et al.*, *Science* **302**, 449 (2003).
4. I. Lee, S. V. Date, A. T. Adai, E. M. Marcotte, *Science* **306**, 1555 (2004).
5. S. L. Wong *et al.*, *Proc. Natl. Acad. Sci. U.S.A.* **101**, 15682 (2004).
6. D. R. Rhodes *et al.*, *Nat. Biotechnol.* **23**, 951 (2005).
7. S. J. Boulton *et al.*, *Science* **295**, 127 (2002).
8. K. C. Gunsalus *et al.*, *Nature* **436**, 861 (2005).
9. See supporting material on Science Online.
10. M. Ashburner *et al.*, *Nat. Genet.* **25**, 25 (2000).
11. E. M. Schwarz *et al.*, *Nucleic Acids Res.* **34**, D475 (2006).
12. S. Li *et al.*, *Science* **303**, 540 (2004); published online 2 January 2004 (10.1126/science.1091403).
13. K. P. O'Brien, M. Remm, E. L. Sonnhammer, *Nucleic Acids Res.* **33**, D476 (2005).
14. A. Baudot *et al.*, *Bioinformatics* **22**, 248 (2006).
15. G. J. Beitel, S. G. Clark, H. R. Horvitz, *Nature* **348**, 503 (1990).
16. K. Iwasaki, D. W. Liu, J. H. Thomas, *Proc. Natl. Acad. Sci. U.S.A.* **92**, 10317 (1995).
17. D. S. Walker, N. J. Gower, S. Ly, G. L. Bradley, H. A. Baylis, *Mol. Biol. Cell* **13**, 1329 (2002).
18. J. Lee *et al.*, *J. Mol. Biol.* **344**, 585 (2004).
19. N. Moghal, L. R. Garcia, L. A. Khan, K. Iwasaki, P. W. Sternberg, *Development* **130**, 4553 (2003).
20. Y. Wu, M. Han, *Genes Dev.* **8**, 147 (1994).
21. T. R. Clandinin, J. A. DeModena, P. W. Sternberg, *Cell* **92**, 523 (1998).
22. We thank the *Caenorhabditis* Genetics Center for strains; WormBase staff for discussions; L. Chen for advice on statistical analysis; B. Perry for maintaining reagents; and C. Van Buskirk, E. Hallem, B. Hwang, M. Kato, E. Kipreos, R. Kishore, A. Petcherski, and E. Schwarz for critical reading of the manuscript. P.W.S. is an investigator and W.Z. is an associate of the Howard Hughes Medical Institute.

Supporting Online Material

www.sciencemag.org/cgi/content/full/311/5766/1481/DC1

Materials and Methods

Figs. S1 to S6

Tables S1 to S5

References

1 December 2005; accepted 26 January 2006
10.1126/science.1123287

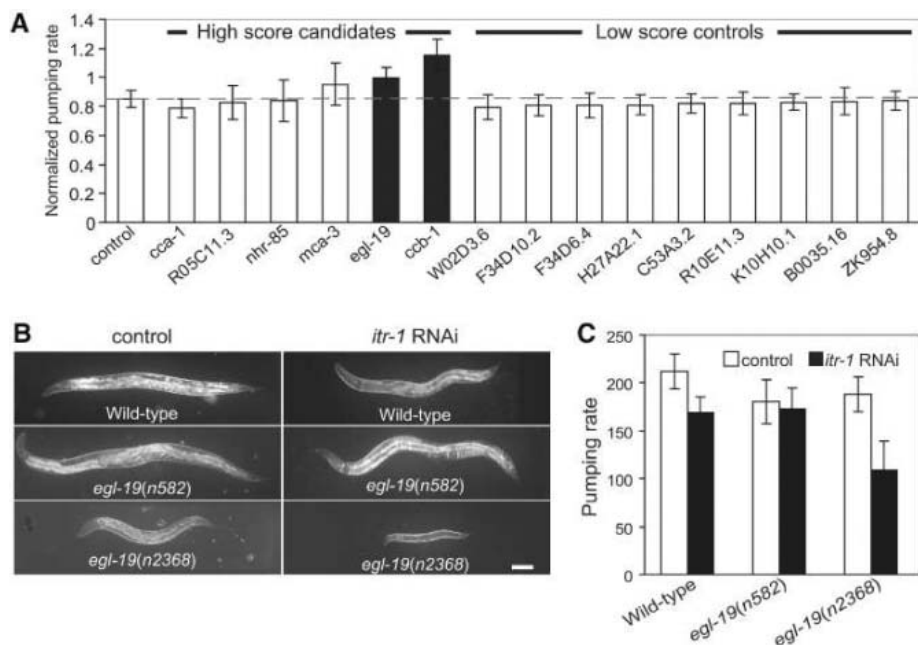


Fig. 3. *itr-1* genetic interactions. **(A)** Normalized pharyngeal pumping rate (*itr-1* rate divided by average wild-type rate) under various RNAi conditions. Bars and error bars represent means and SD, respectively. Under each RNAi condition, we scored the pumping rates of $n \geq 20$ wild-type animals to compute the average wild-type rate and $n \geq 20$ *itr-1* animals for normalized pharyngeal pumping rates. The gray horizontal dashed line indicates the average rate under vector-alone control RNAi; black bars represent data with significant differences from controls ($P < 0.001$). **(B)** Nomarski images of wild-type, loss-of-function *egl-19(n582)*, and gain-of-function *egl-19(n2368)* animals under control and *itr-1* RNAi conditions. Scale bar, 100 μ m. **(C)** Pharyngeal pumping rate (pumps per minute) under control and *itr-1* RNAi conditions. Error bars represent SD.

Behavioral Research Apparatus

Three apparatuses for use in behavioral research, the Stoelting Elevated-Plus Maze, Porsolt "Forced Swim" Test, and Open Field, were designed with video tracking in mind. These apparatuses are particularly intended for use with the StoeltingANY-maze video-tracking software, but they can easily be used with almost any video tracking system. The Open Field enclosure (available



in either non-reflective gray or clear) is equipped with handles for positioning and for removal for cleaning between subjects. The base plate is slotted to ensure that the arena maintains its footprint or can be returned to its appropriate position directly under the camera. The Elevated-Plus maze is constructed of the same non-reflective, neutrally colored materials, making it suitable for video tracking. The closed arms of the maze can be quickly removed for thorough cleaning between animals. The design of the Porsolt "Forced Swim" apparatus allows for behavioral tracking from above or from the side. The apparatus is equipped with handles and a drain for positioning and emptying.

Stoelting For information 630-860-9700 www.stoeltingco.com

Yeast RNA Purification Kit

The MasterPure Yeast RNA Purification Kit provides all the reagents needed to purify RNA from cell types, including *Candida*, *Saccharomyces*, *Schizosaccharomyces*, and filamentous fungi. The kit makes use of a rapid desalting process to remove contaminating macromolecules, avoiding toxic organic solvents, bead beating, and spheroplasting. The resulting RNA is of the high quality necessary for microarray gene expression analysis. The method is faster than spheroplasting and produces RNA of higher quality than that obtained from bead-beating.

Epicentre Biotechnologies For information 800-284-8474 www.EpiBio.com

Taq Full DNA Polymerase

Taq Full DNA polymerase offers superior performance in a full length Taq. It has been optimized for exceptional sensitivity and robust yields, allowing you to amplify from any DNA template, including rare ones. It can be used for both routine and specialized polymerase chain reaction (PCR), including genotyping, reverse transcription-PCR, and primer extension, and for a wide range of templates, including bacterial and plasmid DNA, complementary DNA, and complex genomic DNA.

Clontech Laboratories For information 650-919-7300 www.clontech.com

Drug Discovery Software

A suite of sophisticated yet easy-to-use Excel add-ins that provide pharmaceutical researchers with a robust, flexible, and familiar environment for data analysis is available. Developed specifically for pre-clinical drug research, Assay Master Suite combines five core modules into a comprehensive solution for managing assay data and leverages the power of the "home-grown" Excel macros many researchers now use to analyze

their analytical data. The modules include Filature, an application for converting plate reader data from biological experiments to uniform database format; Calculture, for performing calculations on large batches of plate data; Templature, which is used to design and describe plate layouts; Curvature, which enables researchers to rapidly evaluate large numbers of curves from biological experiments; and Kinetiture, a module that enables graphical analysis of kinetic data generated by plate readers. Assay Master also includes a Microsoft Access database for permanent storage of assay results.

CeuticalSoft For information 518-828-3722 www.ceuticalsoft.com

Transfer Pad

The Swift transfer pad can reduce protein immunoblot transfer times by more than 50%, while producing high efficiency protein transfer. The transfer pad technology allows for the optimal composition of electrolytes in the protein immunoblot sandwich, giving improved transfer times and efficiency.

G-Biosciences/Genotech For information 314-991-6034 www.GBiosciences.com

Differential Scanning Calorimeter

The DSC823e is a powerful differential scanning calorimeter (DSC) with a unique sensor design that results in performance features such as flat baselines, high sensitivity, and excellent peak resolution. With a ceramic sensor, the instrument is suitable for measurements of thermal effects in research and development and quality control environments. It offers high sample throughput and a modular design that allows for future expansion. It features a temperature range from -150° to 700°C .

Mettler Toledo For information 614-438-4696 www.mt.com

Gene Expression Workstation

The Biomek 3000-ArrayPlex Workstation is a robust, affordable RNA preparation solution for gene expression arrays. This new workstation, which includes validated methods, processes between one and 96 samples in a single run with minimal user intervention. It works with a variety of chemistries and chips and has the flexibility to perform other nucleic acid preparation applications. The workstation incorporates the RNAClean kit from Agencourt, featuring magnetic bead technology for the cleanup of complementary DNA and complementary RNA. With RNAClean, the process is simplified and yields are higher with reduced sample-to-sample variability.

Beckman Coulter For information 800-742-2345 www.beckmancoulter.com

For more information visit **Product-Info**, **Science's new online product index** at <http://science.labvelocity.com>

From the pages of Product-Info, you can:

- Quickly find and request free information on products and services found in the pages of *Science*.
- Ask vendors to contact you with more information.
- Link directly to vendors' Web sites.

Newly offered instrumentation, apparatus, and laboratory materials of interest to researchers in all disciplines in academic, industrial, and government organizations are featured in this space. Emphasis is given to purpose, chief characteristics, and availability of products and materials. Endorsement by *Science* or AAAS of any products or materials mentioned is not implied. Additional information may be obtained from the manufacturer or supplier by visiting www.science.labvelocity.com on the Web, where you can request that the information be sent to you by e-mail, fax, mail, or telephone.